

Methods in biomechanics and bionics

Edited by

Zhen Luo, Triwiyanto Triwiyanto and Suvash C. Saha

Published in

Frontiers in Bioengineering and Biotechnology



FRONTIERS EBOOK COPYRIGHT STATEMENT

The copyright in the text of individual articles in this ebook is the property of their respective authors or their respective institutions or funders. The copyright in graphics and images within each article may be subject to copyright of other parties. In both cases this is subject to a license granted to Frontiers.

The compilation of articles constituting this ebook is the property of Frontiers.

Each article within this ebook, and the ebook itself, are published under the most recent version of the Creative Commons CC-BY licence. The version current at the date of publication of this ebook is CC-BY 4.0. If the CC-BY licence is updated, the licence granted by Frontiers is automatically updated to the new version.

When exercising any right under the CC-BY licence, Frontiers must be attributed as the original publisher of the article or ebook, as applicable.

Authors have the responsibility of ensuring that any graphics or other materials which are the property of others may be included in the CC-BY licence, but this should be checked before relying on the CC-BY licence to reproduce those materials. Any copyright notices relating to those materials must be complied with.

Copyright and source acknowledgement notices may not be removed and must be displayed in any copy, derivative work or partial copy which includes the elements in question.

All copyright, and all rights therein, are protected by national and international copyright laws. The above represents a summary only. For further information please read Frontiers' Conditions for Website Use and Copyright Statement, and the applicable CC-BY licence.

ISSN 1664-8714
ISBN 978-2-8325-4227-9
DOI 10.3389/978-2-8325-4227-9

About Frontiers

Frontiers is more than just an open access publisher of scholarly articles: it is a pioneering approach to the world of academia, radically improving the way scholarly research is managed. The grand vision of Frontiers is a world where all people have an equal opportunity to seek, share and generate knowledge. Frontiers provides immediate and permanent online open access to all its publications, but this alone is not enough to realize our grand goals.

Frontiers journal series

The Frontiers journal series is a multi-tier and interdisciplinary set of open-access, online journals, promising a paradigm shift from the current review, selection and dissemination processes in academic publishing. All Frontiers journals are driven by researchers for researchers; therefore, they constitute a service to the scholarly community. At the same time, the *Frontiers journal series* operates on a revolutionary invention, the tiered publishing system, initially addressing specific communities of scholars, and gradually climbing up to broader public understanding, thus serving the interests of the lay society, too.

Dedication to quality

Each Frontiers article is a landmark of the highest quality, thanks to genuinely collaborative interactions between authors and review editors, who include some of the world's best academicians. Research must be certified by peers before entering a stream of knowledge that may eventually reach the public - and shape society; therefore, Frontiers only applies the most rigorous and unbiased reviews. Frontiers revolutionizes research publishing by freely delivering the most outstanding research, evaluated with no bias from both the academic and social point of view. By applying the most advanced information technologies, Frontiers is catapulting scholarly publishing into a new generation.

What are Frontiers Research Topics?

Frontiers Research Topics are very popular trademarks of the *Frontiers journals series*: they are collections of at least ten articles, all centered on a particular subject. With their unique mix of varied contributions from Original Research to Review Articles, Frontiers Research Topics unify the most influential researchers, the latest key findings and historical advances in a hot research area.

Find out more on how to host your own Frontiers Research Topic or contribute to one as an author by contacting the Frontiers editorial office: frontiersin.org/about/contact

Methods in biomechanics and bionics

Topic editors

Zhen Luo — University of Technology Sydney, Australia

Triwiyanto Triwiyanto — Health Polytechnic of the Ministry of Health Surabaya, Indonesia

Suvash C. Saha — University of Technology Sydney, Australia

Citation

Luo, Z., Triwiyanto, T., Saha, S. C., eds. (2024). *Methods in biomechanics and bionics*. Lausanne: Frontiers Media SA. doi: 10.3389/978-2-8325-4227-9

Table of contents

- 05 **An Analysis of Lower Limb Coordination Variability in Unilateral Tasks in Healthy Adults: A Possible Prognostic Tool**
Maryam Ghahramani, Billy Mason, Patrick Pearsall and Wayne Spratford
- 16 **Non-invasive and quantitative analysis of flatfoot based on ultrasound**
Zhende Jiang, Qianpeng Zhang, Lei Ren and Zhihui Qian
- 24 **Validation of an MRI Technique for the 6-DOF Knee Kinematics Measurement**
Shixiong Tang, Liwen Zheng, Yongheng Luo, Ren Wu, Qunyan Tian and Lei Wang
- 37 **Designing anisotropic porous bone scaffolds using a self-learning convolutional neural network model**
Yongtao Lu, Tingxiang Gong, Zhuoyue Yang, Hanxing Zhu, Yadong Liu and Chengwei Wu
- 52 **Optimization and demonstration of two types of spring-roll dielectric elastomer actuators for minimally invasive surgery**
HaoChen Wang, Saihui Cui and Fuzhou Niu
- 66 **Optimization of the driver's seat belt and injury biomechanical analysis in real-world minivan small offset impact accident scenarios**
Xiuju Yang, Jingjing Shi, Qianying Fu, Shanshan Pu, Chunxiao Lian, Kui Li, Zhiyong Yin, Shengxiong Liu and Guixue Wang
- 83 **Biomechanical evaluation of lumbar spondylolysis repair with various fixation options: A finite element analysis**
Yuchen Ye, Shichang Jin, Yang Zou, Yuekun Fang, Panpan Xu, Zhili Zhang, Nan Wu and Changchun Zhang
- 97 **Clinical viability of magnetic bead implants in muscle**
Cameron R. Taylor, William H. Clark, Ellen G. Clarrissimeaux, Seong Ho Yeon, Matthew J. Carty, Stuart R. Lipsitz, Roderick T. Bronson, Thomas J. Roberts and Hugh M. Herr
- 111 **Untethered muscle tracking using magnetomicrometry**
Cameron R. Taylor, Seong Ho Yeon, William H. Clark, Ellen G. Clarrissimeaux, Mary Kate O'Donnell, Thomas J. Roberts and Hugh M. Herr
- 122 **Biomechanical influence of T1 tilt alteration on adjacent segments after anterior cervical fusion**
Wei Wei, Xianping Du, Na Li, Yunjie Liao, Lifeng Li, Song Peng, Wei Wang, Pengfei Rong and Yin Liu
- 133 **Post-stroke rehabilitation of the ankle joint with a low cost monoarticular ankle robotic exoskeleton: Preliminary results**
Guillermo Asín-Prieto, Silvana Mercante, Raúl Rojas, Mariangeles Navas, Daiana Gomez, Melisa Toledo, Aitor Martínez-Expósito and Juan C. Moreno

- 148 **Orthogonal pinhole-imaging-based learning salp swarm algorithm with self-adaptive structure for global optimization**
Zongshan Wang, Hongwei Ding, Jingjing Yang, Peng Hou, Gaurav Dhiman, Jie Wang, Zhijun Yang and Aishan Li
- 171 **Biased instantaneous regional muscle activation maps: Embedded fuzzy topology and image feature analysis**
Carlos De la Fuente, Alejandro Weinstein, Alejandro Neira, Oscar Valencia, Carlos Cruz-Montecinos, Rony Silvestre, Patricio A. Pincheira, Felipe Palma and Felipe P. Carpes
- 181 **The effects of ankle dorsiflexor fatigue on lower limb biomechanics during badminton forward forehand and backhand lunge**
Jianhua Tong, Zhenghui Lu, Xuanzhen Cen, Chaoyi Chen, Ukadike Chris Ugbole and Yaodong Gu
- 192 **Portable 3D-printed hand orthosis with spatial stiffness distribution personalized for assisting grasping in daily living**
Chan Beom Park and Hyung-Soon Park
- 208 **Effects of stance control via hidden Markov model-based gait phase detection on healthy users of an active hip-knee exoskeleton**
Miguel Sánchez-Manchola, Luis Arciniegas-Mayag, Marcela Múnera, Maxime Bourgain, Thomas Provot and Carlos A. Cifuentes
- 223 **Application of numerical simulation studies to determine dynamic loads acting on the human masticatory system during unilateral chewing of selected foods**
Przemysław Stróżyk and Jacek Batchanowski
- 241 **Mechanical assessment of novel compliant mechanisms for underactuated prosthetic hands**
Orion Ramos, Laura de Arco, Carlos A. Cifuentes, Mehran Moazen, Helge Wurdemann and Marcela Múnera



An Analysis of Lower Limb Coordination Variability in Unilateral Tasks in Healthy Adults: A Possible Prognostic Tool

Maryam Ghahramani^{1*}, Billy Mason^{2,3}, Patrick Pearsall⁴ and Wayne Spratford^{2,3}

¹Human-Centred Technology Research Centre, Faculty of Science and Technology University of Canberra, Canberra, NSW, Australia, ²Faculty of Health, University of Canberra, Canberra, NSW, Australia, ³University of Canberra Research Institute for Sport and Exercise Science, Canberra, NSW, Australia, ⁴School of Information Technology and Systems, Faculty of Science and Technology University of Canberra, Canberra, NSW, Australia

OPEN ACCESS

Edited by:

Zhen Luo,
University of Technology Sydney,
Australia

Reviewed by:

Cheng-Feng Lin,
National Cheng Kung University,
Taiwan
Chi-Wen Lung,
Asia University, Taiwan

*Correspondence:

Maryam Ghahramani
Maryam.Ghahramani@
Canberra.edu.au

Specialty section:

This article was submitted to
Biomechanics,
a section of the journal
Frontiers in Bioengineering and
Biotechnology

Received: 28 February 2022

Accepted: 23 May 2022

Published: 17 June 2022

Citation:

Ghahramani M, Mason B, Pearsall P and Spratford W (2022) An Analysis of Lower Limb Coordination Variability in Unilateral Tasks in Healthy Adults: A Possible Prognostic Tool. *Front. Bioeng. Biotechnol.* 10:885329. doi: 10.3389/fbioe.2022.885329

Interlimb coordination variability analysis can shed light into the dynamics of higher order coordination and motor control. However, it is not clear how the interlimb coordination of people with no known injuries change in similar activities with increasing difficulty. This study aimed to ascertain if the interlimb coordination variability range and patterns of healthy participants change in different unilateral functional tasks with increasing complexity and whether leg dominance affects the interlimb coordination variability. In this cross-sectional study fourteen younger participants with no known injuries completed three repeated unilateral sit-to-stands (UniSTS), step-ups (SUs), and continuous-hops (Hops). Using four inertial sensors mounted on the lower legs and thighs, angular rotation of thighs and shanks were recorded. Using Hilbert transform, the phase angle of each segment and then the continuous relative phase (CRP) of the two segments were measured. The CRP is indicative of the interlimb coordination. Finally, the linear and the nonlinear shank-thigh coordination variability of each participant in each task was calculated. The results show that the linear shank-thigh coordination variability was significantly smaller in the SUs compared to both UniSTS and Hops in both legs. There were no significant differences found between the latter two tests in their linear coordination variability. However, Hops were found to have significantly larger nonlinear shank-thigh coordination variability compared to the SUs and the UniSTS. This can be due to larger vertical and horizontal forces required for the task and can reveal inadequate motor control during the movement. The combination of nonlinear and linear interlimb coordination variability can provide more insight into human movement as they measure different aspects of coordination variability. It was also seen that leg dominance does not affect the lower limb coordination variability in participants with no known injuries. The results should be tested in participants recovering from lower limb injuries.

Keywords: interlimb coordination variability, interlimb coordination, unilateral sit to stand, unilateral functional tasks, continuous hops

INTRODUCTION

The biomechanical study of human motion in the fields of sports and health science can help with many aspects such as rehabilitation, injury prevention, and sports performance monitoring and analysis (Lamb and Stöckl, 2014). Many studies have modelled human movement as a dynamical system involving coordinated moving parts (Stergiou, 2004), (Glazier and Davids, 2009). The interaction and coordination of segments cause the effective displacement of the body. It is suggested that the behaviour of a dynamical system can be described by plotting a variable versus its first derivative, known as phase portraits (Rosen, 1970). Continuous relative phase (CRP) is a measure of the phase space relation of two segments evolving throughout a movement (Lamb and Stöckl, 2014), and has been widely used for inter- and intra-limb coordination analysis (Yi et al., 2016) (Lamb and Pataky, 2018) (Chopra et al., 2017). Movement coordination is associated with intersegment dynamics and the ability to construct and maintain proper coordination between joints or segments during motions (Chiu and Chou, 2012). Interlimb coordination measured by CRP has been used for injury recovery assessment such as anterior cruciate ligament reconstructive (ACLR) surgery (Goerger et al., 2020). It has also been proved that the interlimb coordination is affected by injuries, disease, and ageing (Salehi et al., 2020) (Dewolf et al., 2019) (Gueugnon et al., 2019) (Schwarz et al., 2021).

The interlimb coordination variability occurs in repeated motions. Any type of movement variability is a common inter- and intra-individual phenomena. As a movement is repeated, a certain amount of change may be recorded between its subsequent repetitions (Preatoni et al., 2013). Movement variability gives the body the degrees of freedom required to adapt to external and internal environmental conditions and to find the most appropriate movement strategies to execute a task (Preatoni et al., 2013), (Estep et al., 2018). However, increased or decreased movement variability can be indicative of lack of proper motor control caused by injury, disease or ageing (Ghahramani et al., 2020) (Thies et al., 2009), (Rennie et al., 2018). In order to properly investigate the movement variability many studies have focused on both linear and nonlinear variability assessment measures (Estep et al., 2018) (Gibbons et al., 2020). While linear methods are easy to generate and interpret, they neglect the time-dependent changes in pattern or structure of the signal (Stergiou et al., 2006), (Stergiou and Decker, 2011). Generally, motion variability is better captured by nonlinear measures where the temporal changes in the signal pattern is recorded (Stergiou and Decker, 2011). However, nonlinear variability assessment methods such as Sample Entropy (SampEn) have some limitations. This method is dependent on the sampling frequency and higher sample frequencies will lead to smaller SampEn values (Raffalt et al., 2018). Oliveira et al. (Oliveira et al., 2019) suggest that nonlinear variability assessment methods can be strong prognostic tools when used in conjunction with linear methods.

Interlimb coordination variability has been studied in sports (Floria et al., 2019). Assessing the interlimb coordination

variability in repeated motions can give an insight into the stability of the system or its resiliency to perturbation. However, there is a lack of clarity on how it should be interpreted. Some studies have suggested that the coordination variability in sports is an indicator of skill, and the adaptability to generate motor patterns signifies the capability of responding to disturbances or changes in environmental conditions (Preatoni et al., 2013) (Seifert et al., 2016) (Bernstein, 1967). Meanwhile other studies found contradicting results suggesting that high coordination variability is related to an elevated injury risk or decreased level of performance due to the changes in motor control, leading to tissue overload and increased load on the joint (Hamill et al., 2012) (Seifert et al., 2013) (Mansourizadeh et al., 2020). Nevertheless, the interlimb coordination variability analysis can shed light into the dynamics of higher order coordination (Lamb and Pataky, 2018).

While most studies have assessed the coordination variability in a single activity under various conditions (i.e., walking at different speeds (Wang W. et al., 2021)), no study has assessed the interlimb coordination variability in different lower-limb movement tasks of increasing complexity. Quantifying the adjustments in interlimb coordination and coordination variability as the complexity of the functional task changes provide insights on the level of challenge required to induce changes. Modifications in coordination could indicate the need to alter the movement pattern to accomplish the demands of the new task. Changes in the coordination variability in healthy adults might indicate the degree of adaptability that is required to respond to new constraints in the task. On the other hand, increased coordination variability can be indicative of perturbed coordination beyond stability (Kelso, 1995). Hence, it is not clear how the interlimb coordination of people with no known injuries change in similar activities with increasing difficulty. Elucidating how the coordination variability changes in response to different functional activities with similar motion may help us further understand the role of variability in human movement.

The present study focuses on assessing the interlimb coordination variability in a group of adults with no known injuries in a set of unilateral functional tasks with increasing complexity. All unilateral activities consist of knee extension-flexion. In this study the two following questions are meant to be answered: 1- Does the interlimb coordination variability range and patterns of participants with no injuries change in different unilateral functional tasks with increasing complexity? and 2- Does the leg dominance affect the shank-thigh coordination variability in participants with no known injuries? We hypothesized that the interlimb coordination variability increases in tasks with less ecological validity. We also hypothesized that the interlimb coordination variability of the nondominant leg is greater than the dominant one. In order to carefully characterize the shank-thigh coordination variability in the three functional tasks both linear and nonlinear motion variability measures were used.

Therefore, the contributions of this study are: 1) assessing the linear interlimb coordination variability of participants in the three different functional tasks, 2) assessing the nonlinear

interlimb coordination variability, 3) comparing the linear and nonlinear interlimb coordination variability of the participants in the functional tasks with increasing difficulty and complexity 4) assessing the effect of leg dominance on the shank-thigh coordination variability in the three different tasks. The three functional tasks in this study have been selected as they have similar knee extension-flexion motion and due to their application in clinical settings (McQuade and De Oliveira, 2011) (Jonsson and Kärrholm, 1994), as assessments of lower-limb strength (Waldhelm et al., 2020), or due to their similarities to activities of daily living (Grimmer et al., 2020). The results of this study indicate that participants displayed different results in their linear and nonlinear coordination variability. It was also seen that despite our initial hypothesis the leg dominance does not affect the interlimb coordination variability in participants with no known injuries. It is anticipated that the findings of this study may be used as a baseline for future studies investigating interlimb coordination in participants recovering from lower limb injuries such as ACL.

METHODS

Study Participants

Fourteen younger adult participants with no known injuries aged 18–35 (28 ± 7.69) years were recruited to participate in this study and provided informed consent prior to their participation. Upon arrival to the testing facility participants completed an Adult Pre-Exercise Screening System (APSS; Exercise and Sports Science Australia). Using the APSS tool any participant with injury, known disease or symptoms of disease that would have impacted their ability to complete the required movement tasks were identified and excluded from the study.

Study Experiments

This study used a cross-sectional study design to assess coordination variability in three unilateral movement tasks with increasing complexity. Participants' dominant leg was determined by asking participants which leg they would kick a soccer ball with or land from a jump (Weir et al., 2019). Upon arrival to the testing facility participants completed 5-min on a cycle ergometer to warm up the musculature of the lower-body using a previously described protocol (Kelly et al., 2010). Once the warm-up was completed, participants performed a single practice set of the unilateral sit-to-stand (UniSTS), unilateral step-ups (SUs), and three continuous-hops (Hops) before being fitted with inertial sensors (MTw from Xsens Technology). Once the sensors were applied, each participant completed the UniSTS, SUs and Hops in a randomized order using the techniques outlined below. As we were aiming at assessing the interlimb coordination variability three repetitions were included in each task. We also conducted two trials for each task to avoid any possible data loss due to technical issues.

In the UniSTS participants started from a seated position on a box. They placed a single foot on the ground at the midline of the body with arms across their chest. Participants were instructed to stand to an upright position before returning to the seated position

on the box in a controlled manner. The UniSTS was performed for 2 sets of three repetitions each leg (**Figure 1A**). The SUs commenced with a leg placed on top of a 30 cm box, with the other foot placed flat on the floor behind the box as outlined in **Figure 1B**. The box was positioned to allow for 90-degree knee flexion in the front leg when in the start position. When instructed, participants applied pressure through their front foot to bring their rear foot onto the box and finish in a tall standing position. The rear foot was then removed from the box and returned to the floor with the participant finishing the movement back in the start position ready to perform the next repetition. This process was repeated for 2 trials and each trial consisted of a set of three repetitions each leg. The Hops were performed by landing at markers placed 50 cm apart (**Figure 1C**). Whilst hop tests are often performed as a performance task with the aim of covering maximal distance (Ageberg and Cronström, 2018), the distance was set at 50 cm in the current study to allow for intra- and inter-trial standardization. This approach also ensured that data observed was due to differences in interlimb coordination and not distance covered during the task. Participants were instructed to jump forwards off a single leg and land on the same leg for a total of three repetitions each side. The Hops were performed in a continuous linear motion and were repeated for a total of two sets of three continuous repetitions each side.

Measurement System

Four inertial sensors (MTw from Xsens Technology) were attached on each participant; two on the shanks, placed on the medial surface of the tibia and two on the thighs placed on the lateral side superior to the knee joint. The shank and thigh angular rotation in the sagittal plane were recorded with the sampling rate of 60 Hz before data was transmitted to a computer for further analysis using MATLAB (R2021a). To ensure that extra movements did not affect the analysis, any data points recorded before and after the movement tasks were removed by reviewing the recorded sessions in Xsens MVN Analyze software. The data was pre-processed within MVN analyze which applies a Kilman filter to the data.

In order to assess the shank-thigh coordination variability, the phase angle of the two segments must first be determined (Ippertsiel et al., 2018). In a similar method to Lamb and Stockl (Lamb and Stöckl, 2014) the amplitude of each segment angular rotation data is firstly centered around zero. Having the segment angular rotation $\theta(t)$ the centered angular rotation for the time t_i noted as $\theta_{centred}(t_i)$ is as follows:

$$\theta_{centred}(t_i) = \theta(t_i) - \min(\theta(t)) - \frac{\max(\theta(t)) - \min(\theta(t))}{2} \quad (1)$$

$\min(\theta(t))$ and $\max(\theta(t))$ are indicative of the minimum and the maximum value of $\theta(t)$ respectively. Subsequently each centered angular rotation set is transformed into a complex analytical signal of $\zeta(t)$ using the Hilbert transform (Ippertsiel et al., 2018).

$$\zeta(t) = \theta_{centred}(t) + iH(t) \quad (2)$$

The Hilbert transform of signal $U(t)$ is the convolution of $U(t)$ with the signal $h(t) = \frac{1}{\pi t}$. The Cauchy principal value is used in

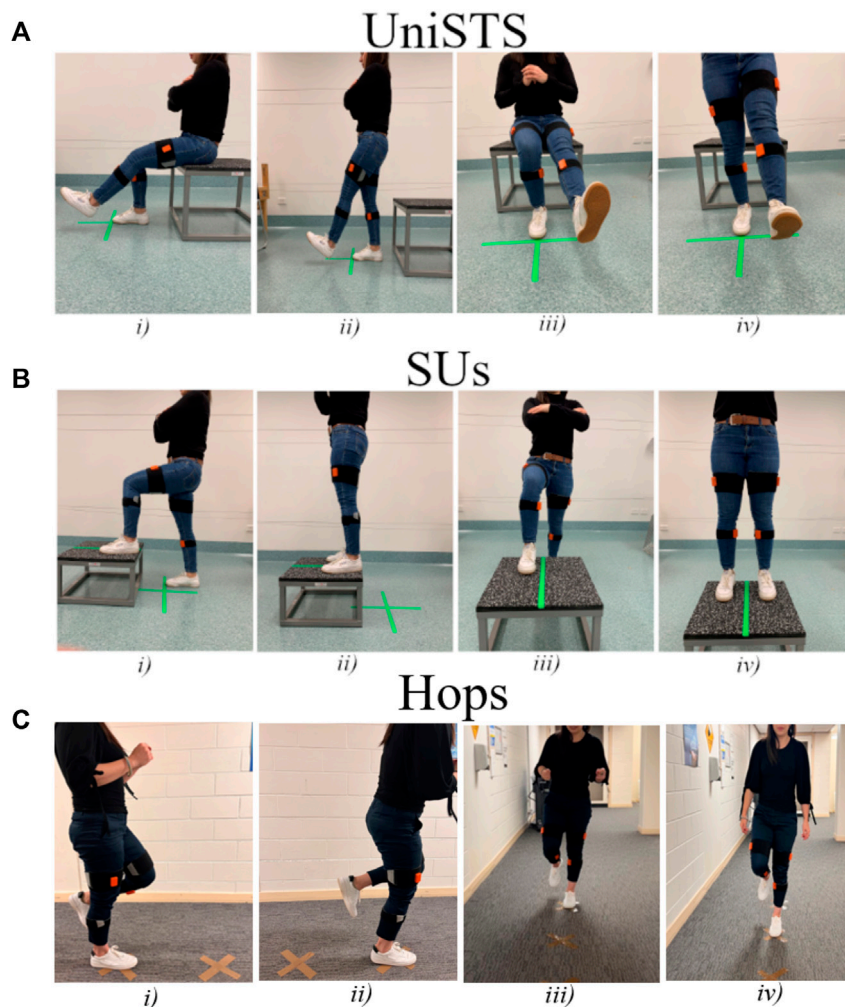


FIGURE 1 | The standardization procedures for **(A)** UniSTS, **(B)** SUs, and **(C)** Hops in starting and ending position, with a sagittal plane view and frontal plane view. Two inertial sensors were attached to the shanks and two to the thighs of the participants.

the Hilbert Transform (Gabor, 1946). Using Hilbert transform, the phase difference between two arbitrary, non-stationary, non-sinusoidal signals can be determined. The phase angle at each time point t_i ; $\varnothing(t_i)$ is calculated as the inverse tangent of imaginary part of the complex analytical representation of the segment data $\zeta(t)$ divided by its real part.

$$\varnothing(t_i) = \arctan\left(\frac{H(t_i)}{\theta_{centered}(t_i)}\right) \quad (3)$$

Continuous relative phase (CRP) analysis was then used to describe patterns of phase relationship between the two segments' angular rotation as the difference between the phase angle of each segment at t_i :

$$CRP(t_i) = \varnothing_1(t_i) - \varnothing_2(t_i) \quad (4)$$

A value of 0° for the CRP of the segments is indicative of them being fully in-phase, whereas CRP of 180° represents a fully out-of-phase coupling. CRP shows how the two segments are coupled

in their movements during the functional task (Stergiou et al., 2001). When two segments are out-of-phase they are moving in opposite directions and two in-phase segments move in a similar fashion and are totally coordinated. As stated by Lamb and Stockl (Lamb and Stöckl, 2014), in order to find meaningful and interpretable results to describe phase relationships properly from a dynamical systems perspective only segment angles should be used for calculating the CRP. For this purpose, the CRP for the shank-thigh segments was calculated.

The mean CRP over each repetition in every functional task is referred to as the mean relative phase (MRP). Finally, the standard deviation of the MRP (sdMRP) over the different repetitions in every functional task was calculated to assess linear coordination variability (Meyns et al., 2020). A schematic overview of the calculation of shank-thigh coordination measures is shown in **Figure 2**.

Sample Entropy (SampEn) is chosen for the nonlinear coordination variability analysis (Delgado-Bonal and Marshak, 2019). SampEn looks into the probability of two or more adjacent

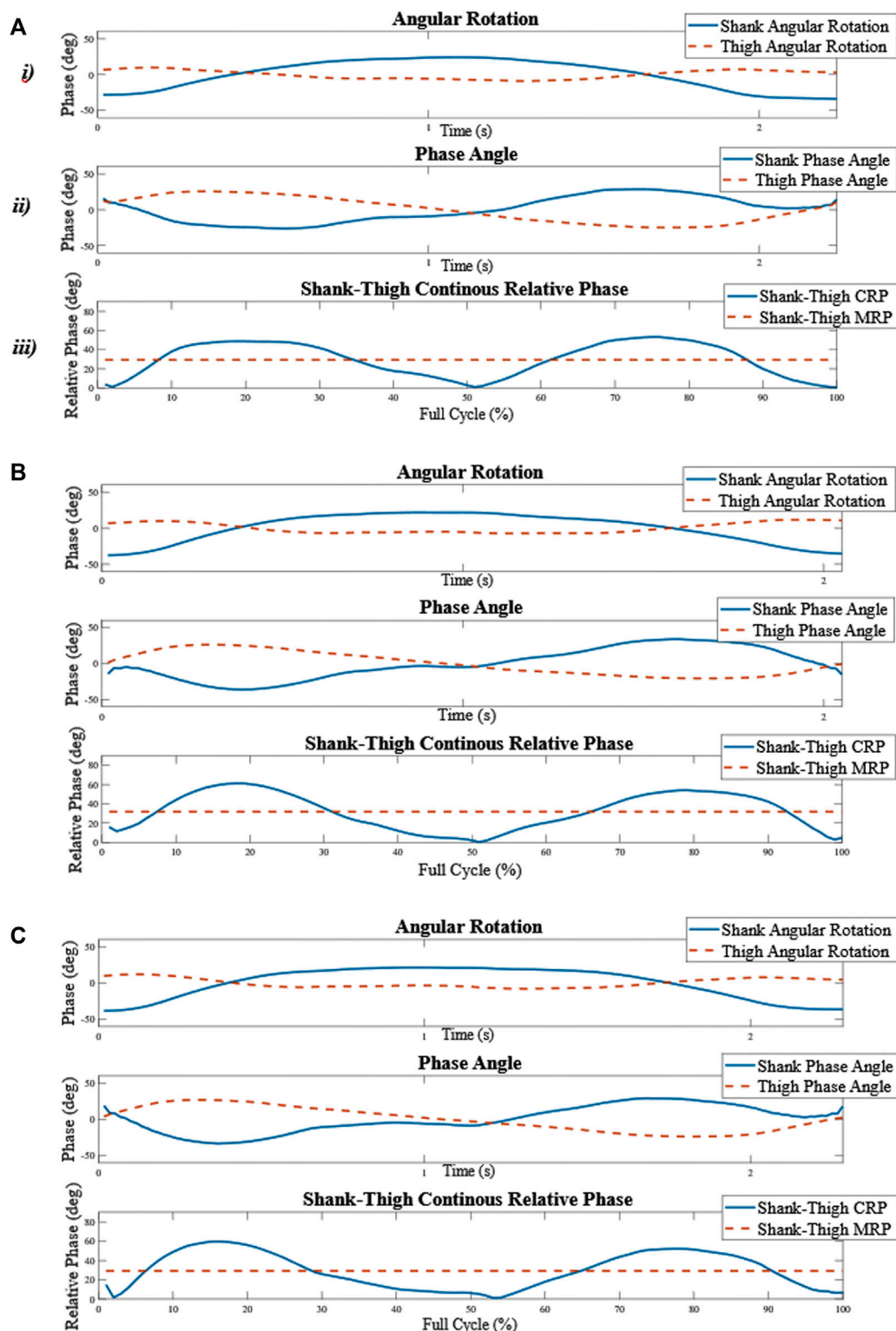


FIGURE 2 | Schematic overview of the calculation of the shank-thigh coordination measures. **(A) i)** The angular rotation of the right thigh and lower leg in the sagittal plane in one repetition of the SUS. **(A) ii)** The right shank-thigh continuous relative phase (CRP) over the full cycle of one repetition of the SUS. **(A) iii)** The mean of the CRP over the functional cycle is calculated and averaged for each repetition in each functional task for each participant and is referred to as the MRP. **(B–C)** The process was repeated for the second and the third repetitions. The standard deviation of the MRP over the three repetitions in every task is referred to as the linear coordination variability (sdMRP).

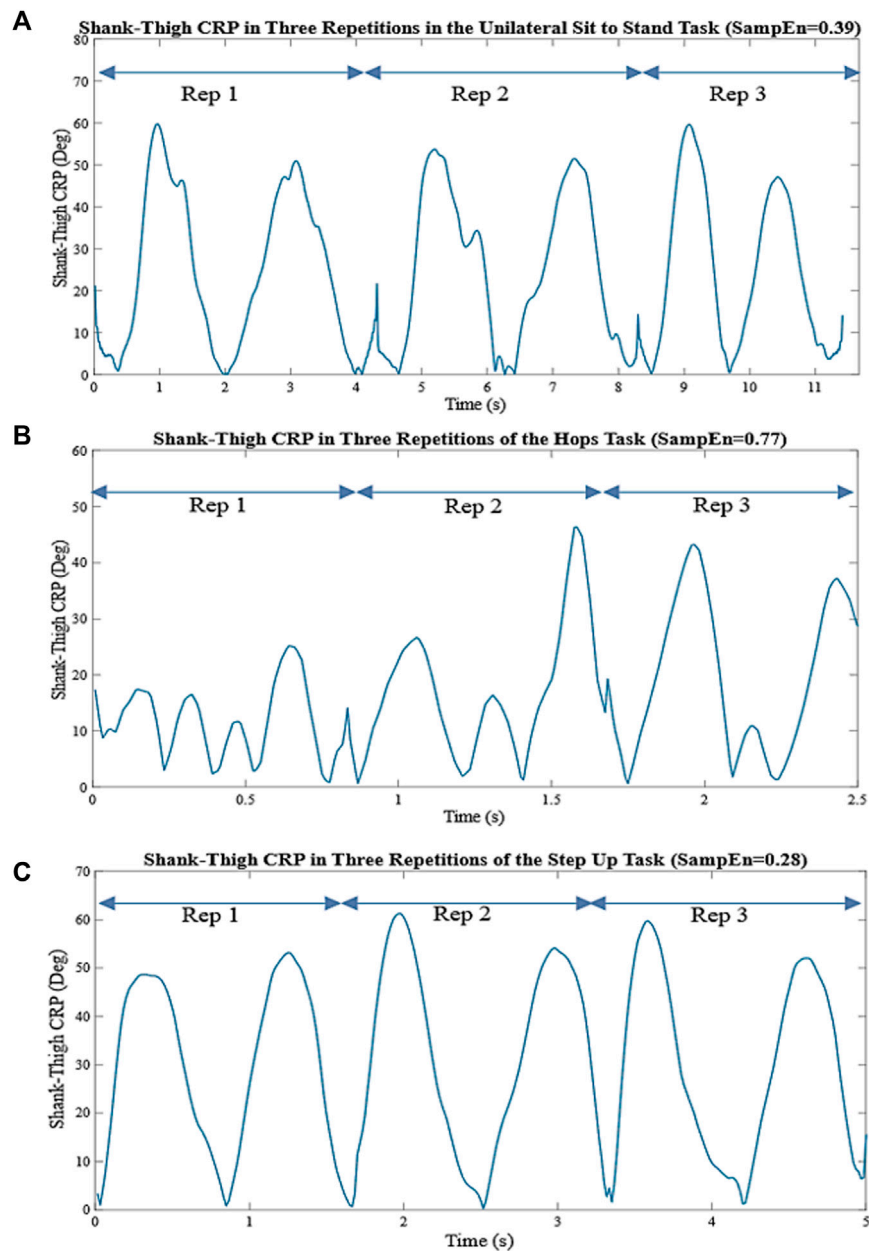


FIGURE 3 | (A) Shank-thigh CRP in three repetitions of the UnISTS. **(B)** Shank-thigh CRP in three repetitions of the Hops. **(C)** Shank-thigh CRP in three repetitions of the SUs. The nonlinear coordination variability is measured by the SampEn applied to the overall shank-thigh CRP in all repetitions. The higher SampEn is indicative of larger interlimb coordination variability and irregularity.

values in a time series being used to predict the next value. If SampEn is applied to a periodic signal the result will be 0, and if SampEn is above 1 it is indicative that the signal is with little to no clear periodic patterns. In order to calculate nonlinear coordination variability, firstly the shank-thigh CRP in each repetition in each functional task (CRP₁-CRP₃) was arranged in a vector as:

$$X = [\text{CRP}_1; \text{CRP}_2; \text{CRP}_3] \quad (5)$$

Then SampEn was applied to X. SampEn can be defined as:

$$\text{SampEn}(m, r, N) = -\ln\left(\frac{A}{B}\right) \quad (6)$$

Where m is the embedded dimension (typically 2 for most cases); r is the tolerance interval (typically the standard deviation of the signal multiplied by 0.2); and N is the length of the signal X. A is defined as the number of vector pairs having $d[X_{m+1}(i), X_{m+1}(j)] < r$ and B as the number of vector pairs

TABLE 1 | The right and left shank-thigh linear and nonlinear coordination variability analysis results in the UniSTS, Hops, and SUs and the Wilcoxon signed-rank test results.

	UniSTS	Hops	SUs
Right leg			
<i>sdMRP</i>	5.36 (4.81–6.63)* * <i>p</i> = 0.009 * <i>Z</i> = -2.6 * <i>r</i> = 0.69	5.66 (4.72–7.17) [#]	4.23 (3.86–4.43) [#] # <i>p</i> = 0.009 # <i>Z</i> = -2.6 # <i>r</i> = 0.69
<i>SampEn CRP</i>	0.29 (0.25–0.35)* * <i>p</i> ≤ 0.001 * <i>Z</i> = -3.3 * <i>r</i> = 0.88	0.92 (0.83–1.04) [#] # <i>p</i> ≤ 0.001 # <i>Z</i> = -3.3 # <i>r</i> = 0.88	0.35 (0.30–0.37) [#]
Left leg			
<i>sdMRP</i>	5.81 (5.03–7.91)* * <i>p</i> = 0.002 * <i>Z</i> = -3.2 * <i>r</i> = 0.85	5.67 (4.93–7.06) [#]	4.21 (4.01–4.89) [#] # <i>p</i> = 0.009 # <i>Z</i> = -2.6 # <i>r</i> = 0.69
<i>SampEn CRP</i>	0.29 (0.26–0.35)* * <i>p</i> ≤ 0.001 * <i>Z</i> = -3.3 * <i>r</i> = 0.88	0.98 (0.92–1.23) [#] # <i>p</i> ≤ 0.001 # <i>Z</i> = -3.2 # <i>r</i> = 0.85	0.33 (0.31–0.4) [#]

CI, confidence interval; *sdMRP*, standard deviation of the mean relative phase; *SampEn CRP*, sample entropy of the continuous relative phase. The significant differences ($p < 0.05$, $r > 0.5$) are shown by * for UniSTS vs. SUs, # for Hops vs. SUs, and + for UniSTS vs. Hops.

having $d[X_m(i), X_m(j)] < r$. $X_m(i)$ and $X_m(j)$ are vector pairs of length m where $j \neq i$ to avoid self-counting, and the $d[\cdot]$ denotes the distance function (Delgado-Bonal and Marshak, 2019). In Figure 3, the shank-thigh CRP of a participant in three repetitions of the UniSTS, Hops, and SUs and their relative *SampEn* values are shown.

Statistical Analysis

Using the Kolmogorov-Smirnov test the normality assumption of the results was tested. As most results rejected the null hypothesis ($p < 0.05$) non-parametric tests were used. Using the Friedman test, followed by Wilcoxon non-parametric test the significant differences in each leg's coordination variability in different functional tests were investigated. The effect size r was calculated and considered as small for $r < 0.1$, medium for $0.1 < r < 0.3$, and large for $r > 0.5$ (Rosenthal, 1994). Significant differences of the linear and nonlinear variability results of the dominant leg compared to the nondominant leg were investigated using Kruskal-Wallis ANOVA. The significance level was set by a p -value below 0.05.

RESULTS

Firstly, the right shank-thigh linear coordination variability is compared in the UniSTS, Hops, and SUs test using the Friedman test. The shank-thigh linear coordination variability of the right leg is found significantly different in

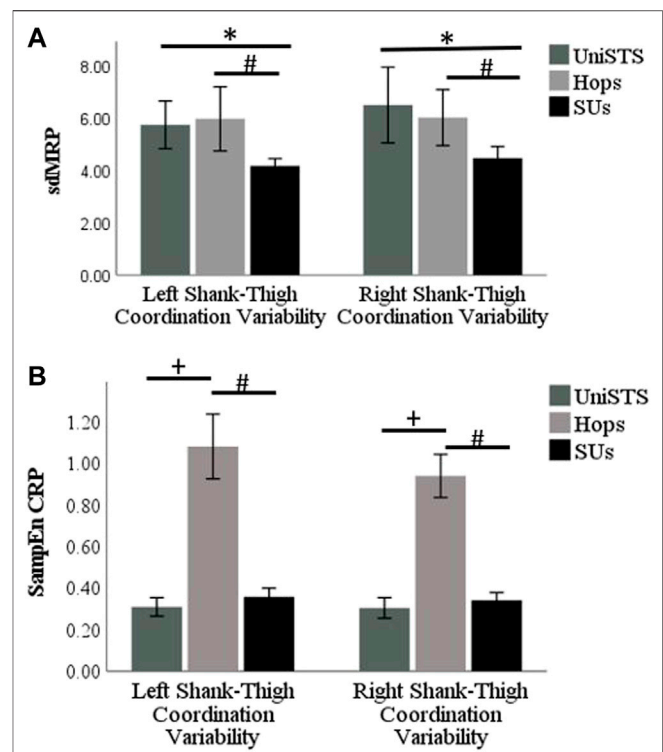


FIGURE 4 | (A) The bar plot of the linear right and left shank-thigh coordination variability results measured by the *sdMRP* of the participants in UniSTS, SUs, and Hops. (B) The bar plot of the non-linear right and left shank-thigh coordination variability results measured by the *SampEn CRP* of the participants in UniSTS, SUs, and Hops. The significant differences ($p < 0.05$, $r > 0.5$) are shown by * for UniSTS vs. SUs, # for Hops vs. SUs, and + for UniSTS vs. Hops.

TABLE 2 | Linear and nonlinear coordination variability analysis of the dominant and nondominant legs results in the UniSTS, Hops, and SUs.

	Dominant leg	Non-Dominant leg
<i>sdMRP Median (CI)</i>		
UniSTS	5.6 (5.03–7.56)	5.35 (4.73–7.03)
Hops	5.98 (5.08–7.5)	5.52 (4.6–6.7)
SUs	4.26 (3.9–4.46)	4.12 (3.96–4.87)
<i>SampEn CRP Median (CI)</i>		
UniSTS	0.29 (0.26–0.35)	0.28 (0.25–0.35)
Hops	0.98 (0.93–1.25)	0.90 (0.84–1.00)
SUs	0.33 (0.31–0.38)	0.37 (0.31–0.39)

CI, confidence interval; *sdMRP*, standard deviation of the mean relative phase; *SampEn CRP*, sample entropy of the continuous relative phase.

the UniSTS, Hops, and SUs ($\chi^2(2) = 7.00$, $p = 0.03$). Similarly, the shank-thigh non-linear coordination variability of the right leg is found significantly different in the UniSTS compared to that in Hops, and SUs ($\chi^2(2) = 23.29$, $p < 0.001$). The same process was repeated for the left leg. The shank-thigh linear coordination variability of the left leg is found significantly different in the three tests ($\chi^2(2) = 10.71$, $p = 0.005$). The left leg's

nonlinear shank-thigh coordination variability is found significantly different in the UniSTS, Hops, and SUs ($\chi^2(2) = 24.15, p < 0.001$).

The median and the confidence interval of the shank-thigh coordination variability results for each leg in different tasks and the results of the Wilcoxon signed-rank test for pairwise comparison are shown in **Table 1**. The bar plot of the results on the linear and nonlinear right and left shank-thigh coordination variability are shown in **Figure 4**.

In another comparison in order to test the effect of leg dominance on the coordination variability the dominant and nondominant shank-thigh coordination variability were compared separately within each individual functional task. Despite our initial hypothesis, the effect of the leg dominance on the shank-thigh coordination variability is not apparent. No significant differences were found in the linear shank-thigh coordination variability of the dominant leg compared to the nondominant one in any functional task. Similarly, the nonlinear shank-thigh coordination variability did not show any significant differences when compared in the dominant leg to the nondominant one in any of the tasks (**Table 2**).

DISCUSSION

This study focused on the shank-thigh coordination variability in different unilateral functional tasks in adults with no known injuries. In this study both the linear and nonlinear shank-thigh coordination variability were assessed. The results of shank-thigh sdMRP is significantly smaller in the SUs compared to both UniSTS and the Hops in both legs. However, the results yielded from both right and left shank-thigh SampEn are significantly larger in the Hops compared to both UniSTS and SUs. This difference in the nonlinear and the linear coordination variability shows that they cover different aspects of human motion. In order to have better understanding on the interlimb coordination variability and its role in human movement, it is beneficial to assess both measures. It was also found that the dominant shank-thigh coordination variability did not have any significant differences compared to the nondominant shank-thigh coordination variability in any of the tasks. The results of this study can be used as a baseline for future studies investigating interlimb coordination in participants recovering from lower limb injuries. A better understanding of the range of coordination variability in healthy adults aids with the injury recovery monitoring and physiotherapy.

Motor control associates with intersegmental dynamics and the ability to construct and maintain proper coordination between joints or segments during motions (Chiu and Chou, 2012) (Needham et al., 2014). Analyzing the interlimb coordination variability can help with understanding the dynamics of higher order coordination and to investigate the stability of the human movement system, or its resiliency to perturbation. (Lamb and Stöckl, 2014). Most studies focus on one activity with different speed or under different condition (Wang Y. et al., 2021). To the best of our knowledge this is the first study to examine shank-thigh coordination variability in unilateral

tasks with knee extension-flexion of increasing complexity. According to Clark et al. (Clark et al., 1993) shank-thigh coordination is cyclic and dissipative and therefore energy must be supplied to continue the behavior. The three functional tasks with similar knee extension-flexion have different difficulty levels that can act as external constraints. Any external constraint can cause the fluctuation in the stability of human motion system and affect the interlimb coordination (Glazier et al., 2006).

The linear shank-thigh coordination variability in the SUs is found to be significantly smaller compared to UniSTS and the SUs in both right and left legs. This could be due to the level of familiarity the participants have with the SUs movement compared to the UniSTS and the Hops. The refined motor control process required for consistent movement is developed through a learning process (Guarrera-Bowlby and Gentile, 2004). As the motor control adopts a functionally preferred state of interlimb coordination, the dynamics of order parameters are highly ordered and stable leading to the consistent patterns of interlimb coordination (Kelso, 1995). The step-up is a closed chain movement which mimics stair ascent and other common activities of daily living (Pijnappels et al., 2010). However, both dynamic hops and the open chain UniSTS tasks are of less ecological validity.

In addition to the linear interlimb coordination variability analysis, we assessed the nonlinear coordination variability using SampEn. While most studies rely on linear interlimb coordination variability analysis, non-linear measures of variability are found to be a potentially powerful prognostic tool when used in conjunction with linear measures (Oliveira et al., 2019). In the nonlinear shank-thigh coordination variability, Hops are found to have significantly larger SampEn results, i.e., larger nonlinear shank-thigh coordination variability compared to the SUs and the UniSTS. There are some everyday situations, e.g., car egress, which are to some extent similar to the unilateral sit-to-stand (Steingrebe et al., 2018). However, continuous unilateral hopping is far less common in activities of daily living. Moreover, during the Hops larger forces and acceleration in the vertical and anterior-posterior directions are needed compared to SUs and UniSTS to move the body and the center of mass both horizontally and vertically. The nonlinear interlimb coordination variability assessed by the SampEn investigates the irregularity of the patterns of the signal through repetitions. When it comes to the interlimb coordination, the ability to have more regular patterns is more difficult in complex or less familiar tasks (as seen in **Figure 4**). While larger motion variability is not always indicative of lack of stability, the large irregularity of interlimb coordination patterns in the Hops in the absence of any external perturbation can be considered as a lack of proper motor control (Van Emmerik et al., 2016). This result suggests that in addition to the common linear interlimb coordination variability (sdMRP), the nonlinear assessment of the coordination variability by SampEn should be considered.

Despite our initial hypothesis our results indicate that leg dominance did not have any effect on the coordination variability in participants with no known injuries. There were no significant

differences in the shank-thigh coordination variability of participants' dominant and nondominant legs in any of the unilateral functional tasks. This result indicates symmetry in shank-thigh coordination variability of participants regardless of the task. Similar to our results, it is reported by some studies that in healthy adults, leg dominance does not influence lower limb functionality (McGrath et al., 2016), (Greska et al., 2017), (Steingrebe et al., 2018). It is anticipated that injured participants show asymmetry in their dominant and nondominant lower limb coordination variability specifically in their nonlinear coordination variability. In a pilot study by Albano et al. (Albano et al., 2021) uninjured participants showed symmetrical knee joint variability. Meanwhile, the injured participants with no rehabilitation showed a noteworthy asymmetry. This result is interesting in itself and should be tested in participants recovering from lower limb injuries.

Limitation and Future Work

The findings of this study should be interpreted in light of some limitations. One limitation of this study is that some participants had more active lifestyles compared to others within the sample. This might have affected their range of coordination variability specially in the Hops and the UniSTS which are more demanding tasks compared to the SUs. It would be beneficial to repeat this study on an athletic population. In a study by Wang et al. (Wang W. et al., 2021) athletes showed smaller coordination variability while running compared to nonathletes suggesting that coordination variability may depend on motor skill level. Another limitation is that the height and the mass of the participants were not considered in the analysis. These factors might have affected the shank-thigh coordination variability results. In future studies other general and pathological factors of the participants that might affect their interlimb coordination should be taken into consideration.

CONCLUSION

The results of this study show that the combination of nonlinear and linear interlimb coordination variability analysis can provide more information on human movement. Participants had significantly smaller linear shank-thigh coordination variability in the SUs when compared to the UniSTS and Hops. There were no significant differences found between the linear interlimb coordination variability of the latter two tasks. However, nonlinear coordination variability is found to be significantly larger in the Hops compared to the two other tasks. This indicates

irregularity in the interlimb coordination patterns which can be due to the larger vertical and horizontal forces required for the task, which may in turn reveal inadequate motor control during the movement. It was also seen that leg dominance does not affect the interlimb coordination of the participants with no known injuries. The results of this study should be tested on athletes with more familiarity in unilateral functional tasks and can be used as a benchmark for participants recovering from lower limb injuries.

DATA AVAILABILITY STATEMENT

The raw data supporting the conclusions of this article will be made available by the authors, without undue reservation.

ETHICS STATEMENT

This study was approved (project number: 20215831) by the University of Canberra Human Research Ethics Committee. The patients/participants provided their written informed consent to participate in this study.

AUTHOR CONTRIBUTIONS

MG is the lead investigator in this project. She is the corresponding author. BM contributed to the study design, the recruitment of participants and data collection sections of the paper. PP was in charge for the linear and nonlinear coordination variability analysis. WS was the senior member and contributed to the study design, the recruitment of participants, data collection and the overall understanding of the project. All the authors contributed to manuscript revision and read and approved the submitted version.

FUNDING

This study was funded by the Early Career Researcher Development Plan (ECARD) program, University of Canberra.

ACKNOWLEDGMENTS

We thank all subjects for participating in this study.

REFERENCES

- Ageberg, E., and Cronström, A. (2018). Agreement between Test Procedures for the Single-Leg Hop for Distance and the Single-Leg Mini Squat as Measures of Lower Extremity Function. *BMC Sports Sci. Med. Rehabil.* 10 (1), 15–17. doi:10.1186/s13102-018-0104-6
- Albano, D., Lambiase, G., Romano, B., and Vastola, R. (2021). Nonlinear Analysis of Knee Kinematic Variability after ACL Reconstruction for the Return to Sport. *J. Phys. Educ. Sport* 21 (2), 922–926. doi:10.7752/jpes.2021.02114
- Bernstein, N. A. (1967). *The Coordination and Regulation of Movements*. New York: Pergamon.
- Chiu, S.-L., and Chou, L.-S. (2012). Effect of Walking Speed on Inter-joint Coordination Differs between Young and Elderly Adults. *J. Biomechanics* 45, 275–280. doi:10.1016/j.jbiomech.2011.10.028
- Chopra, S., Favre, J., and Crevoisier, X. (2017). Qualitative Analysis of Foot Intersegment Coordination in the Sagittal Plane Following Surgery for End-Stage Ankle Osteoarthritis. *J. Orthop. Res.* 35 (6), 1304–1310. doi:10.1002/jor.23379
- Clark, J., Truly, T., and Phillips, S. (1993). "On the Development of Walking as a Limit-Cycle System," in *Dynamical Systems in Development: Application*. Editors E. Thelen and E. Smith (Cambridge: MIT Press), 71–93.

- de Oliveira, E. A., Andrade, A. O., and Vieira, M. F. (2019). Linear and Nonlinear Measures of Gait Variability after Anterior Cruciate Ligament Reconstruction. *J. Electromyogr. Kinesiol.* 46, 21–27. doi:10.1016/j.jelekin.2019.03.007
- Delgado-Bonal, A., and Marshak, A. (2019). Approximate Entropy and Sample Entropy: A Comprehensive Tutorial. *Entropy (Basel)* 21 (6). doi:10.3390/e21060541
- Dewolf, A. H., Meurisse, G. M., Schepens, B., and Willems, P. A. (2019). Effect of Walking Speed on the Intersegmental Coordination of Lower-Limb Segments in Elderly Adults. *Gait posture* 70, 156–161. doi:10.1016/j.gaitpost.2019.03.001
- Estep, A., Morrison, S., Caswell, S., Ambegaonkar, J., and Cortes, N. (2018). Differences in Pattern of Variability for Lower Extremity Kinematics between Walking and Running. *Gait Posture* 60, 111–115. doi:10.1016/j.gaitpost.2017.11.018
- Floria, P., Sánchez-Sixto, A., Harrison, A. J., and Ferber, R. (2019). The Effect of Running Speed on Joint Coupling Coordination and its Variability in Recreational Runners. *Hum. Mov. Sci.* 66, 449–458. doi:10.1016/j.humov.2019.05.020
- Gabor, D. (1946). Theory of Communication. Part I: The Analysis of Information. *J. Institution Electr. Engineers-Part III Radio N. D. Commun. Eng.* 93 (26), 429–441. doi:10.1049/ji-3-2.1946.0074
- Ghahramani, M., Stirling, D., and Naghdy, F. (2020). The Sit to Stand to Sit Postural Transition Variability in the Five Time Sit to Stand Test in Older People with Different Fall Histories. *Gait Posture* 81, 191–196. doi:10.1016/j.gaitpost.2020.07.073
- Gibbons, C. T., Amazeen, P. G., and Likens, A. D. (2020). Distinguishing Two Types of Variability in a Sit-To-Stand Task. *Mot. Control* 24, 168–188. doi:10.1123/mc.2018-0022
- Glazier, P. S., and Davids, K. (2009). Constraints on the Complete Optimization of Human Motion. *Sports Med.* 39, 15–28. doi:10.2165/00007256-200939010-00002
- Glazier, P. S., Wheat, J. S., Pease, D. L., and Bartlett, R. M. (2006). “The Interface of Biomechanics and Motor Control: Dynamic Systems Theory and the Functional Role of Movement Variability,” in *Movement System Variability*. Editors K. Davids, S. Bennet, and S. Newell (Champaign, IL: Human Kinetics), 46–69.
- Goerger, B. M., Marshall, S. W., Beutler, A. I., Blackburn, J. T., Wilkens, J. H., and Padua, D. A. (2020). Longitudinal Analysis of Inter-limb Coordination before and after Anterior Cruciate Ligament Injury: The JUMP-ACL Study. *J. SCI. SPORT Exerc.* 2 (3), 265–271. doi:10.1007/s42978-020-00089-8
- Greska, E. K., Cortes, N., Ringleb, S. I., Onate, J. A., and Van Lunen, B. L. (2017). Biomechanical Differences Related to Leg Dominance Were Not Found during a Cutting Task. *Scand. J. Med. Sci. Sports* 27 (11), 1328–1336. doi:10.1111/sms.12776
- Grimmer, M., Elshamashory, A. A., and Beckerle, P. (2020). Human Lower Limb Joint Biomechanics in Daily Life Activities: a Literature Based Requirement Analysis for Anthropomorphic Robot Design. *Front. Robot. AI* 7, 13. doi:10.3389/frobt.2020.00013
- Guarrera-Bowlby, P. L., and Gentile, A. M. (2004). Form and Variability during Sit-To-Stand Transitions: Children versus Adults. *J. Mot. Behav.* 36 (36), 104–114. doi:10.3200/JMBR.36.1.104-114
- Gueugnon, M., Stapley, P. J., Gouteron, A., Lecland, C., Morisset, C., Casillas, J.-M., et al. (2019). Age-Related Adaptations of Lower Limb Intersegmental Coordination during Walking. *Front. Bioeng. Biotechnol.* 7, 173. doi:10.3389/fbioe.2019.00173
- Hamill, J., Palmer, C., and Van Emmerik, R. E. (2012). Coordinative Variability and Overuse Injury. *Sports Med. Arthrosc. Rehabil. Ther. Technol.* 4 (1), 45–49. doi:10.1186/1758-2555-4-45
- Ippersiel, P., Robbins, S., and Preuss, R. (2018). Movement Variability in Adults with Low Back Pain during Sit-To-Stand-To-Sit. *Clin. Biomech.* 58, 90–95. doi:10.1016/j.clinbiomech.2018.07.011
- Jonsson, H., and Kärrholm, J. (1994). Three-dimensional Knee Joint Movements during a Step-Up: Evaluation after Anterior Cruciate Ligament Rupture. *J. Orthop. Res.* 12 (6), 769–779. doi:10.1002/jor.1100120604
- Kelly, S. B., Alvar, B. A., Black, L. E., Dodd, D. J., Carothers, K. F., and Brown, L. E. (2010). The Effect of Warm-Up with Whole-Body Vibration vs. Cycle Ergometry on Isokinetic Dynamometry. *J. Strength & Cond. Res.* 24 (11), 3140–3143. doi:10.1519/jsc.0b013e3181f9278f
- Kelso, J. S. (1995). *Dynamic Patterns: The Self-Organization of Brain and Behavior*. Cambridge, MA: MIT Press.
- Lamb, P. F., and Pataky, T. C. (2018). The Role of Pelvis-Thorax Coupling in Controlling Within-Golf Club Swing Speed. *J. Sports Sci.* 36 (9), 2164–2171. doi:10.1080/02640414.2018.1442287
- Lamb, P. F., and Stöckl, M. (2014). On the Use of Continuous Relative Phase: Review of Current Approaches and Outline for a New Standard. *Clin. Biomech.* 29 (5), 484–493. doi:10.1016/j.clinbiomech.2014.03.008
- Mansourizadeh, R., Letafatkar, A., Franklyn-Miller, A., Khaleghi-Tajzi, M., and Baker, J. S. (2020). Segmental Coordination and Variability of Change in Direction in Long-Standing Groin Pain. *Gait Posture* 77, 36–42. doi:10.1016/j.gaitpost.2020.01.013
- McGrath, T. M., Waddington, G., Scarvell, J. M., Ball, N. B., Creer, R., Woods, K., et al. (2016). The Effect of Limb Dominance on Lower Limb Functional Performance - a Systematic Review. *J. Sports Sci.* 34 (4), 289–302. doi:10.1080/02640414.2015.1050601
- McQuade, K. J., and De Oliveira, A. S. (2011). Effects of Progressive Resistance Strength Training on Knee Biomechanics during Single Leg Step-Up in Persons with Mild Knee Osteoarthritis. *Clin. Biomech.* 26 (7), 741–748. doi:10.1016/j.clinbiomech.2011.03.006
- Meyns, P., Van de Walle, P., Desloovere, K., Janssens, S., Van Sever, S., and Hallemans, A. (2020). Age-related Differences in Interlimb Coordination during Typical Gait: An Observational Study. *Gait Posture* 81, 109–115. doi:10.1016/j.gaitpost.2020.07.013
- Needham, R., Naemi, R., and Chockalingam, R. (2014). Quantifying Lumbar-Pelvis Coordination during Gait Using a Modified Vector Coding Technique. *J. Biomechanics* 47 (5), 1020–1026. doi:10.1016/j.jbiomech.2013.12.032
- Pijnappels, M., Delbaere, K., Sturnieks, D. L., and Lord, S. R. (2010). The Association between Choice Stepping Reaction Time and Falls in Older Adults-Aa Path Analysis Model. *Age Ageing* 39 (1), 99–104. doi:10.1093/ageing/afp200
- Preatoni, E., Hamill, J., Harrison, A. J., Hayes, K., Van Emmerik, R. E. A., Wilson, C., et al. (2013). Movement Variability and Skills Monitoring in Sports. *Sports Biomech.* 12 (2), 69–92. doi:10.1080/14763141.2012.738700
- Raffalt, P. C., McCamley, J., Denton, W., and Yentes, J. M. (2018). Sampling Frequency Influences Sample Entropy of Kinematics during Walking. *Med. Biol. Eng. Comput.* 57, 759–764. doi:10.1007/s11517-018-1920-2
- Rennie, L., Löfgren, N., Moe-Nilssen, R., Opheim, A., Dietrichs, E., and Franzén, E. (2018). The Reliability of Gait Variability Measures for Individuals with Parkinson's Disease and Healthy Older Adults - the Effect of Gait Speed. *Gait Posture* 62, 505–509. doi:10.1016/j.gaitpost.2018.04.011
- Rosen, R. (1970). *Dynamical Systems Theory in Biology: Vol. 1. Stability Theory and its Application*. Wiley-Interscience.
- Rosenthal, R. (1994). “Parametric Measures of Effect Size,” in *The Handbook of Research Synthesis* (New York: Russell Sage Foundation), 231–244.
- Salehi, R., Mofateh, R., Mehravar, M., Negahban, H., Tajali, S., and Monjezi, S. (2020). Comparison of the Lower Limb Inter-segmental Coordination during Walking between Healthy Controls and People with Multiple Sclerosis with and without Fall History. *Multiple Scler. Relat. Disord.* 41, 102053. doi:10.1016/j.msard.2020.102053
- Schwarz, A., Veerbeek, J. M., Held, J. P. O., Buurke, J. H., and Luft, A. R. (2021). Measures of Interjoint Coordination Post-stroke across Different Upper Limb Movement Tasks. *Front. Bioeng. Biotechnol.* 1551. doi:10.3389/fbioe.2020.620805
- Seifert, L., Button, C., and Davids, K. (2013). Key Properties of Expert Movement Systems in Sport. *Sports Med.* 43 (3), 167–178. doi:10.1007/s40279-012-0011-z
- Seifert, L., Komar, J., Araújo, D., and Davids, K. (2016). Neurobiological Degeneracy: A Key Property for Functional Adaptations of Perception and Action to Constraints. *Neurosci. Biobehav. Rev.* 69, 159–165. doi:10.1016/j.neubiorev.2016.08.006
- Steingrebe, H., Stein, T., Bös, K., and Hoffmann, M. (2018). Biomechanical Analysis of the Knee Joint Load during a Unilateral Sit-To-Stand Movement. *open Sports Sci. J.* 11 (1). doi:10.2174/1875399x01811010078
- Stergiou, N., and Decker, L. M. (2011). Human Movement Variability, Nonlinear Dynamics, and Pathology: Is There a Connection? *Hum. Mov. Sci.* 30 (5), 869–888. doi:10.1016/j.humov.2011.06.002
- Stergiou, N., Harbourne, R. T., and Cavanaugh, J. T. (2006). Optimal Movement Variability. *J. Neurologic Phys. Ther.* 30 (3), 120–129. doi:10.1097/01.npt.0000281949.48193.d9

- Stergiou, N. (2004). *Innovative Analyses of Human Movement: Analytical Tools for Human Movement Research*. Champaign: Human Kinetics.
- Stergiou, N., Jensen, J. L., Bates, B. T., Scholten, S. D., and Tzetzis, G. (2001). A Dynamical Systems Investigation of Lower Extremity Coordination during Running over Obstacles. *Clin. Biomech.* 16 (3), 213–221. doi:10.1016/s0268-0033(00)00090-5
- Thies, S. B., Tresadern, P. A., Kenney, L. P., Smith, J., Howard, D., Goulernas, J. Y., et al. (2009). Movement Variability in Stroke Patients and Controls Performing Two Upper Limb Functional Tasks: a New Assessment Methodology. *J. NeuroEngineering Rehabil.* 6 (1), 2. doi:10.1186/1743-0003-6-2
- Van Emmerik, R. E. A., Ducharme, S. W., Amado, A. C., and Hamill, J. (2016). Comparing Dynamical Systems Concepts and Techniques for Biomechanical Analysis. *J. Sport Health Sci.* 5 (1), 3–13. doi:10.1016/j.jshs.2016.01.013
- Waldhelm, A., Gubler, C., Sullivan, K., Witte, C., Buchheister, D., and Bartz-Broussard, J. (2020). Inter-rater and Test-Retest Reliability of Two New Single Leg Sit-To-Stand Tests. *Intl J. Sports Phys. Ther.* 15 (3), 388–394. doi:10.26603/ijspst20200388
- Wang, W., Qu, F., Li, S., and Wang, L. (2021). Effects of Motor Skill Level and Speed on Movement Variability during Running. *J. Biomechanics* 127, 110680. doi:10.1016/j.jbiomech.2021.110680
- Wang, Y., Zhang, K., Zeng, J., and Yan, S. (2021). Coordination of Lower Limbs in Patients with Knee Osteoarthritis during Walking. *Gait Posture* 83, 160–166. doi:10.1016/j.gaitpost.2020.10.024
- Weir, G., van Emmerik, R., Jewell, C., and Hamill, J. (2019). Coordination and Variability during Anticipated and Unanticipated Sidestepping. *Gait Posture* 67, 1–8. doi:10.1016/j.gaitpost.2018.09.007
- Yi, L. C., Sartor, C. D., Souza, F. T., and Sacco, I. C. N. (2016). Intralimb Coordination Patterns in Absent, Mild, and Severe Stages of Diabetic Neuropathy: Looking beyond Kinematic Analysis of Gait Cycle. *PloS one* 11 (1), e0147300. doi:10.1371/journal.pone.0147300

Conflict of Interest: The authors declare that the research was conducted in the absence of any commercial or financial relationships that could be construed as a potential conflict of interest.

Publisher's Note: All claims expressed in this article are solely those of the authors and do not necessarily represent those of their affiliated organizations, or those of the publisher, the editors and the reviewers. Any product that may be evaluated in this article, or claim that may be made by its manufacturer, is not guaranteed or endorsed by the publisher.

Copyright © 2022 Ghahramani, Mason, Pearsall and Spratford. This is an open-access article distributed under the terms of the Creative Commons Attribution License (CC BY). The use, distribution or reproduction in other forums is permitted, provided the original author(s) and the copyright owner(s) are credited and that the original publication in this journal is cited, in accordance with accepted academic practice. No use, distribution or reproduction is permitted which does not comply with these terms.



OPEN ACCESS

EDITED BY

Suvash C. Saha,
University of Technology Sydney,
Australia

REVIEWED BY

Daniel López-López,
Universidade da Coruña, Spain
Zhongjun Mo,
National Research Center for
Rehabilitation Technical Aids, China
Chueh-Hung Wu,
National Taiwan University, Taiwan

*CORRESPONDENCE

Zhihui Qian,
zhqian@jlu.edu.cn
Lei Ren,
lei.ren@manchester.ac.uk

SPECIALTY SECTION

This article was submitted to
Biomechanics,
a section of the journal
Frontiers in Bioengineering and
Biotechnology

RECEIVED 04 June 2022

ACCEPTED 09 August 2022

PUBLISHED 06 September 2022

CITATION

Jiang Z, Zhang Q, Ren L and Qian Z
(2022), Non-invasive and quantitative
analysis of flatfoot based on ultrasound.
Front. Bioeng. Biotechnol. 10:961462.
doi: 10.3389/fbioe.2022.961462

COPYRIGHT

© 2022 Jiang, Zhang, Ren and Qian. This
is an open-access article distributed
under the terms of the [Creative
Commons Attribution License \(CC BY\)](#).
The use, distribution or reproduction in
other forums is permitted, provided the
original author(s) and the copyright
owner(s) are credited and that the
original publication in this journal is
cited, in accordance with accepted
academic practice. No use, distribution
or reproduction is permitted which does
not comply with these terms.

Non-invasive and quantitative analysis of flatfoot based on ultrasound

Zhende Jiang^{1,2}, Qianpeng Zhang³, Lei Ren^{1,4*} and
Zhihui Qian^{1*}

¹Key Laboratory of Bionic Engineering, Jilin University, Changchun, China, ²Orthopaedic Medical Center, The Second Hospital of Jilin University, Changchun, China, ³Department of Radiology, Second Hospital of Jilin University, Changchun, China, ⁴School of Mechanical, Aerospace and Civil Engineering, University of Manchester, Manchester, United Kingdom

Flatfoot is a common foot deformity that seriously affects the quality of life. The aim of this study is to develop an accurate and noninvasive method for the diagnosis of flatfoot based on B-mode ultrasound. In this study, 51 patients (the flatfoot group) and 43 healthy subjects (the control group) were included. The plantar fascia angle, a new measurement for use in the diagnosis of flatfoot is proposed, as determined using B-mode ultrasound. For comparison, the calcaneal pitch angle and medial cuneiform height were also measured using lateral X-radiography, based on traditional diagnostic methods. The intraclass correlation values of the plantar fascia angle, the calcaneal pitch angle, and the medial cuneiform height were all more than 0.95, and there is a moderate correlation ($r = 0.51$) between the medial cuneiform height and the calcaneal pitch angle, and an excellent correlation ($r = 0.85$) between the plantar fascia angle and the calcaneal pitch angle. The optimal cutoff value, sensitivity, and specificity for medial cuneiform height in flatfoot diagnosis were 12.8 mm, 93.0%, and 54.9%, respectively. The optimal cutoff value, sensitivity, and specificity for plantar fascia angle in flatfoot diagnosis were 9.8°, 97.7%, and 94.1%, respectively. The proposed plantar fascia angle has good sensitivity and specificity in diagnosing flatfoot, therefore supplying a new approach for the noninvasive diagnosis of flatfoot.

KEYWORDS

flatfoot, plantar fascia angle, calcaneal pitch angle, medial cuneiform height, diagnosis

Introduction

The human foot is a complex system comprising 26 bones, 33 joints, and more than 100 muscles, tendons, and ligaments. It plays an important role in human weight-bearing and propulsion (Oleksy et al., 2010). Flatfoot is a common type of foot deformity, in which the foot has little or no arch (Sung, 2016). It has been confirmed that flatfoot is a complex

Abbreviations: PF, plantar fasciitis; FPI-6, foot posture index; ICC, intraclass correlation; 95% CIs, 95% confidence intervals; ROC, receiver operating characteristic; AUC, area under the curve.

deformity, that is, highly related to abnormal changes in the medial longitudinal arch (Pehlivan et al., 2009; Shibuya et al., 2010; Abousayed et al., 2017). Though a study showed that the quality of life seemed not to be influenced by the height of foot arch (Lopez-Lopez et al., 2018), many studies demonstrated that the lower foot arch of flatfoot can lead to abnormal gait and lower-limb alignment, affect the function of shock absorption, and lead to plantar fasciitis (PF), medial tibial stress syndrome, patellar tendon disease, and other problems, and seriously affect the quality of life (Kohls-Gatzoulis et al., 2004; Wearing et al., 2006; Levinger et al., 2010; Van der Worp et al., 2011; Hamstra-Wright et al., 2015).

Diagnostic methods of flatfoot mainly include physical examination and imaging examination (Abousayed et al., 2017). Physical examination is mainly carried out through visual examination, palpation, and mobility measurement. Visual examination mainly involves observing the shape and alignment of the foot; the most commonly used rating tools are the foot posture index (FPI-6) and footprints. FPI-6 allows the foot to be evaluated on three planes; it is composed of six separate evaluation parts, and summarizes the results to reflect the posture of the foot (Oleksy et al., 2010). Palpation is mainly carried out along the posterior tibial tendon to determine whether there is posterior tibial tendonitis or posterior tibial tendon rupture (Abousayed et al., 2017). Mobility measurement is mainly conducted to evaluate muscle strength and movement; for example, the dorsal flexion test is used to judge the tension of the gastrocnemius-soleus muscle complex and the heel lifting test is used to judge the function of the posterior tibial tendon (Abousayed et al., 2017). However, the results of physical examination will be affected by the subjective judgment of podiatrists, and it is troublesome to obtain and measure accurate footprints, so imaging diagnosis is necessary to further clarify the diagnosis and severity of the disease (Bock P, 2018).

The evaluation of X-radiographs of the weight-bearing foot and ankle is still the gold standard for the diagnosis of flatfoot and pes cavus (Abousayed et al., 2017). Anteroposterior X-radiography of the weight-bearing foot can show abduction of the forefoot and the uncovered talus. Many parameters are used to evaluate the uncovered talus, including the talus coverage angle, the percentage of uncovered talus, and the lateral discordant angle (Deland, 2008; Chan et al., 2015). The calcaneal pitch angle and medial cuneiform height of the talus can be measured using lateral X-radiographs of the weight-bearing foot (Younger et al., 2005; Bock et al., 2018). Magnetic resonance imaging and ultrasonography are mainly used for preoperative evaluation of the posterior tibial tendon, spring ligament, and plantar fascia, in order to optimize operation plans (Harish et al., 2008; Arnoldner et al., 2015; Abousayed et al., 2017). A great contribution of the ultrasound is that it opens the opportunity to measure parameters such as the size, shape, angle and biomechanical

properties of the muscle, tendon, ligament and fascia (Romero-Morales et al., 2019; Schillizzi et al., 2020; Romero-Morales et al., 2021), of which the angle of the plantar fascia based on ultrasound was the specifically we are looking at in relation to flatfoot.

X-radiography is important in flatfoot diagnosis (Abousayed et al., 2017). However, X-radiation has potential radiological hazard (Prasarn, 2014). Therefore, the study of rapid, non-radiological, quantifiable and convenient methods for the diagnosis of flatfoot has important clinical significance and social value. As is known, the plantar fascia, as the main structure connecting the calcaneus and the proximal phalanges, maintains the shape and function of the longitudinal arch of the foot (Orchard, 2012; McKeon et al., 2015). When the medial longitudinal arch changes, the characteristics of the plantar fascia will change accordingly. At present, there are many reports on the characteristics of plantar fascia in flatfoot (Wang et al., 2019; Qian et al., 2021). However, to the authors' knowledge, the characteristics of the plantar fascia angle (the angle between the plantar fascia and horizontal line) in flatfoot have not been reported to date.

Previous studies have shown that the calcaneal pitch angle and the medial cuneiform height are effective diagnostic methods for flatfoot (Bock et al., 2018; Flores et al., 2019). Therefore, this study takes the calcaneal pitch angle measured from X-radiographs of the lateral weight-bearing foot as the diagnostic gold standard; the plantar fascia angle in patients with flatfoot was measured to explore the relationship between the plantar fascia angle and the diagnosis of flatfoot. The value of the plantar fascia angle in diagnosing flatfoot was evaluated by comparing it with the medial cuneiform height. It is hypothesized that the plantar fascia angle would be influenced by the height of the arch, and the plantar fascia angle would be an effective method for the diagnosis of flatfoot. The purpose of this study is to propose a non-invasive method for flatfoot diagnosis based on ultrasound.

Methods

Ethics statement

This study was based on the principles outlined in the Declaration of Helsinki, and was approved by the Ethics Committee of the Second Hospital of Jilin University (No.2020085). All volunteers who participated in the study signed a written informed consent agreement.

Patients

This is a prospective study. The sample size calculated by G-Power (Kang, 2021) was 22 when $\alpha = 0.05$, power = 0.95, based on pre-experiments. The inclusion criteria of the experimental group were: ①patients treated in the outpatient center of the



FIGURE 1
Position for ultrasound measurement of plantar fascia angle.

Second Hospital of Jilin University from April 2021 to December 2021; ② ages of the patients ≥ 18 years old; ③ the calcaneal pitch angle of the patients were less than 20° . Healthy adults with similar age, sex, height, and weight were selected as the control group. The exclusion criteria were: ① a history of foot trauma or surgery; ② a diagnosis of systemic disease, such as rheumatoid arthritis, diabetes, or gout; ③ a diagnosis of local disease, such as plantar fibromatosis.

Test device and procedure

A Wisonic ultrasonic scanner (Navis, Wisonic) was used in B mode to measure the plantar fascia angle. The linear transducer frequency was 10–2 MHz. During measurement, each subject lay prone on the examination bed, with the lower limbs straight and the feet hanging over the edge of the examination bed in a neutral position (Haen et al., 2017) (Figure 1). The upper body and legs were relaxed.

The probe was placed under the navicular and medial cuneiform along the long axis of the plantar fascia, and the mark point of the probe was towards to the calcaneus, so that the proximal end of plantar fascia could be presented on the left side of the ultrasound image. In this study, the sampling depth was 3 cm, and the mechanical index was 0.7. The probe was gently placed on the plantar surface and two-dimensional ultrasound images were taken.

After ultrasonic examination, X-radiography of the weight-bearing foot was performed by an experienced radiologist. The calcaneal pitch angle and medial cuneiform height were measured from the lateral X-radiograph (Figure 2A) by an experienced radiologist. The calcaneal pitch angle is the angle between a line drawn along the most inferior part of the calcaneus and the supporting surface. (Abousayed et al., 2017) The medial cuneiform height is the distance from the lowest point of medial cuneiform to the line that connect the lowest point of calcaneus and the lowest point of the sesamoids of the first metatarsal (Bock P, 2018). The plantar fascia angle (Figure 2B) is defined as the angle between the plantar fascia and the horizontal line (the line parallel to the probe and skin), which was measured by an experienced ultrasonographer, who was unknown to the results of X-Ray. The plantar fascia angle, calcaneal pitch angle, and medial cuneiform height were measured three times each, to ensure reproducibility.

Statistical analysis

The data were analyzed using IBM Statistical Package for the Social Sciences (SPSS) version 26.0 (SPSS Inc., IL). Continuous variables (age, height, weight, calcaneal pitch angle, plantar fascia angle, and medial cuneiform height) were expressed as mean \pm standard deviation. The χ^2 test was used to analyze differences between the sexes in the flatfoot and control groups. Firstly, intraclass correlation (ICC) analysis of plantar fascia angle, calcaneal pitch angle, and medial cuneiform height was conducted, and the 95% confidence intervals (95% CIs) and ICC values were calculated. Secondly, Pearson correlation analysis was conducted between the calcaneal pitch angle, plantar fascia angle, and medial cuneiform height. The absolute value of the Pearson correlation coefficient (r) was classified as poor (0.00 ± 0.20), fair (0.21 ± 0.40), moderate (0.41 ± 0.60), good (0.61 ± 0.80), or excellent (0.81 ± 1.00) (Landis JR, 1977). Thirdly, receiver operating characteristic (ROC) curves for all parameters were obtained to calculate sensitivity, specificity, area under the curve (AUC), and optimal cutoff value. The AUCs were compared using the Z test. Finally, sex, age, side (left or right) and PF (With or Without) were set as classification parameters to compare their influences on plantar fascia angle and medial cuneiform height. Statistical significance was considered for $p < 0.05$.

Results

Basic characteristics

51 patients with flatfoot and 43 healthy subjects were included in the study. Firstly, the basic characteristics of the two groups were compared and analyzed; the results are shown in

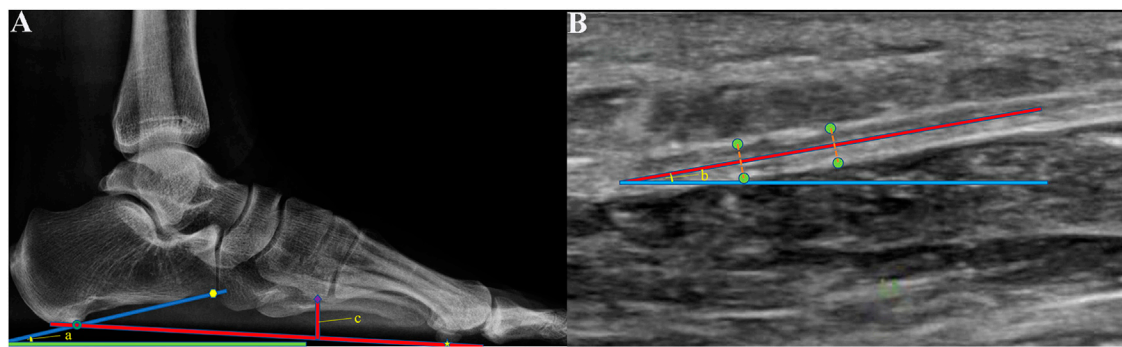


FIGURE 2

(A) Calcaneal pitch angle (angle a) and medial cuneiform height (c) were measured from X-radiographs of the weight-bearing foot. Calcaneal pitch angle is the angle between the supporting surface (green line) and the line (dark blue line) connected the lowest point of calcaneus (dark green circle) and the lowest point of the anterior edge of the calcaneus (yellow point). Medial cuneiform height is the distance from the lowest point of the medial cuneiform (the purple rhombic point) to the line that connected the lowest point of calcaneus (dark green circle) and the lowest point of the sesamoid under the first metatarsal (yellow five-point star). (B) Plantar fascia angle (angle b) was measured using B-mode ultrasound. It was defined as the angle between the middle line (red line) of the plantar fascia and the horizontal line (the blue line parallel to the probe and skin). The green points were the edge of the plantar fascia.

TABLE 1 Basic characteristics of flatfoot and control groups.

Basic characteristic	Flatfoot group	Control group	P
Sex (M/F)	23/28	24/19	0.301
Age (years)	39.81 ± 13.983	35.81 ± 13.162	0.161
Height (cm)	168.27 ± 7.228	169.21 ± 6.236	0.135
Weight (kg)	65.45 ± 10.473	65.02 ± 8.651	0.080

TABLE 2 Intraclass correlation (ICC) values and 95% confidence intervals (95% CIs) of the measured parameters.

Parameter	ICC	95% CI
Plantar fascia angle	0.973	(0.962, 0.981)
Calcaneal pitch angle	0.993	(0.989, 0.995)
Medial cuneiform height	0.982	(0.975, 0.988)

Table 1. The χ^2 test was used for sex comparison, and the independent sample *t* test was used for comparisons of age, height, and weight. Values of *p* are all greater than 0.05. That is, there was no statistical difference in sex, age, height, and weight between the flatfoot group and the control group.

Intraclass correlation analysis

Intraclass correlation analysis of plantar fascia angle, calcaneal pitch angle, and medial cuneiform height was conducted; the results are shown in Table 2. The ICC values

of the three parameters are all greater than 0.9; this indicates that the three parameters had good intra-observer reproducibility.

Pearson correlation analysis

Figure 3A is a scatter plot of medial cuneiform height with respect to calcaneal pitch angle for all subjects; Figure 3B is a scatter plot of plantar fascia angle with respect to calcaneal pitch angle for all subjects. There is a moderate correlation ($r = 0.51$, $p < 0.001$) between medial cuneiform height and calcaneal pitch angle; the correlation between plantar fascia angle and calcaneal pitch angle is excellent ($r = 0.85$, $p < 0.001$).

Diagnostic performance evaluation

The ROC curves for the medial cuneiform height and the plantar fascia angle are shown in Figure 4. The AUC for the medial cuneiform height is 0.775 (0.679–0.871); that for the plantar fascia angle is 0.973 (0.935–1.000). The optimal cutoff value, sensitivity, and specificity for the medial cuneiform height in flatfoot diagnosis are 12.8 mm, 93.0%, and 54.9%, respectively; the optimal cutoff value, sensitivity, and specificity for the plantar fascia angle in flatfoot diagnosis are 9.8°, 97.7%, and 94.1%, respectively. The results for the AUC were compared using the Z test. The AUC for the plantar fascia angle is more significant than that for the medial cuneiform height ($Z = 2.55$, $p = 0.0108$); this suggests that the plantar fascia angle has better diagnostic efficiency in the diagnosis of flatfoot. The AUC for the plantar fascia angle is not more statistically significant than that for the calcaneal pitch angle ($Z = 1.42$, $p = 0.1556$); this

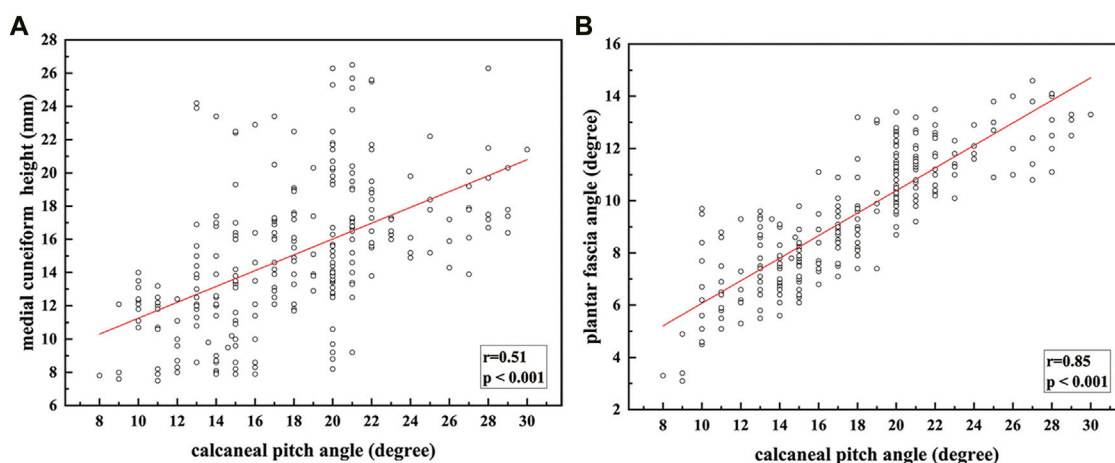


FIGURE 3

Fitting relationship between calcaneal pitch angle and: (A) medial cuneiform height; (B) plantar fascia angle.

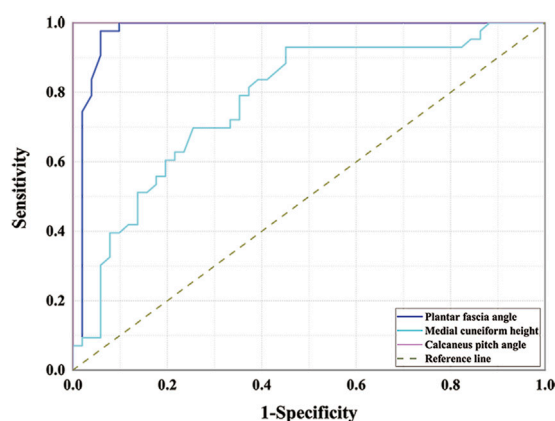


FIGURE 4

Receiver operating characteristic curves for medial cuneiform height and plantar fascia angle.

suggests that the plantar fascia angle has the same diagnostic efficiency as calcaneal pitch angle in the diagnosis of flatfoot.

Influences factors

The influences of sex, age, and side (left or right) on plantar fascia angle and medial cuneiform height are shown in Table 3. There was no difference in sex and side ($p > 0.05$), while statistical differences were found between groups of different ages in plantar fascia angle. Between subjects younger and older than 40 years, the value of p was 0.023. Between subjects younger and older than 50 years, the value of p was 0.001. These results show

that the plantar fascia angle is decreased for subjects older than 40 years.

The influence of PF was shown in Table 4. The results showed that the plantar fascia angle would not be influenced by PF both in the flatfoot group and the healthy control group.

Discussion

Flatfoot is a common foot disease, which can seriously affect the quality of life (Kohls-Gatzoulis et al., 2004; Wearing et al., 2006; Levinger et al., 2010; Van der Worp et al., 2011; Hamstra-Wright et al., 2015). At present, X-radiography of the weight-bearing foot is still the gold standard for the diagnosis of flatfoot (Abousayed et al., 2017). However, radiological diagnosis has led to a 600% increase in medical radiation exposure of the United States population (Lin et al., 2012). X-radiation is a known carcinogen that can cause malignancy (Prasarn, 2014), which can be accumulated (Giordano et al., 2009; Giordano et al., 2011; Taher et al., 2013). Thus, exploration of a nonionizing examination method is of great significance in the clinical field. In this study, ultrasound was used to measure the angle of the plantar fascia for the diagnosis of flatfoot. The calcaneal pitch angle measured from a lateral X-radiograph of the weight-bearing foot was used as a gold standard, and the diagnostic effect of the plantar fascia angle was studied and compared with the diagnostic efficiency of medial cuneiform height.

According to the results, there is no statistical difference in the basic characteristics between the flatfoot group and the control group ($p > 0.05$). Analysis of the measured results showed that the ICC values are all greater than 0.95, indicating that the values of the three parameters have good intra-observer reproducibility. Studies have also shown that the

TABLE 3 The influences of sex, age, side (left or right) on plantar fascia angle and medial cuneiform height.

Group		Plantar fascia angle (degree)	P	Medial cuneiform height (mm)	P
Sex	Female (47)	9.20 ± 2.30	0.197	14.33 ± 3.95	0.090
	Male (47)	9.81 ± 2.31		15.82 ± 4.47	
Side	Left (41)	9.78 ± 2.41	0.318	15.08 ± 3.71	0.982
	Right (53)	9.29 ± 2.24		15.06 ± 4.68	
Age	<30 y (31)	9.55 ± 2.13	0.889	15.04 ± 5.53	0.970
	≥30 y (63)	9.48 ± 2.42		15.08 ± 3.53	
	<40 y (52)	9.99 ± 2.09	0.023*	15.51 ± 4.61	0.269
	≥40 y (42)	8.90 ± 2.46		14.53 ± 3.77	
	<50 y (68)	10.00 ± 2.20	0.001*	15.35 ± 4.26	0.312
	≥50 y (26)	8.21 ± 2.14		14.35 ± 4.27	

*Difference was statistically significant.

TABLE 4 The influences of plantar fasciitis on plantar fascia angle.

Group		Plantar fascia angle (degree)	P
Flatfoot (51)	With PF (9)	8.09 ± 1.28	0.386
	Without PF (42)	7.77 ± 1.82	
Healthy Control (43)	With PF (5)	11.53 ± 0.75	0.903
	Without PF (38)	11.49 ± 1.26	

PF is the abbreviation of plantar fasciitis.

calcaneal pitch angle and the medial cuneiform height have a high degree of reliability between observers (Bock et al., 2018). Pearson correlation analysis was conducted between the medial cuneiform height, plantar fascia angle, and calcaneal pitch angle; the results show an excellent correlation between plantar fascia angle and calcaneal pitch angle ($r = 0.85$), better than that between medial cuneiform height and calcaneal pitch angle ($r = 0.51$).

In addition, the area under the ROC curve was used to test the diagnostic efficiency. The AUCs for the medial cuneiform height and plantar fascia angle are 0.775 and 0.973, respectively. Both of these measures have good diagnostic effect. The AUC for the plantar fascia angle is more significant than that for the medial cuneiform height ($Z = 2.55$, $p = 0.0108$); this suggests that the plantar fascia angle has better diagnostic efficiency in the diagnosis of flatfoot. The AUC for the plantar fascia angle is not more statistically significant than that for the calcaneal pitch angle ($Z = 1.42$, $p = 0.1556$); this suggests that the plantar fascia angle has the same diagnostic efficiency as calcaneal pitch angle in the diagnosis of flatfoot.

The sensitivity and specificity of the two methods for the diagnosis of flatfoot were calculated using the Youden index. The results show that the optimal cutoff value of plantar fascia angle to diagnose flatfoot is 9.8° ; that is, when the measured plantar fascia angle is less than 9.8° , a diagnosis of flatfoot is indicated.

The sensitivity and specificity of using this value to diagnose flatfoot are 97.7 and 94.1%, respectively. The optimal cutoff value of medial cuneiform height to diagnose flatfoot is 12.8 mm; that is, when the measured medial cuneiform height is less than 12.8 mm, flatfoot can be diagnosed. The sensitivity and specificity of using this value to diagnose flatfoot are 93.0 and 54.9%, respectively. The specificity of the plantar fascia angle is greater than that of medial cuneiform height. The specificity of the medial cuneiform height might be low because the medial cuneiform height is likely to be influenced by the varus and valgus of the foot.

The subject's sex and the side of the affected foot did not influence the results for plantar fascia and medial cuneiform height ($p > 0.05$). However, the plantar fascia angle was affected in subjects older than 40 years. The results show statistical differences in plantar fascia angle between groups of different ages. Between subjects younger and older than 40 years, the value of p was 0.023. Between subjects younger and older than 50 years, the value of p was 0.001. Tas and Cetin (Tas and Cetin, 2019) also report that age is a potential parameter that might affect the morphologies and mechanical properties of plantar muscles. Changes in morphology and mechanical properties of plantar muscles would influence the medial longitudinal arch, leading to a change in the plantar fascia angle. In addition, the results of the study showed that the plantar fascia angle was not affected by plantar fasciitis. It may be for the reason that the plantar fasciitis was always happened at the insertion portion of plantar fascia (Orchard, 2012), while the plantar fascia angle was measured at the portion of the plantar fascia under the navicular and medial cuneiform, so plantar fascia angle would not be influenced by plantar fasciitis.

Ultrasound is a good tool in disease diagnosis; it is convenient, low-cost, and nonionizing. In the diagnosis of flatfoot, the plantar fascia angle measured using B-mode ultrasound has good sensitivity and specificity, as well as good intra-observer reproducibility. At the same time, it

is portable and noninvasive; thus, it is more applicable in the diagnosis of flatfoot for disabled patients and children.

There are limitations in this study. Firstly, the flatfoot in this study was not graded according to severity. The role of plantar fascia angle in diagnosing the severity of flatfoot needs further study. Secondly, flatfoot can present different clinical manifestations, such as with or without hindfoot valgus, forefoot abduction, etc. (Hillstrom et al., 2013). These different clinical manifestations may influence the test results; this is to be considered in future work. Thirdly, the different conditions of the ankle/foot in X-ray (weight-bearing) and ultrasound (non-weight-bearing) would be a limitation for this study. However, even under the condition of non-weight-bearing, the plantar fascia angle still showed significant statistical difference between flatfoot ($7.83 + 1.74^\circ$) and the healthy control ($11.49 + 1.21^\circ$), $p < 0.001$; In addition, the plantar fascia angle showed an excellent correlation with calcaneal pitch angle and the sensitivity and specificity in diagnosing flatfoot is also excellent.

Conclusion

Plantar fascia angle has an excellent sensitivity and specificity in diagnosing flatfoot, and there is good intra-observer reproducibility within this study, thus, it could seem to be an effective method to diagnose flatfoot, especially when it was used for flatfoot screening. However, further studies in larger populations with different flatfoot grades and different clinical manifestations are warranted to confirm these promising results.

Data availability statement

The original contributions presented in the study are included in the article/supplementary material, further inquiries can be directed to the corresponding authors.

References

- Abousayed, M. M., Alley, M. C., Shakked, R., and Rosenbaum, A. J. (2017). Adult-Acquired flatfoot deformity. *JBS Rev.* 5, e7. doi:10.2106/jbjs.Rvw.16.00116
- Arnoldner, M. A., Gruber, M., Syre, S., Kristen, K. H., Trnka, H. J., Kainberger, F., et al. (2015). Imaging of posterior tibial tendon dysfunction--Comparison of high-resolution ultrasound and 3T MRI. *Eur. J. Radiol.* 84, 1777–1781. doi:10.1016/j.ejrad.2015.05.021
- Bock, P., Pittermann, M., Chraim, M., and Rois, S. (2018). The inter- and intraobserver reliability for the radiological parameters of flatfoot, before and after surgery. *Bone Jt. J.* 100, 596–602. doi:10.1302/0301-620x.100b5.bjj-2017-1279
- Chan, J. Y., Greenfield, S. T., Soukup, D. S., Do, H. T., Deland, J. T., and Ellis, S. J. (2015). Contribution of lateral column lengthening to correction of forefoot

Ethics statement

The studies involving human participants were reviewed and approved by the Ethics Committee of the Second Hospital of Jilin University. The patients/participants provided their written informed consent to participate in this study.

Author contributions

ZJ was responsible for the experiments and manuscript preparation. QZ participated in measurement of data. LR and ZQ worked as supervisors for all procedures.

Funding

This research was supported by the project of National Natural Science Foundation of China (No. 52175270, 52005209), the Project of Scientific and Technological Development Plan of Jilin Province (No.20220508130RC), the Key Project of the National Natural Science Foundation of China (No.91848204), and the Interdisciplinary Research Funding Program for Doctoral Students of Jilin University (No. 101832020DJX049).

Conflict of interest

The authors declare that the research was conducted in the absence of any commercial or financial relationships that could be construed as a potential conflict of interest.

Publisher's note

All claims expressed in this article are solely those of the authors and do not necessarily represent those of their affiliated organizations, or those of the publisher, the editors and the reviewers. Any product that may be evaluated in this article, or claim that may be made by its manufacturer, is not guaranteed or endorsed by the publisher.

abduction in stage IIb adult acquired flatfoot deformity reconstruction. *Foot Ankle Int.* 36, 1400–1411. doi:10.1177/1071100715596607

Deland, J. T. (2008). Adult-acquired flatfoot deformity. *J. Am. Acad. Orthop. Surg.* 16, 399–406. doi:10.5435/00124635-200807000-00005

Flores, D. V., Mejia Gomez, C., Fernandez Hernando, M., Davis, M. A., and Pathria, M. N. (2019). Adult acquired flatfoot deformity: Anatomy, biomechanics, staging, and imaging findings. *Radiographics* 39, 1437–1460. doi:10.1148/rg.2019190046

Giordano, B. D., Rehtine, G. R., 2nd and Morgan, T. L. (2009). Minimally invasive surgery and radiation exposure. *J. Neurosurg. Spine* 11, 375–376. doi:10.3171/2009.2.spine09181

- Giordano, B. D., Grauer, J. N., Miller, C. P., Morgan, T. L., Reichtine, G. R., and 2nd (2011). Radiation exposure issues in orthopaedics. *J. Bone Jt. Surg.* 93, e69–10. doi:10.2106/JBJS.J.01328
- Haen, T. X., Roux, A., Soubeyrand, M., and Laporte, S. (2017). Shear waves elastography for assessment of human achilles tendon's biomechanical properties: An experimental study. *J. Mech. Behav. Biomed. Mater.* 69, 178–184. doi:10.1016/j.jmbm.2017.01.007
- Hamstra-Wright, K. L., Bliven, K. C., and Bay, C. (2015). Risk factors for medial tibial stress syndrome in physically active individuals such as runners and military personnel: A systematic review and meta-analysis. *Br. J. Sports Med.* 49, 362–369. doi:10.1136/bjsports-2014-093462
- Harish, S., Kumbhare, D., O'Neill, J., and Popowich, T. (2008). Comparison of sonography and magnetic resonance imaging for spring ligament abnormalities: Preliminary study. *J. Ultrasound Med.* 27, 1145–1152. doi:10.7863/jum.2008.27.8.1145
- Hillstrom, H. J., Song, J., Kraszewski, A. P., Hafer, J. F., Mootanah, R., Dufour, A. B., et al. (2013). Foot type biomechanics part 1: Structure and function of the asymptomatic foot. *Gait Posture* 37, 445–451. doi:10.1016/j.gaitpost.2012.09.007
- Kang, H. (2021). Sample size determination and power analysis using the G*Power software. *J. Educ. Eval. Health Prof.* 18, 17. doi:10.3352/jeehp.2021.18.17
- Kohls-Gatzoulis, J., Angel, J. C., Singh, D., Haddad, F., Livingstone, J., and Berry, G. (2004). Tibialis posterior dysfunction: A common and treatable cause of adult acquired flatfoot. *BMJ* 329, 1328–1333. doi:10.1136/bmj.329.7478.1328
- Landis, K. G., Jr, and Koch, G. G. (1977). The measurement of observer agreement for categorical data. *Biometrics* 33, 159–174. doi:10.2307/2529310
- Levinger, P., Murley, G. S., Barton, C. J., Cotchett, M. P., Mcsweeney, S. R., and Menz, H. B. (2010). A comparison of foot kinematics in people with normal- and flat-arched feet using the Oxford Foot Model. *Gait Posture* 32, 519–523. doi:10.1016/j.gaitpost.2010.07.013
- Linnet, M. S., Slovis, T. L., Miller, D. L., Kleinerman, R., Lee, C., Rajaraman, P., et al. (2012). Cancer risks associated with external radiation from diagnostic imaging procedures. *CA A Cancer J. Clin.* 62, 75–100. doi:10.3322/caac.21132
- Lopez-Lopez, D., Vilar-Fernandez, J. M., Barros-Garcia, G., Losa-Iglesias, M. E., Palomo-Lopez, P., Becerro-De-Bengoa-Vallejo, R., et al. (2018). Foot arch height and quality of life in adults: A strobe observational study. *Int. J. Environ. Res. Public Health* 15, 1555. doi:10.3390/ijerph15071555
- Mckee, P. O., Hertel, J., Bramble, D., and Davis, I. (2015). The foot core system: A new paradigm for understanding intrinsic foot muscle function. *Br. J. Sports Med.* 49, 290. doi:10.1136/bjsports-2013-092690
- Oleksy, Ł., Mika, A., Łukomska-Górny, A., and Marchewka, A. (2010). Intrarater reliability of the Foot Posture Index (FPI-6) applied as a tool in foot assessment in children and adolescents. *Med. Rehabil.* 14, 18–28.
- Orchard, J. (2012). Plantar fasciitis. *BMJ* 345, e6603. doi:10.1136/bmj.e6603
- Pehlivan, O., Cilli, F., Mahiroglu, M., Karabudak, O., and Koksak, O. (2009). Radiographic correlation of symptomatic and asymptomatic flexible flatfoot in young male adults. *Int. Orthop.* 33, 447–450. doi:10.1007/s00264-007-0508-5
- Prasarn, M. L. (2014). Commentary on: Intraoperative fluoroscopy, portable X-ray, and CT: Patient and operating room personnel radiation exposure in spinal surgery. *Spine J.* 14, 2992–2994. doi:10.1016/j.spinee.2014.07.006
- Qian, Z., Jiang, Z., Wu, J., Chang, F., Liu, J., Ren, L., et al. (2021). Morphology and mechanical properties of plantar fascia in flexible flatfoot: A noninvasive *in vivo* study. *Front. Bioeng. Biotechnol.* 9, 727940. doi:10.3389/fbioe.2021.727940
- Romero-Morales, C., Martin-Llantino, P. J., Calvo-Lobo, C., Palomo-Lopez, P., Lopez-Lopez, D., Pareja-Galeano, H., et al. (2019). Comparison of the sonographic features of the achilles tendon complex in patients with and without achilles tendinopathy: A case-control study. *Phys. Ther. Sport* 35, 122–126. doi:10.1016/j.ptsp.2018.12.003
- Romero-Morales, C., Bravo-Aguilar, M., Ruiz-Ruiz, B., Almazan-Polo, J., Lopez-Lopez, D., Blanco-Morales, M., et al. (2021). Current advances and research in ultrasound imaging to the assessment and management of musculoskeletal disorders. *Dis. Mon.* 67, 101050. doi:10.1016/j.disamonth.2020.101050
- Schillizzi, G., Alviti, F., D'Ercole, C., Elia, D., Agostini, F., Mangone, M., et al. (2020). Evaluation of plantar fasciopathy shear wave elastography: A comparison between patients and healthy subjects. *J. Ultrasound* 24, 417–422. doi:10.1007/s40477-020-00474-7
- Shibuya, N., Jupiter, D. C., Ciliberti, L. J., Vanburen, V., and La Fontaine, J. (2010). Characteristics of adult flatfoot in the United States. *J. Foot Ankle Surg.* 49, 363–368. doi:10.1053/j.jfas.2010.04.001
- Sung, P. S. (2016). The ground reaction force thresholds for detecting postural stability in participants with and without flat foot. *J. Biomech.* 49, 60–65. doi:10.1016/j.jbiomech.2015.11.004
- Taher, F., Hughes, A. P., Sama, A. A., Zeldin, R., Schneider, R., Holodny, E. I., et al. (2013). 2013 young investigator award winner: How safe is lateral lumbar interbody fusion for the surgeon? A prospective *in vivo* radiation exposure study. *Spine* 38, 1386–1392. doi:10.1097/BRS.0b013e31828705ad
- Tas, S., and Cetin, A. (2019). An investigation of the relationship between plantar pressure distribution and the morphologic and mechanic properties of the intrinsic foot muscles and plantar fascia. *Gait Posture* 72, 217–221. doi:10.1016/j.gaitpost.2019.06.021
- Van Der Worp, H., Van Ark, M., Roerink, S., Pepping, G. J., Van Den Akker-Scheek, I., and Zwerver, J. (2011). Risk factors for patellar tendinopathy: A systematic review of the literature. *Br. J. Sports Med.* 45, 446–452. doi:10.1136/bjsm.2011.084079
- Wang, K., Liu, J., Wu, J., Qian, Z., Ren, L., and Ren, L. (2019). Noninvasive *in vivo* study of the morphology and mechanical properties of plantar fascia based on ultrasound. *IEEE Access* 7, 53641–53649. doi:10.1109/access.2019.2909409
- Wearing, S. C., Smeathers, J. E., Urry, S. R., Hennig, E. M., and Hills, A. P. (2006). The pathomechanics of plantar fasciitis. *Sports Med.* 36, 585–611. doi:10.2165/00007256-200636070-00004
- Younger, A. S., Sawatzky, B., and Dryden, P. (2005). Radiographic assessment of adult flatfoot. *Foot Ankle Int.* 26, 820–825. doi:10.1177/107110070502601006



Validation of an MRI Technique for the 6-DOF Knee Kinematics Measurement

Shixiong Tang^{1,2}, Liwen Zheng^{3*}, Yongheng Luo¹, Ren Wu⁴, Qunyan Tian⁴ and Lei Wang⁵

¹Department of Radiology, The Second Xiangya Hospital, Central South University, Changsha, China, ²Clinical Research Center for Medical Imaging in Hunan Province, Changsha, China, ³Department of Rehabilitation, The Second Xiangya Hospital, Central South University, Changsha, China, ⁴Department of Orthopedics, The Second Xiangya Hospital, Central South University, Changsha, China, ⁵School of Information Science and Engineering, Central South University, Changsha, China

OPEN ACCESS

Edited by:

Suvash C. Saha,
University of Technology Sydney,
Australia

Reviewed by:

Björn Rath,
Klinikum Wels-Grieskirchen, Austria
Md. Mamun Molla,
North South University, Bangladesh

*Correspondence:

Liwen Zheng
zhengliwen@csu.edu.cn

Specialty section:

This article was submitted to
Biomechanics,
a section of the journal
Frontiers in Bioengineering and
Biotechnology

Received: 25 March 2022

Accepted: 09 June 2022

Published: 14 September 2022

Citation:

Tang S, Zheng L, Luo Y, Wu R, Tian Q
and Wang L (2022) Validation of an
MRI Technique for the 6-DOF Knee
Kinematics Measurement.
Front. Bioeng. Biotechnol. 10:904012.
doi: 10.3389/fbioe.2022.904012

Background: For total knee arthroplasty (TKA), the optimal rotational position of the femoral component is felt to be critically important. The current knee joint kinematics measurement technology is unable to identify the exact rotation axis of the knee joint, the main reasons being low measurement accuracy and insufficient three-dimensional data (2D-3D image matching technology). In order to improve the effect of TKA surgery, we proposed a knee joint kinematics measurement method, based on the MRI technology, and verified its measurement accuracy. We then employed this method to identify the personalized optimal rotation axis of the knee joint for TKA patients.

Purposes: The purpose of the study was 1) to propose a method for measuring knee joint kinematics and verify its accuracy and 2) to propose a method for determining the optimal rotation axis of knee joint for TKA surgery, based on accurate kinematic measurement results.

Materials and Methods: The experiment was divided into two parts: *in vitro* and *in vivo*. The purpose of the *in vitro* experiment was to verify the measurement accuracy of our method. We fixed two aquarium stones (approximately 10 cm * 10 cm * 10 cm in size, close to the size of the distal femur and proximal tibia) firmly on the fixed and moving arms of the goniometer/vernier caliper with glue and immersed the aquarium stones in the water to capture MRI images. The MRI images were then processed with MATLAB software, and the relative motion of the two aquarium stones was measured. The measurement accuracy of our method was verified via the scale reading of the moving arm on the goniometer/vernier caliper. *In vivo*, 36 healthy elderly participants (22 females, 14 males) were recruited from the local community; our method was then employed to measure the relative motion of the tibia and femur and to observe the rollback and screw home motion of the medial/lateral condyle of the femur, which was identified as specific kinematic features of the knee joint.

Results: *In vitro*, all measurements were accurate to <1 mm and <1°. *In vivo*, all knee measurements showed rollback motion (the rollback distance of the medial femoral condyle was 18.1 ± 3.7 mm and that of the lateral condyle was 31.1 ± 7.3 mm) and screw home motion.

Conclusion: In the application scenario of knee joint kinematics measurement, our method has an accuracy of $<1^\circ$ of rotation angle and <1 mm of translation for all reference points, and it can be employed to identify the most stable axis of the knee joint.

Significance: Using our method to accumulate data on the knee rotation axis of more subjects to establish an average rotation axis of a given population may help in knee prosthesis design and reduce the patient dissatisfaction rate. Individually measuring the patient's rotation axis before TKA surgery and adjusting the prosthesis installation in TKA may further reduce the patient dissatisfaction rate, and automatic computer measurement may be realized in the future, but it is still time-consuming for now.

Keywords: total knee arthroplasty, knee joint kinematics, prosthesis design, characteristic area, characteristic area frame, subcortical vascular segment, most stable rotation axis

INTRODUCTION

Total knee arthroplasty (TKA) is a commonly used surgery that treats end-stage osteoarthritis (OA). It is estimated that by 2030, the number of patients undergoing TKA in the United States will reach 3.5 million every year (Kurtz et al., 2007). So far, 8%–25% of patients undergoing TKA are dissatisfied with the outcome of the

surgery (Justin et al., 2012; Baker et al., 2013; Dunbar et al., 2013; Schulze and Scharf, 2013). In order to improve the efficacy of the surgery, researchers performed numerous kinematics researches, in recent decades, focusing on the rotation axis, which is felt to be critically important for TKA, and the design of the knee joint prosthesis components depends on the assumption of the correct rotational axis.

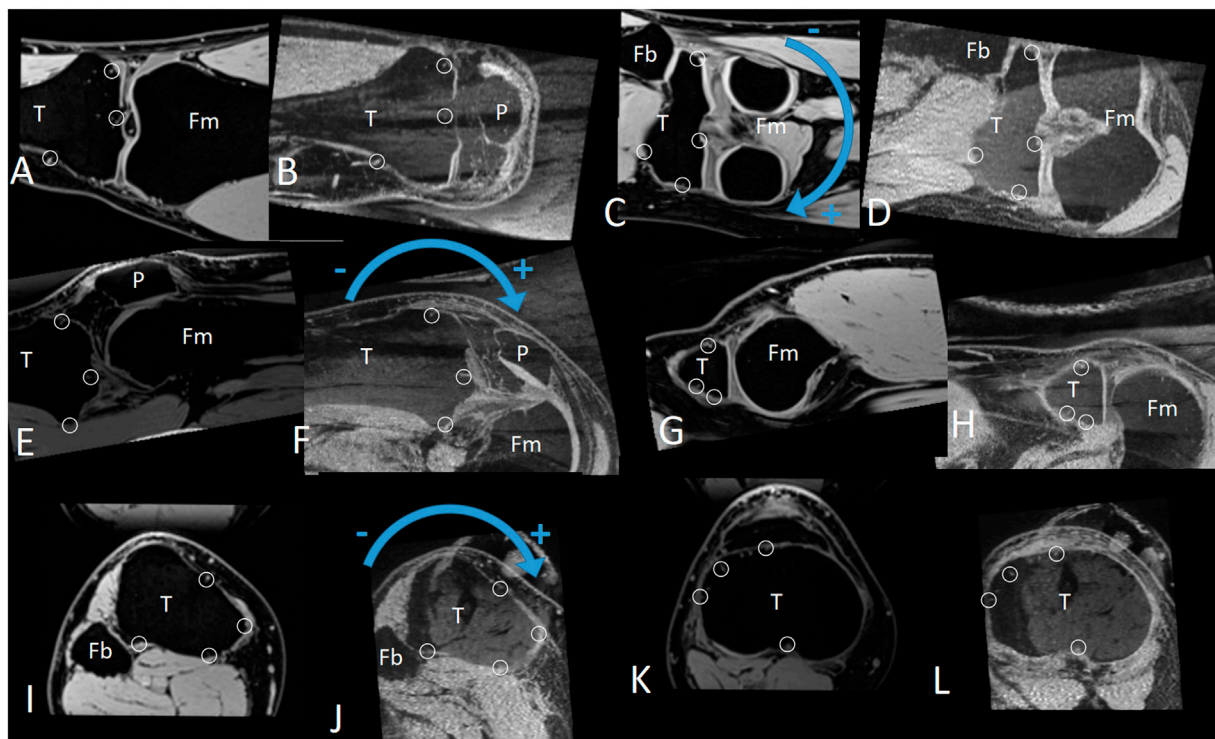
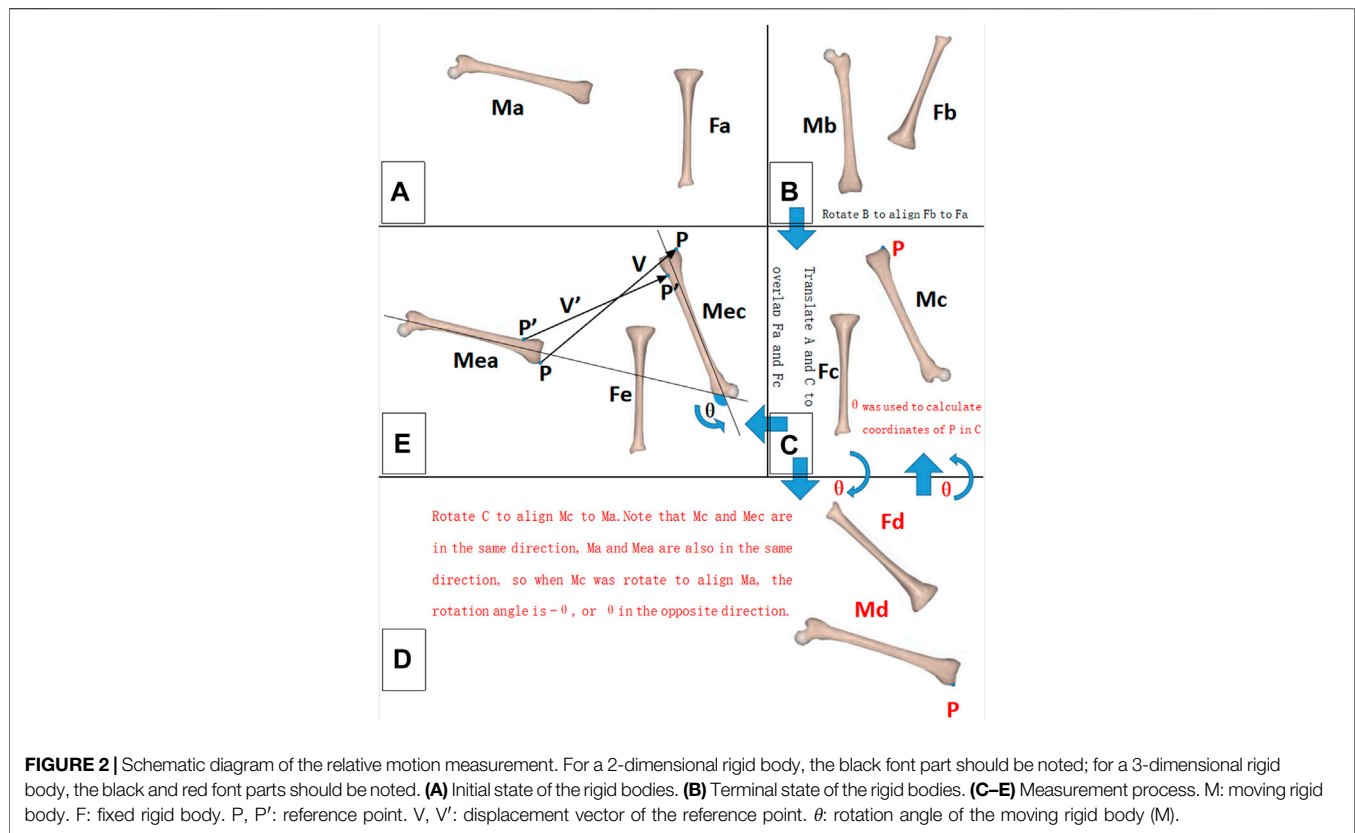


FIGURE 1 | The positive and negative directions of the coronal, sagittal, and horizontal plane rotation, as well as the characteristic area frame (CAF, composed by multiple characteristic areas). (A–D) Coronal plane. (E–H) Sagittal plane. (I–L) Horizontal plane. Small circles: Subcortical vascular segment (SCVS) selected as the characteristic area. T: tibia. P: patella. Fm: femur. Fb: fibula.



To accurately locate the rotation axis, a simple and effective method for describing the relative motion between the femur and tibia is required. It is easy to imagine that the relative motion of two rigid bodies refers to the change of orientation and displacement of one body (the moving rigid body, the femur is used as the moving rigid body in this experiment) at different time points, with the other body (the fixed rigid body, the tibia is regarded as the fixed rigid body in this experiment) as a reference. In the actual measurement, the mutual position of the two rigid bodies at a certain moment can be defined as the initial state of motion (in this study, the knee joint was extended as the initial state), and one or more terminal states of motion can be determined (different angles of knee joint flexion), then the orientation and displacement changes of the moving rigid body (femur) can be measured in each terminal state, relative to the initial state, and thus, these changes can be quantitatively described. In recent studies, researchers generally described knee kinematics using 6 degrees of freedom (DOF) (Li et al., 2009; Fitzpatrick et al., 2016; Guan et al., 2017; Sta et al., 2021). Although the details of these descriptions differ, the principle of the rigid body rotation with 3 DOF (3 rotation directions in 3-dimensional space) and rigid body displacement with the other 3 DOF (3 coordinate axes in 3-dimensional space) remain the same. Reddy et al. established a description method of 6-DOF. They believed that the most important aspect was to determine the 3 rotational DOF. Upon determining the rotation angle, the

measurement and calculation of the 3 translational DOF would be very simple (Reddy et al., 1989).

In addition to the describing method, the precise recording of the moving process is also critical. In order to examine the rotation axis, many studies selected the contact point (Mohsen et al., 2016; Cacciola et al., 2020; Takashi and Mochizuki, 2021) or reference point (Meneghini et al., 2017) to be the measurement object. Freeman and Pinskerova (2005) believed that the contact points are not suitable for analyzing the axis of rotation, because they do not define a point in the femur. Skin sensor (Schache et al., 2006; Van Campen et al., 2011) has low accuracy due to soft tissue movement (Dennis et al., 2005; Freeman and Pinskerova, 2005; Beach et al., 2019). In addition, there are substantial individual differences in the measurement of bony eminence (Şahin et al., 2013).

In addition, non-invasive measurement methods are more easily accepted by patients and applied in the clinic. For example, the cortical bone screw has high accuracy, but it is invasive (Ramsey and Wretenberg, 1999), so it is generally used only in cadaver studies. Imaging examinations (X-ray, CT, MRI) are non-invasive, but the radiation dose of CT is relatively large. In the scenario of kinematic measurement that requires repeated CT scans of the knee joint, the potential health risks of experimental subjects/clinical patients are particularly worrying. X-ray is less radioactive, and 2D-3D image matching technique is developed, based on X-ray fluoroscopy, whose accuracy is very high (Giphart et al., 2012; Kono et al.,

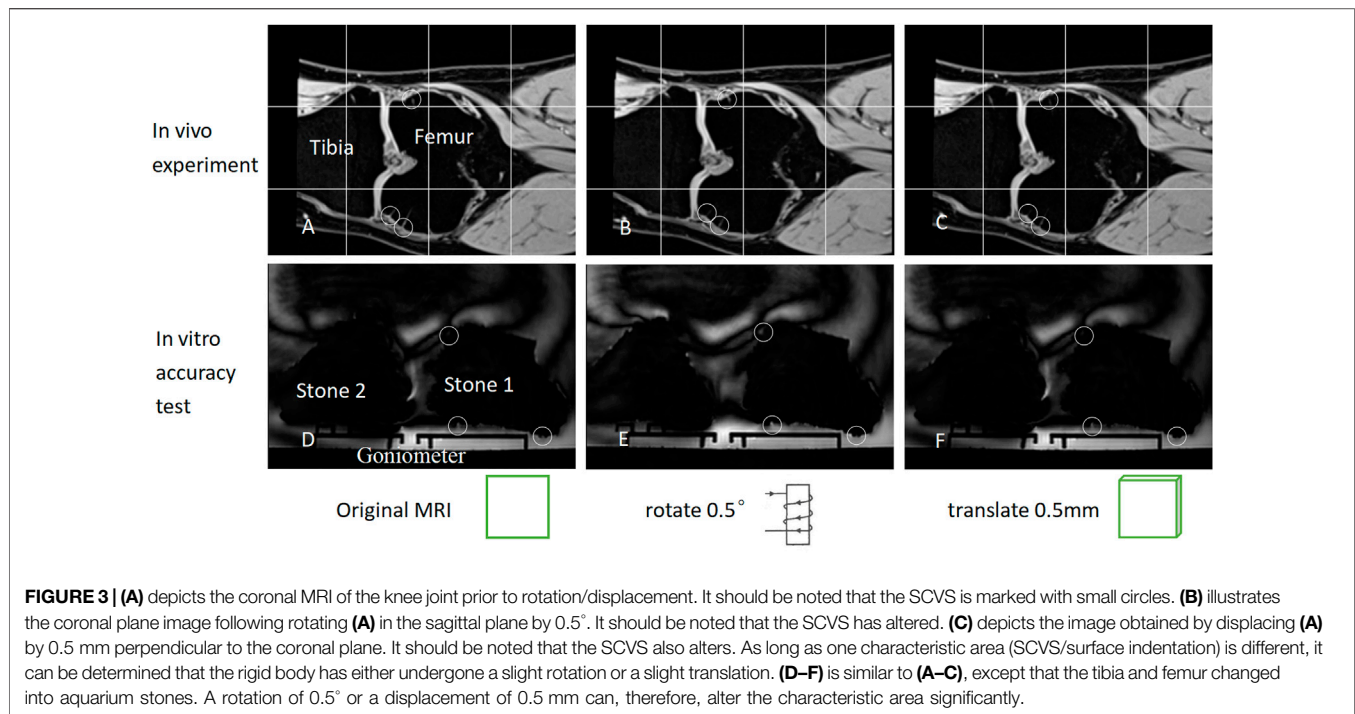


FIGURE 3 | (A) depicts the coronal MRI of the knee joint prior to rotation/displacement. It should be noted that the SCVS is marked with small circles. (B) illustrates the coronal plane image following rotating (A) in the sagittal plane by 0.5° . It should be noted that the SCVS has altered. (C) depicts the image obtained by displacing (A) by 0.5 mm perpendicular to the coronal plane. It should be noted that the SCVS also alters. As long as one characteristic area (SCVS/surface indentation) is different, it can be determined that the rigid body has either undergone a slight rotation or a slight translation. (D–F) is similar to (A–C), except that the tibia and femur changed into aquarium stones. A rotation of 0.5° or a displacement of 0.5 mm can, therefore, alter the characteristic area significantly.

2018). But they have a common deficiency: Only the reference points with local features (e.g., metal beads and contact points.) can be tested to validate the translation accuracy (Yamazaki et al., 2015; Shih et al., 2020). It cannot validate the translation accuracy of other reference points without local features. This deficiency can be made up for with weight-bearing MRI techniques, which are less popular but still an active research area (Bruno et al., 2018). Some researchers employed MRI to measure the knee joint kinematics (Hollister et al., 1993; Scarvell et al., 2004; Park et al., 2014; Dzialo et al., 2018; Yu et al., 2021) but the accuracy was not very good. We believe that the main obstacle is the lack of a reference object that can be accurately measured and widely used. The main innovation of our study is the use of the subcortical vascular segment (SCVS) as the universal reference. We use multiple (6–8 each in sagittal plane/coronal plane/horizontal plane, 18–24 in total) SCVS to create a large (length/width/height > 4 cm) characteristic area frame (CAF), which is then used to locate the reference points on the femur/the tibia. Because of their small size and distinctive features, SCVS are more accurately located than traditional anatomical markers, such as tibial tubercle.

Our purpose is 2-fold: 1) To propose an MRI-based non-invasive *in vivo* knee kinematics measurement method and to verify its measurement accuracy; 2) to describe a method for determining the optimal rotation axis of knee joint for TKA surgery, based on accurate kinematic measurement results, and discuss the logic of this method. Our assumption is that the measurement accuracy of this kinematics measurement method is <1 mm and $<1^\circ$.

MATERIALS AND METHODS

This study employed the geometric center axis (GCA) coordinate system (Most et al., 2004; Eckhoff et al., 2007; Iranpour et al., 2010; Van Campen et al., 2011). The 3-dimensional rotation of the bone was described by the Carden angle (Tupling and Pierrynowski, 1987). The rotational order was: sagittal plane to horizontal plane to coronal plane. The rotation unit was degree, with positive numbers representing backward/internal rotation/valgus, and negative numbers representing forward/external rotation/varus (Figure 1).

Principles of Measurement and Description for Relative Motion

To help understand our method of measuring relative motion, let's first look at the case of a 2-dimensional rigid body (Figure 2, black text). The relative motion between the fixed rigid body F and moving rigid body M can be described *via* two parameters: 1) the rotation angle θ of M 2) the displacement vector V of any reference point P on M. Since the entire 2-dimensional rigid body can be easily visualized to the image, we can measure the rotation angle θ and the displacement vector V directly on the image. Obviously, V is different for different reference points P. If the displacement parameter V of P is measured, the displacement parameter V' of any other reference point P' can be calculated by using relative position P'-P (Eq. 1).



FIGURE 4 | There are many small indentations on the surface of the aquarium stones (small red circles). In their MRI image, those indentations that meet the CAF standard are used as characteristic areas, to improve the measurement accuracy.

$$V' = (P' - P) \begin{bmatrix} \cos \theta & -\sin \theta \\ \sin \theta & \cos \theta \end{bmatrix} + V \quad (1)$$

The situation of a 3-dimensional rigid body is similar to that of a 2-dimensional rigid body, except for one troublesome aspect, we cannot see the full picture of a 3-dimensional rigid body in MRI images, so we cannot measure θ and V directly as we can with a 2-dimensional rigid body. We solved this problem by noting that Mea and Ma are in the same direction and Mec and Mc are in the same direction. As long as we rotated A so that Ma and Mc were in the same direction, the rotation operation would be equivalent to θ , or if we rotated C so that Mc was in the same direction as Ma , this rotation operation would be equivalent to $-\theta$ (Figure 2, red text section). The measurer tried different rotation operations. Given the directions of Ma and Mc are in the same direction, the current rotation operation will be the measurement result of θ . The measurement accuracy of this method depended on the accurate determination that Ma faced the same direction as Mc after the rotation operation. To improve the accuracy, we innovatively proposed the concept of the CAF (composed by multiple SCVS) as a tool to confirm the same direction of two identical rigid bodies (Figure 1). After determining θ , V can be directly measured, because after the θ rotation operation (with P as the rotation center) the CAF of Mea is parallel with the CAF of Mec (on MRI images the 2 CAFs are identical), so V is the positional difference between the two parallel CAFs. The displacement parameter V' of any other reference point P' was then calculated using Eq. 2. In other words, only V was measured. Hence, all V' was calculated. The measurement accuracies of V and V' were tested separately, as described in the “*In vitro* measurement accuracy test” section.

$$V' = (P' - P)RxRyRz + V,$$

where

$$Rx = \begin{bmatrix} 1 & 0 & 0 \\ 0 & \cos a & -\sin a \\ 0 & \sin a & \cos a \end{bmatrix}$$

$$Ry = \begin{bmatrix} \cos b & 0 & \sin b \\ 0 & 1 & 0 \\ -\sin b & 0 & \cos b \end{bmatrix}$$

$$Rz = \begin{bmatrix} \cos c & -\sin c & 0 \\ \sin c & \cos c & 0 \\ 0 & 0 & 1 \end{bmatrix}$$

$$RxRyRz = \begin{bmatrix} \cos b \cos c & \sin a \sin b \cos c + \cos a \sin c & -\sin b \cos a \cos c + \sin a \sin c \\ -\sin c \cos b & \cos a \cos c - \sin a \sin b \sin c & \cos a \sin b \sin c + \sin a \cos c \\ \sin b & -\sin a \cos b & \cos a \cos b \end{bmatrix}, \quad (2)$$

$$\theta = [a, b, c]$$

Regarding Eq. 2, the rotation matrix in our formula was the same as in the study of Reddy et al. (1989). We divided the rotation matrix into three matrices, representing the rotation of the sagittal, coronal, and horizontal planes. This did not affect the calculation results; however, it made the formula more readable.

In the 3-dimensional situation, θ and V had 3 parameters each, for a total of 6 DOF. Although P also had 3 parameters, P was determined by V using Eq. 2, so the parameters of P were not free. In other words, the method we used to describe relative motion had 6 DOF.

***In Vitro* Measurement Accuracy Test**

Since the CAF (Figure 1) generally has a significant impact on measurement accuracy, we set a unified standard for it in this study: 1) The length/width of each characteristic area (SCVS/surface indentation of aquarium stones) was ≤ 5 pixels (2.5 mm); 2) The characteristic areas were distributed in two different MRI planes, with ≥ 80 layers (4 cm) interval between the planes in the direction of each coordinate axis; and 3) When comparing the similarity between the CAF of both rigid bodies, each characteristic area as well as the interval between the layers where the characteristic area was located were made the same. Under such a standard, CAF is sensitive to a small rotation of the rigid body, and a 0.5° deflection in the direction of the rigid body can cause a visible change in the CAF (Figure 3). If the same CAF can be found on two rigid bodies, it means that the two rigid bodies are identical and have little difference in direction. Therefore, depending on CAF, it can be determined that the direction of the moving rigid body in the terminal state after rotation is the same as that of the moving rigid body in the initial state, thus accurately measuring the rotation parameter θ (as described in the “Principles of measurement and description for relative motion” section mentioned earlier). Similarly, the standardized CAF is also sensitive to a small displacement of the rigid body. In fact, 0.5 mm displacement of the rigid body can cause a significant alteration in CAF (Figure 3), so the displacement parameter V can also be accurately measured.

A two-arm goniometer was used to measure rotation angle, and a vernier caliper represented the length. The angle and length were measured and tested on the sagittal, coronal, and horizontal planes.

Aquarium stones (approximately 10 cm * 10 cm * 10 cm in size, close to the size of the distal femur and proximal tibia) were employed as the rigid bodies to be examined. The exact size of aquarium stones was unknown and their shape was not regular,

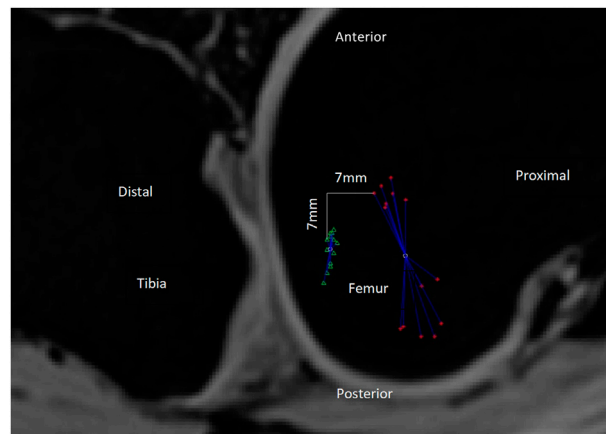


FIGURE 5 | PC value is the standard deviation of the distances between the reference point's trajectory coordinates and the average coordinate. As shown in the figure, the green triangle's trajectory is more gathered than that of the red asterisk, so the PC value of the green triangle should be less than that of the red asterisk. The actual calculation result of the PC value is indeed the case [13.7 mm (red asterisk) and 4.5 mm (green triangle), respectively]. The smaller the PC value, the more gathered is the trajectory and the more stable is the reference point during the 0–130° knee flexion. In this Figure 2D distances are used as an illustration, but in the actual experiment, 3D distances are used to calculate the PC value. Red asterisk: the trajectory of the medial condyle of TEA. Green triangle: the trajectory of the reference point 7 mm distal and posterior to the medial condyle of TEA. White circles: there are two white circles, representing the average position of the red asterisk and the green triangle, respectively. Blue line segments: each line segment represents the distance between a reference point coordinate and the average position of all coordinates.

but this did not affect the measurement of the relative motion between the stones, using our method, much like the irregular shape of the tibia and femur. There are a lot of small indentations on the surface of the aquarium stones, which can be used as a measurement reference like SCVS (**Figure 4**). We employed glue to firmly fix the two aquarium stones on the moving and fixed arms of the goniometer/vernier caliper. The stones have a low signal on MRI. During MRI examination, we soaked it in water, so that the indentations on the surface of aquarium stones were clearly visualized on MRI. These indentations simulated knee joint SCVS in MRI images and played the role of the characteristic area, to improve measurement accuracy.

The parameter settings of the MRI examination were the same as the “*In vivo* experiments” described as follows. An MRI image was captured at the initial motion state of the goniometer 0°/vernier caliper 0 mm (**Figure 2A**). Next, the moving arm of the goniometer/vernier caliper was moved to different target scales and MRI images were captured again (terminal state of motion, **Figure 2B**). The relative motion of the 3-dimensional rigid body was measured using the method described in the “Principle of measurement and description for relative motion” section, and the measurement results were subtracted from the scale of the goniometer/vernier caliper to obtain measurement accuracy.

During the test, the rotation measurement accuracy of the entire rigid body was first tested. Since the knee joint flexion angle generally does not exceed 150°, we tested multiple rotation angles within 150°. Next, the displacement measurement accuracy of the reference points at different positions was tested. First, a reference point P was randomly selected in the area near the center and inside the aquarium, stones to measure its displacement parameter V, to test the displacement measurement accuracy of this reference point P. Then, the displacement measurement

accuracy of all reference points within a certain range around P (these reference points can be anywhere near P, represented by P') was tested. Because the size of the skeletal portion of the knee joint is generally no larger than 10 cm * 10 cm * 10 cm, if P is in the center of the knee joint, it is enough to test the displacement accuracy of the reference point P' within 5 cm around P. Since the reference point P randomly selected during the actual measurement may not be the exact center of the knee joint, to ensure that the validation range includes the entire proximal tibia and distal femur, we extended the test range and tested the displacement accuracy of all reference points P' within the range of 7 cm around P with 1 cm intervals. (3-dimensional cube grids of 14 cm * 14 cm * 14 cm, grid spacing of 1 cm, and grid intersections were regarded as reference points P', with a total of $15 * 15 * 15 = 3,375$ reference points and 3,374 reference points except for P).

In Vivo Experiments

From December 2019 to February 2021, 36 subjects (22 females and 14 males) with age >50 years were recruited from residential areas around the hospital with random house numbers. The study was reviewed and approved by the hospital Ethics Committee, and all subjects signed informed consent before the initiation of the study.

We employed the method of Gogia et al. (1987) to measure the knee flexion angle involving the greater trochanter of the femur, fibular head, and lateral malleolus as surface markers. The subject laid on his side with the knee joint to be examined above the contralateral lower limb. A customized and MRI-compatible device was used to apply a 15 kg force toward the head side to the sole of the foot of the subject. Following each MRI imaging, the subject rested for 2–3 min prior to the

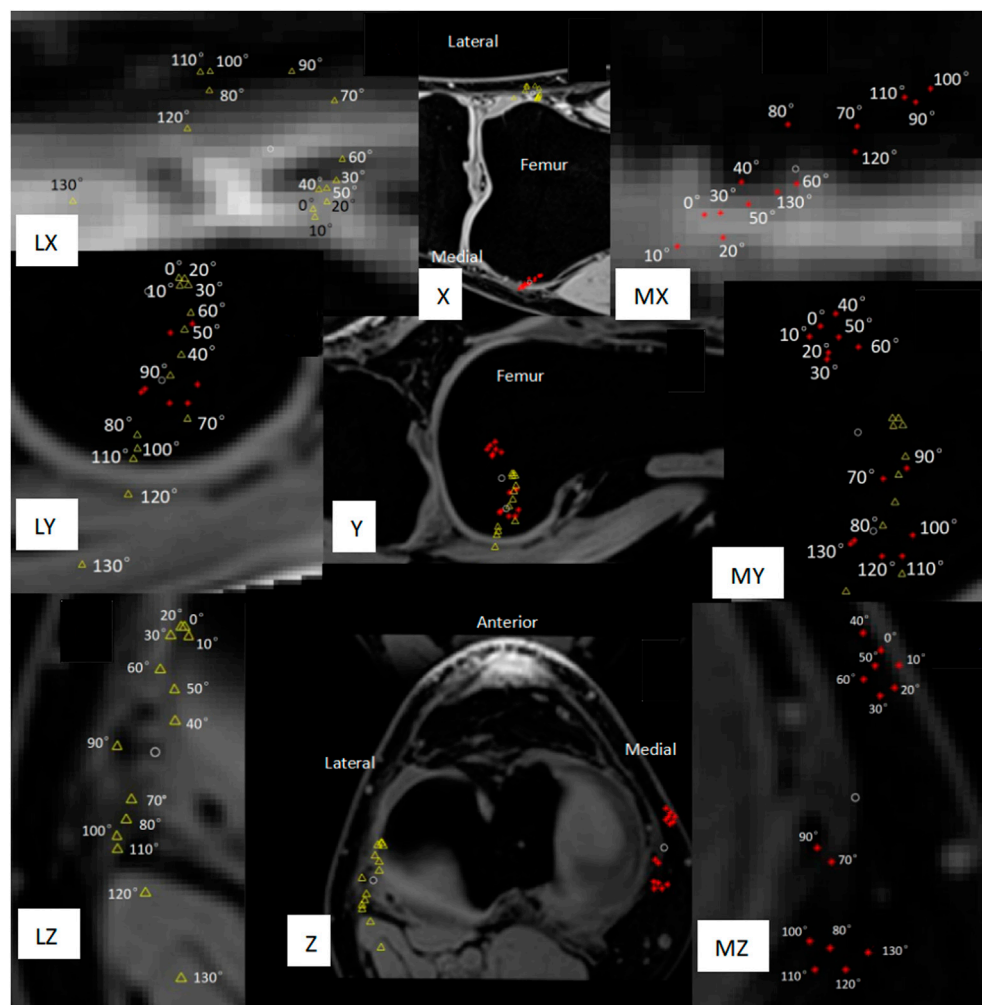


FIGURE 6 | Movement trajectory of the medial/lateral condyle of the femur with the tibia as a fixed rigid body. The red asterisk represents the medial condyle, the yellow triangle represents the lateral condyle, and the two white circles represent the average position of the movement trajectory of the medial condyle and the lateral condyle, respectively. PC is the standard deviation of the distance between the white circle and each red asterisk/yellow triangle around it. (X) Coronal plane. (Y) Sagittal plane. (Z) Horizontal plane. (MX, MY, MZ) Local magnification of the movement trajectory of the femoral medial condyle. (LX, LY, LZ) Local enlargement of the movement trajectory of the femoral lateral condyle. (Z, LZ, MZ) The reverse screw home phenomenon at the flexion of 40°–70° and screw home of flexion over 70° should be noted.

initiation of the MRI imaging of the next knee flexion angle. MRI was conducted on a clinical 3-T (UMR790, United Imaging, Shanghai) that used fat-suppressed T1-weighted 3D sequence: TR/TE 10.44/4.88; echo train length 22; field of view 160 mm * 160 mm; matrix 320 * 320; receiver bandwidth 150; slice thickness 0.5 mm with no gap; at 2 excitations; and examination time 4 min 43 s. 14 MRI images with knee flexion from 0° to 130° were captured at intervals of 10°. All MRI data were exported in DICOM format. The MATLAB software was used to implement the measurement steps mentioned in the “Principle of measurement and description for relative motion” section. SCVS was used as a characteristic area; these structures were common in MRI under the above-mentioned imaging conditions and met the conditions required for accurate

measurement (see the “*In vitro* measurement accuracy test” section for details).

Method to Determine the Optimal Rotation Axis of the Knee Joint for Total Knee Arthroplasty Surgery

The tibia was the fixed rigid body and the femur was the moving rigid body. A femur reference point had 14 coordinates during the knee flexion from 0° to 130° (each coordinate was measured/calculated in an MRI image, there are 14 MRI images with knee flexion from 0° to 130° captured at intervals of 10°), and the standard deviation of distance from the average coordinate was used to measure the positional change (PC) of this reference point during the knee flexion from 0° to 130°

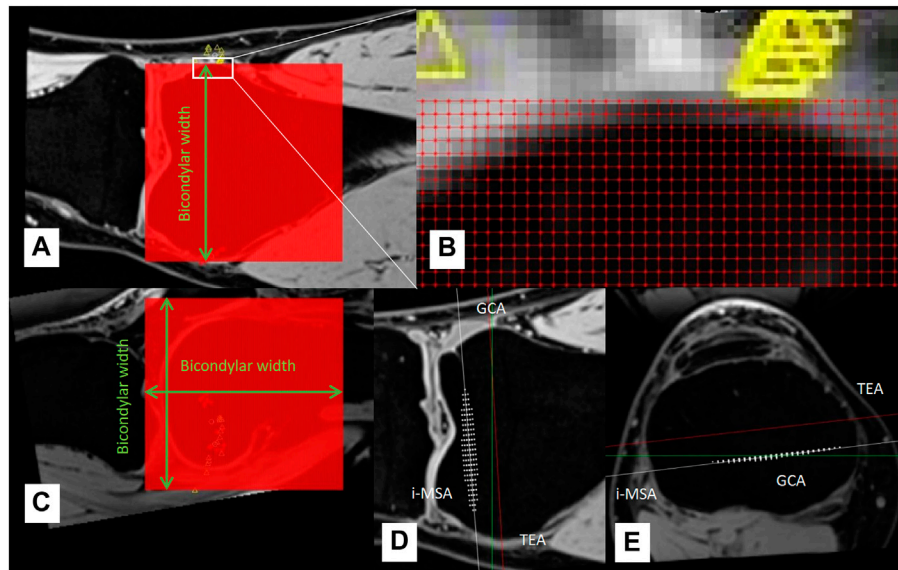


FIGURE 7 | (A–C) A cube grid with the side length of bicondylar width was established at the distal end of the femur, the grid spacing was 1 mm, and all grid intersections were candidate reference points. **(D–E)** White asterisks represent the 0.2% reference points with the smallest PC, which was used to determine rotation axis (individual most stable rotation axis, i-MSA).

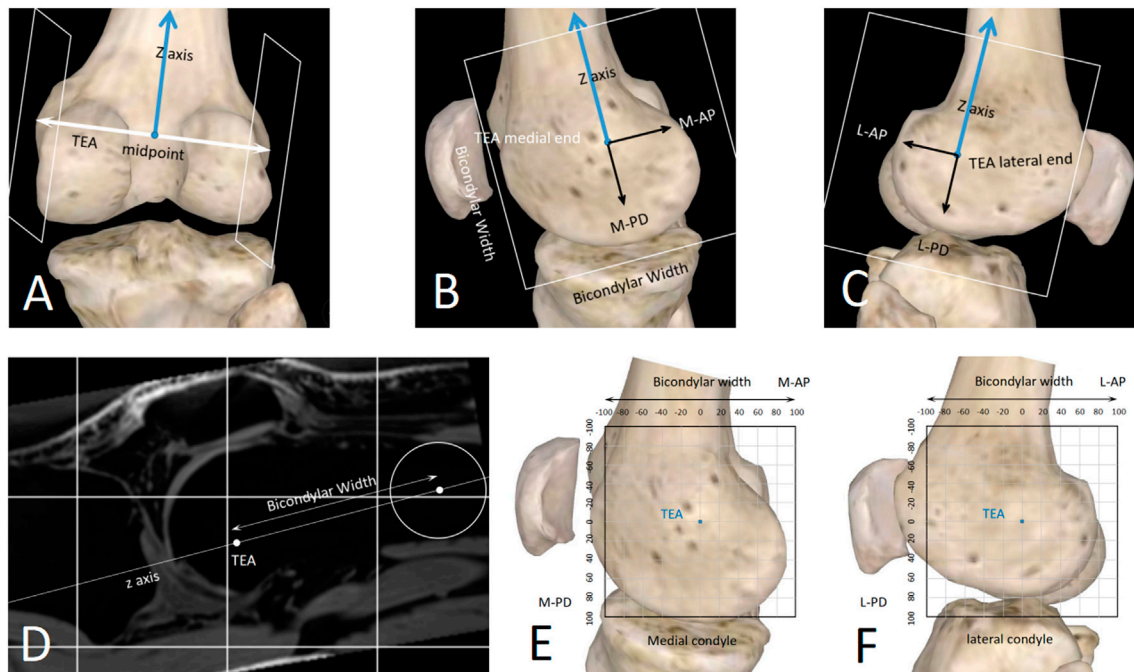


FIGURE 8 | A standardized method to describe spatial position of any straight line close to the knee joint. **(A–D)** The sagittal planes of the TEA medial/lateral ends were determined with the distal femur anatomy. **(E,F)** 2D coordinate systems were established in the sagittal planes. The unit length can be millimeter (sagittal-mm coordinate system) or bicondylar width (sagittal-BCW coordinate system).

(Figures 5, 6). Obviously, the smaller the PC of a reference point, the more stable the reference point was during knee movement. We employed the method in Figures 7A–C to determine the range of candidate reference points. Subsequently, we calculated the respective PC of all reference points and selected the 0.2% reference point with the smallest PC value to fit a straight line with the least square method, which was then used as the rotation axis (Figures 7D,E).

Difference Between/Within the Measurers

In the *in vitro* accuracy test experiment, two musculoskeletal radiologists (SXT and YHL) with over 5 years of experience independently confirmed the CAF of aquarium stones twice, and the interval between the two measurements was more than 1 week. The relative motion between aquarium stones was calculated using MATLAB software. For the accuracy test of θ , V , and V' , an inter-class consistency (ICC) was used to assess the intra-measurer and inter-measurer consistency. The mean \pm standard deviation was used to describe their accuracy (Table 1), and their consistency was also evaluated by ICC.

In the *in vivo* experiment, the knee joint CAF was independently confirmed by the same two measurers, and the

ICC equaled 1.000. Hence, the results of the measurer SXT were used as the experimental data.

In all experiments, the measurers do not know the exact value of kinematics parameters, they only confirm the CAF. Even if the measurers know the kinematics measurement data, they cannot estimate the position of the reference points P and P' , because it can only be obtained after a lot of calculations. These calculations were performed using MATLAB software, and these calculated results are blind to the measurers.

RESULTS

In Vitro Measurement Accuracy Test

The accuracy verification results are summarized in Table 1. Overall, all the angles/lengths that were tested in the experiment have a measurement accuracy of $<1^\circ/1$ mm. It seems that the clinical 3T MRI is sufficient to obtain good accuracy. In addition, the range of angles/lengths validated here is sufficient for knee joint measurements.

In Vivo Experiment

In this study, the knee joints of 36 healthy elderly subjects (14 men and 22 women) were measured. The general

TABLE 1 | All angles/lengths tested in the experiment have a measurement accuracy of $<1^\circ/1$ mm; see text for details.

Actual length/angle	Accuracy (95% CI)*#	Intra-measurer ICC*	Inter-measurer ICC*
Measurement accuracy of V and θ			
Length (mm)			
1	[0.00,0.00]/[0.00,0.00]/[0.00,0.00]	1.000/1.000/1.000	1.000/1.000/1.000
2	[0.00,0.00]/[0.00,0.00]/[0.00,0.00]		
5	[0.00,0.00]/[0.00,0.00]/[0.00,0.00]		
10	[0.00,0.00]/[-0.79,0.04]/[-0.68,0.18]		
20	[0.00,0.00]/[0.00,0.00]/[-0.09,0.034]		
50	[-0.61,0.86]/[-0.68,0.18]/[-0.67,0.42]		
100	[-0.61,0.86]/[-0.68,0.18]/[-0.68,0.18]		
Angle (deg)			
1	[0.00,0.00]/[0.00,0.00]/[0.00,0.00]	1.000/1.000/1.000	1.000/1.000/1.000
5	[0.00,0.00]/[0.00,0.00]/[0.00,0.00]		
10	[-0.81,0.31]/[0.00,0.00]/[-0.59,-0.16]		
20	[-0.31,0.81]/[0.15,0.85]/[-0.29,0.54]		
50	[-0.09,0.34]/[-1.00,0.00]/[-0.35,0.35]		
80	[-0.18,0.68]/[0.00,1.00]/[-0.18,0.68]		
150	[-0.81,0.68]/[-0.33,0.85]/[-0.67,0.18]		
Actual length	Accuracy (95% CI)*^	Intra-measurer ICC*	Inter-measurer ICC*
Measurement accuracy of V'			
Length (mm)			
1	[-0.02,0.01]/[-0.00,0.02]/[-0.01,0.01]	1.000/1.000/1.000	1.000/1.000/1.000
2	[-0.02,0.01]/[-0.01,0.01]/[-0.02,0.01]		
5	[-0.01,0.02]/[-0.03,0.01]/[-0.02,-0.01]		
10	[-0.01,0.02]/[-0.78,0.04]/[-0.68,0.20]		
20	[-0.00,0.01]/[-0.02,0.01]/[-0.10,0.35]		
50	[-0.63,0.86]/[-0.67,0.17]/[-0.69,0.41]		
100	[-0.61,0.87]/[-0.68,0.17]/[-0.69,0.18]		

*Measurement results in different directions are separated by “/,” indicating the results of the coronal plane/sagittal plane/horizontal plane.

#Two measurers were measured twice; there are a total of four measurement results used to calculate the mean and standard deviation of the accuracy of V .

^There are a total of 3,374 reference points within the range of 7 cm from V , and there are a total of $4 \times 3,374 = 13,496$ measurement results, which are used to calculate the mean and standard deviation of the accuracy V' .

TABLE 2 | General information of *in vivo* test subjects.

	Male	Female
Cases	14	22
Age (y)	65.3 ± 9.6 (53–79)	63.5 ± 6.2 (52–77)
Height (cm)	168.6 ± 5.4 (162–179)	160.3 ± 4.1 (152–167)
Weight (kg)	76.1 ± 6.5 (64–87)	63.7 ± 8.2 (52–77)
BMI	26.8 ± 2.8 (23.4–32.4)	24.8 ± 3.2 (20.2–30.0)
Left knee	8 (57%)	10 (45%)

information on the subjects is provided in **Table 2**. Among the 36 measured knee joints, the trajectory of a common medial/lateral femoral condyle is shown in **Figure 6**. Roll-back motion was observed in all 36 knee joints, and the rollback distance of the medial femoral condyle was 18.1 ± 3.7 mm, and that of the lateral femoral condyle was 31.1 ± 7.3 mm. In addition, the screw home phenomenon was observed in all knee joints, most lateral femoral condyle (21/36, 58%) began to move significantly backward only during knee flexion over 70° .

DISCUSSION

This study proposed a method to describe and measure knee joint kinematics. Our work showed that the rotation angle parameter θ of the rigid body is uniform (**Eq. 2** and **Figure 2**), so the verification of the rotation angle in this study was also uniform. However, the displacement parameter V was not uniform, and the displacement V' of different reference points P' was different (**Eq. 2** and **Figure 2**), so the V and V' needed to be verified separately. Verification experiments showed that the accuracy of the knee joint measurement was $<1^\circ$ and 1 mm with our method. This method can be used to determine the optimal rotation axis of each patient's knee joint before TKA, prior to the adjustment of prosthesis installation during TKA in a personalized manner, which may improve the surgery effect of TKA and improve the satisfaction rate of patients.

In the “Materials and Methods” section we describe a method for determining the optimal axis of rotation for TKA surgery, based on kinematic measurements. Regarding this method, this study focuses on its logic; therefore, the measurement results of the rotation axis are not listed. It is easy to imagine that: 1) if the tibia is used as a fixed rigid body, each reference point on the femur will have its own motion trajectory during knee flexion from 0° to 130° , and the PC of the motion trajectory can be used to measure the stability of this reference point during knee joint movement such that the smaller the PC, the more stable the reference point; 2) strict pivot movement will produce an absolutely stable rotation axis, and the PCs of all reference points on this axis should be 0. In reality, knee joint movement is mainly pivot motion (flexion and extension), accompanied by internal and external rotation, varus-valgus rotation, rollback, screw home, medial pivot, and other unknown movements that may exist. So, the movement of the knee joint is not a strict pivot motion. Although we could not find an absolutely stable rotation axis, in this study, we still observed

all the reference points of the distal femur at 1 mm intervals and calculated the PC of each reference point to find which reference points produce a smaller PC. Theoretically, the rotation axis of the femoral prosthesis should be installed in a straight line formed by the reference points with a smaller PC, so that the prosthesis is more stable after TKA and the knee motion is closer to the natural knee.

Our *in vivo* measurements were broadly consistent with those of other researchers, but our results revealed more detail about knee joint movement. Rollback (**Figure 6Y, Z**) and screw home phenomena (**Figure 6Z, LZ, MZ**) were observed in our measurements. The measurement results of Tanifuji et al. (2013) showed that the distance of rollback of the medial and lateral ends of transepicondylar axis (TEA) was 18.1 ± 3.7 mm and 31.1 ± 7.3 mm, respectively. Our measurement results were 21.5 ± 4.2 mm and 31.1 ± 7.1 mm, therefore, the data were consistent. In addition, our results showed that the medial end of TEA moved 3.1 ± 1.6 mm to the proximal side and the lateral end moved 5.4 ± 2.9 mm to the distal side during rollback. Kono et al. (2018), Tanifuji et al. (2013) believed that the lateral condyle of TEA moved forward by about 3 mm during knee flexion from 0° to 40° , and moved backward during knee flexion over 40° , which was also similar to our measurement results of the relative movement trajectory of the TEA lateral condyle. However, our results further showed that the most lateral TEA condyle (21/36, 58%) began to move significantly backward only during knee flexion over 70° . These details may help design new prostheses that better conform to the natural knee kinematics.

Although the *in vitro* accuracy verification experiment in this study used aquarium stone as the measurement object, which was not exactly the same as the *in vivo* experiment of knee joint measurement, we believe that this difference does not have a significant impact on the measurement accuracy of angle and length. Because MRI mainly relies on gradient magnetic fields (determine layer) and 2-dimensional Fourier transformation (determine the image for each layer) for localization, they are related to the MRI machine and not related to whether the object being examined is inside or outside the body. The important factor affecting measurement accuracy is the CAF criteria (*In vitro* measurement accuracy test, materials, and methods) preset before the measurement. In this study, the CAF criteria for both *in vivo* and *in vitro* experiments were uniform.

Our method may have some important implications. Currently, there are 3 clinically applied rotational guides for aligning the rotation of the TKA femoral component: TEA, 3° external from the posterior condylar axis (PCA), and Whiteside's line. These lines, however, are mainly summarized based on the experience of clinicians, which are not necessarily accurate and cannot reflect the individual differences in knee joint rotation axis in each patient. In fact, regarding the rotation alignment of the TKA prosthesis, Poilvache believed that the use of any specific prosthesis alignment technique will result in impaired implant durability or dissatisfaction in some patients, the external rotation angle of the femoral prosthesis appears to be variable and must be adjusted for each knee (Poilvache, 2002). Our method can find the individual most stable rotation axis (i-MSA) (**Figure 7**),

which makes it possible to individually install TKA prostheses in the surgery.

Because our method is time-consuming, currently it is difficult to preoperatively measure the i-MSA for every TKA patient. To benefit more TKA patients, we propose the concept of population averaged most stable rotational axis (a-MSA). For TKA patients who have not measured i-MSA, a-MSA is a low-cost alternative that can be considered. We believe that a-MSA should be described in the TEA coordinate system [a similar coordinate system has been proposed by Yu et al. (2021) (Figure 8)] because it is constant in TKA patients (OA does not cause bone defect in TEA). The researchers should have measured the i-MSA of many healthy subjects in advance, then determine the 4 parameters (M-AP, M-PD, L-AP, L-PD) of each subject's i-MSA in the TEA-coordinate system (Figure 8), and finally, take the average value of each parameter to get the corresponding parameters of a-MSA. For a new patient about to undergo TKA surgery, his or her a-MSA can be determined on preoperative knee MRI according to the 4 parameters of a-MSA. This avoids the time-consuming measurement steps of i-MSA. Further studies will be needed in the future to compare the PC values of a-MSA and conventional rotational axes, and to assess whether a-MSA is more stable than conventional rotational axes. We believe it is less stable than i-MSA but more stable than TEA and GCA.

Interpreting our findings needs caution. Trying to reproduce an individual patient's kinematics may improve outcomes, but this is not absolute, because clinical outcomes are multifactorial. More research and validation should be performed to continuously refine TKA prosthesis design and their surgical insertion.

This study has some limitations. First, our method currently only measures static knee kinematics. Due to the current level of technological development, MRI examination is time-consuming, so it cannot dynamically record the knee kinematics like X-ray fluoroscopy. But MRI has a unique advantage; it can obtain enough 3-dimensional data to make it possible to find the optimal rotation axis. If the future development of imaging techniques can significantly speed up MRI examinations, our method could be used to measure dynamic knee kinematics. Secondly, our method requires manual confirmation of CAF, so the measurement process is time-consuming for now (It takes 40–50 min to measure a knee joint for a radiologist), which is not conducive to the widespread clinical application of this method. However, a-MSA may be used as a low-cost alternative; it only takes 4–5 min to measure. Thirdly, the study only

examined the knee joints of healthy people and did not assess the knee joints of TKA patients with end-stage osteoarthritis. Such knee joints are often combined with bone defects, which may have a significant impact on the knee joint kinematics. However, it is a common defect in current studies, as most studies use healthy knee joints as the measurement object (Asano et al., 2005; Tanifuji et al., 2011; Tanifuji et al., 2013; Kono et al., 2018; Hans et al., 2021). At present, the kinematics of healthy knee joints has not been fully clarified. If the healthy knee joints have been studied thoroughly in the future it may then be necessary to further study the effect of different osteoarthritic grades on knee kinematics.

In conclusion, in the application scenario of knee joint kinematics measurement, our method has an accuracy of $<1^\circ$ of rotation angle and <1 mm of translation for all reference points, and it can be employed to identify the most stable axis of the knee joint.

DATA AVAILABILITY STATEMENT

The original contributions presented in the study are included in the article/supplementary material; further inquiries can be directed to the corresponding author.

ETHICS STATEMENT

The studies involving human participants were reviewed and approved by the Clinical Research Ethics Committee of the Second Xiangya Hospital of Central South University. The patients/participants provided their written informed consent to participate in this study. Written informed consent was obtained from the individual(s) for the publication of any potentially identifiable images or data included in this article.

AUTHOR CONTRIBUTIONS

LZ and RW contributed to the conception and design of the study. ST and YL performed data measurement. LZ and LW developed the methodology and software. QT performed the statistical analysis. LZ wrote the first draft of the manuscript. All authors contributed to manuscript revision, read, and approved the submitted version.

REFERENCES

- Asano, T., Akagi, M., and Nakamura, T. (2005). The Functional Flexion-Extension Axis of the Knee Corresponds to the Surgical Epicondylar Axis. *J. Arthroplasty* 20 (8), 1060–1067. doi:10.1016/j.arth.2004.08.005
- Baker, P. N., Rushton, S., Jameson, S. S., Reed, M., Gregg, P., and Deehan, D. J. (2013). Patient Satisfaction with Total Knee Replacement Cannot Be Predicted from Pre-operative Variables Alone: A Cohort Study from the National Joint Registry for England and Wales. *Bone Jt. J.* 95-B (95-B), 1359–1365. doi:10.1302/0301-620X.95B10.32281
- Beach, A., Regazzola, G., Neri, T., Verheul, R., and Parker, D. (2019). The Effect of Knee Prosthesis Design on Tibiofemoral Biomechanics during Extension Tasks Following Total Knee Arthroplasty. *Knee* 26 (5), 1010–1019. doi:10.1016/j.knee.2019.07.008
- Bruno, F., Barile, A., Arrigoni, F., Laporta, A., Russo, A., Carotti, M., et al. (2018). Weight-bearing MRI of the Knee: a Review of Advantages and Limits. *Acta Biomed.* 89 (89), 78–88. doi:10.23750/abm.v89i1-S.7011

- Cacciola, G., De Martino, I., and De Meo, F. (2020). Does the Medial Pivot Knee Improve the Clinical and Radiographic Outcome of Total Knee Arthroplasty? A Single Centre Study on Two Hundred and Ninety Seven Patients. *Int. Orthop. (SICOT)* 44 (2), 291–299. doi:10.1007/s00264-019-04462-3
- Dennis, D. A., Mahfouz, M. R., Komistek, R. D., and Hoff, W. (2005). *In Vivo* Determination of Normal and Anterior Cruciate Ligament-Deficient Knee Kinematics. *J. Biomechanics* 38 (2), 241–253. doi:10.1016/j.jbiomech.2004.02.042
- Dunbar, M. J., Richardson, G., and Robertsson, O. (2013). I Can't Get No Satisfaction after My Total Knee Replacement: Rhymes and Reasons. *Bone Jt. J.* 95-B (95-B), 148–152. doi:10.1302/0301-620X.95B11.32767
- Dzialo, C. M., Pedersen, P. H., Simonsen, C. W., Jensen, K. K., de Zee, M., and Andersen, M. S. (2018). Development and Validation of a Subject-specific Moving-axis Tibiofemoral Joint Model Using MRI and EOS Imaging during a Quasi-Static Lunge. *J. Biomechanics* 72 (27), 71–80. doi:10.1016/j.jbiomech.2018.02.032
- Eckhoff, D., Hogan, C., DiMatteo, L., Robinson, M., and Bach, J. (2007). An Abjs Best Paper. *Clin. Orthop. Relat. Res.* 461 (461), 238–244. doi:10.1097/blo.0b013e318112416b
- Fitzpatrick, C. K., Maag, C., Clary, C. W., Metcalfe, A., Langhorn, J., and Rullkoetter, P. J. (2016). Validation of a New Computational 6-DOF Knee Simulator during Dynamic Activities. *J. Biomech.* 49 (49), 3177–3184. doi:10.1016/j.jbiomech.2016.07.040
- Freeman, M. A. R., and Pinskerova, V. (2005). The Movement of the Normal Tibio-Femoral Joint. *J. Biomechanics* 38 (2), 197–208. doi:10.1016/j.jbiomech.2004.02.006
- Giphart, J. E., Zirker, C. A., Myers, C. A., Pennington, W. W., and LaPrade, R. F. (2012). Accuracy of a Contour-Based Biplane Fluoroscopy Technique for Tracking Knee Joint Kinematics of Different Speeds. *J. Biomechanics* 45 (16), 2935–2938. doi:10.1016/j.jbiomech.2012.08.045
- Gogia, P. P., Braatz, J. H., Rose, S. J., and Norton, B. J. (1987). Reliability and Validity of Goniometric Measurements at the Knee. *Phys. Ther.* 67 (2), 192–195. doi:10.1093/ptj/67.2.192
- Guan, S., Gray, H. A., Schache, A. G., Feller, J., de Steiger, R., and Pandey, M. G. (2017). *In Vivo* six-degree-of-freedom Knee-Joint Kinematics in Overground and Treadmill Walking Following Total Knee Arthroplasty. *J. Orthop. Res.* 35 (35), 1634–1643. doi:10.1002/jor.23466
- Hans, A. G., Guan, S., Thomeer, T. L., and Pandey, M. G. (2021). Moment Arm of the Knee-Extensor Mechanism Measured *In Vivo* across a Range of Daily Activities. *J. Biomechanics* 123, 110484. doi:10.1016/j.jbiomech.2021.110484
- Hollister, A. M., Jatana, S., Singh, A. K., Sullivan, W. W., and Lupichuk, A. G. (1993). The Axes of Rotation of the Knee. *Clin. Orthop. Relat. Res.* 290, 2259–2268. doi:10.1097/00003086-199305000-00033
- Iranpour, F., Merican, A. M., Baena, F. R. Y., Cobb, J. P., and Amis, A. A. (2010). Patellofemoral Joint Kinematics: The Circular Path of the Patella Around the Trochlear axis. *J. Orthop. Res.* 28 (5), 589–594. doi:10.1002/jor.21051
- Justin, D. B., Petrucci, D., Adili, A., Piccirillo, L., Wismer, D., and Winemaker, M. (2012). Patient Perspective Survey of Total Hip vs Total Knee Arthroplasty Surgery. *J. Arthroplasty* 27 (6), 865–869. doi:10.1016/j.arth.2011.12.031
- Kono, K., Tomita, T., Futai, K., Yamazaki, T., Tanaka, S., Yoshikawa, H., et al. (2018). *In Vivo* three-dimensional Kinematics of Normal Knees during Different High-Flexion Activities. *Bone & Jt. J.* 100-B (1100), 50–55. doi:10.1302/0301-620X.100B1.bjj-2017-0553.r2
- Kurtz, S., Ong, K., Lau, E., Mowat, F., and Halpern, M. (2007). Projections of Primary and Revision Hip and Knee Arthroplasty in the United States from 2005 to 2030. *J. Bone & Jt. Surg.* 89 (4), 780–785. doi:10.2106/jbjs.f.00222
- Li, G., Kozanek, M., Hosseini, A., Liu, F., Van de Velde, S. K., and Rubash, H. E. (2009). New Fluoroscopic Imaging Technique for Investigation of 6DOF Knee Kinematics during Treadmill Gait. *J. Orthop. Surg. Res.* 4 (13), 6. doi:10.1186/1749-799X-4-6
- Meneghini, R. M., Deckard, E. R., Ishmael, M. K., and Ziemba-Davis, M. (2017). A Dual-Pivot Pattern Simulating Native Knee Kinematics Optimizes Functional Outcomes after Total Knee Arthroplasty. *J. Arthroplasty* 32 (32), 3009–3015. doi:10.1016/j.arth.2017.04.050
- Mohsen, A. S., Boulos, A., Saevansson, S. K., Yoo, S., Miller, S., and Anglin, C. (2016). Changes in Knee Kinematics Following Total Knee Arthroplasty. *Proc. Inst. Mech. Eng. H.* 4 (230), 265–278. doi:10.1177/09544119166632491
- Most, E., Axe, J., Rubash, H., and Li, G. (2004). Sensitivity of the Knee Joint Kinematics Calculation to Selection of Flexion Axes. *J. Biomechanics* 37 (11), 1743–1748. doi:10.1016/j.jbiomech.2004.01.025
- Park, A., Duncan, S. T., Nunley, R. M., Keeney, J. A., Barrack, R. L., and Nam, D. (2014). Relationship of the Posterior Femoral axis of the "kinematically Aligned" Total Knee Arthroplasty to the Posterior Condylar, Transepicondylar, and Anteroposterior Femoral Axes. *Knee* 21 (21), 1120–1123. doi:10.1016/j.knee.2014.07.025
- Poivache, P. (2002). *The Epicondylar Axis for Femoral Component Rotation. Surgical Techniques in Total Knee Arthroplasty*. New York: Springer.
- Ramsey, D. K., and Wretenberg, P. F. (1999). Biomechanics of the Knee: Methodological Considerations in the *In Vivo* Kinematic Analysis of the Tibiofemoral and Patellofemoral Joint. *Clin. Biomech.* 14 (9), 595–611. doi:10.1016/S0268-0033(99)00015-7
- Reddy, N. P., Askew, M. J., Baniewicz, F. M., Melby, A., Fuller, K. A., Steurer, P. A., et al. (1989). A Technique for Quantitative Assessment of Three-Dimensional Motion with Applications to Human Joints. *Proc. Inst. Mech. Eng. H.* 203 (4), 207–213. doi:10.1243/pime_proc_1989_203_041_01
- Şahin, N., Atıcı, T., Kurtoglu, U., Turgut, A., Ozkaya, G., and Ozkan, Y. (2013). Centre of the Posterior Cruciate Ligament and the Sulcus between Tubercle Spines Are Reliable Landmarks for Tibial Component Placement. *Knee Surg. Sports Traumatol. Arthrosc.* 21 (10), 2384–2391. doi:10.1007/s00167-012-2120-5
- Scarvell, J. M., Smith, P. N., Refshauge, K. M., Galloway, H. R., and Woods, K. R. (2004). Comparison of Kinematic Analysis by Mapping Tibiofemoral Contact with Movement of the Femoral Condylar Centres in Healthy and Anterior Cruciate Ligament Injured Knees. *J. Orthop. Res.* 22 (22), 955–962. doi:10.1016/j.jorthres.2003.12.016
- Schache, A. G., Baker, R., and Lamoireux, L. W. (2006). Defining the Knee Joint Flexion-Extension axis for Purposes of Quantitative Gait Analysis: An Evaluation of Methods. *Gait Posture* 24 (1), 100–109. doi:10.1016/j.gaitpost.2005.08.002
- Schulze, A., and Scharf, H. P. (2013). Zufriedenheit nach Knieendoprothesenimplantation. *Orthopäde* 42 (10), 858–865. doi:10.1007/s00132-013-2117-x
- Shih, K.-S., Lin, C.-C., Lu, H.-L., Fu, Y.-C., Lin, C.-K., Li, S.-Y., et al. (2020). Patient-specific Instrumentation Improves Functional Kinematics of Minimally-Invasive Total Knee Replacements as Revealed by Computerized 3D Fluoroscopy. *Comput. Methods Programs Biomed.* 188 (188), 105250. doi:10.1016/j.cmpb.2019.105250
- Sta, S., Ogor, J., Letissier, H., Stindel, E., Hamitouche, C., and Dardenne, G. (2021). Towards Markerless Computer Assisted Surgery: Application to Total Knee Arthroplasty. *Int. J. Med. Robot.* 17 (5), e2296. doi:10.1002/rcs.2296
- Takashi, S., and Mochizuki, T. (2021). Three-dimensional Morphology of the Distal Femur Based on Surgical Epicondylar axis in the Normal Elderly Population. *Knee* 30, 125–133. doi:10.1016/j.knee.2021.03.022
- Tanifuji, O., Sato, T., Kobayashi, K., Mochizuki, T., Koga, Y., Yamagiwa, H., et al. (2011). Three-dimensional *In Vivo* Motion Analysis of Normal Knees Using Single-Plane Fluoroscopy. *J. Orthop. Sci.* 16 (16), 710–718. doi:10.1007/s00776-011-0149-9
- Tanifuji, O., Sato, T., Kobayashi, K., Mochizuki, T., Koga, Y., Yamagiwa, H., et al. (2013). Three-dimensional *In Vivo* Motion Analysis of Normal Knees Employing Transepicondylar axis as an Evaluation Parameter. *Knee Surg. Sports Traumatol. Arthrosc.* 21 (10), 2301–2308. doi:10.1007/s00167-012-2010-x
- Tupling, S. J., and Pierrynowski, M. R. (1987). Use of Cardan Angles to Locate Rigid Bodies in Three-Dimensional Space. *Med. Biol. Eng. Comput.* 25 (25), 527–532. doi:10.1007/BF02441745
- Van Campen, A., De Groote, F., Bosmans, L., Scheys, L., Jonkers, I., and De Schutter, J. (2011). Functional Knee axis Based on Isokinetic Dynamometry Data: Comparison of

- Two Methods, MRI Validation, and Effect on Knee Joint Kinematics. *J. Biomechanics* 44 (15), 2595–2600. doi:10.1016/j.jbiomech.2011.08.022
- Yamazaki, T., Futai, K., Tomita, T., Sato, Y., Yoshikawa, H., Tamura, S., et al. (2015). 3D Kinematics of Mobile-Bearing Total Knee Arthroplasty Using X-Ray Fluoroscopy. *Int. J. Comput. Assist. Radiol. Surg.* 10 (10), 487–495. doi:10.1007/s11548-014-1093-x
- Yu, Z., Cai, H., Yang, B., Yao, J., Zhang, K., Tian, H., et al. (2021). Relationship between Patellofemoral Finite Helical axis and Femoral Trans-epicondylar axis Using a Static Magnetic Resonance-Based Methodology. *J. Orthop. Surg. Res.* 16 (16), 212. doi:10.1186/s13018-021-02328-2

Conflict of Interest: The authors declare that the research was conducted in the absence of any commercial or financial relationships that could be construed as a potential conflict of interest.

Publisher's Note: All claims expressed in this article are solely those of the authors and do not necessarily represent those of their affiliated organizations, or those of the publisher, the editors, and the reviewers. Any product that may be evaluated in this article, or claim that may be made by its manufacturer, is not guaranteed or endorsed by the publisher.

Copyright © 2022 Tang, Zheng, Luo, Wu, Tian and Wang. This is an open-access article distributed under the terms of the Creative Commons Attribution License (CC BY). The use, distribution or reproduction in other forums is permitted, provided the original author(s) and the copyright owner(s) are credited and that the original publication in this journal is cited, in accordance with accepted academic practice. No use, distribution or reproduction is permitted which does not comply with these terms.



OPEN ACCESS

EDITED BY

Zhen Luo,
University of Technology Sydney,
Australia

REVIEWED BY

Yuhang Chen,
Heriot-Watt University, United Kingdom
Valentin Mateev,
Technical University, Sofia, Bulgaria

*CORRESPONDENCE

Yadong Liu,
doctoryadong@163.com

SPECIALTY SECTION

This article was submitted
to Biomechanics,
a section of the journal
Frontiers in Bioengineering and
Biotechnology

RECEIVED 20 June 2022

ACCEPTED 07 September 2022

PUBLISHED 27 September 2022

CITATION

Lu Y, Gong T, Yang Z, Zhu H, Liu Y and
Wu C (2022), Designing anisotropic
porous bone scaffolds using a self-
learning convolutional neural
network model.
Front. Bioeng. Biotechnol. 10:973275.
doi: 10.3389/fbioe.2022.973275

COPYRIGHT

© 2022 Lu, Gong, Yang, Zhu, Liu and
Wu. This is an open-access article
distributed under the terms of the
[Creative Commons Attribution License](#)
(CC BY). The use, distribution or
reproduction in other forums is
permitted, provided the original
author(s) and the copyright owner(s) are
credited and that the original
publication in this journal is cited, in
accordance with accepted academic
practice. No use, distribution or
reproduction is permitted which does
not comply with these terms.

Designing anisotropic porous bone scaffolds using a self-learning convolutional neural network model

Yongtao Lu^{1,2}, Tingxiang Gong¹, Zhuoyue Yang³, Hanxing Zhu⁴,
Yadong Liu^{5*} and Chengwei Wu^{1,6}

¹Department of Engineering Mechanics, Dalian University of Technology, Dalian, China, ²DUT-BSU Joint Institute, Dalian University of Technology, Dalian, China, ³Xi'an Aerospace Propulsion Institute, Xi'an, China, ⁴School of Engineering, Cardiff University, Cardiff, United Kingdom, ⁵Department of Orthopedics, Dalian Municipal Central Hospital Affiliated of Dalian University of Technology, Dalian, China, ⁶State Key Laboratory of Structural Analysis for Industrial Equipment, Dalian University of Technology, Dalian, China

The design of bionic bone scaffolds to mimic the behaviors of native bone tissue is crucial in clinical application, but such design is very challenging due to the complex behaviors of native bone tissues. In the present study, bionic bone scaffolds with the anisotropic mechanical properties similar to those of native bone tissues were successfully designed using a novel self-learning convolutional neural network (CNN) framework. The anisotropic mechanical property of bone was first calculated from the CT images of bone tissues. The CNN model constructed was trained and validated using the predictions from the heterogenous finite element (FE) models. The CNN model was then used to design the scaffold with the elasticity matrix matched to that of the replaced bone tissues. For the comparison, the bone scaffold was also designed using the conventional method. The results showed that the mechanical properties of scaffolds designed using the CNN model are closer to those of native bone tissues. In conclusion, the self-learning CNN framework can be used to design the anisotropic bone scaffolds and has a great potential in the clinical application.

KEYWORDS

scaffold design, convolutional neural network, anisotropic property, bone tissue, finite element modeling

1 Introduction

Every year, millions of bone replacement surgeries have to be performed worldwide to fix the large bone defects (Dang et al., 2018). In these surgeries, the autograft and allograft are the techniques widely used in the clinic, but in autograft there is the issue associated with the lack of bone supply and in allograft there are issues, such as the disease transmission (Finkemeier, 2002; Laurencin et al., 2006). Because of these, the bone scaffold has emerged as a promising method for fixing large bone defects. However, there

are still many issues to be solved, such as the stress shielding. The structural design is one of the main approaches to solve these challenges but it is still in its early stage and requires extensive research.

In the structural design of bone scaffolds, the design target is to have a bionic scaffold which can mimic the behaviors of the defected native bone tissues in all aspects including the geometrical features, the mechanical and biological functions, etc. However, it should be noted that geometrically the native bone possesses irregular shapes and mechanically the bone is anisotropic in different scales, which poses a big challenge in the bionic design of bone scaffolds. In the past, many efforts have been made to achieve the bionic design of bone scaffolds. For example, the microstructure of bone scaffolds has been evolved from the periodic regular lattices to the triply periodic minimal surface (TPMS) based structures and further to the irregular, non-periodic structures (Vijayavenkataraman et al., 2018; Huo et al., 2021). The periodic regular lattices (e.g., the cube, the hexagon) are widely used in the early stage of the design of bone scaffold (Bucklen et al., 2008). The TPMS based scaffold is one of the main types of structures widely used nowadays because of the bionic features of the TPMS, such as a mean curvature of zero. Most recently, the focus of the scaffold design has been put on the anisotropic behaviors of TPMS scaffolds (Ataee et al., 2018; Bonatti and Mohr, 2019; Kang et al., 2020; Peng et al., 2021). For example, Peng et al. (2021) has managed to increase the range of scaffold anisotropy by modifying the geometrical parameters of Gyroid cellular structure. In addition, the techniques such as grading and hybrid design, etc. are used to design the scaffolds with anisotropic mechanical properties (Liu et al., 2018; Al-Ketan et al., 2019; Chen et al., 2019). However, because the TPMS based scaffolds are based on the periodic units and additionally the number of design variables in the TPMS scaffolds is limited, the design space for the anisotropic mechanical properties of the TPMS scaffolds is limited. Designing the irregular and non-periodic bone scaffolds using some advanced mathematical algorithms (e.g., the Voronoi algorithm) (Gómez et al., 2016; Wang et al., 2018) is one of the strategies to achieve a larger design space for the anisotropic mechanical properties, but high complexities are involved in the advanced mathematical algorithms which hinders its development and application. Therefore, a novel and efficient approach for designing the scaffolds with controllable anisotropy is still highly needed.

In recent years, the machine learning has been evolved as a novel and fast-growing technique, which has been successfully applied in many fields, e.g., the accurate prediction of musculoskeletal force (Rane et al., 2019), the automatic tracking of joint kinematics (Burton et al., 2021), etc. In the design of porous materials, the machine learning based technique has also been widely explored in the recent years. For example, Zheng et al. (2021) has managed the inverse design of auxetic metamaterials using deep learning; Gu et al. (2018) has managed the design of bioinspired hierarchical composite using machine

learning; a deep-learning based model was proposed by Tan et al. (2020) for the efficient design of microstructural materials. The advantage of the machine learning technique is that once the machine learning model is well trained and validated, it can serve as an efficient surrogate model for generating the real-time outputs from new inputs. Additionally, the machine learning based technique is able to deal with structural design involving a large number of design variables, which is extremely crucial in the design of porous scaffolds, because the design space for the scaffold anisotropy can be easily expanded by adding more design variables. Therefore, the machine learning technique has the great potential in designing the fully bionic bone scaffolds. Nevertheless, to the best of our knowledge, the design of bone scaffolds with anisotropic mechanical properties using the machine learning technique has not been fully elaborated. The aim of the present study was to design bionic bone scaffolds with the mechanical properties similar to those of native bone tissues using the emerging machine learning technique.

This paper is organized in the following scheme. The calculation of the elasticity matrix of native bone tissue and the details on the self-learning convolutional neural network based design framework are illustrated in Section 2. In Section 3, the performance of the developed framework is demonstrated using a two-dimensional (2D) bone sample. In Section 4, the predictive accuracy of the machine learning based model and the design results are discussed and conclusions are drawn in the end.

2 Materials and methods

2.1 Calculation of the elasticity matrices for the native bone and bone scaffold

In the present study, a 2D bone example is presented to demonstrate the application of the machine learning based method in the design of the anisotropic porous bone scaffold. The anisotropic bone scaffold to be designed is to replace the defected bone tissues and an ideal scaffold should possess the mechanical properties similar to those of the replaced bone tissue. Therefore, the first step in the scaffold design is to work out the mechanical properties of bone tissue, which are calculated from the CT images of native human bone tissue. The CT images used were acquired in the previous studies (Lu et al., 2015). Briefly, thirty-five cadavers were harvested from the female patients with a mean age of 81.3 ± 7.2 year-old (range: 65 to 90 year-old). The spinal segments of T11/T12/L1 were dissected and the specimens were scanned in the frozen state using the HR-pQCT scanner (XtremeCT, Scanco Medical AG, Bruettisellen, Switzerland) operated at 59.4 kV, 900.0 μ As with an image voxel size of $82.0 \times 82.0 \times 82.0 \mu\text{m}^3$. In the present study, only the cancellous fraction was used and thus the volumes

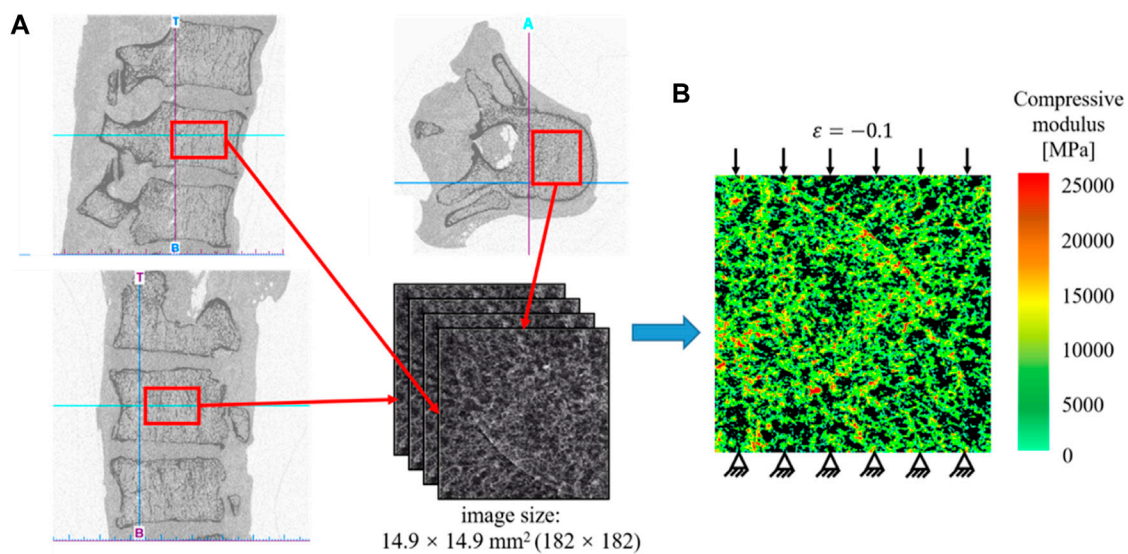


FIGURE 1

(A) Extraction of the CT data of the human cancellous bone. (B) Establishment of the heterogeneous finite element model for calculating the effective elastic mechanical modulus of bone tissue.

of interest covering only the cancellous bone were cropped out from the CT images of the spinal segments (Figure 1A).

Because the native bone tissue exhibits the anisotropic mechanical properties, the homogenized elasticity matrix of the bone was calculated to describe the anisotropic mechanical properties of the native bone tissue, which were calculated from the finite element (FE) analysis as follows (Figure 1). First, the heterogeneous FE models of the cancellous fraction were generated using the standard method previously developed (Lu et al., 2019a). Briefly, the cancellous fraction (Figure 1A) with the dimension of $14.9 \times 14.9 \text{ mm}^2$ was cropped out from the HR-pQCT images of human vertebral body. The grayscale image was first smoothed using a Gaussian filter ($\sigma = 1.2$, $\text{support} = 2.0$) to reduce the influence of image noise. Then, the grayscale values were converted to vBMD values based on the linear calibration equation provided by the HR-pQCT scanner. The vBMD values were further converted into bone ash density according to the relationship of $\rho_{\text{ash}} = 0.877 \times \rho_{\text{HA}} + 0.079$, where ρ_{ash} is the bone ash density, unit in mg/cm^3 and ρ_{HA} is the HA-equivalent vBMD, unit in mg/cm^3 . Heterogeneous FE model (Figure 1B) was generated by converting the bone ash density to the elastic modulus for each bone element using the density-modulus relationship previously published. Poisson's ratio for the bone elements was set to 0.30. The FE meshes were generated by converting each bone pixel into 2D 4-node plane stress element (PLANE182). The elastic modulus calculated at each image pixel was mapped to the FE mesh using an in-house developed MATLAB (R2017a, MathWorks, Natick,

Massachusetts, United States) code. It should be noted that to ensure the connectivity of bone tissues in the FE analysis, the 2D FE bone models were generated from the processed 2D images, each of which was created by keeping the maximal grayscale values in the pixels calculated from 15 2D images randomly selected from the original 2D image datasets. The 2D images and the corresponding 2D FE models were derived from the transverse plane of the human vertebral plane.

The plane stress problem is assumed and the following constitutive model is used to describe the anisotropic mechanical behavior of the bone tissue (Xiao et al., 2021):

$$\begin{bmatrix} \sigma_x \\ \sigma_y \\ \tau_{xy} \end{bmatrix} = \begin{bmatrix} c_{11} & c_{12} & c_{13} \\ c_{12} & c_{22} & c_{23} \\ c_{13} & c_{23} & c_{33} \end{bmatrix} \begin{bmatrix} \epsilon_x \\ \epsilon_y \\ \gamma_{xy} \end{bmatrix} \quad (1)$$

where σ_x and σ_y are the normal stresses in the x and y directions, respectively, τ_{xy} is the shear stress in the x - y plane, ϵ_x and ϵ_y are the normal strains in the x and y directions, respectively, γ_{xy} is the shear strain in the x - y plane and $c_{11}, c_{12}, \dots, c_{33}$ are the elastic constants. Because of the symmetric property of the elasticity matrix, there are six independent constants in the constitutive model, which can be determined using the following three loading scenarios (the FE model was solved three times for the following three loading scenarios to obtain the elastic constants) (Figure 2).

First, the strain in the x direction is set to -0.1 while the other two strains are set to zeros, i.e., $\epsilon_x = -0.1$, $\epsilon_y = 0.0$, $\gamma_{xy} = 0.0$ (Figure 2A). Under this loading scenario, the elastic constants of c_{11} , c_{12} and c_{13} can be calculated as below:

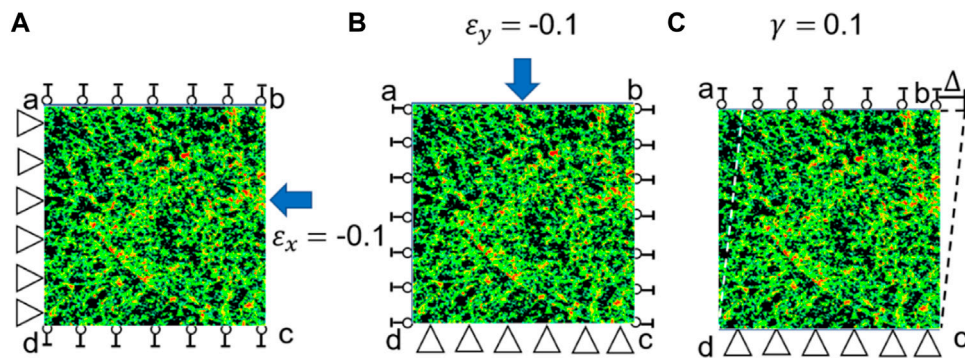


FIGURE 2

Three loading scenarios used for calculating the elasticity matrix of bone tissue. (A) Uniaxial compression in the x direction ($\epsilon_x = -0.1$), (B) uniaxial compression in the y axis ($\epsilon_y = -0.1$) and (C) shear loading in the x-y plane ($\gamma_{xy} = 0.1$).

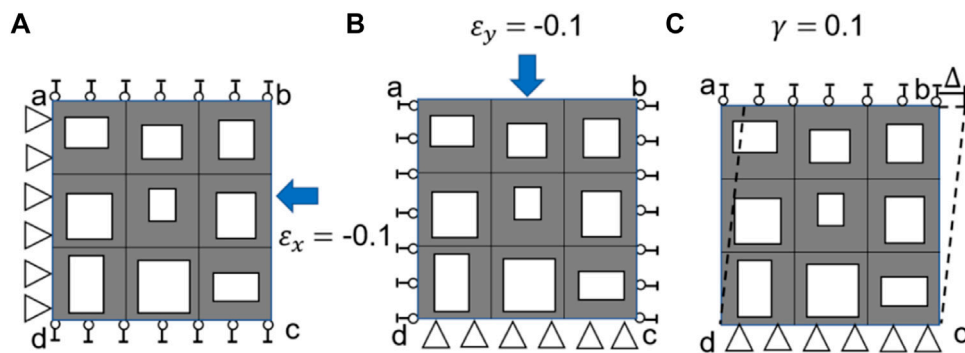


FIGURE 3

Three loading scenarios used for calculating the elasticity matrix of bone scaffold, (A) uniaxial loading in the x direction, (B) uniaxial loading in the y direction and (C) shear loading in the x-y plane.

$$c_{11} = \frac{\sigma_x}{\epsilon_x}, c_{12} = \frac{\sigma_y}{\epsilon_x}, c_{13} = \frac{\tau_{xy}}{\epsilon_x} \quad (2)$$

Second, the strain in the y direction is set to -0.1 and other two strains are set to zeros, i.e., $\epsilon_x = 0.0$, $\epsilon_y = -0.1$, $\gamma_{xy} = 0.0$ (Figure 2B). Under this loading scenario, the elastic constants of c_{22} and c_{23} can be calculated as:

$$c_{22} = \frac{\sigma_y}{\epsilon_y}, c_{23} = \frac{\tau_{xy}}{\epsilon_y} \quad (3)$$

Third, the shear strain is set to 0.1 and other two strains are set to zeros, i.e., $\epsilon_x = 0.0$, $\epsilon_y = 0.0$, $\gamma_{xy} = 0.1$ (Figure 2C). Under this loading scenario, the elastic constants of c_{33} can be calculated as:

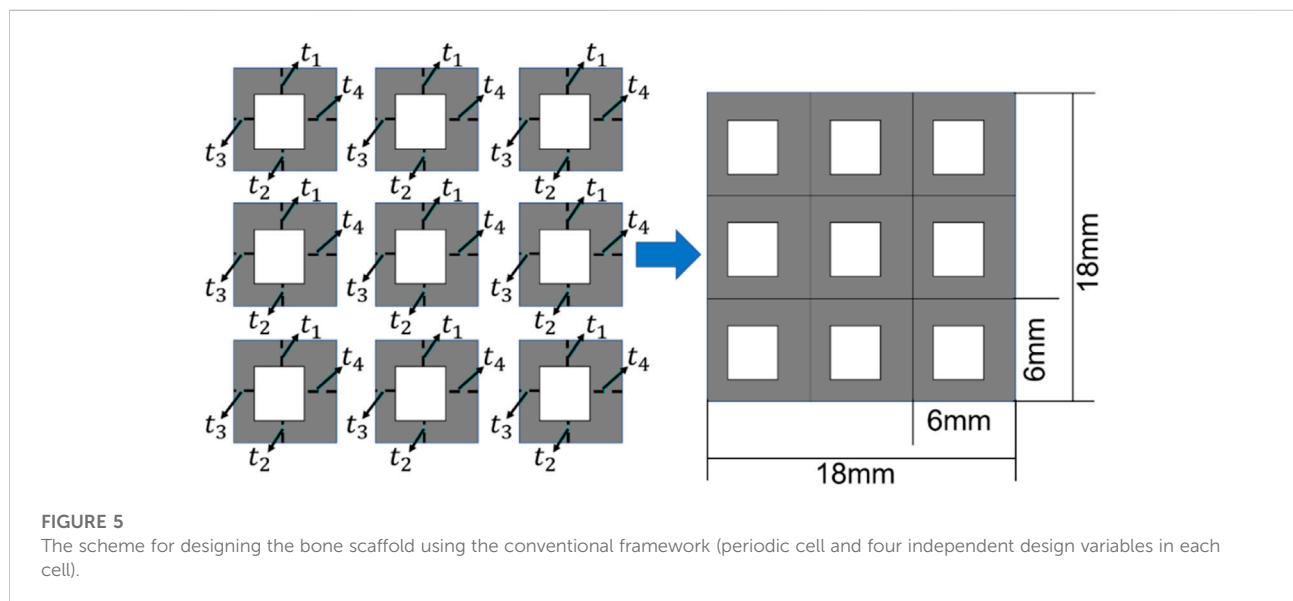
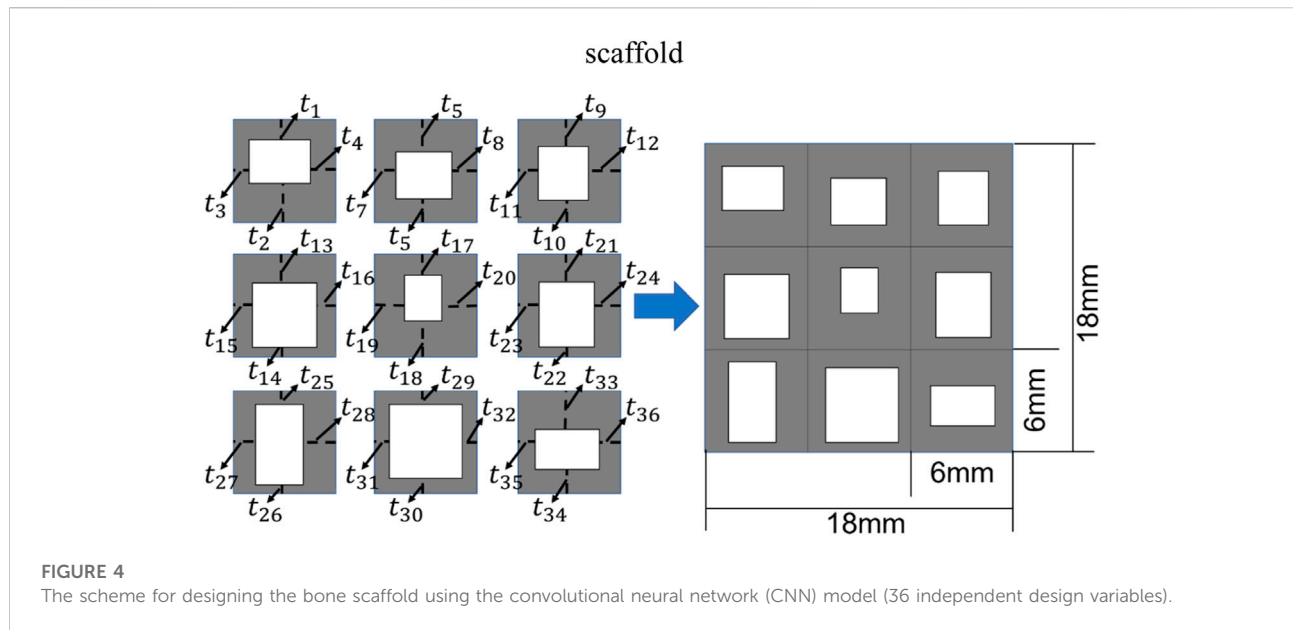
$$c_{33} = \frac{\tau_{xy}}{\gamma_{xy}} \quad (4)$$

It should be noted that the same loading scenarios (Figure 3) and procedure described above was used to calculate the elasticity

matrix of the bone scaffold (also meshed using PLANE182) in the subsequent analysis.

2.2 Design setting for the bone scaffold

In the present study, the 2D bone scaffold with the anisotropic mechanical properties was intended to be designed. The porous bone scaffold with 3×3 cells was used for the demonstration (Figure 4). Nevertheless, the readers can also use the same framework to design the scaffolds with more cells. The dimension of the scaffold was set to $18.0 \times 18.0 \text{ mm}^2$, which is the size similar to the defected human vertebral part. In each cell of the scaffold, the four dimensional parameters, i.e., the four thicknesses, were set as the independent design variables. Therefore, there are 36 independent design variables ($t_1 \sim t_{36}$) for the entire scaffold. It is obvious that it is very time consuming to



perform the structural optimization involving 36 independent design variables using the conventional optimization methods, such as the solid isotropic material with penalization (SIMP) method and the level set method (LSM) (Davoodi et al., 2021). In order to demonstrate the advantage of using 36 independent design variables in the scaffold design, the design using the conventional design framework, i.e., using the periodic cell and four design variables in each cell, was also performed for the comparison purpose (Figure 5).

Considering the minimal structural thickness, which can be produced by the additive manufacturing (e.g., the selective laser melting), is approximately 0.2 mm, the minimal dimension of the design variable was set to 0.2 mm and the thickness of the scaffold was increased or decreased by 0.2 mm in the iterations. The scaffold designed was intended to replace the defected bone tissues. Therefore, to make the scaffold clinically relevant and to increase the computational efficiency, three discrete values, i.e., 0.2, 0.4 and 0.6 mm, were set as the design ranges for both the 36 design

variables in the CNN method and the four design variables in the conventional design framework. Because of the constraint on the structural dimensions, the porosity of the scaffold is consequently constrained.

Regarding the characterization of the mechanical property of the bone scaffold, because all the dimensional parameters were set as the independent design, the scaffold designed can exhibit the anisotropic mechanical behavior and thus the constitutive relation presented Eq. 1 was used to describe the mechanical properties of scaffold. In the present study, the Ti-6Al-4V was considered as the base material for producing the porous scaffold. Therefore, in the FE models of 2D bone scaffolds, the Young's modulus of the solid part was set to 113.8 GPa and the Poisson's ratio was set to 0.34 (Niinomi, 1998).

In the design of bone scaffolds, the differences in the six elastic constants calculated from the bone and scaffolds may be very large. The constant with a large difference will make a significantly large contribution to the design objective function, leading to the ignorance of the constants with small differences. It is revealed in the authors' previous study that the contributions of the elastic constants c_{13} and c_{23} to the anisotropic properties of the scaffold are ignorable (Lu et al., 2019b; Li et al., 2019). Therefore, to make the influencing role of each constant approximately the same in the optimization process, the following weighting factors were introduced:

$$w_{ij} = \begin{bmatrix} \frac{1}{1-\nu^2} & \nu \cdot \frac{1}{1-\nu^2} & 0 \\ \nu \cdot \frac{1}{1-\nu^2} & \frac{1}{1-\nu^2} & 0 \\ 0 & 0 & \frac{1}{2(1+\nu)} \end{bmatrix} \quad (5)$$

where ν is the Poisson's ratio of the base material.

The relative differences between the elastic constants of the bone scaffold and those of the bone tissue were calculated using the following formula:

$$a_{ij} = \left(\frac{c'_{ij} - c_{ij}}{c_{ij}} \right)^2 \quad (i, j = 1, 2, 3) \quad (6)$$

where c'_{ij} are the elastic constants of the bone scaffold and c_{ij} are the elastic constants of the bone tissue. In the equation above, a power of two is used to magnify the difference between different samples. Additionally, it is used to convert the negative values to positive values so as to increase the prediction accuracy.

Then the objective function used in the optimization process was defined as:

$$f = \sum \frac{w_{ij}}{\hat{w}} a_{ij} \quad (i, j = 1, 2, 3) \quad (7)$$

where $\hat{w} = \sum w_{ij}$.

2.3 Machine learning based framework for the optimization of bone scaffold

In the design of anisotropic bone scaffold, there are 36 independent design variables and each variable has three values to be chosen from. Therefore, there are 3^{36} possible designs. It will take a long time to perform the optimization using the FE simulations and the calculation time will be exponentially increased when the number of design variable is increased. To increase the calculation efficiency and make the design clinically practical, a novel self-learning convolutional neural network (CNN) based optimization framework was developed to design the scaffolds. The CNN model constructed is shown in Figure 6, where three convolutional layers and three full-connection layers were used in the model. The convolution kernels were trained in a hierarchical manner, which consisted of low-level features to generate more complex patterns. All convolution kernels were set to a size of 3×3 . The maximal pooling was applied after the convolutional layers to simplify the information of the output neurons (Li et al., 2019). To improve the accuracy of the CNN model, a dropout rate of 10% was used in the three pooling layers. Each new design of scaffold was converted into the 6×6 matrix expressed in Matlab (Figure 7) and serve as the input for the CNN model. The conversion of the design into Matlab matrix enabled the automation of the entire optimization process and increased the calculation process. The output of the CNN is the objective function given in Eq. 8. It should be noted that the CNN architecture presented in the present study is not new but is guided by the work done by Li et al. (2019), which was created to solve a similar problem. Different CNN architectures or machine learning techniques may also be used to achieve the same purpose, i.e., designing anisotropic bone scaffolds. The CNN model presented in the present paper can take the image (in terms of the matrix) as the input and is just one demonstration of the technique in designing anisotropic porous bone scaffolds. The reason that the convolutional layers are used in the CNN architecture is that the computational efficiency can be largely increased, because the convolutional layer can deal with the two-dimensional input while the fully connected layer can only deal with the one-dimensional input.

The training and cross-validation of the CNN model is shown in Figure 8. In the training of the CNN model, first, 10,000 bone scaffolds were randomly generated, 8,000 of which were used for the training of the CNN model (Figure 8A) and the remaining 2,000 were used for the cross-validation of the CNN model (Figure 8B). The elastic constants of bone scaffolds calculated from the FE analysis were served as the ground truths for the training and cross-validation. In the training process, the CNN model learned a valid representation describing the geometric features of the bone scaffolds. A loss function was defined to quantify the differences between the elastic constants predicted from the CNN model and those

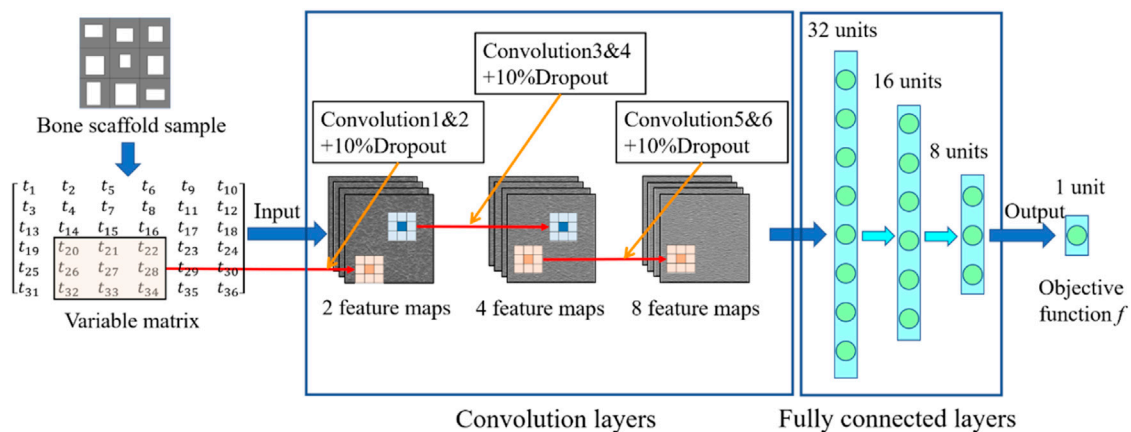


FIGURE 6

The CNN model developed in the present study.

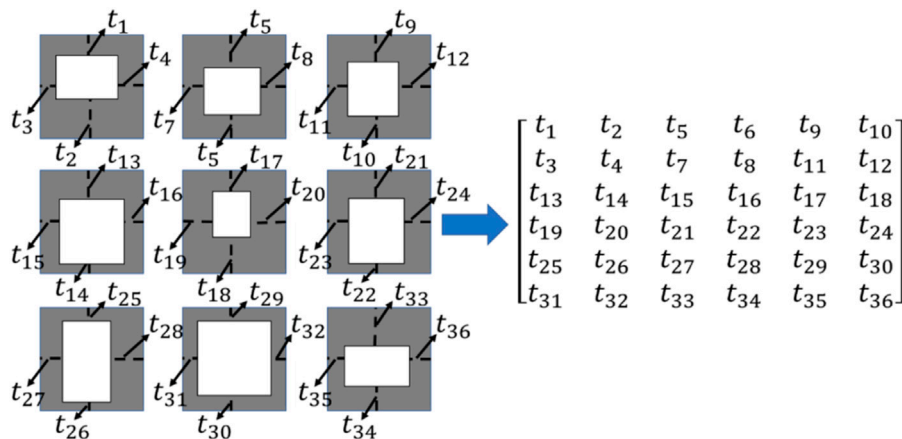


FIGURE 7

Conversion of the scaffold design into the matrix expressed in Matlab.

calculated from the FE analysis. The kernels and biases in the convolutional layers and weights in the fully connected layers were then adjusted using the backpropagation algorithm (Rubio et al., 2011). Iterative adjustments were made to minimize the loss function using a large datasets of bone scaffolds. In the present study, the mean absolute error (MAE) between the FE prediction and the CNN prediction was set as the objective (loss) function:

$$\text{MAE}[Y, f(X)] = \frac{1}{n} \sum_{i=1}^n |Y_i - f_i(X)| \quad (8)$$

where Y_i is the objective function presented in Eq. 7 which was calculated using the FE method, $f_i(X)$ is the corresponding

value calculated using the CNN method and n is the number of the samples used for the cross-validation of the CNN model ($n = 2,000$).

To assess the predictive power of the CNN model constructed, 500 new bone scaffolds were processed. The values of these bone scaffolds, calculated as the objective function for optimization, i.e., that presented in Eq. 8, were calculated using the trained CNN model and the FE method, respectively. The FE predictions were served as the ground truths and the predictive power of the CNN model was obtained by comparing the values obtained from the CNN and the FE models. The linear correlation analysis was performed between the CNN and FE predictions using the 500 data samples. Because the

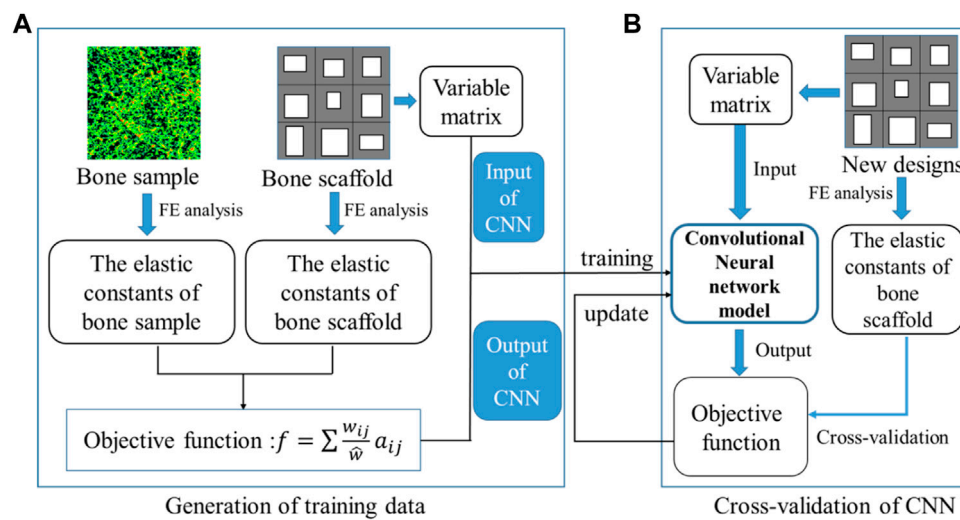


FIGURE 8 Training and cross-validation of the convolutional neural network model for predicting the elastic constants of bone scaffold, (A) generation of the training data and (B) cross-validation of the CNN model.

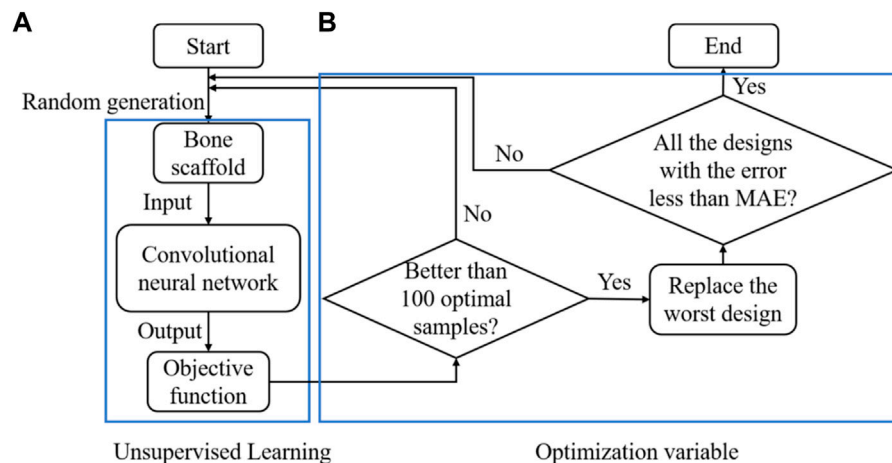


FIGURE 9 The design of the anisotropic scaffold using the self-learning CNN model, (A) unsupervised learning and (B) optimization variable.

variance between the CNN and FE predictions increased with the amplitude of the values, the log transformed values were plotted and analyzed, in which the following transformation formula was used:

$$\text{Log}_f = (\log(f) + 1) / \log(f_{\max}) \quad (9)$$

where f is the objective function, calculated using Eq. 7, before the log transformation, Log_f is the corresponding value after the log transformation and f_{\max} is the maximal value in the optimal sample dataset.

In summary, the CNN-based framework for designing the anisotropic scaffold is shown in Figure 9. It should be noted that a self-learning process was introduced into the scaffold design to accelerate the optimization process. The self-learning process consists of two parts: unsupervised learning (Figure 9A) and optimization variable (Figure 9B). Specifically, the process can be briefly explained as below: in the iterations, 10,000 new samples were generated from which the first 100 optimal designs were selected as the initial optimal samples. The process was repeated and the first 100 optimal designs were updated after each iteration, i.e., if the design is better than those in the

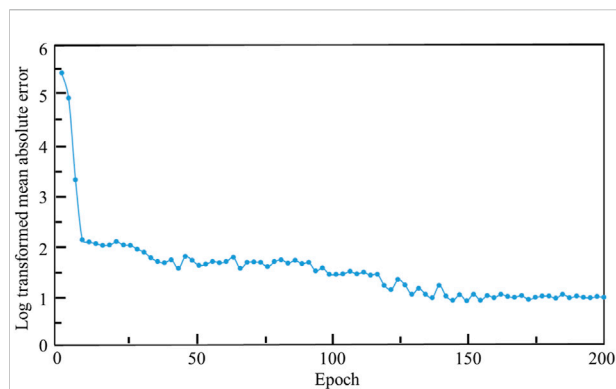


FIGURE 10

The relationship between the log transformed mean absolute error, where $Y = \ln(\text{MAE}) + 1$ is used, and the epoch.

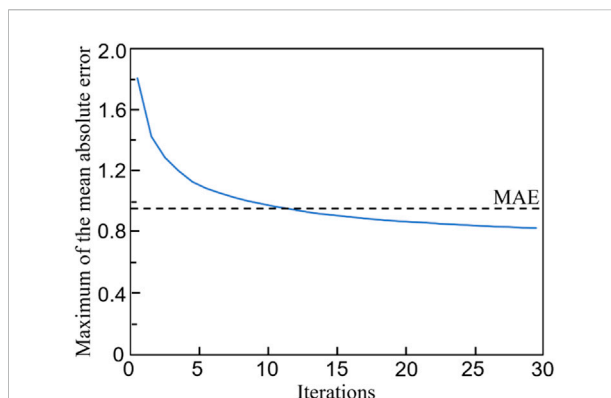


FIGURE 11

The evolution of the maximum mean absolute error (MAE) in 100 optimal samples with the number of iterations.

100 optimal designs and then it is used to replace the worst design in the 100 designs. Because some errors are presented in the CNN model and the MAE is the average prediction error between the prediction and the actual values, to avoid the exclusion of the optimal samples, all the designs with the error less than MAE remained in the iterations.

Using the framework presented in Figure 9, the bone scaffold was designed to mimic the anisotropic mechanical behavior of a specific defected bone sample, which is one of the main design objectives in scaffold design (Gómez et al., 2016; Kang et al., 2020). To demonstrate the ability of the CNN based framework in designing the scaffolds for different bone samples and also to take into account the variances among different bones, 12 bone samples with different porosities and structures, obtained from the HR-pQCT images, were processed and the corresponding scaffolds were designed using the CNN and conventional methods. Statistical analysis was performed and the normality check for all the data samples was performed using the statistical program PASW statistics (SPSS Inc., Chicago, IL) and the probability of type I error was set to $\alpha = 0.05$, i.e., $p < 0.05$ was considered normal distribution.

To quantify the differences between the mechanical properties of the bone scaffolds and those of the bone samples, the relative error (RE) was used, which is defined as below:

$$\text{RE} = \frac{P^{\text{CNN}} - P^{\text{RVE}}}{P^{\text{RVE}}} \times 100\% \quad (10)$$

where P^{RVE} is the elastic constant calculated from the bone samples, P^{CNN} is the corresponding elastic constant calculated from the bone scaffold designed using the self-learning CNN or conventional method.

To enable the process of a large amount of bone scaffolds, all the pre-processing and post-processing were automated using the in-house developed Matlab (R2019, MathWorks, Natick,

Massachusetts, United States) code and the FE analysis was performed using the Ansys (v18.0, ANSYS, Inc., Canonsburg, PA, United States). The CNN model was constructed using the Tensorflow 2.0 module in Python 3.7. The training process was conducted on a desktop computer setting to i7-8700 CPU, 32G RAM, and the Nvidia GTX1060. The batch size was set to 128 and the training was iterated for 200 epochs. The training process took approximately 2.0 h.

3 Results

3.1 Cross-validation and prediction power of the convolutional neural network model

The relationship between the mean absolute error (MAE) and the training iterations is shown in Figure 10. Because the initial values of the weights and biases are randomly assigned, the MAEs of the first a few iterations are high. However, after several iterations, the MAE descends rapidly and the MAE is below 1.0 after 120 training epochs. Therefore, no over-fitting is observed in the cross-validation of the CNN model developed. In the process of self-learning accelerated optimization, the changes of samples were recorded. It can be seen that this procedure ensured the errors in all the 100 optimal designs are less than MAE after some iterations (Figure 11). Afterwards, an optimal sample can be obtained from these 100 samples.

The linear correlation between the log transformed objective functions obtained from the CNN and FEM is shown in Figure 12A. A high coefficient of determination (R^2) has been achieved, i.e. $R^2 = 0.95$, implying a good prediction power of the CNN model. To further demonstrate the prediction power of the CNN model, Bland-Altman diagram of the objective function (f)

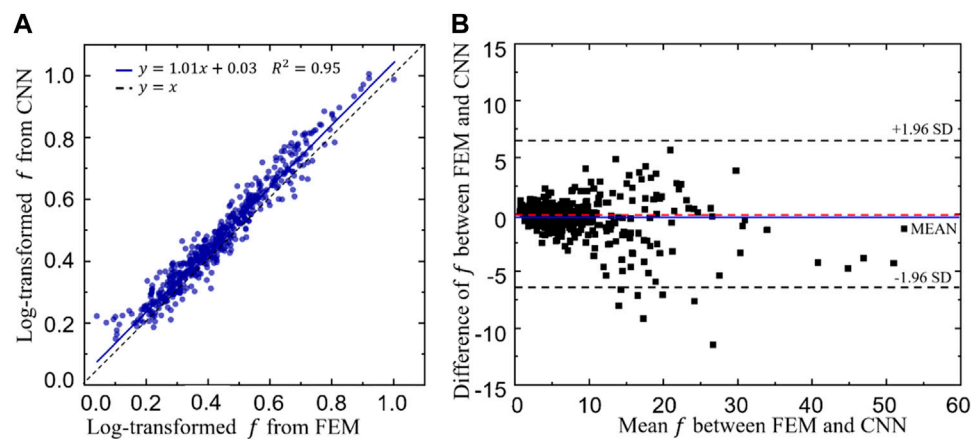


FIGURE 12
(A) The relationship between the log transformed objective functions predicted from the convolutional neural network (CNN) model and those calculated from the finite element method (FEM). (B) Bland-Altman diagram of the objective function (f) between the FEM and CNN predictions.

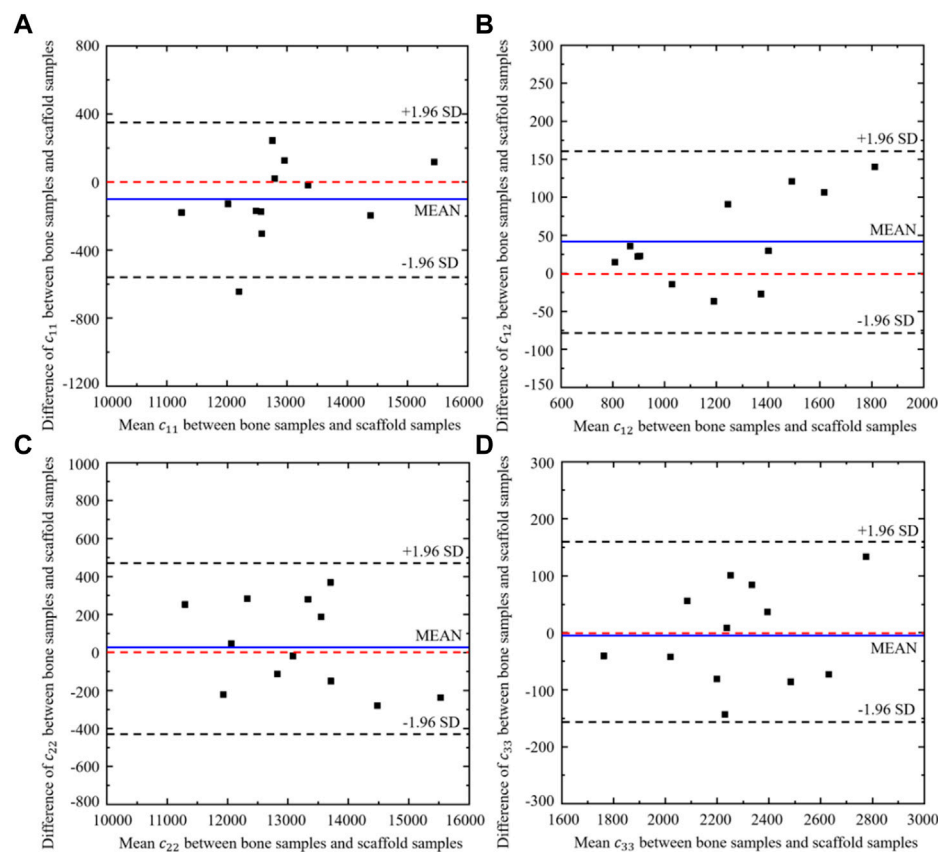
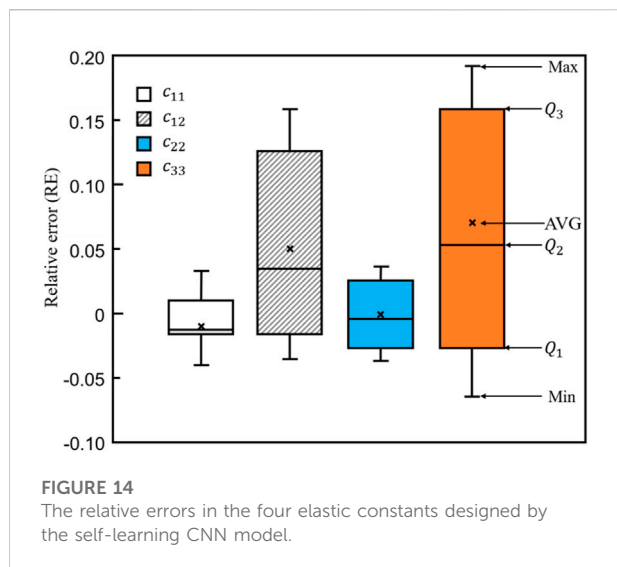


FIGURE 13
Bland-Altman diagram of elastic constants between the scaffold designed from CNN model and the corresponding bone samples ($n = 12$).



between the FEM and CNN predictions is presented in Figure 12B, where the values in the x axis represent the mean objective functions obtained from the CNN and FEM predictions (both calculated using Eq. 8 and the values in the y axis represent the difference between the objective functions. It is shown in the figure that the mean difference, represented in the blue line, is very close to zero. Additionally, 493 out of 500 samples (98.6%) fall in the confidence interval from -1.96 standard deviation (SD) to $+1.96$ SD (corresponding to 6.28) and only seven samples are out of this interval, implying a high degree of agreement between the CNN and the FEM predictions.

3.2 Design results from the self-learning convolutional neural network model

Twelve different bone samples are selected as the tissues to be replaced and the corresponding 12 bone scaffolds are designed using the self-learning CNN model developed. To assess the performance of the self-learning CNN model, the agreement between the elastic constants of the bone samples and those of the designed scaffolds was assessed using the Bland-Altman diagram (Figure 13), where the values in the x axis represent the mean elastic constants obtained from the bone samples and the bone scaffolds and the values in the y axis represent the differences between the elastic constants of the bone samples and those of bone scaffolds. It is shown in the figure that for the constants c_{22} and c_{33} , the mean differences are very close to zero. The mean differences are -94.0 and 40.5 for the constants c_{11} and c_{12} , respectively, which are also close to zero. The 95% confidence intervals for c_{11} , c_{12} , c_{22} and c_{33} are $[-565, 377]$, $[-76, 157]$, $[-427, 482]$ and $[-156, 161]$, respectively. 91.7% samples of c_{11} and all the c_{12} , c_{22} and c_{33} samples fall in the 95% confidence

intervals, implying a high degree of agreement in these constants between the bone samples and the bone scaffolds.

To further demonstrate the differences between bone scaffolds and bone samples, the relative errors in the four elastic constants, calculated using Eq. 10, are presented in Figure 14, where MAX and MIN represent the maximum and minimum values in the dataset, respectively. Q_1 , Q_2 and Q_3 represent the lower quartile, the median and the upper quartile values in the dataset and AVG represents the average value in the dataset. It is shown in the figure that the average errors are -0.01 , 0.03 , 0.01 and 0.05 for c_{11} , c_{12} , c_{22} and c_{33} , respectively. The ranges from Q_1 to Q_3 are much smaller for c_{11} and c_{22} ($[-0.02, 0.01]$ and $[-0.03, 0.03]$, respectively) than those for c_{12} and c_{33} ($[-0.02, 0.13]$ and $[-0.03, 0.16]$, respectively), implying c_{11} and c_{22} can be better matched to those of the native bone tissue using the self-learning CNN model.

3.3 Comparison of the results obtained from the convolutional neural network and conventional methods

To demonstrate the superior performance of the self-learning CNN model over the conventional method, the relative errors in the four elastic constants are presented in Figure 15. It is shown in the figure that for all the four constants, the average errors are closer to zero in the CNN group than those in the conventional method group. Furthermore, the relative errors from Q_1 to Q_3 are much smaller in the CNN group than those in the conventional method group, implying the relative errors are more scattered distributed in the scaffold designed using the conventional method. Figure 15 revealed that using the self-learning CNN model developed, not only a larger range of bone scaffolds can be designed, but also the mechanical properties of bone scaffolds designed from the CNN model are closer to those of the targeted bone samples. Distribution of the von Mises stress in one representative optimal scaffold designed from the CNN model is shown in Figure 16, where variable thicknesses are present in the structure.

4 Discussion

In the present study, a novel self-learning convolutional neural network (CNN) model was developed and its performance in designing the bone scaffolds with the anisotropic mechanical properties matched to the targeted bone tissue was demonstrated. The novelty of the present study lies in the novel design of anisotropic bone scaffolds using the emerging self-learning CNN technique.

The present study was motivated by the fact that it is crucial to design bone scaffolds with the anisotropic mechanical properties matched to those of the replaced defected bone

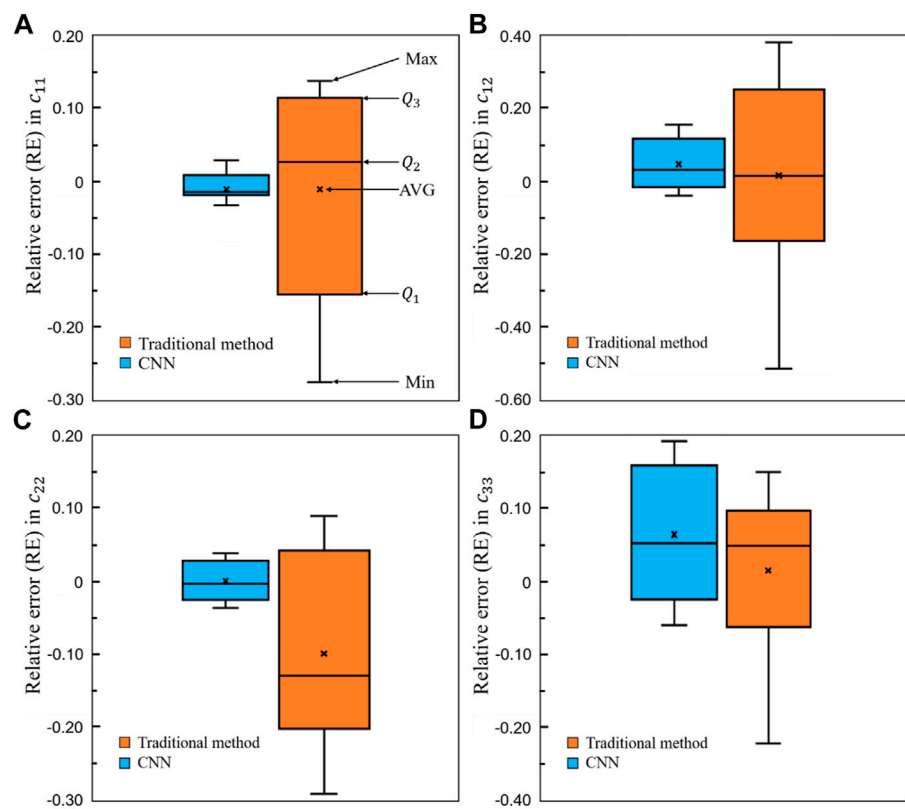


FIGURE 15
Comparison of the relative errors in the four elastic constants between the self-learning CNN and conventional methods ($n = 12$).

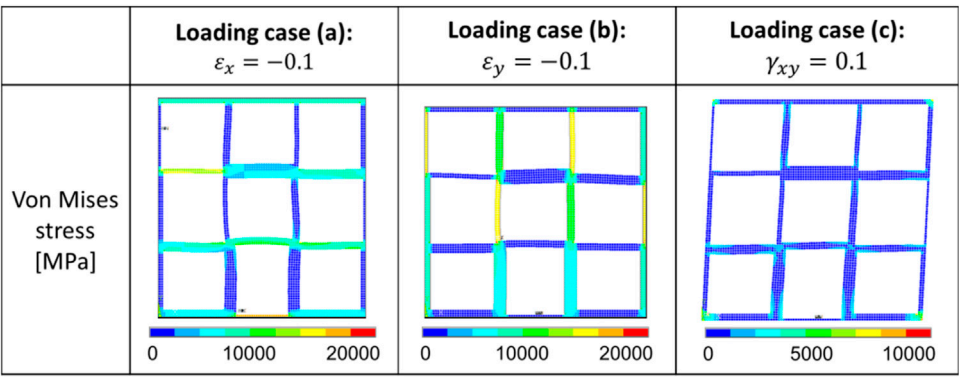


FIGURE 16
Distribution of the von Mises stress in one representative optimal scaffold under the three different loading cases.

tissues, but it is very challenging to realize this using the conventional design approaches because of the large amount of design variables involved. The emerging machine learning technique has the potential to solve the challenges. Indeed, it is

revealed in the present study that the design and optimization of one anisotropic scaffold took approximately only 20 min excluding the time used in the training and cross-validation of the CNN model, which took approximately 2 days (including

pre-processing of the 10,000 bone scaffolds, the model generation, the FE calculation, the post-processing, etc.). In contrast, it would take much more time to complete the design and optimization involving the same number of design variables, i.e., 36, using the conventional method, such as LSM. It should be noted that the more the independent design variables are involved in the design (e.g., in the 3D case), the more obvious efficient the self-learning CNN method is. The other advantage of the CNN technique is that because there is no constraint on the number of design variable, the design space can be largely expanded. As a consequence, new novel material designs can be made possible using the CNN model. Therefore, the CNN method has the great potential to be used as a novel and crucial tool in the design of 3D porous implants.

Regarding the ability of the self-learning CNN model in designing the scaffolds with anisotropic mechanical properties matched to those of the defected bone, a high ability has been achieved in the present study, which was assessed using the elasticity matrix. It should be noted that when evaluating the mechanical properties of bionic bone scaffolds, it is crucial to use the elasticity matrix of the structure, because the porous scaffolds are not isotropic. Nevertheless, in most previous studies (Dang et al., 2018; Zheng et al., 2021), the mechanical properties of scaffolds under just one or two loading scenarios are investigated and consequently their conclusions are limited to certain conditions.

The bionic scaffold with the mechanical properties matched to those of the native bone tissue is crucial in the clinical application, because when the scaffold is implanted in the human body, it has to be working together with the surrounding soft and hard tissues. If the mechanical properties of the implanted scaffold are too high, the stress shielding may occur and eventually affect the life expectancy of the scaffold [(Gómez et al., 2016), (Bloyer et al., 2007)]. If the mechanical properties of the implanted scaffold are too low, the scaffold may fail to afford the external loadings. Additionally, because of the daily activities of human body, all sorts of loading scenarios may occur in the bone (Huang et al., 2017) and consequently the anisotropic mechanical properties should be taken into account in the design of scaffold. Over the thousand years' evolution, the native bone tissues have been optimized to be the best structures in daily activities. Therefore, the designed artificially bone scaffold should possess the mechanical properties similar to those of the native bone tissues. The present study has advanced the design of bone scaffold towards this goal and it is demonstrated that the bone scaffolds designed using the CNN model indeed possess the anisotropic mechanical properties very similar to those of the native bone tissue.

Some shortcomings in the present study should be noted. First, only one topology (i.e., rectangular) of the scaffold was investigated. The primary aim of the present study was to demonstrate the application of the CNN technique in the design of scaffolds with anisotropic mechanical properties. Nevertheless, in the future, the scaffolds with other topologies,

such as sphere shape, etc. should also be investigated. Second, the simplified method (Figures 2, 3) for reconstructing the elastic matrices of bone and anisotropic scaffolds is used in the present study. More rigorous method such as periodic boundary condition should be incorporated in the future to have an accurate representation of the elastic matrix of the fully anisotropic structure. Third, due to the complexities in the design problem, only the 2D examples were presented and the plane stress scenario was assumed. In the current setting, there are 36 independent design variables and 3^{36} possible designs. Extending the current framework to the 3D scenario will create the computational "disaster." The authors of the present study are in the process to solve this technical challenge for 3D case. Nevertheless, the present study is the first towards the application of the self-learning CNN technique in designing bionic scaffolds with the anisotropic mechanical properties. Regarding the assumption of plane stress scenario, it is believed to be reasonable for the purpose of the present study, i.e., demonstrating the feasibility of the CNN model in designing the anisotropic scaffold involving many design variables. Fourth, only the elastic mechanical properties of the scaffolds were investigated. It should be noted that some other mechanical properties, especially the long-term properties of the bone scaffold, such as the fatigue (Huo et al., 2022), are the crucial factors influencing the life performance of the scaffold and thus should also be investigated in the future. Additionally in the clinical application of bone scaffolds, not only the mechanical properties but also other properties, such as the permeability, the cell behavior, should also be taken into account. Therefore, one of the future works in this direction is to investigate the overall performance of the anisotropic scaffold designed by CNN using the permeability test, the cell culture, the animal testing, etc. Last but not the least, the image datasets from the elderly patients (81.3 ± 7.2 year-old) are used. Nevertheless, this is a methodology paper, in which the high resolution images, i.e., HR-pQCT of human vertebrae (not possible in the clinic scenario so far), are used to obtain the accurate representation of the anisotropic mechanical properties of vertebral body. In the future, the 3D analysis using the images with the clinic resolution needs to be performed and tested before the clinical translation of the method.

In conclusion, 2D bone scaffolds with the anisotropic mechanical properties matched to those of the defected native bone tissue were successfully designed using a self-learning convolutional neural network model. It is revealed in the present study that not only the design space of the scaffolds can be expanded using the CNN method, but also the scaffolds designed by the CNN model possess the anisotropic mechanical properties better matched to those of the native bone tissue. Furthermore, the CNN model is efficient, because once the CNN model is well trained, it takes approximately only 20 min to complete the design of bone scaffold involving 36 independent design variables. Therefore, the CNN model developed possesses great potentials in the design of anisotropic bone scaffolds in the clinical setting.

Data availability statement

The original contributions presented in the study are included in the article/supplementary material, further inquiries can be directed to the corresponding authors.

Author contributions

YL, TG, ZY: conceptualization, methodology, formal analysis, investigation, writing—original draft. HZ: conceptualization, analysis, writing—review and editing. YaL, CW: resources, writing—review and; editing, supervision.

Funding

This work was supported by the National Natural Science Foundation of China (12072066, 12172083, U1908233), the Doctoral Scientific Research Foundation of Liaoning Province (2020-BS-280), the Natural Science

References

- Al-Ketan, O., Rashid, K., and Al-Rub, A. (2019). Multifunctional mechanical metamaterials based on triply periodic minimal surface lattices. *Adv. Eng. Mat.* 21 (10), 1900524. doi:10.1002/adem.201900524
- Ataee, A., Li, Y., Fraser, D., Song, G., and Wen, C. (2018). Anisotropic Ti-6Al-4V gyroid scaffolds manufactured by electron beam melting (EBM) for bone implant applications. *Mater. Des.* 13, 345–354. doi:10.1016/j.matdes.2017.10.040
- Bloyer, D. R., McNaney, J. M., Cannon, R. M., Saiz, E., Tomsia, A. P., and Ritchie, R. O. (2007). Stress-corrosion crack growth of Si-Na-K-Mg-Ca-P-O bioactive glasses in simulated human physiological environment. *Biomaterials* 28 (33), 4901–4911. doi:10.1016/j.biomaterials.2007.08.005
- Bonatti, C., and Mohr, D. (2019). Smooth-shell metamaterials of cubic symmetry: Anisotropic elasticity, yield strength and specific energy absorption. *Acta Mater.* 164, 301–321. doi:10.1016/j.actamat.2018.10.034
- Bucklen, B. S., Wettergreen, W. A., Yuksel, E., and Liebschner, M. A. K. (2008). Bone-derived CAD library for assembly of scaffolds in computer-aided tissue engineering. *Virtual Phys. Prototyp.* 3 (1), 13–23. doi:10.1080/17452750801911352
- Burton, W. S., Myers, C. A., Jensen, A., Hamilton, L., Shelburne, K. B., Banks, S. A., et al. (2021). Automatic tracking of healthy joint kinematics from stereoradiography sequences. *Comput. Biol. Med.* 139, 104945. doi:10.1016/j.combiomed.2021.104945
- Chen, Z., Xie, Y. M., Wu, X., Wang, Z., Li, Q., and Zhou, S. (2019). On hybrid cellular materials based on triply periodic minimal surfaces with extreme mechanical properties. *Mater. Des.* 183, 108109. doi:10.1016/j.matdes.2019.108109
- Dang, M., Saunders, L., Niu, X., Fan, Y., and Ma, P. (2018). Biomimetic delivery of signals for bone tissue engineering. *Bone Res.* 6 (3), 25–216. doi:10.1038/s41413-018-0025-8
- Davoodi, E., Montazerian, H., Mirhakimi, A. S., Zhianmanesh, M., Ibadode, O., Shahabad, S. I., et al. (2021). Additively manufactured metallic biomaterials. *Bioact. Mater.* 15, 214–249. doi:10.1016/j.bioactmat.2021.12.027
- Finkemeier, C. G. (2002). Bone-grafting and bone-graft substitutes. *J. Bone Jt. Surgery-American Volume* 84 (3), 454–464. doi:10.2106/00004623-200203000-00020
- Gómez, S., Vlad, M. D., López, J., and Fernández, E. (2016). Design and properties of 3D scaffolds for bone tissue engineering. *Acta Biomater.* 42, 341–350. doi:10.1016/j.actbio.2016.06.032
- Gu, G. X., Chen, C. T., Richmond, D. J., and Buehler, M. J. (2018). Bioinspired hierarchical composite design using machine learning: Simulation, additive manufacturing, and experiment. *Mat. Horiz.* 5 (5), 939–945. doi:10.1039/C8MH00653A
- Huang, K. L., Marcora, E., Pimenova, A. A., Di-Narzo, A. F., Kapoor, M., Jin, S. C., et al. (2017). A common haplotype lowers PU.1 expression in myeloid cells and delays onset of Alzheimer's disease. *Nat. Neurosci.* 20 (8), 1052–1061. doi:10.1038/nn.4587
- Huo, Y., Lu, Y., Meng, L., Meng, L., Wu, J., Gong, T., et al. (2021). A critical Review on the design, manufacturing and assessment of the bone scaffold for large bone defects. *Front. Bioeng. Biotechnol.* 9, 753715. doi:10.3389/fbioe.2021.753715
- Huo, Y., Lyu, Y., Bosiakov, S., and Han, F. (2022). A critical Review of the design, manufacture, and evaluation of bone joint replacements for bone repair. *Materials* 15 (1), 153. doi:10.3390/ma15010153
- Kang, J., Dong, E., Li, D., Dong, S., Zhang, C., and Wang, L. (2020). Anisotropy characteristics of microstructures for bone substitutes and porous implants with application of additive manufacturing in orthopaedic. *Mater. Des.* 191, 108608. doi:10.1016/j.matdes.2020.108608
- Laurencin, C., Khan, Y., and El-Amin, S. F. (2006). Bone graft substitutes. *Expert Rev. Med. Devices* 3 (1), 49–57. doi:10.1586/17434440.3.1.49
- Li, X., Liu, Z., Cui, S., Luo, C., Li, C., and Zhuang, Z. (2019). Predicting the effective mechanical property of heterogeneous materials by image based modeling and deep learning. *Comput. Methods Appl. Mech. Eng.* 347, 735–753. doi:10.1016/j.cma.2019.01.005
- Liu, F., Mao, Z., Zhang, P., Zhang, D., Jiang, J., and Ma, Z. (2018). Functionally graded porous scaffolds in multiple patterns: New design method, physical and mechanical properties. *Mater. Des.* 160, 849–860. doi:10.1016/j.matdes.2018.09.053
- Lu, Y., Krause, M., Bishop, N., Sellenschloh, K., Glüer, C. C., Püschel, K., et al. (2015). The role of patient-mode high-resolution peripheral quantitative computed tomography indices in the prediction of failure strength of the elderly women's thoracic vertebral body. *Osteoporos. Int.* 26 (1), 237–244. doi:10.1007/s00198-014-2846-7
- Lu, Y., Zhu, Y., Krause, M., Huber, G., and Li, J. (2019a). Evaluation of the capability of the simulated dual energy X-ray absorptiometry-based two-dimensional finite element models for predicting vertebral failure loads. *Med. Eng. Phys.* 69, 43–49. doi:10.1016/j.medengphys.2019.05.007
- Lu, Y., Zhao, W., Cui, Z., Zhu, H., and Wu, C. (2019b). The anisotropic elastic behavior of the widely-used triply-periodic minimal surface based scaffolds. *J. Mech. Behav. Biomed. Mat.* 99, 56–65. doi:10.1016/j.jmbbm.2019.07.012

Foundation of Dalian (21Z11019, 2021RQ025), the DUT-BSU grant (ICR 2103) and the Fundamental Research Funds for the Central Universities, China (DUT21TD105, DUT21LK21).

Conflict of interest

The authors declare that the research was conducted in the absence of any commercial or financial relationships that could be construed as a potential conflict of interest.

Publisher's note

All claims expressed in this article are solely those of the authors and do not necessarily represent those of their affiliated organizations, or those of the publisher, the editors and the reviewers. Any product that may be evaluated in this article, or claim that may be made by its manufacturer, is not guaranteed or endorsed by the publisher.

- Niinomi, M. (1998). Mechanical properties of biomedical titanium alloys. *Mater. Sci. Eng. A* 243 (1), 231–236. doi:10.1016/S0921-5093(97)00806-X
- Peng, X., Huang, Q., Zhang, Y., Zhang, X., Shen, T., Shu, H., et al. (2021). Elastic response of anisotropic Gyroid cellular structures under compression: Parametric analysis. *Mater. Des.* 205, 109706. doi:10.1016/j.matdes.2021.109706
- Rane, L., Ding, Z., and McGregor, A. H. (2019). Deep learning for musculoskeletal force prediction. *Ann. Biomed. Eng.* 47 (3), 778–789. doi:10.1007/s10439-018-02190-0
- Rubio, J. J., Angelov, P., and Pacheco, J. (2011). Uniformly stable backpropagation algorithm to train a feedforward neural network. *IEEE Trans. Neural Netw.* 22 (3), 356–366. doi:10.1109/TNN.2010.2098481
- Tan, R. K., Zhang, N. L., and Ye, W. (2020). A deep learning-based method for the design of microstructural materials. *Struct. Multidiscipl. Optim.* 61 (4), 1417–1438. doi:10.1007/s00158-019-02424-2
- Vijayavenkataraman, S., Zhang, L., Zhang, S., Zhang, S., His, F., Jerry, Y., et al. (2018). Triply periodic minimal surfaces sheet scaffolds for tissue engineering applications: An optimization approach toward biomimetic scaffold design. *ACS Appl. Bio Mat.* 1 (2), 259–269. doi:10.1021/acsabm.8b00052
- Wang, G., Shen, L., Zhao, J., Liang, H., Xie, D., Tian, Z., et al. (2018). Design and compressive behavior of controllable irregular porous scaffolds: Based on voronoi-tessellation and for additive manufacturing. *ACS Biomater. Sci. Eng.* 4 (2), 719–727. doi:10.1021/acsbiomaterials.7b00916
- Xiao, P., Haque, E., Zhang, T., Dong, X. N., Huang, Y., and Wang, X. (2021). Can DXA image-based deep learning model predict the anisotropic elastic behavior of trabecular bone? *J. Mech. Behav. Biomed. Mater.* 124, 104834. doi:10.1016/j.jmbbm.2021.104834
- Zheng, X., Chen, T. T., Guo, X., Samitsu, S., and Watanabe, I. (2021). Controllable inverse design of auxetic metamaterials using deep learning. *Mater. Des.* 211, 110178. doi:10.1016/j.matdes.2021.110178



OPEN ACCESS

EDITED BY
Zhen Luo,
University of Technology Sydney,
Australia

REVIEWED BY
Somnath Sarangi,
Indian Institute of Technology Patna,
India
Jakub Lengiewicz,
University of Luxembourg, Luxembourg

*CORRESPONDENCE
Fuzhou Niu,
fzniu@uusts.edu.cn

SPECIALTY SECTION
This article was submitted to
Biomechanics,
a section of the journal
Frontiers in Bioengineering and
Biotechnology

RECEIVED 10 August 2022
ACCEPTED 16 September 2022
PUBLISHED 04 October 2022

CITATION
Wang H, Cui S and Niu F (2022),
Optimization and demonstration of two
types of spring-roll dielectric elastomer
actuators for minimally invasive surgery.
Front. Bioeng. Biotechnol. 10:1016350.
doi: 10.3389/fbioe.2022.1016350

COPYRIGHT
© 2022 Wang, Cui and Niu. This is an
open-access article distributed under
the terms of the [Creative Commons
Attribution License \(CC BY\)](#). The use,
distribution or reproduction in other
forums is permitted, provided the
original author(s) and the copyright
owner(s) are credited and that the
original publication in this journal is
cited, in accordance with accepted
academic practice. No use, distribution
or reproduction is permitted which does
not comply with these terms.

Optimization and demonstration of two types of spring-roll dielectric elastomer actuators for minimally invasive surgery

HaoChen Wang¹, Saihui Cui² and Fuzhou Niu^{1*}

¹School of Mechanical Engineering, Suzhou University of Science and Technology, Suzhou, China,
²Zhongshan Hospital Affiliated to Fudan University, Shanghai, China

Resulting from the restricted size of incisions and confined surgical space, the existing rigid and slender minimally invasive surgery (MIS) instruments are inefficient in providing an optimum articulation to handle certain minimally invasive surgery tasks. Thus, developments of novel articulating actuators are of urgent requirement. In this paper, with the aim to enhance the flexibility and maneuverability of surgical instruments in diverse minimally invasive surgery scenarios, two types of spring-roll dielectric elastomer (DE) actuators, namely linear-type and bending-type, are proposed. The actuators' parameters were optimized and calibrated using a novel step-by-step procedure, based on the characterization and modeling of dielectric elastomer material (VHB 4905). Critical design factors including dimensions of the core spring, the pre-stretch ratio of the dielectric elastomer, and the excitation level of the actuator were identified, while the boundary conditions for the modeling of the actuator were derived from the requirements of minimally invasive surgery applications. The dielectric elastomer actuators' deformation behavior and force response were analyzed both theoretically and experimentally, and the results from the two approaches were in good agreement. The linear-type actuator could achieve a maximum strain of 29% and a blocking force up to 5.05 N, while the bending-type actuator could achieve angulation over 70° and a blocking force of up to 0.22 N. The proposed actuators are lightweight, compact, and cost-effective, which could provide novel design inspiration for minimally invasive surgery instruments.

KEYWORDS

dielectric elastomer actuator, minimally invasive surgery (MIS), design optimization, spring-roll configuration, optimal design method

1 Introduction

Specialized miniature instruments with high-level flexibility and maneuverability can enable the surgeon to perform minimally invasive surgery through tiny incisions and/or natural orifice environments, benefiting in less hospitalization stay and postoperative complication rate compared to traditional surgery. However, the restricted incisions could cause various surgical difficulties including limited surgical operation spaces, lacks of visibility, and constraints on the degrees of freedom (DOFs) of the MIS instruments. In particular, the slender and rigid structure of traditional MIS instruments can only provide a limited range of hardness and accuracy, which can not meet the requirements of precision medical surgical tasks (Vajsbaher et al., 2018). In some common minimally invasive medical procedures, such as single-port laparoscopic surgery (SPLS) or natural orifice endoscopic surgery (NOTES), the whole body of an MIS instrument should work through a narrow single hole (Tei et al., 2021; Hurni et al., 2022), where the surgical field and flexibility of the operation are severely constrained. To deal with the above problems, novel actuators should be designed with adequate mechanical simplicity and robustness to obtain better flexibility and maneuverability.

Dielectric elastomers (DE) are a type of smart materials that could be electrically activated to change their shape. Dielectric elastomers can offer superior performance in terms of energy density and strain capacity compared to other conventional actuation methods (Imboden et al., 2022). Among the DE actuators, acrylic DE actuators are well known for their high strain and mechanical energy density. In particular, the acrylic VHB DE material shows the largest strain up to 380% and actuation pressure up to 7.2 Mpa (Sahu et al., 2022), which enables it a better response and performance surpassing that of natural muscle. Such characteristics make it particularly suitable for applications in robotics, prosthetics, and animatronics (Ji et al., 2019; Li et al., 2019; Di et al., 2021; Guo et al., 2021).

An ideal DE actuator for MIS application should be lightweight, miniature, flexible and safe, while capable of providing sufficient force output for the surgical operation (Le et al., 2016; Runciman et al., 2019). In particular, the outer diameter of the actuator should be less than 10 mm to fit most of the trocar ports. The length of a single actuator should be less than 50 mm to allow at least 3–4 actuators for the articulation of the MIS tools (the usual depth of penetration of MIS tools inside the patient's abdominal cavity is around 150 mm (Soper et al., 2008)). The blocking force of the bending actuator should be in a range of 0.1–5 N and the linear-type actuator in 5–10 N which are the common operating force in MIS (Golahmadi et al., 2021), while an adequate strain/angulation should also be achieved for the whole articulated system. The power and control unit of the actuator should be moderate for an adequate set-up time and

room for surgical operation (Lonner et al., 2021). Accordingly, the design requirements are summarized in Table 1, which are benchmarked against the performances of other actuators which were developed for MIS and already reported in the literature (Moers et al., 2012; Gerboni et al., 2016; Decroly et al., 2020; Wang and El Wahed, 2020; Wang et al., 2020; Decroly et al., 2021; Zhang et al., 2021).

To meet the above requirements, two types of spring-roll configuration DE actuators were designed in this study. As shown in Figure 1, when the coated area of the electrode was subjected to an external electric field, the DE roll of the linear-type spring-roll DE actuator could reduce its thickness in a circumferential direction and hence produce a linear elongation in its axial direction. Alternatively, the coated area of the electrode could be patterned (segregated) to permit a partial activation of the DE and hence produce a bending action of the actuator. The spring-roll DE actuator was designed to replace part of the rigid stem of conventional MIS tools. By aligning multiple linear- or bending-type spring-roll DE actuators, a flexible MIS instrument could be achieved as illustrated in Figure 1.

Even though DE actuators have been proven to offer large axial and bending actuation, the trade-off between their technical capabilities and the design requirements of the targeted devices has always been a major challenge that impedes their practical implementation. Therefore, the optimal design of the spring-roll DE actuator is critical to validate its feasibility and achieve its ultimate MIS applications. Besides, modeling of the DE actuator remains difficult due to the inherent nonlinear hyperelasticity of the DE material. Moreover, performance demonstrations needed to be conducted for verifying its stability and feasibility for articulating the MIS instruments.

In this paper, the three most important design factors that are expected to critically affect the overall performance of the developed actuator were identified, including the dimensions of the core spring, the pre-stretch ratio of the DE in different directions, and the excitation level of the actuator. Based on the characterization and modeling of the DE and the spring, a novel step-by-step optimization process of the above parameters was developed to address the critical trade-off between the technical capability of the spring-roll DE actuators and the design requirements of MIS applications. In addition, this paper also presents robust design and fabrication techniques for linear and bending-type spring-roll DE actuators. The performance of the prototypes was tested in terms of actuation strain and force, and the experimental results show that the developed DE actuator was promising for MIS uses.

The remainder of this paper is organized as follows. Section 2 addresses the optimal design of DE actuators aiming for MIS applications. Section 3 presents the fabrication process and experimental arrangements. Section 4 gives the results and discussions. And, Section 5 gives the conclusions.

TABLE 1 Performance of different actuators and design requirements of DE actuators proposed for MIS applications.

Actuator type	Total length (mm)	Outer diameter (mm)	Strain/Angulation	Blocking force (N)	Power & control unit
Bending-Tendon Driven (Zhang et al., 2021)	48.8	7	180°	0.96~5	N/A
Bending-Electromagnetic (Wang and El Wahed, 2020)	31.6	10	30°	1.42	Moderate
Bending-Hybrid (Wang et al., 2020)	40	11	180°	N/A	Moderate
Bending-Pneumatic Driven (Decroly et al., 2021)	50	6	180°	0.1	Moderate
Bending-Fluidic Driven (Decroly et al., 2020)	17~43	5	270°	0.04	Small
Linear-Fluidic Driven (Gerboni et al., 2016)	4	9	50%	5.6	Small
Linear-Fluidic McKibben (Moers et al., 2012)	62	1.5	15%	6	Small
Design requirements	30~50	5~10	30% (linear) 60° (bending)	5~10 (linear) 0.1~2 (bending)	Moderate

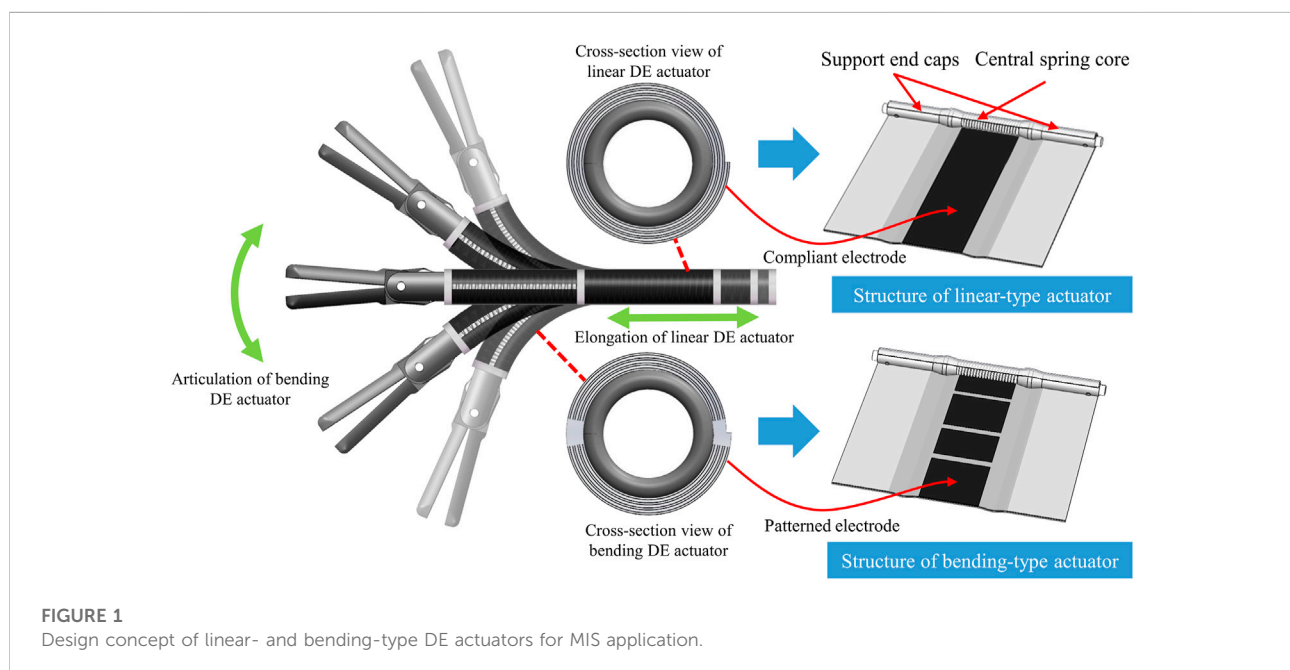


FIGURE 1
Design concept of linear- and bending-type DE actuators for MIS application.

2 Optimal design of dielectric elastomer actuators

2.1 Optimal design strategies

In this study, we use boundary conditions derived from the requirements of MIS applications (Table 1) to define the allowable strain and force outputs of the actuators for an enhanced theoretical modeling compared to the previous study (Li et al., 2019; Guo et al., 2021; Precht et al., 2021). Accordingly, several design parameters which are expected to critically affect the performance of the developed actuator were identified and targeted as shown in Figure 2.

When the spring-roll DE actuator reached a steady status, the elastic stress of the elastomer in the axial direction was balanced with the sum of two stresses, which are the Maxwell stress induced by the external electric excitation and the operating stress provided by the compressed spring, respectively. The Maxwell stress and the operating stress facilitate the expansion of the DE-film whilst the elastic stress impedes such variation as shown below:

$$\sigma_{\text{elastomer}}(x, y, \epsilon) = \sigma_{\text{spring}}(K, L, r_{\text{spring}}, \epsilon) + \sigma_{\text{Maxwell}}(U, \epsilon) \quad (1)$$

Where x and y are the pre-stretch ratios in the X and Y direction respectively; ϵ is the strain of the actuator in the longitudinal

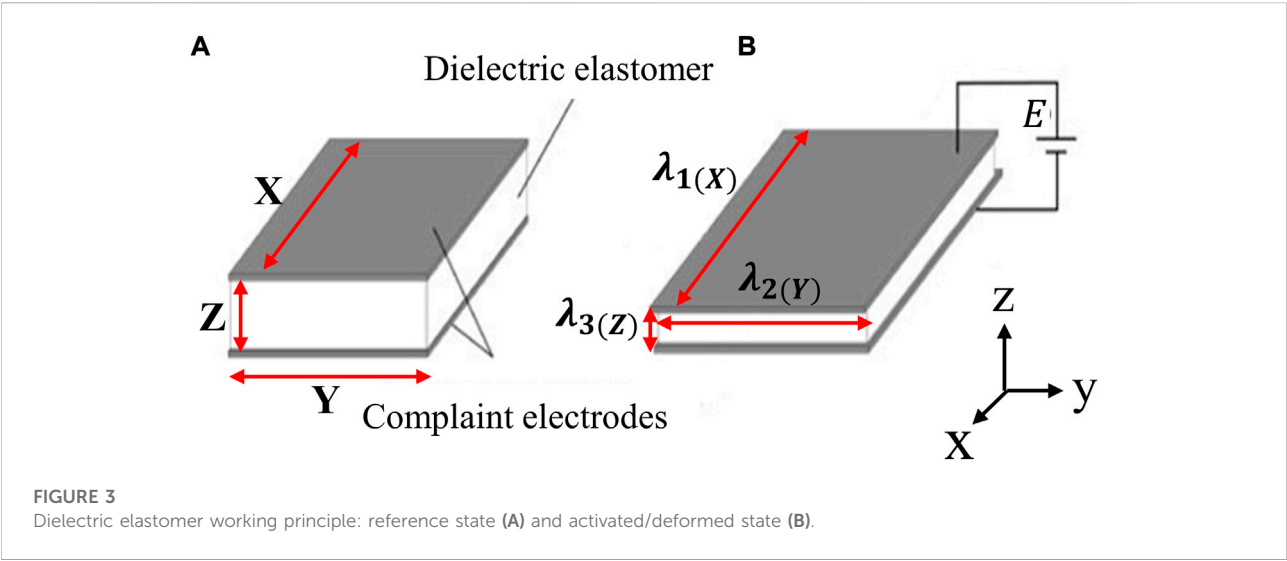
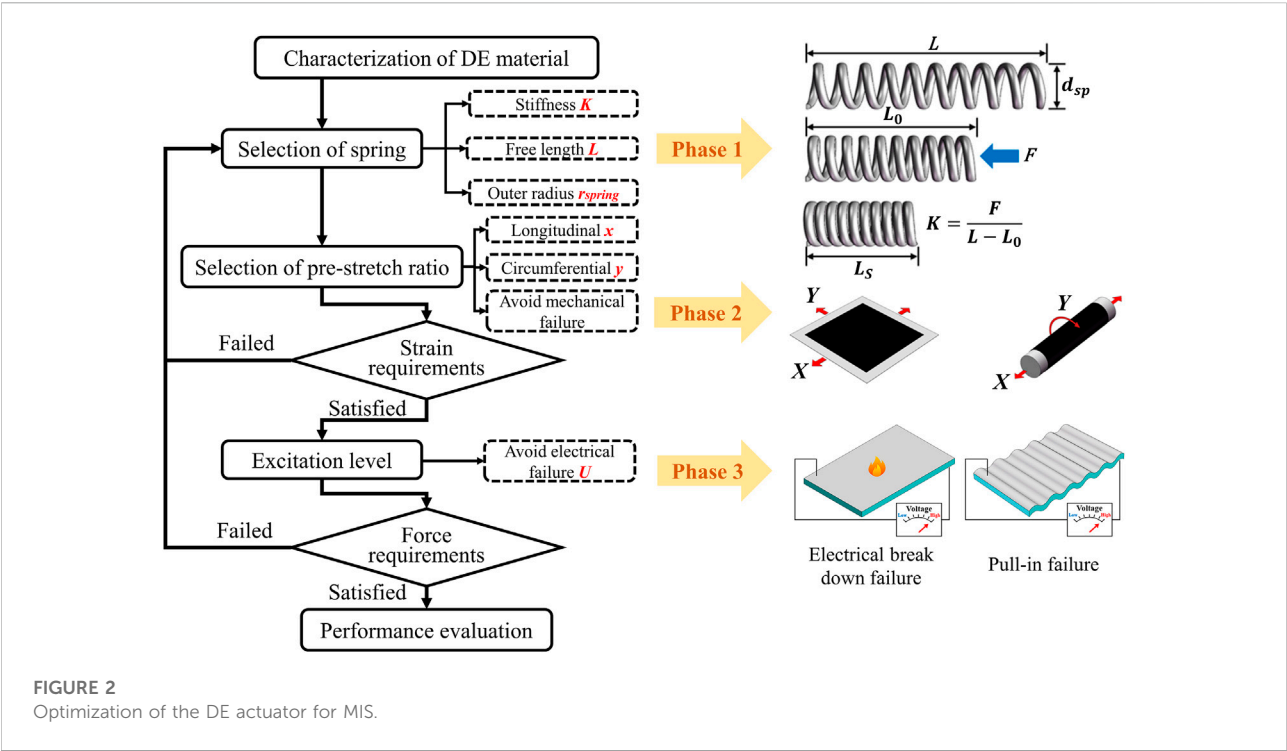


TABLE 2 Parameters of the selected commercialized spring.

Model	Outer diameter (mm)	Inner diameter (mm)	Free length (mm)	Solid length (mm)	Stiffness (N/mm)
3,364	6.35	5.23	63.5	19.89	0.17

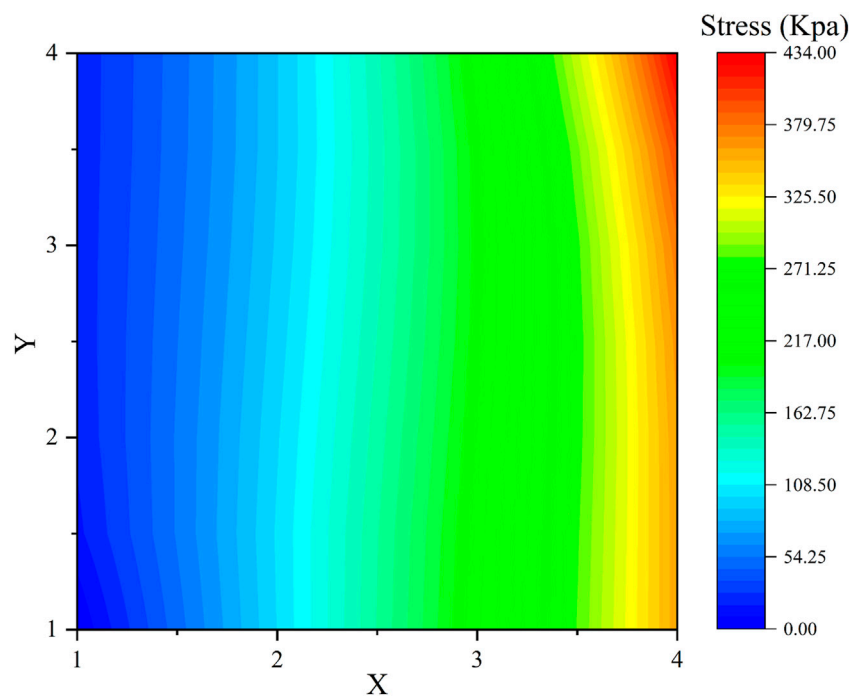


FIGURE 4
Elastic stress of VHB 4905 in the longitudinal direction with different Pre-stretch ratios.

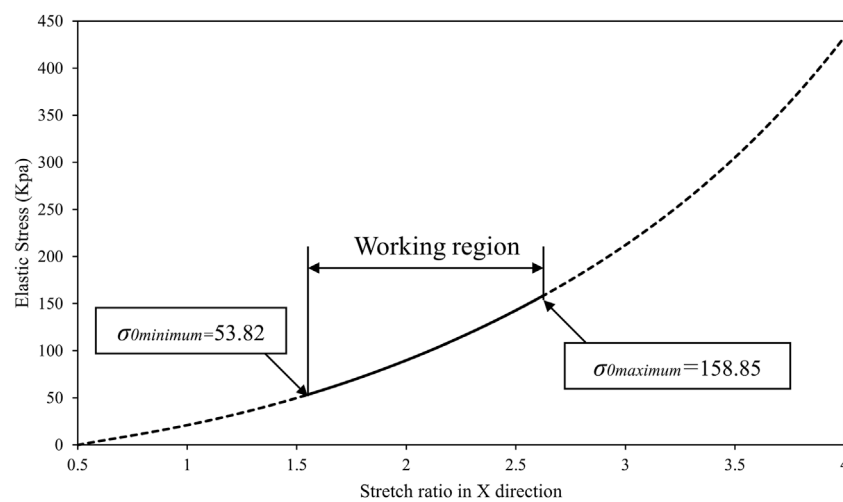


FIGURE 5
Elastic stress of the DE film in the longitudinal direction with x from one to four and y as four against the constrain of spring model 3,364.

direction; K is the stiffness of the spring; L is the free length of the spring; r_{spring} is the outer radii of the spring; U is the applied voltage on the DE.

Accordingly, the optimal design process is mainly divided into three phases, which are corresponded to the optimization of the spring, DE and electrical excitation, respectively. Since

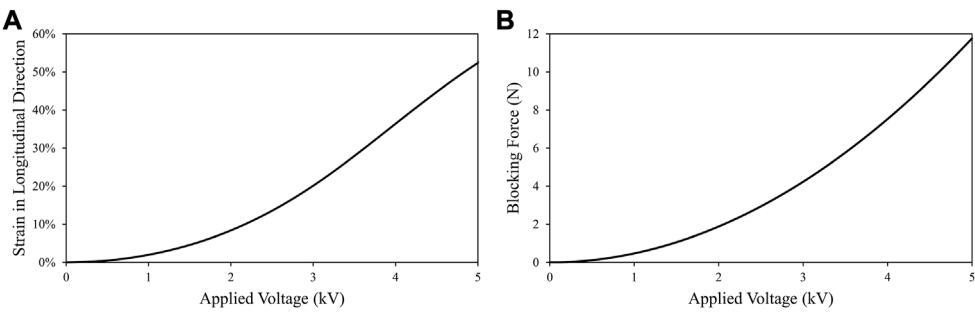


FIGURE 6
Performance estimation of the linear DE actuator with different excitation levels: (A) Strain versus applied voltage; (B) blocking force output versus applied voltage.

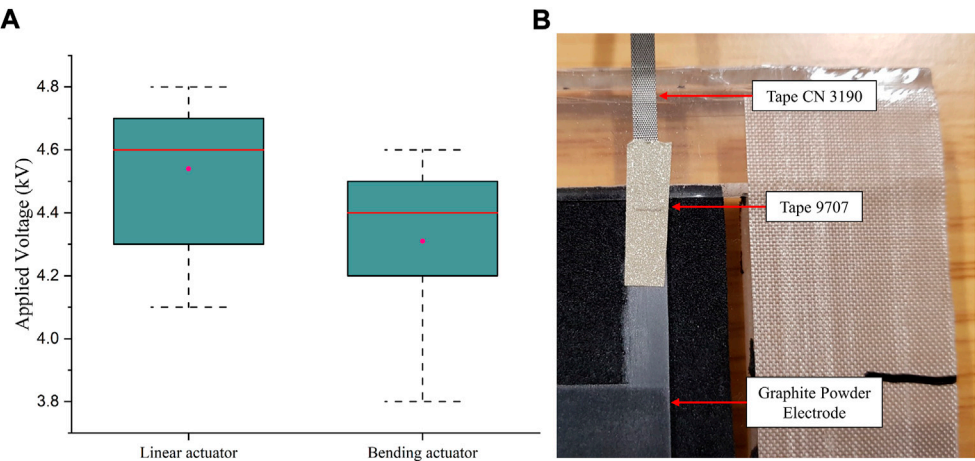


FIGURE 7
Electrical breakdown failure of the DE actuator: (A) Electrical breakdown failure of the bending and linear spring-roll DE actuator; (B) Electrical connection area of the dielectric film.

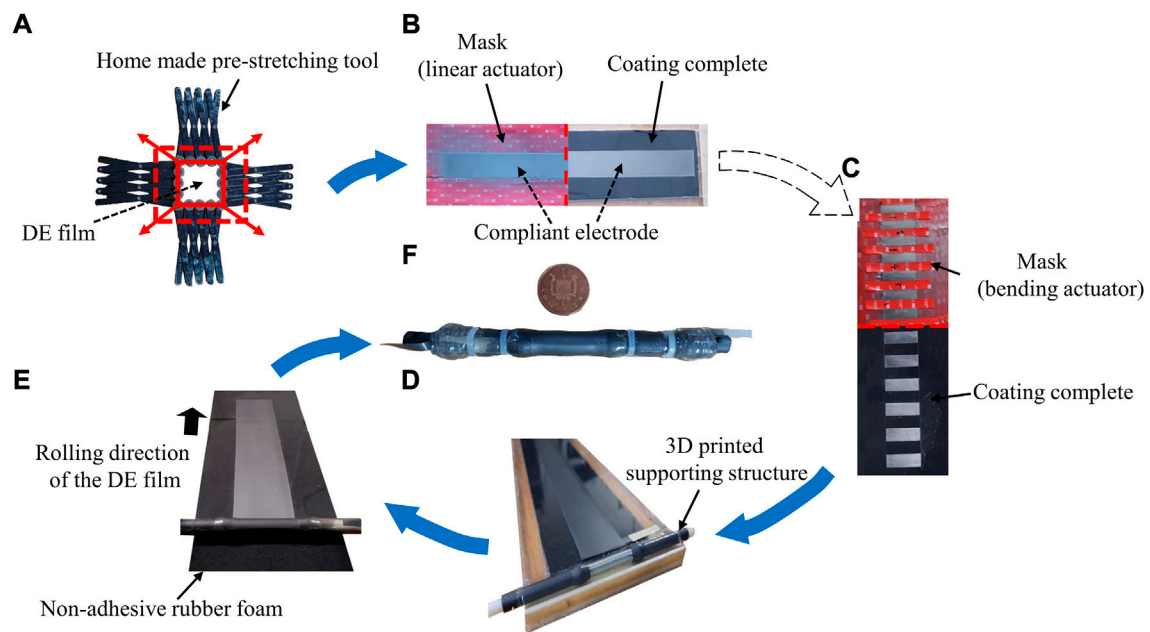
TABLE 3 Design parameters of the optimized spring-roll DE actuator.

Dielectric Elastomer	VHB 4905
Selected spring	Model 3,364 (Entex Spring)
Pre-stretch ratios	$x = 2.5$ and $y = 4$
Outer diameter	10 mm
Length	~24.2 mm
Maximum excitation level	3.5 kV

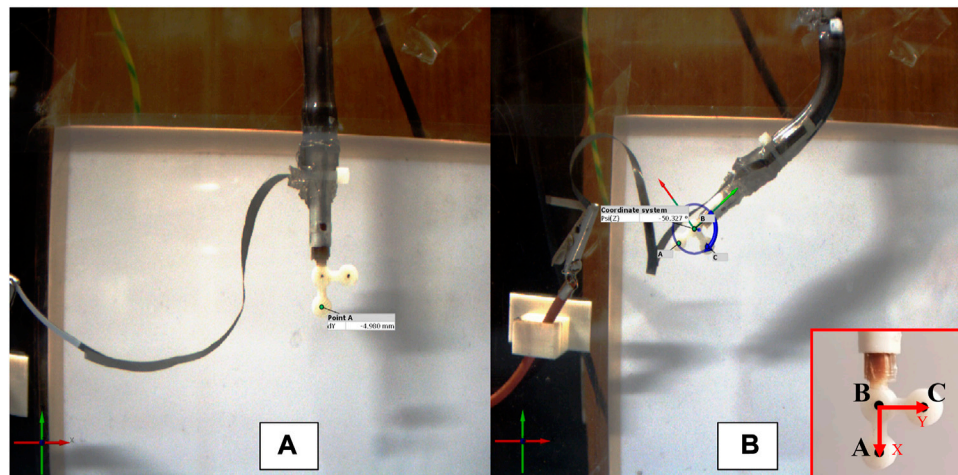
the parameters of spring mainly determine the overall size and capabilities of the actuator, it was analyzed in the first place. Subsequently, the design parameters of DE were discussed as they dictate the actuation state of the actuator. Finally, the

limitation of electrical excitation level was determined experimentally. As presented in Figure 2, the proposed optimization was progressed iteratively to both unfold the complex interaction between the three phases and maximize the strain/force performance of the developed actuator.

The optimization of the bending actuator is similar to the linear actuator, where the major difference is the pattern of the electrode. In this study, the bending actuator is designed as two degrees of freedom actuator as shown in Figure 1 and its analytical model could be derived from the modeling of the linear actuator (Li et al., 2019). Therefore, the optimization process would stress on the linear spring-roll actuator for simplicity. Accordingly, the discussion of those parameters has progressed step by step in the following sections.

**FIGURE 8**

Fabrication procedure of the spring-roll DE actuator: (A) Pre-stretch of the DE; (B) Coating of the compliant electrode for linear-type DE actuator; (C) Coating of the compliant electrode for bending DE actuator; (D) Spring core accommodated in the beginning slot before rolling; (E) Rolling the spring core along the frame and wrapping DE films on it; (F) Fabricated sample beside a one penny coin.

**FIGURE 9**

Marker recognition dot used in the deformation tests of linear-type DE actuator (A) and bending-type DE actuator (B).

2.2 Characterization of dielectric elastomer material

Dielectric elastomers are usually comprised of a thin layer of dielectric film with low in-plane stiffness, which is coated

with compliant electrodes on both sides to form a sandwich-like structure. When an electric excitation (usually in the range of several kV) is applied across the compliant electrodes, electrostatic stress, also known as the Maxwell stress, is generated as a result of the attraction of the

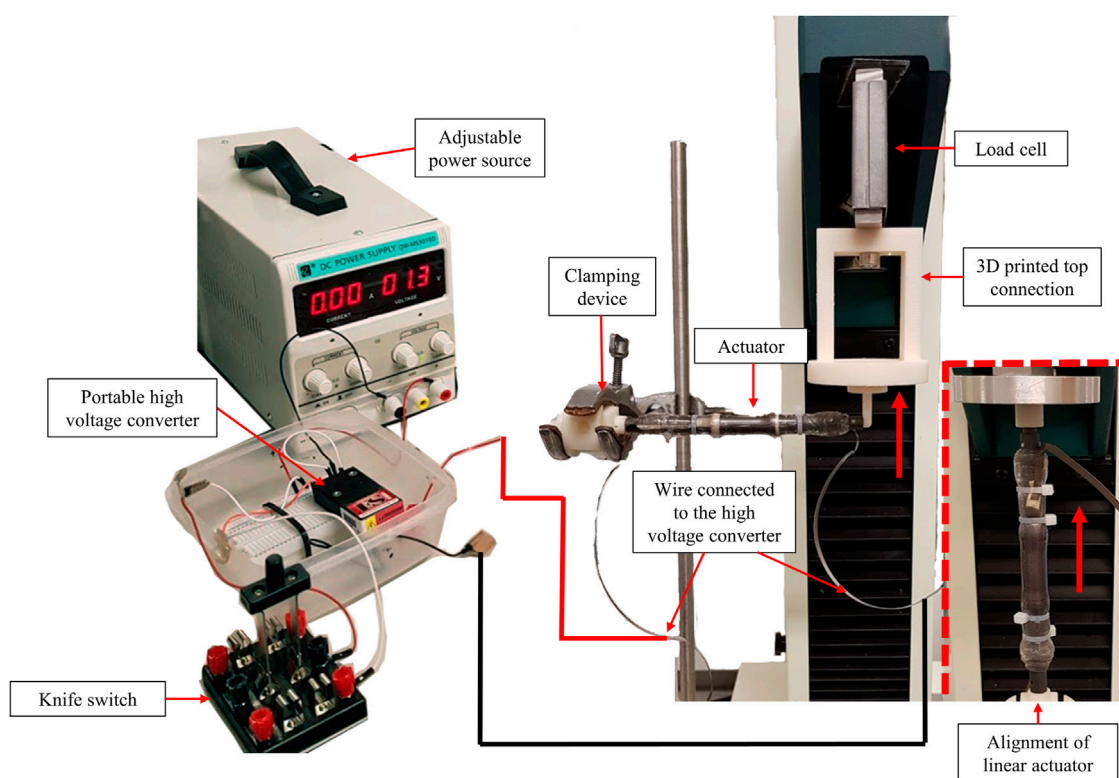


FIGURE 10

Force output test setup for bending-type spring-roll DE actuator (the alignment of the linear-type actuator as shown in the right bottom).

opposite charges induced on the two sides of the dielectric film. The electrostatic stress would squeeze the dielectric film and cause a deformation in a direction that is normal to the direction of the applied field (Precht et al., 2021), as illustrated in Figure 3.

Attributed to the high strain capability and dielectric constant provided by the 3M VHB 4910 film, it has been routinely used for the construction of DE actuators (Li et al., 2019; Guo et al., 2021). However, since the reduction of elastomer thickness could enlarge the outputs of the DE actuator (Li et al., 2019; Guo et al., 2021; Precht et al., 2021), 3M VHB 4905 acrylic film (0.5 mm thickness) was employed as the dielectric elastomer instead of 3M VHB 4910 (1.0 mm thickness) in this investigation. Therefore, the characterization of the VHB 4905 film was required. Reports have indicated that the Yeoh model (hyperelastic model) was deemed to be adequate to describe the deformation and stress behavior of 3M acrylic film (Garcia and Trindade, 2019), which are given by:

$$I_1 = \lambda_1^2 + \lambda_2^2 + \lambda_3^2 \quad (2)$$

$$\frac{\partial W}{\partial I_1} = C_{10} + 2C_{20}(I_1 - 3) + 3C_{30}(I_1 - 3)^2 \quad (3)$$

$$\sigma_i = \lambda_i \frac{\partial W}{\partial \lambda_i} - P_s = \lambda_i \frac{\partial I_1}{\partial \lambda_i} \frac{\partial W}{\partial I_1} - P_s \quad (4)$$

where C_{10} , C_{20} and C_{30} are the material constants, P_s is the hydrostatic pressure which depends on the boundary conditions of the elastomer, λ_1 , λ_2 and λ_3 are the stretch ratios in the X, Y, and Z directions, respectively which compose a Cartesian coordinate system as illustrated in Figure 3. The X, Y, and Z directions are identified as the longitudinal (axial direction of the DE roll), latitude (circumferential direction of the DE roll), and thickness directions of the DE elastomers.

To characterize the VHB 4905 film in the Yeoh model, the required material parameters were obtained from a set of uniaxial tensile tests which were performed on this film using a Tinius-Olsen tensile machine, model H5KS. This enabled the three main constants C_{10} , C_{20} and C_{30} of the Yeoh model to be estimated for the VHB 4905 elastomer film, which were found to be 14,070, -184.93, and 4.042, respectively.

The viscoelastic behavior of the VHB 4905 material was characterized by a relaxation test with stretch ratio inputs

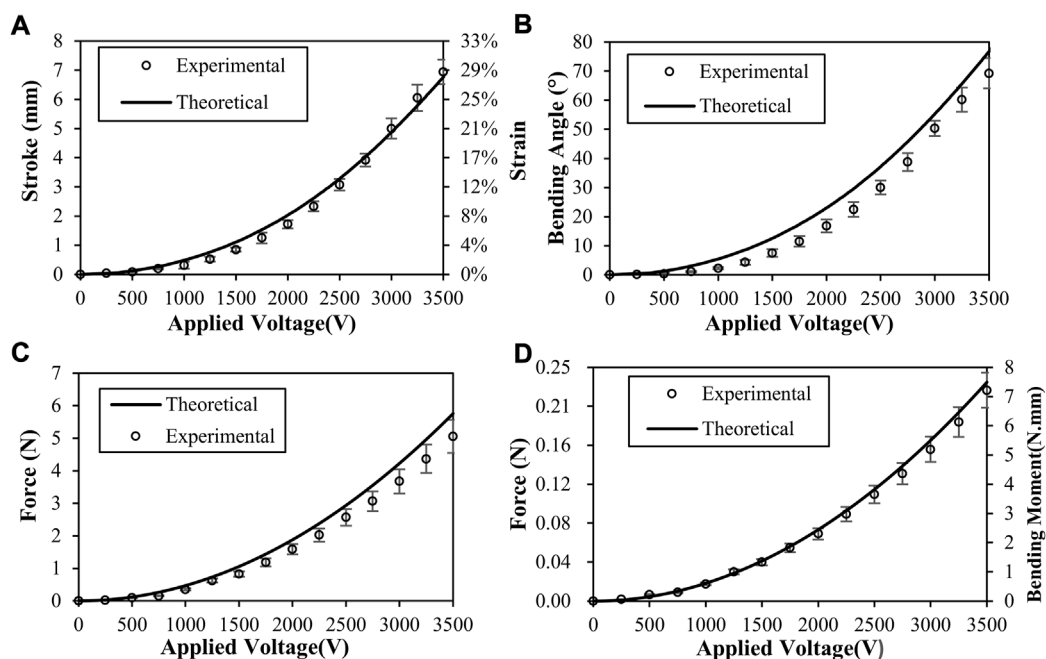


FIGURE 11

(A) Stroke/strain of linear-type spring-roll DE actuator versus applied voltage; (B) Angulation of bending-type spring-roll DE actuator versus applied voltage; (C) Output force of linear-type spring-roll DE actuator versus applied voltage; (D) Lateral blocking force/bending moment versus applied voltage for bending-type spring-roll DE actuator.

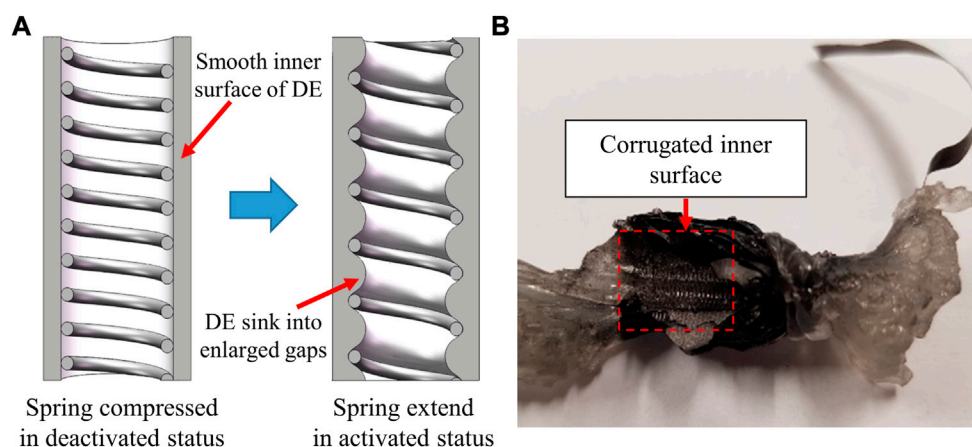


FIGURE 12

Inner surface variation of the spring-roll DE actuator: (A) Spring variation during the activation of the spring-roll DE actuator; (B) Corrugation of the surface of inner layers of the DE actuator.

varied between 100% and 400%. The result indicates that the stress relaxation of the film becomes slower after 60 s as it only drops further 3% (to 97%), after 200 s. Therefore, it was decided in this

study that the deformed shape of the spring-roll DE actuator is recorded after approximately 60 s from the voltage application, during which the DE actuator is assumed to be fully relaxed.

2.3 Selection of spring

The maximum allowable strain (ϵ_{\max}) of the actuator in the axial direction is a prior parameter that directly determines the capability of linear extension and bending angle for the spring-roll DE actuator. The core spring supports the structure of the activated DE rolls and defines the boundary conditions of the elastomer film (as presented later in sub section 4.2, Figure 12). Any stroke above the maximum compressed length will result in an undesired extension of the compression spring and meet the failure of the actuator. Therefore, the operating stress of spring (σ_{spring}) and maximum allowable strain (ϵ_{\max}) could be expressed as shown below:

$$\sigma_{\text{spring}} = \sigma_0 - \frac{\epsilon L_0 K}{\pi(r_{\text{actuator}}^2 - r_{\text{spring}}^2)} \quad (5)$$

$$\epsilon_{\max} = \frac{L}{L_0} - 1 = \frac{L}{L - \frac{\sigma_0 A}{K}} - 1 = \frac{1}{\frac{KL}{\sigma_0 \pi(r_{\text{actuator}}^2 - r_{\text{spring}}^2)} - 1} \quad (6)$$

Where L_0 is the compressed length of the spring in deactivated status; A is the cross-section area of the DE stack rolls in the longitudinal direction; σ_0 is the initial operating stress provided by the compressed spring acting on the DE rolls; r_{actuator} is the outer radii of the deactivated DE actuator.

To maximize σ_{spring} and ϵ_{\max} , a spring with low free length (L), stiffness (K), and outer radius (r_{spring}) should be targeted. Also, a larger r_{actuator} is favored which a maximum value is 5 mm in this design. However, during the fabrication of the prototypes, it was found that if the thickness of the elastomer rolls in the radial direction is larger than the radius of the core spring (r_{spring} too small), the shape of the actuator would be easily twisted by the elastomers and result in failure of the design. Besides, L_0 must be greater than or equal to the solid length (L_s) of the spring to enable the stress balance of the actuator and avoid corresponding mechanical failure. In addition, ϵ_{\max} should exceed 30% according to Table 1, which gives the following boundary conditions:

$$\begin{cases} L_0 = L - \frac{\sigma_0 \pi(r_{\text{actuator}}^2 - r_{\text{spring}}^2)}{K} \geq L_s \\ \epsilon_{\max} = \frac{\sigma_0 \pi(r_{\text{actuator}}^2 - r_{\text{spring}}^2)}{KL - \sigma_0 \pi(r_{\text{actuator}}^2 - r_{\text{spring}}^2)} > 30\% \end{cases} \quad (7)$$

According to Eqs. 5, 6, a promotion on σ_0 could also increase σ_{spring} and ϵ_{\max} , resulting in a better strain performance of the DE actuator. Yet, σ_0 equals to the initial elastic stress of the DE film, which depends on the pre-stretch ratio of the elastomer. Finally, a commercialized spring manufactured by Entex Spring company (model

3,364) was selected and the detailed parameters of the spring are given in Table 2.

2.4 Selection of pre-stretch ratio

The effect of the pre-stretch process on the enhancement of the performance of dielectric elastomer has been proven to be significant by several research groups (Li et al., 2019; Guo et al., 2021; Precht et al., 2021). Such a process could reduce the thickness of single DE layers before the fabrication of the DE actuator, and hence enlarge the electric field and the corresponding Maxwell stress under the same applied voltage level. The DE could be biaxially pre-stretched in two directions, which are the X (longitudinal) and Y (circumferential) directions, respectively.

During the experiments, it was found that the elastomer becomes extremely sensitive and vulnerable when the pre-stretch ratio exceeds four in each direction. Hence the maximum pre-stretch ratio in the X and Y direction was determined to be four to avoid any mechanical failure. According to Eqs. 2–4, the elastic stress of VHB 4905 in the longitudinal direction with different pre-stretch ratios was displayed in Figure 4.

The elastomer film pre-stretching process aims to increase the Maxwell stress as much as possible by reducing the DE film thickness, but at the same time to keep the elastic stress low in the longitudinal direction. It can be seen from Figure 4 that the pre-stretch ratio in the Y direction has little effect on the elastic stress in the X direction. Therefore, by considering both maximizing the pre-stretch ratio as well as lower the corresponding elastic stress, a pre-stretch ratio of four was selected in the Y direction. In contrast, the selection of pre-stretch ratio in the X direction should allow the initial elastic stress to fulfill the conditions of Eq. 7. Accordingly, the elastic stress of the DE film in the longitudinal direction with x from one to four and y as four is displayed in Figure 5.

As presented in the above figure, the allowable pre-stretch ratio x under the constraint of spring model 3,364 is between 1.54 and 2.63 when the pre-stretch ratio y is 4. Therefore, and to be on the safe side particularly when high voltages are involved, the pre-stretch ratio x was eventually chosen as 2.5.

2.5 Excitation level and electrical failure

According to the previous work on DE actuators (Li et al., 2019; Precht et al., 2021), the electrostatic pressure (Maxwell stress) acting along the thickness of the dielectric film could be estimated by the equation below:

$$\sigma_{\text{Maxwell}} = f_0 f_r \left(\frac{\epsilon U}{d} \right)^2 \quad (8)$$

Where f_0 is the free-space permittivity (8.85×10^{-12} F/m), f_r is the dielectric constant of the elastomer film, and d is the thickness of the DE in deactivated status, U is the excitation level (voltage) of the compliant electrode. Accordingly, the Maxwell stress could be enlarged with the increase of the excitation level. By substituting Eqs. 4, 5 and Eq. 8 into Eq. 1, the strain and force output of the developed linear DE actuator *versus* the applied voltage could be estimated as presented in Figure 6.

By considering the design requirements prescribed in Table 1, it could be seen from the above figure that the maximum excitation level of the DE actuator should be above 3.5 kV to achieve a strain of 30% and force output over 5 N. Yet, electrical breakdown failure occurs when the electric field applied across the dielectric elastomer film exceeds the breakdown strength limit of the material (U exceeds the limits), which causes an electrical discharge (spark) across the film and hence limits the maximum excitation level of the DE actuator. This type of failure is fatal as the generated heat would dramatically build up in that region between the compliant electrodes, which then causes the film material to burn and be damaged beyond any possible repair. Many factors could affect the breakdown limits of the DE actuator and controversy remains on the estimation of this parameter in literature (Di et al., 2021; Guo et al., 2021). Therefore, in this study, the maximum excitation level of the DE actuator was investigated experimentally.

Twenty trials were conducted for linear and bending DE actuators (each with ten trails) and the results are displayed in Figure 7. Electrical conductive adhesive transfer tape 9,707 (thickness 0.05 mm) and tape CN3190 (thickness 0.125 mm) from 3M company were used to facilitate the electrical connection of the DE actuator. However, as a result of the non-uniformity of this area, as shown in Figure 7B, the electrical breakdown failure usually occurs when the applied voltage is above approximately 4 kV. Therefore, in consideration of both the safety during the activation and the design requirements, the maximum excitation level was set as 3.5 kV in this study.

Since the spring was compressed during the activation, the Maxwell stress will always be lower than the elastic stress of the DE, and hence the pull-in failure (Plante and Dubowsky, 2006) (Maxwell stress becomes greater than the elastic stress of the DE) could be dismissed. In summary, the design parameters of the optimized spring-roll DE actuator are listed in Table 3.

3 Fabrication and experimental arrangement

3.1 Fabrication of the dielectric elastomer actuator

An ideal compliant electrode of DE actuator should be able to maintain a high electrical conductivity and good stability at large actuator strain and have negligible in-plane stiffness and

thickness. In this study, ALDRICH graphite powder (particle size less than 20 μm) was chosen as the applied electrode since it could be easily smeared on the designated electrode area of the adhesive surface of VHB 4905. Any extra powder material could be blown off from the sticky film surface, and the uniformity of the thickness of the electrode could be guaranteed. To increase its conductivity under large strain level deformations, this electrode material was painted when the DE film was overstretched, which enhanced the maximum strain of the activated area.

Figure 8 shows the major steps that were followed during the fabrication of the spring-roll DE actuator. A homemade pre-stretching tool was designed and manufactured in this study to permit the stretching of the VHB 4905 elastomer film uniformly. A masking template was used to expose the required film area for the coating of the compliant electrode. The whole central area of the DE was exposed for the production of linear actuator, whilst only parts of the central area were exposed for the production of bending actuator. The fabricated DE actuators only weigh around 9 g.

3.2 Experimental arrangement

To determine the deformation of the DE actuator, a Digital Image Correlation (DIC) method, which is a non-invasive technique, was employed in this investigation to estimate the strain of the spring-roll DE actuator using captured digital images. A charge-coupled device (CCD) camera, type CM3-U3-13S2C-CS (supplied by Point Grey Company) was used to capture the deformed actuator images, which were subsequently imported and analyzed in a DIC processing software (GOM correlate). The actuator prototype was placed vertically, while the CCD camera was positioned horizontally using a clamping device. Electrical excitation of the actuator prototype was achieved using a dedicated power supply unit consisting of a portable high voltage DC converter, type XP Power FS50P-12 which was integrated with an adjustable power source, type QW-MS3010D. The power supply unit was calibrated in advance to provide the required voltage for the excitation of the actuator.

During the deformation assessment of the spring-roll DE actuators, a specially designed lightweight end tip (weight less than 1 g) was attached to the lower end of the actuator, as shown in the right bottom of Figure 9, on which three dots (A, B, C) markers were traced so that they could be identified by the software to estimate the displacement of actuator end tip during its activation stage while its top end is firmly fixed. These three dots are used to form a 2D coordinate system. The front surface of the end tip was positioned in the X-Y plane of deformation of the actuator, which was also parallel to the camera lens.

Experimental arrangements were made in which Tinius Olsen, type H5KS tensile machine was used to measure the

force output of the spring-roll DE actuators as shown in Figure 10 for linear- and bending-type DE actuators. Special plastic connecting components were manufactured using a 3D printer, which was used to facilitate the alignment of the DE actuator (vertical for linear-type actuator and horizontal for bending-type actuator).

4 Results and discussions

4.1 Performance of the developed dielectric elastomer spring-roll actuator

Experimentally, each test was repeated five times to validate the results whilst only the average values are reported. The variations of the linear stroke of the linear-type spring-roll DE actuator as a function of the applied voltage level are presented in Figure 11A. Accordingly, the DE roll was able to elongate to about 6.95 mm which is equivalent to an approximately 29% strain under the maximum applied voltage level of 3.5 kV.

Figure 11B shows that the maximum bending angle of the end tip of the spring-roll DE actuator could reach approximately 70°. On a few occasions, bending angles above 90° were observed when the applied voltage was increased beyond the level of 3.5 kV.

As presented in Figure 11C, a maximum blocking force magnitude of about 5.05 N was obtained for the linear-type actuator, which is about 12.3% lower than the theoretical force magnitude calculated as 5.76 N for the same voltage level.

The variation of the lateral blocking forces of the bending-type spring-roll DE actuator with the applied voltage is presented in Figure 11D. It can be seen that the blocking force of the bending-type DE actuator could reach a magnitude of approximately 0.22 N (bending moment about 7.2 N mm). Overall, it is observed that the standard deviation of the results grows with the increase of the excitation level of the DE actuator, which indicates that the performance of the actuator becomes less steady when the applied voltage was high.

4.2 Stability of the developed dielectric elastomer spring-roll actuator

As shown in Figure 11, the experimental deformation and force results of the DE actuators were seen to be in good qualitative agreement with the theoretical prediction. However, a deviation between the two sets of results still exists especially for elevated applied voltage levels. The undershooting of the experimental performance of the actuator may result from the corrugation of the inner surface of the DE. Ideally, the elastomer film should be rolled around the core spring of the spring-roll DE actuator, assuming that the spring has a smooth and flat surface. However, in actual practice

situations, the support surface of the core spring cannot be maintained as a continuous plane surface, especially when the spring extends under the activated DE film action, where gaps between adjacent windings of the spring are enlarged and as a result, the surrounding elastomer film is expected to sink into these gaps and wrinkle in the radial direction as shown in Figure 12. This could be a major reason for the unstable performance of the prototypes when the excitation level was high.

Also, air bubbles, electrode connection, and minor film scars may cause a local electrical breaking down strength weakness or a non-uniform thickness distribution of the DE film across the width of the roll and the coated electrode. These issues are expected to either enhance the electric field locally, which may result in an early electrical breaking down failure, or cause mechanical damage to the DE film.

For future improvements, pad-printed electrodes could be utilized to mitigate this problem and improve the performance of the DE actuator (Ji et al., 2019). Furthermore, the procedures should be completed in a vacuum and dust-free environment to avoid any possible contamination.

4.3 Feasibility of the developed dielectric elastomer spring-roll actuator for minimally invasive surgery.

The output forces of the new actuator were found to be adequate to generate the angulation required by MIS tools with the comparison of actuators listed in Table 1. In addition, the developed DE spring-roll actuator utilizes a battery-operated miniature high voltage DC converter (type XP Power FS50P-12 as shown in Figure 10), which ensured the compatibility of such devices in MIS applications.

The DE material (VHB 4905) used in this study is a commercialized product, which remarkably lower the cost of the developed spring-roll DE actuator (the price of a single prototype could be lower than 16 CNY according to our trials). The weight of a single actuator is around 9 g. Moreover, the inside diameter of the actuator is 5.23 mm, which offers sufficient space for the passage of the guiding wires for the control of the tool's end effector in addition to other possible functional structures.

Yet, the developed actuator has a few inevitable drawbacks. Due to the inherent viscoelastic behavior of the VHB material, the control dynamics of such devices were complicated. The low thickness of the VHB elastomer also adds difficulties to the fabrication of the DE actuator. Furthermore, the high voltage used in the DE actuator was considered to be dangerous by the general public, which impedes the development of DE actuators in the biomedical field. Despite that, haptic devices utilizing DE actuators have been developed by several research groups and the safety of such devices was assessed and deemed to be satisfactory for any contact with human subjects

(Frediani et al., 2014; Boys et al., 2017; Pourazadi et al., 2017; Zhao et al., 2020; Guo et al., 2021).

Some researchers have proposed the utilization of non-compressive gel or soft non-conductive shielding membranes for an adequate separation between the high voltage and the users for compact DE haptic devices (Frediani et al., 2014; Boys et al., 2017), which could be a proper solution for soft DE actuators in medical use. In addition, the risk level of high voltage exposure mainly depends on the current intensity and charge duration exposed to the body, while the excitation of the small DE actuators is usually provided by a dedicated circuitry whose power output is only a few watts. And hence, some suggested that the safety concerns of small DE actuators could be mitigated, since the high voltage exposure of such devices could be avoided by limiting the current (usually less than 20 mA) and energy level of the electrical circuitry (Zhao et al., 2020). In this work, the maximum outputs of the DC converter (XP Power FS50P-12) are only 2 mA and 10 W, which is deemed to be safe even in medical scenarios.

Except for direct contact with the high voltage sources, the DE actuator is seen as a capacitive device under the excitation of the high voltage, which also rise concerns of high voltage discharge through its user. But research has indicated that the capacitance of the DE actuators is usually low, especially for compact DE devices (less than 300 pF per cm² of a DE surface), which is considered to be not necessarily dangerous (Pourazadi et al., 2017). Therefore, with proper electrical shielding arrangements, the implementation of DE actuators for MIS tools is applicable. However, this paper is mainly focused on the optimization and performance evaluation of the DE actuator for MIS, while the detailed electrical shielding system and relative safety assessment will be carried out in future works.

5 Conclusion

This paper has introduced an investigation of dielectric elastomer (DE) spring-roll actuators which were aimed to improve the articulation of the current MIS surgical instruments. A new optimization process of design parameters was proposed to maximize the performance of the developed spring-roll DE actuators. In particular, the deformation behavior of the DE actuators and their force response were analyzed using theoretical and experimental methods, where the results from the two approaches were found to be in good agreement. The linear-type actuator could deliver a maximum strain of 29% and a blocking force up to 5.05 N, while the bending-type DE spring-roll actuator could deliver bending angles over 70° and a blocking force of up to 0.22 N (bending moment 7.2 N mm). Accordingly, the developed DE actuators were considered to be satisfactory for improving the function of the surgical instruments in MIS.

In addition, the spring-roll DE actuator is extremely lightweight and cheap to manufacture. Taking into account the unique soft features of such actuators, they can be used as a disposable devices in MIS applications such as an endoscope instrument, and other medical applications where a high level of dexterity is required. Accordingly, the developed optimization process could also provide design guidance for the spring-roll DE actuator in diverse scenarios by altering the corresponding design requirements.

Although the activation voltage of the spring-roll DE actuator is considered to be relatively high, which may raise safety concerns, practical measures were discussed to dampen such concerns and the corresponding electrical shielding system will be investigated in future works.

Data availability statement

The raw data supporting the conclusions of this article will be made available by the authors, without undue reservation.

Author contributions

HW and FN conceived of the presented idea. HW developed the theory and planned the experiments. SC verified the analytical model. HW took the lead in writing the manuscript. All authors provided critical feedback and helped shape the research, analysis and manuscript.

Funding

This work was supported in part by the National Natural Science Foundation of China under Grant 61903269, in part by the Natural Science Foundation of Jiangsu Province under Grant BK20190941, in part by the QingLan Project of Jiangsu, in part by the China Postdoctoral Science Foundation under Grant 2020M681517, in part by the Jiangsu Postdoctoral Science Foundation under Grant 2020Z063, in part by the Doctoral Innovation and Entrepreneurship Program of Jiangsu Province, and in part by the Natural Science Foundation of Higher Education of Jiangsu Province under Grant 22KJB460036.

Conflict of interest

The authors declare that the research was conducted in the absence of any commercial or financial relationships that could be construed as a potential conflict of interest.

Publisher's note

All claims expressed in this article are solely those of the authors and do not necessarily represent those of their affiliated

organizations, or those of the publisher, the editors and the reviewers. Any product that may be evaluated in this article, or claim that may be made by its manufacturer, is not guaranteed or endorsed by the publisher.

References

- Boys, H., Frediani, G., Poslad, S., Busfield, J., and Carpi, F. (2017). A dielectric elastomer actuator-based tactile display for multiple fingertip interaction with virtual soft bodies. *EAPAD* 10163, 451–462. doi:10.1117/12.2259957
- Decroly, G., Lambert, P., and Delchambre, A. (2021). A soft pneumatic two-degree-of-freedom actuator for endoscopy. *Front. Robot. AI* 8, 768236. doi:10.3389/frobt.2021.768236
- Decroly, G., Mertens, B., Lambert, P., and Delchambre, A. (2020). Design, characterization and optimization of a soft fluidic actuator for minimally invasive surgery. *Int. J. Comput. Assist. Radiol. Surg.* 15 (2), 333–340. doi:10.1007/s11548-019-02081-2
- Di, K., Bao, K., Chen, H., Xie, X., Tan, J., Shao, Y., et al. (2021). Dielectric elastomer generator for electromechanical energy conversion: A mini review. *Sustainability* 13, 9881. doi:10.3390/su13179881
- Frediani, G., Mazzei, D., De Rossi, D. E., and Carpi, F. (2014). Wearable wireless tactile display for virtual interactions with soft bodies. *Front. Bioeng. Biotechnol.* 2, 31. doi:10.3389/fbioe.2014.00031
- Garcia, L. A., and Trindade, M. A. (2019). Finite element modeling and parametric analysis of a dielectric elastomer thin-walled cylindrical actuator. *J. Braz. Soc. Mech. Sci. Eng.* 41 (1), 18–19. doi:10.1007/s40430-018-1527-4
- Gerboni, G., Brancadoro, M., Tortora, G., Diodato, A., Cianchetti, M., and Menciasci, A. (2016). A novel linear elastic actuator for minimally invasive surgery: Development of a surgical gripper. *Smart Mat. Struct.* 25, 105025. doi:10.1088/0964-1726.25.10.105025
- Golahmadi, A. K., Khan, D. Z., Mylonas, G. P., and Marcus, H. J. (2021). Tool-tissue forces in surgery: A systematic review. *Ann. Med. Surg. (Lond)*. 65, 102268. doi:10.1016/j.jamsu.2021.102268
- Guo, Y., Liu, L., Liu, Y., and Leng, J. (2021). Review of dielectric elastomer actuators and their applications in soft robots. *Adv. Intell. Syst.* 3 (10), 2000282. doi:10.1002/aisy.202000282
- Hurni, Y., Romito, F., and Huber, D. (2022). Transvaginal natural orifice transluminal endoscopic surgery for surgical staging of early-stage ovarian cancers: A report of two cases. *Front. Surg.* 16, 833126–833287. doi:10.3389/fsurg.2022.833126
- Imboden, M., Chen, S., Gudozhnik, O., Pollock, C., Javor, J., Bishop, D., et al. (2022). The integration of optical stimulation in a mechanically dynamic cell culture substrate. *Front. Bioeng. Biotechnol.* 10, 934756. doi:10.3389/fbioe.2022.934756
- Ji, X., Liu, X., Cacucciolo, V., Imboden, M., Civet, Y., El Haitami, A., et al. (2019). An autonomous untethered fast soft robotic insect driven by low-voltage dielectric elastomer actuators. *Sci. Robot.* 4, eaaz6451. doi:10.1126/scirobotics.aaz6451
- Le, H. M., Do, T. N., and Phee, S. J. (2016). A survey on actuators-driven surgical robots. *Sensors Actuators A Phys.* 247, 323–354. doi:10.1016/j.sna.2016.06.010
- Li, J., Liu, L., Liu, Y., and Leng, J. (2019). Dielectric elastomer spring-roll bending actuators: Applications in soft robotics and design. *Soft Robot.* 6 (1), 69–81. doi:10.1089/soro.2018.0037
- Lonner, J. H., Goh, G. S., Sommer, K., Niggeman, G., Levicoff, E. A., Vernace, J. V., et al. (2021). Minimizing surgical instrument burden increases operating room efficiency and reduces perioperative costs in total joint arthroplasty. *J. Arthroplasty* 36 (6), 1857–1863. doi:10.1016/j.arth.2021.01.041
- Moers, A. J. M., De Volder, M. F. L., and Reynaerts, D. (2012). Integrated high pressure microhydraulic actuation and control for surgical instruments. *Biomed. Microdevices* 14 (4), 699–708. doi:10.1007/s10544-012-9650-y
- Plante, J. S., and Dubowsky, S. (2006). Large-scale failure modes of dielectric elastomer actuators. *Int. J. Solids Struct.* 43 (25–26), 7727–7751. doi:10.1016/j.ijsolstr.2006.03.026
- Pourazadi, S., Shagerdmootaab, A., Chan, H., Moallem, M., and Menon, C. (2017). On the electrical safety of dielectric elastomer actuators in proximity to the human body. *Smart Mat. Struct.* 26, 115007. doi:10.1088/1361-665X/aa89b1
- Prechtl, J., Kunze, J., Moretti, G., Bruch, D., Seelecke, S., and Rizzello, G. (2021). Modeling and experimental validation of thin, tightly rolled dielectric elastomer actuators. *Smart Mat. Struct.* 31 (1), 015008–015029. doi:10.1088/1361-665X/ac34be
- Runciman, M., Darzi, A., and Mylonas, G. P. (2019). Soft robotics in minimally invasive surgery. *Soft Robot.* 6 (4), 423–443. doi:10.1089/soro.2018.0136
- Sahu, D., Sahu, R. K., and Patra, K. (2022). In-plane actuation performance of graphene oxide filled VHB 4910 dielectric elastomer. *J. Appl. Polym. Sci.* 139 (5), 51594–51605. doi:10.1002/app.51594
- Soper, N. J., Swanström, L. L., and Eubanks, S. (2008). *Mastery of endoscopic and laparoscopic surgery*. Philadelphia: Lippincott Williams & Wilkins.
- Tei, M., Sueda, T., Matsumura, T., Furukawa, H., Koga, C., Wakasugi, M., et al. (2021). Systematic review of single port vs. multi port surgery for rectal cancer. *Mol. Clin. Oncol.* 14 (2), 24. doi:10.3892/mco.2020.2186
- Vajsbaher, T., Schultheis, H., and Francis, N. K. (2018). Spatial cognition in minimally invasive surgery: A systematic review. *BMC Surg.* 18 (1), 94–16. doi:10.1186/s12893-018-0416-1
- Wang, H., Cui, S., Wang, Y., and Song, C. (2020). A hybrid electromagnetic and tendon-driven actuator for minimally invasive surgery. *Actuators* 9, 92. doi:10.3390/act9030092
- Wang, H., and El Wahed, A. K. (2020). Development of a novel latching-type electromagnetic actuator for applications in minimally invasive surgery. *Actuators* 9, 41. doi:10.3390/act9020041
- Zhang, D., Sun, Y., and Lueth, T. C. (2021). Design of a novel tendon-driven manipulator structure based on monolithic compliant rolling-contact joint for minimally invasive surgery. *Int. J. Comput. Assist. Radiol. Surg.* 16 (9), 1615–1625. doi:10.1007/s11548-021-02442-w
- Zhao, H., Hussain, A. M., Israr, A., Vogt, D. M., Duduta, M., Clarke, D. R., et al. (2020). A wearable soft haptic communicator based on dielectric elastomer actuators. *Soft Robot.* 7 (4), 451–461. doi:10.1089/soro.2019.0113



OPEN ACCESS

EDITED BY
Zhen Luo, University of Technology
Sydney, Australia

REVIEWED BY
Fang Wang,
Changsha University of Science and
Technology, China
Zhihua Cai,
Hunan University of Science and
Technology, China

*CORRESPONDENCE
Zhiyong Yin,
530250681@qq.com
Shengxiong Liu,
89484883@qq.com
Guixue Wang,
wangx@cqu.edu.cn

SPECIALTY SECTION
This article was submitted to
Biomechanics,
a section of the journal
Frontiers in Bioengineering and
Biotechnology

RECEIVED 09 June 2022
ACCEPTED 14 September 2022
PUBLISHED 20 October 2022

CITATION
Yang X, Shi J, Fu Q, Pu S, Lian C, Li K,
Yin Z, Liu S and Wang G (2022),
Optimization of the driver's seat belt and
injury biomechanical analysis in real-
world minivan small offset impact
accident scenarios.
Front. Bioeng. Biotechnol. 10:965206.
doi: 10.3389/fbioe.2022.965206

COPYRIGHT
© 2022 Yang, Shi, Fu, Pu, Lian, Li, Yin, Liu
and Wang. This is an open-access article
distributed under the terms of the
[Creative Commons Attribution License](https://creativecommons.org/licenses/by/4.0/)
(CC BY). The use, distribution or
reproduction in other forums is
permitted, provided the original
author(s) and the copyright owner(s) are
credited and that the original
publication in this journal is cited, in
accordance with accepted academic
practice. No use, distribution or
reproduction is permitted which does
not comply with these terms.

Optimization of the driver's seat belt and injury biomechanical analysis in real-world minivan small offset impact accident scenarios

Xiuju Yang¹, Jingjing Shi², Qianying Fu², Shanshan Pu²,
Chunxiao Lian², Kui Li³, Zhiyong Yin^{1,4*}, Shengxiong Liu^{2*} and
Guixue Wang^{1*}

¹Key Laboratory for Biorheological Science and Technology of Ministry of Education, State and Local Joint Engineering Laboratory for Vascular Implants, College of Bioengineering, Chongqing University, Chongqing, China, ²Department of Biomedical Engineering, College of Pharmacy and Bioengineering, Chongqing University of Technology, Chongqing, China, ³Chongqing Key Laboratory of Vehicle Crash/Bio-Impact and Traffic Safety, Department 4, Institute of Surgery Research, Daping Hospital, Army Medical University, Chongqing, China, ⁴China Automotive Engineering Research Institute Co., Ltd., Chongqing, China

To minimize injuries and protect the safety of the driver in minivan small offset collisions, an optimized pre-tensioned force-limiting seat belt was proposed herein. An accident with detailed information, such as medical reports, vehicle inspection reports, and accident scene photographs, was reconstructed using HyperMesh software. The effectiveness of both the accident model and the pre-tensioned force-limiting seat belt was evaluated. To obtain the optimal seat belt parameters for driver protection, first, force-limiting A, pre-tensioned force B, and pre-tensioned time C factors were selected in designing an orthogonal test with different factor levels. The influence laws of each factor on the injury biomechanical characteristics of the driver were analyzed via the direct analysis method. Moreover, each kind of critical injury value of the human body was synthesized, and the radial basis function surrogate model was constructed. The three seat belt parameters were optimized using the NSGA-II multi-objective genetic algorithm. The results showed that the optimal balance variable parameter of the seat belt was 4751.618 N–2451.839 N–17.554 ms (A–B–C). Finally, the optimal scheme was verified in a system simulating a minivan small offset collision. The results showed that after optimization, the skull von Mises stress was reduced by 36.9%, and the stress of the cervical vertebra cortical bone and cancellous bone decreased by 29.1% and 30.8%, respectively. In addition, the strains of the ribs and lungs decreased by 31.2% and 30.7%, respectively.

KEYWORDS

small offset collision, accident reconstruction, driver injury, pre-tensioned force-limiting seat belt, multi-objective genetic algorithm, biomechanics analysis, genetic algorithm

1 Introduction

Minivans have a large market share in China because of their low price, large internal space, and compact engine and cab layout. The energy absorption space of the front-end of minivans is small, their body materials are made of plain carbon steel, and their safety configuration is low. Hence, the invasion of the occupants' cabin during small offset collisions is severe, seriously threatening the safety of drivers (Li et al., 2015; Prochowski et al., 2016; Shi et al., 2016).

The safety of drivers in a minivan collision is an important issue. The structural crashworthiness and the design of the restraint systems of minibuses are the focus of current research (Hassan and Meguid, 2018; Hu et al., 2018). By contrast, the structural crashworthiness of minivans is mainly evaluated *via* numerical simulations. Moreover, previous studies concentrated on optimizing the energy absorption mechanism, characteristics, and crashworthiness of the thin-walled structures of minivans. Anghileri et al. (2005) identified the damage parameters of a model of "bi-phase" materials *via* PAM-CRASH. They determined these parameters from the dynamic axial crushing of thin-walled cylinder tubes with different fiber orientations by using an inverse method combined with the multi-objective optimization method to identify damage and failure mechanisms in composite materials. Cho et al. (2006) evaluated the crashworthiness of rectangular and circular dent-type crush initiators to analyze the influence of the ratio of wall thickness and size on crashworthiness. They found that the rectangular dent-type crush initiator absorbs more crash energy than the circular dent-type crush initiator. The crashworthiness of automobiles can be improved by using energy-absorbing structures (Park, 2011; Ovesy and Masjedi, 2014).

Given that collision forces throw the occupants out of the vehicle, researchers developed various restraint systems (Zhai et al., 2015; Tian et al., 2016; Liu et al., 2017a; Albanese et al., 2020). Previous studies primarily focused on optimizing the performance of safety belts, airbags, crash dummies, and seats to effectively avoid or reduce the secondary collision of compartment structures and occupants in minivans. Zhai et al. (2017) clarified the influence of the variable optimization of airbags, seat belts, and pretension times on the head and chest injury of occupants by using a genetic algorithm. They found that head and chest injuries can be greatly reduced by designing reasonable energy-absorbing structures and matching the restraint systems of vehicles. Liu et al. (2016) examined the influence of seat belt hang-point positions, elongations, and initial strains on occupant impact injury. They established a simulation model of seat belt restraint systems by using MADYMO software and constructed an approximate model by using the radial function. Then, they optimized the seat belt parameters. They reported that the optimized seat belts can effectively reduce the injuries of the occupants. Gu et al.

(2020) simulated and optimized the anchorage of seat belts. They stated that the safety performance of vehicles can be increased, and the contact surface between the anchorage stiffener plate and the inner plate of the B-pillar can be enhanced by improving the structure of the anchorage stiffener plate. NSGA-II is an improved version of the non-dominated sorting genetic algorithm (NSGA), and it has high operation efficiency, good distribution of the solution set, good convergence, and robustness (Deb et al., 2002; Wang et al., 2020). The researchers used the NSGA-II genetic algorithm to optimize the key parameters of the occupant pre-tensioned force-limiting seat belt restraint system (Ge et al., 2017). The results show that this method can quickly and effectively obtain the optimal matching parameters of the pre-tensioned force-limiting seat belt restraint system and ensure the safety of vehicle occupants.

Simulation research on minivans is relatively perfect. However, because of the large number of calculation parameters involved, the calculation time is long and the error is large. Gao et al. (2019) compared and analyzed four approximate models of minivans, namely, response surface, radial basis neural network, Kriging polynomial, and orthogonal polynomial. They stated that replacing the real model with an approximate model can substantially reduce the calculation time and ensure the feasibility of optimization. In this study, small offset collisions were simulated, and the effect of different seat belt variables on the Total Human Model for Safety (THUMS), that is, the head, neck, thorax, and legs were examined. An accident was reconstructed using detailed crash information. An accident model was then tested to determine its effectiveness. We analyzed the effects of seat belts, including those that are commonly used and those that are pre-tensioned force-limiting, on the head, neck, thorax, and legs of drivers. On this basis, we used the NSGA-II genetic algorithm to optimize the key parameters of the pre-tensioned force-limiting seat belt. The results show that the optimized pre-tensioned force-limiting seat belt plays a good protective effect on the driver. Finally, to test the effectiveness of the optimized scheme, the optimized seat belt parameters were substituted into the simulation model.

2 Materials and methods

2.1 Accident data

Our work is supported by an in-depth accident investigation carried out by a research team at the Surgical Institute of Army Military University in Chongqing, China, who gathered data on more than 2,700 traffic incidents from 2013 to 2018 and created a database (Duan et al., 2020). To ascertain how each collision happened, pertinent information is gathered from the traffic police division. Typical small offset collision crashes relating a minivan were selected from our database for this study. This

TABLE 1 Details about the collision, vehicle, and driver.

Collision information	Weather	Light rain	
	Ground	Wet asphalt	
	Collision type	25% offset collision	
	Impact velocity (km/h)	54	
Driver information	Age	38	
	Gender	Male	
	Stature (cm)	160	
Vehicle information	Vehicle type	Minivan	
	Curb weight (kg)	1,015	
	Wheelbase (mm)	2,500	
	Length × width × height (mm)	3,860 × 1,500 × 1,900	
Driver injury	Injury part	AIS	Injury information
	Head	3	Mid-frontal scattered with contusions and lacerations. Left eyebrow with arcuate wound. Depth of the wound cavity reached the muscular layer. Concave fracture of the left eyebrow arch and skull fracture
	Neck	2+	Fracture of the thyroid cartilage in the neck
	Thorax	4	Closed fracture of the sternum, rib fracture, and lung contusion
	Lower limb	3	Large open laceration on the left medial thigh. Amputation wounds were seen in both lower limbs
Extent of vehicle damage	The front windshield cracked. The hood was dented and deformed. Front bumper skin with peeled and concave deformation. The left front wheel and suspension were deformed. The left A-pillar was deformed. The left front door and the left center door were deformed. The window and sealing rubber of the left front door and the left middle door detached. Left and right front headlights detached		



accident has detailed photos of the accident scene, police traffic accident scene map, injury report, vehicle trace deformation, and other information. The details of the accident collision process is as follows: the location of the accident is a two-way four lane, the weather is light rain, and the ground is the wet asphalt pavement; a small offset collision of 25% occurs between the left front of a minivan and the left front of a sedan; when the collision occurs, the collision velocity of the minivan is 54 km/h (Liu et al., 2017b; Wang et al., 2022a), and the driver uses the seat belt, but without the airbag. The abridged injury scale (AIS), which was amended in 2005, was used to categorize the injury information of the drivers involved in the accidents. The AIS values of 1, 2, 3, 4, 5,

and 6 correspond to minor, moderate, serious, severe, critical, and untreated injuries, respectively, according to the criteria. The details of the collision, vehicle, and driver of the accident are shown in Table 1.

2.2 Accident reconstruction

Figure 1A shows the workflow involved in reconstructing the accident. The THUMS model (version 4.0.2) was used to adjust the dummy position with an initial force or an initial velocity (Magee and Thornton, 1978). The vehicle finite element model

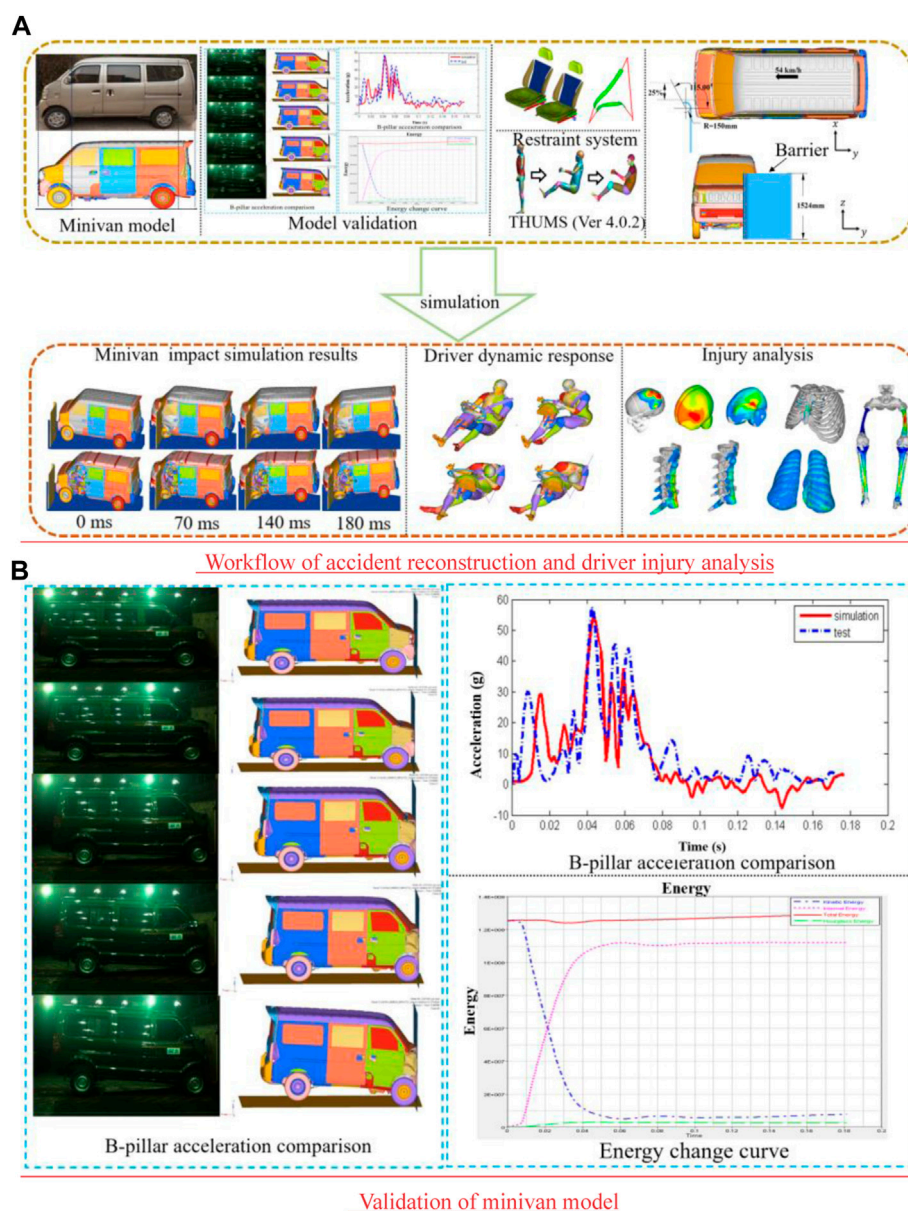


FIGURE 1

Accident reconstruction. (A) Workflow of accident reconstruction and driver injury analysis and (B) validation of the minivan model.

was constructed based on the prototype of the minivan in this case. Vehicle models included body, windshield, seating system, steering system, dashboard, and pedals. The model had 727,826 units, and its materials and characteristics satisfied the collision standards' fundamental criteria. Figure 1B shows that after the finite-element model of the minivan is constructed, the validity and accuracy of the model are verified. Lei and Yin (2016) conducted 100% rigid wall frontal crash experiments on real vehicles and finite-element vehicle models. The results of the real-vehicle test and simulation show that the dynamic response

process of the minivan in simulation is basically consistent with the results of a real-vehicle collision. The acceleration value and change trend of the B-pillar are basically consistent, and the total energy is basically stable, which conforms to the requirements of the energy conservation law. Therefore, the finite-element model of the minivan can effectively simulate and analyze the small offset collision. In accordance with China Insurance Automotive Safety Index (C-IAI) regulations, a rigid barrier with a simplified arc structure was adopted in this work. The height of the barrier was 1,524 mm, the radian of the arc surface was

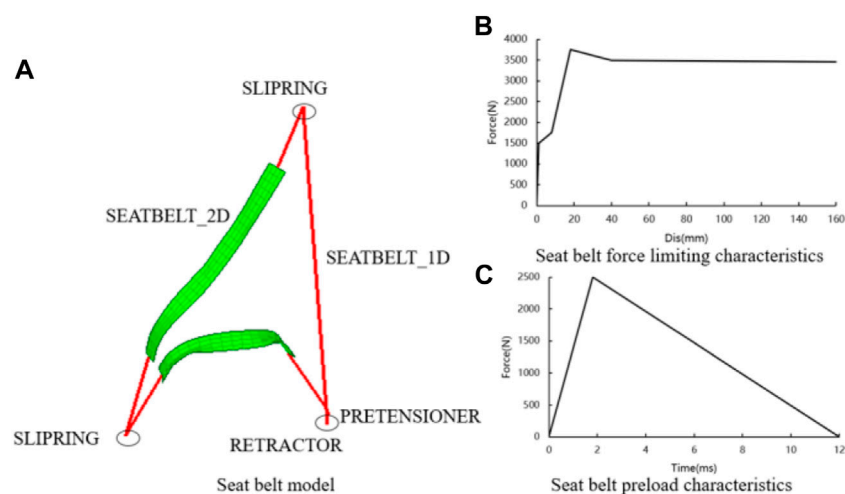


FIGURE 2
Pre-tensioned force-limiting seat belt. (A) composition of pre-tensioned force-limiting seatbelt, (B) force limiting characteristic curve of seatbelt, and (C) pre-tightening curve of seatbelt.

115°, and the radius of the arc surface was 150 mm. Based on the performance of the seat belt in the crash vehicle, the ordinary three-point seat belt model was established.

A boundary condition included the relative position of the minivan to the barrier as well as the ground impact. Using the crash information, the contact location seen between the vehicle and the barrier was set, and the barrier was completely constrained. The barrier is situated on the left side of the minivan body, and there is a 25% overlap rate with the vehicle body. The vehicle acted as the slave surface, the barrier acted as the main surface, the dynamic friction coefficient was 0.1, and the static friction coefficient was 0.2. The type of contact between the THUMS model and the vehicle interior was defined as automatic face-to-face contact (Wang et al., 2022b). An asphalt pavement, which is considered a rigid body, was used in the test (Hu et al., 2011). The wet asphalt pavement had a friction coefficient of 0.3. The vehicle impact velocity was set at 54 km/h.

2.3 Establishment of the seat belt finite-element model

2.3.1 Establishment of the finite-element model of the ordinary seat belt

A seat belt, which protects the vehicle occupants in the event of a crash, is an effective, compulsory safety device in vehicle restraint systems. The most commonly used type is a three-point seat belt consisting of a seat belt fixed at one end, a D-ring, and a retractor. In this study, an ordinary three-point seat belt, which mainly includes a seat belt webbing, a rewinding device, a D-ring, and a seat belt anchorage, was modeled using Primer software.

The 1D seat belt unit and the 2D shell unit comprised the seat belt webbing.

2.3.2 Establishment of a finite-element model of a pre-tensioned force-limiting seat belt

By the definition of the belt webbing using the card *ELEMENT_SEATBELT_RETRACTOR in Primer software, the force-limiting seat belt was implemented. A pre-tensioner is a device that controls the retraction part of the seat belt using a rewinding device. The pre-tensioned function was realized through the card *ELEMENT_SEATBELT_PRETENSIONER definition (Figure 2).

The police investigation found that the minivan was not equipped with airbags. Seat belts are the most important restraint systems. To reduce the risk of injury to the driver, the model of the pre-tensioned force-limiting seat belt was optimized for three variables. Limiting forces A, pre-tensioned forces B, and pre-tensioned times C were the design variables. Those variables were designed in the range of $4500 \text{ N} \leq A \leq 5500 \text{ N}$, $1500 \text{ N} \leq B \leq 2500 \text{ N}$, and $16 \text{ ms} \leq C \leq 24 \text{ ms}$, respectively.

2.4 Injury criteria

The degree of head injury is evaluated using the head injury criterion (HIC). As a measure of head injury, the HIC is widely accepted and used. The theoretical expression is as follows (Marjoux et al., 2008):

$$HIC = \max_{T_0 \leq t_1 \leq t_2 \leq T_E} \left\{ (t_2 - t_1) \left[\frac{1}{t_2 - t_1} \int_{t_1}^{t_2} a(t) dt \right]^{2.5} \right\}. \quad (1)$$

In this expression, T_0 represents the beginning of the simulation and T_E represents the end of the simulation. The starting time and the ending time when the HIC reaches its maximum value are indicated by t_1 and t_2 , respectively. In the integral time throughout the collision, $a(t)$ represents the combined acceleration of the head in the X, Y, and Z directions. A head injury value is the maximum calculated in the integral time throughout the collision. HIC_{15} , i.e., $t_2 - t_1 = 15$ ms, was used for small offset collisions in the 2018 China-New Car Assessment Programme (C-NCAP).

Based on the THUMS with high biological fidelity, three biomechanical parameters were used to analyze the head injury of drivers. They were skull von Mises stress, intracranial pressure, and intracranial von Mises stress. In addition, the tolerance limits were 10 MPa, 235 KPa, and 15–20 kPa, respectively (Chan and Liu, 1974; Willinger et al., 2000).

The biomechanical neck injury (N_{ij}) predictor is a useful index for determining the severity of occupant injuries. N_{ij} is calculated as follows:

$$N_{ij} = \left| \frac{F_z}{F_{zc}} \right| + \left| \frac{M_{ocy}}{M_{yc}} \right|, \quad (2)$$

where F_z denotes the axial force and M_{ocy} denotes the bending moment. The critical intercept values F_{zc} and M_{yc} correspond to the axial force and the neck bending moment, respectively. In collision accidents, the FMVSS208 standard specifies that the N_{ij} tolerance limit value is 1 (Wen et al., 2011).

Cervical cortical bone stress and cancellous bone stress were used to determine the extent of neck tissue injury. Studies have shown that cervical vertebra fractures occur when cortical bone stress and cancellous bone stress exceed 236 and 59 MPa, respectively (Chi and Geng, 2019).

The contiguous 3 ms injury criteria and maximal thorax compression are important indices for occupant chest injury in frontal collisions. According to FMVSS208, the maximal resultant linear acceleration of a thorax during a continuous span of 3 ms cannot surpass 60 g, i.e., $C_{3ms} \leq 60$ g (Marjoux et al., 2008). When the chest compression reaches 55 mm, there is a 50% probability of rib fracture (Mertz et al., 1997). Rib and lung strains are also used to evaluate the driver's chest injury. Studies have shown a risk of fracture when the rib strain exceeds 3%, and the threshold of lung strain is 30% (Schaefer et al., 1958; Kallieris et al., 1997).

In this study, leg injury was evaluated by the axial force of the thigh F_{femur} , femur, and tibia strain. The study showed that the axial force of the thigh should not exceed 10 kN (Viano and Arepally, 1990), and the strain of the femur and tibia would be more than 3% (Kuppa et al., 2001).

In small offset collisions, drivers suffer from different degrees of injury to various body parts. The degree of injury to the human body was evaluated. To evaluate the injuries to the head, thorax,

and legs comprehensively, the weighed injury criteria (WIC) were used. The WIC are calculated as follows (Viano and Arepally, 1990):

$$WIC = 0.6 \left(\frac{HIC_{15}}{700} \right) + \frac{0.35 \left(\frac{C_{3ms}}{60} + \frac{C_{comp}}{63} \right)}{2} + 0.05 \left(\frac{F_L + F_R}{20} \right), \quad (3)$$

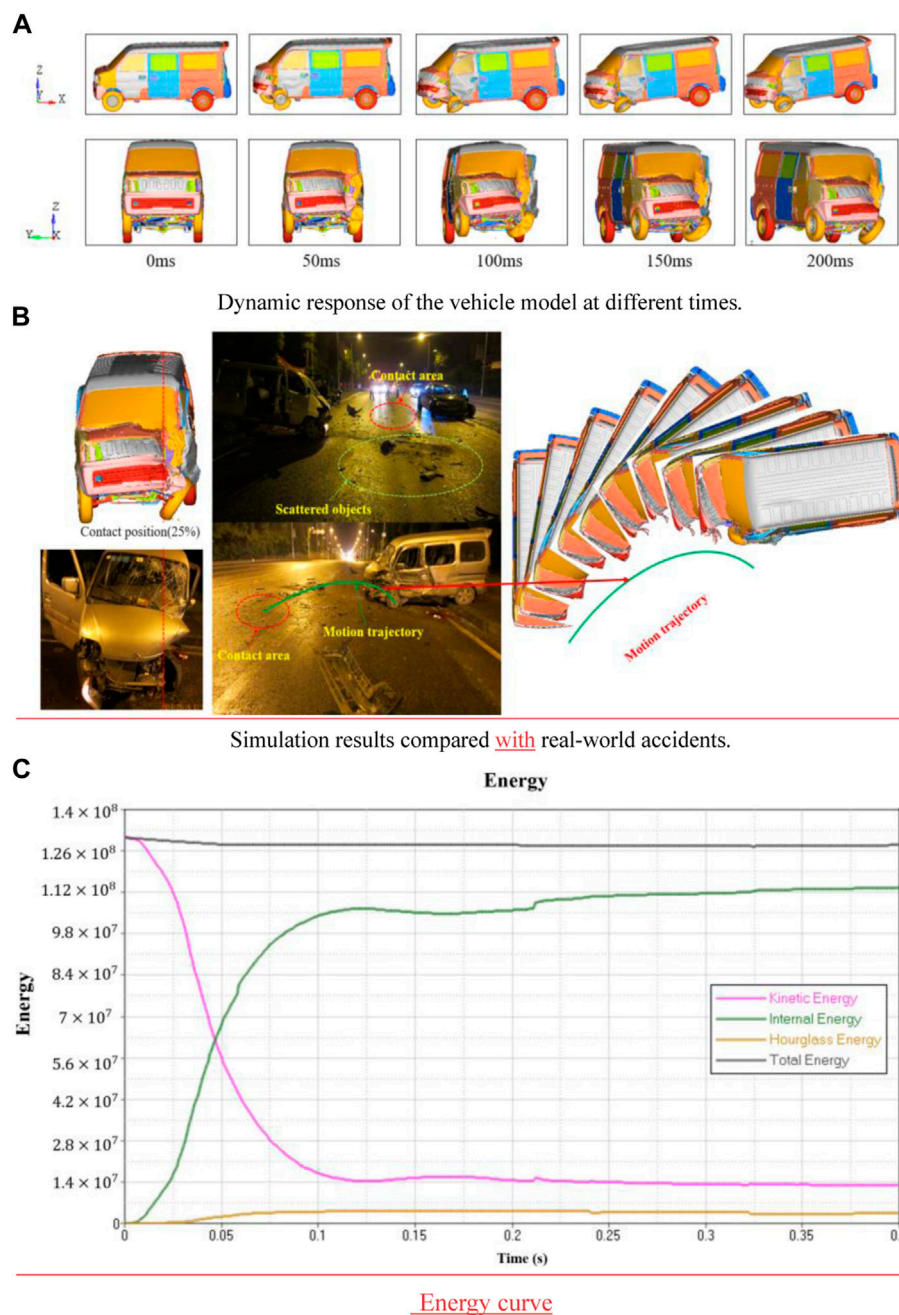
where C_{comp} denotes the compressive amount of the thorax and F_L is the maximum axial force for the left thigh bone, whereas F_R is the maximum axial force for the right thigh bone.

3 Results and discussion

3.1 Validation of the accident model

The simulation of the changes that occurred in the minivan during the small offset collision is outlined in Figure 3A. The deformation of the vehicle was observed at different times. During the small offset collision, the front windshield broke, and the hood, the front bumper, the left front wheel, the suspension, and the left A-pillar were deformed. The simulation results were consistent with the actual deformation of the vehicle during the accident. The vehicle model and the barrier contact positions were consistent with accident vehicle collision positions as shown in Figure 3B. The impacted area of the vehicle was inferred from the main concentrated area of the scattered objects at the accident site and the final stopping position of the vehicle. The motion track of the vehicle at the time of the accident was obtained. In accordance with the observations of real-world accidents, the reconstructed collision track had a good correlation with the accident collision track. The energy change curve of the minivan during the small offset collision can be used as an important index to evaluate the reliability of the simulation results. Figure 3C illustrates that the simulation model is in an energy conservation state during the whole collision process, with a smooth curve and small fluctuation. The conversion between kinetic energy and internal energy and the ratio of hourglass energy to total energy are all within the acceptable 5% range. Therefore, the aforementioned results verify the effectiveness of the collision model.

The dynamic reaction of a driver wearing an ordinary seat belt and another driver wearing a pre-tensioned force-limiting seat belt was compared to identify the differences between the pre-tensioned force-limiting seat belt and the ordinary seat belt (Figure 4). During the entire period of the collision, the dummy moved forward and toward the left because of longitudinal deceleration and the acceleration force along the Z direction. The dummy's knees first came into contact with the vehicle's interior after the collision, as shown in Figure 4A. The dummy then continuously moved forward and toward the left because of

**FIGURE 3**

Dynamic response of the vehicle model and comparison between the simulation results and real-world accidents. **(A)** Dynamic response of the vehicle model at different times. **(B)** Simulation results compared with real-world accidents. **(C)** Energy curve.

the effects of inertia. The chest hit the steering wheel. Finally, the dummy stopped moving forward because of the tension of the seat belt. The legs of the dummy were first hit by the vehicle's interior, as shown in Figure 4B. The pre-tensioned force-limiting seat belt prevented the direct violent collision between the chest and the steering wheel. Moreover, the seat belt shortened the

distance moved by the head as it leaned forward, thereby protecting the head.

According to the dynamic response of the THUMS dummies, 14 injury indexes were used to evaluate the risk of injury to the head, thorax, and legs. The amount of protection provided by the ordinary seat belt and the pre-tensioned force-limiting seat belt

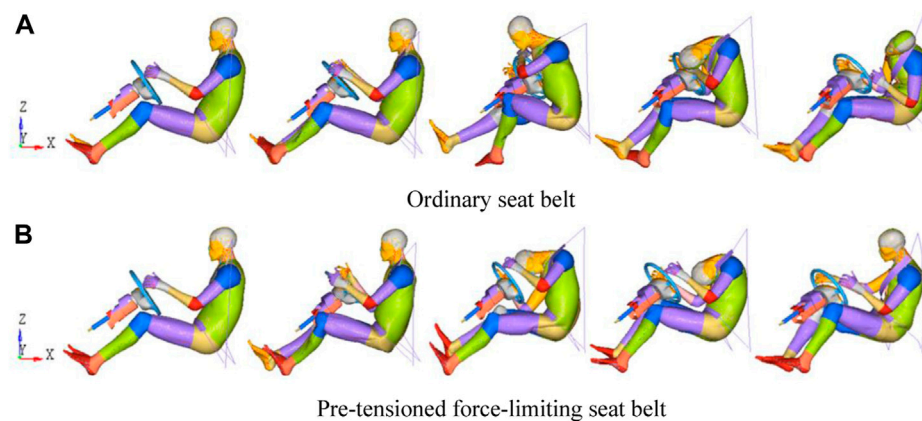


FIGURE 4

Dynamic reaction of a dummy wearing an ordinary seat belt and a dummy wearing a pre-tensioned force-limiting seat belt. (A) Ordinary seat belt. (B) Pre-tensioned force-limiting seat belt.

TABLE 2 Injury values for dummies' heads, necks, chests, and legs.

	Injury criteria	Injury threshold	Ordinary seat belt	Pre-tensioned force-limiting seat belt	Reduction (%)
Head	Skull von Mises stress (MPa)	10	31.8	23.6	25.8
	Intracranial pressure (kPa)	235	277.8	198.7	28.5
	Intracranial von Mises stress (kPa)	15–20	19.1	14.6	23.6
	HIC	700	834.6	521.3	37.5
Neck	N_{ij}	1	1.24	0.87	29.8
	Cortical bone stress (MPa)	236	159.8	123.4	22.8
	Cancellous bone stress (MPa)	59	16.3	11.7	28.2
Chest	C_{3ms} (g)	60	103.4	92.4	10.6
	C_{comp} (mm)	50	45.3	37.8	16.6
	Rib strain	3%	43.4%	32.4%	25.3
	Lung strain	30%	29.2%	22.5%	22.9
Leg	F_L (KN)	10	15.5	13.2	14.8
	F_R (KN)	10	12.1	10.5	13.2
	Femur strain	3%	6.1%	4.9%	19.7
	Tibia strain	3%	9.7%	8.3%	14.4
WIC		1	1.212	0.881	27.3

against the injuries to the dummies' head, neck, chest, and legs was compared (Table 2).

The simulation results indicated that the HIC, von Mises stress, intracranial pressure, and intracranial von Mises stress with ordinary seat belts were larger than the injury thresholds, a

condition that may lead to skull fracture and serious injury. This mostly agrees with the driver's head injury, which is listed as AIS 3 in Table 1. These injuries may have been caused as the driver's head hit the windshield, the steering wheel, and the instrument panel, consistent with the report of Pappachan and Alexander

TABLE 3 Simulation results of the driver's head injury value.

Index	HIC			Skull von Mises stress (MPa)			Intracranial pressure (kPa)			Intracranial von Mises stress (kPa)		
	A	B	C	A	B	C	A	B	C	A	B	C
K1	3,092.6	3,178.6	2,978.8	143.9	156.1	145.4	1,191.9	1,227.1	1,135.5	95.5	89.6	81.9
K2	2,720.8	3,384.6	3,161.3	127.9	164.9	153.1	1,046.2	1,301.2	1,121.7	81.8	96.6	89.3
K3	3,293.5	3,573.8	3,586.4	168.9	172.1	171.6	1,245.9	1,275.6	1,291.7	92.2	101.1	101.0
K4	3,780.9	3,376.9	3,380.0	186.9	162.8	162.3	1,441.4	1,192.6	1,200.0	103.1	95.0	95.9
K5	3,727.2	3,101.1	3,508.5	178.2	149.9	173.4	1,176.4	1,105.3	1,352.9	96.0	86.3	100.5
k1	618.52	635.72	595.76	28.78	31.22	29.08	238.38	245.42	227.10	19.10	17.92	16.38
k2	544.16	676.92	632.26	25.58	32.98	30.62	209.24	260.24	224.34	16.36	19.32	17.86
k3	658.70	714.76	717.28	33.78	34.42	34.32	249.18	255.12	258.34	18.44	20.22	20.20
k4	756.18	675.38	676.00	37.38	32.56	32.46	288.28	238.52	240.00	20.62	19.00	19.18
k5	745.44	620.22	701.70	35.64	29.98	34.68	235.28	221.06	270.58	19.20	17.26	20.10
R	212.02	94.54	121.52	11.8	4.44	5.60	79.04	39.18	46.24	4.26	2.96	3.82

The meaning of the bold value we provide is to highlight the highest value of R among the three variables A, B and C in the text.

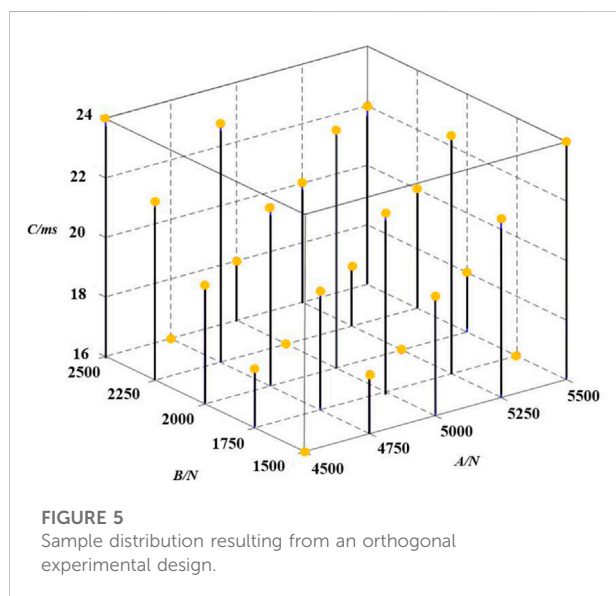


FIGURE 5
Sample distribution resulting from an orthogonal experimental design.

(2012). Injury values of N_{ij} , cortical bone, cancellous bone stress, chest (C_{3ms}), ribs, lungs, heart, and liver were larger than the injury thresholds, a condition that may lead to serious neck and chest injuries. This mostly agrees with the driver's AIS 2+ neck injury and AIS 4 chest injury noted in Table 1 (Hao et al., 2018; Lu et al., 2016). These injuries might have been caused as the chest was restrained by the seat belt and hit the steering wheel. The maximum axial force of the driver's left and right legs was 13.5 kN and 12.1 kN, respectively. That means the driver's left thigh was more seriously injured. A strain of 6.8% on the femur and 9.7% on the tibia, above the injury threshold, shows that the driver suffered serious injury to his lower extremities. The

observation was consistent with the injury report: large open laceration on the left medial thigh. Amputation wounds were seen in both lower limbs. It is due to the fact that the impact region is on the vehicle's front-left side and is heavily contaminated, and the left lower limb is in contact with the A-pillar lower hinge, sill, and foot pedal (xiao et al., 2018).

The results of the comparison of vehicle deformations and the driver's injuries verified the credibility of the crash simulation model, consistent with the results obtained by Shigeta et al. (2009) and Watanabe et al. (2012).

The pre-tensioned force-limiting seat belts reduced the chances of head, neck, chest, and leg injuries compared with the ordinary seat belts, as shown in Table 3. Therefore, pre-tensioned force-limiting seat belts offer better protection for the driver.

3.2 Effects of different parameters of pre-tensioned force-limiting seat belts on driver injury

Further improved safety protection was provided to the driver by the pre-tensioned force-limiting seat belt. The three variables with a great influence on the restraint performance of the pre-tensioned force-limiting seat belt, namely, seat belt force-limiting A, pre-tensioned force B, and pre-tensioned time C, were optimized. With the three factors at 5 levels and 25 samples, an orthogonal experimental design was applied. Figure 5 shows how the sample points are distributed spatially.

The injuries of the drivers in different seat belt variables were analyzed via the direct analysis method. Various design variables were examined for their influences on the dummy injuries.

TABLE 4 Simulation results of the driver's neck injury value.

Index	N_{ij}			Cortical bone stress (MPa)			Cancellous bone stress (MPa)		
	A	B	C	A	B	C	A	B	C
K1	4.48	5.31	4.01	642.7	759.2	572.8	60.1	70.5	52.6
K2	4.02	4.65	3.93	580.5	665.8	564.4	54.7	61.9	52.7
K3	4.11	4.18	4.55	589.4	601.3	655.7	55.2	55.9	60.5
K4	4.52	4.28	4.70	643.9	616.5	673.9	59.6	57.4	62.7
K5	4.90	3.61	4.84	703.9	517.6	693.6	63.7	47.6	64.8
k1	0.896	1.062	0.802	128.54	151.84	114.56	12.02	14.10	10.52
k2	0.804	0.930	0.786	116.10	133.16	112.88	10.94	12.38	10.54
k3	0.822	0.836	0.910	117.88	120.26	131.14	11.04	11.18	12.10
k4	0.904	0.856	0.940	128.78	123.30	134.78	11.92	11.48	12.54
k5	0.980	0.722	0.968	140.78	103.52	138.72	12.74	9.52	12.96
R	0.176	0.34	0.182	24.68	48.32	25.84	1.80	4.58	2.44

The meaning of the bold value we provide is to highlight the highest value of R among the three variables A, B and C in the text.

TABLE 5 Simulation results of the driver's chest injury value.

Index	C_{comp} (mm)			C_{3ms}			Rib strain			Lung strain		
	A	B	C	A	B	C	A	B	C	A	B	C
K1	187.7	165.8	151.7	466.3	422.7	387.1	164.1%	145.8%	133.2%	113.4%	102.8%	94.5%
K2	171.2	172.8	140.7	428.1	439.5	359.6	147.9%	150.9%	124.1%	103.5%	106.9%	87.1%
K3	163.9	176.2	179.6	419.2	449.3	453.5	143.5%	155.2%	155.7%	101.7%	109.1%	110.8%
K4	165.3	158.8	185.6	430.8	402.1	468.0	147.6%	138.4%	162.1%	105.1%	98.0%	113.6%
K5	160.8	175.3	191.3	415.1	445.9	491.3	140.6%	153.4%	168.6%	101.6%	108.5%	119.3%
k1	37.54	33.16	30.34	93.26	84.54	77.42	32.82%	29.16%	26.64%	22.68%	20.56%	18.90%
k2	34.24	34.56	28.14	85.62	87.90	71.92	29.58%	30.18%	24.82%	20.70%	21.38%	17.42%
k3	32.78	35.24	35.92	83.84	89.86	90.70	28.70%	31.04%	31.14%	20.34%	21.82%	22.16%
k4	33.06	31.76	37.12	86.16	80.42	93.60	29.52%	27.68%	32.42%	21.02%	19.60%	22.72%
k5	32.16	35.06	38.26	83.02	89.18	98.26	28.12%	30.68%	33.72%	20.32%	21.70%	23.86%
R	5.38	3.48	10.12	10.24	9.44	26.34	4.70%	3.36%	8.90%	2.48%	2.22%	6.44%

The meaning of the bold value we provide is to highlight the highest value of R among the three variables A, B and C in the text.

Tables 3–Tables 6 show that the sum of the test results across factors and levels is represented by K_i ($i = 1, 2, 3, 4$, and 5). The average of the test results under each factor and level is k_i ($i = 1, 2, 3, 4$, and 5). An indication of the range of test results within the same factor and at various levels is R .

The change in seat belt force-limiting A would have the largest effect just on the head and legs, whereas the strongest influence on the neck was caused by the change in seat belt pre-tensioning force B, according to a comparison of the range R . The change in seat belt pre-tensioned time C had the largest influence on the chest. The head and the chest were the least sensitive to changes in seat belt pre-tensioned force B, whereas the neck injury values and leg injury values were the lowest affected by seat belt force-limiting A and pre-tensioned time C, respectively.

The effect extent of each factor on the driver's head, neck, chest, and leg injury was determined using the range analysis findings of the orthogonal experimental design to comprehend the effect of varying degrees of each element on the driver's injury more intuitively.

Figure 6 as shows the pretensioned force-limiting seat belt variables' effect laws on head, neck, thorax, and leg injuries. As shown in Figure 6A, seat belt force-limiting A increased, the injury values of the head, chest, and leg of the drivers first decreased, then increased, and again decreased, and the neck injury decreased first and then increased. When force-limiting A was larger than 4,750 N, the head, neck, and leg injuries were at their lowest degrees. The lowest value of chest injury occurred when the limiting force A was 5,500 N. As seat belt pre-tensioned

TABLE 6 Simulation results of the driver's leg injury value.

Index	F_{femur} (KN)			Femur strain			Tibia strain		
	A	B	C	A	B	C	A	B	C
K1	64.7	65.9	52.6	24.1%	24.9%	19.8%	41.0%	42.9%	34.5%
K2	44.3	59.2	55.5	16.8%	22.3%	21.0%	29.1%	38.7%	36.2%
K3	52.0	55.8	61.6	19.9%	21.0%	23.4%	34.3%	36.3%	40.1%
K4	64.1	49.8	55.9	24.3%	18.9%	21.1%	42.3%	32.7%	36.7%
K5	53.0	47.4	52.5	20.2%	18.2%	20.0%	35.1%	31.2%	34.3%
k1	12.94	13.18	10.52	4.82%	4.98%	3.96%	8.20%	8.58%	6.90%
k2	8.86	11.84	11.10	3.36%	4.46%	4.20%	5.82%	7.74%	7.24%
k3	10.40	11.16	12.32	3.98%	4.20%	4.68%	6.86%	7.26%	8.02%
k4	12.82	9.96	11.18	4.86%	3.78%	4.22%	8.46%	6.54%	7.34%
k5	10.60	9.48	10.50	4.04%	3.64%	4.00%	7.02%	6.24%	6.86%
R	4.08	3.7	1.82	1.50%	1.34%	0.72%	2.64%	2.34%	1.16%

force B was increased, the severity of injuries to the neck and legs improved. A head injury's value increased first and then decreased, but a chest injury's value decreased first, then increased, and eventually decreased. When pre-tensioned force B was 2,000 N, the driver's chest injury value rapidly declined before abruptly increasing. The lowest injury value for the chest was 2,250 N. The lowest injury values for the head, neck, and leg occurred when pre-tensioned force B was 2,500 N. As pre-tensioned time C continuously increased, the injury values of the neck and chest decreased and then increased. However, the change trend of leg injury was the opposite. The value of the driver's head injury increased first, then decreased, and again increased. Except for intracranial pressure, the lowest value of head injury occurred when pre-tensioned time C was 16 ms. When pre-tensioned time C was 18 ms, the neck (except for cancellous bone stress) and chest injury values were the lowest. Except for the femur strain, the lowest value of leg injury occurred when preload time C was 24 ms.

When one injury objective achieved the ideal value, the other injury objective presumably reached the worst condition, according to the reaction laws of each injury value to the variables of the pre-tensioned force-limiting seat belt. Thus, drivers could not reach the optimal injury value. Through the use of Isight optimization software, the multi-objective variables of the drivers were simultaneously optimized, and the best compromised seat belt variables were derived.

4 Multi-objective optimization of the pre-tensioned force-limiting seat belt

Based on comprehensive consideration, the WIC for drivers' heads, thoraxes, and legs were chosen, with neck injury predictor N_{ij} as the design goal. Additionally, seat belt force-limiting A,

pre-tensioned force B, and pre-tensioned time C were employed as design variables. To construct the model, sample points were selected using the orthogonal test design method.

4.1 Approximate model of radial basis function and error analysis

Isight optimization software was used to construct an RBF model to explore the relationship between WIC and N_{ij} as well as the force-limiting A, pre-tensioned force B, and pre-tensioned time C of the seat belt (Yin et al., 2014). The approximate definition of the response function of the design variable is

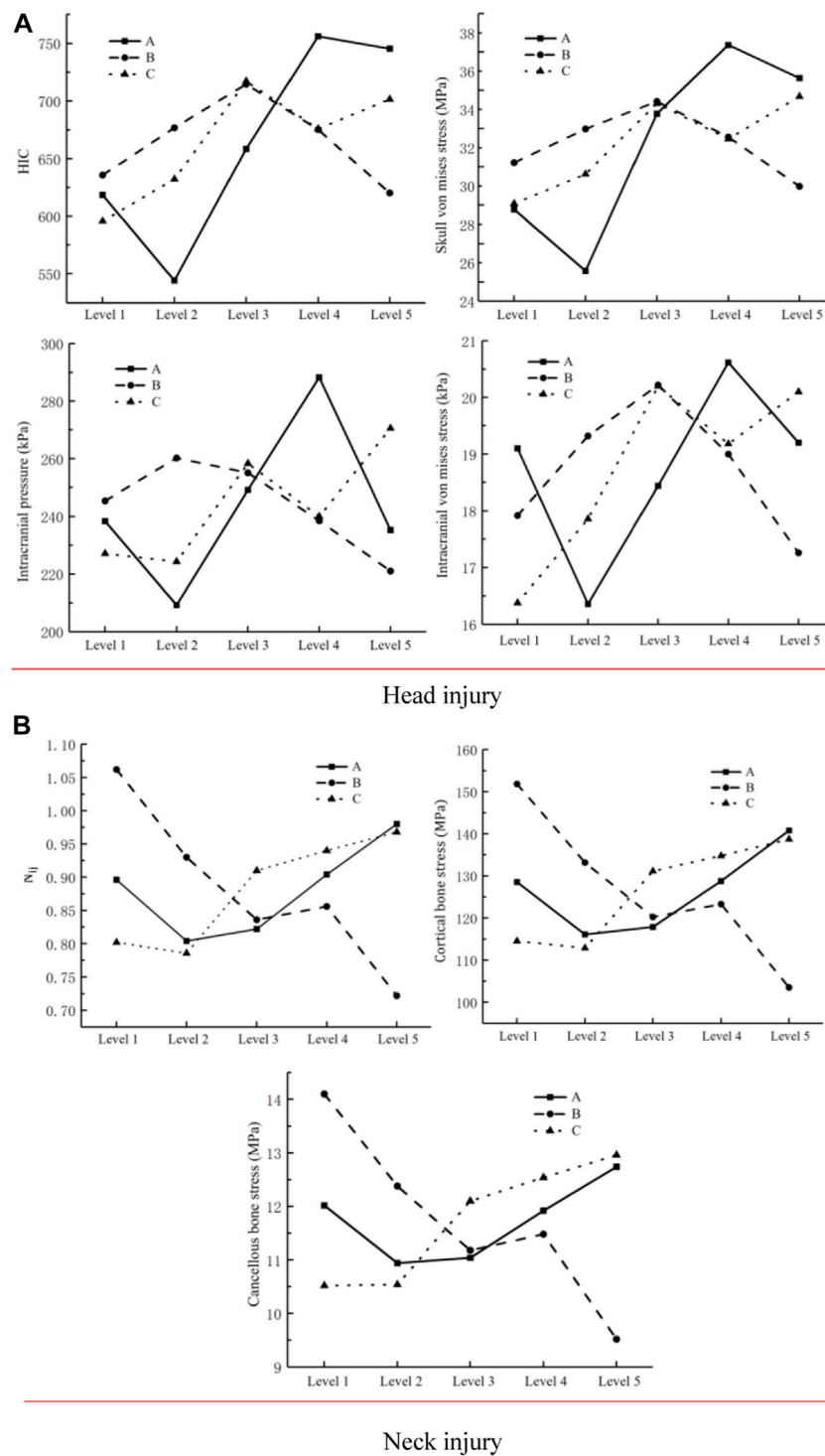
$$Y(X) = \tilde{y}(x) + \varepsilon = \left(\sum_{i=1}^N a_i g_i(\|x - x_i\|^{c_i} + a_{N+1}) \right) + \varepsilon, \quad (4)$$

where the approximate function of the objective is $\tilde{y}(x)$. ε denotes the relative error (RE) between the approximate and true values. g_i is the basis function whose number of terms is indicated by N. $x - x_i$ represents the Euclidean distance of the basis function, whereas the undetermined coefficient is represented by a_i . The shape parameter is indicated by c_i .

The response surface fitted by the RBF model was assessed using the relative error (RE), maximum error (ME), root mean square error (RMSE), and coefficient of determination (R^2) to determine its plausibility. The specific formula is as follows:

$$RE = 100\% \times \frac{|\tilde{y}_i - y_i|}{y_i}, \quad (5)$$

$$ME = 100\% \times (\tilde{y}_i - y_i), \quad (6)$$

**FIGURE 6**

Pre-tensioned force-limiting seat belt variables' effect laws on head, neck, thorax, and leg injuries. (A) Head injury. (B) Neck injury. (C) Chest injury. (D) Leg injury.

$$RMSE = \sqrt{\frac{\sum_{i=1}^M (\tilde{y}_i - y_i)^2}{M}}, \quad (7)$$

$$R^2 = 1 - \frac{SSE}{SST} = 1 - \frac{\sum_{i=1}^m (\tilde{y}_i - y_i)^2}{\sum_{i=1}^m (y_i - \bar{y})^2}, \quad (8)$$

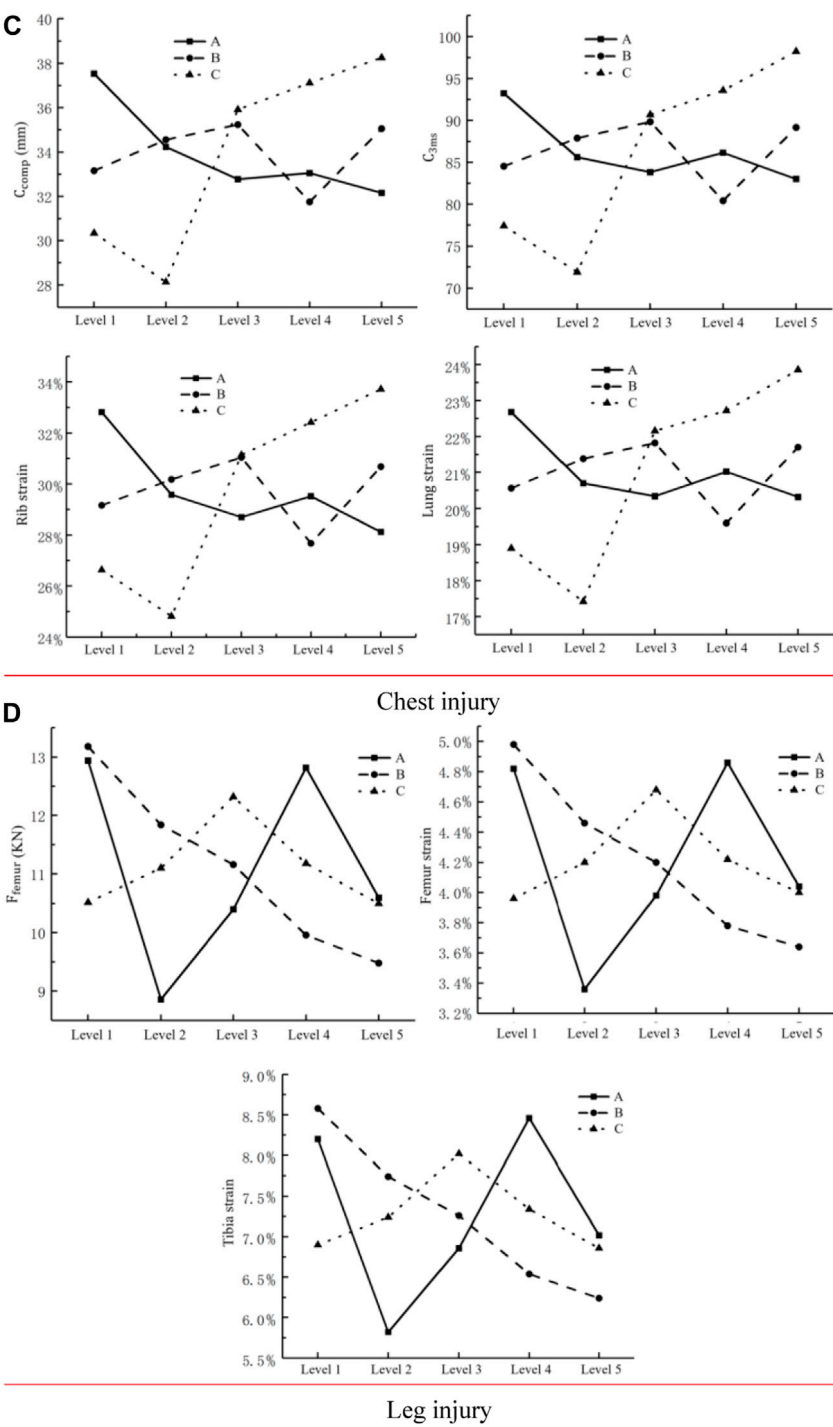


FIGURE 6

where M indicates the number of sampled data points used for testing the model's accuracy. \bar{y}_i represents the predicted value of the model, whereas y_i represents the simulation analysis value of the response. The average value of the sample in the simulation

analysis is \bar{y} . The R^2 determination coefficient is in the range of (0, 1). As the value approaches 1, the more accurate the model becomes. RE, ME, and RMSE maximum allowable errors are limited to 0.2, 0.3, and 0.2 in this model, respectively, and the

TABLE 7 Error estimation of the response surface model.

Response	RE	ME	RMSE	R ²
WIC	1.58959E-14	4.73414E-14	1.93778E-14	0.9982
N _{ij}	1.02088E-14	2.74912E-14	1.22938E-14	0.9923

smaller the value is, the better the plausibility of the model is. An analysis of 25 sample points was conducted. Table 7 shows that the built RBF response surface model has high accuracy and may be utilized to investigate multi-objective optimization issues further.

4.2 Multi-objective optimization model

In this work, the mathematical model of multi-objective optimization of the relationship between weighted injury criterion, neck injury predictor, and key parameters is established as follows:

$$\begin{cases} \min WIC = WIC(A, B, C), \\ \min N_{ij} = N_{ij}(A, B, C), \\ s.t. \ 4500N \leq A \leq 5500N, \\ \quad 1500N \leq B \leq 2500N, \\ \quad 16ms \leq C \leq 24ms. \end{cases} \quad (9)$$

Figure 7 shows that the multi-objective genetic algorithm NSGA-II was used to obtain the multi-objective Pareto frontier within the optimal solutions of pre-tensioned force-limiting seat belt parameters (Cao et al., 2016). The optimal solutions of WIC and N_{ij} may be found from the response surface model, as shown in the figure. In addition, WIC and N_{ij} always demonstrated an inverse relationship, that is, a conflict existed between N_{ij} and WIC, and the optimal solution could not be obtained at the same time.

In Figure 7, the H point represents the minimum value of N_{ij} (0.455), whereas the G point denotes the minimum value of WIC (0.466). G and H are the two best single objective values corresponding to the different response surface models in the Pareto frontier. In this study, the method of distance minimization was used to obtain the optimal value of the weighted injury criterion and neck injury predictor. The optimal values of the neck injury predictor and the weighted injury criterion were obtained by identifying the balance between N_{ij} and WIC in the optimization so that each body part was only slightly injured. The comprehensive optimal point was found when the criterion of minimizing the sum of the distances from the two Pareto response values to the optimal point to the corresponding minimum values in the solution set was the least, according to the principle of distance minimization (Yang et al., 2019). The calculation formula is as follows:

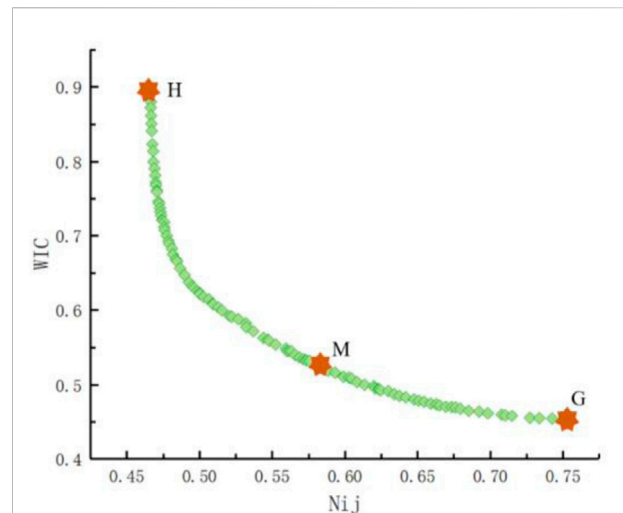


FIGURE 7
Pareto frontier of the optimal solutions of the parameters of the pre-tensioned force-limiting seat belt.

$$\min Z = \left(\sum_{i=1}^n (f_i^k - \min(f_i))^2 \right), \quad (10)$$

where $n = 2$ denotes the number of optimization goals, i.e., the two WIC and N_{ij} optimization objectives; f_i^k is the response value of the i th optimization objective at the k th Pareto response point. The M value in Figure 7 is the equilibrium solution of the conflict between the two responses, based on the multi-objective optimal solution sets calculated from Eq. 10. The response model computed a neck injury (N_{ij}) value of 0.560 at the equilibrium point M, and the WIC value was 0.545 ($A = 4751.618$ N, $B = 2,451.839$ N, and $C = 17.554$ ms).

4.3 Results

The optimal parameter values (4751.618–2,451.839–17.554) obtained from the optimization results were substituted into the crash simulation model for verification calculations. The simulation results were $N_{ij} = 0.589$ and $WIC = 0.572$, and the errors were 4.92% and 4.72%, respectively. Based on the aforementioned data, all errors were determined to be within a reasonable range, which further confirmed the accuracy of the surrogate model. The optimized results were then compared with the previous simulation results, as shown in Table 8.

The optimized pre-tensioned force-limiting seat belt protected the head, neck, thorax, and legs, as well as the entire weighted injury. Based on the injury indexes of each key part of the driver and weighted injury indexes in the optimized pre-tensioned force-limiting seat belt, the optimized pre-tensioned force-limiting seat belt was proven to be more protective and effective.

TABLE 8 Comparisons of the pre-tensioned force-limiting seat belt before and after optimization.

	Injury criteria	Before	After	Reduction (%)
Head	Skull von Mises stress (MPa)	23.6	14.9	36.9
	Intracranial pressure (kPa)	198.7	133.8	32.7
	Intracranial von Mises stress (kPa)	14.6	9.3	36.3
	HIC	521.3	328.5	37.5
Neck	N_{ij}	0.87	0.589	32.3
	Cortical bone stress (MPa)	123.4	87.5	29.1
	Cancellous bone stress (MPa)	11.7	8.1	30.8
Chest	C_{3ms} (g)	92.4	58.2	37.0
	C_{comp} (mm)	37.8	23.7	37.3
	Rib strain	32.4%	22.3%	31.2
	Lung strain	22.5%	15.6	30.7
Leg	F_L (KN)	13.2	12.1	8.3
	F_R (KN)	10.5	9.7	7.6
	Femur strain	4.9%	4.4%	10.2
	Tibia strain	8.3%	7.6%	8.4
WIC		0.881	0.572	35.1

5 Limitations and future work

There are still certain restrictions to the present research. First of all, although the verification results of the reconstruction of the small offset collision of the minivan in this study are ideal, there will still be some errors due to the lack of video information at the time of the accident. Later accident reconstruction is expected to collect small offset collisions with video information. Second, this study only qualitatively analyzed the injury caused to the minivan driver using the pre-tensioned force-limiting seat belt. In the next step, it is necessary to study the optimization of the matching parameters between the pre-tensioned force-limiting seat belt and the airbag, so as to maximize the security value of the driver. Finally, this study only studied the protection of the minivan driver. Future research can focus on the safety performance of the occupant restraint system to reduce the risk of occupant injury.

6 Conclusion

The results show that in a small offset collision at 48 km/h, the pre-tensioned force-limiting seat belt with variables of 4751.618–2,451.839–17.554 had an evident protective effect on the driver's head, neck, chest, and leg injuries, as well as the whole weighted injury. Therefore, the optimized pre-tensioned force-limiting seat belt can help drivers reach the

optimal protection state in minivans when involved in small offset collisions.

- (1) By reconstructing a small offset collision involving a minivan, the risk of injury to each part of the driver's body was evaluated. Based on the results of the simulation, the model can properly portray the drivers' dynamic characteristics as well as effectively evaluate the danger of injury to specific parts of the driver. Therefore, the crash simulation model was verified feasible.
- (2) As pre-tensioned force B changed, it profoundly affected the degree of neck injury suffered by the driver, whereas the most apparent effect of the change in force-limiting A was on the legs and head. Changing the pre-tightening time C of the seat belt had a clear protective effect on the thorax. The head and chest were the least sensitive to changes in seat belt pre-tensioned force B. In addition, changing force-limiting A and pre-tightening time C caused the least injury to the neck and legs, respectively.
- (3) Under the optimized seat belt variables at 4751.618 N, 2,451.839 N, and 17.554 ms for force-limiting A, pre-tensioned force B, and pre-tensioned time C, the head injury HIC and skull von Mises stress decreased by 37.5% and 36.9%, respectively. N_{ij} and cancellous bone stress injuries were reduced by 32.3% and 30.8%, respectively. Moreover, C_{3ms} and C_{comp} were reduced by 37.0% and 37.3%, respectively. Thigh axial force F_L was decreased by 8.3%, and weight injury was reduced by 35.1%. The pre-tensioned force-limiting seat

belt has great potential for increasing driver protection in small offset collisions.

Data availability statement

The original contributions presented in the study are included in the article/Supplementary Material; further inquiries can be directed to the corresponding authors.

Author contributions

XY: conceptualization, investigation, methodology, and writing—original draft. JS: data curation. QF: visualization and investigation. SP: formal analysis and software. CL: methodology and validation. KL: funding acquisition and editing. ZY: conceptualization, funding acquisition, resources, and supervision. SL: supervision and writing—review and editing. GW: funding acquisition, resources, and supervision.

Funding

This work was financially supported by the National Key Research and Development Program of China

References

- Albanese, B., Bohman, K., Bilston, L., Koppel, S., Brown, J., Olivier, J., et al. (2020). Influence of child restraint system design features on comfort, belt fit and posture. *Saf. Sci.* 128, 104707. doi:10.1016/j.ssci.2020.104707
- Anghileri, M., Chirwa, E. C., Lanzi, L., and Mentuccia, F. (2005). An inverse approach to identify the constitutive model parameters for crashworthiness modelling of composite structures. *Compos. Struct.* 68 (1), 65–74. doi:10.1016/j.compstruct.2004.03.001
- Cao, L. B., Ouyang, Z. G., Xu, Z., and Zhang, G. J. (2016). Research on the optimization of reversible restraint systems. *J. Mech. Eng.* 52 (10), 133–141. doi:10.3901/JME.2016.10.133
- Chan, H. S., and Liu, Y. K. (1974). The asymmetric response of a fluid-filled spherical shell—a mathematical simulation of a glancing blow to the head. *J. Biomechanics* 7 (1), 43–59. doi:10.1016/0021-9290(74)90069-4
- Chi, W. C., and Geng, S. (2019). Research of seat in whiplash based on THUMS human model. *Intern. Combust. Engine & Parts* 24 (3), 5–7. doi:10.19475/j.cnki.issn1674-957x.2019.24.003
- Cho, Y. B., Bae, C. H., Suh, M. W., and Sin, H. C. (2006). A vehicle front frame crash design optimization using hole-type and dent-type crush initiator. *Thin-Walled Struct.* 44 (4), 415–428. doi:10.1016/j.tws.2006.03.011
- Deb, K., Pratap, A., Agarwal, S., and Meyarivan, T. (2002). A fast and elitist multiobjective genetic algorithm: NSGA-II. *IEEE Trans. Evol. Comput.* 6 (2), 182–197. doi:10.1109/4235.996017
- Duan, A. W., Zhou, M. X., Qiu, J. L., Feng, C. J., Yin, Z. Y., and Li, K. (2020). A 6-year survey of road traffic accidents in southwest China: Emphasis on traumatic brain injury. *J. Saf. Res.* 73, 161–169. doi:10.1016/j.jsr.2020.02.010
- Gao, D. W., Zhang, N., and Chen, H. F. (2019). Prediction accuracy of collision indicators for minibuses based on an approximate model. *J. Highw. Transp. Res. Dev.* 13 (1), 94–103. doi:10.1061/jhtrcq.0000671
- Ge, R. H., Zhang, S. X., and Hong, L. (2017). Optimization of front-row occupant restraint system with NSGA-II genetic algorithm. *Auto-motive Eng.* 39, 1382–1389. doi:10.19562/j.chinasae.Qcgc.2017.12.005
- (2016YFC0800702-3) and Chongqing Science and Technology Bureau, China (cstc2021jcyj-msxmX0109 and cstc2020jscx-msxmX0132). The authors acknowledge the Institute of Surgery, Army Military University, China, for providing the data in this study.
- Gu, K. L., Ge, C. Y., and Zhang, R. (2020). Correlation analysis and structure optimization of seatbelt anchorage strength for Vehicle. *Sci. Technol. Eng.* 23 (2), 16–18. doi:10.3969/j.issn.1674-6546.2020.02.005
- Hao, Y., Yang, S., Han, F. F., Ren, P. F., He, N., and Fang, R. (2018). Analysis of the influence of the seatbelt fire to the chest damage in mid-low speed frontal impact. *Automob. Appl. Technol.* 2, 71–74. doi:10.16638/j.cnki.1671-7988.2018.02.024
- Hassan, M. T. Z., and Meguid, S. A. (2018). Effect of seat belt and head restraint on occupant's response during rear-end collision. *Int. J. Mech. Mat. Des.* 14 (2), 231–242. doi:10.1007/s10999-017-9373-6
- Hu, Y. Z., Gan, S., Liu, X., Lian, G. J., Zhou, L., Liu, Z. C., et al. (2018). Deformation control and structure crashworthiness optimization for a certain minivan in the event of a frontal collision. *Sci. Technol. Eng.* 18 (18), 105–111. doi:10.3969/j.issn.1671-1815.2018.18.016
- Hu, Y. Z., Zeng, B. Q., and Xie, S. G. (2011). *The simulation and analysis of automobile safety based on IS-dyna and HyperWorks*. Beijing: Tsinghua University press.
- Kallieris, D., Rizzetti, A., and Mattern, R. (1997). Some observation to the skull-brain trauma. *Adv. Group Aerosp. Res. Dev. Conf.* 597, 1–4.
- Kuppa, S., Wang, J., Haffner, M., and Eppinger, R. (2001). Lower extremity injuries and associated injury criteria. *Proc. 17th ESV Conf.* 457, 1–15.
- Lei, C., and Yin, Z. Y. (2016). Study of driver injury based on reconstruction of minibus collisions. *J. Chongqing Univ. Technol. Nat. Sci.* 30 (2), 71–76. doi:10.3969/j.issn.1674-8425(2).2016.02.013
- Li, W. J., Li, G., and Liu, F. J. (2015). Frontal structure safety analysis of minibuses based on Chinese in-depth accident studies. *Int. Conf. Transportation Eng.* 0, 2973–2978. doi:10.1061/9780784479384.379
- Liu, S. X., Yang, X. J., Cui, J. G., and Yin, Z. Y. (2017a). A novel pixel-based method to estimate the instantaneous velocity of a vehicle from CCTV images. *J. Forensic Sci.* 62 (4), 1071–1074. doi:10.1111/1556-4029.13381

- Liu, X., Wu, G., and Yin, L. Y. (2016). Optimal design of a seat belt restraint system based on approximate model management. *J. Vib. Shock* 35 (6), 132–136. doi:10.13465/j.cnki.jvs.2016.06.024
- Liu, Y. Y., Lu, J., Yuan, X. C., Du, B. T., and Yue, P. (2017b). Effects of steering column characteristic on driver's injury. *Sci. Technol. Eng.* 25 (2), 47–50. doi:10.3969/j.issn.1674-6546.2017.02.011
- Lu, F., Zhang, J. Y., Ma, Y., Liu, J. Y., and Ye, W. T. (2016). The analysis and application of the neck mechanical response of rear seat dummy in frontal crash. *Automot. Eng.* 38 (7), 828–834. doi:10.3969/j.issn.1000-680X.2016.07.007
- Magee, C. L., and Thornton, P. H. (1978). *Design considerations in energy absorption by structural collapse*. Warrendale, Pennsylvania, United States: Society of Automotive Engineers, 55–60. doi:10.4271/780434
- Marjoux, D., Baumgartner, D., Deck, C., and Willinger, R. (2008). Head injury prediction capability of the HIC, HIP, SIMon and ULP criteria. *Accid. Analysis Prev.* 40 (3), 1135–1148. doi:10.1016/j.aap.2007.12.006
- Mertz, H. J., Prasad, P., and Irwin, A. L. (1997). Injury risk curves for children and adults in frontal and rear collisions. *Proc. 41st Stapp Car Crash Conf.* 41, 973318–973330. doi:10.4271/973318
- Ovesy, H. R., and Masjedi, P. K. (2014). Investigation of the effects of constitutive equations on the free vibration behavior of single-celled thin-walled composite beams. *Mech. Adv. Mater. Struct.* 21 (10), 836–852. doi:10.1080/15376494.2012.725266
- Pappachan, B., and Alexander, M. (2012). Biomechanics of cranio-maxillofacial trauma. *J. Maxillofac. Oral Surg.* 11, 224–230. doi:10.1007/s12663-011-0289-7
- Park, G. J. (2011). Technical overview of the equivalent static Loads method for non linear static response structural optimization. *Struct. Multidiscipl. Optim.* 43 (3), 319–337. doi:10.1007/s00158-010-0530-x
- Prochowski, L., Dębowski, A., Żuchowski, A., and Zielonka, K. (2016). Evaluation of the influence of velocity on dynamic passenger loads during a frontal minivan impact against an obstacle. *IOP Conference Series: Materials Science and Engineering, IOP Conf. Ser. Mat. Sci. Eng.* 148 (1), 012024–24. doi:10.1088/1757-899X/148/1/012024
- Schaefer, K. E., McNulty, W. P., Carey, C., and Liebow, A. (1958). Mechanisms in development of interstitial emphysema and air embolism on decompression from depth. *J. Appl. Physiology* 13 (1), 15–29. doi:10.1152/jappl.1958.13.1.15
- Shi, L. L., Lei, C., Li, K., Fu, S. S., Wu, Z. W., and Yin, Z. Y. (2016). Finite element simulation of lower limb injuries to the driver in minibus frontal collisions. *Chin. J. Traumatology* 19 (003), 146–150. doi:10.1016/j.cjtee.2016.01.015
- Shigeta, K., Kitagawa, Y., and Yasuki, T. (2009). Development of next generation human body FE model capable of organ injury prediction. *Proc. 21st Annu. Enhanc. Saf. Veh.* 09, 0111. doi:10.1016/0921-8696(89)90628-2
- Tian, G. H., Cheng, H. D., Shun, P. Y., and Wu, X. L. (2016). Simulation of dual-stage gas generator airbag. *Sci. Technol. Eng.* 32 (11), 23–25. doi:10.3969/j.issn.1674-6546.2016.11.005
- Viano, D. C., and Arepally, S. (1990). Assessing the safety performance of occupant restraint systems. *Stapp Car Crash Conf.* 27, 1913–1939. doi:10.4271/902328
- Wang, F., Wu, J. Z., Hu, L., Yu, C., Wang, B. Y., Huang, X. Q., et al. (2022b). Evaluation of the head protection effectiveness of cyclist helmets using full-scale computational biomechanics modelling of cycling accidents. *J. Saf. Res.* 80, 109–134. doi:10.1016/j.jsr.2021.11.005
- Wang, F., Yin, J. J., Hu, L., Wang, M. L., Liu, X., Miller, K., et al. (2022a). Should anthropometric differences between the commonly used pedestrian computational biomechanics models and Chinese population be taken into account when predicting pedestrian head kinematics and injury in vehicle collisions in China? *Accid. Analysis Prev.* 173, 106718. doi:10.1016/j.aap.2022.106718
- Wang, W. W., Dai, S. J., Zhao, W. Z., Wang, C. Y., Ma, T., and Chen, Q. Y. (2020). Reliability-based optimization of a novel negative Poisson's ratio door anti-collision beam under side impact. *Thin-Walled Struct.* 154 (1), 106863. doi:10.1016/j.tws.2020.106863
- Watanabe, R., Miyazaki, H., Kitagawa, Y., and Yasuki, T. (2012). Research of collision speed dependency of pedestrian head and chest injuries using human FE model (THUMS version 4). *Accid. Reconstr. J.* 22, 11–0043.
- Wen, H., Lin, L. Y., Chen, D. Q., Wu, F., and Zhu, L. L. (2011). Features of survived casualties and treatment after “July 23” EMU railway accident at Wenzhou station. *Chin. J. Emerg. Med.* 20 (12), 1248–1250.
- Willinger, R., Baumgartner, D., Chinn, B., and Neale, M. (2000). Head tolerance limits derived from numerical replication of real world accidents. *Proc. Int. Res. Counc. Biomechanics Inj. Conf.* 28, 209–221.
- Xiao, L., Li, L., Duan, D. W., and Liu, Y. B. (2018). Modification design of a sedan based on 25% overlap frontal crash test. *Automot. Eng.* 040 (002), 184–191. doi:10.19562/j.chinasae.qcgc.2018.02.011
- Yang, W., Xie, S., Li, H., and Chen, Z. (2019). Design and injury analysis of the seated occupant protection posture in train collision. *Saf. Sci.* 117, 263–275. doi:10.1016/j.ssci.2019.04.028
- Yin, H. F., Wen, G. L., Liu, Z. B., and Qing, Q. X. (2014). Crashworthiness optimization design for foam-filled multi-cell thin-walled structures. *Thin-Walled Struct.* 75, 8–17. doi:10.1016/j.tws.2013.10.022
- Zhai, K. N., Li, X. Y., Wang, Z. Y., and Yang, S. (2017). Multi-objective optimization of the driver restraint system in the offset crash. *Automob. Appl. Technol.* 16, 93–95.
- Zhai, X. J., Wu, Y. Q., Liu, W. G., Zhou, D. Y., Zhang, H. Y., Zhu, H., et al. (2015). Optimization of steering column's arrangement angles based on occupant protection. *Sci. Technol. Eng.* 11 (2), 26–30. doi:10.3969/j.issn.1674-6546.2015.02.005



OPEN ACCESS

EDITED BY

Suvash C. Saha,
University of Technology Sydney,
Australia

REVIEWED BY

Yongtao Lu,
Dalian University of Technology (DUT),
China
Francesco Travascio,
University of Miami, United States

*CORRESPONDENCE

Changchun Zhang,
zccanhu1968@126.com

[†]These authors have contributed equally
to this work and share first authorship

SPECIALTY SECTION

This article was submitted
to Biomechanics,
a section of the journal
Frontiers in Bioengineering and
Biotechnology

RECEIVED 21 August 2022

ACCEPTED 05 October 2022

PUBLISHED 21 October 2022

CITATION

Ye Y, Jin S, Zou Y, Fang Y, Xu P, Zhang Z,
Wu N and Zhang C (2022),
Biomechanical evaluation of lumbar
spondylolysis repair with various fixation
options: A finite element analysis.
Front. Bioeng. Biotechnol. 10:1024159.
doi: 10.3389/fbioe.2022.1024159

COPYRIGHT

© 2022 Ye, Jin, Zou, Fang, Xu, Zhang,
Wu and Zhang. This is an open-access
article distributed under the terms of the
[Creative Commons Attribution License](https://creativecommons.org/licenses/by/4.0/)
(CC BY). The use, distribution or
reproduction in other forums is
permitted, provided the original
author(s) and the copyright owner(s) are
credited and that the original
publication in this journal is cited, in
accordance with accepted academic
practice. No use, distribution or
reproduction is permitted which does
not comply with these terms.

Biomechanical evaluation of lumbar spondylolysis repair with various fixation options: A finite element analysis

Yuchen Ye^{1,2†}, Shichang Jin^{1†}, Yang Zou¹, Yuekun Fang²,
Panpan Xu², Zhili Zhang¹, Nan Wu¹ and Changchun Zhang^{1,2*}

¹Department of Orthopaedics, First Affiliated Hospital, Bengbu Medical College, Bengbu, China, ²Anhui Province Key Laboratory of Tissue Transplantation, Bengbu Medical College, Bengbu, China

Objective: This study was designed to compare the biomechanical properties of lumbar spondylolysis repairs using different fixation methods by using three-dimensional finite element analysis.

Methods: Five finite element models (A, B, C, D, and E) of L4-S1 vertebral body were reconstructed by CT images of a male patient (A: intact model; B: spondylolysis model; C: spondylolysis model with intrasegmental direct fixation by Buck screw; D: spondylolysis model with intersegmental indirect fixation by pedicle screw system; E: spondylolysis model with hybrid internal fixation). L5-S1 level was defined as the operative level. After the intact model was verified, six physiological motion states were simulated by applying 500 N concentrated force and 10 Nm torque on the upper surface of L4. The biomechanical properties of the three different internal fixation methods were evaluated by comparing the range of motion (ROM), maximum stress, and maximum displacement.

Results: Compared with Model B, the ROM and maximum displacement of Model C, D, and E decreased. The maximum stress on L5/S1 disc in models A, B, and C was much higher than that in Model D and E under extension and lateral bending conditions. Under axial rotation and lateral bending conditions, the maximum stress of interarticular muscle and internal fixation system in Model B and Model C was significantly higher than that in Model D and Model E. In contrast to Model D, the stress in Model E was distributed in two internal fixation systems.

Conclusion: In several mechanical comparisons, hybrid fixation had better biomechanical properties than other fixation methods. The experimental results show that hybrid fixation can stabilize the isthmus and reduce intervertebral disc stress, which making it the preferred treatment for lumbar spondylolysis.

KEYWORDS

lumbar spondylolysis, finite element analysis, biomechanical, surgical therapy, internal fixation

Introduction

Lumbar spondylolysis refers to bone discontinuity or bone defect in the transition area of the upper and lower articular and transverse processes of the lumbar spine, and it is one of the important causes of low back pain in youth (Leone et al., 2011; Gagnet et al., 2018). The incidence of lumbar spondylolysis is around 6%–8% in the general population, but it can reach 63% in people who engage in certain physical activities (Sairyo et al., 2005; Goetzinger et al., 2020). The pathogenesis of lumbar spondylolysis is still controversial. However, the most likely mechanism is that stress fractures can occur under the presence of high intensity and frequency of lumbar activity in the congenital weak or dysplastic anatomic weak area of the vertebral spondylolysis (Terai et al., 2010). Based on previously reported cases, lumbar spondylolysis is more common in L4 and L5 vertebrae, as much as 80% of spondylolysis fractures occurred in L5, and may be associated with varying degrees of spondylolisthesis (Berger and Doyle, 2019).

Presently, nonsurgical treatment is still the main treatment for young people with spondylolysis (Goetzinger et al., 2020). However, surgical treatment is required for patients with refractory low back pain or a poor response to nonoperative treatment (Bouras and Korovessis, 2015; Berger and Doyle, 2019). According to previous reports, many techniques for isthmus repair have been described, including the Scott wiring technique, hook-wire constructs, the trans laminar interfragmentary screw, and pedicle screw hook structure with bone graft (Yamamoto et al., 2008; Berjano et al., 2020; Kumar et al., 2021; Tarpada et al., 2021).

Currently, there are two common methods of internal fixation in clinical practice. One is Buck's technique, proposed by Buck in 1970, to directly fix the isthmus repair, (JE, 1970; Snyder et al., 2014) and the other is the indirect fixation of the isthmus with the intersegmental pedicle screw internal fixation system used by various scholars (Huang et al., 2019; Zhang et al., 2021). Extensive studies have confirmed the effectiveness and safety of both methods. Buck's technique also conserves segmental motion, allowing for rapid postoperative recovery and minimal blood loss (Giudici et al., 2011). Another pedicle screw system ameliorated the low postoperative fusion rate. The strong grip of the pedicle screw itself and the squeezing effect of the screw system on the isthmus bone graft ensure isthmus fusion (Huang et al., 2019; Zhang et al., 2021). However, the above two fixation methods also have certain defects. For example, although the Buck technique can fix the isthmus directly, it cannot solve the problem of stress concentration in the lumbosacral region (Sairyo et al., 2006a; Sterba et al., 2018; Haj-Ali et al., 2019). On the other hand, the pedicle screw technique can disperse stress from the lumbosacral region, but it cannot ensure isthmus stability. In order to solve the problem of stress concentration in the lumbosacral region. It can also disperse stress from the lumbosacral region to ensure the stability of the isthmus.

Therefore, the author also proposed a hybrid fixation method and added it to comparing fixation methods for spondylolysis repair.

Finite element analysis has successfully been used in spine biomechanics research, with the development of computer science (Chosa et al., 2004; Wang et al., 2006). Ramakrishna et al. used finite element analysis to demonstrate the role of sacral slope in the progression of bilateral isthmus defects to lumbar spondylolisthesis in L5 (Ramakrishna et al., 2017). Marwan et al. analyzed the stress distribution of the isthmus, pedicle, and intervertebral disc in a lumbar finite element model by CT reconstruction of a patient with spondylolysis (El-Rich et al., 2006). Sairyo et al. evaluated the biomechanical properties of the Buck technique in repairing lumbar spondylolysis using the finite element method (Sairyo et al., 2006b). Matsukawa et al. compared the biomechanical stability of cortical bone trajectory screws and pedicle screws for isthmus repair (Matsukawa et al., 2016).

In the past, most scholars focused on the finite element study of lumbar spondylolysis with intrasegmental fixation methods (Li et al., 2022a), whereas the comparative study with intersegmental fixation was lacking. In this study, we conducted biomechanical evaluation and comparison of the three surgical methods (Figure 1), including intrasegmental direct fixation, intersegmental indirect fixation, and hybrid fixation, through finite element analysis to offer a theoretical basis for the surgical treatment of young lumbar spondylolysis.

Materials and methods

Construction of the finite element model

This study of the original CT data from a 20-year-old patient diagnosed with L5 bilateral spondylolysis (Supplementary Figure S1); the scan slice thickness was 0.6 mm. All 481 CT images were transmitted to Mimics (Mimics 20.0, Materialize, Leuven, Belgium) in DICOM, a medical image processing software, and adjust the appropriate gray scale to obtain a clear bone profile (Wan and Higgins, 2003). Following the completion of the mask processing, the files were exported to STL format. These STL files were then imported into Geomagic Studio 12 (Geomagic, United States) software to reconstruct solid surfaces by inversion. Subsequently, Solid Works software (Dassault Systems, United States) was used to assemble internal fixation and fabricate the disc, articular cartilage, and bone graft. The intervertebral disc was reconstructed according to vertebral anatomy, and the isthmus defect was filled with bone graft. Then Hypermesh software (Altair Technologies, Fremont, CA, United States) was used to mesh solid models of bone and ligament structures. Finally, the finite element analysis software Abaqus 6.10 (Dassault Systemes, France) was used to

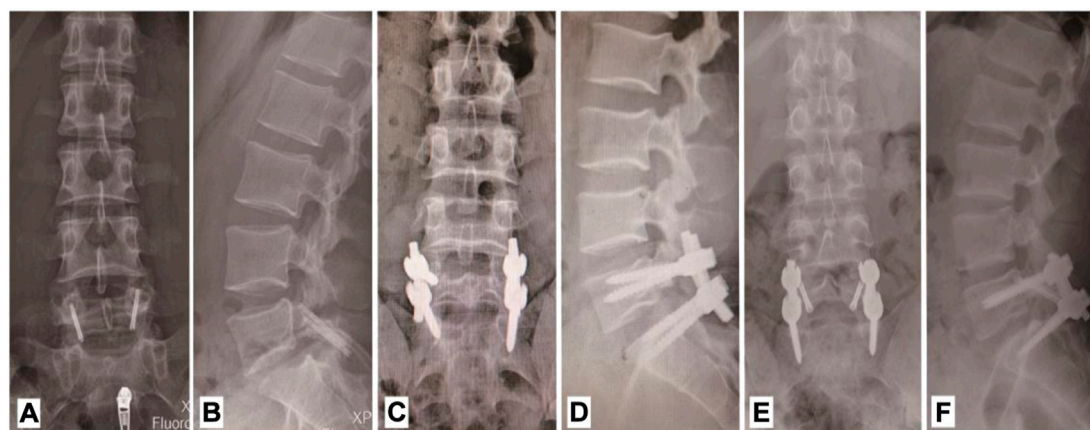


FIGURE 1

X-ray images of three internal fixation options. (A,B) Anteroposterior-lateral radiograph with intra-segmental direct fixation. (C,D) Anteroposterior-lateral radiograph with intra-segmental direct fixation. (E,F) Anteroposterior-lateral radiograph with hybrid fixation.

add soft tissues, such as ligaments, set control conditions, and submit computational solutions.

There are five finite element models established in this experiment (Figure 2). Model A: Intact L4-S1 vertebral model with normal L5 vertebral body after repair; Model B: Original model of CT scan showed bilateral spondylolysis of L5 without internal fixation; Model C: Intrasegmental internal fixation model, in which Buck screws were placed axially on the L5 pars interarticulars of Model B; Model D: Intersegmental internal fixation model, in which L5 and S1 of Model B placing the pedicle screw fixation system; Model E: Hybrid internal fixation model, in which Buck screw and intersegmental pedicle screw fixation system were placed simultaneously on Model B. The operation of the internal fixation model was simulated, and its mechanical properties were analyzed. The model provides a real surgery, said and make the analysis of the mechanical properties are possible.

Material properties

The finite element model included L4-S1 vertebral body, facet joints, intervertebral disc, ligament system, and internal fixation device. According to the CT image grayscale and bone density, cortical bone and cancellous bone of the vertebral body were assigned different material properties (Baca and Horak, 2007; Song et al., 2021). The intervertebral disc consists of the nucleus pulposus, annulus fibrosus, and upper and lower endplates, which are assigned different material properties. For the model with an internal fixation system, bone grafts were added and assigned using autogenous cancellous bone material properties. The ligament system includes the anterior longitudinal ligament, posterior longitudinal ligament,

ligamentum flavum, interspinous ligament, supraspinal ligament, saccular ligament, and transverse ligament. They are configured as homogeneous orthotropic linear elastic materials by obtaining data from references (Baca and Horak, 2007; Song et al., 2021). The detailed materials and properties of the components are illustrated in Table 1.

Mesh generation

To mesh various solid models, the type of model includes the tetrahedral element, pentahedral element (transition element), shell element (cortical bone), and nonlinear truss element (ligament, only in tension and not in compression). The global element size of the model is 1 mm (determined by model validity verification), and local encryption is carried out in the concerned part to ensure calculation accuracy and speed. The tetrahedral element adopts C3D4 element, the pentahedral element adopts the C3D6 element type, the shell element adopts S4R element type, and the truss element adopts T3D2 element (Li et al., 2022a).

Loading and boundary conditions

A uniformly distributed 500 N vertical downward concentrated force was applied on the upper surface of L4 to close to physiological state. Then, a torsional moment of 10 nm was imposed to simulate the six spinal physiological activities of flexion, extension, left axial rotation (LAR), right axial rotation (RAR), left lateral bending (LLB), and right lateral bending (RLB). ROM of segment L5-S1 was recorded

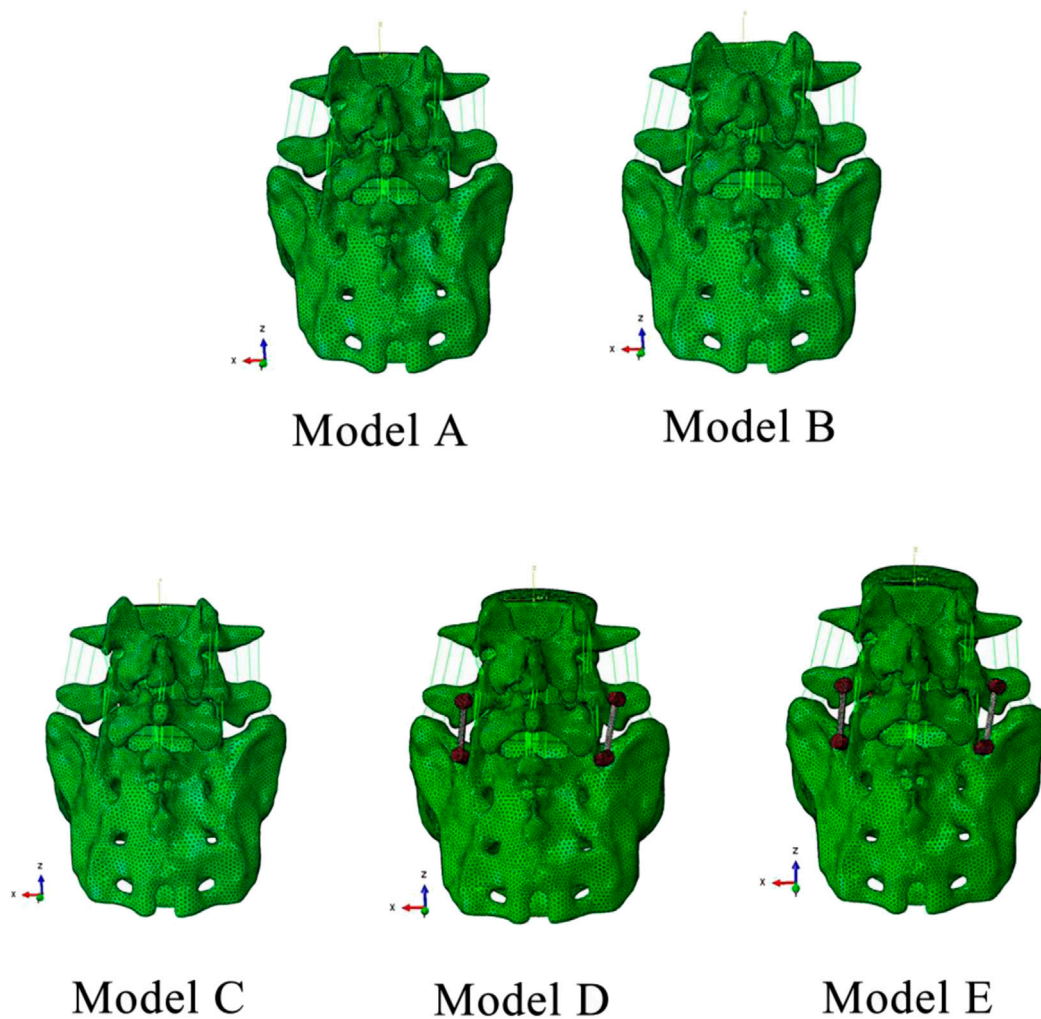


FIGURE 2

Five finite element models. Model A: Intact model; Model B: Spondylolysis model; Model C: Spondylolysis model with Buck screw; Model D: Spondylolysis model with pedicle screw fixation system; Model E: Spondylolysis model with hybrid fixation.

and compared with adjacent segments. The maximum displacement, intervertebral disc stress, facet stress, internal fixation stress, and stress distribution were compared under various models.

Indirect validity verification

Indirect validation studies aim to extensively evaluate the reliability of models created using automated algorithms by contrasting results from multiple models (i.e., multiple samples) with experimental data in the literature (Campbell et al., 2016). In this study, we reconstructed the completed model using the original model and then compared the

generated complete model with the results of other lumbar FE models in the literature.

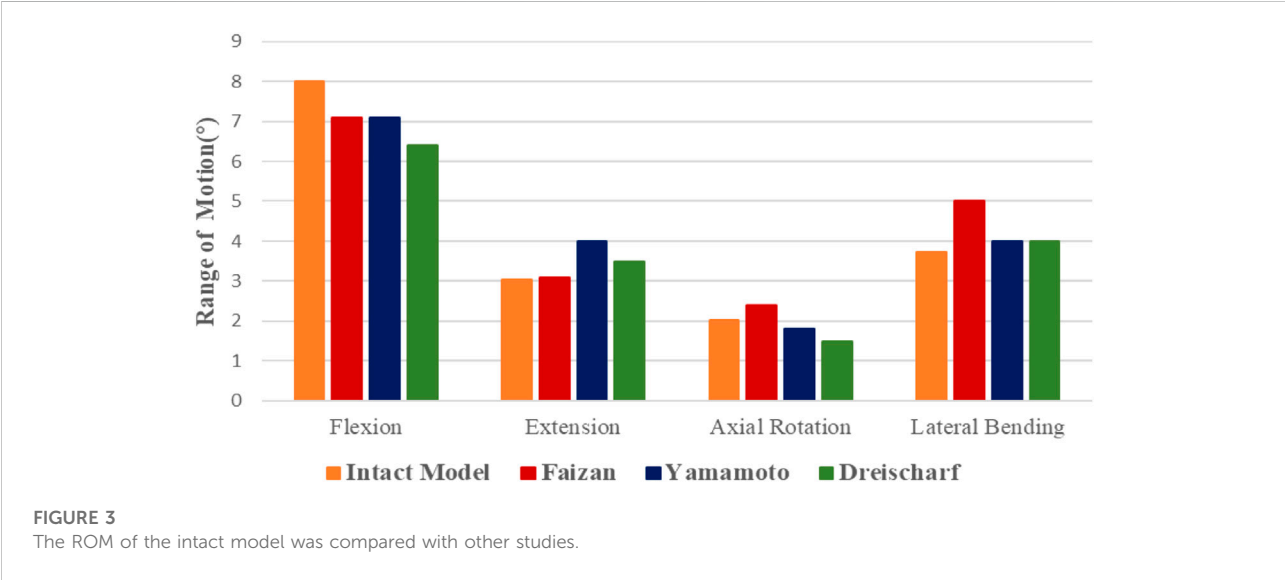
Results

Mesh generation results

In this study, L4-S1 lumbar spine model was reconstructed, and three different internal fixation systems were analyzed using finite element methods. The basic benchmarking model has 595,295, 181,448 elements of a pedicle screw rod system, 59,708 elements of a simple small screw, 79,958 elements of a screw system, and 64 elements of a truss unit.

TABLE 1 Material properties of finite element models (Elmasry et al., 2018; Li et al., 2022a).

Structure	Young's modulus (MPa)	Poisson's ratio
Cortical bone	12000	0.3
Cancellous bone	100	0.2
Cartilaginous endplate	1200	0.29
Posterior structure	3500	0.25
Annulus fibrosus	6	0.45
Nucleus pulposus	1	0.49
Anterior longitudinal ligament	20	0.3
Posterior longitudinal ligament	20	0.3
Supraspinous ligament	15	0.3
Interspinous ligament	11.6	0.3
Ligamentum flavum	19.5	0.3
Capsular ligament	32.9	0.3
Intertransverse ligament	58.7	0.3
Internal fixation (titanium alloy)	110000	0.3



Indirect validation results

We used the intact model (Model A) as a benchmark against other previously published validation studies (Yamamoto et al., 1989; Dreischarf et al., 2014; Faizan et al., 2014). ROMs of the model subjected to a concentrated force of 500 N and a torque of 10 Nm under four states of motion were compared: bending, stretching, lateral bending, and axial rotation. The load conditions of the model referred to are basically consistent with Model A (Figure 3). The results show that ROM of Model A and

other scholar's research results are basically consistent, indirect proved the validity of the proposed research model.

Range of motion

In all six motion modes, the ROM of model B increased compared with the intact model, with an increase range of 1.36%–205.50%. As displayed in Figure 4, compared with the complete model, the ROM of Model B increased in all six motion modes, with an increasing range of 1.36%–205.50%. Among

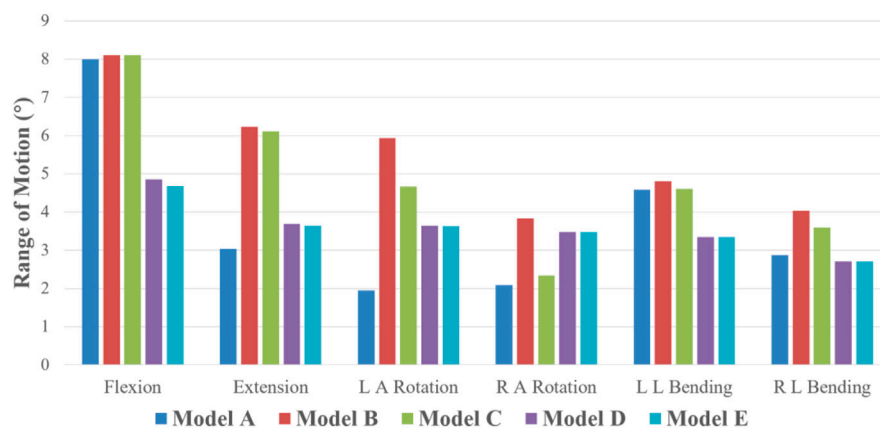


FIGURE 4
ROM of five finite element models under six motion states.

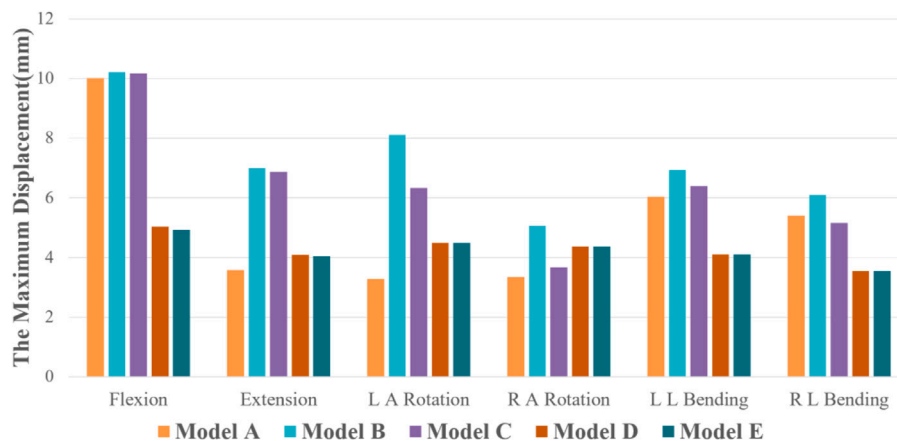


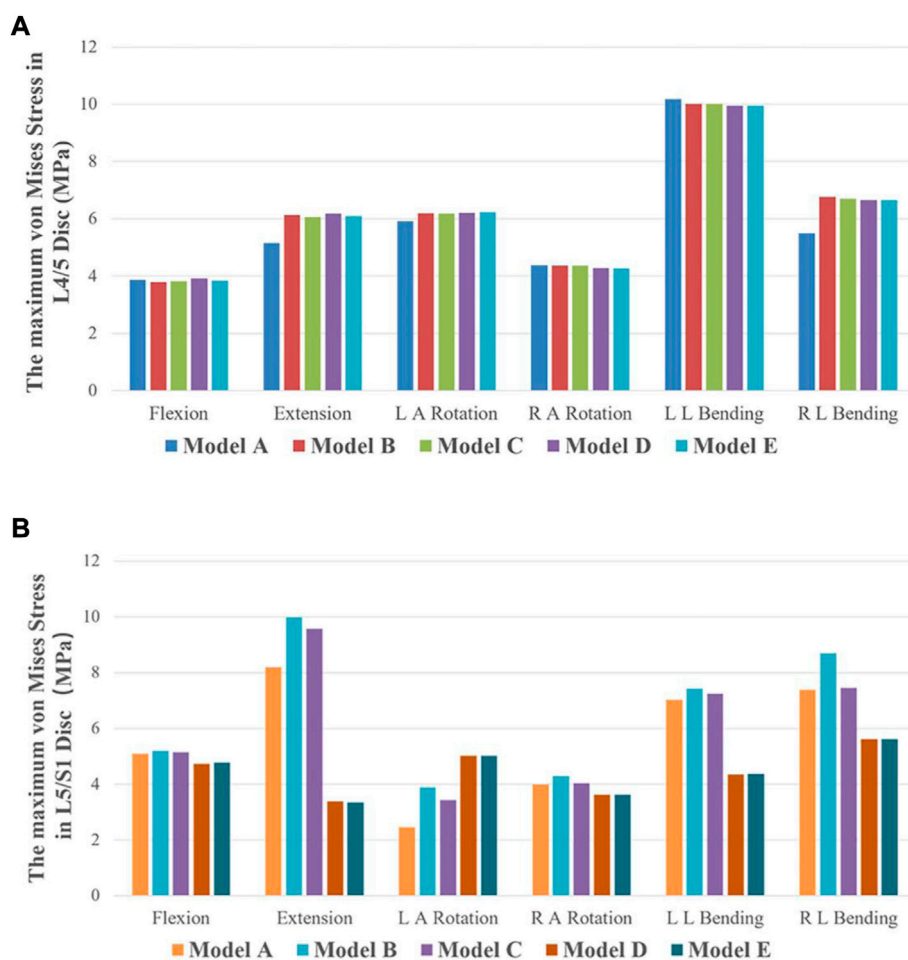
FIGURE 5
The maximum displacement of five finite element models under six motion states.

them, the activity increased significantly under left axis rotation and extension, which were 3.99° and 3.20° , respectively. In addition, in Model B, the activities of left and right axis rotation were 5.93° and 3.84° , respectively, and the activities of left and right lateral flexion were 4.812° and 4.04° , respectively, with noticeable differences, which may be related to the asymmetry of bilateral pedicle spondylolysis in this patient. Compared with Model B, ROM of the three internal fixation models (Model C, D, and E) decreased in all five motion modes except flexion. Among them, the decline range of Model C is 2.02%–38.93%, that of Model D is 9.35%–40.79%, and that of Model E is 9.38%–41.56%. In the comparison of the three internal fixation models, ROM value of Model C decreases the most in the right axis rotation state, while ROM value of Model D

and E decreases the most in the extension state, which may be associated to the method of intersegmental internal fixation.

Maximum displacement of model

As displayed in Figure 5, compared with Model A, the maximum displacement of Model B under six motion states increases with the exceeded range of 1.99%–147.20%, and the displacement difference is the largest under axial rotation. At the same time, the maximum displacement of Model C, D, and E decreased compared with model B under the six motion states. Model C, D, and E decreased by 0.39%–22.06%, 13.78%–50.68%, and 13.86%–51.78%, respectively. The displacement difference

**FIGURE 6**

The maximum von Mises stress of discs in five finite element models under six motion states. (A) The maximum von Mises stress of L4/L5 IVD in the five models. (B) The maximum von Mises stress of L5/S1 IVD in the five models.

between model C and model B is mainly reflected in the axial rotation state, while the displacement difference between Model D and E is significant, except for the axial rotation state on the right side. In addition, the displacement values of Model D and E were not significantly different from those of Model A, except in the flexion state.

Regarding the pars interarticularis (Supplementary Figure S2), the maximum displacement values of Model B and C under the six motion states were all close. Simultaneously, Model D and E under six motion states is significantly different from that of Model B and C. The maximum isthmus displacement of Model D was 22.47% lower than that of Model E in the flexion state, but there was no significant difference between the two models in the other five motion states (extension, lateral bending, axial rotation).

Maximum von Mises stress of the intervertebral disc

The disc stress analysis of the five models showed that the anterior and posterior edges of the disc were concentrated under flexion and posterior extension condition, respectively. In both left and right axial rotation conditions, the stress is concentrated in the anterior and lateral disc. In the left and right lateral bending, the stress distribution is concentrated in the left and right margins of the disc. The maximum stress values of L4/5 and L5/S1 intervertebral discs under different motion states in our five models were compared. As depicted in Figure 6, no significant difference was found between the maximum von Mises stress of L4/5 intervertebral discs (adjacent intervertebral discs) in Model A, B, C, D, and E under the six

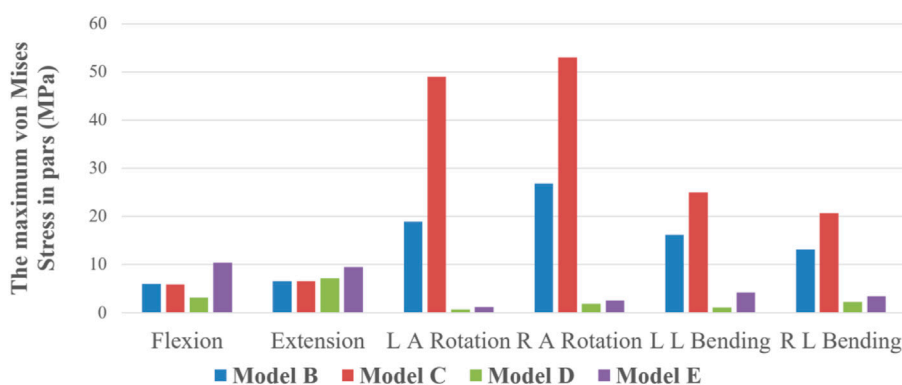


FIGURE 7

The maximum von Mises Stress on pars interarticularis of Model B, C, D, and E under six states of motion.

motion states. In addition to flexion and RAR, the maximum stress on L5/S1 disc was significantly different among the five models. The stress on L5/S1 disc in Model A, B, and C was observably higher than that in Model D and E under extension and lateral bending conditions. Under the LAR, the stress on L5/S1 disc in Model D and E was slightly higher than that in Model A, B, and C. The maximum stress values of Model A, B, and C in the six motion states are as follows: Model B > Model A > Model C. However, the maximum stress values of Model D and E showed no significant difference under any motion state.

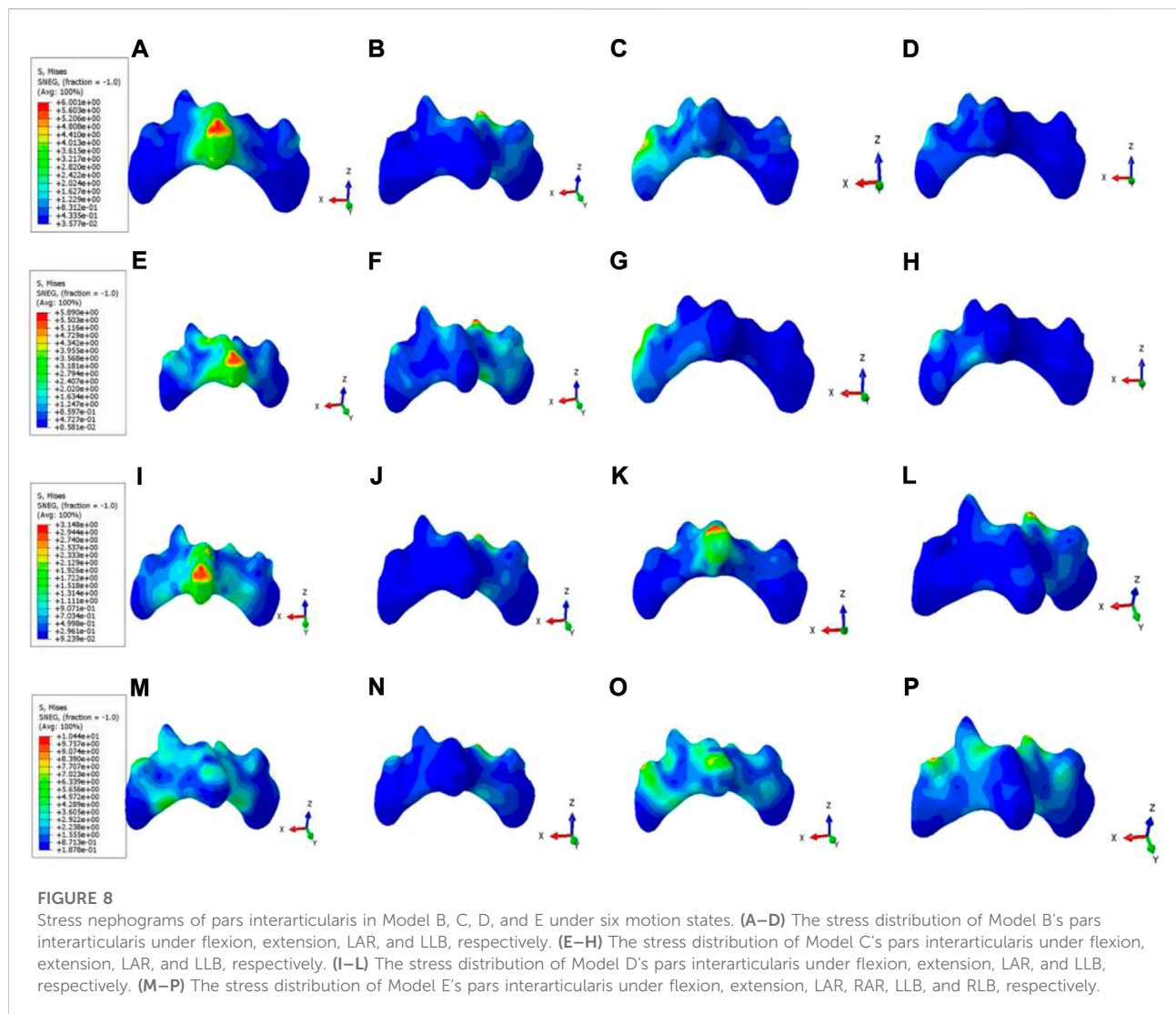
Maximum stress value and stress distribution of pars interarticularis

Model B and C: In the flexion condition, the pars interarticularis stress is concentrated above the spinous process. In the extension and left and right axial rotation conditions, the stress is mainly concentrated on the broken end of the isthmus and below the isthmus. In the left lateral bending and right lateral bending condition, the stress is concentrated on the left and right isthmus fracture end, respectively. **Model D:** In the flexion condition, the stress is mainly distributed around the spinous process. In the posterior extension, right axial rotation and left and right lateral bending condition, the stress is concentrated on the broken end of the isthmus. **Model E:** In six different motion states, large stress distribution and no obvious concentration trend. As demonstrated in Figure 7, this difference is negligible in the maximum von Mises stress at the pars interarticularis of Model B, C, D, and E under flexion and extension. However, the maximum von Mises stress sustained by the pars interarticularis in Model B and C was much greater than that in Model D and E under axial rotation and lateral bending conditions. Among them, the maximum von Mises stress in the

pars interarticularis of Model C was much greater than that of Model B under axial rotation. Combined with stress nephograms analysis (Figure 8), it can be found that the lateral area of the pars interarticularis of Model B and C were subjected to maximum stress under RAR state, which was 26.87 and 52.98 MPa, respectively. Under the left and right lateral flexion states, the stress of Model B and C was mainly concentrated at the broken end of the isthmus. In addition, compared with Model D, the stress distribution of Model E is more dispersed under the six motion states.

Maximum stress and stress distribution of internal fixation systems

Model C: In six different motion states, stress of internal fixation occurred at the junction of the left Buck screw and the isthmus defect. **Model D:** In the flexion and extension condition, the stress mainly focused on the junction of the pedicle screw and the connecting rod. In the left axial rotation and right lateral bending condition, the stress is concentrated at the junction of the right pedicle screw and the connecting rod. In the right axial rotation and left lateral bending condition, the stress is concentrated at the junction of the left pedicle screw and the connecting rod. **Model E:** During the flexion condition, the stress distribution at the junction of the Buck screw to the isthmus defect and between the pedicle screw and the connecting rod. In the extension condition, the stress is distributed between the pedicle screw and the connecting rod. In the left axial rotation and right lateral bending condition, the stress is concentrated at the junction of the right pedicle screw and the connecting rod. In the right axial rotation and left lateral bending condition, the stress is concentrated at the junction of the left pedicle screw and the connecting rod. As revealed in Figure 9, the maximum von Mises stress of internal fixation in model C was significantly



higher than that in Model D and E, except for flexion and extension, and most of the stress was concentrated at the junction of the isthmus defect and screw. Among these, the maximum stress was 2701 MPa, which occurred at the junction between the left Buck screw and the isthmus defect under the RAR state. However, the maximum stress values of Model D and E had no significant difference in the other five motion states except for the flexion state, and the stress distribution was slightly different (Figure 10). Compared with Model D, the stress in Model E was distributed in two internal fixation systems of the Buck screw and pedicle screw under flexion and extension, and the stress area was relatively dispersed. Simultaneously, compared with Model C, the stress distribution of Model E under axial rotation and lateral flexion motion mainly focused on the junction between the pedicle screw and the connecting rod, which greatly reduced the shear force of the isthmus fracture end on the Buck screw.

Discussion

Based on the underlying pathological mechanism of lumbar spondylolysis and previous literature reports, the key to surgical repair is to fully remove the scar tissue at the broken end of the isthmus and fill it with bone graft, complemented with strong internal fixation, and restore the continuity and integrity of the bone while ensuring the relative stability of the pars interarticularis (Wiltse and Jackson, 1975; Cheung et al., 2006; Mohammed et al., 2018). Therefore, the choice of internal fixation has become the focus of debate among scholars. At present, the mainstream isthmus repair operation is mainly divided into two categories: direct intrasegmental repair, represented by the Buck technique, and indirect intersegmental repair, represented by the pedicle screw technique. According to direct repair, direct compression and fixation of the broken end of the isthmus within the segment can

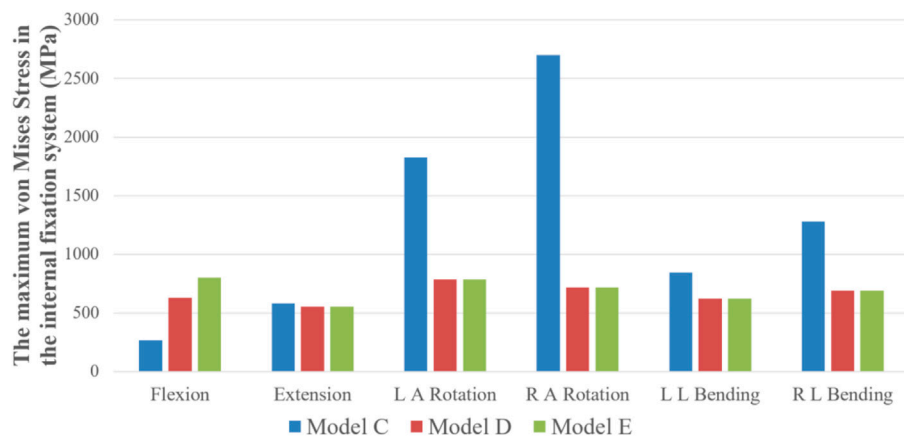


FIGURE 9

The maximum von Mises stress on the internal fixation system of Model C, D, and E under six states of motion.

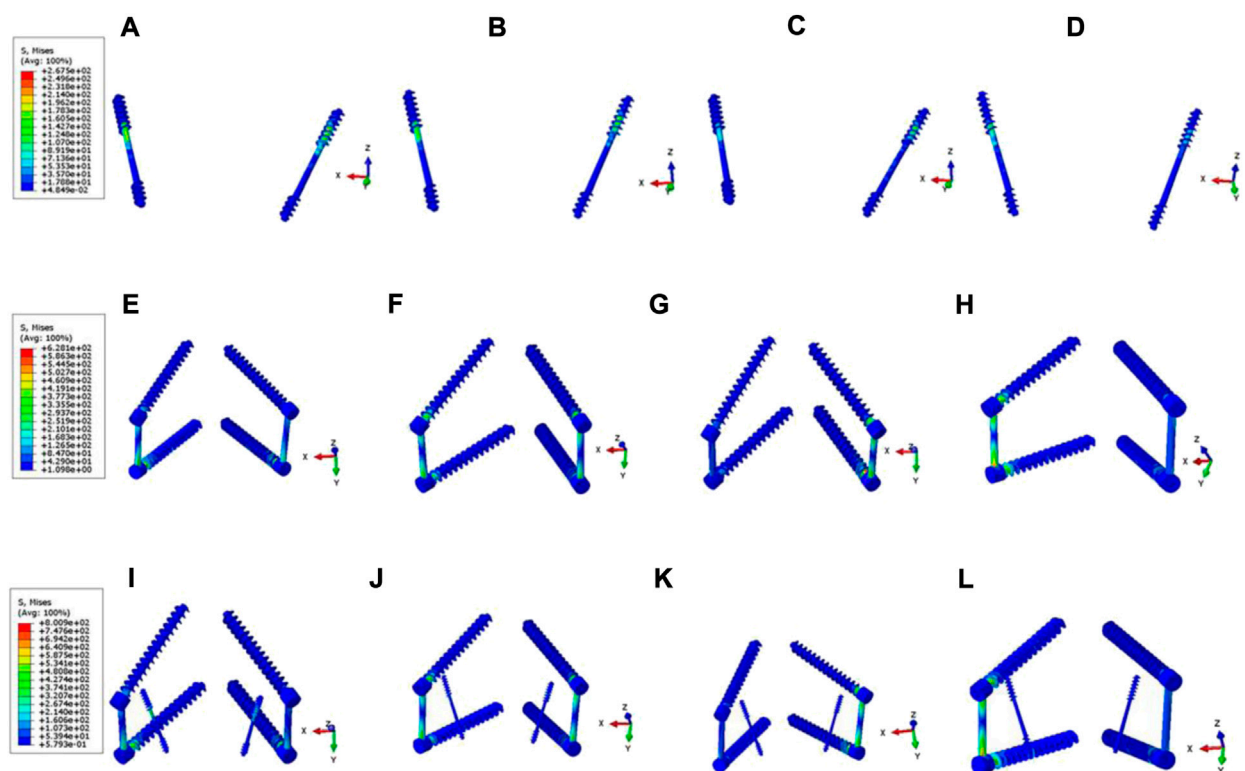


FIGURE 10

Stress nephograms of internal fixation system in Model C, D, and E under six motion states. (A–D) The stress distribution of Model C's internal fixation system under flexion, extension, LAR, and LLB, respectively. (E–H) The stress distribution of Model D's internal fixation system under flexion, extension, LAR, RAR, LLB, and RLB, respectively. (I–L) The stress distribution of Model E's internal fixation system under flexion, extension, LAR, RAR, LLB, and RLB, respectively.

reduce the trauma and preserve the original motion segment (Mohammed et al., 2018). Meanwhile, the concept of indirect repair suggests that intersegmental fixation can limit the ROM of responsible segments in the initial stage of isthmus bone grafting repair, ensure relative stability, and eliminate part of the stress from the lumbosacral region, creating a suitable biomechanical condition for bone fusion in the isthmus (Sterba et al., 2018).

Several researchers have previously analyzed the advantages and disadvantages of various internal fixation methods for the biomechanical evaluation of isthmus repair using computer simulation and finite element algorithm. For example, using the finite element method, Sairyo et al. examined the impact of Buck direct repair on disc stress (Sairyo et al., 2006b). Li et al. conducted a three-dimensional finite element analysis to compare the biomechanical effects of the pedicle screw U-rod internal fixation system and the pedicle screw lamina hook internal fixation system in the treatment of lumbar spondylolysis (Li et al., 2022a). These studies were based on a vertical comparison of the therapeutic effects of different types of internal fixation in intrasegmental repair. This study compared the biomechanical properties of direct intrasegmental and indirect intersegmental repair based on Buck screw fixation and pedicle screw fixation systems. In addition, we designed a new surgical strategy for comparison, aiming to explore whether the hybrid procedure can combine the advantages of the two mainstream procedures while making up for the shortcomings of a single procedure.

This study set up five kind of three-dimensional finite element model based on CT images. First, we use the Model A and Model B between intact model and spondylolysis model to compare the biomechanical differences we compared with Model A, the ROM and maximum displacement of Model B increased under six motion states, especially under extension and axial rotation states. This also suggests that lumbar spondylolysis can lead to decreased spine stability, and long-term instability can lead to vertebral spondylolisthesis. Moreover, combined with the results of intervertebral disc stress analysis, it can be concluded that changes in activity can lead to the biomechanical imbalance of relevant segments, instantaneous rotation center deviation, increased intervertebral disc tissue stress, and risk of degeneration (Sairyo et al., 2006c; Haj-Ali et al., 2019). Compared with Model B, the ROM and maximum displacement of Model C, D, and E decreased due to the addition of an internal fixation device. Among them, Model D and E have smaller ROM and displacement values than Model C, proving that intersegmental fixation can provide better stability in the early postoperative period than intrasegmental fixation. Furthermore, the pedicle screw system can effectively share the stress of the intervertebral disc in a state of spondylolysis due to the supporting role between the segments.

To further compare the stress of the L5 pars interarticularis in different models, we analyzed the maximum displacement and stress nephograms. The results demonstrated that compared with

Model B and C, Model D and E with the pedicle screw system for intersegmental fixation significantly reduced the absolute displacement of the pars interarticularis. The results of the stress nephograms depicted that the stress on the pars interarticularis of model C was substantially higher than that of Model B under axial rotation and lateral bending, which might be attributed to the extra binding force of the Buck screw on the pars interarticularis under these conditions. Meanwhile, due to the limitation of intersegmental fixation on the activity of corresponding segments, the maximum displacement and stress of the L5 isthmus in Model D and E were not significantly different. However, due to the existence of multiple internal fixations, the stress distribution on the isthmus defect in Model E was more dispersed than in Model D. This dispersed stress may indicate that there is less shear force in the isthmus of Model E, which is more conducive to the formation of fibrous callus in the early postoperative stage and the shaping of callus in the later stage (Ishida et al., 2018).

On the other hand, the failure risk of loosening and fracture of postoperative internal fixation depends on the magnitude and distribution of stress (Giudici et al., 2011). The stress nephograms demonstrated that the maximum stress magnitude of three internal fixation models under six motion states appeared in the axial rotation state of Model C, which was 2701 mPa. Based on the analysis of the stress distribution of Model A and B, we believe that the vertebral body exerts strong shear force on the broken end of the isthmus and the directly fixed internal fixation device under the axial rotating state due to bone discontinuity in the isthmus region of the vertebral body. This is also consistent with the results of the isthmus stress distribution. Due to the lack of restriction of intersegmental fixation on relative movement (e.g., axial rotation and lateral bending) between vertebral bodies, the isthmus region under direct intrasegmental fixation is subjected to high shear stress. As the Buck technique was based on a screw that fixed the bone at both ends of the isthmus with a single axis and the lack of an effective connection between the two screws, it reduced the limitation of the relative motion of axial rotation and lateral bending between the vertebral bodies (Fan et al., 2010). Subsequently, such low stability may not be conducive to the osseous fusion between the broken ends of the isthmus, and even internal fixation loosening and fracture may occur, resulting in internal fixation failure and surgical failure (Giudici et al., 2011; Tsai et al., 2022). Therefore, compared with direct intrasegmental fixation, indirect intersegmental fixation can provide greater stability and bear less stress. In addition, by comprehensively analyzing the stress cloud of the isthmus and internal fixations, we believe that the mixed fixation method can present a more dispersed stress distribution than the simple intersegmental fixation method. To sum up, we believe that at the early stage after isthmus repair, indirect intersegmental fixation can provide higher stability and smaller shear force at the broken end than direct intrasegmental fixation. In contrast, hybrid fixation can

create a more dispersed stress distribution based on simple intersegmental fixation, reducing the risk of internal fixation failure.

In addition, although intersegmental fixation can provide higher initial stability than intrasegmental fixation, the cost of such stability is the long-term loss of partial movement of moving segments after surgery, resulting in reduced lumbosacral flexibility (Li et al., 2022b). This loss in activity may result in lower quality of life and postoperative satisfaction in young patients. Combined with previous reports, we believe that Buck technology combined with short-term intersegmental pedicle screw fixation can ensure the initial osseous fusion of the isthmus. At the same time, the intersegmental fixation device can be removed surgically as early as possible. ROM of the lumbosacral region can be restored through early functional exercise (Meng et al., 2022). Certainly, the hybrid fixation is recently proposed as a new technology combining intrasegmental fixation and intersegment fixation technology, and the material application cost is slightly higher compared with the other two technologies. Fortunately, the initial clinical applications showed that the costs were all within the expected range.

This study compared the biomechanical effects of three kinds of operation based on computer modeling and finite element analysis. First of all, we have to admit the limitations of finite element research, such as: the computer simulated disc constructed by the final version of the fiber ring, upper and lower cartilage is somewhat different from the disc in the real state. For model validation, an indirect verification method is used, which may need to be combined with cadaver specimens for biomechanical at a stage. In addition, this study only compared the advantages and disadvantages of the three surgical methods through computer simulation, which provided a theoretical basis for clinical treatment; however, it lacked practical research. Whether indirect intersegmental fixation is more effective than direct intrasegmental fixation in correcting sagittal balance in patients with lumbar spondylolysis needs to be confirmed by collecting clinical cases and measuring sagittal parameters (Roussouly et al., 2006; Vialle et al., 2007). Meanwhile, postoperative isthmus repair is a long-term dynamic process, and the biomechanical assessment in this study is only based on a 3D model. Hence it lacks credibility in the time dimension (Sakamaki and Sairyo, 1976; Sterba et al., 2018). In conclusion, the degree of intervertebral disc degeneration and the recovery of sagittal balance are objective evaluation criteria after isthmus repair. In contrast, the subjective feelings, such as the degree of pain relief and the improvement in function, need to be analyzed through further clinical studies.

Conclusion

This study compared three lumbar spondylolysis repair methods based on finite element analysis from a

biomechanical perspective. The results demonstrated that although the direct intrasegmental fixation based on the Buck technique could retain the original ROM of the lumbosacral region to a large extent, the relative stability was poor, and the intervertebral disc, isthmus region, and internal fixator had to bear large and relatively concentrated stress under axial rotation and lateral bending. Indirect intersegmental fixation based on pedicle screw technology can provide some initial stability, but stress can become excessively concentrated on the screw and rod joints. The hybrid fixation technique can effectively disperse the stress distribution of the intervertebral disc, isthmus region, and internal fixator under various motion states while ensuring initial phase stability. In conclusion, we believe that hybrid fixation can effectively reduce the risk of internal fixation failure and disc degeneration and provide early stability for bone fusion. Simultaneously, to avoid the loss of lumbosacral flexibility due to intersegmental fixation, we recommend using “temporary” fixation to provide individualized surgical strategies for young patients with lumbar spondylolysis.

Data availability statement

The original contributions presented in the study are included in the article/Supplementary Material, further inquiries can be directed to the corresponding author.

Ethics statement

All experimental protocols were approved by the Independent Ethics Committee of Bengbu Medical College (2021289), and the subjects gave informed consent to this work. Written informed consent was obtained from the individual(s) for the publication of any potentially identifiable images or data included in this article.

Author contributions

YY and SJ contributed equally to the work. CZ contributed to the conception and design. YZ, YF, PX, and ZZ are responsible for the provision of the study materials and data collection. PX, ZZ, and NW contributed to the data analysis and interpretation. YY and SJ contributed to the manuscript writing. All authors read and approved the final manuscript.

Funding

This work was supported by the Natural Science Foundation of Anhui Province (1908085MC90), Natural Science Key Project

of Bengbu Medical College (2021byzd082), Natural Science Key Project of Bengbu Medical College (2021byzd171) and Graduate Innovation Program of Bengbu Medical College (Byycx21086).

Acknowledgments

Thanks for the cooperation of all the patients.

Conflict of interest

The authors declare that the research was conducted in the absence of any commercial or financial relationships that could be construed as a potential conflict of interest.

References

- Baca, V., and Horak, Z. (2007). Comparison of isotropic and orthotropic material property assignments on femoral finite element models under two loading conditions. *Med. Eng. Phys.* 29 (8), 935. doi:10.1016/j.medengphys.2006.10.002
- Berger, R. G., and Doyle, S. M. (2019). Spondylolysis 2019 update. *Curr. Opin. Pediatr.* 31 (1), 61–68. doi:10.1097/mop.0000000000000706
- Benjano, P., Ristori, G., Ismael Aguirre, M. F., Langella, F., Damilano, M., Cecchinato, R., et al. (2020). A novel technique for spondylolysis repair with pedicle screws, rod and polyester band: Case report with technical note and systematic literature review. *Spine* 45 (24), E1682–e1691. doi:10.1097/brs.00000000000003697
- Bouras, T., and Koroivessis, P. (2015). Management of spondylolysis and low-grade spondylolisthesis in fine athletes. A comprehensive review. *Eur. J. Orthop. Surg. Traumatol.* 25 (1), S167–S175. doi:10.1007/s00590-014-1560-7
- Campbell, J. Q., Coombs, D. J., Rao, M., Rullkoetter, P. J., and Petrella, A. J. (2016). Automated finite element meshing of the lumbar spine: Verification and validation with 18 specimen-specific models. *J. Biomech.* 49 (13), 2669–2676. doi:10.1016/j.jbiomech.2016.05.025
- Cheung, E. V. H. M., Cavalier, R., and Pizzutillo, P. D. (2006). Spondylolysis and spondylolisthesis in children and adolescents II. Surgical management. *J. Am. Acad. Orthop. Surg.* 14 (8), 488–498. doi:10.5435/00124635-200608000-00006
- Chosa, E., Totoribe, K., and Tajima, N. (2004). A biomechanical study of lumbar spondylolysis based on a three-dimensional finite element method. *J. Orthop. Res.* 22 (1), 158–163. doi:10.1016/s0736-0266(03)00160-8
- Dreischarf, M., Zander, T., Shirazi-Adl, A., Puttlitz, C., Adam, C., Chen, C., et al. (2014). Comparison of eight published static finite element models of the intact lumbar spine: Predictive power of models improves when combined together. *J. Biomech.* 47 (8), 1757–1766. doi:10.1016/j.jbiomech.2014.04.002
- El-Rich, M. A. C., Villemure, I., and Labelle, H. (2006). A biomechanical study of L5-S1 low-grade isthmic spondylolisthesis using a personalized finite element model. *Stud. Health Technol. Inf.* 123, 431–434.
- Elmasry, S. S., Asfour, S. S., and Travascio, F. (2018). Finite element study to evaluate the biomechanical performance of the spine after augmenting percutaneous pedicle screw fixation with kyphoplasty in the treatment of burst fractures. *J. Biomech. Eng.* 140 (6). doi:10.1115/1.4039174
- Faizan, A. K. A., Kiapour, A. M., and Goel, V. K. (2014). Biomechanical analysis of various footprints of transforaminal lumbar interbody fusion devices. *J. Spinal Disord. Tech.* 27 (4), E118–E127. doi:10.1097/bsd.0b013e3182a11478
- Fan, J., Yu, G. R., Liu, F., Zhao, J., and Zhao, W. D. (2010). Direct repair of spondylolysis by TSRH's hook plus screw fixation and bone grafting: Biomechanical study and clinical report. *Arch. Orthop. Trauma Surg.* 130 (2), 209–215. doi:10.1007/s00402-009-0897-6
- Gagnet, P., Kern, K., Andrews, K., Elgafy, H., and Ebraheim, N. (2018). Spondylolysis and spondylolisthesis: A review of the literature. *J. Orthop.* 15 (2), 404–407. doi:10.1016/j.jor.2018.03.008
- Giudici, F., Minoia, L., Archetti, M., Corriero, A. S., and Zagra, A. (2011). Long-term results of the direct repair of spondylolisthesis. *Eur. Spine J.* 20 (1), S115–S120. doi:10.1007/s00586-011-1759-9
- Goetzinger, S., Courtney, S., Yee, K., Welz, M., Kalani, M., and Neal, M. (2020). Spondylolysis in young athletes: An overview emphasizing nonoperative management. *J. Sports Med.* 2020, 9235958. (Hindawi Publ Corp). doi:10.1155/2020/9235958
- Haj-Ali, R., Wolfson, R., and Masharawi, Y. (2019). A patient specific computational biomechanical model for the entire lumbosacral spinal unit with imposed spondylolysis. *Clin. Biomech. (Bristol, Avon)* 68, 37–44. doi:10.1016/j.clinbiomech.2019.05.022
- Huang, Y., Liu, J., Guo, L., Meng, Y., Hao, D., and Du, J. (2019). Temporary short segment fixation in treating adolescent lumbar spondylolysis. *World Neurosurg.* 123, e77–e84. doi:10.1016/j.wneu.2018.11.046
- Ishida, K., Aota, Y., Mitsugi, N., Kuniya, T., Morii, T., Kawai, T., et al. (2018). Spondylolysis repair using a pedicle screw hook or claw-hook system. -a comparison of bone fusion rates. *Spine Surg. Relat. Res.* 2 (2), 135–139. doi:10.22603/ssrr.2017-0011
- JE, B. (1970). Direct repair of the defect in spondylolisthesis. Preliminary report. *J. Bone Jt. Surg. Br. volume* 52 (3), 432–437. doi:10.1302/0301-620x.52b3.432
- Kumar, N., Madhu, S., Pandita, N., Ramos, M. R., Tan, B. W., Lopez, K. G., et al. (2021). Is there a place for surgical repair in adults with spondylolysis or grade-I spondylolisthesis-a systematic review and treatment algorithm. *Spine J.* 21 (8), 1268–1285. doi:10.1016/j.spinee.2021.03.011
- Leone, A., Cianfoni, A., Cerase, A., Magarelli, N., and Bonomo, L. (2011). Lumbar spondylolysis: A review. *Skelet. Radiol.* 40 (6), 683–700. doi:10.1007/s00256-010-0942-0
- Li, L., Jiang, S., Zhao, J., Zhao, M., Zhou, X., Li, K., et al. (2022). Comparison of two internal fixation systems in lumbar spondylolysis by finite element methods. *Comput. methods programs Biomed.* 218, 106713. doi:10.1016/j.cmpb.2022.106713
- Li, Y., Li, H., Chang, X., Hu, Z., Mu, X., Liu, C., et al. (2022). Retrospective comparative study of pedicle screw fixation via quadrant retractor and Buck's technique in the treatment of adolescent spondylolysis. *Orthop. Surg.* 14 (1), 111–118. doi:10.1111/os.13165
- Matsukawa, K., Yato, Y., Imabayashi, H., Hosogane, N., Asazuma, T., and Chiba, K. (2016). Biomechanical evaluation of lumbar pedicle screws in spondylolytic vertebrae: Comparison of fixation strength between the traditional trajectory and a cortical bone trajectory. *J. Neurosurg. Spine* 24 (6), 910–915. doi:10.3171/2015.11.spine15926
- Meng, H., Gao, Y., Lu, P., Zhao, G. M., Zhang, Z. C., Sun, T. S., et al. (2022). Risk factor analysis of disc and facet joint degeneration after intersegmental pedicle screw fixation for lumbar spondylolysis. *J. Orthop. Surg. Res.* 17 (1), 247. doi:10.1186/s13018-022-03082-9
- Mohammed, N., Patra, D. P., Narayan, V., Savardekar, A. R., Dossani, R. H., Bollam, P., et al. (2018). A comparison of the techniques of direct pars interarticularis repairs for spondylolysis and low-grade spondylolisthesis: A meta-analysis. *Neurosurg. focus* 44 (1), E10. doi:10.3171/2017.11.focus17581
- Ramakrishna, V. A. S., Chamoli, U., Viglione, L. L., Tsafnat, N., and Diwan, A. D. (2017). The role of sacral slope in the progression of a bilateral spondylolytic defect

Publisher's note

All claims expressed in this article are solely those of the authors and do not necessarily represent those of their affiliated organizations, or those of the publisher, the editors and the reviewers. Any product that may be evaluated in this article, or claim that may be made by its manufacturer, is not guaranteed or endorsed by the publisher.

Supplementary material

The Supplementary Material for this article can be found online at: <https://www.frontiersin.org/articles/10.3389/fbioe.2022.1024159/full#supplementary-material>

at L5 to spondylolisthesis: A biomechanical investigation using finite element analysis. *Glob. Spine J.* 8 (5), 460–470. doi:10.1177/2192568217735802

Roussouly, P. G. S., Berthonnaud, E., Labelle, H., and Weidenbaum, M. (2006). Sagittal alignment of the spine and pelvis in the presence of L5-s1 isthmic lysis and low-grade spondylolisthesis. *Spine (Phila Pa 1976)* 31 (2), 2484–2490. doi:10.1097/01.brs.0000239155.37261.69

Sairyo, K., Goel, V. K., Faizan, A., Vadapalli, S., Biyani, S., and Ebraheim, N. (2006). Buck's direct repair of lumbar spondylolysis restores disc stresses at the involved and adjacent levels. *Clin. Biomech. (Bristol, Avon)* 21 (10), 1020–1026. doi:10.1016/j.clinbiomech.2006.06.011

Sairyo, K., Goel, V. K., Masuda, A., Vishnubhotla, S., Faizan, A., Biyani, A., et al. (2006). Three dimensional finite element analysis of the pediatric lumbar spine. Part II: Biomechanical change as the initiating factor for pediatric isthmic spondylolisthesis at the growth plate. *Eur. Spine J.* 15 (6), 930–935. doi:10.1007/s00586-005-1033-0

Sairyo, K., Goel, V. K., Masuda, A., Vishnubhotla, S., Faizan, A., Biyani, A., et al. (2006). Three-dimensional finite element analysis of the pediatric lumbar spine. Part I: Pathomechanism of apophyseal bony ring fracture. *Eur. Spine J.* 15 (6), 923–929. doi:10.1007/s00586-005-1026-z

Sairyo, K., Katoh, S., Sasa, T., Yasui, N., Goel, V. K., Vadapalli, S., et al. (2005). Athletes with unilateral spondylolysis are at risk of stress fracture at the contralateral pedicle and pars interarticularis: A clinical and biomechanical study. *Am. J. Sports Med.* 33 (4), 583–590. doi:10.1177/0363546504269035

Sakamaki, T. K. S., and Sairyo, K. (1976). Normal and spondylolytic pediatric spine movements with reference to instantaneous axis of rotation. *Spine* 27 (2), 141–145. doi:10.1097/00007632-200201150-00004

Snyder, L. A. S. H., O'Brien, M. F., Thind, H., Theodore, N., and Kakarla, U. K. (2014). Spondylolysis outcomes in adolescents after direct screw repair of the pars interarticularis. *J. Neurosurg. Spine* 21 (3), 329–333. doi:10.3171/2014.5.spine13772

Song, C., Chang, H., Zhang, D., Zhang, Y., Shi, M., and Meng, X. (2021). Biomechanical evaluation of oblique lumbar interbody fusion with various fixation options: A finite element analysis. *Orthop. Surg.* 13 (2), 517–529. doi:10.1111/os.12877

Sterba, M., Arnoux, P. J., Labelle, H., Warner, W. C., and Aubin, C. E. (2018). Biomechanical analysis of spino-pelvic postural configurations in spondylolysis

subjected to various sport-related dynamic loading conditions. *Eur. Spine J.* 27 (8), 2044–2052. doi:10.1007/s00586-018-5667-0

Tarpada, S. P. K. D., Levine, N. L., Morris, M. T., and Cho, W. (2021). Comparing surgical treatments for spondylolysis: Review on current research. *Clin. Spine Surg. A Spine Publ.* 34 (8), 276–285. doi:10.1097/bsd.0000000000001115

Terai, T. S. K., Goel, V. K., Ebraheim, N., Biyani, A., Faizan, A., Sakai, T., et al. (2010). Spondylolysis originates in the ventral aspect of the pars interarticularis: A clinical and biomechanical study. *J. Bone Jt. Surg. Br. volume* 92 (8), 1123–1127. doi:10.1302/0301-620x.92b8.22883

Tsai, S. H. L. C. C., Chen, W. C., Lin, T. Y., Wang, Y. C., Wong, C. B., Yolcu, Y. U., et al. (2022). Does direct surgical repair benefit pars interarticularis fracture? A systematic review and meta-analysis. *Pain Physician* 25 (3), 265–282.

Vialle, R., Ilharreborde, B., Dauzac, C., Lenoir, T., Rillardon, L., and Guigui, P. (2007). Is there a sagittal imbalance of the spine in isthmic spondylolisthesis? A correlation study. *Eur. spine J.* 16 (10), 1641–1649. doi:10.1007/s00586-007-0348-4

Wan, S. Y., and Higgins, W. E. (2003). Symmetric region growing. *IEEE Trans. Image Process.* 12 (9), 1007–1015. doi:10.1109/tip.2003.815258

Wang, J. P. Z. Z., Cheng, C. K., Chen, C. S., Yu, C. h., Chang, T. K., Wei, S. W., et al. (2006). Finite element analysis of the spondylolysis in lumbar spine. *Biomed. Mat. Eng.* 16 (5), 301–308.

Wiltse, L. L. W. E. J., and Jackson, D. W. (1975). Fatigue fracture: The basic lesion in isthmic spondylolisthesis. *J. Bone Jt. Surg. Am.* 57 (1), 17–22.

Yamamoto, I. P. M., Crisco, T., and Oxland, T. (1989). Three-dimensional movements of the whole lumbar spine and lumbosacral joint. *Spine* 1976 14 (11), 1256–1260. doi:10.1097/00007632-198911000-00020

Yamamoto, T., Iinuma, N., Miyamoto, K., Sugiyama, S., Nozawa, S., Hosoe, H., et al. (2008). Segmental wire fixation for lumbar spondylolysis associated with spina bifida occulta. *Arch. Orthop. Trauma Surg.* 128 (10), 1177–1182. doi:10.1007/s00402-007-0521-6

Zhang, Z. C., Zhang, Y., Zhang, L. Z., Guan, K., Zhao, G. M., Ren, D. J., et al. (2021). Repair of symptomatic bilateral L5 spondylolysis with autogenous iliac crest graft and temporary intersegmental pedicle screw fixation in youth. *J. Orthop. Surg. Res.* 16 (1), 422. doi:10.1186/s13018-021-02534-y



OPEN ACCESS

EDITED BY

Suvash C. Saha,
University of Technology Sydney,
Australia

REVIEWED BY

Gregory S. Sawicki,
Georgia Institute of Technology,
United States
Silvia Muceli,
Chalmers University of Technology,
Sweden

*CORRESPONDENCE

Hugh M. Herr,
hherr@media.mit.edu

[†]These authors share first authorship

SPECIALTY SECTION

This article was submitted to
Biomechanics,
a section of the journal
Frontiers in Bioengineering and
Biotechnology

RECEIVED 02 August 2022

ACCEPTED 05 October 2022

PUBLISHED 25 October 2022

CITATION

Taylor CR, Clark WH, Clarrissimeaux EG,
Yeon SH, Carty MJ, Lipsitz SR,
Bronson RT, Roberts TJ and Herr HM
(2022), Clinical viability of magnetic
bead implants in muscle.
Front. Bioeng. Biotechnol. 10:1010276.
doi: 10.3389/fbioe.2022.1010276

COPYRIGHT

© 2022 Taylor, Clark, Clarrissimeaux,
Yeon, Carty, Lipsitz, Bronson, Roberts
and Herr. This is an open-access article
distributed under the terms of the
[Creative Commons Attribution License](#)
(CC BY). The use, distribution or
reproduction in other forums is
permitted, provided the original
author(s) and the copyright owner(s) are
credited and that the original
publication in this journal is cited, in
accordance with accepted academic
practice. No use, distribution or
reproduction is permitted which does
not comply with these terms.

Clinical viability of magnetic bead implants in muscle

Cameron R. Taylor^{1†}, William H. Clark^{2†}, Ellen G. Clarrissimeaux¹,
Seong Ho Yeon¹, Matthew J. Carty^{1,3}, Stuart R. Lipsitz³,
Roderick T. Bronson³, Thomas J. Roberts² and Hugh M. Herr^{1,3*}

¹K. Lisa Yang Center for Bionics, Massachusetts Institute of Technology, Cambridge, MA, United States,

²Department of Ecology, Evolution, and Organismal Biology, Brown University, Providence, RI,

United States, ³Harvard Medical School, Boston, MA, United States

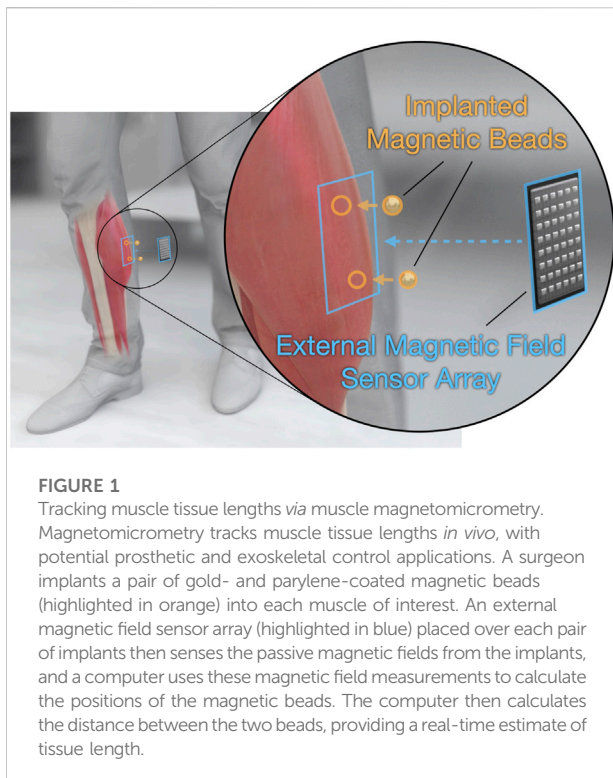
Human movement is accomplished through muscle contraction, yet there does not exist a portable system capable of monitoring muscle length changes in real time. To address this limitation, we previously introduced magnetomicrometry, a minimally-invasive tracking technique comprising two implanted magnetic beads in muscle and a magnetic field sensor array positioned on the body's surface adjacent the implanted beads. The implant system comprises a pair of spherical magnetic beads, each with a first coating of nickel-copper-nickel and an outer coating of Parylene C. In parallel work, we demonstrate submillimeter accuracy of magnetic bead tracking for muscle contractions in an untethered freely-roaming avian model. Here, we address the clinical viability of magnetomicrometry. Using a specialized device to insert magnetic beads into muscle in avian and lagomorph models, we collect data to assess gait metrics, bead migration, and bead biocompatibility. For these animal models, we find no gait differences post-versus pre-implantation, and bead migration towards one another within muscle does not occur for initial bead separation distances greater than 3 cm. Further, using extensive biocompatibility testing, the implants are shown to be non-irritant, non-cytotoxic, non-allergenic, and non-irritating. Our cumulative results lend support for the viability of these magnetic bead implants for implantation in human muscle. We thus anticipate their imminent use in human-machine interfaces, such as in control of prostheses and exoskeletons and in closed-loop neuroprosthetics to aid recovery from neurological disorders.

KEYWORDS

human-machine interfaces, implantable technology, biocompatibility, muscle tracking, wearable technology, magnetomicrometry, bionics, prosthetic control

1 Introduction

The field of human bionics seeks to advance methods for the high-fidelity control of wearable robots to restore and augment human physicality. Delivering on this objective requires new interfacing strategies for determining intent. Today's standard interface for extrinsic control of wearable robots is surface electromyography (sEMG). This technique senses myoelectric signals *via* a skin surface electrode, but suffers from signal noise and



drift caused by motion artifacts and impedance variations (Clancy et al., 2002; Calado et al., 2019). While significant advances have been made in robotic control *via* sEMG (Farina et al., 2017), even myoelectric signals measured using invasive strategies (Weir et al., 2008) cannot fully communicate intended muscle forces or joint movements without also incorporating measurements of muscle length and speed (Zajac 1989). Recent work has suggested the use of ultrasound combined with sEMG to improve upon robotic position control (Zhang et al., 2021; Rabe and Fey 2022). However, a real-time sensing technology has not yet been developed that can directly and reliably measure muscle length and speed in humans.

To address this need, we recently developed a strategy for tracking muscle tissue lengths. This technique, known as magnetomicrometry (MM), uses implanted pairs of magnetic beads to wirelessly track muscle tissue lengths in real time (see Figure 1) (Taylor et al., 2021). In parallel work, we further validate the performance of MM in mobile usage (Taylor, et al., 2022a), lending additional support to its utility for prosthetic and exoskeletal control. Due to its very low time delay, high accuracy, and minimally invasive nature (Taylor et al., 2019), MM has the potential to provide an improved extrinsic controllability over wearable robots.

Towards translating MM for human use, we here develop an improved coating strategy for 3-mm-diameter spherical magnetic bead implants and a translatable surgical protocol

for implantation. With this new strategy, we apply a first coat of gold and a top coat of Parylene to the magnetic beads, following stringent medical device standards for coating, cleaning, and sterilization. We then address three features that are essential for the clinical use of magnetic bead implants: 1) lack of implant discomfort 2) lack of implant migration, and 3) implant biocompatibility.

1.1 Comfort

These implants are intended for permanent implantation like the tantalum beads used in radiostereographic analysis (RSA). Since the standardization of RSA in 1974 (Selvik 1974), tens of thousands of spherical tantalum beads have been implanted into patients with no adverse reactions (Kärrholm 1989), including into muscle tissues (Clites et al., 2018). However, though the magnetic beads we present here are spherical like those used for RSA, they have a diameter three times larger than RSA beads, necessitating an analysis of implant comfort.

Changes in movement patterns have been routinely analyzed to capture the secondary musculoskeletal effects of discomfort or pain, commonly referred to as antalgic gait (Vincent et al., 2013; Nonnekes et al., 2020; Auerbach and Tadi 2021). Following this previous literature, this work analyzes changes in the percentage of stance phase relative to swing phase in an animal model as a measure of comfort after implantation of these magnetic beads. Specifically, we hypothesize that the percentage of stride time in stance is unaffected by the long-term implantation of the magnetic beads. To evaluate this hypothesis, we use an *in vivo* turkey model to implant magnetic bead pairs in the right gastrocnemius muscle, and we analyze the percentage of stride time in stance for walking and running before and after implantation.

1.2 Migration

To provide a consistent measurement of tissue length and to ensure patient health, the magnetic implants must 1) not move relative to the surrounding tissue, 2) not move relative to one another, and 3) not migrate out of the muscle. Spherical steel beads and cylindrical titanium-encapsulated magnetic beads implanted individually into the tongue muscle in animal models proved to be stable against migration in short-term studies (6–24 days) (Mimche et al., 2016; Sokoloff et al., 2017). In previous work, we also showed that magnetic beads implanted in pairs do not migrate over a long-term study (191 days) if sufficiently separated from one another at the time of implantation (Taylor et al., 2021). Although we only investigated migration of magnets at a single magnetization strength, we used these results to determine a distance threshold for migration. We then presented a theoretical

method for adjusting that distance threshold based on the strength of the magnets and the resultant attractive forces between the magnets. In this investigation, we hypothesize that distance thresholds for magnetic bead pair migration can be predicted from empirical data of different magnet strengths using a simple model of the attractive force, which is a function of the distance between the beads. To evaluate this hypothesis, we use an *in vivo* turkey model to implant magnetic bead pairs in the lateral gastrocnemius and tibialis cranialis muscles, and we monitor long-term magnetic bead positions for migration.

1.3 Biocompatibility

The biocompatibility of magnetic bead implants must also be verified before clinical use. In previous work, as a proof of concept, we used non-clinical-grade Parylene-coated magnets (7 μm coating thickness) with a non-clinical-grade insertion process, and we found only minor inflammation (Taylor et al., 2021). Recent work by Iacovacci et al. (2021) extends those results, showing that Parylene-coated magnets (10 μm coating thickness) are non-cytotoxic, non-pyrogenic, and systemically non-toxic, resistant to wear under repeated muscle-like mechanical compression, resistant to corrosion in a simulated post-surgical inflammatory environment, and non-irritant under 28-day sub-acute toxicity evaluation. In this study, we investigate the biocompatibility of magnetic beads as long-term implants in muscle. We hypothesize that the implantation of magnetic beads with suitable biocompatible coatings does not cause adverse tissue reactions, using a first coating of nickel-copper-nickel (10–25 μm coating thickness), a second coating of gold (at least 5 μm coating thickness), and an outer coating of Parylene C (21 μm coating thickness). Using a bead insertion methodology from a clinical-grade device, we examine tissue responses to the implants. Specifically, the coated magnets are evaluated for irritation using a 2-week and 26-week intramuscular implantation, as well as an intracutaneous protocol. Further, a cytotoxic testing protocol is employed using a 72-h minimal essential media elution extraction methodology, and sensitization testing is conducted using a non-allergenic testing methodology.

2 Materials and methods

We implanted magnetic beads in ten wild turkeys over an eight-month period. All turkey experiments were approved by the Institutional Animal Care and Use Committees (IACUC) at Brown University and the Massachusetts Institute of Technology. We obtained the wild turkeys (*Meleagris gallopavo*, adult, seven male [7.7–11.32 kg], three female [3.7, 4.2, and 4.3 kg]) from local breeders and cared for them in the Animal Care Facility at Brown University on an *ad libitum* water and poultry feed diet.

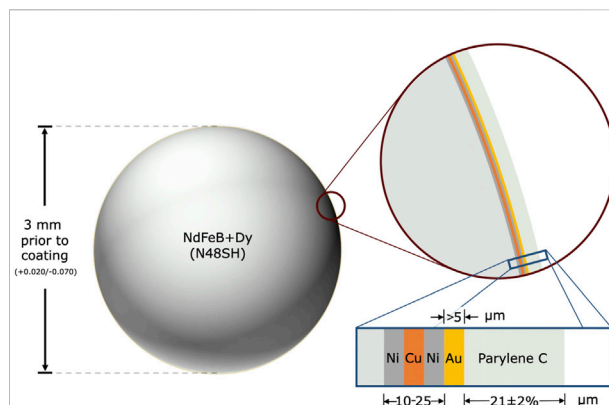


FIGURE 2

Spherical magnetic beads for implantation in muscle. The magnetic bead implants are composed of sintered neodymium-iron-boron (Nd: 26%–33%, Fe: 63.2%–68.5%, B: 1.0%–1.2%, Dy-Tb: 0%–1.5%, Nb: 0.3%–1.4%, Al: 0.1%–1.0%), with dysprosium and terbium added to increase the maximum working temperature to 150°C, which allows the implants to be autoclaved when needed. The base of each magnetic bead implant is approximately 3 mm in diameter (surface area $\sim 0.283 \text{ cm}^2$) and has an approximate residual flux density of 1.36–1.42 T. The implant is coated in 10–25 μm nickel-copper-nickel (see inset with blue border), with the outermost nickel coating being 99.99% pure. It is then coated in at least 5 μm of 99.9% pure gold and approximately 21 μm of Parylene C, resulting in a diameter after coating of approximately 3.001–3.129 mm.

All biocompatibility testing protocols were reviewed and approved by the WuXi AppTec IACUC prior to the initiation of testing. Twelve rabbits and seventeen guinea pigs were used in the biocompatibility testing portion of this work. Albino rabbits (*Oryctolagus cuniculus*, young adult, four female, eight male) and albino guinea pigs (*Cavia porcellus*, young adult male) were obtained from Charles River Laboratories and maintained in the WuXi AppTec animal facility according to NIH and AAALAC guidelines on an *ad libitum* water and certified commercial feed diet.

2.1 Magnetic bead implants

We manufactured the magnetic bead implants following medical device standards for coating, cleaning, and sterilization. SM Magnetics manufactured the base for the magnetic bead implants. The base was a 3-mm-diameter sphere composed of sintered neodymium-iron-boron and dysprosium (grade N48SH) and plated with nickel-copper-nickel (see Figure 2). This base material was delivered unmagnetized to Electro-Spec, Inc., who cleaned the spheres and tumble barrel plated them with 5 μm gold in adherence to ASTM B488, Type III, Code A, Class 5. Specialty Coating Systems (SCS) cleaned these gold-plated beads with isopropyl alcohol and deionized water in an ISO-7 clean room and applied adhesion



FIGURE 3

Magnetic bead set. Each magnetic bead set consists of eight coated, cleaned, and magnetized beads subsequently inserted into a magnetic bead cartridge for packaging, sterilization, storage, and deployment. The surgeon deploys the magnetic beads directly from the cartridge using the custom Halifax magnetic bead insertion device (see Figure 4).

promoter (AdPro) to the gold surface. SCS then coated the beads with 21 μm Parylene C *via* vapor deposition polymerization.

To ensure the implants were free from debris, SCS shipped the Parylene-coated beads in double vacuum packaging to KKS Ultraschall AG, who prepared the implants for magnetization by cleaning and packaging them in polyvinyl chloride tubes and caps received from SM Magnetics. Specifically, in their ISO-8 clean room, KKS ultrasonically cleaned these tubes and caps, inserted 32 beads into each tube, placed the caps on each end, and individually double-packaged each tube into two sealed, well-fitting bags. SM Magnetics then placed each double-packaged tube into a magnetizing coil and used a first magnetizing pulse to align the beads, followed by a second magnetizing pulse to magnetize the beads.

To prepare the beads for surgical insertion, Halifax Biomedical, Inc. (HBI) manufactured cartridges to hold the biocompatibly-coated magnetic beads (see Figure 3). For the in-house portion of this work, we placed the beads in these cartridges directly from the tubes *via* pressing and shearing, then autoclaved the bead set. For outside laboratory biocompatibility testing (WuXi AppTec), HBI inserted the beads into these cartridges (eight beads per cartridge, ISO-7 clean room)

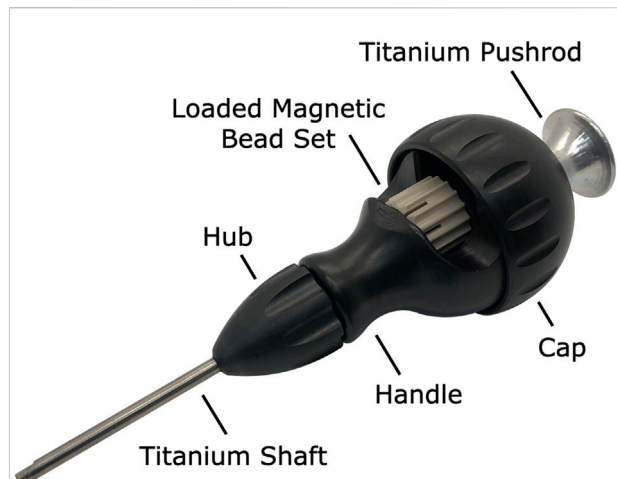


FIGURE 4

Custom Halifax magnetic bead insertion device. A custom magnetic bead insertion device enables the surgeon to implant the magnetic beads directly into the muscle without directly handling the implants. The device reuses the design for tantalum bead insertion already clinically in use, widening the shaft and pushrod to accommodate the 3-mm-diameter beads and replacing the shaft and pushrod with titanium to eliminate any attraction of the magnetic beads to the device materials. A replaceable cap allows a new magnetic bead set to be loaded into the device, and an insertable pushrod allows the surgeon to deploy a magnetic bead from the magnetic bead set into the muscle *via* the shaft. The hub unscrews from the handle to facilitate thorough cleaning and sterilization.

directly from the tubes *via* pressing and shearing, triple-packaged each cartridge into a clamshell container, and sterilized each bead set *via* gamma sterilization before providing them to the biocompatibility testing facility.

2.2 Insertion device

We contracted HBI to manufacture a customized magnetic bead insertion device (see Figure 4) using the same components used in their tantalum bead inserter, but with the shaft and pushrod made from medical-grade titanium alloy to prevent the magnetic beads from sticking to the metal during the implantation procedure. The shaft and pushrod were also widened slightly to accommodate a larger bead compared to standard tantalum bead implants and shortened to simplify the implantation procedure for the magnets, which are not inserted as deeply as tantalum beads. In addition, the 8-bead magnetic bead set was designed to be advanced by two clicks between insertions, allowing it to be a drop-in replacement for the typically-used tantalum bead sets containing 16 smaller beads. For the outside laboratory biocompatibility testing, we provided the biocompatibility testing facility with the insertion device.

2.3 Implantation

We performed all implantation procedures under sterile conditions in spaces approved for veterinary interventions. For each procedure, we placed the turkey under general anesthesia and draped the turkey in typical sterile fashion, as described in previous work (Taylor et al., 2021). We identified the target muscle *via* surface anatomic landmarks and further confirmed its location *via* ultrasound. We then identified specific insertion sites within the muscle, ensuring an intermagnet distance greater than 3 cm, and marked these planned insertion sites with a sterile operative pen. At each insertion site, we made a 1 cm length incision through all layers of skin using a No. 11 surgical scalpel. We then dissected through the underlying subcutaneous fat layer down to the underlying fascia, then incised the fascia with the No. 11 surgical scalpel to expose the underlying target muscle. Finally, we made a 1 cm length incision through the epimysium to expose the underlying muscle fibers.

After loading a magnetic bead set into the Halifax Insertion Device, we marked the planned implantation depth for each insertion site (approximately 6 mm for the proximal site and 2–3 mm for the distal site, to ensure that the magnets were implanted into the belly of the muscle) on the shaft of the insertion device and on a pair of fine surgical scissors (using a sterile operative pen and sterile ruler). With the aid of the fine surgical scissors, we pretunneled the intramuscular insertion path to the marked depth. We then placed the shaft of the Halifax magnetic bead inserter into the pretunneled path, using the depth marking as a guide. Keeping the insertion device in position, we deployed each magnetic bead implant by firmly grasping the insertion device and inserting the pushrod into the device until the knob of the pushrod contacted the cap, then withdrew the insertion device with the pushrod still in contact with the cap. Additional surgical instruments were utilized as necessary due to animal-specific anatomy (i.e., when the muscle was found to be too thin or too shallow).

After insertion, we reapproximated the epimysial edges at each site using 4-0 chromic interrupted sutures. While suturing, we took care to not bring ferromagnetic surgical instruments closer than necessary to the implants to avoid inadvertent displacement of the magnetic beads. Finally, we confirmed the implantation depth and distance between the magnetic beads *via* MM and ultrasound, approximated the skin edges at each implantation site using 4-0 polypropylene interrupted percutaneous sutures, then confirmed the magnetic bead positions once again.

2.4 Comfort

We defined comfort as the absence of change in the percentage of stride time in the stance phase for the walking

and running animals following magnetic bead implantation. Following the same techniques listed above, we implanted a magnetic bead pair in the mid-belly of the right gastrocnemius of the three female turkeys.

To minimize variability in movement patterns, we trained each turkey to walk and run on an enclosed treadmill at 1.5, 2.0, 2.5, 3.0, and 3.5 m/s. In total, there were 15 training sessions: nine times prior to implantation and six times following implantation. During training, we randomized treadmill speed every 2 min for a total of 10 min. We collected pre-implantation biomechanics at session 9 and post-implantation biomechanics at session 15 (3 weeks post-implantation) on a high-speed camera (Flare 12M180MCX, IO Industries) at 120 Hz. For each speed, we visually confirmed that the turkey's movement pattern had stabilized before collecting data.

We also manually identified toe strikes and toe offs for at least 20 consecutive gait cycles at each speed, during selected periods of gait that visually minimized irregular movements (e.g., jumping, standing). Post process, we confirmed consistent movement patterns by excluding strides that were greater than three standard deviations from the mean percentage of right leg stride time in stance, then subsequently replaced inconsistent strides with the next stride recorded.

After collecting the data, we performed statistical tests to determine whether there was an effect of surgery or speed on percentage of stride time in stance using SPSS Statistics 27 (IBM). A linear mixed model tested for the fixed main effect of speed (i.e., 1.5, 2.0, 2.5, 3.0, and 3.5 m/s) and fixed main effect of unilateral implants (i.e., pre-surgery and post-surgery) on the percentage of right leg stride time in stance. Using the theory of generalized estimating equations (Liang and Zeger 1986; Lipsitz et al., 1994), the linear mixed model for estimating means in a repeated measures model is robust to non-normality of the outcomes, so our estimated effects can be considered unbiased estimates. When significant main effects were found, *post-hoc* Tukey tests identified pairwise differences between individual speeds. We report effect sizes as η_p^2 and Cohen's *d* for main effects and pairwise comparisons, respectively. Values of $d > 0.2$, 0.5, and 0.8 indicate small, moderate, and large effects, respectively (Cohen 2013). All statistical tests used an alpha level of 0.05.

2.5 Migration

In the seven male turkeys, we intentionally placed the magnetic beads at a range of distances and in multiple muscles to explore different circumstances in which the magnetic beads might migrate toward one another. The distance between magnets was measured as described in previous work (Taylor et al., 2021), except that the computed tomography scans were performed over a longer time period (immediately following implantation and then again after

8 months). As in previous work, each leg was scanned individually, with the respective leg positioned as medial and as cranial as possible to ensure repeatability of the bird's posture.

2.6 Biocompatibility

To analyze tissue response to the clinical-grade implants inserted using the Halifax magnetic bead inserter, in-house observations were made first, with a total of eight histological samples taken from four of the male turkeys, each at 8 months post-implantation. Histology was performed as in previous work (Taylor et al., 2021), with the addition of Masson's Trichrome staining to highlight the fibrous tissue.

To test the device biocompatibility under good laboratory practice (GLP) compliance (USFDA, Code of Federal Regulations, Title 21, Part 58 - Good Laboratory Practice for Nonclinical Laboratory Studies), we submitted fully manufactured magnetic bead sets and insertion devices to WuXi AppTec for intramuscular implantation, cytotoxicity, intracutaneous irritation, and sensitization testing. All magnetic beads used in the testing were deployed from the magnetic bead cartridges using the insertion device, and all tests were conducted in compliance with international standard ISO 10993-12:2012, Biological Evaluation of Medical Devices, Part 12: Sample Preparation and Reference Materials.

2.6.1 Intramuscular implantation testing

To test for local effects of the magnetic beads contacting skeletal muscle, three magnetic beads and three negative control articles (high density polyethylene, HDPE) were implanted into the left and right paravertebral muscles, respectively, in nine rabbits. Four rabbits were used for the two-week implantation test, and the remaining five rabbits were reserved for the twenty-six-week implantation test. At the test endpoints, the muscles were explanted, fixed in 10% neutral buffered formalin, and sent to the study pathologist for analysis.

Each implantation site was analyzed *via* clinical, gross, and histopathologic information. Each site was examined microscopically and scored for inflammation and tissue response on a scale from 0 (no inflammation/response) to 4 (severe inflammation/response). The average of the magnetic bead site scores minus the control article site scores was used to determine an irritant ranking score, with a negative value considered 0.0. As directed in the ISO standard, a score from 0.0 up to 2.9 was considered to indicate that the magnetic bead implants were non-irritant. The intramuscular implantation tests were conducted in accordance with the ISO Test Method for Implantation in Muscle, ISO 10993-6: 2016, Biological Evaluation of Medical Devices - Part 6: Tests For Local Effects After Implantation.

2.6.2 Cytotoxicity testing

To test for toxicity of the implants to mammalian cells, 54 magnetic beads were extracted at a ratio of 3 cm²/1 ml (surface area per volume) in Eagle's minimal essential medium (E-MEM) supplemented with 5% volume-per-volume fetal bovine serum (FBS) for 72 h at 37°C, then shaken well. A negative control (HDPE) extraction, positive control (0.1% zinc diethyldithiocarbamate, ZDEC, polyurethane film) extraction, and cell control were also prepared in parallel to and under equivalent conditions as the magnetic bead extraction.

Completed extractions were added to fully-formed cell culture wells containing L-929 mouse fibroblast cells (American Type Culture Collection, ATCC # CCL-1) after removal of the culture maintenance medium. Specifically, 1 ml of each extraction was inserted into each of three cell culture wells, and the cell culture wells were incubated in a humidified atmosphere for 72 h.

The cell cultures were examined microscopically and scored for cytopathic effects (lysis, crenation, plaques, and excessive rounding of cells) at 24, 48, and 72 h on a scale from 0 (no reactivity) to 4 (severe reactivity). As directed in the ISO standard, a score of 0, 1, or 2 was considered to indicate that the magnetic bead implants were non-cytotoxic. This cytotoxicity testing was conducted in compliance with ISO 10993-5:2009, Biological Evaluation of Medical Devices, Part 5: Tests for *In Vitro* Cytotoxicity.

2.6.3 Sensitization testing

To test for the induction of allergic reactions, magnetic beads were extracted at a ratio of 3 cm²/1 ml (surface area per volume) into each of 5.1, 8.1, and 10.1 ml of 0.9% normal saline (54, 86, and 107 magnetic beads) and 5.1, 8.1, and 10.1 ml of sesame oil (54, 86, and 107 magnetic beads). These extractions were freshly prepared for corresponding phases of the test and were performed over 72 h at 50°C, with agitation during the course of the extraction. Vehicle controls (containers of liquid without magnetic beads) were prepared in parallel to and under equivalent conditions as the magnetic bead extractions.

One-tenth of 1 ml of each extraction was injected intracutaneously into the dorsal dermis of eleven guinea pigs (one on each side of the midline). Adjacent these first two injections, two additional 0.1 ml injections of an immunostimulant (equal parts Freund's Complete Adjuvant and 0.9% sterile saline) were injected subcutaneously. An additional 0.05 ml of each extraction was then mixed with 0.05 ml of the immunostimulant, and each was injected subcutaneously adjacent the first injections. All six injections were repeated using negative (vehicle) controls in place of the magnetic bead extractions in each of six additional guinea pigs. Six days post-injection, the injection sites were treated with 10% sodium lauryl sulfate in mineral oil. After 24 h, the sites were then cleaned, and a 2 cm × 4 cm filter paper saturated with magnetic bead extract (or vehicle control, for the negative control group) was applied dermally to the site for 48 h, then removed.

After an additional 15 days, two 2 cm × 2 cm filter papers saturated with magnetic bead extract and vehicle control, respectively, were applied dermally to the right and left flanks, respectively, of each animal for 24 h, then removed. At 24–48 h after patch removal, these 2 cm × 2 cm exposure sites were observed and scored for irritation and sensitization reaction on a scale from 0 (no erythema/edema) to 3 (intense erythema/edema). As directed in the ISO standard, a score of 0 (or a score not exceeding the most severe negative control reaction, if non-zero) was considered to indicate that the magnetic bead implants did not elicit a sensitization response. This sensitization testing was conducted in compliance with ISO 10993-10: 2010, Standard, Biological Evaluation of Medical Devices, Part 10: Tests for Irritation and Skin Sensitization.

2.6.4 Intracutaneous irritation testing

To test for local irritation of dermal tissue due to potential extractables or leachables, magnetic beads were extracted at a ratio of 3 cm²/1 ml (surface area per volume) into each of 6 ml of 0.9% normal saline (64 magnetic beads) and 6 ml of sesame oil (64 magnetic beads). These extractions were performed over 72 h at 50°C, with agitation during the course of the extraction, and vehicle controls (containers of liquid without magnetic beads) were prepared in parallel to and under equivalent conditions as the magnetic bead extractions.

One milliliter of each extraction and of each vehicle control was then injected intracutaneously into the dorsal dermis in each of three rabbits. Specifically, the magnetic bead extractions were injected to the right of the midline, and the vehicle controls were injected to the left of the midline. Each extraction was delivered as five 0.2 ml injections at locations spatially distributed along the cranial-caudal axis, with the normal saline extractions being delivered medial to the sesame oil extractions.

The injection sites were observed and scored for gross evidence of erythema and edema at 24, 48, and 72 h on a scale from 0 (no erythema/edema) to 4 (severe erythema/edema). As directed in the ISO standard, a difference in score of less than 1.0 between the magnetic bead extraction and vehicle control extraction was considered to indicate that the magnetic bead implants met the requirements of the intracutaneous reactivity test. This intracutaneous irritation testing was conducted in compliance with ISO 10993-10: 2010, Standard, Biological Evaluation of Medical Devices, Part 10: Tests for Irritation and Skin Sensitization.

3 Results

3.1 Comfort

The percent of the total stride time spent in stance during treadmill running was evaluated before and after surgery for the leg that received implants (the right leg) in three turkeys. We did not observe a significant surgery main effect ($p = 0.234$, $\eta_p^2 =$

0.002) or a significant speed-surgery interaction effect ($p = 0.492$, $\eta_p^2 = 0.006$) on the percentage of right leg stride time in stance (Figure 5). Out of 600 total strides analyzed ($n = 20$ consecutive strides for three birds and five speeds at each of pre-versus post-surgery biomechanical collections), five strides were replaced due to irregular movement (i.e., greater than 3 standard deviations from the mean). Linear mixed model analysis revealed a significant main effect of speed ($p < 0.001$, $\eta_p^2 = 0.752$) on the percentage of right leg stride time in stance. The percentage of right leg stride time in stance significantly decreased with increasing speed (p -values < 0.001).

3.2 Migration

To analyze the effect of distance on migration, we implanted magnetic beads into a total of 16 turkey muscles across seven turkeys. The results of this migration study are shown in Figure 6. Magnetic bead pairs were implanted at various distances apart and their separation distances were determined *via* computed tomography scan both immediately following implantation and after 8 months post-implantation. Full migration occurred in three implants at and below 2.01 cm, but did not occur in one implant at 1.83 cm or in any implants at or above 2.12 cm. As indicated in the plot, one of the muscles was implanted with three magnets in line with one another, for a separate investigation. See Supplementary Table S1 for a numerical presentation of the initial and final separation distances.

3.3 Biocompatibility

For the turkey portion of the biocompatibility analysis, no inflammation was observed around any of the implant sites (see Figure 7 for a representative histological cross section).

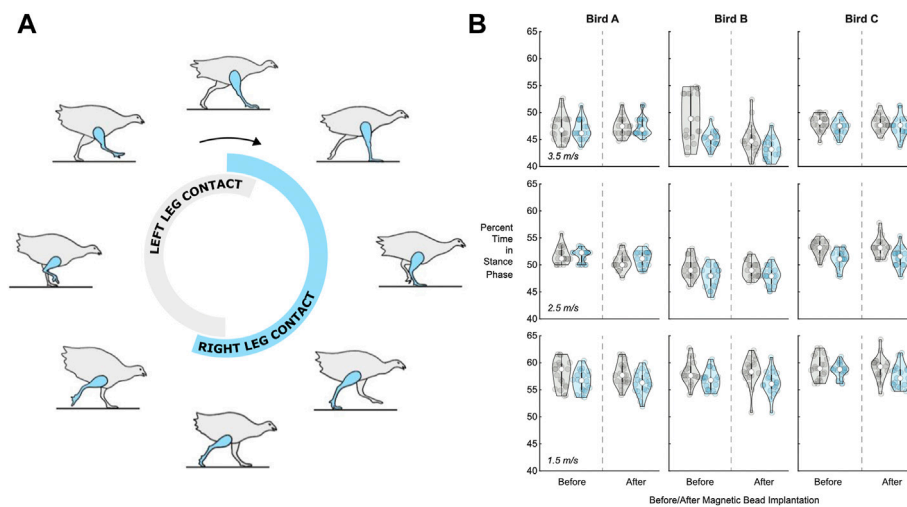
The GLP testing results demonstrated *via* extensive biocompatibility testing that the implants were non-irritant, non-cytotoxic, non-allergenic, and non-irritating (see Table 1).

3.3.1 Intramuscular implantation testing

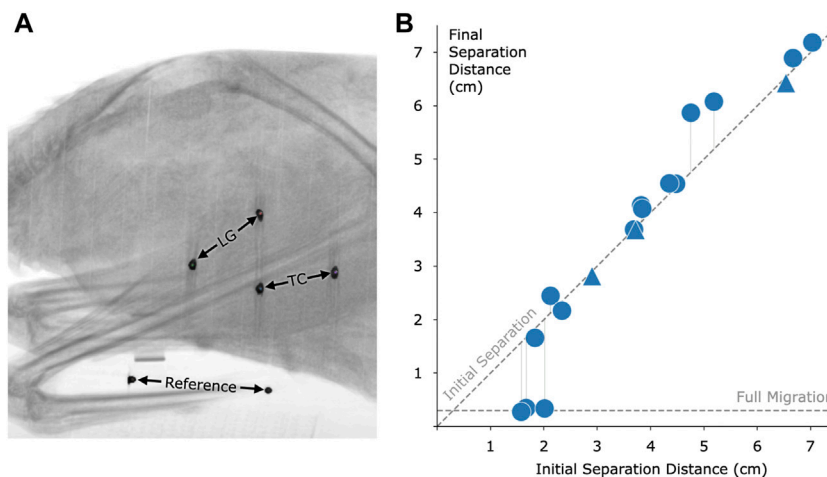
The two-week and twenty-six-week intramuscular implantation tests in rabbits each resulted in an irritant ranking score of 0.0 (rounded up from negative) for the magnetic bead implants, indicating that the fully manufactured magnetic beads in this study are non-irritants as compared to the control articles. No abnormal clinical signs were noted, and no difference was noted macroscopically between the test and control sites in any of the rabbits. All rabbits survived to the scheduled study endpoint.

3.3.2 Cytotoxicity testing

The cytotoxicity test resulted in a score of 0 for the magnetic bead extraction at 24, 48, and 72 h, indicating

**FIGURE 5**

Percentage of stride time in stance phase before and after surgery. **(A)** Turkey gait cycle showing the portion of gait when the leg is in contact with the ground (the stance phase) during running. The contact time for the right leg, which received the implants, is shown in blue, while the contact time for the left leg is shown in gray, for reference. **(B)** Violin plots for left leg (gray, for reference) and right leg (blue) percentage of stride time in stance phase ($n = 20$ strides) for each bird (A, B, and C) at 1.5 m/s (bottom), 2.5 m/s (middle), and 3.5 m/s (top). See [Supplementary Table S1](#) for the full dataset in table form.

**FIGURE 6**

Magnetic bead pair stability against migration in muscle. **(A)** Computed tomography image of one of the turkeys with the implanted magnetic beads. In this case, magnets were implanted in the lateral gastrocnemius (LG) and tibialis cranialis (TC) muscles. A consistent reference, seen at the bottom of the figure, was included in all scans to ensure repeatable distance measurements. **(B)** Effect of initial implant separation on migration of the magnetic beads, seen by comparing the vertical position of each data point to the diagonal dashed line. The horizontal dashed line, labeled Full Migration, indicates the distance between bead centers when they are touching (3 mm center to center). The final magnetic bead pair separation is the separation at 8 months post-implantation. We observed a lack of full migration for all implant pairs at or above an initial separation distance of 2.12 cm. Triangles indicate pairwise distances between three magnets that were placed approximately in line within a single muscle. Refer to [Supplementary Table S1](#) for this data in a numerical representation.

that the magnetic bead implants of this study are non-cytotoxic under the conditions of the cytotoxicity test. The negative and cell controls also received scores of 0 (no reactivity, discrete intracytoplasmic granules, no cell lysis,

and no reduction of cell growth), while the positive control received a score of 4 (severe reactivity and complete or nearly-complete destruction of the cell layers), indicating that the test was functioning normally.

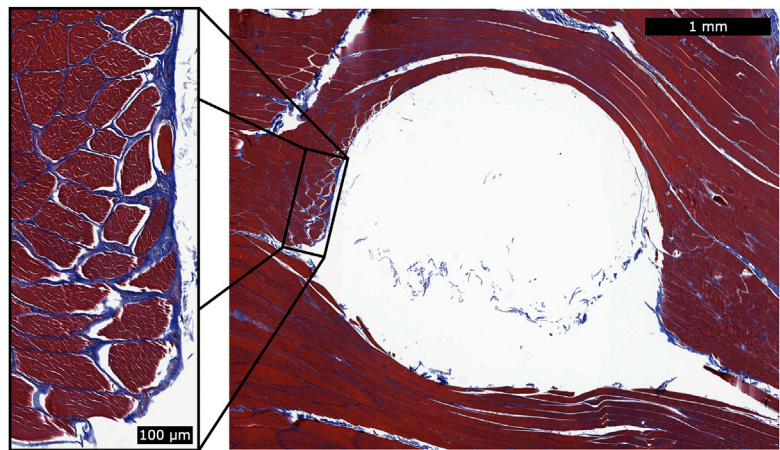


FIGURE 7
Histology for a single magnetic bead implant. This representative histology sample shows a cross section of the implantation site after removal of the spherical magnetic bead implant. We applied Masson’s trichrome staining to highlight the fibrous tissue in blue. During explantation, some of the fibrous capsule remained attached to the implant and thus was generally unobservable in the histological analysis. However, a thin fibrous wall remained (see magnified inset), and the fibrous tissue had integrated into the muscle fibers. This observation suggests that the fibrous tissue may contribute to holding the implant in position relative to the surrounding muscle tissue. No inflammation was observed surrounding the implantation sites.

TABLE 1 Biocompatibility testing results. The following table lists the tests that were performed on the magnetic bead implants under GLP, along with the ISO standards that were followed and the corresponding test results.

Test	ISO standard	Result
Implantation—2 weeks	10993-6:2016	0.0 (non-irritant)
Implantation—26 weeks	10993-6:2016	0.0 (non-irritant)
Cytotoxicity	10993-5:2009	0 (non-cytotoxic)
Sensitization	10993-10:2010	0 (non-allergenic)
Irritation	10993-10:2010	0.0 (non-irritating)

3.3.3 Sensitization testing

The sensitization test resulted in a score of 0 for dermal observations of all exposure sites for both the normal saline and sesame oil extractions, indicating that the magnetic bead implants did not elicit a sensitization response, and thus that the implants are non-allergenic under the conditions of the test. No abnormal clinical signs were noted, and all animals survived to the scheduled study endpoint.

3.3.4 Intracutaneous irritation testing

The intracutaneous irritation test resulted in a comparative score of 0.0 for erythema and edema against the vehicle control for both the normal saline and sesame oil extractions, indicating that the magnetic beads met the requirements of the intracutaneous reactivity test, and thus that the implants are non-irritating under the conditions of the test. No abnormal

clinical signs were noted, and no dermal reactions were observed at the test or control sites in any of the rabbits at any of the observation points. All animals survived to the scheduled study endpoint.

4 Discussion

In this study, we investigate the clinical viability of magnetic bead implants in muscle. Using a specialized device to insert magnetic beads into muscle in avian and lagomorph models, we collect data to assess bead migration, gait metrics, and bead biocompatibility. We find that implanted-leg stance time is preserved from pre- to post-implantation of the magnetic beads in muscle, migration does not occur when the magnets are implanted a sufficient distance from one another, and no inflammation occurs in response to the magnetic bead implantation. In addition, GLP-compliant testing confirms that the implants are non-irritant, non-cytotoxic, non-allergenic, and non-irritating. These results suggest that MM is a viable approach to muscle tissue length tracking in humans.

4.1 Comfort

In support of our hypothesis, we found no evidence of magnetic bead implant discomfort from measures of pre- and post-implant gait. Following a series of training sessions pre- and post-implantation, we did not observe an effect of surgery on the

percentage of right leg stride time in stance across a range of walking and running speeds. The absence of any sign of antalgic gait in a relatively small animal 3 weeks following implantation supports the idea that the implant would not cause significant discomfort in humans, where the implant would represent a much smaller fraction of muscle volume.

4.2 Migration

In previous work, no magnets migrated toward one another from an initial separation distance of 2.15 cm or above (Taylor et al., 2021). Due to the now increased magnetization strength of the magnetic implants (N48 versus N35, or approximately 1.4 T versus 1.183 T), we hypothesized that no implants at this increased strength would migrate from an initial separation of 2.34 cm or greater, a predicted increase of $\sqrt{1.4/1.183}$, or about 9% (using the migration model of Supplementary Material S1, Taylor et al., 2021). In this investigation, no implants were found to migrate from this distance, but also no implants were found to migrate from the even closer distance of 2.12 cm. Having observed in previous work that one pair of magnets only partially migrated from a starting location of 1.67 cm, we further hypothesized that we may see magnets not fully migrate from an initial separation distance as low as 1.82 cm. In support of this hypothesis, in this study we observed a magnetic bead pair that did not migrate from a starting separation distance of 1.83 cm, even though another bead pair did migrate from 2.01 cm. These results highlight the lack of a precise cutoff for a migration distance threshold, due to the inherent limitations of solely relying on initial separation distance to the exclusion of all other factors.

The migration model used here to predict the migration cutoffs may help in understanding one aspect of migration but is insufficient on its own to fully capture what is happening within the body with magnetic bead implant pairs. While in this study we employed the same material type for coating as in previous work, our updated coating, cleaning, and insertion processes resulted in no observed inflammation, which may have reduced the likelihood of migration. Variations in the magnetization strength of each implant due to magnetic bead size tolerances and magnetic material alignment may also be a cause for both in-study and cross-study variations, as could small differences in the surgical procedure (e.g., the position of the insertion path). Finally, our model holds as a fundamental assumption that the maximum contraction ratio is equivalent between any two beads, regardless of implant location, suggesting that the minimum distance between the beads occurs during full muscle contraction and can be predicted from the distance between the beads at rest. However, muscle contraction is not spatially uniform (for instance, widening as it shortens), which weakens this assumption when the beads are not placed in precisely the same locations within the muscle. Further, this

assumption is also weakened by the possibility of subject-to-subject variability in contraction ratios. Importantly, a highly conservative estimate of the migration threshold should be used to account for the many biological factors of the implants and implantation process. As such, we maintain the importance of an initial 3 cm separation distance at the time of implantation for these 3-mm-diameter spherical magnetic beads to ensure stability against migration.

It is critical that these 3-mm-diameter magnetic bead implants be verified to be at least 3 cm from *all* other implants for all possible joint configurations, including distinct muscle contraction states resulting in all possible joint configurations. We wish to also underscore the importance of implanting at, or beyond, the minimum distance threshold even when only a single magnetic bead is implanted per muscle, as has been proposed in previous work (Tarantino et al., 2017). It is critical that this verification be included in the surgical implantation protocol design for implantation in all future human studies.

4.3 Biocompatibility

In a previous study, we observed the histological results of implants coated with a proof-of-concept coating and insertion technique. In this investigation, we developed and employed a hospital-ready insertion technique to implant magnetic beads with standard medical coatings of gold and Parylene C. We chose Parylene C due to its widespread commercial use in medical devices (Golda-Cepa et al., 2020). We applied the thickest Parylene C coating possible while still maintaining a smooth finish. We applied the underlying layer of gold solely for an added measure of safety, using the maximum thickness class provided by the ASTM B488 standard. With the improved techniques and protocols of this study, we did not observe inflammation caused by the implants. We contracted a GLP laboratory to formally investigate the implants for biocompatibility using this finalized clinical-grade insertion device and implants, and the implants were shown to be non-irritant, non-cytotoxic, non-allergenic, and non-irritating. These results support the clinical biocompatibility of these implants for human use.

4.4 Animal model

Turkey models share musculoskeletal characteristics with all vertebrates and have been used to develop and further an understanding of human biomechanics. Early work with turkeys identified the strut-like function of muscles in series with tendons in running turkeys (Roberts et al., 1997; Gabaldón et al., 2008), and this functionality was later shown in humans in both walking (Fukunaga et al., 2001) and running (Farris and Sawicki 2012; Arnold et al., 2013). Metabolic cost measurements

in guinea fowl (Marsh et al., 2004), which are of the same taxonomic order as turkeys, have also been used to inform energy models of human walking (Doke et al., 2005; Neptune et al., 2008) and exoskeletal assistance (Donelan et al., 2008). This previous literature and the parallels between turkey and human muscle biomechanics and physiology suggest that the turkey model provides a robust representation for the use of these intramuscular implants in humans.

4.5 Limitations

These magnetic bead implants have not yet been subjected to MRI Safety Testing, an important factor in their potential use in humans, as these implants may limit the ability of a patient to get an MRI image. Until MRI Safety Testing is completed for these devices, a patient would need to be instructed to not get an MRI. Though there are cases in which an MRI is allowed when a patient has a magnetic implant, the imaging conditions are highly specific to the particular geometry, strength, coercivity, location, and setup of the permanent magnets, making a study of MRI compatibility necessary (Edmonson et al., 2018).

This technique does not replace, and should not be seen as a potential replacement for, RSA, which is a standard technique for monitoring migration of implants such as knee replacements (Kärrholm 1989). RSA is an excellent technique for monitoring rigid bodies because it allows many small beads to be implanted at once and at any depth, while magnetic beads must be separated by a minimum distance and have a limited implantation depth. MM is designed for use in situations requiring high-accuracy real-time tissue length tracking in relatively superficial muscles.

Magnetic bead tracking is depth-limited due to the signal-to-noise ratio of the sensors and the nature of the magnetic dipole field, which falls off with the inverse cube of distance. With the sensing technology demonstrated in the supplementary work, magnet tracking is optimal for use at a depth between no less than 9 mm [when tracking a 1.4 T 3-mm-diameter spherical magnet with an LIS3MDL sensor, the recalibration point for the sensor is 8.58 mm, as given by Table 5.1 of (Taylor, 2020)] and no greater than 33 mm (see Supplementary Figure S1).

In this work, we evaluated 3-mm-diameter spherical magnetic beads coated in Parylene C. Beads of different sizes, geometries, and coatings would need to be further investigated for comfort, migration, and biocompatibility before clinical use.

4.6 Applications

The use of magnetic beads in human-machine interfacing enables additional strategies for controlling external devices and monitoring tissue states. For instance, the use of magnetic bead pairs to track muscle tissue length *via* MM could allow a robotic

prosthesis to be controlled using muscle tissue lengths in paired agonist and antagonist muscles, providing position and impedance control (see Figures 8A,B). For instance, magnetic bead pairs in the lateral gastrocnemius and tibialis anterior could be used to control the ankle joint, while magnetic bead pairs in the tibialis posterior and peroneus longus could be used to control the subtalar joint. Similarly, muscle tissue lengths could be used to control an exoskeleton to provide restoration or augmentation of weak or healthy muscle movement (see Figure 8C). Magnetic bead implants could also enable closed-loop artificial muscle stimulation, providing feedback about the muscle's length during stimulation to allow high-fidelity control over the muscle (see Figure 8D). For a more detailed discussion of how MM could be used to control a prosthesis or exoskeleton, see Taylor et al., 2021.

While the more urgent applications of muscle tracking address the restoration of natural human abilities, muscle tissue length tracking could enable various human-machine interface tasks, such as the operation of remote machines (e.g., unmanned aerial vehicles or telepresence robots), operation of local machines (e.g., factory or farm equipment), and control of oneself or one's tools in an augmented or virtual reality environment. Muscle length control could also enable improved navigation in a weightless environment, such as in control of underwater thrusters or air thrust rotors. Specifically, muscle tissue length tracking *via* magnetic beads is unaffected by water, in comparison with surface electromyography, where the leads need to be fully waterproofed to work reliably when submerged (Rainoldi et al., 2004). In all these cases, the use of muscle tissue length to control an external device would provide an intuitive and powerful means of interaction, as humans are already proficient at using muscle length to control their own movements.

Each pair of magnetic beads should ideally be implanted along a muscle fascicle to enable biomimetic control. In addition, to maximize signal-to-noise ratio for any MM-based control strategy, the magnetic beads should ideally be implanted as maximally separated as possible within the muscle fascicle. Supplementary Figure S1 demonstrates the accuracy of magnetomicrometry for a single spacing at various depths. The accuracy of magnetomicrometry in a mobile context is addressed more completely in parallel work (Taylor, et al., 2022b).

Magnetic bead implants may also be used for delivering proprioceptive feedback. Illusory kinesthetic feedback *via* muscle tissue vibration has been well tested *via* vibramotors on the skin surface, and works by activating muscle spindles to deliver the sensation of illusory joint positions and movements (Marasco et al., 2018). However, as currently implemented, vibration through the skin may create undesirable cutaneous sensations, distracting from the desired proprioceptive signal. Implanted magnetic beads provide an opportunity to vibrate a muscle from the inside using electromagnetic actuation. The ability to selectively vibrate individual magnets was recently

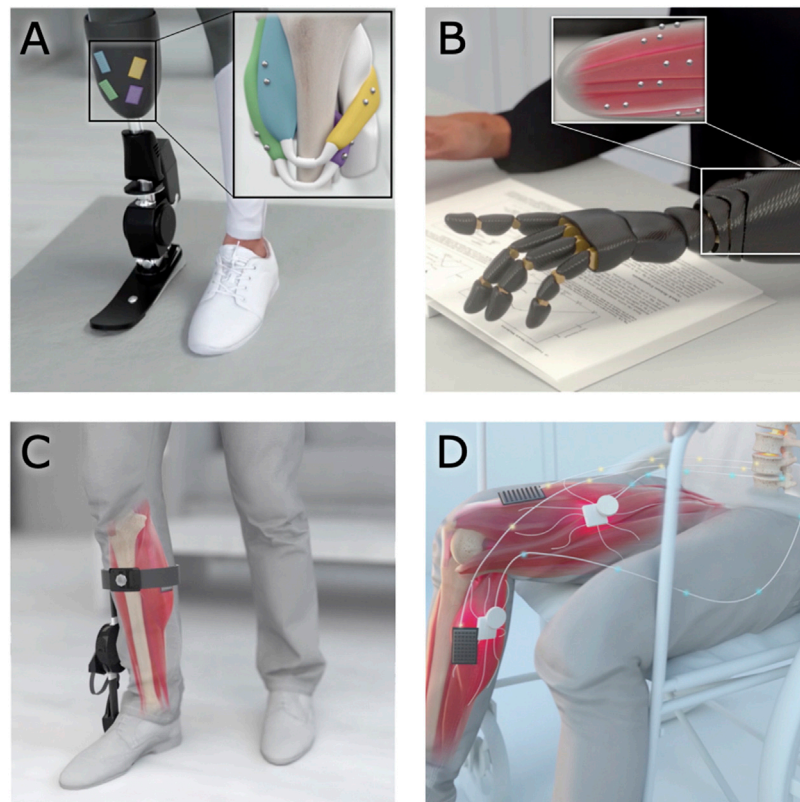


FIGURE 8

Applications of magnetomicrometry. When used to track muscle tissue lengths via magnetomicrometry, magnetic bead implants could enable real-time control in human-machine interfaces. **(A,B)** Magnetic beads implanted into residual muscles could be used to control a prosthetic limb device. **(C)** When implanted in a weakened muscle, the magnetic beads could provide control over an exoskeleton for restoration or augmentation of joint torque. **(D)** Magnetic beads in paralyzed muscles could enable closed-loop artificial muscle stimulation for control of muscle length or force.

demonstrated in benchtop tests of a “myokinetic stimulation interface,” including the ability to modulate the direction of the vibration (Montero et al., 2021). For translation, this strategy will need to balance weight and power requirements, manage simultaneous tracking and stimulation, and compensate for vibration of the surrounding electromagnets. Once these issues are addressed, these passive intramuscular magnetic beads could be employed as bidirectional human-machine interfaces.

When implanted next to cutaneous receptors, such as in fingertips, magnetic implants can confer cutaneous sensing of low-frequency magnetic fields (Hameed et al., 2010). Seeking this additional magnetic sense, the biohacking community has been implanting magnets since the late 1990s or early 2000s (Doerksen 2018), though these implantations are performed as a do-it-yourself operation (Yetisen 2018) and often without anesthesia (Brickley 2019). While we advise against the self-implantation of non-clinical-grade magnetic beads, this history of magnetic bead implantation

suggests an innate human desire to be augmented and a simplicity to the use of passive magnetic beads as a human-machine interface.

4.7 Summary

In this work, we manufacture clinical-grade magnetic bead implants and develop a clinical-grade implantation strategy, and we verify implant comfort, stability against migration, and biocompatibility. Our results demonstrate that when implanted as discussed here, these magnetic beads are viable for use in human muscle.

Data availability statement

The original contributions presented in the study are included in the article/Supplementary Material, further inquiries can be directed to the corresponding author.

Ethics statement

The animal study was reviewed and approved by the Institutional Animal Care and Use Committees at Brown University, the Massachusetts Institute of Technology, and WuXi AppTec.

Author contributions

CT developed the coating strategy and implant manufacturing process, co-designed the custom magnetic bead inserter, coordinated the GLP biocompatibility testing, oversaw experimental design, contributed to surgical procedure design, assisted in surgeries, oversaw the performance of histology, aided in computed tomography data collection, performed migration data analyses, maintained experimental documentation, and led the manuscript preparation. WC contributed to experimental design, assisted in surgeries, performed ultrasound measurements, collected gait symmetry data, performed gait symmetry statistical analyses, performed computed tomography data collection, and contributed to manuscript preparation. EC assisted in collecting and processing gait symmetry data and contributed to manuscript preparation. SY collected and analyzed the magnetomicrometry depth dataset and performed magnetomicrometry measurements during surgeries. MC contributed to surgical procedure design, assisted in surgeries, and contributed to manuscript preparation. SL oversaw the statistical design and statistical analysis of the gait symmetry experiments. RB performed histological analyses and contributed to manuscript preparation. TR assisted with general study management, contributed to experimental design, assisted in surgeries, aided in performing experiments, and contributed to manuscript preparation. HH conceived of the study, oversaw project funding, assisted with general study management, contributed to experimental design, and aided in manuscript preparation.

Funding

This work was funded by the Salah Foundation, the K. Lisa Yang Center for Bionics at MIT, the MIT Media Lab Consortia, NIH grant AR055295, and NSF grant 1832795.

References

- Arnold, Edith M., Hamner, Samuel R., Seth, Ajay, Millard, Matthew, and Delp, Scott L. (2013). How muscle fiber lengths and velocities affect muscle force generation as humans walk and run at different speeds. *J. Exp. Biol.* 216 (11), 2150–2160. doi:10.1242/jeb.075697
- Auerbach, Nadja, and Tadi, Prasanna (2021). *Antalgic gait in adults*. StatPearls [Internet].

Acknowledgments

The authors thank, non-exhaustively, Alexander Best, Mckay Bruning, Andreas Burger, Ziel Camara, Tyler Clites, Steven Charlebois, Charlene Condon, Kathy Cormier, Jimmy Day, Bruce Deffenbaugh, Michelle Dietzel, Asami Ehlert, MacKenzie Ess, Rachel Fleming, Lisa Freed, Robert Gnos, Deborah Grayeski, Alan Grodzinsky, Guillermo Herrera-Arcos, Crystal Jones, Kylie Kelley, Aimee Liu, Richard Marsh, Jesse Mendel, Richard Molin, Chad Munro, Allison O'Konek, Jarrod Petersen, Mitchel Resnick, Lindsey Reynolds, Andy Robinson, Emily Rogers, Amy Rutter, Jessica Sohner, Shriya Srinivasan, Erika Tavares, and Beni Winet for their helpful advice, suggestions, feedback, and support. A preprint of this manuscript was deposited on bioRxiv (Taylor et al., 2022).

Conflict of interest

CT, SY, and HH have filed patents on the magnetomicrometry concept entitled “Method for neuromechanical and neuroelectromagnetic mitigation of limb pathology” (patent WO2019074950A1) and on implementation strategies for magnetomicrometry entitled “Magnetomicrometric advances in robotic control” (US pending patent 63/104942).

The remaining authors declare that the research was conducted in the absence of any commercial or financial relationships that could be construed as a potential conflict of interest.

Publisher's note

All claims expressed in this article are solely those of the authors and do not necessarily represent those of their affiliated organizations, or those of the publisher, the editors and the reviewers. Any product that may be evaluated in this article, or claim that may be made by its manufacturer, is not guaranteed or endorsed by the publisher.

Supplementary material

The Supplementary Material for this article can be found online at: <https://www.frontiersin.org/articles/10.3389/fbioe.2022.1010276/full#supplementary-material>

- Brickley, London (2019). Bodies without borders. *West. Folk.* 78 (1), 5–38. doi:10.2307/26864140

- Calado, Alexandre, Soares, Filomena, and Matos, Demétrio (2019). A review on commercially available anthropomorphic myoelectric prosthetic hands, pattern-recognition-based microcontrollers and SEMG sensors used for prosthetic control, IEEE international Conference on autonomous robot Systems and competitions (ICARSC), 1–6. IEEE.

- Clancy, Edward A., Morin, Evelyn L., and Merletti, Roberto (2002). Sampling, noise-reduction and amplitude estimation issues in surface electromyography. *J. Electromyogr. Kinesiol.* 12 (1), 1–16. doi:10.1016/s1050-6411(01)00033-5
- Clites, Tyler R., Herr, Hugh M., Srinivasan, S. S., Zorzos, A. N. et al (2018). The ewing amputation: The first human implementation of the agonist-antagonist myoneural interface. *Plastic Reconstr. Surg. - Glob. Open* 6 (11), e1997. doi:10.1097/gox.0000000000001997
- Cohen, Jacob (2013). *Statistical power analysis for the behavioral sciences*. New York, NY: Routledge.
- Doerksen, Mark (2018). How to make sense: Sensory modification in grinder subculture. PhD Thesis. Montreal (QC): Concordia University.
- Doke, Jiro, Donelan, J. Maxwell, and Kuo, Arthur D. (2005). Mechanics and energetics of swinging the human leg. *J. Exp. Biol.* 208 (3), 439–445. doi:10.1242/jeb.01408
- Donelan, J. Maxwell, Li, Qinghua, Naing, Veronica, Weber, D. J., and Kuo, Arthur D. (2008). Biomechanical energy harvesting: Generating electricity during walking with minimal user effort. *Science* 319 (5864), 807–810. doi:10.1126/science.1149860
- Edmonson, Heidi A., Carlson, Matthew L., Patton, Alice C., and Watson, Robert E. (2018). MR imaging and cochlear implants with retained internal magnets: Reducing artifacts near highly inhomogeneous magnetic fields. *Radiographics* 38 (1), 94–106. doi:10.1148/rg.2018170135
- Farina, Dario, Vujaklija, Ivan, Sartori, Massimo, Kapelner, Tamás, Negro, Francesco, Jiang, Ning, et al. (2017). Man/machine interface based on the discharge timings of spinal motor neurons after targeted muscle reinnervation. *Nat. Biomed. Eng.* 1 (0025), 1–12. doi:10.1038/s41551-016-0025
- Farris, Dominic James, and Sawicki, Gregory S. (2012). Human medial gastrocnemius force-velocity behavior shifts with locomotion speed and gait. *Proc. Natl. Acad. Sci. U. S. A.* 109 (3), 977–982. doi:10.1073/pnas.1107972109
- Fukunaga, Tetsuo, Kubo, Keitaro, Kawakami, Yasuo, Fukushima, Senshi, Kanehisa, Hiroaki, and ConstantinosMaganaris, N. (2001). *In vivo* behaviour of human muscle tendon during walking. *Proc. R. Soc. Lond. B* 268 (1464), 229–233. doi:10.1098/rspb.2000.1361
- Gabaldón, Annette M., Nelson, Frank E., and Roberts, Thomas J. (2008). Relative shortening velocity in locomotor muscles: Turkey ankle extensors operate at low V/vmax. *Am. J. Physiology-Regulatory, Integr. Comp. Physiology* 294 (1), R200–R210. doi:10.1152/ajpregu.00473.2007
- Golda-Cepa, Monika, Engvall, Klas, Hakkarainen, Minna, and Kotarba, Andrzej (2020). Recent progress on Parylene C polymer for biomedical applications: A review. *Prog. Org. Coatings* 140, 105493. doi:10.1016/j.porgcoat.2019.105493
- Hameed, Jawish, Harrison, Ian, Gasson, Mark N., and Warwick, Kevin (2010). 1–5. IEEE. A novel human-machine interface using subdermal magnetic implantsIEEE 9th International Conference on Cybernetic Intelligent Systems.
- Iacovacci, Veronica, Naselli, Irene, Alice Rita, Salgarella, Clemente, Francesco, Ricotti, Leonardo, and Cipriani, Christian (2021). Stability and *in vivo* safety of gold, titanium nitride and Parylene C coatings on NdFeB magnets implanted in muscles towards a new generation of myokinetic prosthetic limbs. *RSC Adv.* 11 (12), 6766–6775. doi:10.1039/d0ra07989h
- Kärholm, Johan (1989). Roentgen stereophotogrammetry: Review of orthopedic applications. *Acta Orthop. Scand.* 60 (4), 491–503. doi:10.3109/17453678909149328
- Liang, K.-Y., and Zeger, S. L. (1986). Longitudinal data analysis using generalized linear models. *Biometrika* 73 (1), 13–22. doi:10.1093/biomet/73.1.13
- Lipsitz, S. R., Fitzmaurice, G. M., Orav, E. J., and Laird, N. M. (1994). *Performance of generalized estimating equations in practical situations*. Washington, DC: International Biometric Society, 270–278.
- Marasco, Paul D., Jacqueline, S. Hebert, Sensinger, Jon W., Shell, Courtney E., Schofield, Jonathon S., Thumser, Zachary C., et al. (2018). Illusory movement perception improves motor control for prosthetic hands. *Sci. Transl. Med.* 10 (432), eaao6990. doi:10.1126/scitranslmed.aao6990
- Marsh, Richard L., Ellerby, David J., Carr, Jennifer A., Henry, Havalee T., and Buchanan, Cindy I. (2004). Partitioning the energetics of walking and running: Swinging the limbs is expensive. *Science* 303 (5654), 80–83. doi:10.1126/science.1090704
- Mimche, Sylve, Ahn, Dukju, Kiani, Mehdi, Hassan, Elahi, Murray, Kyle, Kirk, Easley, et al. (2016). Tongue implant for assistive technologies: Test of migration, tissue reactivity and impact on tongue function. *Archives Oral Biol.* 71, 1–9. doi:10.1016/j.archoralbio.2016.06.019
- Montero, Jordan, Clemente, Francesco, and Cipriani, Christian (2021). Feasibility of generating 90 Hz vibrations in remote implanted magnets. *Sci. Rep.* 11 (15456), 1–14. doi:10.1038/s41598-021-94240-2
- Neptune, Richard R., Sasaki, Kotaro, and Kautz, Steven A. (2008). The effect of walking speed on muscle function and mechanical energetics. *Gait Posture* 28 (1), 135–143. doi:10.1016/j.gaitpost.2007.11.004
- Nonnekens, Jorik, Růžicka, Evžen, Serranová, Tereza, Reich, Stephen G., Bloem, Bastiaan R., and Hallett, Mark (2020). Functional gait disorders: A sign-based approach. *Neurology* 94 (24), 1093–1099. doi:10.1212/WNL.0000000000009649
- Rabe, Kaitlin G., and Fey, Nicholas P. (2022). Evaluating electromyography and sonomyography sensor fusion to estimate lower-limb kinematics using Gaussian process regression. *Front. Robotics AI* 9. Available at: <https://www.frontiersin.org/articles/10.3389/frobt.2022.716545>.
- Rainoldi, Alberto, Cescon, Corrado, Bottin, Andrea, Casale, Roberto, and Caruso, Ignazio (2004). Surface EMG alterations induced by underwater recording. *J. Electromyogr. Kinesiol.* 14 (3), 325–331. doi:10.1016/j.jelekin.2003.10.002
- Roberts, T. J., Marsh, R. L., Weyand, P. G., and Taylor, C. R. (1997). Muscular force in running turkeys: The economy of minimizing work. *Science* 275 (5303), 1113–1115. doi:10.1126/science.275.5303.1113
- Selvik, Göran (1974). Roentgen stereophotogrammetry: A method for the study of the kinematics of the skeletal system. *Acta Orthop. Scand.* 60 (232), 1–51. (reprinted, 1989). doi:10.3109/17453678909154184
- Sokoloff, Alan J., Yang, Zhongtao, Sargolzaei, Saman, Strait, Karen, Krasnopeyev, Andrey, Easley, Kirk A., et al. (2017). Magnetic implants in the tongue for assistive technologies: Tests of migration; oromotor function; and tissue response in miniature pigs. *Archives Oral Biol.* 81, 81–89. doi:10.1016/j.archoralbio.2017.04.034
- Tarantino, S., Clemente, F., Barone, D., Controzzi, M., and Cipriani, C. (2017). The myokinetic control interface: Tracking implanted magnets as a means for prosthetic control. *Sci. Rep.* 7 (17149), 1–11. doi:10.1038/s41598-017-17464-1
- Taylor, C. R., Abramson, H., and Herr, H. (2019). Low-latency tracking of multiple permanent magnets. *IEEE Sens. J.* 19 (23), 11458–11468. doi:10.1109/jsen.2019.2936766
- Taylor, C. R., Yeon, S. H., Clark, W. H., Clarrissimeaux, E. G., O'Donnell, M. K., Roberts, T. J., et al. (2022b). Untethered muscle tracking using magnetomicrometry. *Front. Bioeng. Biotechnol.* doi:10.3389/fbioe.2022.1010275
- Taylor, C. R., Srinivasan, S. S., Yeon, S. H., Roberts, T. J., and Herr, H. M. (2021). Magnetomicrometry. *Sci. Robot.* 6 (57), eabg0656. doi:10.1126/scirobotics.abg0656
- Taylor, C. R., Clark, W. H., Clarrissimeaux, E. G., Yeon, S. H., Carty, M. J., Lipsitz, S. R., et al. (2022a). Clinical viability of magnetic bead implants in muscle. *Prepr. Biorxiv.* doi:10.1101/2022.08.01.502296
- Taylor, C. R. (2020). Magnetomicrometry: Tissue length tracking via implanted magnetic beads. PhD thesis. Cambridge, MA: Massachusetts Institute of Technology.
- Vincent, H. K., Adams, M. C. B., Vincent, K. R., and Hurley, R. W. (2013). Musculoskeletal pain, fear avoidance behaviors, and functional decline in obesity: Potential interventions to manage pain and maintain function. *Reg. Anesth. Pain Med.* 38 (6), 481–491. doi:10.1097/AAP.0000000000000013
- Weir, R. F., Troyk, P. R., DeMichele, G. A., Kerns, D. A., Schorsch, J. F., and Maas, H. (2008). Implantable myoelectric sensors (IMESs) for intramuscular electromyogram recording. *IEEE Trans. Biomed. Eng.* 56 (1), 159–171. doi:10.1109/tbme.2008.2005942
- Yetisen, Ali K. (2018). Biohacking. *Trends Biotechnol.* 36 (8), 744–747. doi:10.1016/j.tibtech.2018.02.011
- Zajac, Felix E. (1989). Muscle and tendon: Properties, models, scaling, and application to biomechanics and motor control. *Crit. Rev. Biomed. Eng.* 17 (4), 359–411.
- Zhang, Qiang, Iyer, Ashwin, Sun, Ziyue, Kang, Kim, and Sharma, Nitin (2021). A dual-modal approach using electromyography and sonomyography improves prediction of dynamic ankle movement: A case study. *IEEE Trans. Neural Syst. Rehabil. Eng.* 29, 1944–1954. doi:10.1109/TNSRE.2021.3106900



OPEN ACCESS

EDITED BY

Suvash C. Saha,
University of Technology Sydney,
Australia

REVIEWED BY

Ariel Camp,
University of Liverpool, United Kingdom
Eric Diller,
University of Toronto, Canada

*CORRESPONDENCE

Thomas J. Roberts,
thomas_roberts@brown.edu
Hugh M. Herr,
hherr@media.mit.edu

[†]These authors share first authorship

[†]These authors share senior authorship

SPECIALTY SECTION

This article was submitted to
Biomechanics,
a section of the journal
Frontiers in Bioengineering and
Biotechnology

RECEIVED 02 August 2022

ACCEPTED 05 October 2022

PUBLISHED 25 October 2022

CITATION

Taylor CR, Yeon SH, Clark WH,
Clarrissimeaux EG, O'Donnell MK,
Roberts TJ and Herr HM (2022),
Untethered muscle tracking
using magnetomicrometry.
Front. Bioeng. Biotechnol. 10:1010275.
doi: 10.3389/fbioe.2022.1010275

COPYRIGHT

© 2022 Taylor, Yeon, Clark,
Clarrissimeaux, O'Donnell, Roberts and
Herr. This is an open-access article
distributed under the terms of the
[Creative Commons Attribution License](https://creativecommons.org/licenses/by/4.0/)
(CC BY). The use, distribution or
reproduction in other forums is
permitted, provided the original
author(s) and the copyright owner(s) are
credited and that the original
publication in this journal is cited, in
accordance with accepted academic
practice. No use, distribution or
reproduction is permitted which does
not comply with these terms.

Untethered muscle tracking using magnetomicrometry

Cameron R. Taylor^{1†}, Seong Ho Yeon^{1†}, William H. Clark²,
Ellen G. Clarrissimeaux¹, Mary Kate O'Donnell^{2,3},
Thomas J. Roberts^{2**} and Hugh M. Herr^{1**}

¹K. Lisa Yang Center for Bionics, Massachusetts Institute of Technology, Cambridge, MA, United States,

²Department of Ecology, Evolution, and Organismal Biology, Brown University, Providence, RI,
United States, ³Department of Biology, Lycoming College, Williamsport, PA, United States

Muscle tissue drives nearly all movement in the animal kingdom, providing power, mobility, and dexterity. Technologies for measuring muscle tissue motion, such as sonomicrometry, fluoromicrometry, and ultrasound, have significantly advanced our understanding of biomechanics. Yet, the field lacks the ability to monitor muscle tissue motion for animal behavior outside the lab. Towards addressing this issue, we previously introduced magnetomicrometry, a method that uses magnetic beads to wirelessly monitor muscle tissue length changes, and we validated magnetomicrometry *via* tightly-controlled *in situ* testing. In this study we validate the accuracy of magnetomicrometry against fluoromicrometry during untethered running in an *in vivo* turkey model. We demonstrate real-time muscle tissue length tracking of the freely-moving turkeys executing various motor activities, including ramp ascent and descent, vertical ascent and descent, and free roaming movement. Given the demonstrated capacity of magnetomicrometry to track muscle movement in untethered animals, we feel that this technique will enable new scientific explorations and an improved understanding of muscle function.

KEYWORDS

biomechanics, muscle tracking, implantable technology, wearable technology, motion tracking, magnetomicrometry, magnetic beads, magnet tracking

Introduction

Muscle length measurements have driven important discoveries in movement biomechanics (Fowler et al., 1993), informed models of motor control (Prilutsky et al., 1996; Roberts et al., 1997), and provided strategies for prosthetic and robotic design (Eilenberg et al., 2010). For decades, sonomicrometry (SM) has informed how muscles move, providing high accuracy (70 μ m resolution) and high bandwidth (>250 Hz) (Griffiths 1987). Fluoromicrometry (FM) expanded the muscle tracking toolkit, enabling high accuracy (90 μ m precision) and high bandwidth (>250 Hz) for high-marker-count tracking (Brainerd et al., 2010; Camp et al., 2016). Further, image-based ultrasound (U/S) added the capability to non-invasively track muscle geometries (Fukunaga et al., 2001; Sikdar et al., 2014; Clark and Franz, 2021).

Yet, collecting direct muscle length measurements in natural environments remains infeasible, and thus indirect muscle length estimation is still used for observing natural movements. For instance, muscle lengths are estimated using joint angles *via* biophysical models (Delp et al., 2007). These approximations are used due to the limitations of current muscle motion sensing techniques, all of which are tethered or bulky. SM and U/S both require tethered connections to bulky hardware for sensing (Biewener et al., 1998; Clark and Franz, 2021), with SM requiring advanced surgery and percutaneous wires. And while FM does not require a tethered connection, it is limited to a volume approximately the size of a soccer ball, requires equipment the size of a small room, and is time-constrained due to thermal limitations and subject radiation exposure (Brainerd et al., 2010).

Present muscle length tracking technologies also require substantial post-processing time, hindering their use in longitudinal studies. SM requires accounting for and filtering out artifacts such as triggering errors (Marsh 2016), FM requires point labeling in stereo images (Brainerd et al., 2010), and U/S requires fascicle labeling (Van Hooren et al., 2020), all of which require at least some manual processing. While machine learning techniques have shown potential for automatic fascicle length tracking from ultrasound images, the current lack of reliability in tracking cross-activity measurements ($R^2 = 0.05$ for single-subject cross-activity training of a support vector machine) prevents such a strategy from being applicable toward sensing fascicle lengths during natural movement (Rosa et al., 2021).

Researchers need a sensing platform that can operate untethered in natural environments, sensing the full dynamic range of muscle movement in context. To address this need, we developed magnetomicrometry (MM), a minimally-invasive strategy for portable, real-time muscle tracking. MM uses an array of magnetic field sensors to locate and calculate the distance between two implanted magnetic beads with sub-millisecond time delay. This distance provides a measurement of the muscle tissue length between the implanted beads. MM allows continuous recording over an indefinite collection interval extending across hours, with the potential for continuous use across days, weeks, or years.

In prior work, we validated the MM concept against FM *via* tightly controlled *in situ* tests (Taylor et al., 2021). However, it has not previously been empirically demonstrated that the MM technique is robust for recording during untethered locomotion. In the present study we address this question. We investigate the robustness of MM during untethered activity that exhibits soft tissue artifacts (i.e., movement of the magnetic field sensors relative to the muscle) and changes in the relative orientation of the ambient magnetic field.

Herein we present MM as a robust, practical, and effective strategy for measuring muscle tissue length in an untethered freely-moving animal model. We first apply this technique to turkeys running on a treadmill and compare MM to FM to

determine the method's accuracy. We then further investigate the use of MM to track muscle tissue length in freely-moving animals during ramp ascent and descent, vertical ascent and descent, and free roaming movement. We hypothesize that muscle tissue lengths during untethered motion can be tracked *via* MM with submillimeter accuracy and a strong correlation ($R^2 > 0.5$) to FM. Our validation of this tool in a mobile context enables tracking and investigation of muscle physiology in settings previously inaccessible to biomechanics researchers.

Results

Accuracy validation of magnetomicrometry against fluoromicrometry

To verify MM tracking accuracy during untethered activity, we tracked implanted magnetic bead pairs in turkey gastrocnemius muscles (right leg, three turkeys) using both MM and FM while the turkeys walked and ran at multiple speeds on a treadmill (see Figure 1 for the setup and tracking results, see Supplementary Figure S1 for a 3-D scan of the MM sensing array).

We compared the distances between the magnetic bead positions as measured by MM with their distances as measured by FM to evaluate accuracy during the treadmill activity (see Figure 2). The coefficients of determination (R^2 values) between MM and FM were 0.952, 0.860, and 0.967 for Birds A, B, and C, respectively (see also Supplementary Figure S2). The differences between MM and FM were -0.099 ± 0.186 mm, -0.526 ± 0.298 mm, and -0.546 ± 0.184 mm for Birds A, B, and C, respectively (see Supplementary Figure S3).

To determine the study-specific reliability of the manual FM processing (marker position labeling in the X-ray video data), ten gait cycles of raw FM data were independently manually relabeled three times for one bird at one speed. Across these three labelings for these ten gait cycles, manual FM processing was consistent to a standard deviation of 0.098 mm (see Supplementary Figure S4 for more details).

MM's 99-th percentile tracking time delays were 0.698 ms, 0.690 ms, and 0.664 ms for Birds A, B, and C, respectively (see also Supplementary Figure S5), and the MM data did not require any post-processing. In contrast, post-processing the FM data into marker-to-marker distances required approximately 84 manual processing hours spread across multiple months.

Untethered muscle tracking across various activities

To investigate the feasibility of using MM during dynamic, natural motion, we constructed a series of obstacles for the

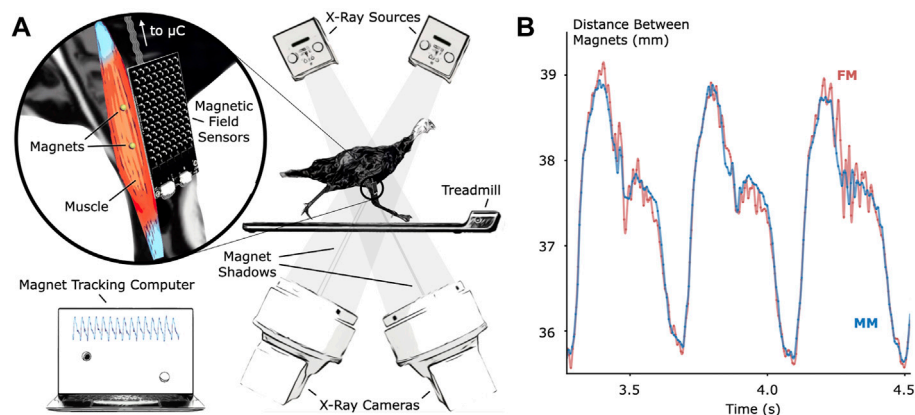


FIGURE 1

Validation of Untethered Muscle Tracking using Magnetomicrometry. (A) A magnetic field sensing array on the surface of the leg tracks the positions of two magnetic beads implanted into the muscle. A feather microcontroller (μC) in the turkey feathers wirelessly transmits the magnetic field data to a magnet tracking computer that calculates and displays the magnetomicrometry (MM) signal in real time. The turkeys walked and ran on a treadmill while x-ray video cameras recorded synchronized fluoromicrometry (FM) data for post-processing. (B) Comparison of MM (blue) with FM (red) to validate the MM accuracy. These representative results during running gait show the submillimeter accuracy of MM during untethered muscle length tracking.

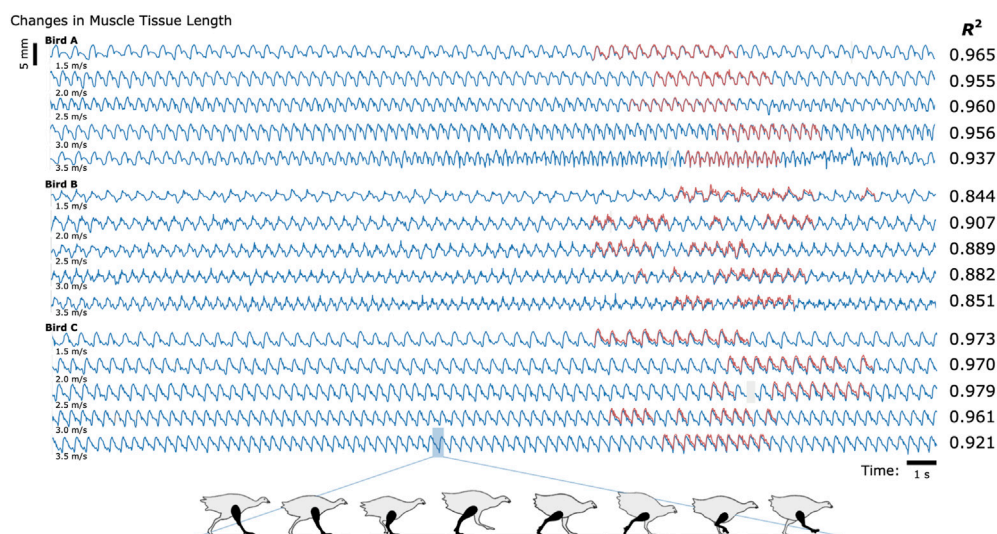


FIGURE 2

Untethered Muscle Tracking During Treadmill Running: Magnetomicrometry Versus Fluoromicrometry. Changes in muscle tissue length measured by MM (blue) and FM (red) for three turkeys at five speeds (30 s shown for each speed). The column to the right of the plots gives the coefficients of determination (R^2) between magnetomicrometry and fluoromicrometry corresponding to each turkey and speed. Gaps in the fluoromicrometry data are due to researcher selection of full gait cycles during which both magnetic beads were visible in both x-ray images. Gaps in the magnetomicrometry data (gray) are due to packet drops during which transmission of the magnetic field signals to the tracking computer (gaps below 50 ms interpolated in gray, gaps above 50 ms highlighted in gray). The turkey gait diagram below the plots shows the corresponding gait phases over one gait cycle.

turkeys to navigate. Specifically, we provided the turkeys with two ramp inclines (10° and 18° , see Figure 3) and three vertical elevation changes (20 cm, 41 cm, and 61 cm, see Figure 4). Because the purpose of these activities was to explore the

range of dynamic motions that could be captured, we did not train the birds to navigate the ramps or vertical elevation changes repetitively, and thus variability is expected within the repeated tasks.

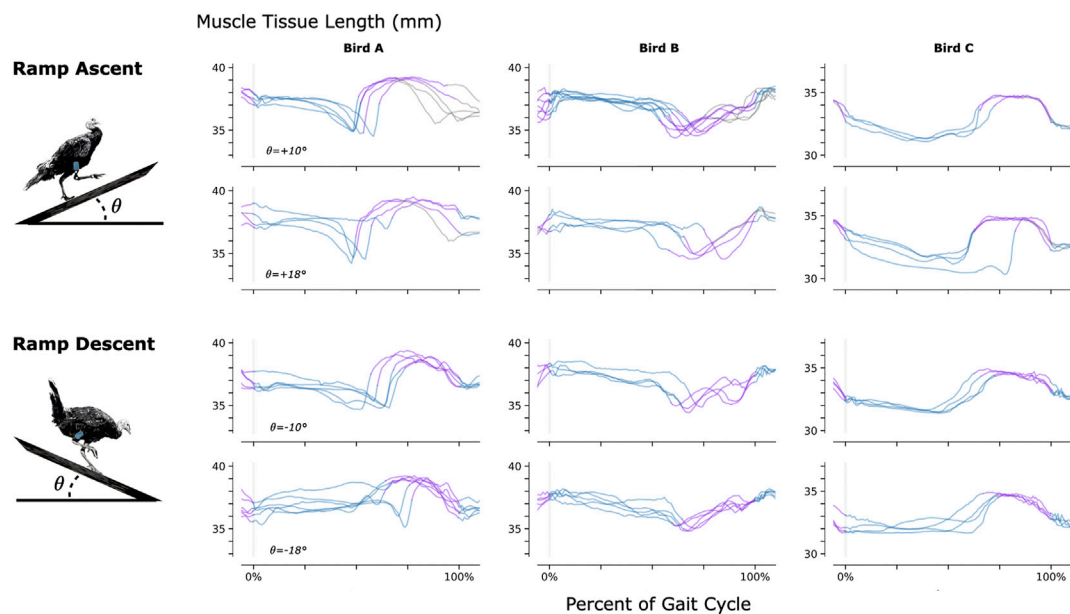


FIGURE 3

Muscle Tissue Length During Non-Synchronous Ramp Ascent and Descent. We used magnetomicrometry to track muscle tissue length during ramp ascent and descent at two inclines for all three birds. Data for each bird and each slope are synchronized at right leg toe strike (indicated by the vertical gray line) and normalized from toe strike to toe strike. Variability between curves reflects gait cycle variability during untrained ramp navigation. Muscle tissue length is plotted in blue for right leg stance, in purple for right leg swing, and in gray where video did not allow gait-phase labeling. We recorded at least three gait cycles of each activity for each bird.

For a video of one of the turkeys (bird A) navigating all of these obstacles with real-time MM data shown, see [Supplementary Movie S1](#).

To further validate the accuracy of MM used during navigation of ramps and vertical elevation changes, we analyzed the magnetic bead tracking data from these activities to find the range of the tracked three-dimensional magnetic bead positions (see [Supplementary Figure S6](#)). We then affixed two magnetic beads 40 mm apart, validated the distance between them using FM (40.000 ± 0.017 mm), and swept this FM-validated magnetic bead pair under the MM sensing array through a volume exceeding these ranges (see [Supplementary Figure S7](#)). We monitored deviations from 40 mm in the MM signal during these benchtop tests and found a 99-th percentile error ($e_{99\%}$) of 1.000 mm (rounded up to the nearest micrometer).

Finally, to explore whether untethered muscle tracking *via* MM is viable in a fully free roaming context, we tracked muscle tissue length while one turkey (Bird A) roamed freely about its enclosure. The results of this data collection are shown in [Figure 5](#).

Discussion

We find that MM enables untethered muscle tissue length tracking with high correlation to FM (R^2 of 0.952, 0.860, and 0.967 for Birds A, B, and C, respectively) and submillimeter

accuracy (AVG \pm SD of -0.099 ± 0.186 mm, -0.526 ± 0.298 mm, and -0.546 ± 0.184 mm for Birds A, B, and C, respectively). These findings enable tracking and investigation of muscle contractile behavior in settings previously inaccessible to biomechanics researchers.

Accuracy validation

The standard we used here to assess the accuracy of muscle length tracking using MM was FM. For magnets implanted superficially in muscles (at depths less than 2 cm), MM exhibits less noise than FM, but FM has the advantage of higher accuracy, especially at greater tissue depths (tracking depths in this study ranged from 11.2 mm to 26.6 mm). Indeed, our tests showed that for unobscured markers moving through the X-ray volume, FM was accurate to 0.030 mm. However, we note that marker tracking noise was a challenge for FM in this particular study due to the use of a large animal and the presence of hardware (the MM sensing array) that regularly obscured the markers during the tracking. These factors resulted in substantial manual labeling noise in the FM signal of 0.098 mm, instead of the 0.030 mm noise we found in our FM accuracy test, affecting the accuracy standard deviations reported above. Accounting for this manual labeling noise gives adjusted accuracy standard deviations of 0.158, 0.281, and

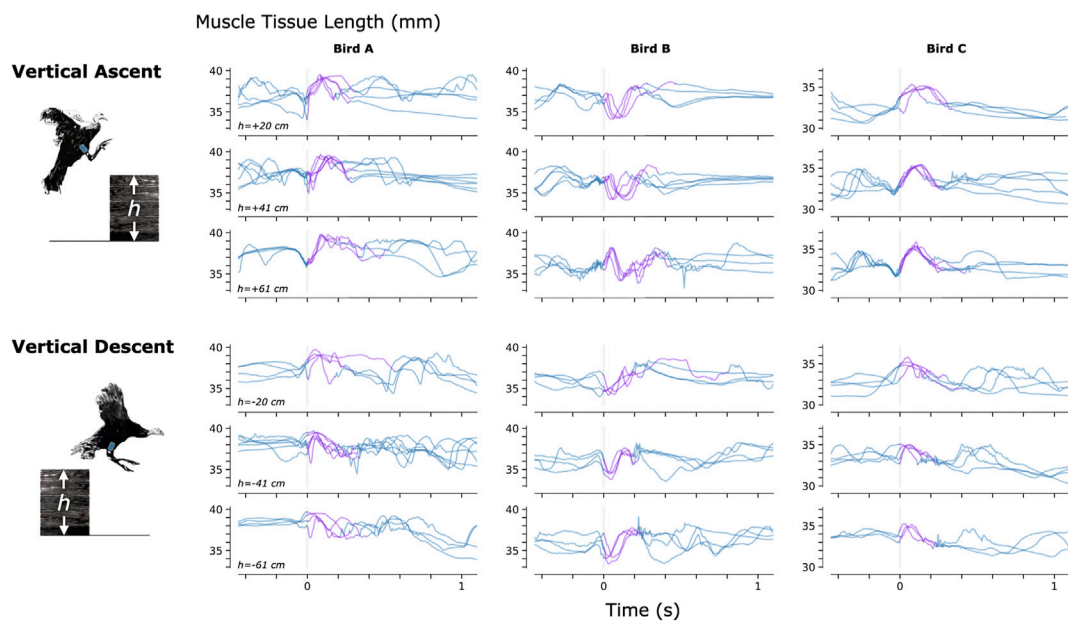


FIGURE 4

Muscle Tissue Length During Non-Synchronous Vertical Ascent and Descent. We used magnetomicrometry to track muscle tissue length during vertical ascent and descent at three heights for all three birds. Data for each bird and each height are synchronized at right leg toe-off (start of the aerial phase, indicated by the vertical gray line). Variability between curves reflects movement variability during untrained vertical ascent and descent. Muscle tissue length during contact with the ground is plotted in blue, and muscle tissue length during the aerial phase is plotted in purple. All data are shown, including scenarios in which significant wing-flapping occurred during jump up or down. We captured at least three recordings of each activity for each bird.

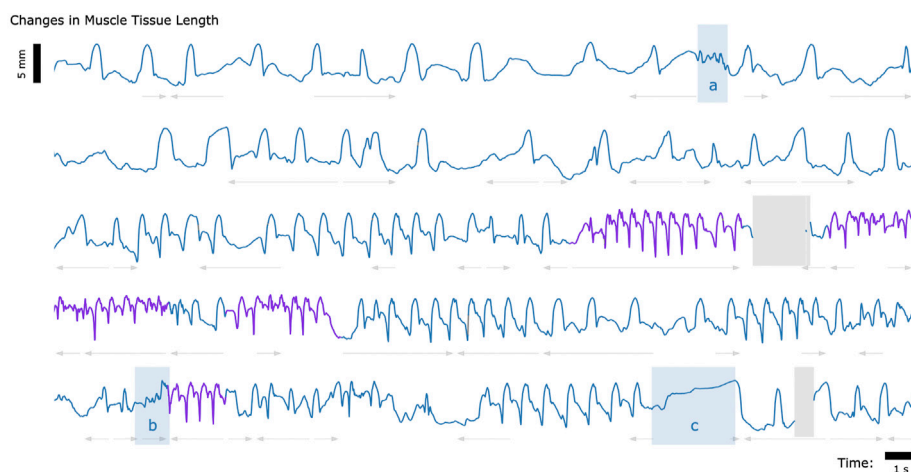


FIGURE 5

Muscle Tissue Length During Free Roaming Movement. Magnetomicrometry data was continuously collected for 150 s during free roaming activity. Muscle tissue length is plotted in blue during standing and walking and plotted in purple during running. Blue highlighted regions indicate muscle tissue length during (a) feather ruffling, (b) jumping, and (c) balancing on one leg. Gray arrows indicate when the turkey was turning left (left arrows) or turning right (right arrows). Gaps due to wireless transmission packet drops are shown in gray, as described in Figure 2.

0.156 mm, for Birds A, B, and C, respectively (see [Supplementary Figure S3](#)).

Constraints to imaging volume make FM impractical during large-animal variable terrain activity, so we performed retrospective benchtop accuracy testing to further validate the MM data collected during navigation of the ramps and vertical elevation changes (see [Supplementary Figure S7](#)). Soft tissue artifacts during dynamic movements, such as tissue deformation or movement, result in depth and position changes of the magnetic beads relative to the MM sensing array. The benchtop tests investigated the accuracy of the MM measurements across the range of depths and positions of the magnetic beads that we observed during those activities (see [Supplementary Figure S6](#)). The error we observed in the benchtop tests ($e_{99\%} < 1$ mm) was acceptable in comparison with the magnitude of the muscle contractions we observed during the variable terrain activity (average MM signal magnitude was 4.5 mm peak-to-peak). This suggests that MM robustly tracked the muscle tissue lengths during the variable terrain activities, despite any soft tissue artifacts that may have occurred during the dynamic movements required by those activities. These tests, however, highlight the importance of sensor placement. Higher accuracy is achieved when the MM sensing array is properly placed—centered over the implanted beads. MM with perfect magnetic field sensing would, in theory, be unaffected by movement of the board relative to the implanted beads, but the errors we observed suggest that the sensors are nonlinear. Magnet tracking nonlinearity compensation (e.g., *via* sensor calibration or three-dimensional sensor geometries) is thus an important area for future research. Meanwhile, in future work, larger sensing arrays with broader coverage would be advantageous to mitigate the need for careful placement of the array.

Ambient magnetic fields

The software-based magnetic disturbance compensation we employed here ([Taylor et al., 2019](#)) was sufficient to compensate for ambient magnetic fields during untethered muscle tracking in the presence of large hydraulic ferromagnetic lift tables, a large, active treadmill motor, and a room full of active X-ray equipment. However, our uniform disturbance compensation strategy may be insufficient for the exceptional situation where a large ferromagnetic object is immediately adjacent to (within a few centimeters of) the tracked muscle. Thus, software-based compensation for spatially-non-uniform ambient magnetic fields may still be a valuable direction for future work to extend the robustness of MM to that potential scenario. Alternatively, ferromagnetic shielding could be used to physically perform disturbance compensation ([Tarantino et al., 2017](#)), but the shield would need to be sufficiently far away to prevent it from acting like a magnetic mirror, creating “image” magnets

that would need to be tracked as well ([Hammond 1960](#)). Further, effective shielding would need to be thick enough to redirect most or all magnetic field disturbances, presenting a trade-off between the weight and the efficacy of the shielding.

Range of behaviors

[Figures 3–5](#) provide a sample of the range of behaviors that can be tracked using magnetomicrometry. Consistency in the curves was not strived for, expected, or desired. Rather, we intentionally preserved anomalous events in those data, such as single or multiple wing flaps during vertical ascent and descent and variable speed during ramp navigation, to explore the range of motor activities during which we could track the muscle activity.

Applications

MM has the potential to work across scales (see [Figure 6](#)), from the ability to track both full-body and muscle movement of small organisms to the ability to track large magnetic beads implanted deep into large animal models. Mathematically, if the number of sensors is fixed and all system dimensions are scaled, the error as a percent of scaled magnetic bead excursion will remain unchanged ([Taylor et al., 2019](#)). However, larger sensing arrays can in principle be used when tracking very small or very large animals, resulting in an increase in tracking accuracy at those extremes. For instance, when tracking small animal muscle tissue, additional sensors can be embedded into the animal’s environment, and when tracking large animal muscle tissue, the increased animal size accommodates the mounting of additional sensors to the animal. Thus, context-specific magnetic bead tracking systems can take advantage of the unique geometries afforded at each scale.

Not only can MM be used across size scales, but across time scales as well. Because there is no need for post-processing, MM data can be collected continuously, enabling the potential for longitudinal studies, including investigations into mechanisms such as neural degradation or plasticity over time.

MM’s muscle length and velocity signals are different from, and complementary to, the signals from electromyography (EMG). While EMG provides a measure of muscle activation, which results more directly from neural commands, muscle length and velocity give information on the shape of the muscle, which in turn can refine our understanding of muscle physiology during a given motion task. Indeed, the combination of MM and EMG will allow for increased physiological understanding in new contexts where animals are in their natural environments.

In parallel work, we also demonstrate the viability of magnetic bead implants for human use, verifying comfort,

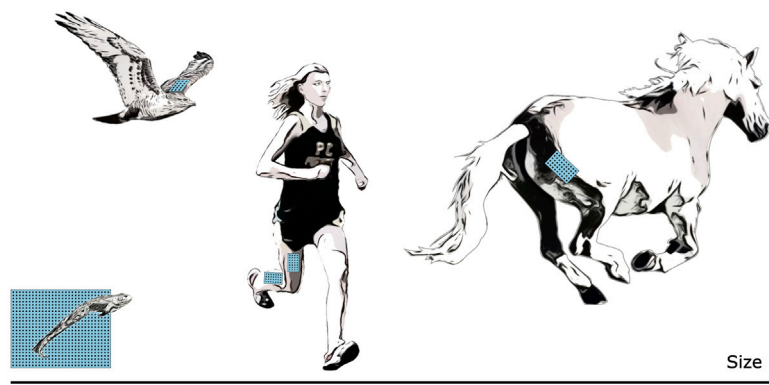


FIGURE 6

Muscle Tracking Across Scales. By changing the size of the magnetic field sensing array, we can track the distance between magnets at closer or farther distances, allowing us in principle to track muscle tissues at a range of scales, including frogs, hawks, persons, horses, or other animals. For small animals, such as the frog shown at bottom left, a fixed array below or beside the animal could track both the position of the animal and the muscle tissue length.

lack of implant migration, and biocompatibility (Taylor, Clark, et al., 2022). Due to the untethered nature of MM, this technique has applications in prosthetic and exoskeletal control. In its most straightforward implementation, a motor controller could directly control a robotic joint using the distance between two beads in each muscle of a flexor-extensor pair. However, the ability for MM to track additional muscles and to work in combination with EMG enables a range of new strategies for human-machine interfacing.

Limitations

In this study, we implanted the magnetic beads approximately 3.5 cm away from one another, based on previous work (Taylor et al., 2021), to ensure that the magnetic beads would not migrate toward one another. If smaller or larger (or differently shaped) magnetic bead implants are used (for instance, in a smaller or larger animal model), the effect of separation distance on stability against migration would need to be re-investigated for the different sizes (and different magnetization strengths) of the implants.

For the benchtop accuracy validation tests, we assumed that the tracked bead positions were a good approximation for the true bead positions. We used the magnetic bead position tracking information from the variable terrain MM data to determine the boundaries of the volume to test. Then, at the start of the tests, we used tracked bead positions to locate the centered, minimum-depth position (the closest position within the full scale range of the sensors), then used blocks of known dimensions to sweep through the benchtop-emulated tissue depth and enforce the volume boundaries. Noting that MM was accurate to within a millimeter

throughout the volume, we found these assumptions reasonable for these tests.

As for any muscle tissue tracking, the location of the implanted tracking devices will determine the length measured. For studies where the aim is to relate measured length changes to muscle contractile properties (e.g., length-tension or force-velocity relationships), it is essential that the markers are aligned along the fascicle axis. In the present study we embedded magnets at locations in the turkey muscles that would ensure the magnets stayed in place over a period of months, and at depths that were favorable for sensor function. Thus, patterns of length change do not directly represent patterns of muscle fascicle length change and can be influenced significantly by dynamic changes in muscle architecture during contraction. This is reflected in the opposite muscle tissue length changes seen during the swing phase of Bird B relative to Birds A and C during ramp navigation (see Figure 3). MM, FM, and SM all suffer from this same issue, and thus for any of these techniques, careful surgical placement is warranted.

Sensing improvements

The suite of electronics for MM is immediately upgradeable as new industry standards develop. The tracking system benefits from global developments in low-cost magnetic field sensors due to the widespread manufacturing of inertial measurement units for devices such as cell phones, video game controllers, and autonomous vehicles. Continuing improvements in magnetic field sensors, capacitors, and microcontrollers will cause direct improvements to the accuracy, efficiency and speed of the tracking system and will allow the tracking of even smaller implants at greater depths.

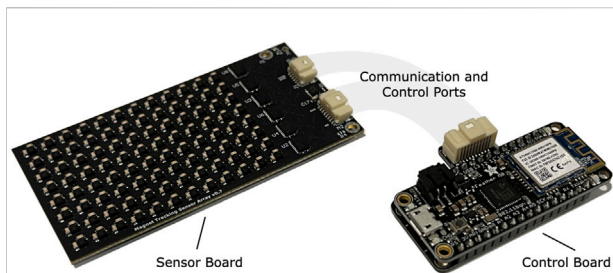


FIGURE 7

Magnetomicrometry Embedded System. We fabricated a custom sensor board (left) and a custom control board (right) for this study. The sensor board holds the magnetomicrometry sensing array, consisting of 96 magnetic field sensors arranged with a spacing of 5.08 mm. Digital multiplexers on the sensor board allow time-domain multiplexing, enabling a single microcontroller on the control board to communicate with and control all magnetic field sensors on the sensor board. The control board merges the data from the sensor board and streams the data wirelessly to the magnet tracking computer. The sensor board and control board weigh 24 g and 12 g, respectively.

Summary

Here, we demonstrate the use of MM for untethered muscle tracking. We validate, against FM, the submillimeter accuracy of MM in an awake, active turkey model ($R^2 \geq 0.860$, $\mu \leq 0.546$ mm, $\sigma \leq 0.298$ mm) with a real-time computing time delay of less than a millisecond ($\eta_{0.99} \leq 0.698$ ms). We further demonstrate the use of MM in untethered muscle tracking during ramp ascent and descent, vertical ascent and descent, and free roaming movement. These results encourage the use of MM in future biomechanics investigations, as well as in prosthetic and exoskeletal control. We hope that MM will enable a variety of new experiments and technologies, and we look forward to the further development and application of this technology.

Methods

All animal experiments were approved by the Institutional Animal Care and Use Committees at Brown University and the Massachusetts Institute of Technology. Wild turkeys (*Meleagris gallopavo*, adult female) were obtained from local breeders and maintained in the Animal Care Facility at Brown University on an *ad libitum* water and poultry feed diet. We used three animals in this study.

Surgical procedure

One pair of 3-mm-diameter Parylene-coated magnetic beads (N48SH) were implanted into the right lateral gastrocnemius muscle of each turkey, with a target magnetic bead separation distance of 3.5 cm. For details on the surgical procedure and

implants, see Taylor et al., 2022. A 1-month recovery period was given before the start of the data collection.

Magnetomicrometry

For this study, we designed a custom magnetic field sensing array (see Figure 7). The sensing array was equipped with 96 magnetic field sensors (LIS3MDL, STMicroelectronics) spaced 5.08 mm apart in an 8-by-12 grid. Each sensor was supplied with nonmagnetic capacitors (VJ1206Y105KCXAT and VJ0603Y104KCXAT, Vishay). Seven digital multiplexers on the sensing array allowed time-domain multiplexing (one 74HC138BQ,115 multiplexing into six 74HC154BQ,118, Nexperia) via a wired connection. The sensing array was connected through a custom adapter board to an off-the-shelf wireless microcontroller embedded system (Feather M0 WiFi microcontroller, Adafruit), which was powered by a lithium-ion polymer battery (3.7 V, 1800 mA-h, 29 g). The microcontroller sampled the magnetic field signals at 155 Hz and wirelessly transmitted them to the magnet tracking computer via a WiFi router (Nighthawk R6900P, Netgear). The tracking algorithm ran in real-time on the magnet tracking computer, a Dell Precision 5550 laptop (Ubuntu 20.04 operating system) with 64 GB of random-access memory and an Intel i7 8-Core Processor, running at 2.30 GHz. The tracking algorithm used, including the strategy for disturbance compensation, is fully-detailed in previous work (Taylor et al., 2019).

We affixed the sensing array to the limb using Opsite Flexifix adhesive film (Smith & Nephew). To secure the array, we first applied a base layer of the adhesive film to the skin. We then positioned the sensing array over the leg and wrapped the adhesive film around the sensing array and the leg. To maintain a sufficient minimum distance between the magnetic beads and the sensing array, we positioned layers of foam between the base adhesive and the array. We then secured the control board and battery within the back feathers of the turkey.

Accuracy validation of magnetomicrometry against fluoromicrometry

We used the W. M. Keck Foundation XROMM Facility at Brown University (Brainerd et al., 2010) to perform FM. We collected X-ray video from two intersecting X-ray beams oriented at 51 degrees relative to one another. We mounted a treadmill with a wooden base (TM145, Horizon Fitness) between the X-ray cameras and the X-ray sources and built a housing over the treadmill with a movable wall to position the birds within the capture window.

The turkeys walked and ran at five speeds (1.5, 2.0, 2.5, 3.0, and 3.5 m/s) in a randomized order until at least ten gait cycles

were visible within the FM capture volume for each speed. We collected FM data at 155 Hz.

Time syncing was performed *via* a coaxial cable connection from FM to an off-the-shelf microcontroller development board (Teensy 4.1, Adafruit). The time-syncing microcontroller relayed the time sync signal to the magnet tracking computer *via* a custom adapter board.

Untethered muscle tracking across various activities

We constructed a hallway to guide the turkeys through the variable terrain activities. We stacked plyometric boxes (Yes4All) in the hallway to heights of 20 cm, 41 cm, and 61 cm for vertical ascent and descent. Upon completion of the vertical ascent and descent tests, we placed ramps (Happy Ride Folding Dog Ramp, PetSafe) up to and down from the plyometric boxes at inclines of 10° and 18° for the turkeys to ascend and descend. Separate from the variable terrain activities, we then allowed one turkey (Bird A) to roam freely within its enclosure while we continued to record MM.

Benchtop magnetomicrometry validation for the variable terrain activity

For benchtop testing, we used super glue (Krazy Glue) to affix each of two N48SH magnetic beads into two 1 × 1 round LEGO plates. We attached these round LEGO plates to a 1 × 6 LEGO technic block, one at each end, to separate the pair of magnetic beads by a fixed distance of 40 mm (see [Supplementary Figure S7A](#)). We imaged this pair of beads using FM to validate the 40 mm fixed distance between them. Specifically, after the MM accuracy validation of two of the birds, we collected FM data with the magnet pair statically in the volume and used the average of the last 3 seconds from each of these two FM collections to confirm the distance between the two beads.

To determine the volume to sweep this FM-validated 40-mm-distanced bead pair during benchtop testing, we analyzed the magnetic bead tracking data from all ramps and vertical elevation changes to determine the full range of the three-dimensional magnetic bead positions relative to the MM sensing array across all three turkeys (see [Supplementary Figure S6](#)).

We first aligned and centered the magnet pair under the array, and we used the tracked magnet z-positions to place the magnets at the closest depth that was possible while still within the full-scale sensing range of the sensors (~1 cm). We then used 3.2-mm-thick 1 × 6 LEGO plates to enforce the remaining depths (see [Supplementary Figure S7A](#)). At each depth, we manually swept from center out and back along the *x* and *y* axes to the point where the farthest magnet reached just beyond the test

volume requirements derived from the variable terrain activity (see [Supplementary Figure S7B](#)).

Data analysis

We post-processed the FM data using XMA Lab ([Knörlein et al., 2016](#)). All FM and MM data were left unfiltered.

We aligned the MM and FM data using the time sync signal and linearly interpolated the FM data at the MM measurement time points. Then, due to imprecision of the time sync signal from the X-ray system, we used local optimization to further align the MM and FM signals while iteratively interpolating FM. During one trial (one data collection for one turkey at one speed), where the tracking computer did not receive a time sync, we used global optimization to align the MM and FM signals. To validate the use of global optimization for synchronization, we tested this same global optimization on all other trials and found that the global optimization successfully located all time sync signals.

We estimated the noise from manual FM processing by independently processing one set of ten gait cycles three times (manually re-processing the video data twice without reference to the previously processed data). We then calculated the variance at each time point and used the square root of the average variance as our estimate of the FM manual processing noise (see [Supplementary Figure S4](#)). We calculated the adjusted MM noise by subtracting the average variance of the FM manual processing noise from the variance of the difference between the MM and FM signals for each bird, then taking the square root.

In [Figure 3](#), for gait cycles where only one toe strike was visible in the video, we normalized the gait cycle using the timing of the peak MM signals in the previous and current gait cycles.

In [Supplementary Figure S7](#), all data are shown plotted as a scatterplot with a smoothing cubic spline approximation, using a smoothing parameter of 0.8 ([Boor, 1978](#)). The plotted standard deviation was calculated as the root-mean-square of the spline-adjusted values, also smoothed with a smoothing parameter of 0.8.

Data availability statement

All data needed to support the conclusions in the paper are included in the main text and [Supplementary Materials](#). In addition, the raw magnetomicrometry and processed fluoromicrometry data is available *via* Zenodo at <https://doi.org/10.5281/zenodo.6952783> ([Taylor et al., 2022a](#)).

Ethics statement

The animal study was reviewed and approved by the Institutional Animal Care and Use Committees at Brown University and the Massachusetts Institute of Technology.

Author contributions

CT developed the magnetomicrometry strategy, led the experimental conception and design, assisted in surgeries, performed data collection, documentation, and analysis, and led the manuscript preparation. SY designed, validated, and oversaw the fabrication of the magnetic field sensing embedded system, set up the WiFi-enabled real-time measurement framework, contributed to experimental conception and design, assisted in surgeries, performed data collection, documentation, and analysis, and contributed to manuscript preparation. WC, EC contributed to experimental conception and design, assisted in surgeries, performed data collection, documentation, and analysis, and contributed to manuscript preparation. MO contributed to experimental conception and design, assisted in surgeries, and contributed to manuscript preparation. TR contributed to experimental conception and design, led the surgeries, assisted in data collection and analysis, and contributed to manuscript preparation. HH conceived the magnetomicrometry strategy, oversaw project funding, assisted with general study management, contributed to experimental conception and design, assisted in data analysis, and aided in manuscript preparation.

Funding

This work was funded by the Salah Foundation, the K. Lisa Yang Center for Bionics at MIT, the MIT Media Lab Consortia, NIH grant AR055295, and NSF grant 1832795.

Acknowledgments

The authors thank, non-exhaustively, Elizabeth Brainerd, Andreas Burger, Ziel Camara, John Capano, Matthew Carty, Tyler Clites, Charlene Condon, Kathy Cormier, Jimmy Day, Bruce Deffenbaugh, Jennie Ehlert, Wendy Ehlert, Rachel Fleming, Lisa Freed, Robert Gnos, Deborah Grayeski, Alan Grodzinsky, Samantha Gutierrez-Arango, Ayse Guvenilir, Kale Hansen,

Mallory Hansen, Guillermo Herrera-Arcos, Crystal Jones, Kylie Kelley, Duncan Lee, Aimee Liu, Richard Marsh, Richard Molin, Chad Munro, Paris Myers, Jarrod Petersen, Mitchel Resnick, Lindsey Reynolds, Andy Robinson, Jacob Rose, Amy Rutter, Shriya Srinivasan, Erika Tavares, Sara Taylor and Beni Winet for their helpful advice, suggestions, feedback, and support. Inclusion in this list of acknowledgments does not indicate endorsement of this work. A preprint of this manuscript was deposited on bioRxiv (Taylor, Yeon, et al., 2022b).

Conflict of interest

CT, SY, and HH have filed patents on the magnetomicrometry concept entitled “Method for neuromechanical and neuroelectromagnetic mitigation of limb pathology” (patent WO2019074950A1) and on implementation strategies for magnetomicrometry entitled “Magnetomicrometric advances in robotic control” (US pending patent 63/104942).

The remaining authors declare that the research was conducted in the absence of any commercial or financial relationships that could be construed as a potential conflict of interest.

Publisher's note

All claims expressed in this article are solely those of the authors and do not necessarily represent those of their affiliated organizations, or those of the publisher, the editors and the reviewers. Any product that may be evaluated in this article, or claim that may be made by its manufacturer, is not guaranteed or endorsed by the publisher.

Supplementary material

The Supplementary Material for this article can be found online at: <https://www.frontiersin.org/articles/10.3389/fbioe.2022.1010275/full#supplementary-material>

References

- Biewender, A. A., Corning, W. R., and Tobalske, B. W. (1998). *In vivo* pectoralis muscle force-length behavior during level flight in pigeons (*Columba livia*). *J. Exp. Biol.* 201 (24), 3293–3307. doi:10.1242/jeb.201.24.3293
- Boor, C. D. (1978). *A Practical Guide to Splines*. 1st ed. New York, NY: Applied Mathematical Science/Springer. Available at: <https://link.springer.com/book/9780387953663>.
- Brainerd, E. L., Baier, D. B., Gatesy, S. M., Hedrick, T. L., Metzger, K. A., Gilbert, S. L., et al. (2010). X-ray reconstruction of moving morphology (XROMM): Precision, accuracy and applications in comparative biomechanics research. *J. Exp. Zool. A Ecol. Genet. Physiol.* 313A (5), 262–279. doi:10.1002/jez.589
- Camp, A. L., Astley, H. C., Horner, A. M., Roberts, T. J., and Brainerd, E. L. (2016). Fluoromicrometry: A method for measuring muscle length dynamics with biplanar videofluoroscopy. *J. Exp. Zool.* 325 (7), 399–408. doi:10.1002/jez.2031
- Clark, W. H., and Franz, J. R. (2021). Age-related changes to triceps surae muscle-subtendon interaction dynamics during walking. *Sci. Rep.* 11 (1), 21264. doi:10.1038/s41598-021-00451-y
- Delp, S. L., Anderson, F. C., Arnold, A. S., Loan, P., Habib, A., John, C. T., et al. (2007). OpenSim: Open-Source software to create and analyze dynamic simulations of movement. *IEEE Trans. Biomed. Eng.* 54 (11), 1940–1950. doi:10.1109/TBME.2007.901024
- Eilenberg, M. F., Geyer, H., and Herr, H. (2010). Control of a powered ankle-foot prosthesis based on a neuromuscular model. *IEEE Trans. Neural Syst. Rehabil. Eng.* 18 (2), 164–173. doi:10.1109/TNSRE.2009.2039620

- Fowler, E. G., Gregor, R. J., Hodgson, J. A., and Roy, R. R. (1993). Relationship between ankle muscle and joint kinetics during the stance phase of locomotion in the cat. *J. Biomechanics* 26 (4), 465–483. doi:10.1016/0021-9290(93)90010-C
- Fukunaga, T., Kubo, K., Kawakami, Y., Fukushima, S., Kanehisa, H., and Maganaris, C. N. (2001). *In vivo* behaviour of human muscle tendon during walking. *Proc. R. Soc. Lond. B* 268 (1464), 229–233. doi:10.1098/rspb.2000.1361
- Griffiths, R. I. (1987). Ultrasound transit time gives direct measurement of muscle fibre length *in vivo*. *J. Neurosci. Methods* 21 (2–4), 159–165. doi:10.1016/0165-0270(87)90113-0
- Hammond, P. (1960). Electric and magnetic images. *Proc. IEE C. Monogr. UK* 379, 306–313. doi:10.1049/pi-c.1960.0047
- Knörlein, B. J., Baier, D. B., Gatesy, S. M., Laurence-Chasen, J. D., and Brainerd, E. L. (2016). Validation of XMA Lab software for marker-based XROMM. *J. Exp. Biol.* 219 (23), 3701–3711. doi:10.1242/jeb.145383
- Marsh, R. L. (2016). Speed of sound in muscle for use in sonomicrometry. *J. Biomechanics* 49 (16), 4138–4141. doi:10.1016/j.jbiomech.2016.10.024
- Prilutsky, B. I., Herzog, W., and Allinger, T. L. (1996). Mechanical power and work of cat soleus, gastrocnemius and plantaris muscles during locomotion: Possible functional significance of muscle design and force patterns. *J. Exp. Biol.* 199 (4), 801–814. doi:10.1242/jeb.199.4.801
- Roberts, T. J., Marsh, R. L., Weyand, P. G., and Taylor, C. R. (1997). Muscular force in running turkeys: The economy of minimizing work. *Science* 275 (5303), 1113–1115. doi:10.1126/science.275.5303.1113
- Rosa, L. G., Zia, J. S., Inan, O. T., and Sawicki, G. S. (2021). Machine learning to extract muscle fascicle length changes from dynamic ultrasound images in real-time. *PloS One* 16 (5), e0246611. doi:10.1371/journal.pone.0246611
- Sikdar, S., Qi, W., and Cortes, N. (2014). Dynamic ultrasound imaging applications to quantify musculoskeletal function. *Exerc. Sport Sci. Rev.* 42 (3), 126–135. doi:10.1249/JES.0000000000000015
- Tarantino, S., Clemente, F., Barone, D., Controzzi, M., and Cipriani, C. (2017). The myokinetic control interface: Tracking implanted magnets as a means for prosthetic control. *Sci. Rep.* 7 (17149), 1–11. doi:10.1038/s41598-017-17464-1
- Taylor, C. R., Abramson, H. G., and Herr, H. M. (2019). Low-latency tracking of multiple permanent magnets. *IEEE Sens. J.* 19 (23), 11458–11468. doi:10.1109/jsen.2019.2936766
- Taylor, C. R., Clark, W. H., Clarrissimeaux, E. G., Yeon, S. H., Carty, M. J., Lipsitz, S. R., et al. (2022). Clinical viability of magnetic bead implants in muscle. *Front. Bioeng. Biotechnol.* doi:10.3389/fbioe.2022.1010276
- Taylor, C. R., Srinivasan, S. S., Yeon, S. H., O'Donnell, M. K., Roberts, T. J., and Herr, H. M. (2021). Magnetomicrometry eabg0656. *Sci. Robot.* 6 (57). doi:10.1126/scirobotics.abg0656
- Taylor, C. R., Yeon, S. H., Clark, W. H., Clarrissimeaux, E. G., O'Donnell, M. K., Roberts, T. J., et al. (2022b). Untethered muscle tracking using magnetomicrometry. *bioRxiv*. doi:10.1101/2022.08.02.502527
- Taylor, C. R., Yeon, S. H., Clark, W. H., Clarrissimeaux, E. G., O'Donnell, M. K., Roberts, T. J., et al. (2022a). Untethered muscle tracking supplementary materials. *Zenodo*. doi:10.5281/zenodo.6952783
- Van Hooren, B., Teratsias, P., and Hodson-Tole, E. F. (2020). Ultrasound imaging to assess skeletal muscle architecture during movements: A systematic review of methods, reliability, and challenges. *J. Appl. Physiology* 128 (4), 978–999. doi:10.1152/japplphysiol.00835.2019



OPEN ACCESS

EDITED BY

Zhen (Jeff) Luo,
University of Technology Sydney,
Australia

REVIEWED BY

Alessio Gizzi,
Campus Bio-Medico University, Italy
Kirill Vadimovich Nourski,
The University of Iowa, United States

*CORRESPONDENCE

Pengfei Rong,
rongpengfei66@163.com
Yin Liu,
liuyin99@foxmail.com

SPECIALTY SECTION

This article was submitted to
Biomechanics,
a section of the journal
Frontiers in Bioengineering and
Biotechnology

RECEIVED 05 May 2022

ACCEPTED 13 October 2022

PUBLISHED 26 October 2022

CITATION

Wei W, Du X, Li N, Liao Y, Li L, Peng S,
Wang W, Rong P and Liu Y (2022),
Biomechanical influence of T1 tilt
alteration on adjacent segments after
anterior cervical fusion.
Front. Bioeng. Biotechnol. 10:936749.
doi: 10.3389/fbioe.2022.936749

COPYRIGHT

© 2022 Wei, Du, Li, Liao, Li, Peng, Wang,
Rong and Liu. This is an open-access
article distributed under the terms of the
[Creative Commons Attribution License](https://creativecommons.org/licenses/by/4.0/)
(CC BY). The use, distribution or
reproduction in other forums is
permitted, provided the original
author(s) and the copyright owner(s) are
credited and that the original
publication in this journal is cited, in
accordance with accepted academic
practice. No use, distribution or
reproduction is permitted which does
not comply with these terms.

Biomechanical influence of T1 tilt alteration on adjacent segments after anterior cervical fusion

Wei Wei^{1,2}, Xianping Du³, Na Li¹, Yunjie Liao¹, Lifeng Li¹,
Song Peng¹, Wei Wang¹, Pengfei Rong^{1*} and Yin Liu^{1*}

¹Department of Radiology, The Third Xiangya Hospital, Central South University, Changsha, China, ²Postdoctoral Research Station of Clinical Medicine, The Third Xiangya Hospital, Central South University, Changsha, China, ³School of Marine Engineering and Technology, Sun Yat-Sen University, Guangzhou, China

Background: Anterior cervical fusion (ACF) has become a standard treatment approach to effectively alleviate symptoms in patients with cervical spondylotic myelopathy and radiculopathy. However, alteration of cervical sagittal alignment may accelerate degeneration at segments adjacent to the fusion and thereby compromise the surgical outcome. It remains unknown whether changes in T1 tilt, an important parameter of cervical sagittal alignment, may cause redistribution of biomechanical loading on adjacent segments after ACF surgery.

Objective: The objective was to examine the effects of T1 tilt angles on biomechanical responses (i.e. range of motion (ROM) and intradiscal VonMises stress) of the cervical spine before and after ACF.

Methods: C2–T1 FE models for pre- and postoperative C4–C6 fusion were constructed on the basis of our previous work. Varying T1 tilts of -10° , -5° , 0° , 5° , and 10° were modeled with an imposed flexion–extension rotation at the T1 inferior endplate for the C2–T1 models. The flexion–extension ROM and intradiscal VonMises stress of functional spinal units were compared between the pre- and postoperative C2–T1 FE models of different T1 tilts.

Results: The spinal segments adjacent to ACF demonstrated higher ROM ratios after the operation regardless of T1 tilt. The segmental ROM ratio distribution was influenced as T1 tilt varied and loading conditions, which were more obvious during displacement-control loading of extension. Regardless of T1 tilt, intradiscal VonMises stress was greatly increased at the adjacent segments after the operation. As T1 tilt increased, intradiscal stress at C3–C4 decreased under 30° flexion and increased under 15° extension. The contrary trend was observed at the C6–C7 segment, where the intradiscal stress increased with the increasing T1 tilt under 30° flexion and decreased under 15° extension.

Conclusion: T1 tilt change may change biomechanical loadings of cervical spine segments, especially of the adjacent segments after ACF. Extension may be more susceptible to T1 tilt change.

KEYWORDS

cervical spine, T1 tilt, fusion, finite element model, biomechanics

Introduction

Numerous studies have highlighted the importance of maintaining the sagittal balance of the spine after a fusion procedure, as indicated by the spinopelvic angle of the lumbosacral region and sagittal curvature of the cervical spine. Specifically, the sagittal balance of the spine after the procedure is closely related to clinical symptoms, surgical outcome, and health-related quality of life (Gum et al., 2012; Ryan et al., 2014; Jun et al., 2015; Liu et al., 2015). Unlike the more fixed spinopelvic structures, cervical sagittal alignment varies greatly (Yu et al., 2015; Diebo et al., 2016). It is still under discussion which parameter is better to define the cervical sagittal balance, due to the higher range of motion (ROM) and unique anatomical characteristics of the neck.

Considering the anchoring effect of the thoracic cage, the potential of T1 tilt in defining cervical sagittal balance has recently received more attention (Knott et al., 2010; Iyer et al., 2016). First described by Knott and others in 2010 (Knott et al., 2010), T1 tilt is defined as the angle between the plane of the superior endplate of the T1 vertebral body and the horizontal plane. Clinical (Iyer et al., 2016; Machino et al., 2016; Weng et al., 2016; Chen et al., 2017) and limited cadaveric (Hofler et al., 2020) studies have demonstrated the close correlation of T1 tilt with cervical lordosis angles and foramen height; they also showed that T1 tilt may be associated with accelerated degeneration and symptoms in aging population, as well as with postoperative prognosis. Yet, its importance may be underestimated as T1 may not be clearly shown on routine radiographic examination of the cervical spine. So far, it remains largely unknown whether and how T1 tilt modifies the biomechanical loadings of the cervical spine, let alone that under cervical decompression surgeries, such as anterior cervical fusion (ACF), which brings structural changes and alters the biomechanical loading pattern on this flexible region. These changes may lead to non-union at the operated segments and long-term complications at the adjacent segments (Klineberg et al., 2007; Tobert et al., 2017). Therefore, the biomechanical influence of T1 tilts on the adjacent segments after fusion surgeries remains to be clarified.

External biomechanical loadings and internal adaptation may contribute to changes in the sagittal balance of the spine. Similar to the lordosis angle, T1 tilt status may be influenced by various factors such as age, thoracic kyphosis, and neck-shoulder musculature tension (Ling et al., 2018). All these factors make it difficult to examine the *in-vivo* biomechanical influence of the T1 tilt change in a noninvasive way or separate it from other cervical sagittal balance parameters in both clinical and cadaveric experiments. Finite element (FE) modeling has been widely used not only to study the biomechanical alteration at the surgically treated vertebra under physiological (Palanca et al., 2021;

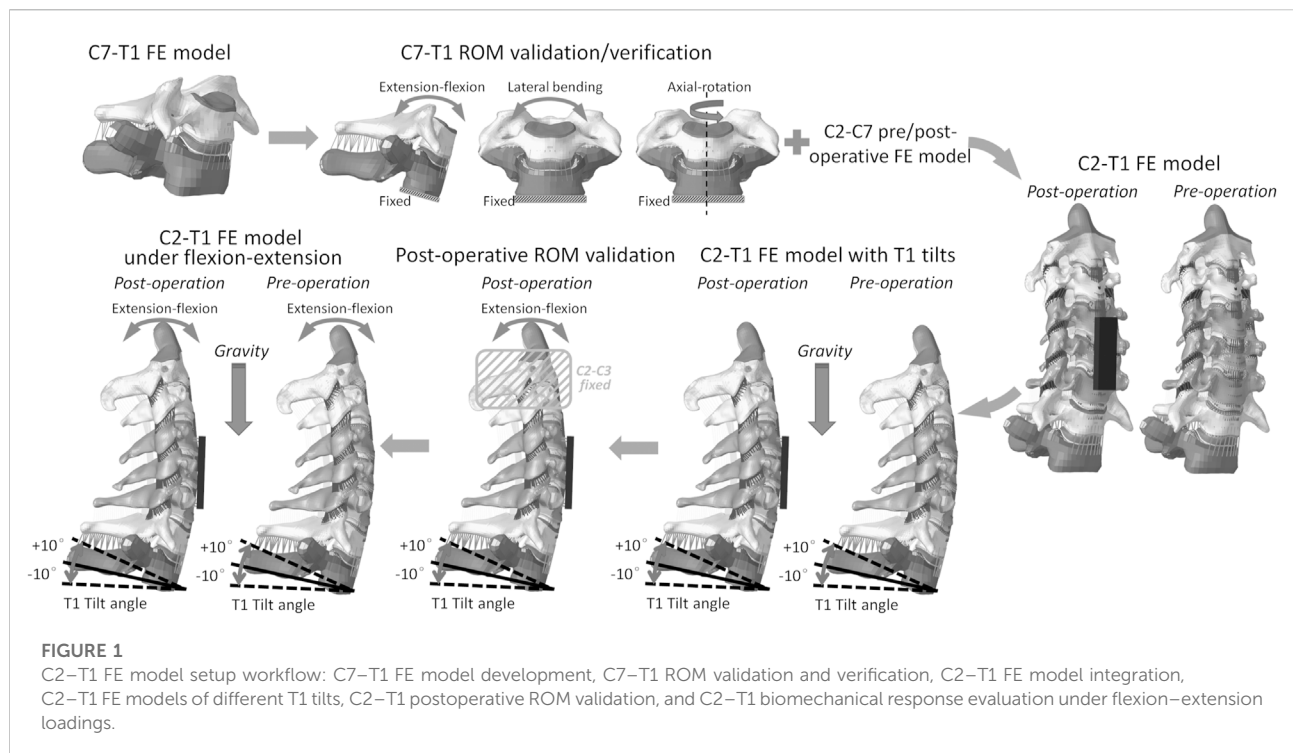
Dall'Ara and San Cheong, 2022) and pathological (Bianchi et al., 2022) conditions, but also detect loading variation at adjacent segment after ACF with different surgical approaches (Kumaresan et al., 1996; Hussain et al., 2013) or with different bone density (Natarajan et al., 2000). Our previous study (Liu et al., 2017a) with C2–C7 FE models demonstrated that a decrease in cervical lordosis could alter the biomechanical loading pattern at adjacent segments after C4–6 ACF and it may contribute to the development of adjacent segment pathology (ASP). However, the effect of lordosis increase was not studied, and the modeling setting indicated by the C2–C7 Cobb angle may bring bias for the middle part of the spine. T1 tilt may be a more precise parameter in defining cervical lordosis. Therefore, the objective of the present study was to further clarify how the neck biomechanical responses, including ROM and intradiscal stress, would transform with different cervical lordosis indicated by T1 tilts before and after ACF.

Materials and methods

C7–T1 FE model development and validation

The C2–C7 FE models were previously developed to study the effects of changes in cervical lordosis on adjacent segment biomechanical loading after ACF (Liu et al., 2017a) and to evaluate the risk of cervical ligament injuries in Sanda combat (Liu et al., 2017b). In brief, mesh convergence tests were first conducted to determine the mesh resolution of the C2–C7 FE model based on the VonMises stress on the vertebrae and intervertebral discs (Liu et al., 2017b). Material properties that were commonly used in other cervical spine FE models were also applied in our C2–C7 FE models (Liu et al., 2017a; Liu et al., 2017b). To verify the material property settings, the C2–C7 FE models for pre- and postoperative C4–C6 fusion were validated against the functional spinal unit (FSU) ROM under multiple loading levels in the directions of flexion, extension, lateral bending, and axial rotation (Liu et al., 2017a). The pre- and post-operative differences in biomechanical responses, including ROM and intradiscal VonMises stress, at adjacent segments were quantified under compression-bending loading to elucidate the adjacent segment pathology after ACF (Liu et al., 2017a). These C2–C7 FE models were further used here to evaluate the effect of T1 tilt on the adjacent segment biomechanical transition.

To study the effect of T1 tilt on adjacent segment biomechanical loading after ACF, we first developed and validated an FSU C7–T1 FE model. After validation, the model was integrated with the C2–C7 FE model. The geometry of T1 and the C7–T1 intervertebral disc was firstly



reconstructed from the CT and MRI dataset that had previously been used for the C2-C7 FE models (Liu et al., 2017b). Similar to our previous modeling procedure (Liu et al., 2017a; Liu et al., 2017b), the T1 vertebral body and C7-T1 disc were modeled with six-node hexahedral elements, while all the ligaments were modeled with tension-only truss elements. The same materials as in our previous works (Liu et al., 2017a; Liu et al., 2017b) were assigned to the corresponding model components (e.g., cortical and cancellous bone, endplate, annulus fibrosus, cartilage).

A pure moment of 0.5 Nm, 1.0 Nm, 1.5 Nm, 2.0 Nm, and 2.5 Nm was applied to the C7 superior endplate for flexion, extension, lateral bending, and axial rotation directions, while the T1 inferior endplate was fixed (Figure 1). The simulated C7-T1 ROMs in flexion and extension were then compared with the previous experimental measurements (Camacho et al., 1997; Wheeldon et al., 2006; Nightingale et al., 2007) for the model validation purpose. Since C7-T1 ROMs under loading143 control conditions were not found for lateral bending or axial rotation direction in the literature, the simulated ROMs in these two directions were reported here only for the model verification purpose.

C2-T1 model setup for different T1 tilts

The validated C7-T1 FE model was then assembled with our previously developed C2-C7 FE model (Liu et al., 2017a; Liu et al., 2017b) to construct the pre- and postoperative C2-T1 FE

models. To acquire C2-T1 FE models with different T1 tilts, the pre- and postoperative FE models were applied (Figure 1) with loading conditions similar to those in previous experimental tests (Hofler et al., 2020). The superior part of the C2 vertebral body was constrained and only allowed for horizontal and vertical translation. The inferior endplate of T1 was constrained and only allowed for the flexion-extension degree of freedom. An imposed flexion-extension rotation of -10° , -5° , 0° , 5° , and 10° was applied to the T1 inferior endplate to mimic T1 extension (negative), neutral (zero), and flexion (positive) tilt. A 5 kg mass was attached to the C2 superior endplate to mimic the weight of the head. In total, 10 FE models were constructed including pre- and postoperative C2-T1 with five different T1 tilt degrees (i.e. -10° , -5° , 0° , 5° , and 10°). The C2-C7 angle and sagittal vertical axis (SVA) were measured for each model when the model balance was reached under gravity loading, with the same method as described in (Hofler et al., 2020) and displayed in (Supplementary Figure SA1).

ROM validation for C2-T1 postoperative FE models

To further warrant the model bio-fidelity, the flexion-extension ROM of C2-T1 postoperative FE models with different T1 tilts was evaluated against published data under pure flexion-extension loadings (without gravity) (Aghayev et al., 2014; Hartmann et al., 2015). Similar to the experimental loading

conditions (Aghayev et al., 2014; Hartmann et al., 2015), T1 inferior endplate was fixed for all the degrees of freedom, while C2 and C3 vertebrae were rigidly attached to avoid relative motion during loadings (Figure 1). Pure moments of 1.5 Nm and 2.0 Nm in flexion-extension were applied to the C2 superior endplate of C2–T1 FE models with different T1 tilts. The flexion-extension ROM was measured for C4–C6 and C3–T1 segments and compared with the previously reported data (Aghayev et al., 2014; Hartmann et al., 2015). The flexion-extension ROM was calculated as the sum of flexion ROM and extension ROM.

T1 tilt effects on C2–T1 mobility and intradiscal loadings

The effects of T1 tilt on C2–T1 mobility were evaluated under moment-control and rotation-control loading conditions. In both conditions, the T1 inferior endplate was always fixed for all the degrees of freedom, while the C2 vertebral body was set free. For the moment-control simulations, a bending moment of -2.0 Nm, -1.0 Nm, 1.0 Nm, and 2.0 Nm was loaded to the C2 vertebral body. For the rotation-control simulations, a flexion of 30° and an extension of 15° (or equivalent to -15° flexion) were imposed on the C2 vertebral body. The gravity loading was always maintained in all of the simulations.

The FSU ROM was measured under each loading condition and compared between the pre- and postoperative C2–T1 models of different T1 tilts. The ROM ratios of the adjacent FSUs were also calculated by dividing the FSU ROMs by C2–T1 ROM. The intradiscal VonMises stress was extracted from the FE solid elements located in the anterior, posterior, left, and right regions of the annulus fibrosus. These biomechanical evaluations would also serve as a sensitivity analysis of fluctuations in mechanical loadings to the upper neck (i.e. C2) for pre- and postoperative models of different T1 tilts. All FE simulations in this study were performed with the explicit solver in LS-DYNA 971 R11.1 (LSTC. Livermore, CA, United States) on an Intel Xeon (2.20 GHz) workstation with 24 processors.

Statistical analysis

Levene's test ($p \leq 0.05$ as a statistically significant result) was used to verify whether the intradiscal VonMises stress complied with a normal distribution in pre- and postoperative models of different T1 tilts. When the normal distribution was verified, one-way analysis of variance (ANOVA) was used to compare the intradiscal VonMises stress between pre- and postoperative models of different T1 tilts and Tukey's honest significant difference (HSD) test was used for pairwise comparisons to identify the significance level of difference. Statistical significance was defined as a two-tailed p -value < 0.05 and the statistical analysis was performed with the software Rstudio 1.2 (Rstudio, Inc, Boston, MA, United States).

Results

ROM validation C2–T1 postoperative FE models

C2–T1 postoperative FE models were validated (in Figure 2) after the ROM validation of the C7–T1 under various rotation moments (see Supplementary Figure SA2). The C7–T1 flexion–extension ROMs (displayed in Supplementary Figure SA2) matched well with the reported data (Camacho et al., 1997; Wheeldon et al., 2006; Nightingale et al., 2007). The C7–T1 ROM was 2.0° – 3.8° with a lateral bending moment of 0.5 – 2.5 Nm, and 3.1° – 6.6° with an axial rotation moment of 0.5 – 2.5 Nm (displayed in Figure A2B). C2–T1 postoperative FE models with T1 tilts of -10° , -5° , 0° , 5° , and 10° were validated against previous studies (Aghayev et al., 2014; Hartmann et al., 2015), as displayed in Figure 2. The flexion–extension ROMs of the operated segment C4–C6 were within the reported experimental range (0.3° – 8.8°) (Hartmann et al., 2015) when the T1 tilt was between -5° and 5° . The C4–C6 flexion–extension ROMs were about 1.1° higher than the reported upper border when the T1 tilt was $\pm 10^\circ$ (Hartmann et al., 2015). C3–T1 ROMs with all T1 tilts were well within the reported rotation range (37.3° – 64.9°) (Aghayev et al., 2014).

SVA and C2–C7 angle with varying T1 tilts under gravity

The C2–C7 SVA increased with the increasing T1 tilt under gravity for both preoperative (0.1° – 16.9°) and postoperative (-0.1° – 18.2°) C2–T1 models (Table 1). When T1 tilt was -10° and -5° , the preoperative SVA was 0.2 – 1.9 mm higher than the postoperative SVA. When T1 tilt was 0° – 10° , the preoperative SVA was 1.1 – 1.4 mm lower than the postoperative SVA. Similarly, the pre- and postoperative C2–C7 Cobb angles also increased with the increasing T1 tilt. The C2–C7 Cobb angle changes between pre- and post-operative were below 2.4% and less obvious than SVA changes.

ROM change with varying T1 tilts under moment control

The ROM ratios of the adjacent FSUs, which were calculated by dividing the FSU ROMs by C2–T1 ROMs, are displayed in Figure 3. With the increasing T1 tilt, the ROM ratios of C2–C3 and C3–C4 decreased under flexion loadings and increased under extension loadings for both the pre- and post-operative models. In contrast, as T1 tilt increased, the ROM ratios of C7–T1 increased under flexion loadings and decreased under extension loadings for both the pre- and postoperative models. The effects of T1 tilt on the ROM ratios of lower FSUs (i.e., C6–C7 and C7–T1) were less significant than

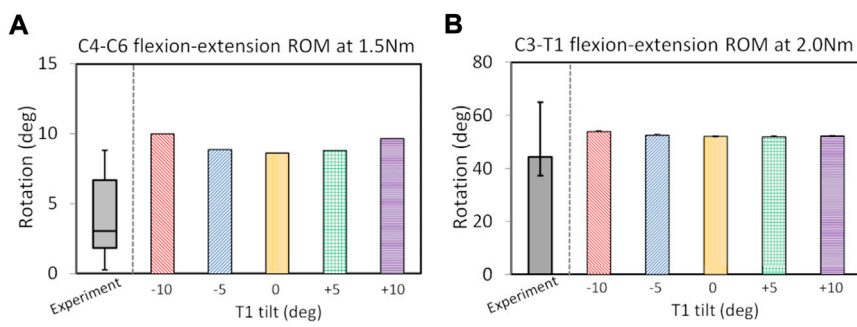


FIGURE 2
ROM validation under pure flexion-extension loadings for postoperative C2-T1 FE models of different T1 tilts against experimental measurements: for C4-C6 segment (A) and C3-T1 segment (B). The boxplot in (A) depicts the minimum, 25% percentile, median, 75% percentile and maximum values from (Hartmann et al., 2015); the error bar plot in (B) depicts the 25% percentile, median and 75% percentile values from (Aghayev et al., 2014).

TABLE 1 Cervical SVAs and C2-C7 angles measured in the pre- and post-operative C2-T1 FE models of different T1 tilts.

T1 tilt (°)	Preoperative					Postoperative				
	-10	-5	0	+5	+10	-10	-5	0	+5	+10
SVA (mm)	0.1	6.1	8.6	12.4	16.9	-0.1	4.2	9.7	13.8	18.2
C2-C7 angle (°)	11.6	17.2	22.2	27.1	32.1	11.7	16.8	22.1	27	32

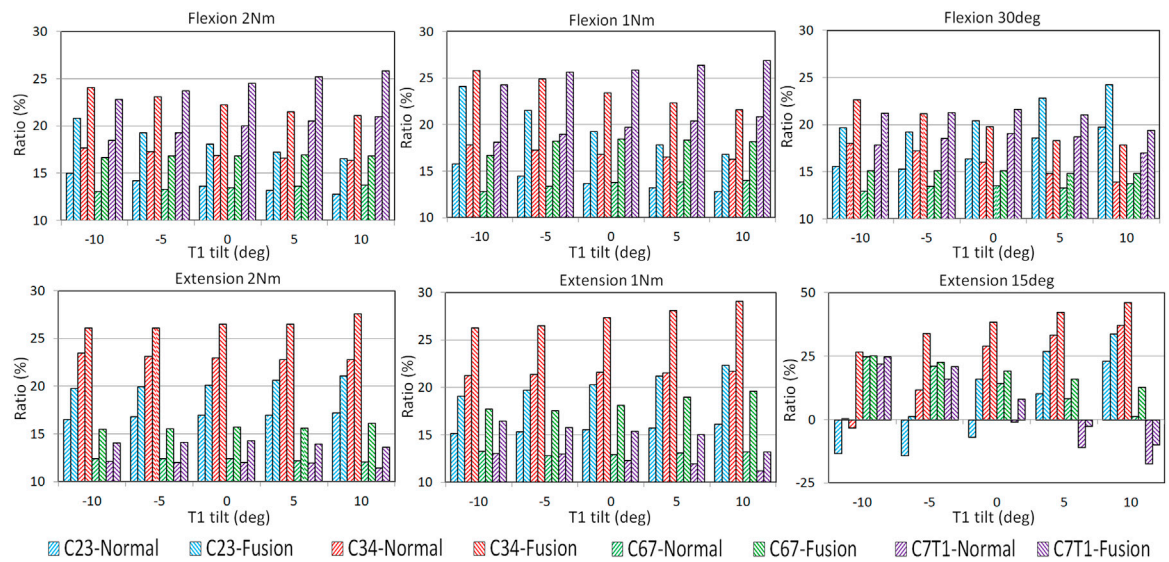


FIGURE 3
FSU ROM ratios of pre- and post-operative C2-T1 FE models with different T1 tilts under flexion and extension loadings.

the effects on the ROM ratios of upper FSUs (i.e., C2–C3 and C3–C4) for pre- and postoperative models (Figure 3; Supplementary Tables SA1, SA2).

For all T1 tilts, post-operative segmental ROM ratio was increased at the adjacent FSUs than pre-operative, resulting from the limited mobility of the operated C4–C6 segment (Figure 3). For flexion, the greatest increase of the post-operative ROM ratio was located at C2–C3 with -10° T1 tilt (53.2% under 1Nm and 38.6% under 2 Nm). For extension, the greatest increase of the post-operative ROM ratio was located at C6–C7 with 10° T1 tilt (48.5% under 1 Nm and 33.9% under 2 Nm).

ROM change with varying T1 tilts under rotation control

Similar to moment-control loadings, the adjacent FSUs sustained higher ROMs after operation regardless of T1 tilt. Under rotation-control loadings, T1 tilt alteration showed a greater influence on post-operative motion distribution under extension than flexion.

Under the 30° flexion loading, the segmental increase of ROM ratio was more obvious at upper adjacent segments (ranging from 22.6% at C2–C3 with 5° T1 tilt to 28.8% at C3–C4 with 10° T1 tilt) than in the lower adjacent segments (ranging from 7.2% at C6–C7 with 10° T1 tilt to 18.4% at C7–T1 with -10° T1 tilt).

Under the 15° extension loading, the ROM ratios of C2–C3 and C3–C4 increased with increasing T1 tilts for both the pre- and postoperative models. In contrast, the ROM ratios of C6–C7 and C7–T1 decreased with increasing T1 tilts for both the pre- and postoperative models. Under the 15° extension loading, C2–C3 of the preoperative models with -10° to 0° T1 tilts and C3–C4 of the preoperative model with -10° T1 tilt had a flexion rotation to compensate for the cervical extension rotation. This compensation trend was also observed at C7–T1 for the preoperative models with 0° – 10° T1 tilts and the postoperative models with 5° – 10° T1 tilts. The greatest post-operative ROM ratio increase was at C3–C4 with -10° T1 tilt (909.1%) and at C6–C7 with 10° T1 tilt (884.6%), and the lowest increase of ROM ratio was at C6–C7 with -10° T1 tilt (1.6%) and at C6–C7 with -5° T1 tilt (7.1%).

Intradiscal stress change with varying T1 tilts under rotation control

The intradiscal maximal stress concentration was markedly increased at both adjacent segments after fusion for any T1 tilt angle (Figures 4, 5). Compared with the intact models, the average intradiscal stress of C3–C4 and C6–C7 was always higher after C4–C6 fusion at all the four (i.e., anterior, posterior, left, and right) regions under 30° flexion and 15° extension loadings (Figures 4–7). The difference in intradiscal

stress was significant before and after the operation for the C3–C4 anterior region with all T1 tilts under flexion of 30° and with -5° to 10° T1 tilts under the extension of 15° (Figures 6, 7). The difference in intradiscal stress was significant for the C3–C4 posterior region with -10° to -5° T1 tilts under 30° flexion and with all T1 tilts under 15° extension (Figures 6, 7). The anterior and posterior regions of C6–C7 annulus fibrosus also sustained significantly higher stress after operation under flexion of 30° for all T1 tilts and under the extension of 15° for -5° to 5° T1 tilts (Figures 6, 7). The lateral (i.e., left and right) regions of the C3–C4 intervertebral disc always had significantly higher stress after operation for all T1 tilts under 15° extension, while the difference was not significant for the lateral regions of the C6–C7 intradisc under this loading (Figures 6, 7).

As T1 tilt increased, the stress at the four regions of C3–C4 annulus fibrosus decreased under the flexion of 30° and increased under the extension of 15° in both pre- and postoperative models. An opposing trend was observed at the C6–C7 segment; namely, the stress at the four regions of C6–C7 annulus fibrosus increased with the increasing T1 tilt under the flexion of 30° and decreased under the extension of 15° .

Discussion

This study demonstrated that the T1 tilt change may significantly influence the biomechanical loading pattern of the cervical spine both before and after ACF, especially during the rotation-control loading of extension movement, after validation of all the post-fusion models with previously published cadaveric studies (Aghayev et al., 2014; Hartmann et al., 2015). To the best of our knowledge, this is the first study on the effect of T1 tilt change on postoperative biomechanical response of the adjacent segments, which may help to understand the effect of T1 tilt on maintaining the posture and optimizing the biomechanical loading of the cervical spine.

Biomechanical loadings may be modified at the adjacent segment post-arthrodesis, as the pressure and strain exerted on the adjacent level may be altered, which is a likely cause of ASP after surgery. Significant increases were indeed observed for the ROM (Prasarn et al., 2012) and intradiscal pressure (Eck et al., 2002) at the adjacent segment post-arthrodesis while insignificant difference was also noted at these segments in other studies (Fuller et al., 1998; Rao et al., 2005). On the basis of our previous study (Liu et al., 2017a), our current study studied more comprehensive status of lordosis change as indicated by T1 tilt alteration. In this study, the ROM of the fused segments (i.e., C4–C6) decreased, while the ROMs of the adjacent segments increased under both the moment-control and rotation-control loadings, regardless of T1 tilt. However, the ROM and intradiscal strain distribution at adjacent segment varied greatly among post-operative models with varying T1 tilts in our study, which were in agreement with these previous *in-*

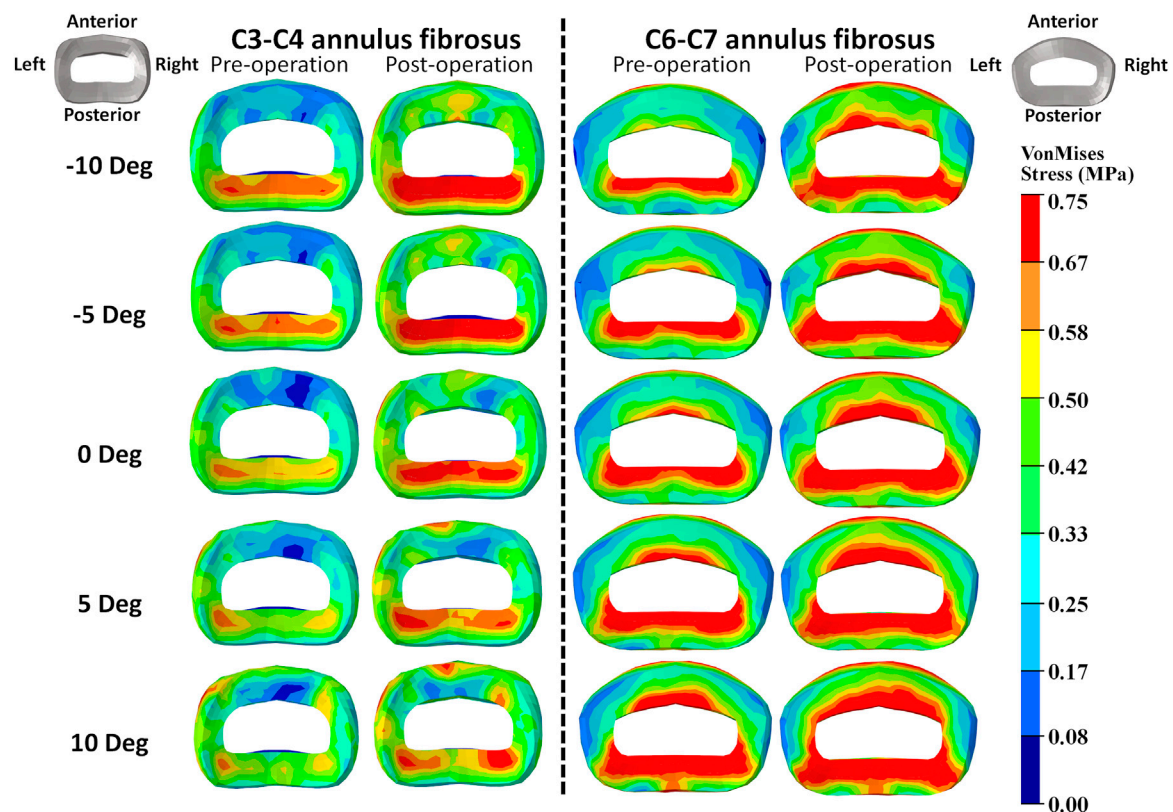


FIGURE 4
Annulus fibrosus VonMises stress distribution of C2–T1 pre- and postoperative FE models with different T1 tilts under the 30° flexion loading.

vitro studies (Fuller et al., 1998; Fuller et al., 1998; Rao et al., 2005; Rao et al., 2005). Considering the fact that T1 tilt or cervical lordosis has rarely been mentioned in previous studies, this may be one contributing factor for previous discrepancies observed among *in-vitro* studies.

Interestingly, the variance of postoperative biomechanical response among different T1 tilts seemed to be more obvious in extension. This was in agreement with some clinical studies. Change in T1 tilt has been found to be associated with aging and clinical symptoms (Machino et al., 2016; Weng et al., 2016). In a large cohort study by Machino et al. (2016), the extension ROM of the cervical spine decreased significantly in patients with cervical spondylotic myelopathy during aging, but the flexion ROM showed no significant changes. Although the degree of T1 tilt was not mentioned in that cohort (Machino et al., 2016), cervical lordosis significantly increased with aging. In addition, the upper segments (i.e., C2–C4) exhibited a flexion movement in the rotation-control loading of extension with -10° to 0° T1 tilts, while the lower segments (i.e., C7–T1) exhibited a flexion movement with 0° – 10° T1 tilts. A similar phenomenon was also reported by Tamai et al. (2018). In their study, the T1 segmental motion of 145 patients was examined using an MRI

kinematic analysis. A cervical rotation opposite to the direction of loadings occurred in 20% of patients who could still keep their head position stable during flexion-extension. It is unknown why the extension was more susceptible to the sagittal alignment change and what this compensatory segmental movement could mean in a clinical scenario. It has been postulated by Machino et al. (2016) that the compromised function of musculature at the posterior neck might play a role, but musculature was not included in our study. Therefore, we assume that it may be associated with the relatively decreased space at the posterior column caused by cervical spine hyperlordosis and resulting in greater resistance during extension. These findings also indicated that a full range of extension should be avoided in ACF patients to alleviate the greater biomechanical loading change at adjacent segments, especially in those with increased T1 tilt or hyperlordosis, compared with the same range of flexion.

Parameters of sagittal balance, such as C2–7 Cobb angle, SVA, and T1 tilt were closely correlated with each other, and it was difficult to clearly discriminate the relationship among them (Ling et al., 2018). Most of the studies on cervical sagittal balance were clinical observational studies. Only one cadaveric experiment of Hofler et al. (2020) reported that T1 tilt was

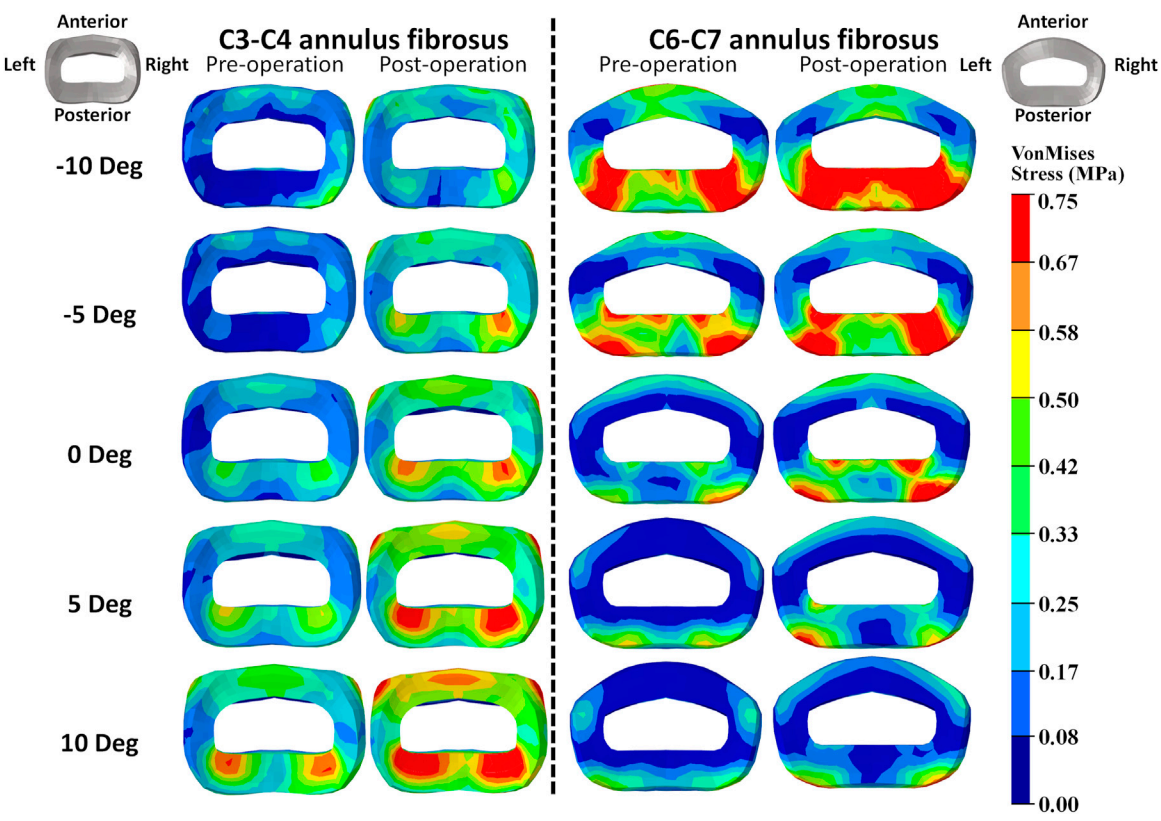


FIGURE 5
Annulus fibrosus VonMises stress distribution of C2–T1 pre- and postoperative FE models with different T1 tilts under 15° extension loading.

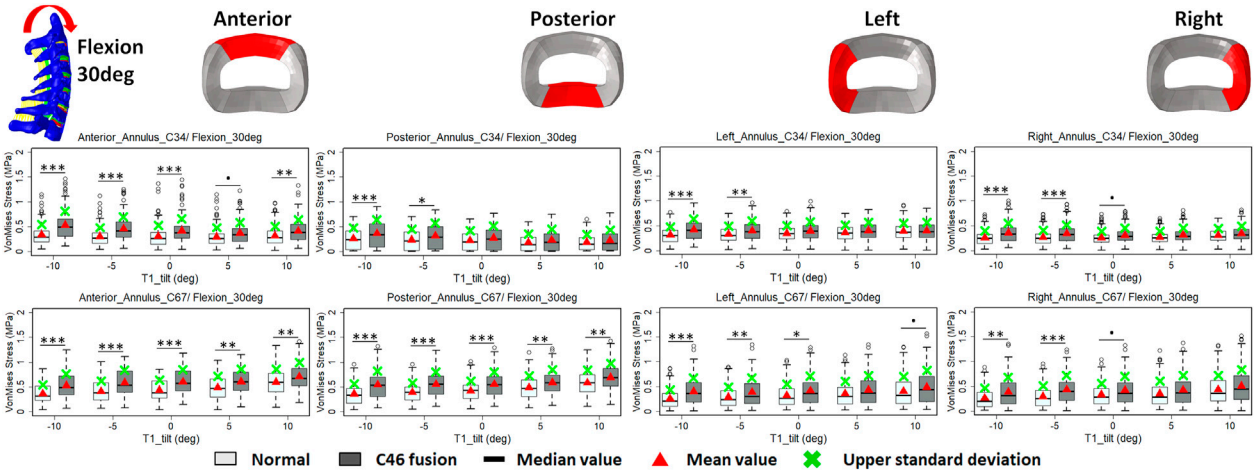
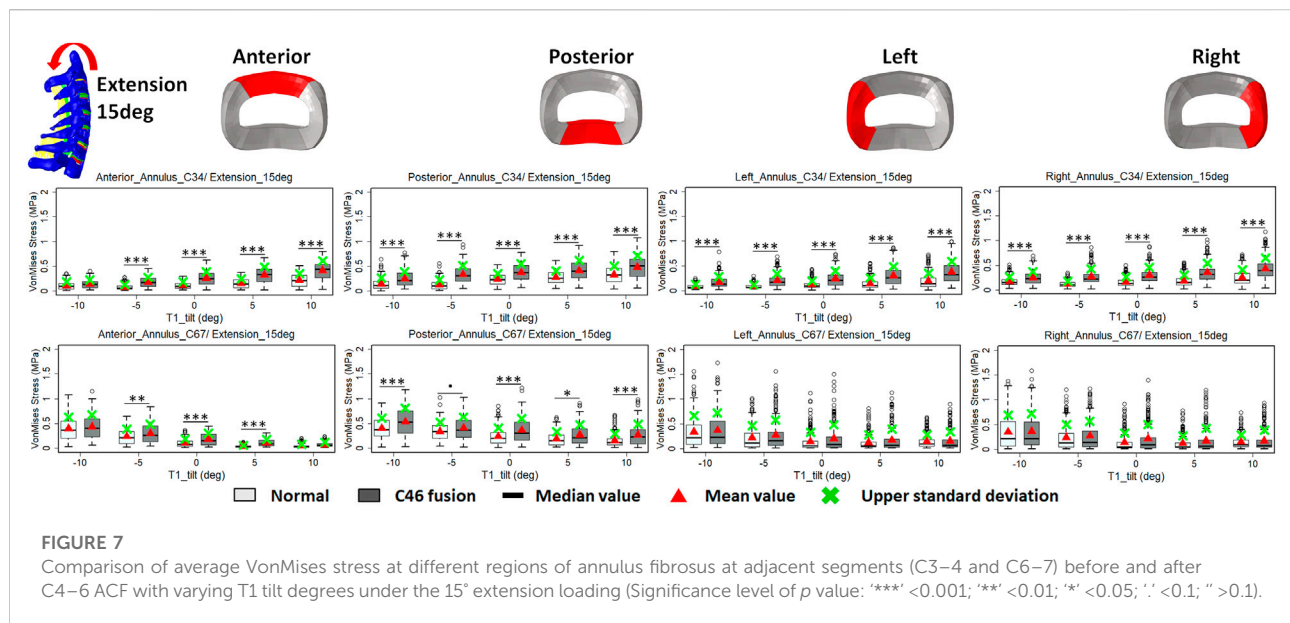


FIGURE 6
Comparison of average VonMises stress at different regions of annulus fibrosus at adjacent segments (C3–4 and C6–7) before and after C4–6 ACF with varying T1 tilt degrees under the 30° flexion loading (Significance level of p value: **** < 0.001 ; ** < 0.01 ; * < 0.05 ; ' < 0.1 ; ' > 0.1).



closely associated with cervical SVA (CSVA) and lordosis, but their study did not examine the effect of T1 tilt change in ACF. Our study was in well agreement with Hofler et al. (2020), and our results indicated that ACF may bring slightly more influence to SVA than C2–C7 Cobb angle. However, it remains unclear which one, lordosis or SVA, is the initiating factor for a cervical sagittal alignment change. The cause of the alignment change remains to be explored.

There were limitations to this study. First, as the study mainly focused on the biomechanical load distribution of the cervical spine, the head and upper cervical spine (C0–C1) were not included in our current models; thus, the influence of these structures was not considered. Second, the musculature was not included in the current FE models, as the muscles can be greatly different in dimensions or mechanical properties among the population. Consequently, the effect of the musculature in maintaining spinal alignment and stability was not considered. Similarly, individual variations such as the osseous microstructure and morphological differences were not considered in this study, which may cause local alterations or redistribution of loading patterns. Future modeling may be improved by including these comprehensive structures (i.e. C0–C1, musculature, and osseous microstructures) with varying tissue properties. The intradiscal loadings of the neck were examined in terms of VonMises stress as done in many previous studies. Yet, it would be interesting to quantify the maximal principal stresses in the intervertebral discs to predict the probability of intervertebral disc injuries under certain loadings. In addition, our study was based on FE models with a relatively normal cervical curvature influenced by T1 tilt change under physiological motions. We assumed that the physiological loadings (the flexion-extension moment up to 2.5 Nm or a rotation up to 30°) should not lead to vertebral fractures or tissue failures. Yet, this assumption needs to be

verified for the normal cervical curvature and other pathological curvatures (e.g. sigmoid curvature and kyphosis) when our future models are validated against spinal fracture loading conditions.

In summary, our results demonstrated that a change in sagittal balance may lead to a change in biomechanical loadings across cervical spine segments, especially at the adjacent segments after ACF. Cervical extension movement was more susceptible to cervical sagittal alignment change. The effects of cervical sagittal alignment on the flexibility and intradiscal loadings of the neck should be considered for presurgical planning for patients with cervical sagittal imbalance.

Data availability statement

The raw data supporting the conclusions of this article will be made available by the authors, without undue reservation.

Ethics statement

Written informed consent was obtained from the individual(s) for the publication of any potentially identifiable images or data included in this article.

Author contributions

RP, LY, Wang. W, and Wei. W designed the study, Wei W, LN and DX developed the model and finished the simulation, LY, LL, PS and Wei W collected the data, Wei W and LY analyzed the data, LY, RP, and Wei W co-wrote the manuscript.

Funding

This study was supported by the Key Research and Development Program of Hunan Province (2022SK2025), the Youth Project of Hunan Provincial Natural Science Foundation (2018JJ3799) and the New Xiangya Talent Project of the Third Xiangya Hospital of Central South University (JY201712).

Conflict of interest

The authors declare that the research was conducted in the absence of any commercial or financial relationships that could be construed as a potential conflict of interest.

References

- Aghayev, K., Doulgeris, J. J., Gonzalez-Blohm, S. A., Eleraky, M., Lee, W. E., 3rd, and Vrionis, F. D. (2014). Biomechanical comparison of a two-level anterior discectomy and a one-level corpectomy, combined with fusion and anterior plate reconstruction in the cervical spine. *Clin. Biomech. (Bristol, Avon)* 29, 21–25. doi:10.1016/j.clinbiomech.2013.10.016
- Bianchi, D., Falcinelli, C., Molinari, L., Gizzi, A., and Di Martino, A. (2022). Osteolytic vs. Osteoblastic metastatic lesion: Computational modeling of the mechanical behavior in the human vertebra after screws fixation procedure. *J. Clin. Med.* 11 (10), 2850. doi:10.3390/jcm11102850
- Camacho, D. L., Nightingale, R. W., Robinette, J. J., Vanguri, S. K., Coates, D. J., and Myers, B. S. (1997). Experimental flexibility measurements for the development of a computational head-neck model validated for near-vertex head impact. *SAE Transactions* 106 (6), 3989–4002.
- Chen, Y., Luo, J., Pan, Z., Yu, L., Pang, L., Zhong, J., et al. (2017). The change of cervical spine alignment along with aging in asymptomatic population: A preliminary analysis. *Eur. Spine J.* 26, 2363–2371. doi:10.1007/s00586-017-5209-1
- Dall'Ara, E., and San Cheong, V. (2022). "Chapter 6 - Bone biomechanics," in *Human orthopaedic Biomechanics*. Editor B. Innocenti and F. Galbusera Academic Press, 97–120. doi:10.1016/B978-0-12-824481-4.00007-X
- Diebo, B. G., Challier, V., Henry, J. K., Oren, J. H., Spiegel, M. A., Vira, S., et al. (2016). Predicting cervical alignment required to maintain horizontal gaze based on global spinal alignment. *Spine (Phila Pa 1976)* 41, 1795–1800. doi:10.1097/brs.0000000000001698
- Eck, J. C., Humphreys, S. C., Lim, T. H., Jeong, S. T., Kim, J. G., Hodges, S. D., et al. (2002). Biomechanical study on the effect of cervical spine fusion on adjacent-level intradiscal pressure and segmental motion. *Spine (Phila Pa 1976)* 27, 2431–2434. doi:10.1097/00007632-200211150-00003
- Fuller, D. A., Kirkpatrick, J. S., Emery, S. E., Wilber, R. G., and Davy, D. T. (1998). A kinematic study of the cervical spine before and after segmental arthrodesis. *Spine (Phila Pa 1976)* 23, 1649–1656. doi:10.1097/00007632-199808010-00006
- Gum, J. L., Glassman, S. D., Douglas, L. R., and Carreon, L. Y. (2012). Correlation between cervical spine sagittal alignment and clinical outcome after anterior cervical discectomy and fusion. *Am. J. Orthop.* 41, E81–E84.
- Hartmann, S., Thomé, C., Keiler, A., Fritsch, H., Hegewald, A. A., and Schmölz, W. (2015). Biomechanical testing of circumferential instrumentation after cervical multilevel corpectomy. *Eur. Spine J.* 24, 2788–2798. doi:10.1007/s00586-015-4167-8
- Hofler, R. C., Muriuki, M. G., Havey, R. M., Blank, K. R., Frazzetta, J. N., Patwardhan, A. G., et al. (2020). Neutral cervical sagittal vertical axis and cervical lordosis vary with T1 tilt. *J. Neurosurg. Spine*, 1–7. doi:10.3171/2020.2.SPINE191363
- Hussain, M., Nassr, A., Natarajan, R. N., An, H. S., and Andersson, G. B. (2013). Biomechanics of adjacent segments after a multilevel cervical corpectomy using anterior, posterior, and combined anterior-posterior instrumentation techniques: A finite element model study. *Spine J.* 13 (6), 689–696. doi:10.1016/j.spinee.2013.02.062
- Iyer, S., Nemani, V. M., Nguyen, J., Elysee, J., Burapachaisri, A., Ames, C. P., et al. (2016). Impact of cervical sagittal alignment parameters on neck disability. *Spine (Phila Pa 1976)* 41, 371–377. doi:10.1097/brs.0000000000001221
- Jun, H. S., Kim, J. H., Ahn, J. H., Chang, I. B., Song, J. H., Kim, T. H., et al. (2015). T1 slope and degenerative cervical spondylolisthesis. *Spine (Phila Pa 1976)* 40, E220–E226. doi:10.1097/brs.0000000000000722
- Klineberg, E., Mclain, R. F., and Bell, G. R. (2017). Cervical spondylotic myelopathy: Anterior approach: Multilevel anterior cervical discectomy and fusion versus corpectomy. *Seminars in spine surgery* 19, 27–34. doi:10.1053/j.semss.2007.01.007
- Knott, P. T., Mardjetko, S. M., and Tschy, F. (2010). The use of the T1 sagittal angle in predicting overall sagittal balance of the spine. *Spine J.* 10, 994–998. doi:10.1016/j.spinee.2010.08.031
- Kumaresan, S., Yoganandan, N., and Pintar, F. A. (1996). Finite element analysis of anterior cervical spine interbody fusion. *Bio-medical Mater. Eng.* 7 (4), 221–230. doi:10.3233/bme-1997-7401
- Ling, F. P., Chevillotte, T., Leglise, A., Thompson, W., Bouthors, C., and Le Huec, J. C. (2018). Which parameters are relevant in sagittal balance analysis of the cervical spine? A literature review. *Eur. Spine J.* 27, 8–15. doi:10.1007/s00586-018-5462-y
- Liu, S., Lafage, R., Smith, J. S., Protopsaltis, T. S., Lafage, V. C., Challier, V., et al. (2015). Impact of dynamic alignment, motion, and center of rotation on myelopathy grade and regional disability in cervical spondylotic myelopathy. *J. Neurosurg. Spine* 23, 690–700. doi:10.3171/2015.2.spine14414
- Liu, Y., Li, N., Wei, W., Deng, J., Hu, Y., Ye, B., et al. (2017a). Prognostic value of lordosis decrease in radiographic adjacent segment pathology after anterior cervical corpectomy and fusion. *Sci. Rep.* 7, 14414. doi:10.1038/s41598-017-14300-4
- Liu, Y., Li, N., Xiong, W., Wei, W., Ye, B., and Wang, W. (2017b). Risk assessment of cervical ligament injury in Sanda combat (Chinese boxing) by using the finite element head-neck model. *Yiyong Shengwu Lixue. J. Med. Biomech.* 32, 38. doi:10.16156/j.1004-7220.2017.01.007
- Machino, M., Yukawa, Y., Imagama, S., Ito, K., Katayama, Y., Matsumoto, T., et al. (2016). Age-related and degenerative changes in the osseous anatomy, alignment, and range of motion of the cervical spine: A comparative study of radiographic data from 1016 patients with cervical spondylotic myelopathy and 1230 asymptomatic subjects. *Spine (Phila Pa 1976)* 41, 476–482. doi:10.1097/brs.0000000000001237
- Natarajan, R. N., Chen, B. H., An, H. S., and Andersson, G. B. (2000). Anterior cervical fusion: A finite element model study on motion segment stability including the effect of osteoporosis. *Spine* 25 (8), 955–961. doi:10.1097/00007632-200004150-00010
- Nightingale, R. W., Carol Chancey, V., Ottaviano, D., Luck, J. F., Tran, L., Prange, M., et al. (2007). Flexion and extension structural properties and strengths for male cervical spine segments. *J. Biomech.* 40, 535–542. doi:10.1016/j.jbiomech.2006.02.015

Publisher's note

All claims expressed in this article are solely those of the authors and do not necessarily represent those of their affiliated organizations, or those of the publisher, the editors and the reviewers. Any product that may be evaluated in this article, or claim that may be made by its manufacturer, is not guaranteed or endorsed by the publisher.

Supplementary material

The Supplementary Material for this article can be found online at: <https://www.frontiersin.org/articles/10.3389/fbioe.2022.936749/full#supplementary-material>

- Palanca, M., De Donno, G., and Dall'Ara, E. (2021). A novel approach to evaluate the effects of artificial bone focal lesion on the three-dimensional strain distributions within the vertebral body. *PLoS ONE* 16 (6), e0251873. doi:10.1371/journal.pone.0251873
- Prasarn, M. L., Baria, D., Milne, E., Latta, L., and Sukovich, W. (2012). Adjacent-level biomechanics after single versus multilevel cervical spine fusion. *J. Neurosurg. Spine* 16, 172–177. doi:10.3171/2011.10.spine11116
- Rao, R. D., Wang, M., Mcgrady, L. M., Perlewitz, T. J., and David, K. S. (2005). Does anterior plating of the cervical spine predispose to adjacent segment changes? *Spine (Phila Pa 1976)* 30, 2788–2792. doi:10.1097/01.brs.0000190453.46472.08
- Ryan, D. J., Protosaltis, T. S., Ames, C. P., Hostin, R., Klineberg, E., Mundis, G. M., et al. (2014). T1 pelvic angle (TPA) effectively evaluates sagittal deformity and assesses radiographical surgical outcomes longitudinally. *Spine (Phila Pa 1976)* 39, 1203–1210. doi:10.1097/brs.0000000000000382
- Tamai, K., Buser, Z., Paholpak, P., Sessumpun, K., Hsieh, P. C., Nakamura, H., et al. (2018). MRI kinematic analysis of T1 sagittal motion between cervical flexion and extension positions in 145 patients. *Eur. Spine J.* 27, 1034–1041. doi:10.1007/s00586-017-5385-z
- Tobert, D. G., Antoci, V., Patel, S. P., Saadat, E., and Bono, C. M. (2017). Adjacent segment disease in the cervical and lumbar spine. *Clin. Spine Surg. A Spine Publ.* 30, 94–101. doi:10.1097/bsd.0000000000000442
- Weng, C., Wang, J., Tuchman, A., Wang, J., Fu, C., Hsieh, P. C., et al. (2016). Influence of T1 slope on the cervical sagittal balance in degenerative cervical spine: An analysis using kinematic MRI. *Spine (Phila Pa 1976)* 41, 185–190. doi:10.1097/brs.0000000000001353
- Wheeldon, J. A., Pintar, F. A., Knowles, S., and Yoganandan, N. (2006). Experimental flexion/extension data corridors for validation of finite element models of the young, normal cervical spine. *J. Biomech.* 39, 375–380. doi:10.1016/j.jbiomech.2004.11.014
- Yu, M., Zhao, W. K., Li, M., Wang, S. B., Sun, Y., Jiang, L., et al. (2015). Analysis of cervical and global spine alignment under Roussouly sagittal classification in Chinese cervical spondylotic patients and asymptomatic subjects. *Eur. Spine J.* 24, 1265–1273. doi:10.1007/s00586-015-3832-2



OPEN ACCESS

EDITED BY

Zhen (Jeff) Luo,
University of Technology Sydney,
Australia

REVIEWED BY

Ukadike Chris Ugbohue,
University of the West of Scotland,
United Kingdom
Robert Peter Matthew,
University of California, San Francisco,
United States

*CORRESPONDENCE

Juan C. Moreno,
jc.moreno@csic.es

SPECIALTY SECTION

This article was submitted to
Biomechanics,
a section of the journal
Frontiers in Bioengineering and
Biotechnology

RECEIVED 09 August 2022

ACCEPTED 10 November 2022

PUBLISHED 25 November 2022

CITATION

Asín-Prieto G, Mercante S, Rojas R,
Navas M, Gomez D, Toledo M,
Martínez-Expósito A and Moreno JC
(2022), Post-stroke rehabilitation of the
ankle joint with a low cost
monoarticular ankle robotic
exoskeleton: Preliminary results.
Front. Bioeng. Biotechnol. 10:1015201.
doi: 10.3389/fbioe.2022.1015201

COPYRIGHT

© 2022 Asín-Prieto, Mercante, Rojas,
Navas, Gomez, Toledo, Martínez-
Expósito and Moreno. This is an open-
access article distributed under the
terms of the [Creative Commons
Attribution License \(CC BY\)](#). The use,
distribution or reproduction in other
forums is permitted, provided the
original author(s) and the copyright
owner(s) are credited and that the
original publication in this journal is
cited, in accordance with accepted
academic practice. No use, distribution
or reproduction is permitted which does
not comply with these terms.

Post-stroke rehabilitation of the ankle joint with a low cost monoarticular ankle robotic exoskeleton: Preliminary results

Guillermo Asín-Prieto¹, Silvana Mercante², Raúl Rojas²,
Mariangeles Navas², Daiana Gomez², Melisa Toledo²,
Aitor Martínez-Expósito^{1,3} and Juan C. Moreno^{1*}

¹Neural Rehabilitation Group, Cajal Institute, CSIC—Spanish National Research Council, Madrid, Spain,
²J. N. Lencinas Hospital, Mendoza, Argentina, ³Department of Anatomy, Histology and Neuroscience,
Universidad Autónoma de Madrid, Madrid, Spain

Introduction: Stroke generates a high rate of disability and, in particular, ankle spasticity is a sequelae that interferes with the execution of daily activities. Robotic devices have been proposed to offer rehabilitation treatments to recover control of ankle muscles and hence to improve gait function.

Objective: The aim of this study is to investigate the effects of passive stretching, combined with active and resisted movement, accompanied by visual feedback, by means of playful interactive software using a low-cost monoarticular robot (MEXO) in patients with stroke sequelae and spastic ankle.

Methods: An open, uncontrolled, non-randomised, quasi-experimental study of 6 weeks duration has been completed. A protocol has been defined to determine the usability, safety and potential benefits of supplementary treatment with the MEXO interactive system in a group of patients. Nine volunteer patients with sequelae of stroke who met the inclusion criteria were included. They received conventional treatment and in addition also received treatment with the MEXO monoarticular robot three times a week during 6 weeks. Each session consisted of 10 min of passive stretching followed by 20 min of active movement training with visual feedback (10 min active without resistance, 10 min with resistance) and a final phase with 10 min of passive stretching. The following variables were measured pre- and post-treatment: joint range of motion and ankle muscle strength, monopodal balance, muscle tone, gait ability and satisfaction with the use of assistive technology.

Results: Statistically significant improvements were obtained in joint range measured by goniometry and in balance measured by monopodal balance test. Also in walking capacity, through the measurement of travelled distance.

Discussion and significance: Device usability and patient safety were tested. Patients improved joint range and monopodal balance. The MEXO exoskeleton might be a good alternative for the treatment of spastic ankle joint in people with a stroke sequela.

KEYWORDS

hemiplegia, rehabilitation, robotics, gait, ankle

1 Introduction

Stroke is a global health problem due to its high mortality rate and level of physical and mental disability. According to the World Health Organization, stroke is the third leading cause of death in first world countries, after heart disease and cancer. It is also the second leading cause of death in geriatric patients and is the leading cause of disability worldwide. Every year, 15 million individuals suffer a stroke, of whom 5.5 million die and another 5 million are left with a lifelong disability. In 2015, an estimated 17.7 million people died from cardiovascular causes, accounting for 31% of all deaths worldwide. Of these deaths, 7.4 million were due to coronary heart disease, and 6.7 million were due to cardiovascular diseases (World Health Organization, 2017).

Stroke is defined as “an episode of acute neurological dysfunction presumed to be caused by ischemia or haemorrhage, persisting ≥ 24 h or until death” (Sacco et al., 2013). Once a stroke has occurred, hemiparesis and spasticity are usually the most common sequela [there is a big panoply of secondary complications though (Teasell, 1992)]. Focal neurological deficits in the acute phase compromise the mobility of patients, with a notable reduction in physical activity and, therefore, in physical condition. Immobility and inactivity cause loss of muscle mass, increased body fat, limited joint mobility and reduced bone mineral density. Ankle spasticity is one of the most common movement disorders after stroke. Spastic hypertonic ankles can severely decrease patients’ mobility and independence (Zhou et al., 2015).

The basic mechanism of muscle tone control is the myotatic reflex which is originated by activation of the primary afferent endings of the neuromuscular spindle and mediated by the spinal cord (Liddell and Sherrington, 1924). The discharge of the primary endings has both static and dynamic components that give rise to the tonic and phasic components of the stretch reflex. Spasticity develops when, due to injury, the stretch reflex arc is isolated from its supraspinal modulatory system resulting in abnormal excitation of alpha and gamma motor neurons (Spaich and Tabernig, 2002).

Physical therapy for the rehabilitation of patients with spastic ankle consists of providing repetitive exercises for the ankle muscles, so that plantar flexion and dorsiflexion lead to the reintegration of the distance between the feet during the swing phase of the gait cycle (Smania et al., 2010). However, the ankle is an anatomical complex that produces joint movements with two degrees of freedom: dorsi/plantarflexion and inversion/eversion (Jones, 2019). Repetitive therapy sessions are required to restore lost motion in terms of joint ranges and forces (Hussain et al., 2017).

Conventional physiotherapy has evolved from techniques focused on strengthening and analytical movement practice, to approaches focused on regaining functional movements, such as gait through training, and the use of, for example, treadmills with partial body weight support (Belda-Lois et al., 2011). Robots have

been developed and have begun to be applied in the field of biomedicine. These robotic-assisted devices used in gait rehabilitation in patients with neurological pathologies have achieved good results in the recovery of lower limb functionality, they seem to have decreased the physical effort made by therapists and intensified gait training in patients (Calderón-Bernal et al., 2015). According to the type of structure, the authors define a monoarticular robotic therapeutic “exoskeleton” as an electromechanical device which closely fits the user’s body and is designed to mobilize one human joint through a physiological range of motion to train the recovery of user’s capacity.

This type of robotic exoskeletons that focus on a single joint can therefore facilitate movements and also help to correct vicious postures. As one of the most common post-stroke sequelae is increased tone and consequent decreased mobility at the ankle joint, there are exoskeletons which are designed to correct the equinus position of the foot and assist its movement, such as the ankle robot or anklebot (Calderón-Bernal et al., 2015; Forrester et al., 2011), which position the foot during the swing phase and assist in facilitating foot mobility, and can be used in standing, seated and supine positions, as well as an interactive video game system where the foot movement is visualised (Chang et al., 2017).

Another prototype used in ankle rehabilitation is MAFO, a motorised ankle and foot orthosis, capable of performing dorsiflexion and plantar flexion movements and providing visual biofeedback on electromyographic signals; this device has been designed as a tool for recovery, simplification and improvement of motor learning thus facilitating ankle functionality, and not developed to be a walking orthosis (Asín-Prieto et al., 2013).

In gait rehabilitation, it is worth mentioning the importance of motor control of the ankle, as several studies applying robotic therapy have shown improvements in the performance of the joint, pointing out by the authors that the motor ability of the ankle could be improved, explained by the increase in motor cortical excitability for the tibialis anterior, thus achieving voluntary control of the ankle flexor musculature and an increase in the flexo-extension of the ankle (Calderón-Bernal et al., 2015).

Recently, significant research efforts have been made to improve the mechanism design, actuation, control algorithms and interaction for these robotic orthoses and parallel ankle robots (Jimenez-Fabian and Verlinden, 2012; Kwon et al., 2019; Asín-Prieto et al., 2020). The goal behind the research is that the design of these robotic devices should provide natural movement patterns for patients with neurological disorders, and the actuation system used with these robots should provide safe and efficient human-robot interaction. The goal of developing advanced control algorithms is to personalise robotic assistance according to the level of disability and stage of rehabilitation of the patient (Hussain et al., 2017).

Miao et al. (2018) reviewed the designs of existing ankle rehabilitation robots. They reported that while most robotic-assisted ankle rehabilitation techniques have been shown to be effective for ankle physiotherapy, they might have design drawbacks that have prevented their wide-range applications. Their review states that an optimal ankle rehabilitation robot design should be characterised with a centre of rotation aligned with the ankle joint, that the number of ranges of motion depends on specific applications, and that the single range of motion robot is developed especially for ankle stretching along dorsi- and plantarflexion; while multiple ranges of motion devices are more suitable for complete ankle rehabilitation exercises. They also add that the adjustability of the system, its method of fixation to the users' foot, and the mechanical stops, affect their clinical application.

In a comprehensive review of recent developments in the field of robotic-assisted ankle rehabilitation, significant advances in mechanism design, control, and experimental evaluations of ankle rehabilitation robots are reported. However, the authors consider that it is necessary to develop improved methods for motion detection and definition of reference trajectories, as well as more objective quantitative evaluations that must be performed to establish the clinical importance of these robots (Hussain et al., 2021).

The device used in this study is the Motorised ankle-foot EXOskeleton (MEXO), a research prototype device developed at the Neural Rehabilitation Group at Cajal Institute of the Spanish National Research Council (CSIC) in Spain.

Given the high prevalence of patients with post-stroke hemiplegia attending the Rehabilitation Service of the J. N. Lencinas Hospital (Mendoza, Argentina), it is of interest to study the effects of possible treatments to improve the functionality of the affected ankle, thus improving walking in them. So far, the most commonly used treatment in this service to improve forefoot drop in hemiplegic patients has been conventional physio-kinesiotherapy, ankle-foot orthosis and functional electrostimulation (FES).

The development of this work was part of the REASISTE Research Network (Ibero-American Network for rehabilitation and assistance of patients with neurological damage using low-cost robotic exoskeletons), funded by CYTED (Ibero-American Programme of Science and Technology for Development) and aimed to contribute to the validation and safety of cost-effective robotic rehabilitation equipment and its possible transfer to treatment spaces.

2 Objective

The main objective of the study is to measure the effects of passive stretching, combined with active and resisted movement, on the ankle and its impact on gait functionality, accompanied by visual feedback, by means of an interactive playful software using

low-cost Monoarticular robotic EXOskeleton MEXO in patients with sequelae of stroke and spastic ankle; in the Rehabilitation Service of the J. N. Lencinas Hospital (Mendoza, Argentina) during the period 2020–2021. Secondary objectives are to evaluate pre- and post-treatment ankle variables such as joint range, muscle strength, muscle tone, functional gait performance (speed–distance–fall risk–walking ability), to check the usability of the device and patient safety, and also to measure the degree of patient satisfaction with this assistive technology.

3 Materials and methods

This is an open, pre-post, uncontrolled, non-randomised, 6-week, quasi-experimental study. The study population is made up of patients attending the Rehabilitation Service who present with hemiparesis following a stroke, with an evolution time of more than 3 months, during the period 2020–2021.

3.1 Protocol

All included patients received conventional treatment and treatment with the MEXO exoskeleton three times a week for 6 weeks. The conventional rehabilitation treatment, lasting 60 min, consisted of passive mobilizations, active exercises and strength training with isotonic exercises. Also, proprioceptive training and balance exercises. Following this treatment, they received treatment with MEXO with each session consisting of 10 min of passive stretching followed by 20 min of active movement training with playful visual feedback (10 min active without resistance, 10 min with resistance) and a final 10-min phase of passive stretching.

Pre-treatment, during treatment sessions, and post-treatment data were collected for the variables listed in Table 1.

3.2 Ethical considerations

The study was evaluated and approved by the Teaching and Research Committee of the José Nestor Lencinas Hospital and by the COPEIS (Provincial Health Research Ethics Committee) of the province of Mendoza (Argentina).

All the patients were informed about their participation in the study. All stroke survivors in the Rehabilitation Service who met the inclusion criteria and who did not meet the exclusion criteria were eligible to participate in this study. All patients who participated in the study agreed to the treatment with the MEXO exoskeleton.

The following inclusion criteria was considered: hemiparesis resulting from a single stroke event, age between 18 and 65 years old, post-stroke time equal or greater than 3 months, independent walking, passive ankle joint range at dorsiflexion

TABLE 1 Variable description.

Variable	Concept	Measuring instrument
Ankle joint range	The angle in degrees from the start point to the end point of the movement	Goniometer
Ankle muscle strength	Ability of a muscle to exert tension against a load during muscle contraction	Medical Research Council (MRC) Score 0 to 5
Monopodal balance	The time in seconds that the patient can stand on one foot or the other	Time in seconds
Muscle tone	Permanent state of partial, passive and continuous contraction of muscles	Modified Ashworth Scale. Score from 1 to 5
Satisfaction with the use of Assistive Technology	Satisfaction in relation to health can be defined as an attitude about a service, product, a service provision or an individual's state of health, according to expectations, wishes or needs.	QUEST scale. Items 1 to 5.
Walkability:		
- Distance travelled	Distance in metres travelled in a set period of time	2 min test
- Time	Time it takes to cover a given distance	10-m test
- Walking ability	Assessment of a subject's chances of successfully completing an ambulation	Timed up and go; and time and items from 1 to 5

of at least 90 degrees, dorsiflexor muscle strength of at least two according to Medical Research Council (MRC) index, ankle plantarflexor spasticity of ± 2 according to Modified Ashworth Scale, ability to understand and follow instructions, informed consent form signed. The exclusion criteria includes comorbidities affecting gait, history of frequent falls, debilitating or immunosuppressive disease, alteration of mental functions that prevent the patient from following instructions.

3.3 Description of the equipment

The MEXO device has been developed at the Neural Rehabilitation Group of Cajal Institute CSIC in the scope of the REASISTE Iberoamerican Network that supports the development of cost-effective robotic solutions for therapy. It consists of a mobile platform adjustable to different anthropometries that allows dorsal and plantar flexion of the right or left foot, by means of a manual clutch in the motor-gearbox assembly. It has a position sensor of the ankle angle and measures the force that the motor exerts. It also has adjustable mechanical stops with screws that prevent the platform from reaching extreme positions, which are previously defined by the therapist before starting the treatment by means of passive mobilisation. As a safety measure, the device is equipped with an emergency stop switch, which interrupts the power supply to the entire device.

MEXO is intended for controlling the movement of the human ankle providing an improved visual feedback by means of interactive software (video game) aimed at people with neuromotor impairments such as cerebral palsy, stroke and incomplete spinal cord injury. The exoskeleton is a stationary system that allows active/passive mobilisation of the ankle in the sagittal plane, allowing the required stretching

exercises to be performed in such a way that the angular trajectory of the user's ankle follows a specific trajectory depending on the video game with which it is synchronised. The MEXO device is used in a seated position, and has ergonomic adaptations for contact, support, alignment and fixation to each user's limb.

The exoskeleton has three operation modes:

- **Passive mode:** The user's ankle follows the movement rigidly imposed by the exoskeleton, thus leading to passive stretching. In this mode, the actuator clutch is engaged. Thus, the system imposes a joint trajectory within the limits of the subject's joint assessed in the passive joint evaluation. The maximum range of motion in this mode goes from a dorsiflexion of 25 degrees up to a plantarflexion of 55 degrees, with a total of 80 degrees travel, and it is possible to adjust extreme limits in case of joint limitation by the patient, for which the robot's travel must correspond to the passive joint evaluation. The speed of the movement goes from a maximum full range travel time of 6 s (slow speed, 13.33 degrees/second) taking into account the speed-spasticity ratio, to a minimum of 2 s (fast speed, 40 degrees/second).
- **Active mode:** The exoskeleton actuator would not exert any force, and the user has to actively perform the stretches. In this mode, the actuator clutch is not engaged, and the work is performed mainly on the flexor muscles of the foot (tibialis anterior and peroneus) due to the effect of gravity, and secondarily on the extensors (calf and soleus) in the search for maximum joint amplitude. The range of motion in this mode also goes from a dorsiflexion of 25 degrees up to a plantarflexion of 55 degrees, with a total of 80 degrees travel, and it is possible too to adjust extreme limits in case of joint limitation by the patient, for which the robot's

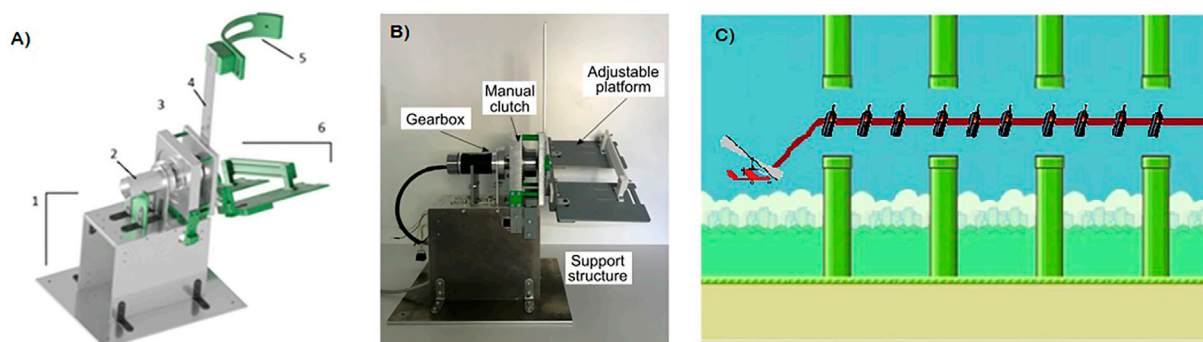


FIGURE 1

Structural components and visual paradigm of MEXO: (A) Mechanical components, 1- structural support, 2- motor and gearbox assembly, 3- clutch, 4- leg structure bar, 5- strap and 6- insole; (B) Front view of the MEXO robot; and (C) Visual interface.

travel must correspond to the active muscle evaluation. The speed of the movement can be regulated (within the limits set for the passive mode) according to the patient's muscular resistance. In the visual paradigm bio-feedback, the gyrocopter (Figures 1C) goes up and down with the dorsi/plantarflexion, and the efficiency or error in the movement produced by the patient is recorded. The challenge of this mode is to achieve good score, and sustain this correct and wide movement over time (overcoming the possible fatigue).

- **Resistive mode:** In this case, the exoskeleton actuator introduces disturbances to the movement of the visual trajectory, so that the user must perform movements that counteract these disturbances in order to try to complete the trajectory as accurately as possible. In this mode, the actuator clutch is engaged. The system applies a single resistance pattern to the movement that simulates the sagittal force profile of ground reaction during the stance phase of the gait, and performs a pause (rest) that would correspond to the swing phase. The work is mainly on the extensor muscles (calf and soleus) by making an eccentric–concentric contraction simulating muscle activation during the stance phase of gait. The challenge of this mode is to achieve a good score and sustain this movement pattern over time against the perturbations. The range of motion in this mode goes from a dorsiflexion of 15 degrees (the robot overcomes the patient's strength –eccentric–) up to a plantarflexion of 25 degrees (patient overcomes robot force –concentric–). With a total of 40 degrees travel, and a unique movement pattern that simulates the stance phase of gait and a pause (rest) that would correspond to the swing phase, it is possible to adjust extreme limits in case of joint limitation by the patient, for which the robot's range of movement must correspond to the active muscle evaluation. The speed of the movement can be regulated

(within the limits set for the passive mode) according to the patient's muscular resistance, and in this “Resistive mode”, the resistance offered by the robot to the patient can also be regulated (from five to 20 N); these parameters are adjusted according to the patient's muscular resistance. As in the previous mode, the visual paradigm bio-feedback shows the gyrocopter going up and down with dorsi/plantarflexion, and the efficiency or error in the movement produced by the patient against the resistance given by the robot is recorded, with pause cycles shown on the screen with the word “Descansa” (Rest in Spanish).

The main components of the exoskeleton (depicted in Figures 1A,B) are the following:

- **Structural support:** The structure consists of a series of aluminium plates that form the main support for the exoskeleton and raise it above the ground surface. The base of this support can be anchored to the ground by means of screws fixed or a counterweight fixed to the base.
- **Motor and gearbox assembly:** The exoskeleton actuator consists of a brushless direct current motor, coupled to a planetary gearbox (Maxon Motor, www.maxongroup.com). Both components were specifically selected so that the actuator can develop the required torque on the patient's ankle during rehabilitation exercises.
- **Clutch:** The actuator has a clutch with a manual disengagement/engagement system attached to the motor and side panels. When the system is disengaged, the ankle joint of the exoskeleton moves freely with the user's foot, while when the system is engaged it is the motor–gearbox assembly that executes this movement.
- **Leg structure bar:** On this bar the height position of the strap is adjusted so that the adaptation of the exoskeleton on the user's leg is optimal.

TABLE 2 Clinical and demographic characteristics of patients.

	P1	P2	P3	P4	P5	P6	P7	P8	P9
Age	58	57	54	53	42	60	50	56	64
Gender	F	M	M	F	F	M	M	M	F
Stroke evolution time in months	8	6	7	3	3	3	20	10	4
Walking assistance	No	No	No	No	No	No	Cane	Cane	No
Affected hemibody	Left	Right	Right	Left	Right	Right	Right	Right	Left
Type of stroke	H	I	I	I	I	I	H	H	H
Spasticity in flexion	0	1	1	0	0	0	1	0	0
Spasticity in extension	0	1	1	0	0	0	0	0	0

- Strap: Component that embraces the user's leg and is adjusted to it by means of a BOA fastener, so that the exoskeleton is adapted to the user's leg.
- Insole: This component, made up of two platforms, is adjustable in width and length so that it can be adapted to different foot sizes depending on the user who is going to use the device. The foot, with the user's footwear is attached to the insole by means of several Velcro straps and BOA fasteners.

The equipment includes safety measures both at an electronic level (emergency stop switch, which interrupts the power supply to the entire device) and at a mechanical level (physical stops limiting ankle dorsi-plantarflexion).

MEXO is connected to a standard PC which contains the set of software functions to perform the therapy. The computer receives information from the MEXO's position sensor to move the game avatar through the virtual scenario. The avatar's range of motion is adapted according to the patient's joint range capabilities, so as not to overly penalise its performance. In addition to the avatar's position, the game sets the motor resistance when the "resisted" game mode is selected. The software that integrates the device is divided into two fundamental elements: control and visual paradigm. The control is executed on the control board of the device (Arduino MEGA), and is responsible for: 1) reading the current on the motor and the angle, 2) sending this information *via* serial port to the computer that executes the visual interface (implemented in MATLAB), and 3) controlling the motor for the different operating modes. The visual paradigm, shown in Figure 1C, is implemented in such a way that it receives the angle information from the control board of the device, and moves the item on the screen according to this information (dorsiflexion and plantarflexion move the gyrocopter up and down respectively). It is also responsible for sending the corresponding commands for the different control modes.

3.4 Participants

Patient demographics are shown in Table 2. 16 patients were evaluated, with finally nine completing the entire treatment. Five patients had to drop out due to restrictions imposed by the Ministry of Health, Social Development and Sports due to the COVID-19 pandemic situation and two for complications with transportation in the area. The mean age of the patients was 54.9 years ranging from 42 to 64 years; four were female and five male; the mean time since stroke was 7.1 months ranging from three to 20 months. Only two patients required walking assistance. There were three patients with left, and six with right, hemibody involvement, four with haemorrhagic and five with ischaemic stroke.

3.5 Data analysis

With the data obtained, a descriptive and hypothesis testing analysis was carried out comparing the changes in the variables collected before and after the treatment (pre-post analysis) using the Wilcoxon test. We also conducted correlation analyses (Pearson and Spearman, depending on normality tests –Kolmogorov-Smirnov-based Lilliefors test–, i.e., Pearson for normally distributed variables on both components of the pair, Spearman otherwise).

4 Results

The results of the variables studied pre- and post-treatment are summarised in Table 3.

Pre- and post-intervention comparisons were made in the patient group for all variables. The mean, standard deviation, median, minimum, maximum, mode and normality values are expressed in Table 4; and the pre- and post-treatment statistical significance in Table 5.

TABLE 3 Variables studied pre and post treatment.

Patient	Goniometry (deg)				Spast. (Ash)		Muscle strength (MRC)		Monopodal balance test (deg)		T2min (m)	T10m (sec)	TUGT (sec)	PROM (deg)	AROM (deg)	AScore (%)	ARMSE (deg)	RScore (%)	RRMSE (deg)
	Flex (+)		Ext (–)		F	E	F	E	Right	Left									
	FP	A	FP	A															
1-PRE	5	2	54	50	0	0	–4/5	–4/5	40	19	157	6	7	67.16	72.98	74.59	5.72	67.86	6.80
1-POST	17	13	48	60	0	0	+4/5	+4/5	59	23.49	165	7.29	7	80.69	75.23	86.51	5.18	76.75	6.51
2-PRE	0	0	40	38	1	1	–4/5	–4/5	10	38	160	8	6	75.65	62.64	85.56	5.05	75.29	7.43
2-POST	0	3	41	41	1	1	4/5	4/5	12	34	160	6	6	81.19	64.93	91.72	3.18	83.69	4.05
3-PRE	5	5	38	38	1	1	–4/5	–4/5	6	5	157	6	6	63.51	64.33	82.59	4.58	76.04	5.43
3-POST	10	10	50	40	0	0	+4/5	+4/5	40	30	188	5.32	6	77.93	73.50	95.57	3.29	98.80	2.65
4-PRE	3	2	45	50	0	0	3/5	3/5	6	2	157	9.39	10.32	71.81	71.37	80.19	5.37	68.91	6.26
4-POST	25	20	60	60	0	0	+4/5	+4/5	40	17.5	160	5.65	6.56	78.20	83.04	99.80	3.02	97.81	3.70
5-PRE	0	0	30	25	0	0	+4/5	+4/5	5.6	4.11	160	8.68	6.9	73.97	74.05	87.06	4.53	83.58	4.87
5-POST	15	15	35	35	0	0	+4/5	+4/5	12.58	16.8	180	5.84	2.74	83.60	71.71	101.49	2.55	94.68	3.70
6-PRE	10	0	65	60	0	0	–4/5	+4/5	1.3	2.9	89	9.6	10.7	69.92	9.19	66.01	7.48	55.46	9.25
6-POST	10	0	65	60	0	0	+4/5	+4/5	4.20	8.69	111	8.6	9.8	65.62	174.66	100.72	1.92	83.33	3.92
7-PRE	10	10	35	35	1	0	4/5	4/5	1.99	18.05	107	9.14	12.7	61.18	44.95	55.16	6.50	51.62	5.90
7-POST	0	5	50	50	1	0	+4/5	+4/5	3.5	30.5	123	8.3	10.58	57.27	50.03	79.05	4.80	54.36	7.54
8-PRE	3	3	40	40	0	0	4/5	4/5	1.03	1.09	100	7.6	8.99	64.59	58.26	59.74	7.93	62.54	5.89
8-POST	14	10	50	45	0	0	+4/5	+4/5	1	1.53	130	6.54	9.02	73.58	53.59	84.39	6.93	87.35	4.65
9-PRE	7	10	30	50	0	0	+4/5	4/5	1	-	70	12.6	12.78	76.43	72.44	46.67	9.49	38.28	13.82
9-POST	15	10	42	47	0	0	5/5	5/5	0.91	0.72	82	13.6	14.1	66.92	39.80	65.58	5.94	49.18	10.80

FP, forced passive; A, active; T2min, 2 min walking test; T10m, 10 m walking test; TUGT, timed up and go test; deg, degrees; sec, seconds; m, metres; PROM, passive range of motion; AROM, active range of motion; AScore, active score; ARMSE, active root mean squared error; RScore, resistive score; RRMSE, resistive root mean squared error; Spast., spasticity; Ash, ashworth; F, flex; E, ext.

TABLE 4 Values of mean (AVG), standard deviation (STD), median (MDN), minimum (MIN), maximum (MAX), mode (MOD) and normality (NRM) pre- and post-treatment of the variables.

		GFFP	GFA	GEFP	GEA	AshwF	AshwE	MSF	MSE	RMBT	LMBT	T2min	T10m	TUGT	PROM	AROM	ASCr	ARMSE	RScr	RRMSE
AVG	PRE	4.22	3.56	41.89	42.89	0.33	0.22	0.33	1.22	8.10	10.52	128.56	8.56	9.04	69.36	58.91	70.84	6.30	64.40	7.29
	POST	11.78	9.56	49.00	48.67	0.22	0.11	4.11	4.11	19.24	18.14	144.33	7.46	8.31	73.89	76.28	89.42	4.09	80.66	5.28
STD	PRE	3.19	4.00	11.42	10.51	0.50	0.44	4.12	3.93	12.35	12.30	36.53	2.02	2.72	5.54	20.85	14.56	1.70	14.07	2.76
	POST	8.00	6.19	9.29	9.51	0.44	0.33	0.33	0.33	21.45	12.47	34.92	2.58	2.82	8.82	39.40	11.91	1.69	17.95	2.57
MDN	PRE	5.00	2.00	40.00	40.00	0.00	0.00	3.00	4.00	5.60	4.56	157.00	8.68	8.99	69.92	64.33	74.59	5.72	67.86	6.26
	POST	14.00	10.00	50.00	47.00	0.00	0.00	4.00	4.00	12.00	17.50	160.00	6.54	7.00	77.93	71.71	91.72	3.29	83.69	4.05
MIN	PRE	0.00	0.00	30.00	25.00	0.00	0.00	-4.00	-4.00	1.00	1.09	70.00	6.00	6.00	61.18	9.19	46.67	4.53	38.28	4.87
	POST	0.00	0.00	35.00	35.00	0.00	0.00	4.00	4.00	0.91	0.72	82.00	5.32	5.74	57.27	39.80	65.58	1.92	49.18	2.65
MAX	PRE	10.00	10.00	65.00	60.00	1.00	1.00	4.00	4.00	40.00	38.00	160.00	12.60	12.78	76.43	74.05	87.06	9.49	83.58	13.82
	POST	25.00	20.00	65.00	60.00	1.00	1.00	5.00	5.00	59.00	34.00	188.00	13.60	14.10	83.60	174.66	101.49	6.93	98.80	10.80
MOD	PRE	5.00	0.00	30.00	50.00	0.00	0.00	-4.00	4.00	6.00	1.09	157.00	6.00	6.00	61.18	9.19	46.67	4.53	38.28	4.87
	POST	0.00	10.00	50.00	60.00	0.00	0.00	4.00	4.00	40.00	0.72	160.00	5.32	6.00	57.27	39.80	65.58	1.92	49.18	2.65
NRM	PRE	Yes	Yes	Yes	Yes	No	No	No	No	No	No	No	Yes	Yes	Yes	Yes	Yes	Yes	Yes	Yes
	POST	Yes	Yes	Yes	Yes	No	No	No	No	No	Yes	Yes	Yes	Yes	Yes	No	Yes	Yes	Yes	Yes

GFFP, goniometry flexion FP; GFA, goniometry flexion A; GEFP, goniometry extension FP; GEA, goniometry extension A; AshwF, ashworth flexion; AshwE, ashworth extension; MSF, muscle strength-flexion; MSE, muscle strength extension; RMBT, right monopodal balance test; LMBT, left monopodal balance test; T2min, 2 min walking test; T10m, 10 m walking test; TUGT, timed up and go test; PROM, passive ROM; AROM, active ROM; ASCr, active score; ARMSE, active RMSE; RScr, resistive score; RRMSE, resistive RMSE.

TABLE 5 *p*-value of treatment variables (**p* < 0.05).

Variables	Signedrank	<i>p</i> value
Goniometry flexion FP	4.00	<i>p</i> = 0.0469*
Goniometry flexion A	2.50	<i>p</i> = 0.0625
Goniometry extension FP	3.00	<i>p</i> = 0.0391*
Goniometry extension A	2.50	<i>p</i> = 0.0312*
Ashworth flexion	1.00	<i>p</i> = 1
Ashworth extension	1.00	<i>p</i> = 1
Muscle strength flexion	0.00	<i>p</i> = 0.0312*
Muscle strength extension	0.00	<i>p</i> = 0.0625
Right monopodal balance test	3.00	<i>p</i> = 0.0195*
Left monopodal balance test	5.00	<i>p</i> = 0.0391*
2 min walking test	0.00	<i>p</i> = 0.0078*
10-m walking test	35.50	<i>p</i> = 0.1367
Timed up and go test	16.00	<i>p</i> = 0.3125
Passive range of motion	9.00	<i>p</i> = 0.1289
Active range of motion	15.00	<i>p</i> = 0.4258
Active score	0.00	<i>p</i> = 0.0039*
Active RMSE	45.00	<i>p</i> = 0.0039*
Resistive score	0.00	<i>p</i> = 0.0039*
Resistive RMSE	41.00	<i>p</i> = 0.0273*

Pre-post intervention comparisons in the patient group were plotted for the variables “goniometry”, “monopodal balance”, “active root mean squared error”, “active performance”, “resistive root mean squared error” and “resistive performance”. Comparisons of the intervention effect in the group (variables collected pre- and post-treatment pre-post analysis using the Wilcoxon test) for these two variables are presented in Figure 2 for “monopodal balance” and “goniometry”. Mean values with standard deviation, together with mean and deviation for the values corresponding to the first and last score and rmse value (normalized to 1,000 repetitions) for the intrasubject linear fitting for the variables “active root mean squared error”, “active performance”,

“resistive root mean squared error” and “resistive performance” are presented in Figure 3. We used the measurements before and after the training days to perform the statistical analyses.

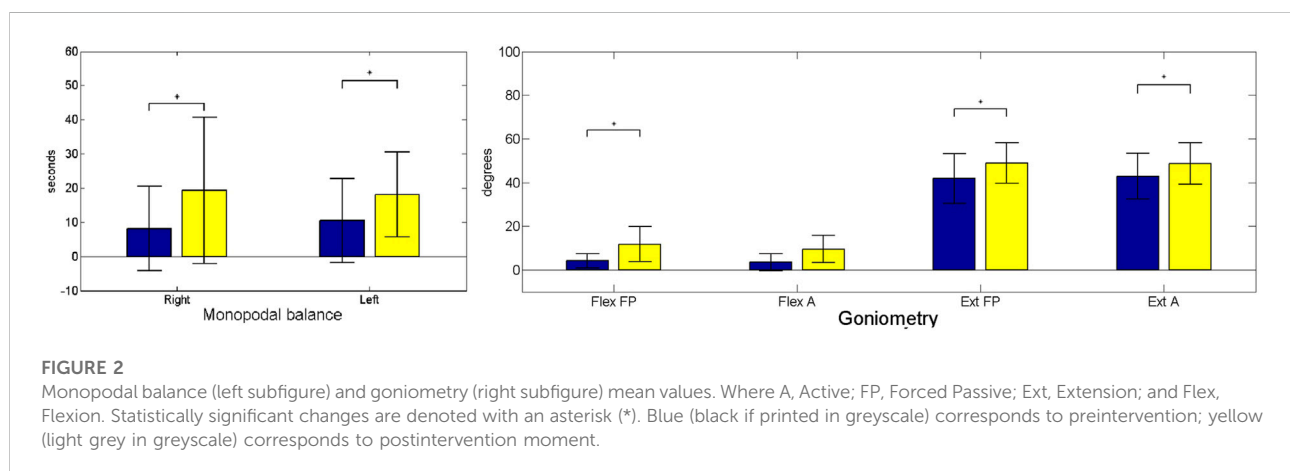
Table 5 shows the pre- and post-intervention statistical inference. The results of the study showed significant changes in monopodal balance, as well as in FP flexion, FP extension, A extension kinematics, together with the 2-min walking test, and muscle strength during flexion. Furthermore, we also found significant changes in score and root mean squared error for both active and resistive training paradigms.

We also evaluated the User Satisfaction with Assistive Devices Technology by means of the QUEST Quebec Survey version 2.0 (Demers et al., 2002) adapted to the MEXO exoskeleton. Two unrelated questions were removed from the “Device” section, and another two from the “Services” section. Unrelated dimensions that were removed with respect to the apparatus are dimensions and weight. Regarding the service, the delivery process dimension and repair and maintenance were also eliminated (refer to Table 6 for results).

Figure 4 shows the most important aspects for the patients, extracted from the questionnaires.

Table 7 shows the mean, standard deviation, median, minimum, maximum, mode and normality values for QUEST results.

Tables 8, 9 show the correlations with a value of *p* greater than 0.05 (*p* > 0.05) for both Spearman and Pearson correlation tests respectively. Spearman has been applied to those data that do not comply with normality (both variables, or at least one of them). Pearson has been applied to those variable pairs where both comply with normality. Correlations for EU (Ease of Use), Co (Comfort), Q (Quality), Fu (Follow-up) and OS (Overall satisfaction with Services) could not be performed, due to they having null variance (all patients scored 5 points on all these variables). We observed moderate to strong correlations in all the correlating pairs. Some interesting correlations are those that find increased monopodal balance for increased active ROM; decreased Timed Up and Go Test time for increased root



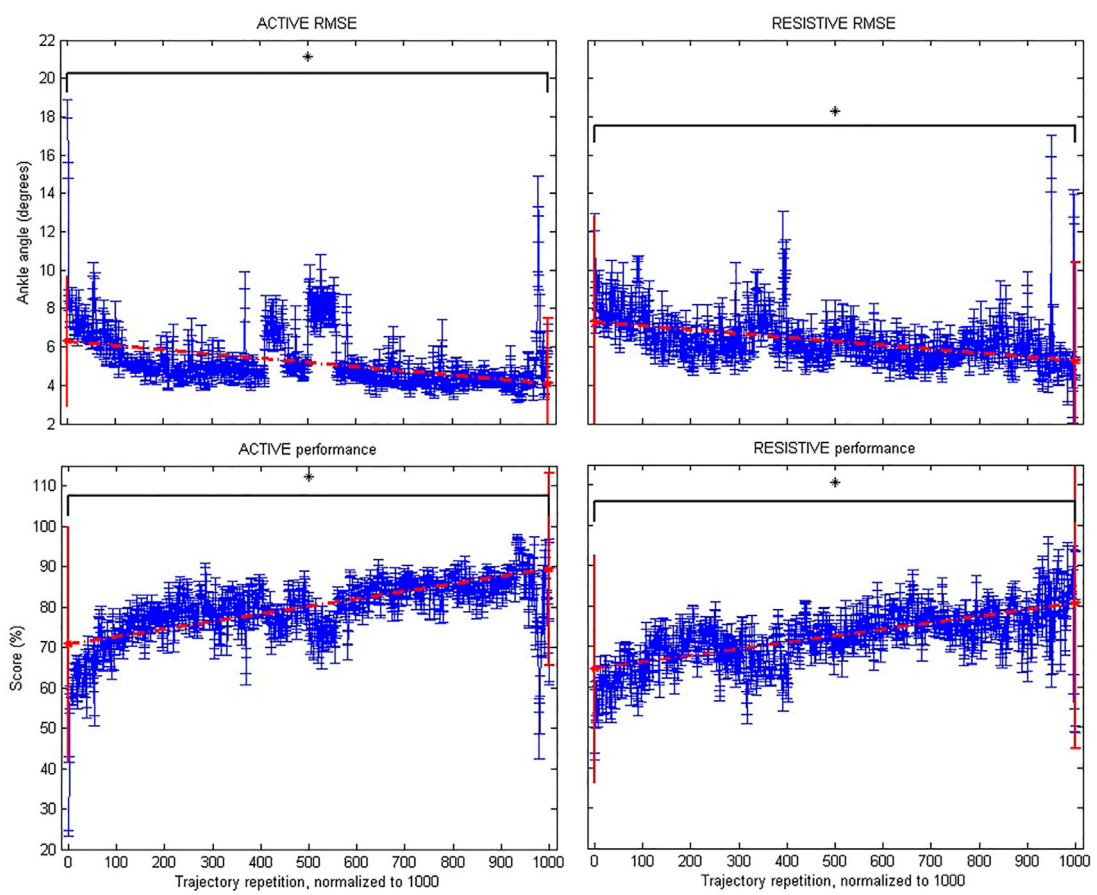


FIGURE 3
Robotic metrics: Active root mean squared error (upper left subfigure); Active performance (lower left); Resistive root mean squared error (upper right); and Resistive performance (lower right). Statistically significant changes are denoted with an asterisk (*).

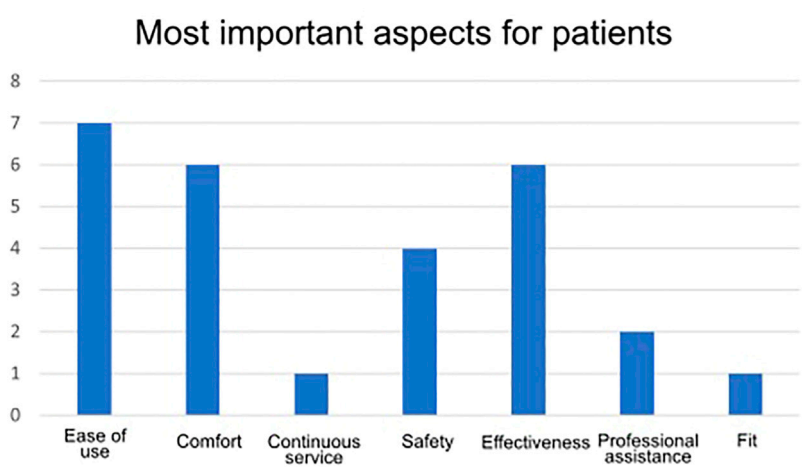


FIGURE 4
Most important aspects for patients.

TABLE 6 Results of the QUEST questionnaire.

Assessed dimensions	Patient #	P1	P2	P3	P4	P5	P6	P7	P8	P9
“Device” section	Ease of adjustment	4	4	5	5	5	4	5	4	4
	Safety	5	5	5	5	5	4	5	5	3
	Durability	5	4	4	5	5	5	5	5	4
	Ease of use	5	5	5	5	5	5	5	5	5
	Comfort	5	5	5	5	5	5	5	5	5
	Effectiveness	5	5	5	5	5	5	5	5	3
“Services” section	Quality	5	5	5	5	5	5	5	5	5
	Follow-up	5	5	5	5	5	5	5	5	5
“Additional questions”	Overall satisfaction level with the device	5	4	4	5	5	4	5	5	4
	Overall satisfaction with services	5	5	5	5	5	5	5	5	5
“Selection of three most important questions”		- S	- F	- EU	- EU	- EU	- S	- S	- P	- C
		- Co	- EU	- S	- Co	- Co	- Co	- Ef	- EU	- EU
		- P	- Ef	- Ef	- Ef	- Ef	- Ef	- EU	- Co	- Cs

S, safety; Co, comfort; P, professional assistance; F, fit; EU, ease of use; Ef, effectiveness; Cs, continuous service.

TABLE 7 Values of mean, standard deviation, median, minimum, maximum, mode and normality of QUEST results.

EA	S	D	EU	Co	Ef	Q	Fu	OD	OS
Average									
4.44	4.67	4.67	5.00	5.00	4.78	5.00	5.00	4.56	5.00
Standard deviation									
0.53	0.71	0.50	0.00	0.00	0.67	0.00	0.00	0.53	0.00
Median									
4.00	5.00	5.00	5.00	5.00	5.00	5.00	5.00	5.00	5.00
Minimum									
4.00	3.00	4.00	5.00	5.00	3.00	5.00	5.00	4.00	5.00
Maximum									
5.00	5.00	5.00	5.00	5.00	5.00	5.00	5.00	5.00	5.00
Mode									
4.00	5.00	5.00	5.00	5.00	5.00	5.00	5.00	5.00	5.00
Normality									
No	No	No	No	No	No	No	No	No	No

EA, ease of adjustment; S, safety; D, durability; EU, ease of use; Co, comfort; Ef, effectiveness; Q, quality; Fu, follow-up; OD, overall satisfaction level with the device; OS, overall satisfaction level with services.

mean squared error in the resistive paradigm; or decreased score for the 10 m walking test for both active and resistive scores.

5 Discussion

Among the exoskeleton prototypes tested for ankle dysfunctions, the present study is a novel local study in

Mendoza (Argentina) that investigates the effects of passive stretching combined with active and resisted ankle movement. It also investigates the impact of passive stretching on gait using the MEXO robotic exoskeleton in patients with stroke sequelae.

Patients received the therapy for 6 weeks, accompanying conventional treatment. Pre- and post-treatment results were compared for the studied variables. There were three variables that showed a net increase at the end of the treatment: kinematics

TABLE 8 Spearman correlations table ($p > 0.05$) for PRE and POST-treatment variables.

Variable 1	Variable 2	Spearman correlation coefficient
AROM POST	AScore POST	-0.73
T10m POST	S	-0.86
T2min POST	S	-0.91
RMBT POST	AROM POST	0.88
RMBT POST	T2min POST	-0.75
T10m POST	S	-0.73
T2min POST	S	0.73
RMBT POST	AROM POST	0.70
RMBT POST	T2min POST	0.81
RRMSE PRE	S	-0.73
RScore PRE	RMBT POST	0.69
ARMSE PRE	RMBT POST	-0.72
T10m PRE	S	-0.73
T2min PRE	S	0.75
T2min PRE	PROM POST	0.86
T2min PRE	TUGT POST	-0.91
T2min PRE	T10m POST	-0.74
T2min PRE	T2min POST	0.82
T2min PRE	RScore PRE	0.89
T2min PRE	ARMSE PRE	-0.92
T2min PRE	AScore PRE	0.91
T2min PRE	TUGT PRE	-0.82
LMBT PRE	LMBT POST	0.73
RMBT PRE	T2min POST	0.73
RMBT PRE	LMBT POST	0.75
RMBT PRE	RMBT POST	0.88
RMBT PRE	ARMSE PRE	-0.70
RMBT PRE	TUGT PRE	-0.69
RMBT PRE	T2min PRE	0.79
MSE PRE	RMBT POST	-0.75
MSE PRE	RMBT PRE	-0.88
MSF PRE	MSE PRE	0.77
AshwF PRE	LMBT POST	0.82
AshwF PRE	GFFP POST	-0.79
GFFP PRE	AROM POST	0.76
GFFP PRE	T2min PRE	-0.70

AROM, active range of motion; AScore, active score; T10m, 10 m walking test; S, safety; T2min, 2 min walking test; RMBT, right monopodal balance test; RRMSE, resistive root mean squared error; RScore, resistive score; ARMSE, active root mean squared error; PROM, passive range of motion; TUGT, timed up and go test; LMBT, left monopodal balance test; MSE, muscle strength extension; MSF, muscle strength-flexion; AshwF, ashworth flexion; GFFP, goniometry flexion FP.

(goniometry), balance through the monopodal test, and distance covered through the 2-min walking test. Muscle tone, the 10-m walking test, and the Timed Up and Go test showed no significant changes. In goniometry, in active flexion, the improvement was not significant, but it was significant in

Forced Passive flexion and Forced Passive and Active extension. Calderón Bernal et al. (2015) reported that human gait is a repetitive functional movement, so that therapy, as in the case of the exoskeleton, should be intensive and aimed at stimulating central pattern generators. They also stated that treatment sessions could improve ankle motor skills explained by an increase in cortical motor excitability for the tibialis anterior, thus achieving an increase in dorsi-plantarflexion of the ankle. Several previous studies with other devices reported improvements in passive joint range, muscle strength, and walking speed (Forrester et al., 2011; Zhou et al., 2015; Chang et al., 2017). The walking speed obtained indirectly, taking into account the distance covered in a 2-minute walking test, was 1.07 m/s pre-treatment and 1.20 m/s post-treatment, thus presenting an improvement of 0.13 m/s. According to Duncan et al. (2011), a speed greater than 0.8 m/s is considered to be high. Other authors, such as Chang et al. (2017) and Forrester et al. (2011), found mainly an increase in walking speed. Balance also showed statistically significant improvements, in line with other studies using other prototypes, albeit measured by the Berg balance scale (Chang et al., 2017). It can be observed that the MEXO exoskeleton allows the therapists' action to be alleviated, increasing the quality of the sessions, their repeatability, length, intensity, and the number of repetitions; as well as the objectivity in the measurement of variables; as robotic devices, machines they are, provide therapists the capability to exactly repeat precise movements, as well as objectively measured, *via* embedded or parallel sensors, physical variables than can be correlated to clinical scales. If these data imply an improvement in ankle control, the variation occurs along with that of the clinical scales used to assess improvement after treatment. Consequently, we can consider that these changes in kinematics, balance and covered distance tend to improve similarly to the clinical scales.

The MEXO exoskeleton would be a prototype, according to the classification of Calderón Bernal et al. (2015), of the static and end-effector type, centred on a single joint. In this case aided by gamification. All patients were able to use the visual feedback with their limbs having a kinematic and dynamic interaction with the robot generating a closed loop between the brain and the limb, and between the human and the robot. Active participation during treatment may improve patients' adherence and initiative and make them more interested (Chan, 2002; Zhou et al., 2015; Gui et al., 2017). The real effect of video games may be to improve the ability to learn new tasks by increasing attentional control in the cognitive interaction of the human-virtual environment (Green and Bavelier, 2012; Asín-Prieto et al., 2020).

Similarly to what we found in our previous study that applied a haptic adaptive feedback (HAF) adapted to the user capabilities with a more complex (yet similarly designed) tool (Asín-Prieto et al., 2020), the patients improved their range of motion and clinical scales score (for T10m and TUGT). In the HAF study, we also gathered the performance data within the game task, and correlated it with the clinical scales, finding that an improvement

TABLE 9 Pearson correlations table ($p > 0.05$) for PRE and POST–treatment variables.

Variable 1	Variable 2	Pearson correlation coefficient	Variable 1	Variable 2	Pearson correlation coefficient
RRMSE POST	RScore POST	−0.94	RScore POST	AScore PRE	0.82
RRMSE POST	AScore POST	−0.92	AScore POST	AScore PRE	0.81
RScore POST	AScore POST	0.88	PROM POST	AScore PRE	0.83
ARMSE POST	AScore POST	−0.81	TUGT POST	AScore PRE	−0.96
RScore POST	PROM POST	0.72	T10m POST	AScore PRE	−0.82
RRMSE POST	TUGT POST	0.84	T2min POST	AScore PRE	0.91
RScore POST	TUGT POST	−0.85	RScore PRE	AScore PRE	0.95
AScore POST	TUGT POST	−0.79	ARMSE PRE	AScore PRE	−0.92
PROM POST	TUGT POST	−0.80	GFA POST	AROM PRE	0.76
RRMSE POST	T10m POST	0.90	RRMSE POST	TUGT PRE	0.67
RScore POST	T10m POST	−0.85	RScore POST	TUGT PRE	−0.70
AScore POST	T10m POST	−0.78	PROM POST	TUGT PRE	−0.86
TUGT POST	T10m POST	0.94	TUGT POST	TUGT PRE	0.86
RRMSE POST	T2min POST	−0.74	T10m POST	TUGT PRE	0.72
RScore POST	T2min POST	0.77	T2min POST	TUGT PRE	−0.85
AScore POST	T2min POST	0.67	RScore PRE	TUGT PRE	−0.88
PROM POST	T2min POST	0.78	ARMSE PRE	TUGT PRE	0.74
TUGT POST	T2min POST	−0.96	AScore PRE	TUGT PRE	−0.84
T10m POST	T2min POST	−0.88	TUGT POST	T10m PRE	0.75
GEA POST	GEFP POST	0.78	T10m POST	T10m PRE	0.78
GFA POST	GFFP POST	0.82	T2min POST	T10m PRE	−0.78
RRMSE POST	RRMSE PRE	0.72	RRMSE PRE	T10m PRE	0.75
TUGT POST	RRMSE PRE	0.79	RScore PRE	T10m PRE	−0.70
T10m POST	RRMSE PRE	0.91	TUGT PRE	T10m PRE	0.78
T2min POST	RRMSE PRE	−0.80	GEA POST	GEA PRE	0.84
RRMSE POST	RScore PRE	−0.82	GEFP POST	GEA PRE	0.73
RScore POST	RScore PRE	0.84	GEA POST	GEFP PRE	0.76
AScore POST	RScore PRE	0.77	GEFP POST	GEFP PRE	0.76
PROM POST	RScore PRE	0.83	GEA PRE	GEFP PRE	0.75
TUGT POST	RScore PRE	−0.97	RRMSE POST	GFA PRE	0.75
T10m POST	RScore PRE	−0.90	RScore POST	GFA PRE	−0.77
T2min POST	RScore PRE	0.95	AScore POST	GFA PRE	−0.82
RRMSE PRE	RScore PRE	−0.77	PROM POST	GFA PRE	−0.69
RRMSE POST	ARMSE PRE	0.72	TUGT POST	GFA PRE	0.72
RScore POST	ARMSE PRE	−0.68	RScore PRE	GFA PRE	−0.71
AScore POST	ARMSE PRE	−0.72	AScore PRE	GFA PRE	−0.74
TUGT POST	ARMSE PRE	0.93	RScore POST	GFFP PRE	−0.71
T10m POST	ARMSE PRE	0.85	PROM POST	GFFP PRE	−0.84
T2min POST	ARMSE PRE	−0.95	TUGT POST	GFFP PRE	0.69
LMBT POST	ARMSE PRE	−0.78	RScore PRE	GFFP PRE	−0.76
RRMSE PRE	ARMSE PRE	0.78	AScore PRE	GFFP PRE	−0.75
RScore PRE	ARMSE PRE	−0.91	TUGT PRE	GFFP PRE	0.71
RRMSE POST	AScore PRE	−0.80	GFA PRE	GFFP PRE	0.83

RRMSE, resistive root mean squared error; RScore, resistive score; AScore, active score; PROM, passive range of motion; ARMSE, active root mean squared error; TUGT, timed up and go test; T10m, 10 m walking test; T2min, 2 min walking test; GFA, goniometry flexion A; AROM, active range of motion; GEA, goniometry extension A; GEFP, goniometry extension FP; GFFP, goniometry flexion FP; LMBT, left monopodal balance test.

in the former could be correlated with better scales in the latter. In the MEXO study we have also used the visual interface (game) as a means of promoting the adherence to the treatment by the patients, and have gathered the performance data, finding moderate to strong correlations between some clinical scales and tests (T10m, TUGT, Monopodal balance) and robotic-videogame system intrinsic measurements (active ROM, resistive RMSE, active and resistive scores). The MEXO study uses the MEXO tool as a simplification towards a low-cost marketable tool based on the tool used in the HAF study.

As referred to by Hussain et al. in terms of the clinical intervention of robots of this type, MEXO allows the patient to practice part of the task (like end-effector robots), perform many repetitions of a movement, which will promote neuroplastic underlying recovery; and maintain and even increase range of motion by mobilising active joints and muscles in different parts of their full range of motion (Hussain et al., 2021).

MEXO, like other robotic ankle exoskeletons, and as reported by Miao et al. (2018), has an optimal design for ankle rehabilitation, through the performance of stretching exercises for the treatment of foot drop, which are usually performed along the dorsiflexion of the ankle, where patients often have difficulty lifting their toes correctly when walking.

Patient satisfaction measured by the QUEST survey was very satisfactory for all patients. The three most important items for the patient were Effectiveness, Comfort and Ease of use. Patient reactions to the training were very positive.

6 Conclusion

Preliminary results in this sample of nine patients have shown safety, usability and patient satisfaction with the use of the exoskeleton.

We aimed at exploring the validity of the combined robotic ankle exoskeleton with a video game, designed to enhance the adherence in the therapy protocol. We approached this objective by providing an appealing and improved visual interface (a video game) while asking them to follow a trajectory depicted as a sequence of collectible onscreen items (resistive and active modes).

Although our actual sample size was small, we found for the studied population that patients obtained positive changes in terms of goniometry and balance, rendering our approach valid and usable for training in stroke survivors. Furthermore, the QUEST Likert-like questionnaire showed that the approach of using the integrated MEXO device was very positively received by all patients, with an overall score of 5 over 5; being the three most important aspects (selected by more than half of the sample), from least to most: Comfort, Effectiveness and Ease of Use.

The MEXO device has been shown to be safe during the execution of this study, with no type of inconvenience arising

with the patients. It has an easily accessible cut-off switch and so far it has never been necessary to use it. No adverse effects or inconveniences have arisen during the use by patients. In conclusion, the integrated tool including non-ambulatory robotic ankle foot orthosis and video game, together with the delivered treatment protocol has been very positively received by patient end-users, and has led to positive results in terms of improvement in clinical scales, balance and range of motion.

6.1 Limitations of this study

The sample size can be considered a limitation of this preliminary exploratory study. All subjects received the same treatment, thus we can obtain conclusions on usability of the system and subjective perception of the end users. However, a randomized controlled trial will be needed to verify the impact of the MEXO robot.

We gathered several representative data, including muscle strength and tone, from a clinical scale point of view. It would have been also useful to provide an objective force measure (torque at the instrumented ankle joint) to compare and even correlate with the clinical scales. Two of the 9 actual participants needed technical aids to walk (in particular, those with a longer time from the lesion). It would be useful to broaden the studied population to survivors with worse walking ability, to try to extend the results to a wider sample of the stroke survivors.

Data availability statement

The raw data supporting the conclusion of this article will be made available by the authors, without undue reservation.

Ethics statement

The studies involving human participants were reviewed and approved by Teaching and Research Committee of the “Jose Nestor Lencinas” Hospital and by the COPEIS (Provincial Health Research Ethics Committee) of the province of Mendoza (Argentina). The patients/participants provided their written informed consent to participate in this study.

Author contributions

Main writing process for the manuscript (GA-P, RR, SM, and JM). Contribution to study conceptualization (RR, SM, and JM), study design (RR and SS), data acquisition (RR, MN, DG, and MT), data analysis (GA-P, AM-E, MN, MT, and JM), and data interpretation (GA-P and JM). Approval of final

manuscript and agreement to be accountable for all aspects of the work while ensuring that questions related to the accuracy or integrity of any part of the work are appropriately investigated and resolved (all).

Funding

This research has been partially funded by the Dicyt, Dirección de Investigaciones Ciencia y Técnica (Gobierno de Mendoza, Argentina). This work has been also partially funded by CSIC Interdisciplinary Thematic Platform (PTI+) NEURO-AGING+ (PTI-NEURO-AGING+). This research has received funding from CSIC's grant MU-201720E072.

Acknowledgments

This work has been performed within the framework of the Red Iberoamericana de Rehabilitación y Asistencia de Pacientes con Daño Neurológico mediante Exoesqueletos de Bajo Coste (REASISTE) coordinated by

José María Azorín. We are also grateful to the team at Biomechanics Unit of Hospital Paraplégicos de Toledo for all the feedback that was provided to optimize both machine and intervention.

Conflict of interest

The authors declare that the research was conducted in the absence of any commercial or financial relationships that could be construed as a potential conflict of interest.

Publisher's note

All claims expressed in this article are solely those of the authors and do not necessarily represent those of their affiliated organizations, or those of the publisher, the editors and the reviewers. Any product that may be evaluated in this article, or claim that may be made by its manufacturer, is not guaranteed or endorsed by the publisher.

References

- Asin-Prieto, G., Barroso, F. A., Moreno, J. C., and Pons, J. L. (2013). Assessment of the suitability of the motorized ankle-foot orthosis as a diagnostic and rehabilitation tool for gait. In *Special Session on Sensory Fusion for Diagnostics and Neurorehabilitation*. (SCITEPRESS) 2, 161–166.
- Asin-Prieto, G., Martínez-Expósito, A., Barroso, F. O., Urendes, E. J., Gonzalez-Vargas, J., Alnajjar, F. S., et al. (2020). Haptic adaptive feedback to promote motor learning with a robotic ankle exoskeleton integrated with a video game. *Front. Bioeng. Biotechnol.* 8, 113. doi:10.3389/fbioe.2020.00113
- Belda-Lois, J.-M., Mena-del Horno, S., Bermejo-Bosch, I., Moreno, J. C., Pons, J. L., Farina, D., et al. (2011). Rehabilitation of gait after stroke: A review towards a top-down approach. *J. neuroengineering rehabilitation* 8, 66–20. doi:10.1186/1743-0003-8-66
- Calderón-Bernal, A., Cano-de la Cuerda, R., Alguacil-Diego, I., Molina-Rueda, F., Cuesta-Gómez, A., and Miangolarra-Page, J. (2015). Terapia robótica para la rehabilitación de la marcha en patología neurológica. *Rehabilitación* 49, 177–192. doi:10.1016/j.rh.2014.11.003
- Chan, R. (2002). Active participation and autonomy: An ultimate target for rehabilitation. *Disabil. Rehabilitation* 24, 983–984. doi:10.1080/09638280210152030
- Chang, J. L., Lin, R. Y., Saul, M., Koch, P. J., Krebs, H. I., and Volpe, B. T. (2017). Intensive seated robotic training of the ankle in patients with chronic stroke differentially improves gait. *NeuroRehabilitation* 41, 61–68. doi:10.3233/nre-171457
- Demers, L., Weiss-Lambrou, R., and Ska, B. (2002). The quebec user evaluation of satisfaction with assistive technology (quest 2.0): An overview and recent progress. *Technol. Disabil.* 14, 101–105. doi:10.3233/tad-2002-14304
- Duncan, P. W., Sullivan, K. J., Behrman, A. L., Azen, S. P., Wu, S. S., Nadeau, S. E., et al. (2011). Body-weight-supported treadmill rehabilitation after stroke. *N. Engl. J. Med. Overseas. Ed.* 364, 2026–2036. doi:10.1056/nejmoa1010790
- Forrester, L. W., Roy, A., Krebs, H. I., and Macko, R. F. (2011). Ankle training with a robotic device improves hemiparetic gait after a stroke. *Neurorehabil. Neural Repair* 25, 369–377. doi:10.1177/1545968310388291
- Green, C. S., and Bavelier, D. (2012). Learning, attentional control, and action video games. *Curr. Biol.* 22, R197–R206. doi:10.1016/j.cub.2012.02.012
- Gui, K., Liu, H., and Zhang, D. (2017). Toward multimodal human-robot interaction to enhance active participation of users in gait rehabilitation. *IEEE Trans. Neural Syst. Rehabil. Eng.* 25, 2054–2066. doi:10.1109/tnsre.2017.2703586
- Hussain, S., Jamwal, P. K., and Ghayesh, M. H. (2017). State-of-the-art robotic devices for ankle rehabilitation: Mechanism and control review. *Proc. Inst. Mech. Eng. H.* 231, 1224–1234. doi:10.1177/0954411917737584
- Hussain, S., Jamwal, P. K., Vliet, P. V., and Brown, N. A. (2021). Robot assisted ankle neuro-rehabilitation: State of the art and future challenges. *Expert Rev. Neurother.* 21, 111–121. doi:10.1080/14737175.2021.1847646
- Jimenez-Fabian, R., and Verlinden, O. (2012). Review of control algorithms for robotic ankle systems in lower-limb orthoses, prostheses, and exoskeletons. *Med. Eng. Phys.* 34, 397–408. doi:10.1016/j.medengphy.2011.11.018
- Jones, O. (2019). *The ankle joint*. Available at: <https://teachmeanatomy.info/lower-limb/joints/ankle-joint/> (accessed April 13, 2022).
- Kwon, J., Park, J.-H., Ku, S., Jeong, Y., Paik, N.-J., and Park, Y.-L. (2019). A soft wearable robotic ankle-foot-orthosis for post-stroke patients. *IEEE Robot. Autom. Lett.* 4, 2547–2552. doi:10.1109/Lra.2019.2908491
- Liddell, E. G. T., and Sherrington, C. S. (1924). Reflexes in response to stretch (myotatic reflexes). *Proc. R. Soc. Lond. Ser. B, Contain. Pap. a Biol. Character* 96, 212–242.
- Miao, Q., Zhang, M., Wang, C., and Li, H. (2018). Towards optimal platform-based robot design for ankle rehabilitation: The state of the art and future prospects. *J. Healthc. Eng.* 2018, 1–9. doi:10.1155/2018/1534247
- Sacco, R. L., Kasner, S. E., Broderick, J. P., Caplan, L. R., Connors, J., Culebras, A., et al. (2013). An updated definition of stroke for the 21st century: A statement for healthcare professionals from the American heart association/American stroke association. *Stroke* 44, 2064–2089. doi:10.1161/str.0b013e318296aeca
- Smania, N., Picelli, A., Munari, D., Geroi, C., Ianes, P., Waldner, A., et al. (2010). Rehabilitation procedures in the management of spasticity. *Eur. J. Phys. Rehabil. Med.* 46, 423–438.
- Spaich, E., and Tabernig, C. (2002). Estimulación eléctrica y espasticidad: Una revisión. *Rehabilitación* 36, 162–166. doi:10.1016/s0048-7120(02)73263-5
- Teasell, R. W. (1992). Long-term sequelae of stroke: How should you handle stroke complications? *Can. Fam. Physician* 38, 381–388.
- World Health Organization (2017). *Enfermedades cardiovasculares*. Available at: <https://www.who.int/es/news-room/fact-sheets/detail/cardiovascular-diseases-cvds>.
- Zhou, Z., Zhou, Y., Wang, N., Gao, F., Wei, K., and Wang, Q. (2015). A proprioceptive neuromuscular facilitation integrated robotic ankle-foot system for post stroke rehabilitation. *Robotics Aut. Syst.* 73, 111–122. doi:10.1016/j.robot.2014.09.023



OPEN ACCESS

EDITED BY

Suvash C. Saha,
University of Technology Sydney,
Australia

REVIEWED BY

Xiangtao Li,
School of Artificial Intelligence, Jilin
University, China
Essam Halim Houssein,
Minia University, Egypt

*CORRESPONDENCE

Hongwei Ding,
wzs_ynu@163.com

SPECIALTY SECTION

This article was submitted to
Biomechanics,
a section of the journal
Frontiers in Bioengineering and
Biotechnology

RECEIVED 14 August 2022

ACCEPTED 17 November 2022

PUBLISHED 01 December 2022

CITATION

Wang Z, Ding H, Yang J, Hou P,
Dhiman G, Wang J, Yang Z and Li A
(2022), Orthogonal pinhole-imaging-
based learning salp swarm algorithm
with self-adaptive structure for
global optimization.
Front. Bioeng. Biotechnol. 10:1018895.
doi: 10.3389/fbioe.2022.1018895

COPYRIGHT

© 2022 Wang, Ding, Yang, Hou,
Dhiman, Wang, Yang and Li. This is an
open-access article distributed under
the terms of the [Creative Commons
Attribution License \(CC BY\)](#). The use,
distribution or reproduction in other
forums is permitted, provided the
original author(s) and the copyright
owner(s) are credited and that the
original publication in this journal is
cited, in accordance with accepted
academic practice. No use, distribution
or reproduction is permitted which does
not comply with these terms.

Orthogonal pinhole-imaging-based learning salp swarm algorithm with self-adaptive structure for global optimization

Zongshan Wang^{1,2}, Hongwei Ding^{1,2*}, Jingjing Yang^{1,2},
Peng Hou³, Gaurav Dhiman^{4,5,6}, Jie Wang⁷, Zhijun Yang^{1,2} and
Aishan Li⁸

¹School of Information Science and Engineering, Yunnan University, Kunming, China, ²University Key Laboratory of Internet of Things Technology and Application, Kunming, China, ³School of Computer Science, Fudan University, Shanghai, China, ⁴Department of Electrical and Computer Engineering, Lebanese American University, Byblos, Lebanon, ⁵Department of Computer Science and Engineering, University Centre for Research and Development, Chandigarh University, Gharuan, India, ⁶Department of Computer Science and Engineering, Graphic Era Deemed to be University, Dehradun, India, ⁷School of Mechanical and Power Engineering, Zhengzhou University, Zhengzhou, China, ⁸Rackham Graduate School, University of Michigan, Ann Arbor, MI, United States

Salp swarm algorithm (SSA) is a simple and effective bio-inspired algorithm that is gaining popularity in global optimization problems. In this paper, first, based on the pinhole imaging phenomenon and opposition-based learning mechanism, a new strategy called pinhole-imaging-based learning (PIBL) is proposed. Then, the PIBL strategy is combined with orthogonal experimental design (OED) to propose an OPIBL mechanism that helps the algorithm to jump out of the local optimum. Second, a novel effective adaptive conversion parameter method is designed to enhance the balance between exploration and exploitation ability. To validate the performance of OPLSSA, comparative experiments are conducted based on 23 widely used benchmark functions and 30 IEEE CEC2017 benchmark problems. Compared with some well-established algorithms, OPLSSA performs better in most of the benchmark problems.

KEYWORDS

particle swarm optimization, exploration and exploitation, metaheuristic algorithms, equilibrium optimizer, global optimization, benchmark

1 Introduction

In recent years, metaheuristics have received incredible attention worldwide, and their great success on global optimization tasks has established superb beliefs for researchers, motivating them to develop more algorithms with good performance. Basically, metaheuristics are classified into four categories, namely swarm-based, human-based, evolution-based and physics-based approaches. Among them, swarm intelligence-based methods have attracted most enthusiastic admiration, and they usually metaphorically

represent some unique swarming behavior of organisms in the nature. The most classical swarm intelligent algorithm, particle swarm optimization (PSO) algorithm (Kennedy and Eberhart, 1995), mimics the flocking behavior of birds as they fly through the sky. Artificial bee colony (ABC) algorithm (Karaboga and Basturk, 2007; Wang et al., 2020), inspired by the collaborative honey-harvesting behavior of bees, has also captured widespread attention and has been successfully applied to solve real-world problems. The ant colony optimization (ACO) algorithm (Blum, 2005) is motivated by the phenomenon that ant colonies transmit information by secreting pheromones to accomplish foraging. The ACO algorithm is admired by researchers because of its unique advantages in solving business travel problems. Besides, many excellent nature-inspired swarm intelligent approaches have been validated to be effective in tricky global optimization projects, they include but are not limited to: bat algorithm (BA) (Yang and Gandomi, 2012), krill herd optimization (KHO) (Gandomi et al., 2012), cuckoo search (CS) algorithm (Gandomi et al., 2013), fruit-fly optimization algorithm (FOA) (Mitić et al., 2015), grey wolf optimizer (GWO) (Mirjalili et al., 2014), moth-flame optimization (MFO) (Mirjalili, 2015), grasshopper optimization algorithm (GOA) (Abualigah and Diabat, 2020), whale optimization algorithm (WOA) (Mirjalili and Lewis, 2016), marine predators algorithm (MPA) (Faramarzi et al., 2020a), white shark optimizer (WSO) (Braik et al., 2022), starling murmuration optimizer (SMO) (Zamani et al., 2022), harris hawks algorithm (Heidari et al., 2019), squirrel search optimization (SSO) algorithm (Jain et al., 2019), dragonfly algorithm (DA) (Mirjalili, 2016), chimp optimization algorithm (ChOA) (Khishe and Mosavi, 2020), rat swarm algorithm (RSA) (Dhiman et al., 2021), Animal migration optimization (AMO) (Li et al., 2014), butterfly optimization algorithm (BOA) (Arora and Singh, 2019), emperor penguin optimizer (EPO) (Dhiman and Kumar, 2018), tunicate swarm algorithm (TSA) (Kaur et al., 2020), horse herd optimization algorithm (HOA) (MiarNaeimi et al., 2021), monarch butterfly optimization (MBO) (Wang et al., 2019), firefly algorithm (Fister et al., 2013; Wang et al., 2022a), and seagull optimization algorithm (SOA) (Dhiman and Kumar, 2019).

Swarm intelligent algorithms have emerged in various scientific and engineering fields, they are based on different metaphors, and their mathematical models consequently differ, which correspond to distinctive search mechanisms. Nevertheless, the framework of these algorithms is broadly the same, all divided into two phases: exploration (cohesion) and exploitation (alignment) (Wang et al., 2022b). In the exploration phase, it is encouraged to maximize the stochasticity of the search agents, which is related to the global search process. In the later iteration, the algorithm shifts from exploration to exploitation, refining the promising regions that have already been explored, which is pertinent to the local search process. Balancing these two phases is a core essential and challenging task for metaheuristic techniques.

Recently, a novel nature-inspired swarm intelligent technique, namely salp swarm algorithm (SSA) (Mirjalili et al., 2017), has been reported by Mirjalili in 2017. SSA simulates the distinctive foraging and navigation behaviors of the marine biological salps. The framework is mainly based on the leader-follower mechanism of the salp swarm. Compared with other population intelligence-based approaches, SSA has many advantages, such as fewer control parameters, easy implementation, and special search pattern. Prior studies have shown that SSA displays better performance than other metaheuristic techniques on numerical optimization problems and engineering design cases. Therefore, SSA is favored and employed to tackle various optimization problems. In (Ewees et al., 2021), Ewees et al. enhanced SSA algorithm using firefly search mechanism for solving unrelated parallel machine scheduling problem. In (Xia et al., 2022), Xia et al. proposed barebone SSA algorithm, and embedded quasi-oppositional based learning strategy. The developed SSA variant was used in medical diagnosis systems. In (Ozbay and Alatas, 2021), Ozbay et al. added inertia weights to the standard SSA to improve the ability of the algorithm to find the optimal solution and utilized the boosted SSA for fake news detection and obtained satisfactory results. In (Faris et al., 2018) introduced a binary version of SSA with a crossover mechanism for feature selection problems. In, Tu et al. (2021) proposed a quantum-behaved SSA approach and studied the application of the advocated approach in wireless sensor networks. In, Wang et al. (2021) developed an improved SSA with opposition based learning mechanism and ranking-based learning strategy for global optimization problems and PV parameter extraction task.

Although the SSA algorithm has shown excellent performance on global optimization problems, it still suffers from premature convergence and insufficient solution accuracy when large-scale optimization tasks and complex restricted engineering design issues. To address these limitations of the standard SSA, many high-performance SSA-based algorithms have been developed. In, Ding et al. (2022) developed a velocity-based SSA algorithm. The proposed algorithm enhances the search efficiency of SSA by limiting the maximum speed of the algorithm. Furthermore, an adaptive mechanism was added to the SSA to balance the exploration and exploitation ability. The introduced algorithm was tested using the CEC 2017 benchmark suite. Experimental results show that the velocity-based SSA algorithm outperforms all competitors. Finally, the proposed algorithm is employed to solve the mobile robot path planning task, and the results show that the algorithm is able to plan reasonable collision-free path for the robot. In (Çelik et al., 2021), devised three simple but efficacious strategies to improve the performance of the standard SSA. First, the control parameter is amended chaotically to enhance the tradeoff between exploration and exploitation. Then, a new mutualistic phase is injected to augment the information exchange between leading salps. Finally,

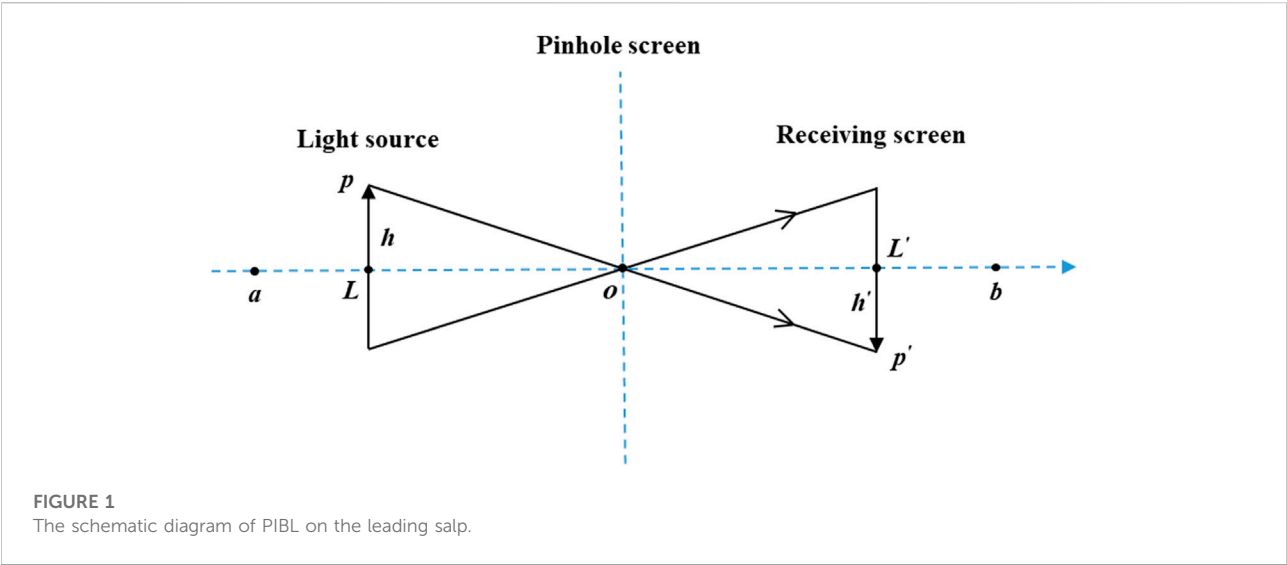


FIGURE 1
The schematic diagram of PIBL on the leading salp.

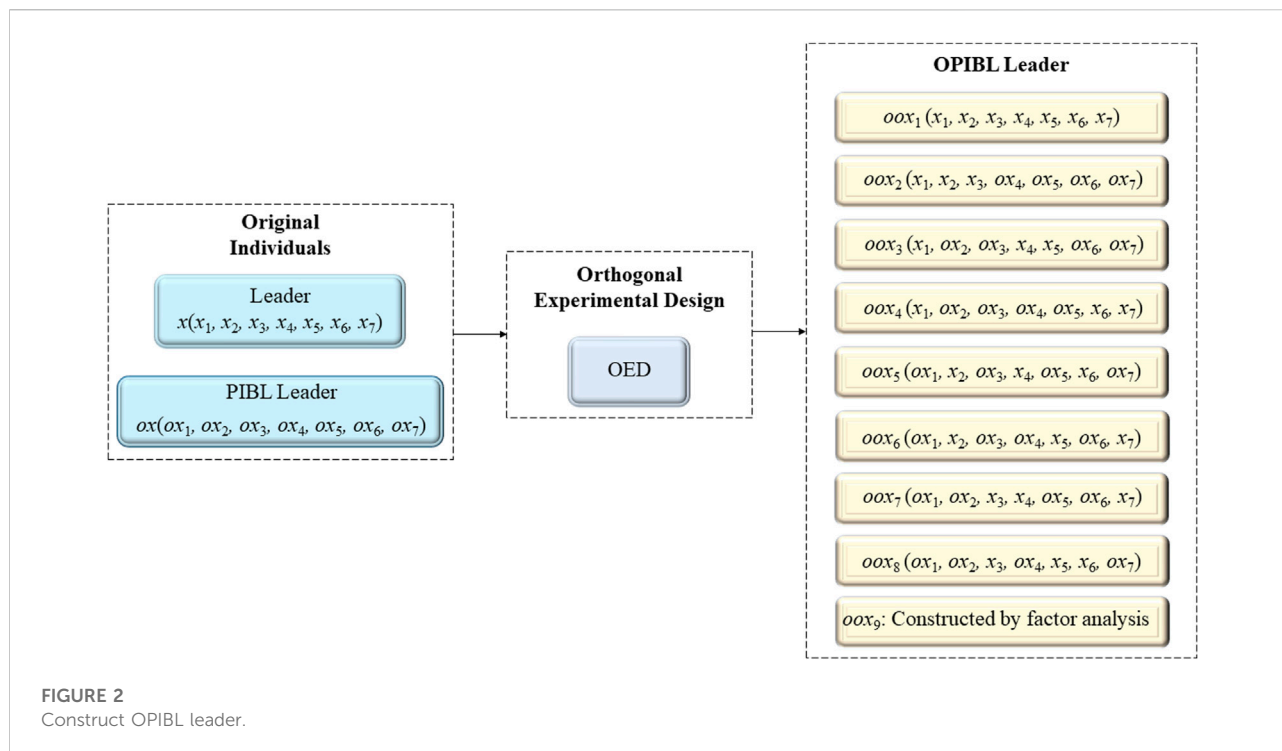
TABLE 1 Orthogonal array of $L_9 (3^4)$.

M	K			
	1	2	3	4
1	1	1	1	1
2	1	2	2	2
3	1	3	3	3
4	2	1	2	3
5	2	2	3	1
6	2	3	1	2
7	3	1	3	2
8	3	2	1	3
9	3	3	2	1

stochastic techniques are applied to improve the dynamics among the followers. In, [Chen et al. \(2022\)](#) made three adjustments to the basic SSA. Opposition-based learning technique is adopted to enrich the population diversity. The leader location update formula is modified to help the salp chain jump out of sub-optimal solution. A social learning tactic inspired by PSO is introduced to accelerate the convergence of the optimizer. In, [Zhang et al. \(2021\)](#) introduced a mutual learning mechanism in the exploitation phase of SSA to improve its performance, and used a tangent factor to update the location of the search agent. In, [Wang et al. \(2022c\)](#) designed an orthogonal quasi-opposition-based learning structure to avoid the population from falling into local optima. Moreover, a dynamic learning paradigm is proposed to effectively improve the search pattern of the followers. In ([Bairathi and Gopalani, 2021](#)), Bairathi et al. proposed a boosted version of SSA for

complex multimodal problems. First, stochastic opposition-based learning is used to enhance the ability to search for unknown regions. Then, multiple search agents are employed to serve as leaders instead of one to intensify the global search ability. Finally, it is compounded with the simulation annealing algorithm to improve the local development ability. In, [Singh et al. \(2022\)](#) proposed a hybrid algorithm of HHO and SSA to cover the unbalanced local search and global exploration of the basic SSA.

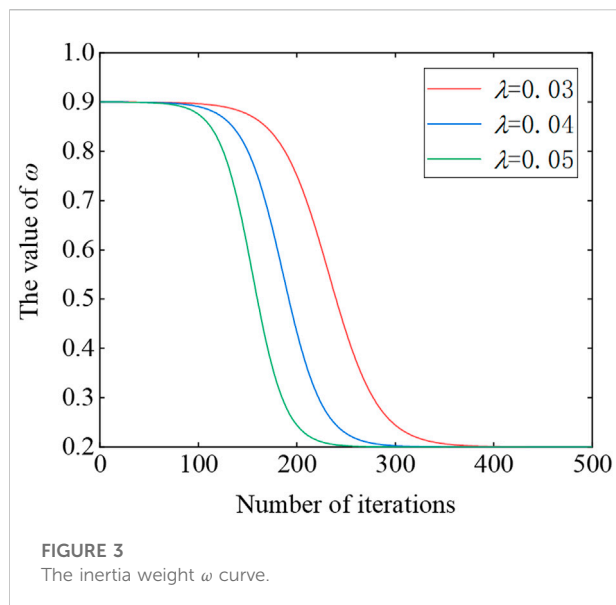
Many existing SSA variants focus mainly on alleviating the shortcomings of lack of convergence accuracy and unbalanced exploitation and exploration suffered by the basic SSA. For this purpose, different strategies have been injected into SSA and achieved remarkable results. However, these two limitations have not been completely solved and there are still research gaps. Moreover, the “No Free Lunch” theorems ([Wolpert and Macready, 1997](#)) logically proves that it is impossible to expect one algorithm to solve all optimization problems. That is to say, while each algorithm has some unique characteristics along with shortcomings. Even for reputable algorithms, they still have some limitations. For example, AMO is a classical metaheuristic algorithm inspired by animal migration behavior. This optimizer can effectively improve the initial random population and converge to the global optima. It has many advantages, including simple search pattern, easy to implement, and strong global optimization ability. Thanks to the success of the AMO algorithm, it has been applied to many different optimization problems, such as clustering ([Hou et al., 2016](#)), the optimal power flow problem ([Dash et al., 2022](#)), and multilevel image thresholding ([Rahkar Farshi, 2019](#)). However, as most metaheuristic techniques, it suffers from premature convergence and often falls into optima. To solve this drawback, many AMO variants have been proposed, such as the opposition-based AMO ([Cao et al., 2013](#)), and Lévy flight



assisted AMO (Gülcü, 2021). Differential evolution (DE) (Storn and Price, 1997) is a global search algorithm, which simulates the biological process in the nature. In DE algorithm, individuals repeatedly perform mutation, crossover, and selection to guide the search process to gradually approach the global optima solution. Because of its simplicity and effectiveness, it has received a lot of attention and has been applied to solve many real-world problems (Wang et al., 2022d). However, DE has some limitations, such as unbalanced exploration and exploitation ability and being sensitive to the selection of the control parameters. To alleviate these drawbacks, Li et al. (2017) proposed a Multi-search DE algorithm with three adjustments. First, the population is divided into multiple subpopulations and the subpopulation group size is dynamically adjusted. Second, three effective mutation strategies are proposed to take on the responsibility for either exploitation or exploration. Finally, a novel parameter adaptation method is designed to solve the automatically adjust the algorithmic parameters. However, there is no mechanism in this DE variant for large-scale problems, which will result in its performance will still be restricted by the phenomenon of “curse of dimensionality” as the number of dimensions increase. The CS is an effective optimization algorithm with two features that make it stands out against other metaheuristic techniques. First, it uses a mutation function based on Lévy flight to improve the quality of the randomly selected solutions at each iteration. Second, it uses one parameter called abandon fraction that does not require fine-tuning. However, CS suffers from the drawback of being prone to

premature convergence (Zhang et al., 2019). To address this limitation, many CS variants were developed. For example, Li et al. (Li and Yin, 2015) used two novel mutation rules and the new rules were combined by a linear decreasing probability rule to balance the exploitation and exploration of the algorithm. Further, the parameter setting was adjusted to enhance the diversity of the population. The performance of the developed CS-based method was tested using 16 classical test functions. Experimental results show that the introduced approach performs better than its competitors, or at least comparable to the peer algorithms. However, according to the statistical results, the proposed algorithm still suffers from the drawback of insufficient convergence accuracy. In this paper, a novel SSA variant called OPLSSA is introduced considering the above two considerations. First, a novel pinhole-imaging opposition-based learning mechanism is designed and combined with the orthogonal experimental design for effectively enhancing the global exploration ability. Second, the follower update pattern is modified by introducing adaptive inertia weights to provide dynamic search with adaptive mechanism. Comprehensive comparison experiments on 23 widely used numerical test functions and 30 CEC 2017 benchmark problems demonstrate that the proposed approach outperforms the traditional SSA, popular SSA-based methods, and well-established population-based intelligent algorithms.

The remainder of this work is structured as follows: The standard SSA, including the principle, mathematical model and shortcoming analysis, is presented in Section 2. The developed



modifications and the advocated OPLSSA algorithm are described in detail in Section 3. The effectiveness of the proposed approach is verified by comparison experiments in Section 4. Finally, the conclusions and future tasks are provided in Section 5.

2 The original salp swarm algorithm

2.1 Description of salp swarm algorithm

The SSA algorithm is a well-established swarm intelligent approach inspired by the unexplained behavior of salp swarm that organize in chains to improve foraging efficiency in oceans. SSA, resembling other population intelligence-based methodologies, commences its search process with a suit of randomly generated search agents, each of which indicates a solution to the pending problem. SSA compartmentalizes the salp population into two groups: leaders and followers. The leader is the key member, which plays a leadership role and at the front of the chain to lead the population in search of food. The followers, on the other hand, move implicitly or outright along the trajectory of the leader.

In SSA, the leading salp changes position depending on the following formula.

$$X_{1,j} = \begin{cases} F_j + c_1 \times ((ub_j - lb_j) \times c_2 + lb_j) & c_3 \geq 0.5 \\ F_j - c_1 \times ((ub_j - lb_j) \times c_2 + lb_j) & c_3 < 0.5 \end{cases} \quad (1)$$

where $X_{1,j}$ and F_j are the locations of the leader and the food source, respectively, c_2 is a random vector, c_3 is a random value, all taking values between the interval $[0,1]$, and c_1 is the key parameter that regulates the transformation of the algorithm from the exploration

in the initial iteration to the exploitation in the later search stages, which is calculated according to the following equation.

$$c_1 = 2 \times e^{-\left(\frac{4 \times l}{L}\right)^2} \quad (2)$$

where l and L denote the current iteration and the maximum iteration, respectively.

The mathematical equation used to change the followers' positions is as follows:

$$X_{i,j} = \frac{1}{2} \times (X_{i,j} + X_{i-1,j}) \quad (3)$$

where $X_{i,j}$ indicates the location of the i -th follower in the j th dimensional search landscape.

Algorithm 1 outlines the pseudo code of the basic SSA.

```

1  Initialize the salp population  $X_i(i=1,2,\dots,N)$  consider  $ub$  and  $lb$ 
2  Obtain food source position based on the fitness
3  while ( $l < L$ ) do
4      Update  $c_1$  by Eq. (2)
5      for  $i=1$  to  $N$ 
6          if  $i==1$  (leader)
7              Update the position of the leading salp by Eq. (1)
8          else if (follower)
9              Update the position of the follower by Eq. (8)
10         end if
11     end for
12     Amend the search agent based on the boundaries
13     Evaluate the salp population based on the fitness
14     Update the food source position
15      $l=l+1$ 
16 end while
17 Output the food source position

```

Algorithm 1. Q-Pseudocode of SSA.

The SSA approach begins the search with a reservation number of randomly generated search agents, and subsequently continuously updates the population position according to the objective value of the optimized function. The fitness of the population is evaluated after each iteration and the best individual is assigned as the current food source, which is the desired goal pursued by the leader, and the followers intuitively or implicitly follow the leading salp, the salp chain thus continuously approaching the food source. Notably, the value of the control parameter c_1 decreases nonlinearly after the lapse of iterations, and the salp chain accordingly switches from moving in large steps to explore the search space to traveling gradually to exploit the already discovered potential areas. The salp swarm repeatedly searches following the aforementioned pattern until the cessation criterion is encountered, at which point the food source is the expected optimal solution.

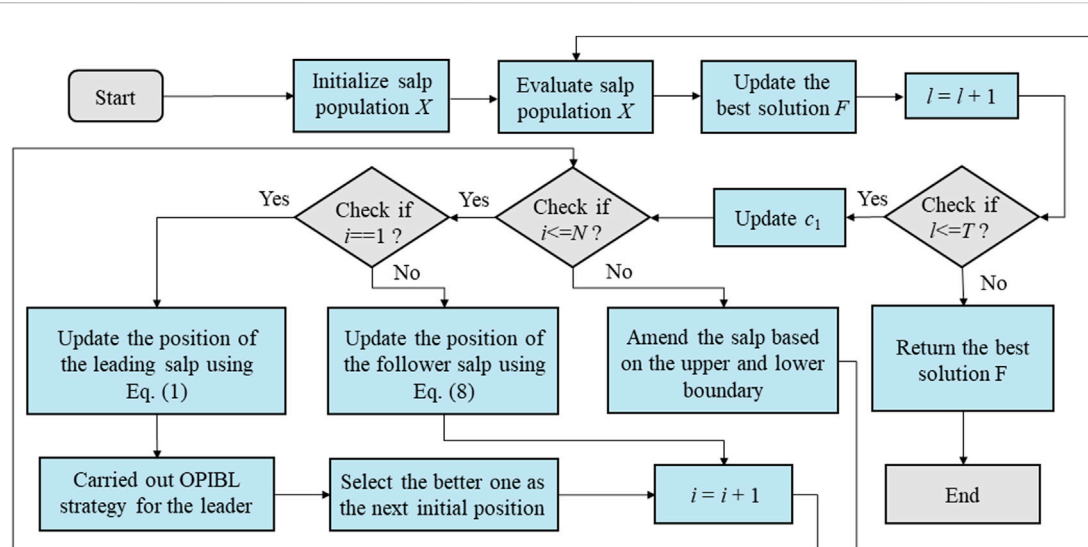


FIGURE 4
The flow chart of OPLSSA.

TABLE 2 The characteristics of the classical benchmark functions.

Function type	Function formulation	Search range	f_{\min}
Unimodal	$f_1(x) = \sum_{i=1}^D x_i^2$	$[-100, 100]$	0
	$f_2(x) = \sum_{i=1}^D i x_i^2$	$[-10, 10]$	0
	$f_3(x) = \sum_{i=1}^D (\sum_{j=1}^i x_j)^2$	$[-100, 100]$	0
	$f_4(x) = \max_i \{ x_i , 1 \leq x_i \leq D\}$	$[-100, 100]$	0
	$f_5(x) = \sum_{i=1}^D (x_i + 0.5)^2$	$[-100, 100]$	0
	$f_6(x) = \sum_{i=1}^D i x_i^4$	$[-1.28, 1.28]$	0
	$f_7(x) = \sum_{i=1}^D i x_i^4 + \text{random}[0, 1]$	$[-1.28, 1.28]$	0
	$f_8(x) = \sum_{i=1}^D x_i ^{(i+1)}$	$[-1, 1]$	0
	$f_9(x) = \sum_{i=1}^D (10^6)^{(i-1)/(D-1)} x_i^2$	$[-100, 100]$	0
	$f_{10}(x) = x_1^2 + 10^6 \cdot \sum_{i=2}^D x_i^6$	$[-100, 100]$	0
	$f_{11}(x) = 10 \cdot x_1^2 + \sum_{i=2}^D x_i^6$	$[-1, 1]$	0
Multimodal	$f_{12}(x) = \sum_{i=1}^D [x_i^2 - 10 \cos(2\pi x_i) + 10]$	$[-5.12, 5.12]$	0
	$f_{13}(x) = -20 \exp(-0.2 \sqrt{\frac{1}{D} \sum_{i=1}^D x_i^2}) - \exp(\frac{1}{D} \sum_{i=1}^D \cos(2\pi x_i)) + 20 + e$	$[-32, 32]$	0
	$f_{14}(x) = \frac{1}{4000} \sum_{i=1}^D x_i^2 - \prod_{i=1}^D \cos(\frac{x_i}{\sqrt{i}}) + 1$	$[-600, 600]$	0
	$f_{15}(x) = \sum_{i=1}^D x_i \cdot \sin(x_i) + 0.1 x_i $	$[-10, 10]$	0
	$f_{16}(x) = \sin^2(\pi x_1) + \sum_{i=1}^{D-1} [x_i^2 \cdot (1 + 10 \sin^2(\pi x_i)) + (x_i - 1)^2 - \sin^2(2\pi x_i)]$	$[-10, 10]$	0
	$f_{17}(x) = 0.1D - (0.1 \sum_{i=1}^D \cos(5\pi x_i) - \sum_{i=1}^D x_i^2)$	$[-1, 1]$	0
	$f_{18}(x) = \sum_{i=1}^D x_i^2 + (\sum_{i=1}^D 0.5 x_i)^2 + (\sum_{i=1}^D 0.5 x_i)^4$	$[-5, 10]$	0
	$f_{19}(x) = \sum_{i=1}^D (0.2 x_i^2 + 0.1 x_i^2 \cdot \sin(2\pi x_i))$	$[-10, 10]$	0
	$f_{20}(x) = [\frac{1}{D-1} \sum_{i=1}^D (\sqrt{x_i} (\sin(50.0 x_i^{0.2}) + 1))]^2$	$[-100, 100]$	0
	$f_{21}(x) = \sum_{i=1}^{D-1} [x_i^2 + 2x_{i+1}^2 - 0.3 \cos(3\pi x_i) - 0.4 \cos(4\pi x_{i+1}) + 0.7]$	$[-15, 15]$	0
	$f_{21}(x) = \sum_{i=1}^{D-1} (x_i^2 + 2x_{i+1}^2)^{0.25} \cdot ((\sin 50(x_i^2 + x_{i+1}^2)^{0.1})^2 + 1)$	$[-10, 10]$	0
	$f_{23}(x) = \sum_{i=1}^{D-1} x_i^6 \cdot (2 + \sin \frac{1}{x_i})$	$[-1, 1]$	0

TABLE 3 Comparisons of nine algorithms on 23 test functions with 100 dimensions.

Function	Results	SSA	LSSA	ASSA	GSSA	OBSSA	ASSO	RDSSA	IWOSSA	OPLSSA
f1	Mean	1.29E+03	2.50E-03	5.11E-02	1.23E-15	3.92E-32	2.02E-26	3.93E-65	1.75E-06	0
	Std	3.17E+02	2.20E-03	3.97E-02	4.22E-15	4.65E-32	3.11E-27	1.75E-64	1.61E-06	0
	f-rank	9	7	8	5	3	4	2	6	1
f2	Mean	8.71E+02	2.00E-01	2.01E-02	7.11E-16	3.00E-32	9.87E-27	8.16E-39	4.69E-07	0
	Std	2.42E+02	1.74E-01	8.20E-03	2.86E-15	3.50E-32	1.48E-27	4.47E-38	4.08E-07	0
	f-rank	9	8	7	5	3	4	2	6	1
f3	Mean	5.02E+04	8.39E+03	1.79E+04	1.43E+04	4.77E-30	1.92E-25	5.28E-34	1.01E+05	0
	Std	2.29E+04	5.89E+03	9.86E+03	8.51E+03	8.26E-30	7.04E-26	2.89E-33	3.21E+04	0
	f-rank	8	5	7	6	3	4	2	9	1
f4	Mean	2.73E+01	2.25E+01	9.3313	2.39E+01	5.52E-17	3.45E-14	5.53E-30	4.47E+01	0
	Std	2.8509	5.2878	2.6632	3.2136	3.56E-17	3.08E-15	2.40E-29	7.0144	0
	f-rank	8	6	5	7	3	4	2	9	1
f5	Mean	2.83E+03	8.1000	1.46E+01	0	0	0	0	1.0667	0
	Std	8.76E+02	5.0402	7.0392	0	0	0	0	1.7991	0
	f-rank	9	7	8	1	1	1	1	6	1
f6	Mean	2.97E-01	1.17E-02	1.06E-07	1.86E-02	3.97E-70	1.44E-59	1.95E-95	3.67E-12	0
	Std	1.91E-01	1.70E-02	1.14E-07	2.55E-02	7.31E-70	4.82E-60	1.07E-94	8.94E-12	0
	f-rank	9	7	6	8	3	4	2	5	1
f7	Mean	2.6326	6.81E-01	8.53E-02	1.13E-01	7.85E-05	1.14E-04	7.41E-04	8.06E-02	8.96E-05
	Std	4.78E-01	2.71E-01	2.09E-02	1.45E-01	9.21E-05	1.03E-04	5.22E-04	4.73E-02	9.53E-05
	f-rank	9	8	6	7	1	3	4	5	2
f8	Mean	3.36E-06	2.59E-10	1.98E-26	7.00E-50	9.10E-39	1.17E-35	2.74E-74	1.33E-17	0
	Std	2.60E-06	1.21E-09	7.55E-26	3.83E-49	2.83E-38	2.33E-35	1.50E-73	4.51E-17	0
	f-rank	9	8	6	3	4	5	2	7	1
f9	Mean	7.14E+07	1.2397	1.26E+02	1.20E-14	2.88E-27	1.36E-21	6.63E-33	9.80E-03	0
	Std	2.67E+07	9.42E-01	5.88E+01	4.08E-14	4.05E-27	5.33E-22	3.63E-32	6.50E-03	0
	f-rank	9	7	8	5	3	4	2	6	1
f10	Mean	6.72E+13	1.36E+09	9.78E+05	1.53E+13	5.34E-35	5.37E-32	2.55E-82	1.69E+05	0
	Std	4.72E+13	3.58E+09	1.12E+06	1.27E+13	1.55E-34	7.22E-32	1.39E-81	5.07E+05	0
	f-rank	9	7	6	8	3	4	2	5	1
f11	Mean	1.7951	1.47E-04	2.78E-10	5.71E-17	7.60E-33	5.19E-30	5.47E-76	5.77E-09	0
	Std	1.5770	3.60E-04	7.29E-10	2.49E-16	2.92E-32	1.15E-29	2.99E-75	2.62E-08	0
	f-rank	9	8	6	5	3	4	2	7	1
f12	Mean	2.36E+02	1.95E+02	2.38E+02	2.88E-11	0	0	0	3.22E+02	0
	Std	3.42E+01	1.13E+02	1.31E+02	1.27E-10	0	0	0	1.14E+02	0
	f-rank	7	6	8	5	1	1	1	9	1
f13	Mean	1.03E+01	8.47E-02	2.93E-02	1.32E-09	8.88E-16	1.96E-14	4.20E-15	6.63E-01	8.88E-16
	Std	1.4847	3.05E-01	1.03E-02	1.80E-09	0	2.27E-15	9.01E-16	3.6301	0
	f-rank	9	7	6	5	1	4	3	8	1
f14	Mean	1.35E+01	2.74E-02	5.33E-02	1.29E-14	0	0	0	3.60E-03	0
	Std	4.7887	4.76E-02	3.61E-02	6.18E-14	0	0	0	8.60E-03	0
	f-rank	9	7	8	5	1	1	1	6	1
f15	Mean	2.86E+01	1.35E+01	1.04E+01	4.42E-14	1.49E-17	1.14E-14	1.65E-26	1.88E+01	0
	Std	6.1418	1.29E+01	6.2120	1.40E-13	5.88E-18	7.75E-16	6.69E-26	1.56E+01	0
	f-rank	9	7	6	5	3	4	2	8	1
f16	Mean	3.51E+02	1.77E+02	4.31E+01	4.73E-08	1.99E-32	7.97E-27	6.69E-47	8.3098	0
	Std	6.68E+02	1.38E+02	2.49E+01	1.69E-07	1.96E-32	1.22E-27	3.63E-46	2.21E+01	0
	f-rank	9	8	7	5	3	4	2	6	1

(Continued on following page)

TABLE 3 (Continued) Comparisons of nine algorithms on 23 test functions with 100 dimensions.

Function	Results	SSA	LSSA	ASSA	GSSA	OBSSA	ASSO	RDSSA	IWOSSA	OPLSSA
f17	Mean	4.9384	1.3822	1.36E-04	0	0	0	0	1.99E-09	0
	Std	6.59E-01	7.74E-01	1.69E-04	0	0	0	0	9.33E-10	0
	f-rank	9	8	7	1	1	1	1	6	1
f18	Mean	7.16E+01	1.78E-02	8.50E-03	9.29E-09	2.09E+02	1.75E-28	4.35E-47	2.16E-02	2.92E-44
	Std	1.95E+01	1.08E-02	4.90E-03	2.12E-08	3.03E+01	3.42E-29	2.38E-46	2.77E-02	8.67E-45
	f-rank	8	6	5	4	9	3	1	7	2
f19	Mean	1.89E+01	3.40E-03	1.48E-04	4.36E-17	8.03E-35	4.02E-29	1.48E-43	2.55E-09	0
	Std	5.7632	4.70E-03	7.83E-05	1.00E-16	9.15E-35	5.04E-30	8.13E-43	1.80E-09	0
	f-rank	9	8	7	5	3	4	2	6	1
f20	Mean	5.0612	2.83E-01	1.8212	5.69E-10	4.79E-09	1.28E-07	6.21E-15	7.26E-02	0
	Std	2.18E-01	238E-01	5.49E-01	5.11E-10	1.36E-09	4.05E-09	2.58E-14	2.26E-01	0
	f-rank	9	7	8	5	4	3	2	6	1
f21	Mean	1.90E+02	1.34E+01	3.94E-01	1.22E-16	0	0	0	1.34E-06	0
	Std	2.88E+01	6.4554	5.12E-01	3.94E-16	0	0	0	7.37E-07	0
	f-rank	9	8	7	5	1	1	1	6	1
f22	Mean	4.1930	4.1724	4.1941	9.39E-01	4.65E-09	1.19E-07	1.86E-02	3.5709	0
	Std	1.88E-01	3.04E-01	1.61E-01	4.69E-01	1.36E-09	4.29E-09	2.18E-02	1.1627	0
	f-rank	8	7	9	5	2	3	4	6	1
f23	Mean	2.59E-04	1.16E-05	5.96E-11	8.13E-05	5.24E-108	1.64E-92	6.43E-209	2.79E-10	0
	Std	1.65E-04	9.04E-06	9.92E-11	1.08E-04	1.72E-107	8.86E-93	0	7.19E-10	0
	f-rank	9	7	5	8	3	4	2	6	1
Average f-rank		8.7391	7.1304	6.7826	5.1739	2.6956	3.2174	1.9565	6.5652	1.0869
Overall f-rank		9	8	7	5	3	4	2	6	1

2.2 Analysis of the shortcomings of salp swarm algorithm

In this subsection, we analyze the key limitations of the basic SSA, which is the inference and motivation behind the current work. The details are as follows:

- 1) First of all, there is only one parameter c_1 to be updated in the basic SSA, which is used to control the movement of the leader and thus maintain a more stable balance between exploration and exploitation. However, strong stochastic factors break this expectation. The food source could not guide the leader salp to the more promising search region as expected, resulting in the algorithm not being able to switch search modes smoothly during the search process, which also reduced the convergence speed.
- 2) Second, the position update equation of the followers in SSA does not have any control parameters, and although this can reduce the computational cost, it will make this movement mechanism sluggish and the algorithm is thus prone to fall into local optimum.

3) In addition, adaptive is a novel and effective technique that helps the algorithm to adjust the movement pattern autonomously during the search process, however, such operator is lacking in SSA.

- 4) Finally, maintaining a desirable balance between exploitation and exploration is the goal pursued by all swarm-based intelligence techniques, and a lot of research has focused on enhancing the capability of SSA algorithms in this regard to strengthen its overall performance, but there is still a gap in this context.

The above analyzed weak points of SSA have promoted the authors to discern that the algorithm has some drawbacks to be rectified, and this is the motivation behind proposing a novel version of SSA. Each of the embedded adjustments will be described in detail in the next section.

3 Essentials of the OPLSSA

As discussed previously, the swarm intelligent algorithm covers two phases, namely exploration and exploitation.

TABLE 4 Statistical conclusions based on Wilcoxon signed-rank test on 100-dimensional benchmark problems.

Function	SSA <i>p</i> -value	LSSA <i>p</i> -value	ASSA <i>p</i> -value	GSSA <i>p</i> -value	OBSSA <i>p</i> -value	ASSO <i>p</i> -value	RDSSA <i>p</i> -value	IWOSSA <i>p</i> -value
f1	1.2118E-12	1.2118E-12	1.2118E-12	1.2118E-12	1.2118E-12	1.2118E-12	1.2118E-12	1.2118E-12
f2	1.2118E-12	1.2118E-12	1.2118E-12	1.2118E-12	1.2118E-12	1.2118E-12	1.2118E-12	1.2118E-12
f3	1.2118E-12	1.2118E-12	1.2118E-12	1.2118E-12	1.2118E-12	1.2118E-12	1.2118E-12	1.2118E-12
f4	1.2118E-12	1.2118E-12	1.2118E-12	1.2118E-12	1.2118E-12	1.2118E-12	1.2118E-12	1.2118E-12
f5	1.2118E-12	1.1808E-12	1.1941E-12	N/A	N/A	N/A	N/A	1.4306E-04
f6	1.2118E-12	1.2118E-12	1.2118E-12	1.2118E-12	1.2118E-12	1.2118E-12	1.2118E-12	1.2118E-12
f7	3.0199E-11	3.0199E-11	3.0199E-11	3.0199E-11	0.6952	0.2062	1.2870E-09	3.0199E-11
f8	1.2118E-12	1.2118E-12	1.2118E-12	1.2118E-12	1.2118E-12	1.2118E-12	4.5736E-12	1.2118E-12
f9	1.2118E-12	1.2118E-12	1.2118E-12	1.2118E-12	1.2118E-12	1.2118E-12	1.2118E-12	1.2118E-12
f10	1.2118E-12	1.2118E-12	1.2118E-12	1.2118E-12	1.2118E-12	1.2118E-12	1.2118E-12	1.2118E-12
f11	1.2118E-12	1.2118E-12	1.2118E-12	1.2118E-12	1.2118E-12	1.2118E-12	1.2118E-12	1.2118E-12
f12	1.2118E-12	1.2118E-12	1.2118E-12	1.4545E-04	N/A	N/A	N/A	1.2118E-12
f13	1.2118E-12	1.2118E-12	1.2118E-12	1.2118E-12	N/A	5.6687E-13	7.1518E-13	1.2118E-12
f14	1.2118E-12	1.2118E-12	1.2118E-12	6.6067E-05	N/A	N/A	N/A	1.2118E-12
f15	1.2118E-12	1.2118E-12	1.2118E-12	1.2118E-12	1.2118E-12	1.2118E-12	1.2118E-12	1.2118E-12
f16	1.2118E-12	1.2118E-12	1.2118E-12	1.2118E-12	1.2118E-12	1.2118E-12	1.2118E-12	1.2118E-12
f17	1.2118E-12	1.2118E-12	1.2118E-12	N/A	N/A	N/A	N/A	1.2118E-12
f18	3.0199E-11	3.0199E-11	3.0199E-11	3.0199E-11	3.0199E-11	3.0199E-11	3.0199E-11	3.0199E-11
f19	1.2118E-12	1.2118E-12	1.2118E-12	1.2118E-12	1.2118E-12	1.2118E-12	1.2118E-12	1.2118E-12
f20	1.2118E-12	1.2118E-12	1.2118E-12	1.2118E-12	1.2118E-12	1.2118E-12	1.2118E-12	1.2118E-12
f21	1.2118E-12	1.2118E-12	1.2118E-12	8.1523E-02	N/A	N/A	N/A	1.2118E-12
f22	8.6253E-13	1.2118E-12	1.2118E-12	1.2118E-12	1.2118E-12	1.2118E-12	1.2078E-12	1.2098E-12
f23	1.2118E-12	1.2118E-12	1.2118E-12	1.2118E-12	1.2118E-12	1.2118E-12	1.2118E-12	1.2118E-12
+/- = /-	23/0/0	23/0/0	23/0/0	21/2/0	17/6/0	17/6/0	17/5/1	23/0/0

Exploration maintains a superiority in global search, and the strong exploration capability is conducive to improving the convergence speed. On the other hand, the domain nature of exploitation is shown in the local search, and the powerful

development capability is beneficial to boost the convergence accuracy. Maintaining a proper equilibrium between exploration and exploitation holds a key position in the performance of swarm intelligent approaches, which is also

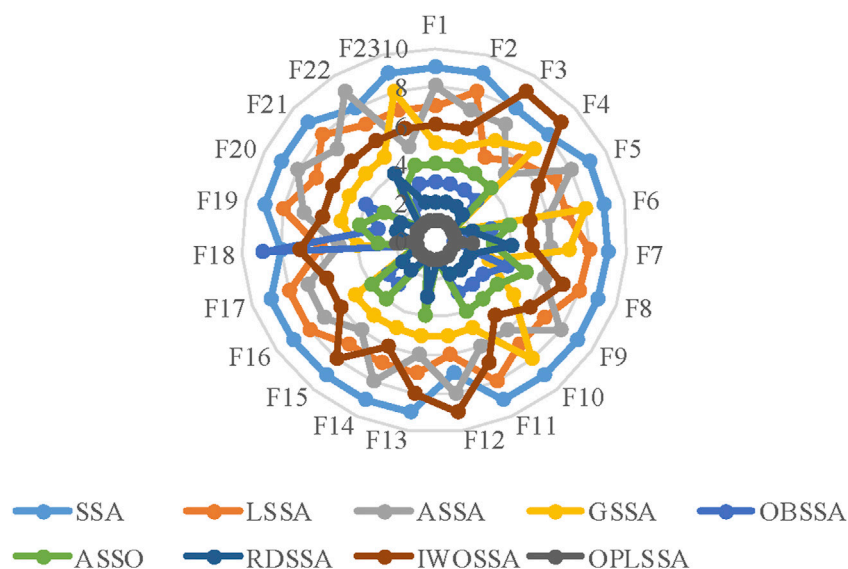


FIGURE 5

Radar plot for consolidated ranks of 23 benchmark problems with the SSA variants.

a research gap that the current community tries to bridge. In this study, two straightforward but applicable mechanisms are integrated into SSA to produce an enhanced balanced SSA variants with better performance. This section provides an in-depth discussion of the designed components and the OPLSSA algorithm.

3.1 Orthogonal pinhole-imaging-based learning

In standard SSA, according to the location changing pattern of the leading salp, a prospective candidate search agent location is gained by directing the leader to the food source. Followers chase the leader explicitly or indirectly, gathering near the perceived global optimum in the later phase of the search. As a result, the standard SSA is inclined to converge prematurely. Therefore, improving the ability of the approach to avoid local optima has been considered as the most critical and necessary research goal in SSA improvement. To enhance the global exploration ability of swarm intelligent metaheuristic techniques, the most common method used in the published literatures is opposition-based learning (OBL). For example, Abualigah et al. (2021) revised the search pattern of the slime mould algorithm (SMA) (Li et al., 2020) by incorporating the OBL mechanism. Dinkar et al. (2021) used the OBL technique to accelerate the convergence rate of equilibrium optimizer (EO) (Faramarzi et al., 2020b), and the reported OBL-based EO approach was used for multilevel threshold

image segmentation. Yu et al. (2021) included an additional OBL phase in the GWO algorithm to help the wolves jump to reverse individuals to enhance the exploration of the search space. Yildiz et al. (2021) mixed OBL with GOA algorithm to improve the ability of the algorithm to exploit unknown regions. In the proposed algorithm, elite individuals generate corresponding elite reverse individuals through the OBL strategy and retain well-quality individuals for the next iteration. Chen et al. (2020) employed quasi-opposition-based learning (QOBL), an OBL variant, to create dynamic jumps during the location update of the WOA algorithm to prevent the algorithm from falling into local optima.

Pinhole imaging is a general physical phenomenon in which a light source passes through a small hole in a plate and an inverted real image is formed on the other side of the plate. Motivated by the discovery that there are close similarities between the pinhole imaging phenomenon and the OBL mechanism, this paper proposes a pinhole-imaging-based learning (PIBL) mechanism and applies it to the current leader to augment the exploration capability of SSA for unknown areas. Figure 1 plots the schematic diagram of the PIBL.

In Figure 1, p is a light source of height h , and its projection on the x -axis is L . Place a pinhole screen on the base point o , and the real image p' formed by the light source through the pinhole screen will fall on the receiving screen on the other side. It is worth noting that p' is the inverted image of p , and the height of p' from the x -axis is h' . At this point, L jumps to L' based on pinhole imaging principle. Therefore, from the pinhole imaging principle, it can be derived that

TABLE 5 Comparisons of nine algorithms on 23 test functions with 100 dimensions.

Function	Results	TSA	MPA	HGS	AOA	IGWO	WEMFO	DMMFO	OGWO	OPLSSA
f1	Mean	3.01E-10	1.80E-19	2.23E-152	9.49E-79	2.21E-12	3.59E-22	3.29E+04	4.59E-15	0
	Std	3.25E-10	1.27E-19	1.22E-151	5.09E-78	1.32E-12	1.93E-21	7.03E+03	5.59E-15	0
	f-rank	8	5	2	3	7	4	9	6	1
f2	Mean	1.41E-10	7.00E-20	8.26E-149	8.91E-78	1.09E-12	1.68E-22	1.48E+04	9.72E-16	0
	Std	1.57E-10	6.87E-20	4.52E-148	4.59E-77	1.41E-12	8.42E-22	2.65E+03	1.36E-15	0
	f-rank	8	5	2	3	7	4	9	6	1
f3	Mean	1.28E+04	9.6728	3.73E-18	1.14E-62	5.69E+03	4.63E-07	2.37E+05	8.28E+02	0
	Std	7.98E+03	1.22E+01	2.04E-17	5.34E-62	3.15E+03	2.53E-06	4.31E+04	1.01E+03	0
	f-rank	8	5	3	2	7	4	9	6	1
f4	Mean	5.59E+01	1.87E-07	4.79E-62	3.47E-38	5.0967	2.04E-10	8.89E+01	1.8357	0
	Std	1.34E+01	8.76E-08	2.62E-61	1.09E-37	3.2803	4.26E-10	2.6732	1.9532	0
	f-rank	7	5	2	3	8	4	9	6	1
f5	Mean	1.34E+01	0	0	0	0	0	3.53E+04	0	0
	Std	9.6264	0	0	0	0	0	6.17E+03	0	0
	f-rank	8	1	1	1	1	1	9	1	1
f6	Mean	4.99E-18	8.77E-41	8.25E-261	4.89E-164	1.72E-22	7.39E-46	1.02E+20	3.51E-28	0
	Std	2.62E-17	1.44E-40	0	0	2.97E-22	4.03E-45	2.86E+01	7.99E-28	0
	f-rank	8	5	2	3	7	4	9	6	1
f7	Mean	5.22E-02	2.00E-03	1.90E-03	7.68E-04	1.44E-02	1.60E-03	9.24E+01	2.10E-03	4.87E-05
	Std	1.70E-02	1.00E-03	2.50E-03	5.45E-04	5.40E-03	1.10E-03	2.96E+01	1.90E-03	5.19E-05
	f-rank	8	5	4	2	7	3	9	6	1
f8	Mean	1.83E-42	4.25E-60	1.52E-77	7.57E-187	2.57E-57	1.66E-82	1.40E-03	1.26E-61	0
	Std	9.92E-42	1.12E-59	8.29E-77	0	1.31E-56	6.92E-82	1.60E-03	6.84E-51	0
	f-rank	8	5	4	2	6	3	9	7	1
f9	Mean	7.98E-07	9.23E-16	3.30E-160	4.07E-74	3.60E-09	6.95E-19	2.07E+08	4.56E-12	0
	Std	1.30E-06	9.36E-16	1.81E-159	1.87E-73	2.68E-09	2.24E-18	9.88E+07	4.89E-12	0
	f-rank	8	5	2	3	7	4	9	6	1
f10	Mean	4.28E-02	8.66E-39	1.95E-54	5.97E-170	4.60E-10	2.88E-48	2.86E+17	5.41E-21	0
	Std	1.11E-01	1.67E-38	1.03E-53	0	1.69E-09	8.27E-48	1.19E+17	1.21E-20	0
	f-rank	8	5	3	2	7	4	9	6	1
f11	Mean	7.21E-20	3.89E-53	1.62E-43	4.26E-183	6.04E-28	8.17E-63	9.86E-01	2.85E-38	0
	Std	2.95E-19	7.53E-53	8.76E-43	0	1.43E-27	4.09E-62	3.91E-01	9.84E-38	0
	f-rank	8	4	5	2	7	3	6	9	1
f12	Mean	9.86E+02	0	0	0	1.46E+02	2.85E+02	8.14E+02	1.1484	0
	Std	1.04E+02	0	0	0	4.72E+01	3.14E+02	6.94E+01	2.7139	0
	f-rank	9	1	1	1	6	7	8	5	1
f13	Mean	1.25E-05	5.03E-11	8.88E-16	1.86E+01	1.53E-07	6.67E-01	1.97E+01	4.91E-09	8.88E-16
	Std	2.86E-05	3.14E-11	0	5.0657	6.66E-08	3.6445	3.34E-01	1.57E-09	0
	f-rank	6	3	1	8	5	7	9	4	1
f14	Mean	1.63E-02	0	0	0	4.70E-03	0	3.02E+02	1.80E-03	0
	Std	1.80E-02	0	0	0	7.10E-03	0	5.85E+01	7.00E-03	0
	f-rank	8	1	1	1	7	1	9	6	1
f15	Mean	1.51E+02	3.83E-12	9.59E-72	6.71E-42	3.70E-03	5.58E+01	5.79E+01	2.05E-04	0
	Std	2.16E+01	3.34E-12	5.25E-71	2.71E-41	1.90E-03	2.67E+01	1.01E+01	4.99E-04	0
	f-rank	9	4	2	3	6	7	8	5	1
f16	Mean	1.38E+02	1.83E-16	5.31E-123	3.44E-61	8.2595	5.44E-21	1.56E+03	2.97E-23	0
	Std	9.02E+01	4.55E-16	2.91E-122	1.88E-60	4.4488	2.95E-20	2.13E+02	1.37E-22	0
	f-rank	8	6	2	3	7	5	9	4	1

(Continued on following page)

TABLE 5 (Continued) Comparisons of nine algorithms on 23 test functions with 100 dimensions.

Function	Results	TSA	MPA	HGS	AOA	IGWO	WEMFO	DMMFO	OGWO	OPLSSA
f17	Mean	3.2947	0	0	0	2.63E-14	0	1.26E+01	5.39E-15	0
	Std	2.8236	0	0	0	8.78E-15	0	1.6209	2.58E-15	0
	f-rank	8	1	1	1	7	1	9	6	1
f18	Mean	9.89E-12	2.99E-19	1.49E-109	2.08E-69	1.72E-12	7.12E-23	5.07E+02	6.62E-16	2.38E-44
	Std	1.45E-11	3.67E-19	8.17E-109	1.14E-68	1.89E-12	3.85E-22	7.89E+01	5.22E-16	4.48E-15
	f-rank	8	5	1	2	7	4	9	6	3
f19	Mean	1.09E+01	7.27E-22	4.13E-136	7.49E-81	1.61E-14	4.56E-27	1.62E+02	5.65E-27	0
	Std	5.97E+01	1.00E-21	2.26E-135	3.45E-80	1.43E-14	1.28E-26	3.67E+01	2.26E-26	0
	f-rank	8	6	2	3	7	4	9	5	1
f20	Mean	2.8523	4.58E-07	2.19E-39	8.39E-22	1.02E-02	2.04E-08	8.4517	7.17E-05	0
	Std	1.4825	4.09E-07	8.26E-39	2.07E-21	3.10E-03	4.15E-08	3.23E-01	4.19E-05	0
	f-rank	8	5	2	3	7	4	9	6	1
f21	Mean	4.3276	0	0	0	2.16E-12	0	2.19E+03	2.95E-15	0
	Std	1.21E+01	0	0	0	1.55E-12	0	4.97E+02	3.28E-15	0
	f-rank	8	1	1	1	7	1	9	6	1
f22	Mean	7.2165	6.13E-01	3.63E-38	1.71E-02	3.0308	4.60E-03	7.4324	8.31E-01	0
	Std	5.16E-01	7.47E-02	1.99E-37	1.78E-02	4.72E-01	6.80E-03	2.66E-01	2.58E-01	0
	f-rank	8	5	2	4	7	3	9	6	1
f23	Mean	8.46E-14	3.86E-55	6.3951	6.12E-235	6.93E-25	1.58E-70	6.23E-01	3.89E-64	0
	Std	2.86E-13	1.06E-54	8.6601	0	2.46E-24	8.54E-70	2.75E-01	2.12E-63	0
	f-rank	7	5	9	2	6	3	8	4	1
Average f-rank		7.9130	4.0435	2.3913	2.5217	6.5217	3.6956	8.7391	5.5612	1.0869
Overall f-rank		8	5	2	3	7	4	9	6	1

$$\frac{(a+b)/2-L}{L'-(a+b)/2} = \frac{h}{h'} \quad (4)$$

Let $h/h' = n$, Eq. 9 can be rewritten as

$$L' = \frac{(a+b)}{2} + \frac{(a+b)}{2n} - \frac{L}{n} \quad (5)$$

Equation 5 is the formula of PIBL on the leading salp. When $n = 1$, the above equation is simplified to

$$L' = a + b - L \quad (6)$$

Equation 6 is the original OBL strategy on the leading salp. Clearly, OBL is very similar to PIBL. In other words, PIBL can be treated as a dynamic version of OBL.

Generalizing Eq. 5 to the D -dimensional spatial, it can be obtained

$$L'_j = (a_j + b_j)/2 + (a_j + b_j)/2k - L_j/n \quad (7)$$

where L_j and L'_j are the j th dimensional values of the leader and the PIBL leader, respectively.

In this paper, we use the proposed PIBL mechanism to help the leader search for unknown regions, thus improving the global search ability of the algorithm and avoiding the premature convergence due to the lack of exploration capability. However, similar to OBL, PIBL also suffers from the problem of “dimensional degradation”, i. e., the current leader improves only in some dimensions after jumping to the PIBL leader, while some other dimensions are even farther from the global optimum. To solve this problem, we introduce orthogonal experimental design (OED) and combine it with the PIBL strategy to design the orthogonal pinhole-imaging-based learning (OPIBL) mechanism.

The OED is an auxiliary tool that can find the optimal combination of experiments by a reasonable number of trials. For example, for an experiment with 3 levels and 4 factors, it would take 81 attempts using a trial-and-error approach. In contrast, by adopting an OED, only 9 sets of representative combinations need to be evaluated to determine the optimal combination of the experiment. $L_9(3^4)$ is shown in Table 1.

In each iteration, the OPIBL mechanism is used for the

TABLE 6 Statistical conclusions based on Wilcoxon signed-rank test on 100-dimensional benchmark problems.

Function	TSA <i>p</i> -value	MPA <i>p</i> -value	HGS <i>p</i> -value	AOA <i>p</i> -value	IGWO <i>p</i> -value	WEMFO <i>p</i> -value	DMMFO <i>p</i> -value	OGWO <i>p</i> -value
f1	1.2118E-12	1.2118E-12	1.2118E-12	1.2118E-12	1.2118E-12	1.2118E-12	1.2118E-12	1.2118E-12
f2	1.2118E-12	1.2118E-12	6.6167E-04	4.5736E-12	1.2118E-12	1.2118E-12	1.2118E-12	1.9346E-10
f3	1.2118E-12	1.2118E-12	8.8658E-07	1.2118E-12	1.2118E-12	1.2118E-12	1.2118E-12	1.2118E-12
f4	1.2118E-12	1.2118E-12	3.4526E-07	1.2118E-12	1.2118E-12	1.2118E-12	1.2118E-12	1.2118E-12
f5	4.5342E-12	N/A	N/A	N/A	N/A	N/A	1.2118E-12	N/A
f6	3.0199E-11	3.0199E-11	1.0702E-09	3.0199E-11	3.0199E-11	3.0199E-11	3.0199E-11	2.3715E-10
f7	3.0199E-11	3.3384E-11	2.1947E-08	2.3715E-10	3.0199E-11	4.9752E-11	3.0199E-11	1.7769E-10
f8	1.2118E-12	1.2118E-12	8.87E-07	1.2118E-12	1.2118E-12	1.2118E-12	1.2118E-12	1.2118E-12
f9	1.2118E-12	1.2118E-12	6.6167E-04	1.2118E-12	1.2118E-12	1.2118E-12	1.2118E-12	1.2118E-12
f10	1.2118E-12	1.2118E-12	5.3750E-06	1.2118E-12	1.2118E-12	1.2118E-12	1.2118E-12	1.2118E-12
f11	1.2118E-12	1.2118E-12	5.3750E-06	1.2118E-12	1.2118E-12	1.2118E-12	1.2118E-12	1.2118E-12
f12	1.2118E-12	N/A	N/A	N/A	1.2118E-12	2.2130E-06	1.2118E-12	1.2108E-12
f13	1.2118E-12	1.2118E-12	N/A	1.6572E-11	1.2118E-12	4.5736E-12	1.2118E-12	1.2118E-12
f14	1.2118E-12	N/A	N/A	N/A	1.2118E-12	N/A	1.2118E-12	1.2118E-12
f15	1.2118E-12	1.2118E-12	3.3149E-04	1.2118E-12	1.2118E-12	1.2118E-12	1.2118E-12	1.2118E-12
f16	1.2118E-12	1.2118E-12	5.3750E-06	1.2118E-12	1.2118E-12	1.2118E-12	1.2118E-12	1.2118E-12
f17	1.2118E-12	N/A	N/A	N/A	1.1010E-12	N/A	1.2118E-12	4.4162E-11
f18	3.0199E-11	3.0199E-11	2.3982E-11	3.0199E-11	3.0199E-11	3.0199E-11	3.0199E-11	3.0199E-11
f19	1.2118E-12	1.2118E-12	1.2717E-05	1.2118E-12	1.2118E-12	1.2118E-12	1.2118E-12	1.2118E-12
f20	1.2118E-12	1.2118E-12	5.5843E-03	1.2118E-12	1.2118E-12	1.2118E-12	1.2118E-12	1.2118E-12
f21	1.2118E-12	N/A	N/A	N/A	1.2118E-12	N/A	1.2118E-12	1.2029E-12
f22	1.2118E-12	1.1037E-12	1.4552E-04	1.2118E-12	1.2118E-12	1.2000E-12	6.4999E-13	1.2118E-12
f23	1.2118E-12	1.2118E-12	1.2118E-12	4.5736E-12	1.2118E-12	1.2118E-12	1.2118E-12	1.2118E-12
+/- = +/-	23/0/0	18/5/0	16/6/1	18/5/0	22/1/0	19/4/0	23/0/0	22/1/0

King, OPLSSA gets the highest rank, followed by HGS, AOA, WEMFO, MPA, OGWO, IGWO, TSA, DMMFO, which further indicates that the performance of OPLSSA is better than its competitors.

leader, the dimension of the problem to be solved is considered as the factor of the OED, and the leader and the PIBL leader are regarded as the two levels of the OED. The designed OPIBL mechanism considers the information of

the current leader and the PIBL leader, and retains the respective dominant dimensions to combine as a promising partial PIBL individual, called OPIBL leader. In this way, the OPIBL mechanism can effectively avoid the “dimensional

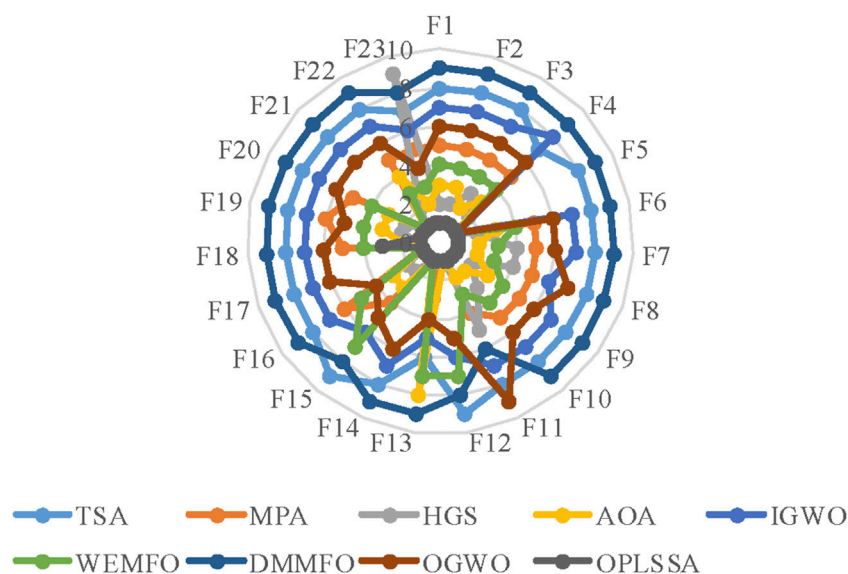


FIGURE 6

Radar plot for consolidated ranks of 23 benchmark problems with OPLSSA and the Frontier algorithms.

degradation” problem caused by PIBL and significantly help the leader to quickly approach the global optimal solution. To visualize the process of the leader jumps to OPIBL leader, we consider a 7-dimensional problem and draw the schematic diagram of the leader jumps to the OPIBL leader according to $L_8(2^7)$, as shown in Figure 2.

In order not to increase the computational complexity of the algorithm, only the leader executes the OPIBL operation. Then, evaluate both the current leader and the OPIBL leader, and reserve the high-quality search agent.

3.2 Adaptive conversion parameter strategy

For nature-inspired swarm intelligent algorithms, strong exploration capability is beneficial to improve the convergence speed, while powerful exploitation ability is conducive to refine the convergence accuracy. Maintaining a proper balance between exploration and exploitation can effectively boost the overall performance of the algorithm, which is a research difficulty that the metaheuristic community has been trying to conquer with great effort. In the basic SSA, the follower updates its position according to Eq. 3. This equation is control parameter-free, the current follower salp only considers its own position and the position of neighboring individual to calculate the next location. Although this mechanism makes SSA more consistent with the advocated minimalism, this rigid position update pattern tends to deviate the population from the global optimum. Furthermore, it is unreasonable that the followers move

without utilizing the current global optimal position. To address this issue, many studies have focused on modifying the follower position update equation to enhance the dynamic nature.

Based on the above analysis, this paper proposes an adaptive position update mechanism for follower salps to replace the original formula, namely

$$X_{i,j} = \frac{1}{2} \times (\omega X_{i,j} + X_{i-1,j}) \quad (8)$$

where ω is an inertia weight factor.

In PSO, the inertia weight coefficient factor changes dynamically during the search process to help the algorithm switch between exploitation and exploration operations. With the progress of the research on metaheuristic techniques, the inertia weight has been introduced into many swarm intelligence-based approaches to improve their performance. For example, GU et al. (2022) implemented the inertia weight to tune the particle's search behavior in chicken swarm algorithm (CSA) (Meng et al., et al.). Jena et al. (Jena and Satapathy, 2021) used a Sigmoid adaptive inertia weight to intensify the performance of the social group optimization (SGO) (Naik et al., 2018). Inspired by the above studies, a novel inertia weight coefficient is proposed in this work with the following mathematical expression:

$$\omega = (\omega_{\max} - \omega_{\min}) \cdot \frac{e^{10-\lambda t} - 2}{e^{10-\lambda t} + 2} + \omega_{\max} \quad (9)$$

TABLE 7 Results obtained by OPLSSA on 10000-dimensional functions.

Function	OPLSSA				
	Best	Worst	Mean	Std	SR%
f1	0	0	0	0	100
f2	0	0	0	0	100
f3	0	0	0	0	100
f4	0	0	0	0	100
f5	0	0	0	0	100
f6	0	0	0	0	100
f7	4.63E-07	2.95E-04	8.56E-05	8.48E-05	70
f8	0	0	0	0	100
f9	0	0	0	0	100
f10	0	0	0	0	100
f11	0	0	0	0	100
f12	0	0	0	0	100
f13	8.88E-16	8.88E-16	8.88E-16	0	100
f14	0	0	0	0	100
f15	0	0	0	0	100
f16	0	0	0	0	100
f17	0	0	0	0	100
f18	3.49E-43	6.13E-43	4.71E-43	7.40E-44	100
f19	0	0	0	0	100
f20	0	0	0	0	100
f21	0	0	0	0	100
f22	0	0	0	0	100
f23	0	0	0	0	100

Me representative test functions were plotted. In experiment 2, the convergence graphs of the OPLSSA algorithm and eight cutting-edge approaches on some representative benchmark functions were illustrated.

where λ is a constant number, ω_{\max} and ω_{\min} are the maximum and minimum values of the inertia weight coefficient, respectively.

Figure 3 plots the schematic diagram of the nonlinear decrease of the inertia weight during the iterative process. From the figure, in the initial stage, the value of ω is larger, and the particle accordingly moves in larger steps in the search space, which is beneficial to the global search. After the lapse of iterations, ω nonlinearly decreases and the particle moves in shorter steps correspondingly, which is advantageous for fine exploit the already explored promising area to improve the convergence accuracy.

3.3 The flowchart of OPLSSA

In summary, Figure 4 shows the flow chart of the developed OPLSSA algorithm.

4 Simulations and comparisons

In this section, 23 classical benchmark test functions are solved using the OPLSSA algorithm to synthetically verify its effectiveness and applicability. The results obtained by the proposed approach on the test cases are recorded and compared with some well-established metaheuristic techniques, including the basic SSA, the forefront swarm intelligent algorithms, and the popular SSA variants. All experiments were implemented under MATLAB 2016b software, operating system used is Microsoft WINDOWS 10 64-bit Home, and simulations supported by Intel (R) Core (TM) i7-7700 CPU at 3.60 GHz with 8.00 GB RAM.

4.1 Experiments on well-known benchmark functions

In this subsection, the selected 23 benchmark functions that include both multimodal and unimodal functions are reported, as shown in Table 2, where Search range represents the boundary of the function search space, and f_{\min} is the best value. Among them, f_1 - f_{11} are unimodal functions, and they are mainly complex spherical or valley value problems. They have only one global optimal solution in the search range but are difficult to find. Therefore, it can be used to test the convergence efficiency and exploration ability of each algorithm. Different from the unimodal functions, the multimodal functions (f_{12} - f_{23}) have multiple local extremes in the search space. Moreover, the scale of this type of problem will increase exponentially as the dimensionality increases. Therefore, the multimodal problem can effectively test the abilities of each algorithm to search globally and to jump out of local optima (Long et al., 2021).

4.1.1 Compared against salp swarm algorithm and salp swarm algorithm variants

To test the performance of the advocated OPLSSA algorithm, 23 classical benchmark functions reported in Table 2 were employed. The dimensions of the involved problems were set to 100. The obtained results were compared with the standard SSA and seven representative SSA variants, including the self-adaptive SSA (ASSA) (Salgotra et al., 2021), adaptive SSA with random replacement strategy (RDSSA) (Ren et al., 2021), lifetime tactic enhanced SSA (LSSA) (Braik et al., 2020), the Gaussian perturbed SSA (GSSA) (Nautiyal et al., 2021), the intensified OBL-based SSA.

(OBSSA) (Hussien, 2021), inertia weight enhanced SSA (ASSO) (Ozbay and Alatas, 2021), and WOA improved SSA (IWOSSA) (Saafan and El-Gendy, 2021). The general parameters of the involved methods were set as recommended in the respective original literature. In OPLSSA, $k = 100$, $\lambda = 0.04$, $\omega_{\max} = 0.55$, $\omega_{\min} = 0.2$. The maximum number of iterations of

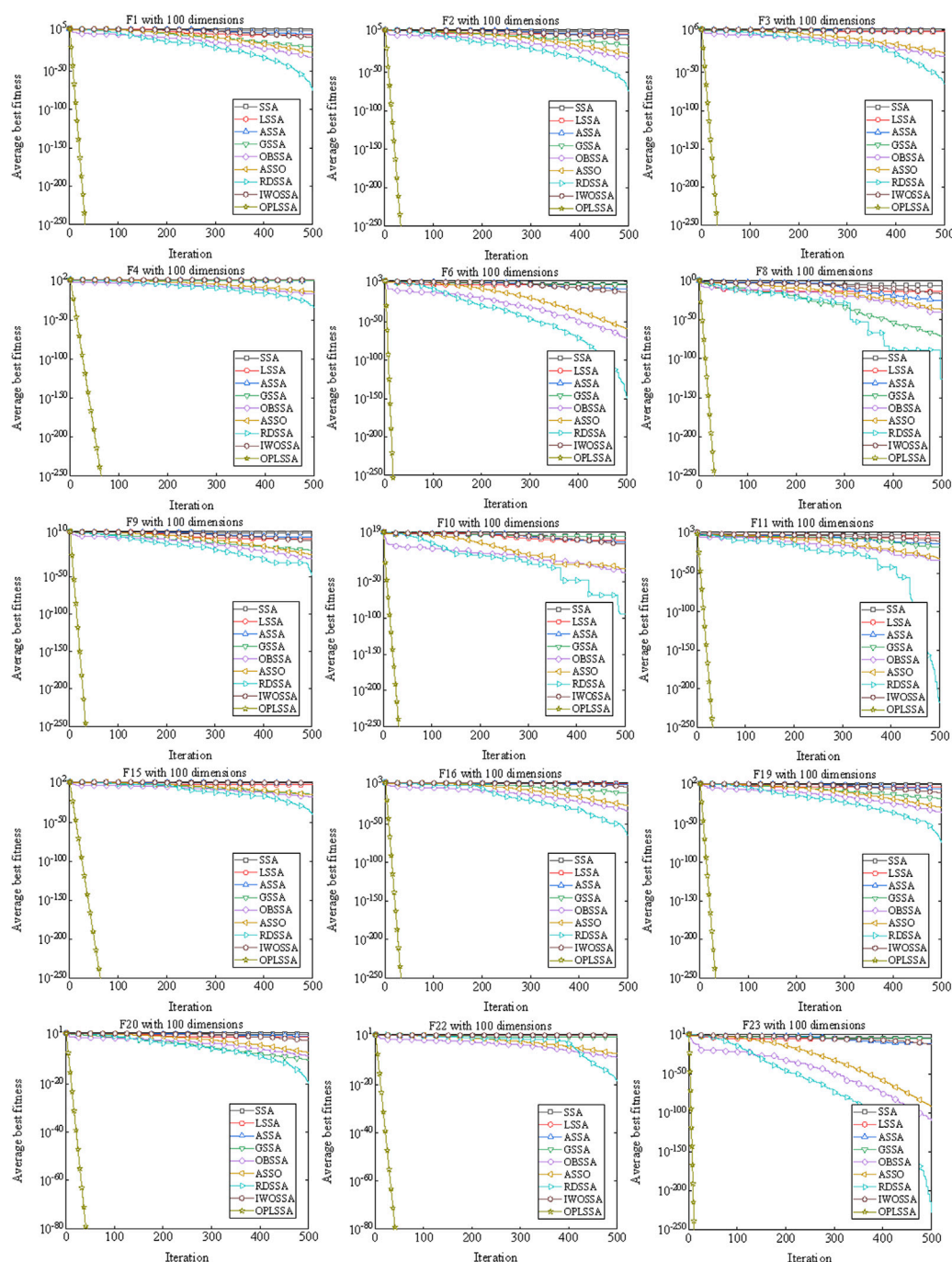


FIGURE 7

Convergence curves of OPLSSA and other SSA-based algorithms on 15 representative benchmarks.

each algorithm for each benchmark was 500, the population size was set to 30, and the number of independent runs was set to 30 to eliminate random errors. The mean value and standard variance of the results obtained from 30 runs were recorded as metrics to evaluate the performance of the algorithms. In

addition, Friedman test was utilized to evaluate the average performance of the algorithms. Wilcoxon signed ranks was used as an auxiliary tool to investigate the differences between OPLSSA and its competitors from a statistical point of view. The results of the nine algorithms on the 23 tested problems are

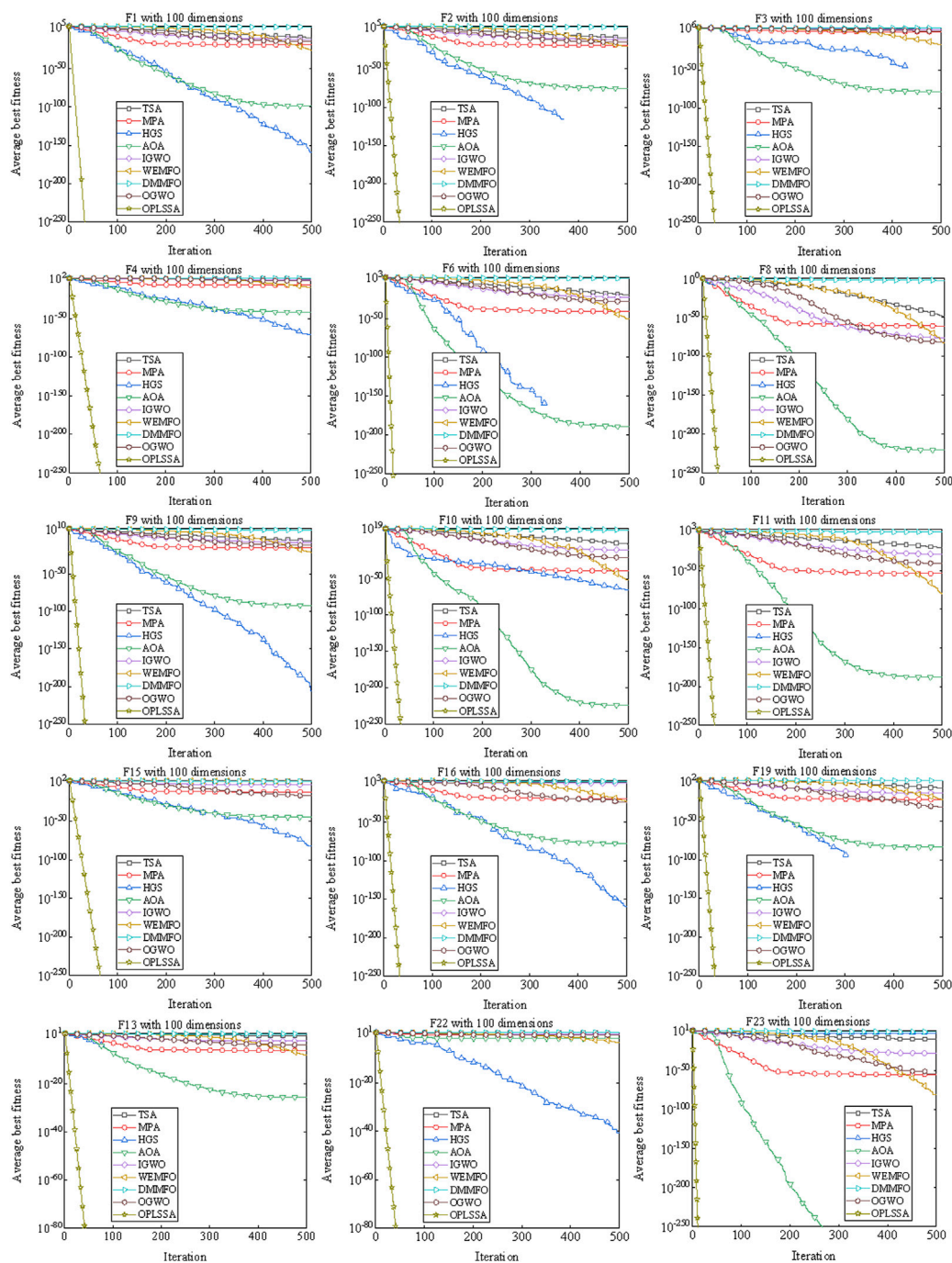


FIGURE 8

Convergence curves of OPLSSA and other Frontier algorithms on 15 representative benchmarks.

shown in Table 3, and the results of the Wilcoxon signed ranks test are reported in Table 4.

From Table 3, the developed OPLSSA is superior to SSA, LSSA, ASSA and IWOSSA on all test functions. Compared to GSSA, OPLSSA presents similar and better performance on two and 21 test cases, respectively. OPLSSA plays a tie with

OBSSA on six benchmarks, it beats OBSSA on six functions, and on another function (i.e. f_7), it is inferior to OBSSA. OPLSSAS defeats ASSO on 18 benchmarks, and on the remaining five problems, both algorithms find the theoretical optimal solution. With respect to RDSSA, OPLSSA wins on 17 test functions, ties with it on five test

TABLE 8 Summary of the 30 CEC 2017 benchmark problems.

Class	No.	Description	Search Range	Optimal
Unimodal	1	Shifted and Rotated Bent Cigar Function	[-100, 100]	100
	2	Shifted and Rotated Sum of Different Power Function	[-100, 100]	200
	3	Shifted and Rotated Zakharov Function	[-100, 100]	300
Multimodal	4	Shifted and Rotated Rosenbrock's Function	[-100, 100]	400
	5	Shifted and Rotated Rastrigin's Function	[-100, 100]	500
	6	Shifted and Rotated Expanded Scaffer's Function	[-100, 100]	600
	7	Shifted and Rotated Lunacek Bi-Rastrigin Function	[-100, 100]	700
	8	Shifted and Rotated Non-Continuous Rastrigin's Function	[-100, 100]	800
	9	Shifted and Rotated Levy Function	[-100, 100]	900
	10	Shifted and Rotated Schwefel's Function	[-100, 100]	1000
Hybrid	11	Hybrid Function 1 (N = 3)	[-100, 100]	1100
	12	Hybrid Function 2 (N = 3)	[-100, 100]	1200
	13	Hybrid Function 3 (N = 3)	[-100, 100]	1300
	14	Hybrid Function 4 (N = 4)	[-100, 100]	1400
	15	Hybrid Function 5 (N = 4)	[-100, 100]	1500
	16	Hybrid Function 6 (N = 4)	[-100, 100]	1600
	17	Hybrid Function 6 (N = 5)	[-100, 100]	1700
	18	Hybrid Function 6 (N = 5)	[-100, 100]	1800
	19	Hybrid Function 6 (N = 5)	[-100, 100]	1900
	20	Hybrid Function 6 (N = 6)	[-100, 100]	2000
Composition	21	Composition Function 1 (N = 3)	[-100, 100]	2100
	22	Composition Function 2 (N = 3)	[-100, 100]	2200
	23	Composition Function 3 (N = 4)	[-100, 100]	2300
	24	Composition Function 4 (N = 4)	[-100, 100]	2400
	25	Composition Function 5 (N = 5)	[-100, 100]	2500
	26	Composition Function 6 (N = 5)	[-100, 100]	2600
	27	Composition Function 7 (N = 6)	[-100, 100]	2700
	28	Composition Function 8 (N = 6)	[-100, 100]	2800
	29	Composition Function 9 (N = 3)	[-100, 100]	2900
	30	Composition Function 10 (N = 3)	[-100, 100]	3000

functions, and is defeated by RDSSA on one (i.e. f_{18}) test function. According to the Friedman ranking achieved by the different approaches for 23 test problems, OPLSSA obtained the top rank, followed by RDSSA, OBSSA, ASSO, GSSA, IWOSSA, ASSA, LSSA and SSA. Furthermore, according to the comparison results of Wilcoxon signed ranks approach, the p -values are less than 0.05 except for two pairwise comparisons (i.e. OPLSSA versus OBSSA, OPLSSA versus ASSO), which demonstrates that OPLSSA has a significant advantage over the comparison algorithms.

Figure 5 plots the radar diagram showing the ranking of the nine SSA-based algorithms on the 23 tested functions as counted in Table 4. From the figure, OPLSSA received competitive rankings on all cases, which proves that the overall performance of the OPLSSA algorithm outperforms its competitors.

4.1.2 Comparison against other swarm intelligent algorithms

In this subsection, the developed OPLSSA algorithm was compared with marine predators algorithm (MPA) (Faramarzi et al., 2020a), hunger game search (HGS) algorithm (Yang et al., 2021), Improved grey wolf optimization (IGWO) algorithm (Nadimi-Shahraki et al., 2021), tunicate swarm algorithm (TSA) (Kaur et al., 2020), adaptive moth flame optimizer (WEMFO) (Shan et al., 2021), Archimedes optimization algorithm (AOA) (Hashim et al., 2021), OBL-based grey wolf optimization (OGWO) algorithm (Yu et al., 2021), diversity and mutation mechanisms enhanced moth-flame optimization (DMMFO) algorithm (Ma et al., 2021). In this comparison experiment, the 23 benchmark problems in Table 2 were employed, and the dimensions of the problems were set to 100. The parameters of the methods were set identically as in

TABLE 9 Results of CEC 2017 at 30-dimensional achieved by the developed algorithm and its competitors.

Function	DA	GOA	TSA	SOA	EGWO	PBO	SSA	OPLSSA
F1	2.04E+08	1.03E+09	1.60E+10	7.37E+09	5.85E+09	1.36E+04	6.34E+02	1.06E+02
F2	NA	NA	NA	NA	NA	NA	NA	NA
F3	5.43E+04	3.09E+04	4.92E+04	2.98E+04	5.28E+04	1.08E+04	1.55E+04	3.00E+02
F4	7.76E+02	4.89E+02	3.36E+03	7.15E+02	1.33E+04	5.46E+02	5.15E+02	4.69E+02
F5	7.67E+02	7.17E+02	8.14E+02	6.90E+02	9.43E+02	6.80E+02	6.15E+02	5.66E+02
F6	6.65E+02	6.32E+02	6.63E+02	6.35E+02	7.04E+02	6.63E+02	6.24E+02	6.03E+02
F7	1.01E+03	8.20E+02	1.23E+03	1.08E+03	1.43E+03	1.79E+03	8.37E+02	8.05E+02
F8	1.04E+03	1.04E+03	1.05E+03	9.48E+02	1.20E+03	9.48E+02	9.14E+02	8.47E+02
F9	9.31E+03	4.44E+03	8.69E+03	3.63E+03	1.58E+04	3.92E+03	3.00E+03	9.19E+02
F10	6.54E+03	5.07E+03	6.64E+03	6.44E+03	9.83E+03	4.21E+03	3.83E+03	2.98E+03
F11	4.34E+03	9.21E+03	4.35E+03	1.88E+03	9.16E+03	1.26E+03	1.21E+03	1.14E+03
F12	8.31E+07	4.87E+06	2.10E+09	2.20E+08	1.67E+09	6.52E+06	1.44E+06	3.85E+05
F13	3.73E+05	2.82E+04	1.13E+09	1.48E+08	3.65E+09	1.80E+05	5.05E+04	1.30E+04
F14	1.46E+05	8.32E+03	1.45E+06	1.17E+05	4.16E+05	1.91E+04	3.92E+03	1.92E+03
F15	4.98E+04	1.86E+05	2.52E+07	1.51E+05	8.07E+07	3.45E+04	1.01E+04	8.98E+03
F16	3.39E+03	3.42E+03	2.94E+03	2.65E+03	7.26E+03	2.72E+03	2.46E+03	1.96E+03
F17	2.80E+03	2.13E+03	2.42E+03	2.06E+03	5.42E+03	2.26E+03	1.97E+03	1.80E+03
F18	2.81E+06	8.82E+04	1.34E+06	4.42E+05	1.19E+07	1.52E+05	1.91E+05	2.95E+04
F19	8.46E+06	4.35E+06	7.80E+06	5.04E+06	3.09E+08	4.82E+05	1.27E+05	9.51E+03
F20	3.02E+03	2.91E+03	2.61E+03	2.63E+03	3.55E+03	2.32E+03	2.32E+03	2.11E+03
F21	2.60E+03	2.51E+03	2.59E+03	2.45E+03	2.77E+03	2.59E+03	2.39E+03	2.36E+03
F22	3.13E+03	2.49E+03	7.68E+03	2.66E+03	7.66E+03	6.24E+03	2.30E+03	2.30E+03
F23	3.37E+03	2.90E+03	3.16E+03	2.82E+03	3.82E+03	3.31E+03	2.74E+03	2.69E+03
F24	3.56E+03	3.01E+03	3.31E+03	2.93E+03	4.09E+03	3.42E+03	2.89E+03	2.90E+03
F25	2.98E+03	2.89E+03	3.42E+03	3.23E+03	5.56E+03	2.88E+03	2.89E+03	2.88E+03
F26	8.75E+03	4.21E+03	7.70E+03	5.09E+03	1.22E+04	7.88E+03	5.42E+03	4.11E+03
F27	3.32E+03	3.29E+02	3.43E+03	3.25E+03	6.03E+03	3.20E+03	3.24E+03	3.19E+03
F28	3.53E+03	4.43E+03	4.49E+03	5.29E+03	7.35E+03	3.30E+03	3.22E+03	3.10E+03
F29	4.85E+03	4.22E+03	4.73E+03	4.01E+03	7.75E+03	4.81E+03	3.83E+03	3.48E+03
F30	1.63E+07	1.93E+06	1.89E+07	1.09E+07	2.48E+09	1.28E+06	3.24E+06	3.02E+05

Subsection 4.1.1. Each algorithm was run 30 times independently on each function to make the obtained results more reliable. Table 5 shows the average and standard deviation of the optimal objective values obtained from the 30 executions. At the bottom of Table 5, the average ranking of the algorithms involved is presented. Table 6 reports the results gained from the Wilcoxon signed ranks test.

From Table 5, OPLSSA beats TSA and DMMFO on all cases. Compared to MPA, OPLSSA finds similar and better values on five and 18 test functions, respectively. HGS and OPLSSA reach the theoretical optimal solution on six benchmarks (i.e. f_5 , f_{12} , f_{13} , f_{14} , f_{17} , f_{21}); OPLSSA shows better performance on 16 cases; on the remaining one function (i.e. f_{18}), the OPLSSA algorithm is inferior to HGS. According to the pairwise comparison between OPLSSA and AOA, they are tied on five test functions; OPLSSA wins on 17 test cases; AOA gains advantage on only one function (i.e.

f_{18}). OPLSSA beats IGWO and OGWO on almost all benchmark functions; for f_5 , all three methods find the theoretical optimal solution. With respect to WEMFO, OPLSSA obtains similar and better results on four and 19 problems, respectively. According to the average ran-

Finally, from the results generated by the Wilcoxon signed ranks test, the p -values derived from all available comparisons are less than 0.05, which reveals that all differences between the performance of OPLSSA and its competitors on the utilized functions are statistically significant.

Figure 6 provides a graphical depiction in the form of a radar chart that emphasizes the average ranking of the OPLSSA approach and the eight involved Frontier swarm intelligent algorithms on the 23 tested functions. From the figure, OPLSSA achieved the highest ranking on almost all tested functions, which represents that this algorithm can be considered as a promising optimization tool.

4.1.3 Scalability test

The performance of well-established metaheuristic algorithms will not deteriorate drastically as the dimensionality of the to-be-solved problem increases. The proposed OPLSSA algorithm aims to improve the overall performance of the basic SSA, and scalability is a key point that must be considered. In this experiment, OPLSSA was applied to address 23 benchmark functions with large scales (i.e. 10000 dimensions) in Table 2. The parameters of the algorithms were set to the same as those used in Subsection 4.1.1. To evaluate the performance of the OPLSSA method in solving challenging optimization problems with high dimensions, a novel metric called success rate (SR%) was introduced, which can be defined as

$$\begin{cases} |f_A - f_T|/f_T \leq 10^{-5}, & f_T = 0 \\ |f_A - f_T| \leq 10^{-5} \leq 10^{-5}, & f_T \neq 0 \end{cases} \quad (10)$$

where f_A is the results achieved by OPLSSA for the test function, f_T stand for the theoretical optimal value of the function.

If the result obtained by the algorithm on the benchmark function satisfies Eq. 10, it means that this solution is successful and *vice versa*. The OPLSSA algorithm is run 30 times independently on each case and the ratio of the number of successes to the total number of runs is the SR%. Table 7 reports the optimal value, worst value, average value, standard deviation, and SR% for the 30 independent runs.

From Table 7, OPLSSA shows competitive performance in solving high-dimensional optimization problems. In terms of solution accuracy, OPLSSA is able to find the theoretical optimal solution on 20 test functions; for f_7 and f_{13} , the solutions obtained are similar to those achieved on 100-dimensional problems; for f_{18} , the value derived is inferior to that found on 100-dimensional benchmark. This proves that the dramatic increase in the problem's dimensionality does not deteriorate the performance of the OPLSSA algorithm, i.e., OPLSSA has superior stability. On the other hand, in terms of SR%, OPLSSA attains a 100% success rate on 22 high-dimensional optimization problems, representing that the developed approach has been successful in all 30 independent tests. The SR% on another function (i.e. f_7) is 70%, meaning that 21 out of 30 runs achieved success. Based on the above discussion, the developed OPLSSA algorithm gets remarkable performance on large scale optimization problems.

4.1.4 Convergence analysis

A well-established swarm intelligent algorithm moves in large steps in the search space in the early iterations to locate the rough position of the global optimal solution. After the lapse of few iterations, the step size is shortened to precisely search the already explored region, thus improving the convergence accuracy. Rapid convergence rate often leads to premature convergence of the algorithm, making the solution accuracy insufficient. Improving the solution precision of the method

requires performing more iterations, which will degrade the convergence speed of the algorithm. The unbalanced convergence speed and convergence precision is a weak open point that destroys the performance of the algorithm. One of the main goals of the improvements to SSA in this work is to enhance the above-mentioned balance of the basic algorithm. To investigate the performance of the OPLSSA algorithm in this regard, two additional sets of experiments were performed. For experimental purpose, some of the representative benchmarks with 100-dimensional in Table 2 were applied. The parameter settings of the employed algorithms were the same as those used in Subsection 4.1.1. In experiment 1, the convergence curves of the standard SSA algorithm and eight SSA variants on so-

By observing Figure 7, the OPLSSA algorithm is able to find more accurate solutions quickly for all functions, while the comparison algorithms are inferior to OPLSSA in terms of convergence rate and convergence accuracy. Similar phenomena can be observed on Figure 8. Overall, the OPLSSA algorithm outperforms the popular SSA variants and the cutting-edge algorithms in terms of convergence rate and convergence accuracy.

4.2 Experiments on CEC 2017 benchmark functions

In this subsection, the effectiveness of OPLSSA algorithm is tested on the IEEE CEC 2017 benchmark functions. This benchmark suite contains 30 test problems. For each function, the search region in each dimension is defined as $[-100, 100]$. All selected functions are initiated in $[-100, 100]^D$, where D is the problem's dimension which is taken as 30 for all functions. All the 30 benchmarks can be classified into four species according to the function character, in which unimodal functions contain F1, F2, and F3, from F4 to F10 belongs to multimodal functions, hybrid functions include from F11 to F20, from F21 to F30 belongs to composition functions. The details of all the 30 benchmark functions are shown in Table 8. Since the mentioned functions are from distinct classes and each has its own characteristic properties, the utilized OPLSSA is challenged from different aspects. The obtained results are compared with other well-established swarm intelligent approaches, including DA (Mirjalili, 2016), TSA (Kaur et al., 2020), EGWO (Long et al., 2018), GOA (Abualigah and Diabat, 2020), SOA (Wang et al., 2022b), PBO (Polap and Woźniak, 2017), and the standard SSA (Mirjalili et al., 2017). The specific parameters of the comparison approaches are set the same as recommended in the respective original literature, and the number of function evaluations is set to $10^4 \times D$, where D is the dimension of the tested problem. The results obtained at CEC 2017 test functions for the involved approaches are reported in Table 9. Note that F2 has been removed due to the erratic behavior it exhibits.

By observing Table 9, OPLSSA outperformed DA, GOA, TSA, SOA, EGWO and PBO on all test cases. OPLSSA can beat PBO on

almost all test functions, while on F22 and F24, the two algorithms obtain similar performance. With respect to SSA, OPLSSA provides better results on 27 test functions and similar values on one case. However, for F24, marginally better results are achieved by SSA. Overall, OPLSSA shows better or at least competitive performance than its peers on all CEC 2017 test functions, which proves that OPLSSA has superior performance. Moreover, according to the pairwise comparisons between SSA and DA, GOA, TSA, SOA, EGWO and PBO, SSA beats all competitors on 20 test functions (i.e. F1, F5, F6, F8, F9, F10, F11, F12, F14, F15, F16, F17, F19, F20, F21, F22, F23, F24, F28, F29), which proves that the SSA algorithms is a competitive swarm intelligence-based approach.

5 Conclusion

This paper proposes an extended version of salp swarm algorithm termed as OPLSSA. Two modifications to SSA have been introduced which make it competitive with other well-established swarm intelligent algorithms: First, the algorithm applied the PIBL mechanism to help the leading salp to jump out of the local optimal. Second, the algorithm uses the concept of adaptive-based mechanism to generate diversity among the followers. Both these modifications helping in boosting the balance between exploration and exploitation. The performance of the proposed algorithm has been tested on 23 classical benchmark functions and 30 IEEE CEC 2017 benchmark suite and compared with several metaheuristic techniques, including SSA-based algorithms and state-of-the-art swarm intelligent algorithms. The experimental results show that OPLSSA performs better or at least comparable to the competitor methods. Therefore, the developed OPLSSA algorithm can be regarded as a promising method for global optimization problems.

In the future works, we have planned to further extend the research on this paper on the following points: for one direction, the two proposed mechanisms will be combined with other swarm intelligence based algorithms with the hope of improving their performance; for another, the proposed OPLSSA algorithm will be employed to resolve real-world problems such as feature selection, PV parameter extraction, mobile robot path planning, multi-threshold image segmentation, and video coding optimization.

References

- Abualigah, L., and Diabat, A. (2020). A comprehensive survey of the grasshopper optimization algorithm: Results, variants, and applications. *Neural comput. Appl.* 32 (19), 15533–15556. doi:10.1007/s00521-020-04789-8
- Abualigah, L., Diabat, A., and Elaziz, M. A. (2021). Review and analysis for the red deer algorithm. *J. Ambient. Intell. Humaniz. Comput.*, 1–11. doi:10.1007/s12652-021-03602-1
- Arora, S., and Singh, S. (2019). Butterfly optimization algorithm: A novel approach for global optimization. *Soft Comput.* 23 (3), 715–734. doi:10.1007/s00500-018-3102-4
- Bairathi, D., and Gopalani, D. (2021). An improved salp swarm algorithm for complex multi-modal problems. *Soft Comput.* 25 (15), 10441–10465. doi:10.1007/s00500-021-05757-7
- Blum, C. (2005). Ant colony optimization: Introduction and recent trends. *Phys. Life Rev.* 2, 353–373. doi:10.1016/j.plrev.2005.10.001
- Braik, M., Hammouri, A., Atwan, J., Al-Betar, M. A., and Awadallah, M. A. (2022). White shark optimizer: A novel bio-inspired meta-heuristic algorithm for

Data availability statement

The original contributions presented in the study are included in the article/supplementary material, further inquiries can be directed to the corresponding author.

Author contributions

ZW and HD conceived and designed the review. ZW wrote the manuscript. PH, GD, JW, ZY, and AL all participated in the data search and analysis. ZW and JY participated in the revision of the manuscript. All authors contributed to the article and approved the submitted version.

Funding

This work was supported by the National Nature Science Foundation of China (grant no. 61461053, 61461054, and 61072079), Yunnan Provincial Education Department Scientific Research Fund Project (grant no. 2022Y008), the Yunnan University's Research Innovation Fund for Graduate Students, China (grant no. KC-22222706) and the project of fund YNWR-QNBJ-2018-310, Yunnan Province.

Conflict of interest

The authors declare that the research was conducted in the absence of any commercial or financial relationships that could be construed as a potential conflict of interest.

Publisher's note

All claims expressed in this article are solely those of the authors and do not necessarily represent those of their affiliated organizations, or those of the publisher, the editors and the reviewers. Any product that may be evaluated in this article, or claim that may be made by its manufacturer, is not guaranteed or endorsed by the publisher.

- global optimization problems. *Knowledge-Based Syst.* 243, 108457. doi:10.1016/j.knsys.2022.108457
- Braik, M., Sheta, A., Turabieh, H., and Alhiary, H. (2020). A novel lifetime scheme for enhancing the convergence performance of salp swarm algorithm. *Soft Comput.* 25 (1), 181–206. doi:10.1007/s00500-020-05130-0
- Cao, Y., Li, X., and Wang, J. (2013). Opposition-based animal migration optimization. *Math. Problems Eng.* 2013, 1–7. doi:10.1155/2013/308250
- Çelik, E., Öztürk, N., and Arya, Y. (2021). Advancement of the search process of salp swarm algorithm for global optimization problems. *Expert Syst. Appl.* 182, 115292. doi:10.1016/j.eswa.2021.115292
- Chen, D., Liu, J., Yao, C., Zhang, Z., and Du, X. (2022). Multi-strategy improved salp swarm algorithm and its application in reliability optimization. *Math. Biosci. Eng.* 19 (5), 5269–5292. doi:10.3934/mbe.2022247
- Chen, H., Li, W., and Yang, X. (2020). A whale optimization algorithm with chaos mechanism based on quasi-opposition for global optimization problems. *Expert Syst. Appl.* 158, 113612. doi:10.1016/j.eswa.2020.113612
- Dash, S. P., Subhashini, K. R., and Chinta, P. (2022). Development of a Boundary Assigned Animal Migration Optimization algorithm and its application to optimal power flow study. *Expert Syst. Appl.* 200, 116776. doi:10.1016/j.eswa.2022.116776
- Dhiman, G., Garg, M., Nagar, A., Kumar, V., and Dehghani, M. (2021). A novel algorithm for global optimization: Rat swarm optimizer. *J. Ambient. Intell. Humaniz. Comput.* 12 (8), 8457–8482. doi:10.1007/s12652-020-02580-0
- Dhiman, G., and Kumar, V. (2018). Emperor penguin optimizer: A bio-inspired algorithm for engineering problems. *Knowledge-Based Syst.* 159, 20–50. doi:10.1016/j.knsys.2018.06.001
- Dhiman, G., and Kumar, V. (2019). Seagull optimization algorithm: Theory and its applications for large-scale industrial engineering problems. *Knowledge-Based Syst.* 165, 169–196. doi:10.1016/j.knsys.2018.11.024
- Ding, H., Cao, X., Wang, Z., Dhiman, G., Hou, P., Wang, J., et al. (2022). Velocity clamping-assisted adaptive salp swarm algorithm: Balance analysis and case studies. *Math. Biosci. Eng.* 19 (8), 7756–7804. doi:10.3934/mbe.2022364
- Dinkar, S. K., Deep, K., Mirjalili, S., and Thapliyal, S. (2021). Opposition-based Laplacian equilibrium optimizer with application in image segmentation using multilevel thresholding. *Expert Syst. Appl.* 174, 114766. doi:10.1016/j.eswa.2021.114766
- Ewees, A. A., Al-qaness, M. A., and Abd Elaziz, M. (2021). Enhanced salp swarm algorithm based on firefly algorithm for unrelated parallel machine scheduling with setup times. *Appl. Math. Model.* 94, 285–305. doi:10.1016/j.apm.2021.01.017
- Faramarzi, A., Heidarinejad, M., Mirjalili, S., and Gandomi, A. H. (2020). Marine predators algorithm: A nature-inspired metaheuristic. *Expert Syst. Appl.* 152, 113377. doi:10.1016/j.eswa.2020.113377
- Faramarzi, A., Heidarinejad, M., Stephens, B., and Mirjalili, S. (2020). Equilibrium optimizer: A novel optimization algorithm. *Knowledge-Based Syst.* 191, 105190. doi:10.1016/j.knsys.2019.105190
- Faris, H., Mafarja, M. M., Heidari, A. A., Aljarah, I., Ala'M, A. Z., Mirjalili, S., et al. (2018). An efficient binary salp swarm algorithm with crossover scheme for feature selection problems. *Knowledge-Based Syst.* 154, 43–67. doi:10.1016/j.knsys.2018.05.009
- Fister, I., Fister, I., Jr, Yang, X. S., and Brest, J. (2013). A comprehensive review of firefly algorithms. *Swarm Evol. Comput.* 13, 34–46. doi:10.1016/j.swevo.2013.06.001
- Gandomi, A. H., Alavi, A. H., and herd, K. (2012). Krill herd: A new bio-inspired optimization algorithm. *Commun. Nonlinear Sci. Numer. Simul.* 17, 4831–4845. doi:10.1016/j.cnsns.2012.05.010
- Gandomi, A. H., Yang, X. S., and Alavi, A. H. (2013). Cuckoo search algorithm: A metaheuristic approach to solve structural optimization problems. *Eng. Comput.* 29, 17–35. doi:10.1007/s00366-011-0241-y
- Gu, Y., Lu, H., Xiang, L., and Shen, W. (2022). Adaptive simplified chicken swarm optimization based on inverted S-shaped inertia weight. *Chin. J. Electron.* 31 (2), 367–386. doi:10.1049/cje.2020.00.233
- Gülü, Ş. (2021). An improved animal migration optimization algorithm to train the feed-forward artificial neural networks. *Arab. J. Sci. Eng.* 47, 9557–9581. doi:10.1007/s13369-021-06286-z
- Hashim, F. A., Hussain, K., Houssein, E. H., Mabrouk, M. S., and Al-Atabany, W. (2021). Archimedes optimization algorithm: A new metaheuristic algorithm for solving optimization problems. *Appl. Intell.* 51 (3), 1531–1551. doi:10.1007/s10489-020-01893-z
- Heidari, A. A., Mirjalili, S., Faris, H., Aljarah, I., Mafarja, M., and Chen, H. (2019). Harris hawks optimization: Algorithm and applications. *Future gener. Comput. Syst.* 97, 849–872. doi:10.1016/j.future.2019.02.028
- Hou, L., Gao, J., and Chen, R. (2016). An information entropy-based animal migration optimization algorithm for data clustering. *Entropy* 18 (5), 185. doi:10.3390/e18050185
- Hussien, A. G. (2021). An enhanced opposition-based salp swarm algorithm for global optimization and engineering problems. *J. Ambient. Intell. Humaniz. Comput.* 2, 1–22.
- Jain, M., Singh, V., and Rani, A. (2019). A novel nature-inspired algorithm for optimization: Squirrel search algorithm. *Swarm Evol. Comput.* 44, 148–175. doi:10.1016/j.swevo.2018.02.013
- Jena, J. J., and Satapathy, S. C. (2021). A new adaptive tuned Social Group Optimization (SGO) algorithm with sigmoid-adaptive inertia weight for solving engineering design problems. *Multimed. Tools Appl.* 1–35. doi:10.1007/s11042-021-11266-4
- Karaboga, D., and Basturk, B. (2007). A powerful and efficient algorithm for numerical function optimization: Artificial bee colony (ABC) algorithm. *J. Glob. Optim.* 39, 459–471. doi:10.1007/s10898-007-9149-x
- Kaur, S., Awasthi, L. K., Sangal, A. L., and Dhiman, G. (2020). Tunicate swarm algorithm: A new bio-inspired based metaheuristic paradigm for global optimization. *Eng. Appl. Artif. Intell.* 90, 103541. doi:10.1016/j.engappai.2020.103541
- Kennedy, J., and Eberhart, R. (1995). Particle swarm optimization. *Proc. ICNN'95-international Conf. neural Netw.* 4, 1942–1948.
- Khishhe, M., and Mosavi, M. R. (2020). Chimp optimization algorithm. *Expert Syst. Appl.* 149, 113338. doi:10.1016/j.eswa.2020.113338
- Li, S., Chen, H., Wang, M., Heidari, A. A., and Mirjalili, S. (2020). Slime mould algorithm: A new method for stochastic optimization. *Future Gener. Comput. Syst.* 111, 300–323. doi:10.1016/j.future.2020.03.055
- Li, X., Ma, S., and Hu, J. (2017). Multi-search differential evolution algorithm. *Appl. Intell. (Dordr.)* 47 (1), 231–256. doi:10.1007/s10489-016-0885-9
- Li, X., and Yin, M. (2015). Modified cuckoo search algorithm with self adaptive parameter method. *Inf. Sci.* 298, 80–97. doi:10.1016/j.ins.2014.11.042
- Li, X., Zhang, J., and Yin, M. (2014). Animal migration optimization: An optimization algorithm inspired by animal migration behavior. *Neural comput. Appl.* 24 (7), 1867–1877. doi:10.1007/s00521-013-1433-8
- Long, W., Jiao, J., Liang, X., and Tang, M. (2018). An exploration-enhanced grey wolf optimizer to solve high-dimensional numerical optimization. *Eng. Appl. Artif. Intell.* 68, 63–80. doi:10.1016/j.engappai.2017.10.024
- Long, W., Jiao, J., Liang, X., Wu, T., Xu, M., and Cai, S. (2021). Pinhole-imaging-based learning butterfly optimization algorithm for global optimization and feature selection. *Appl. Soft Comput.* 103, 107146. doi:10.1016/j.asoc.2021.107146
- Ma, L., Wang, C., Xie, N. g., Shi, M., Ye, Y., and Wang, L. (2021). Moth-flame optimization algorithm based on diversity and mutation strategy. *Appl. Intell.* 17, 5836–5872. doi:10.1007/s10489-020-02081-9
- Meng, X. B., Liu, Y., Gao, X. Z., and Zhang, H. Z. (2021). “A new bio-inspired algorithm: Chicken swarm optimization,” in *Proc. Of international conference on swarm intelligence* (China: Hefei).
- MiarNaeimi, F., Azizyan, G., and Rashki, M. (2021). Horse herd optimization algorithm: A nature-inspired algorithm for high-dimensional optimization problems. *Knowledge-Based Syst.* 213, 106711. doi:10.1016/j.knsys.2020.106711
- Mirjalili, S. (2016). Dragonfly algorithm: A new meta-heuristic optimization technique for solving single-objective, discrete, and multi-objective problems. *Neural comput. Appl.* 27 (4), 1053–1073. doi:10.1007/s00521-015-1920-1
- Mirjalili, S., Gandomi, A. H., Mirjalili, S. Z., Saremi, S., Faris, H., and Mirjalili, S. M. (2017). Salp swarm algorithm: A bio-inspired optimizer for engineering design problems. *Adv. Eng. Softw.* 114, 163–191. doi:10.1016/j.advengsoft.2017.07.002
- Mirjalili, S., and Lewis, A. (2016). The whale optimization algorithm. *Adv. Eng. Softw.* 95, 51–67. doi:10.1016/j.advengsoft.2016.01.008
- Mirjalili, S., Mirjalili, S. M., and Lewis, A. (2014). Grey wolf optimizer. *Adv. Eng. Softw.* 69, 46–61. doi:10.1016/j.advengsoft.2013.12.007
- Mirjalili, S. (2015). Moth-flame optimization algorithm: A novel nature-inspired heuristic paradigm. *Knowledge-based Syst.* 89, 228–249. doi:10.1016/j.knsys.2015.07.006
- Mitić, M., Vuković, N., Petrović, M., and Miljković, Z. (2015). Chaotic fruit fly optimization algorithm. *Knowledge-Based Syst.* 89, 446–458. doi:10.1016/j.knsys.2015.08.010

- Nadimi-Shahraki, M. H., Taghian, S., and Mirjalili, S. (2021). An improved grey wolf optimizer for solving engineering problems. *Expert Syst. Appl.* 166, 113917. doi:10.1016/j.eswa.2020.113917
- Naik, A., Satapathy, S. C., Ashour, A. S., and Dey, N. (2018). Social group optimization for global optimization of multimodal functions and data clustering problems. *Neural Comput. Appl.* 30 (1), 271–287. doi:10.1007/s00521-016-2686-9
- Nautiyal, B., Prakash, R., Vimal, V., Liang, G., and Chen, H. (2021). Improved salp swarm algorithm with mutation schemes for solving global optimization and engineering problems. *Eng. Comput.* 7, 1–23.
- Ozbay, F. A., and Alatas, B. (2021). Adaptive Salp swarm optimization algorithms with inertia weights for novel fake news detection model in online social media. *Multimed. Tools Appl.* 80 (26), 34333–34357. doi:10.1007/s11042-021-11006-8
- Polap, D., and Woźniak, M. (2017). Polar bear optimization algorithm: Meta-heuristic with fast population movement and dynamic birth and death mechanism. *Symmetry* 9, 203. doi:10.3390/sym9100203
- Rahkar Farshi, T. (2019). A multilevel image thresholding using the animal migration optimization algorithm. *Iran. J. Comput. Sci.* 2 (1), 9–22. doi:10.1007/s42044-018-0022-5
- Ren, H., Li, J., Chen, H., and Li, C. (2021). Stability of salp swarm algorithm with random replacement and double adaptive weighting. *Appl. Math. Model.* 95, 503–523. doi:10.1016/j.apm.2021.02.002
- Saafan, M. M., and El-Gendy, E. M. (2021). Iwossa: An improved whale optimization salp swarm algorithm for solving optimization problems. *Expert Syst. Appl.* 15 (176), 114901. doi:10.1016/j.eswa.2021.114901
- Salgotra, R., Singh, U., Singh, S., Singh, G., and Mittal, N. (2021). Self-adaptive salp swarm algorithm for engineering optimization problems. *Appl. Math. Model.* 89, 188–207. doi:10.1016/j.apm.2020.08.014
- Shan, W., Qiao, Z., Heidari, A. A., Chen, H., Turabieh, H., and Teng, Y. (2021). Double adaptive weights for stabilization of moth flame optimizer: Balance analysis, engineering cases, and medical diagnosis. *Knowl. Based. Syst.* 214, 106728. doi:10.1016/j.knsys.2020.106728
- Singh, N., Houssein, E. H., Singh, S. B., and Dhiman, G. (2022). Hssahho: A novel hybrid salp swarm-harris hawks optimization algorithm for complex engineering problems. *J. Ambient. Intell. Humaniz. Comput.*, 1–37. doi:10.1007/s12652-022-03724-0
- Storn, R., and Price, K. (1997). Differential evolution—a simple and efficient heuristic for global optimization over continuous spaces. *J. Glob. Optim.* 11 (4), 341–359. doi:10.1023/a:1008202821328
- Tu, Q., Liu, Y., Han, F., Liu, X., and Xie, Y. (2021). Range-free localization using reliable anchor pair selection and quantum-behaved salp swarm algorithm for anisotropic wireless sensor networks. *Ad Hoc Netw.* 113, 102406. doi:10.1016/j.adhoc.2020.102406
- Wang, G. G., Deb, S., and Cui, Z. (2019). Monarch butterfly optimization. *Neural Comput. Appl.* 31 (7), 1995–2014. doi:10.1007/s00521-015-1923-y
- Wang, X., Wang, Y., Wong, K. C., and Li, X. (2022). A self-adaptive weighted differential evolution approach for large-scale feature selection. *Knowledge-Based Syst.* 235, 107633. doi:10.1016/j.knsys.2021.107633
- Wang, Z., Ding, H., Li, B., Bao, L., and Yang, Z. (2020). An energy efficient routing protocol based on improved artificial bee colony algorithm for wireless sensor networks. *IEEE Access* 8, 133577–133596. doi:10.1109/access.2020.3010313
- Wang, Z., Ding, H., Li, B., Bao, L., Yang, Z., and Liu, Q. (2022). Energy efficient cluster based routing protocol for WSN using firefly algorithm and ant colony optimization. *Wirel. Pers. Commun.* 125, 2167–2200. doi:10.1007/s11277-022-09651-9
- Wang, Z., Ding, H., Wang, J., Hou, P., Li, A., Yang, Z., et al. (2022). Adaptive guided salp swarm algorithm with velocity clamping mechanism for solving optimization problems. *J. Comput. Des. Eng.* 9, 2196–2234. doi:10.1093/jcde/qwac094
- Wang, Z., Ding, H., Yang, J., Wang, J., Li, B., Yang, Z., et al. (2022). Advanced orthogonal opposition-based learning-driven dynamic salp swarm algorithm: Framework and case studies. *IET Control Theory Appl.* 16, 945–971. doi:10.1049/cth2.12277
- Wang, Z., Ding, H., Yang, Z., Li, B., Guan, Z., and Bao, L. (2021). Rank-driven salp swarm algorithm with orthogonal opposition-based learning for global optimization. *Appl. Intell. (Dordr.)* 52, 7922–7964. doi:10.1007/s10489-021-02776-7
- Wolpert, D. H., and Macready, W. G. (1997). No free lunch theorems for optimization. *IEEE Trans. Evol. Comput.* 1, 67–82. doi:10.1109/4235.585893
- Xia, J., Zhang, H., Li, R., Wang, Z., Cai, Z., Gu, Z., et al. (2022). Adaptive barebones salp swarm algorithm with quasi-oppositional learning for medical diagnosis systems: A comprehensive analysis. *J. Bionic Eng.* 19, 240–256. doi:10.1007/s42235-021-00114-8
- Yang, X. S., and Gandomi, A. H. (2012). Bat algorithm: A novel approach for global engineering optimization. *Eng. Comput. Swans.* 29, 464–483. doi:10.1108/02644401211235834
- Yang, Y., Chen, H., Heidari, A. A., and Gandomi, A. H. (2021). Hunger games search: Visions, conception, implementation, deep analysis, perspectives, and towards performance shifts. *Expert Syst. Appl.* 177, 114864. doi:10.1016/j.eswa.2021.114864
- Yildiz, B. S., Pholdee, N., Bureerat, S., Yildiz, A. R., and Sait, S. M. (2021). Enhanced grasshopper optimization algorithm using elite opposition-based learning for solving real-world engineering problems. *Eng. Comput.* 38, 4207–4219. doi:10.1007/s00366-021-01368-w
- Yu, X., Xu, W., and Li, C. (2021). Opposition-based learning grey wolf optimizer for global optimization. *Knowledge-Based Syst.* 226, 107139. doi:10.1016/j.knsys.2021.107139
- Zamani, H., Nadimi-Shahraki, M. H., and Gandomi, A. H. (2022). Starling murmuration optimizer: A novel bio-inspired algorithm for global and engineering optimization. *Comput. Methods Appl. Mech. Eng.* 392, 114616. doi:10.1016/j.cma.2022.114616
- Zhang, H., Feng, Y., Huang, W., Zhang, J., and Zhang, J. (2021). A novel mutual aid Salp Swarm Algorithm for global optimization. *Concurr. Comput. Pract. Exper.* 2021, e6556. doi:10.1002/cpe.6556
- Zhang, X., Li, X. T., and Yin, M. H. (2019). Hybrid cuckoo search algorithm with covariance matrix adaption evolution strategy for global optimisation problem. *Int. J. Bio-Inspired Comput.* 13 (2), 1–110. doi:10.1504/ijbic.2017.10004358



OPEN ACCESS

EDITED BY

Zhen (Jeff) Luo,
University of Technology Sydney,
Australia

REVIEWED BY

Haipeng Liu,
Coventry University, United Kingdom
Venugopal Gopinath,
NSS College of Engineering, India

*CORRESPONDENCE

Felipe P. Carpes,
carpes@unipampa.edu.br

SPECIALTY SECTION

This article was submitted to
Biomechanics,
a section of the journal
Frontiers in Bioengineering and
Biotechnology

RECEIVED 02 May 2022

ACCEPTED 15 November 2022

PUBLISHED 22 December 2022

CITATION

De la Fuente C, Weinstein A, Neira A,
Valencia O, Cruz-Montecinos C,
Silvestre R, Pincheira PA, Palma F and
Carpes FP (2022), Biased instantaneous
regional muscle activation maps:
Embedded fuzzy topology and image
feature analysis.
Front. Bioeng. Biotechnol. 10:934041.
doi: 10.3389/fbioe.2022.934041

COPYRIGHT

© 2022 De la Fuente, Weinstein, Neira,
Valencia, Cruz-Montecinos, Silvestre,
Pincheira, Palma and Carpes. This is an
open-access article distributed under
the terms of the [Creative Commons
Attribution License \(CC BY\)](https://creativecommons.org/licenses/by/4.0/). The use,
distribution or reproduction in other
forums is permitted, provided the
original author(s) and the copyright
owner(s) are credited and that the
original publication in this journal is
cited, in accordance with accepted
academic practice. No use, distribution
or reproduction is permitted which does
not comply with these terms.

Biased instantaneous regional muscle activation maps: Embedded fuzzy topology and image feature analysis

Carlos De la Fuente^{1,2,3}, Alejandro Weinstein⁴, Alejandro Neira⁵,
Oscar Valencia⁶, Carlos Cruz-Montecinos⁷, Rony Silvestre^{1,3},
Patricio A. Pincheira^{8,9}, Felipe Palma⁶ and Felipe P. Carpes^{2*}

¹Carrera de Kinesiología, Departamento de Cs. de la Salud, Facultad de Medicina, Pontificia Universidad Católica, Santiago, Chile, ²Laboratory of Neuromechanics, Universidade Federal do Pampa, Campus Uruguiana, Uruguiana, Brazil, ³Unidad de Biomecánica, Centro de Innovación, Clínica MEDS, Santiago, Chile, ⁴Centro de Investigación y Desarrollo en Ingeniería en Salud, Universidad de Valparaíso, Valparaíso, Chile, ⁵Escuela de Kinesiología, Facultad de Ciencias, Universidad Mayor, Santiago, Chile, ⁶Laboratorio Integrativo de Biomecánica y Fisiología del Esfuerzo, Facultad de Medicina, Escuela de Kinesiología, Universidad de los Andes, Santiago, Chile, ⁷Laboratory of Clinical Biomechanics, Department of Physical Therapy, Faculty of Medicine, Universidad de Chile, Santiago, Chile, ⁸School of Health and Rehabilitation Science, The University of Queensland, Brisbane, QLD, Australia, ⁹School of Human Movement and Nutrition Sciences, The University of Queensland, Brisbane, QLD, Australia

The instantaneous spatial representation of electrical propagation produced by muscle contraction may introduce bias in surface electromyographical (sEMG) activation maps. Here, we described the effect of instantaneous spatial representation (sEMG segmentation) on embedded fuzzy topological polyhedrons and image features extracted from sEMG activation maps. We analyzed 73,008 topographic sEMG activation maps from seven healthy participants (age 21.4 ± 1.5 years and body mass 74.5 ± 8.5 kg) who performed submaximal isometric plantar flexions with 64 surface electrodes placed over the medial gastrocnemius muscle. Window lengths of 50, 100, 150, 250, 500, and 1,000 ms and overlap of 0, 25, 50, 75, and 90% to change sEMG map generation were tested in a factorial design (grid search). The Shannon entropy and volume of global embedded tri-dimensional geometries (polyhedron projections), and the Shannon entropy, location of the center (LoC), and image moments of maps were analyzed. The polyhedron volume increased when the overlap was <25% and >75%. Entropy decreased when the overlap was <25% and >75% and when the window length was <100 ms and >500 ms. The LoC in the x-axis, entropy, and the histogram moments of maps showed effects for overlap ($p < 0.001$), while the LoC in the y-axis and entropy showed effects for both overlap and window length ($p < 0.001$). In conclusion, the instantaneous sEMG maps are first affected by outer parameters of the overlap, followed by the length of the window. Thus, choosing the window length and overlap parameters can introduce bias in sEMG activation maps, resulting in distorted regional muscle activation.

KEYWORDS

muscle, high-density electromyography, UMAP, entropy, barycenter, image moments, segmentation

Introduction

Physical therapists, biomechanists, and engineers regularly infer (quantitative or qualitative interpretation) neuromuscular adaptations from surface electromyography (sEMG) activation maps (Vieira et al., 2011; Campanini et al., 2020; Merletti and Cerone, 2020). An sEMG activation map represents the discrete distribution of the voltage propagation elicited from the train sum of motor unit action potentials (MUAPs) collected from an array of electrodes on the skin (Botter and Vieira, 2015; Guzmán-Venegas et al., 2015; Ghaderi and Marateb, 2017; Jordanić et al., 2017; Vigotsky et al., 2017; Merletti and Muceli, 2019; Merletti and Cerone, 2020). Thus, multiple electrodes allow for obtaining sEMG activation maps that can be interpreted as images (Jordanić et al., 2017; Merletti and Muceli, 2019), similar to brain activation (Beniczky and Schomer, 2020) or a uterus electromyogram (Xu et al., 2022). Each map pixel corresponds to the voltage acquired by each electrode. Thus, the map can be defined by $I_{i,j,t} = \sqrt{\frac{1}{N-1} \sum_{k=1}^N (\text{EMG}[nT]_{i,j} w[n - mR])^2}$. $I_{i,j,t}$ is the pixel intensity that represents the magnitude of the muscle activity located at (i,j) , t is the number of maps obtained after windowing, $\text{EMG}[nT]_{i,j}$ is the sEMG signal located in the array, $w[n]$ is the window or epoch, N is the length of $w[n]$, and R is the hop size that determines the amount of overlap.

Traditionally, sEMG activation map quantification involves feature extraction, where the location of the center (LoC or barycenter) and the Shannon entropy are the most used (Guzmán-Venegas et al., 2015). The LoC is defined by $\text{LoC} = \frac{\sum_{i,j} I_{i,j} \begin{bmatrix} i \\ j \end{bmatrix}}{\sum_{i,j} I_{i,j}}$ (Jordanić et al., 2016; Pincheira et al., 2020).

Meanwhile, the entropy that explores homogeneity is defined by $E = -\sum_{k=1}^N p(k)^2 \log_2 p(k)^2$. $p(k)^2$ is the probability of the square of the root mean square value at electrode k (Farina et al., 2008). In addition, image moments (expected value, variance, skewness, and kurtosis) can also describe image changes in the spatial time domain (Brown and Godman, 2011).

On the other hand, several conditions might introduce undesired dispersion and noise. Therefore, capturing latent map data might be convenient for understanding how synthetic distortions are introduced. The latent data, which retain lower-dimension information that explains higher-dimension data, have been optimized through the Uniform Manifold Approximation and Projection (UMAP) algorithm (McInnes et al., 2020; Ali et al., 2019; Oskolkov, 2019). UMAP projects a fuzzy topological set of high dimensions equivalent to low-dimensional data (McInnes et al., 2020; Ali et al., 2019). The approximation is possible by creating fuzzy topological projections with binary cross-entropy and

projections (McInnes et al., 2020). The binary cross-entropy is modeled by $\sum_{j \in E} [w_h(e) \log \frac{w_h(e)}{w_l(e)} + (1 - w_h(e)) \log \frac{(1 - w_h(e))}{(1 - w_l(e))}]$, while the weight between neighbors is modeled by $w = e^{-d(x_i - x_j) - \rho / \sigma}$. ρ_i is the distance from the i -th data points to its first nearest neighbor (Oskolkov, 2019). The first term ensures fuzzy connectivity (simplex or node connections). In contrast, the second term does not permit the creation of simplexes (McInnes et al., 2020). Hence, UMAP might allow the topological representation of different sEMG maps (high dimensions) resulting from N and R parameters.

Previously, sEMG segmentation influenced the electrical manifestation of fatigue conclusions (De la Fuente et al., 2021). Since sEMG activation maps depend inherently on segmentation, alterations are expected in the sEMG activation map. However, there is still large variability in choosing window lengths, i.e., 50 ms, 100 ms, 150 ms, 250 ms, 500 ms, or 1,000 ms (Botter and Vieira, 2015; Guzmán-Venegas et al., 2015; Jordanić et al., 2016; Falla et al., 2017; Jordanić et al., 2017; Zhu et al., 2017; Martinez-Valdes et al., 2018; Vinti et al., 2018; Watanabe et al., 2018; Hegyi et al., 2019), and truncation methods (non-overlapping (Guzmán-Venegas et al., 2015; Falla et al., 2017; Jordanić et al., 2017)). Therefore, understanding how segmentation may distort regional muscle activation is still a concern. Here, we aimed to describe the effect of instantaneous spatial representation (sEMG segmentation) on embedded fuzzy topological polyhedrons and image features extracted from the sEMG activation maps obtained with high-density sEMG on healthy participants performing a submaximal isometric contraction of medial gastrocnemius.

Materials and methods

Study design

We conducted a factorial experiment to test 30 signal processing conditions (Figure 1). The sample included 73,008 sEMG activation maps obtained from seven healthy participants (aged 21.4 ± 1.5 years, body mass 74.5 ± 8.5 kg, height 1.77 ± 0.01 m, and body mass index 20.9 ± 2.2 kg/m²) who performed a submaximal isometric plantar flexion with the ankle at neutral position (60% with the ankle in a 90° position) in a controlled laboratory set-up (Figure 1). Here, we considered the medial gastrocnemius muscle as a good muscle model due to its application in clinics and biomechanics and because it was previously used in EMG segmentation (Theisen et al., 2016; De la Fuente et al., 2021). The Bioethics Committee of the Andes University (Santiago, Chile) approved this study (# INV-IN201701), which was developed according to the

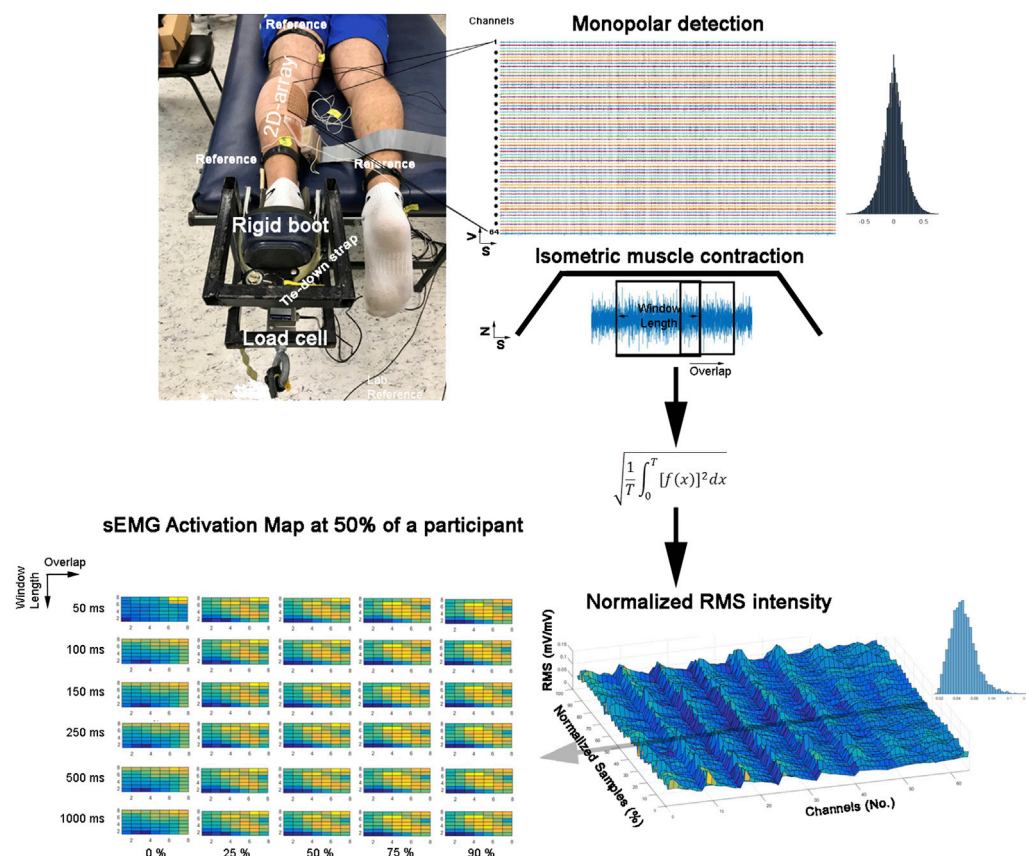


FIGURE 1

Experimental set-up and instantaneous surface electromyographic map generation flow. Colors represent the instantaneous potential amplitude distribution (yellow indicates more intensity, and blue indicates lower intensity).

principles of the Declaration of Helsinki. All participants signed a consent term agreeing to participate in this study.

Data

A total of 73,008 sEMG activation maps were included in the study (data are available in https://www.researchgate.net/publication/365904692_Biased_instantaneous_regional_muscle_activation_maps_embedded_fuzzy_topology_and_image_features_analysis_datapart1 and https://www.researchgate.net/publication/365904985_Biased_instantaneous_regional_muscle_activation_maps_embedded_fuzzy_topology_and_image_features_analysis_datapart2). They were the result of 39 experiments of a total of 42 experiments (6 trials x 7 participants). Of the 42 experiments, three experiments were excluded due to artifacts. These 39 experiments contained 10,240 samples x 64 channels. The 73,008 sEMG activation maps resulted in combining 1,872 maps and 39 experiments. The 1,872 maps resulted from 30 conditions, that is, window lengths

(50, 100, 150, 250, 500, and 1,000 ms) combined with an overlap (0%, 25%, 50%, 75%, and 90%) without repetition. This combination resulted in 100, 136, 199, 423, and 1,014 maps (Pincheira et al., 2021).

Experimental set-up

Participants were lying prone on a bench with their hip, knee, and ankle in a neutral joint position. The ankle of the participants was tightly strapped to a customized rigid structure (Figure 1). Then, they were asked to perform three maximal voluntary isometric contractions against a force transducer placed at a metatarsal head level (Revere Transducers®, 9363-B10-500-20T1R, United States). Each attempt lasted 5 seconds, with a 3-min rest period between repetitions (a period of non-contraction to recover basal muscle energy conditions). Immediately, the participants were asked to perform the submaximal voluntary contraction. The contractions were sustained for 20 s, and the duration of the ascending/descending ramps was 6 s and 8 s, respectively, for the hold

phase. The participants received real-time visual feedback, displaying a trapezoid target (Figure 1). The participants completed six trials.

Electrode location and data acquisition

Prior to data acquisition, the skin was shaved, abraded (Everi: Spes Medica s. r.l, Battipaglia, Italy), and cleaned with alcohol to diminish the skin impedance. Then, a semi-disposable adhesive with 64 electrodes organized in eight rows and eight columns of 1 mm diameter and an inter-electrode distance of 10 mm was attached (GR10MM0808, OT Bioelettronica, Torino, Italy) (Pincheira et al., 2021). The electrode spaces were filled with a conductive cream (Spes Medica s.r.l, Italy) (Pincheira et al., 2021).

The electrode was placed over the most prominent region of the medial gastrocnemius, and the muscle belly was determined by palpation during a resisted plantar flexion. Then, the electrode was aligned in the cephalocaudal axis with respect to the line formed between the medial femoral condyle and malleolus. For the mediolateral axis, the electrode was aligned with respect to the medial contour of the medial gastrocnemius muscle. The superomedial electrode corner was fixed at 30% of the distance of the cephalocaudal axis, as was described previously (Pincheira et al., 2021).

A total of 64 monopolar sEMG signals were collected from the electrodes, amplified with a gain of 200, and digitized at a sampling frequency of 2,048 Hz with a 12-bit resolution and 3-dB bandwidth 10–500 Hz (EMG-USB2: OTBioelettronica, Turin, Italy). The reference electrodes were positioned according to Pincheira et al. (2021) over the contralateral ankle and superior to the electrode near the popliteal fossa (Pincheira et al., 2021). Two additional reference electrodes were placed on the tibial tuberosity and the fibula to improve the EMG signal-to-noise ratio. Once the quality of the signals was assured, the electrodes were firmly secured with an elastic adhesive bandage (Figure 1).

Correct electrode placement was confirmed by assessing sEMG signals online for low baseline noise levels and possible artifacts, cortocircuit, or bad contact during visual inspection during brief plantar flexion contractions (Pincheira et al., 2021). The signal was evaluated at rest (without contraction) and under contraction (Pincheira et al., 2021). Non-saturated signals and out-of-power line interference were appreciated during the acquisition (Pincheira et al., 2021). Nevertheless, three experiments were excluded during offline signal processing after observing in the time and frequency domains. The domains showed increased noise.

Pre-processing

The sEMG signals were mean-centered to zero and segmented at the force plateau signal. Then, the signals

were filtered by a zero-lag second-order Butterworth with a bandpass of 20–400 Hz. Outlier channels were manually identified and confirmed using the Z-score. A mean with 1 pixel of radio was assigned for outlier pixels from channels with confirmed higher Z-scores (<0.01% was assigned). Afterward, the sEMG signals were convolved with a rectangular window. Our convolved sEMG signals were arranged in a matrix 8×8 , and the maps were normalized to the maximum value of the whole matrixes during the plateau (Figure 1).

Window length and overlap (intervention)

The window lengths were chosen based on previous reports (Guzmán-Venegas et al., 2015; Jordanic et al., 2016; Falla et al., 2017; Jordanić et al., 2017; Zhu et al., 2017; Martínez-Valdes et al., 2018; Watanabe et al., 2018; Hegyi et al., 2019). The overlap parameters were 0, 25, 50, 75, and 90%, resulting in 30 different combinations between the window length and overlap $\{(50, 0), (50, 25), \dots, (1000, 75), (1000, 90)\}$ to introduce variability to the sEMG activation maps to study its effects.

Uniform manifold approximation and projection and feature image extraction

The sEMG activation maps of each condition of all participants were concatenated $[73,008 \times 64]$ and introduced to the UMAP algorithm version 1.4.1 (Meehan et al., 2020). The global structure of high-dimensional data (64 dimensions) was embedded into three-dimensional data (McInnes et al., 2020; McInnes, 2018). The number of neighbors was 10, the minimum distance was 0.7, the number of components was three dimensions, the metric was Euclidean, the number of epochs was 200, the learning rate was 1, local connectivity was 1, repulsion strength was 1, the spread was 1, the fuzzy set operation was 1, and the negative sample rate was 5. After assessing the level of connectivity and homogeneity of the structures, we created a 3D polyhedron (finite elements) to obtain their volume and Shannon entropy. In addition, we extracted the image features from sEMG activation maps, LoC, Shannon entropy, and image moment (expected value–moment 1-, variance–moment 2-, skewness–moment 3-, and kurtosis–moment 4-) (Brown and Godman, 2011).

Variables

The following continuous variables were determined: 1) volume of the fuzzy topological structure obtained from the embedded dataset and normalized to a maximum value, 2)

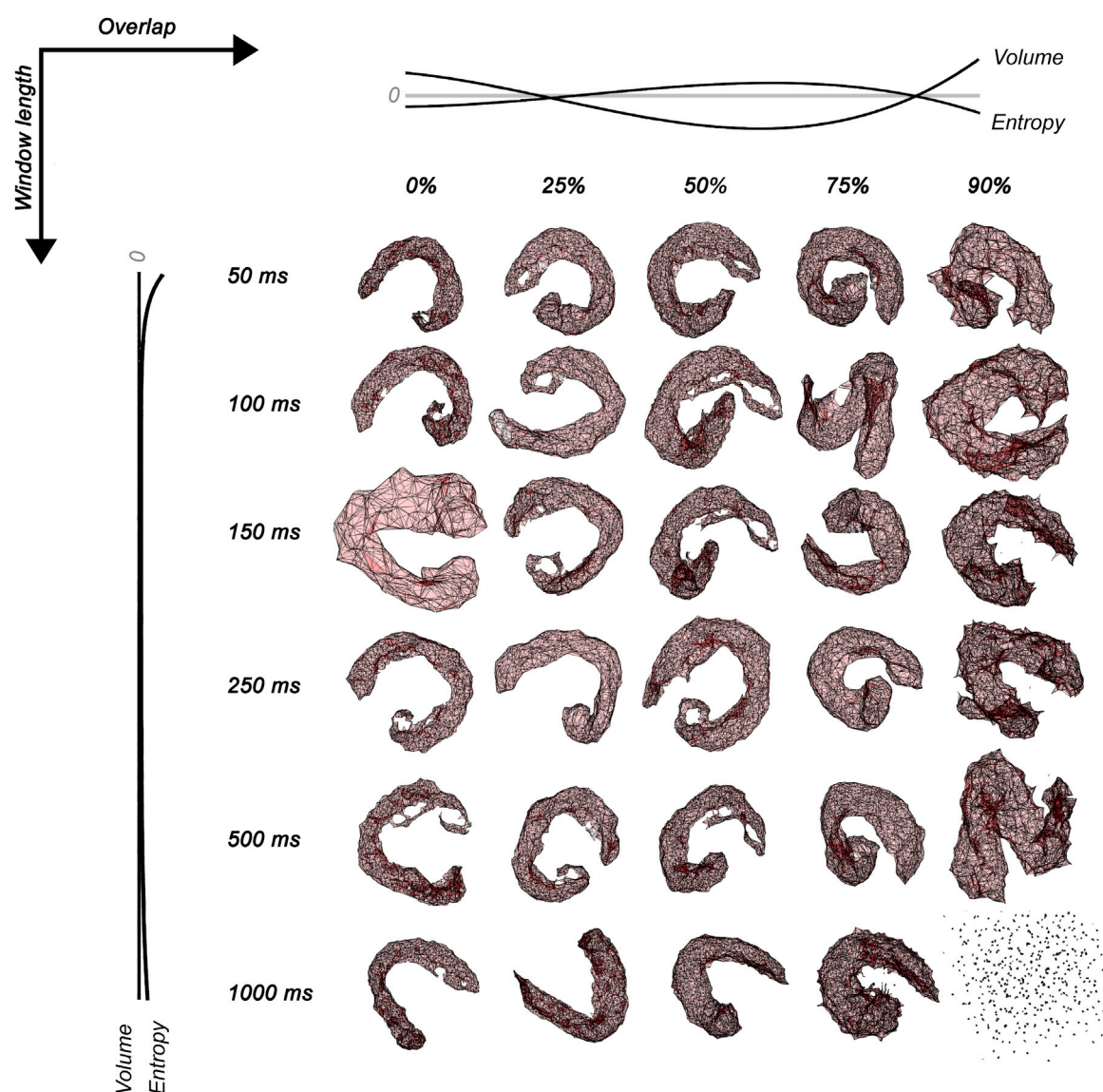


FIGURE 2

Surface electromyographic maps embedded in three dimensions for 30 conditions of signal processing varying window lengths (50 ms, 100 ms, 150 ms, 250 ms, 500 ms, and 1,000 ms) and overlap (0, 25, 50, 75, and 90%). The normalized no-linear fitting for the Shannon entropy and volume of sEMG polyhedrons is also shown in dark lines. Notice that the combination of 1000 ms and 90% of overlap projects no simplexes connections.

entropy of the fuzzy topological structure from the embedded dataset obtained as the Shannon entropy (Farina et al., 2008), 3) LoC obtained from the sEMG activation map in both x and y coordinates (Jordanić et al., 2017), 4) Shannon entropy obtained from the sEMG activation maps (Farina et al., 2008), 5) moment-1 of maps obtained from the sEMG activation map as the expected value (Brown and Godman, 2011), 6) moment-2 of maps obtained from the sEMG activation map as variance (Brown and Godman, 2011), 7) moment-3 of maps obtained from the sEMG activation map as skewness (Brown and Godman, 2011), and 8) moment-4 of

maps obtained from the sEMG activation map as kurtosis (Brown and Godman, 2011).

Data analysis

The sEMG activation maps were described as the expected value and variance. Normality and homoscedasticity assumptions were checked prior to the image analysis feature using two-way ANOVA $2 \times 5 \times 6$ (two factors: window length and overlap; six levels of the length of windows: 50 ms, 100 ms,

TABLE 1 Topographical EMG map outcomes.

	50 ms	100 ms	150 ms	250 ms	500 ms	1,000 ms
LoCx, m.m.						
0%	33 (0.013)	33 (0.013)	33 (0.010)	33 (0.010)	33 (0.010)	33 (0.010)
25%	24 (0.007)	24 (0.006)	24 (0.005)	24 (0.005)	24 (0.005)	24 (0.005)
50%	16 (0.003)	16 (0.003)	16 (0.002)	16 (0.002)	16 (0.002)	16 (0.002)
75%	08 (7.4e-4)	08 (5.7e-4)	08 (5.4e-4)	08 (5.2e-4)	08 (5.2e-4)	08 (5.1e-4)
90%	03 (1.2e-4)	03 (9.7e-5)	03 (9.2e-5)	03 (8.9e-5)	03 (8.7e-5)	03 (8.7e-5)
LoCy, m.m.						
0%	35 (0.012)	35 (0.010)	35 (0.010)	35 (0.010)	35 (0.009)	35 (0.009)
25%	26 (0.007)	26 (0.005)	26 (0.005)	26 (0.005)	26 (0.005)	26 (0.005)
50%	18 (0.003)	18 (0.003)	18 (0.002)	18 (0.002)	18 (0.002)	18 (0.002)
75%	08 (6.6e-4)	08 (5.5e-4)	08 (5.2e-4)	08 (5.0e-4)	08 (5.0e-4)	08 (4.9e-4)
90%	03 (1.2e-4)	03 (9.4e-5)	03 (8.9e-5)	03 (8.6e-5)	03 (8.5e-5)	03 (8.4e-5)
Entropy, d.u.						
0%	3.11 (0.012)	3.11 (0.012)	3.12 (0.012)	3.11 (0.012)	3.11 (0.012)	3.11 (0.023)
25%	3.11 (0.012)	3.11 (0.012)	3.11 (0.012)	3.11 (0.012)	3.11 (0.012)	3.11 (0.012)
50%	3.11 (0.012)	3.11 (0.012)	3.11 (0.012)	3.11 (0.012)	3.11 (0.012)	3.11 (0.012)
75%	3.11 (0.009)	3.11 (0.009)	3.11 (0.009)	3.11 (0.009)	3.11 (0.009)	3.11 (0.009)
90%	2.97 (7.1e-4)	2.97 (7.1e-4)	2.97 (5.1e-4)	2.97 (4.8e-4)	2.98 (4.6e-4)	2.98 (4.7e-4)
Moment-1, d.u.						
0%	0.126 (0.004)	0.128 (0.004)	0.128 (0.004)	0.128 (0.004)	0.128 (0.004)	0.129 (0.004)
25%	0.126 (0.004)	0.128 (0.004)	0.128 (0.004)	0.128 (0.004)	0.128 (0.004)	0.129 (0.004)
50%	0.126 (0.004)	0.128 (0.004)	0.128 (0.004)	0.128 (0.004)	0.128 (0.004)	0.129 (0.004)
75%	0.126 (0.004)	0.128 (0.004)	0.128 (0.004)	0.128 (0.004)	0.128 (0.004)	0.129 (0.004)
90%	0.126 (0.004)	0.128 (0.004)	0.128 (0.004)	0.128 (0.004)	0.128 (0.004)	0.129 (0.004)
Moment-2 x 10 ⁻⁵ , d.u.						
0%	2.14 (8.84e-11)	1.04 (3.71e-11)	1.03 (3.45e-11)	1.03 (3.25e-11)	1.03 (3.20e-11)	1.03 (3.19e-11)
25%	1.89 (8.00e-11)	1.33 (4.77e-11)	1.33 (4.60e-11)	1.33 (4.43e-11)	1.33 (4.39e-11)	1.33 (4.38e-11)
50%	2.14 (8.84e-11)	1.28 (4.33e-11)	1.28 (3.91e-11)	1.28 (3.78e-11)	1.28 (3.73e-11)	1.28 (3.72e-11)
75%	2.24 (7.84e-11)	1.33 (3.99e-11)	1.33 (3.58e-11)	1.33 (3.44e-11)	1.33 (3.40e-11)	1.33 (3.39e-11)
90%	2.33 (7.95e-11)	1.33 (3.99e-11)	1.33 (3.57e-11)	1.33 (3.43e-11)	1.33 (3.39e-11)	1.33 (3.38e-11)
Moment-3, d.u.						
0%	-0.01 (0.41)	0.03 (0.42)	0.04 (0.41)	0.05 (0.41)	0.05 (0.41)	0.05 (0.41)
25%	-0.01 (0.41)	0.03 (0.43)	0.05 (0.43)	0.05 (0.43)	0.06 (0.42)	0.06 (0.42)
50%	0.00 (0.42)	0.03 (0.42)	0.05 (0.41)	0.05 (0.42)	0.06 (0.41)	0.06 (0.41)
75%	0.00 (0.43)	0.03 (0.42)	0.05 (0.42)	0.05 (0.42)	0.06 (0.41)	0.06 (0.41)
90%	0.00 (0.43)	0.03 (0.42)	0.06 (0.42)	0.06 (0.41)	0.06 (0.41)	0.06 (0.41)
Moment-4, d.u.						
0%	2.47 (0.80)	2.52 (0.82)	2.52 (0.83)	2.53 (0.83)	2.54 (0.85)	2.55 (0.85)
25%	2.46 (0.82)	2.49 (0.79)	2.50 (0.82)	2.52 (0.83)	2.52 (0.83)	2.52 (0.83)
50%	2.48 (0.80)	2.51 (0.80)	2.52 (0.82)	2.53 (0.82)	2.54 (0.83)	2.54 (0.83)
75%	2.47 (0.79)	2.50 (0.79)	2.51 (0.81)	2.52 (0.81)	2.53 (0.82)	2.53 (0.81)
90%	2.47 (0.79)	2.50 (0.80)	2.51 (0.81)	2.52 (0.81)	2.53 (0.82)	2.53 (0.82)

d.u. = dimensionless unit.

Data are expressed as the expected value ($E[x]$) of the histogram and variance of the expected value ($E[x - E[x]]^2$).

150 ms, 250 ms, 500 ms, and 1,000 ms; and five levels of sliding: 0%, 25%, 50%, 75%, and 90%) for main effects. Effect sizes were described as the square sum of the effects divided by the total sum of squares to show the explained variance [small: $\eta^2 < 0.04$ (<

4%), medium: between 0.04 (4%) and 0.64 (64%), and large: > 0.64 (64%) (Ferguson, 2009)]. The Tukey–Kramer test was used to find differences between groups. The K-medoid algorithm was applied to explore the differences between

factors. The number of clusters with K-medoids was evaluated as the sum of the ratio between the sum of that within the Euclidean distance and Euclidean distance of each point with their medoid found. Then, the elbow method before convergence was chosen. The alpha error was equal to 0.05 for all statistics. The volume and entropy behavior were studied using a non-linear least square method, and fuzzy sEMG polyhedrons were described in the UMAP space. The zero-crossing of the fitted curve was described. All calculi were made through MATLAB software (MathWorks, Inc., United States).

Results

The polyhedron volume increased when the overlap was <25% and >75%. Entropy decreased when the overlap was <25% and >75% and when the window length was <100 ms and >500 ms. The polyhedron volume R^2 was 73.5% and 16.9% for overlap and window length, respectively. The polyhedron entropy R^2 was 90.1% and <1% for overlap and window length, respectively. The polyhedron zero-crossing for volume in the overlap was at 25%, and between 75% and 90%. The polyhedron zero-crossing for entropy in the overlap was between 25% and 50%, and between 75% and 90%. Non-zero crossings were found for window lengths. Figure 2 shows the volume and entropy behavior of embedded sEMG activation maps.

Map LoC_x (Table 1) showed a main effect for both overlap ($p < 0.001$, $\eta^2 = 0.998$, large effect size) and window length ($\eta^2 < 0.04$, small effect size), and there was interaction ($p < 0.001$, $\eta^2 < 0.04$, small effect size). Overlap showed differences between all multiple comparisons ($p < 0.001$). Window length showed multicomparison differences between 50 ms and all window lengths ($p < 0.001$). Data were grouped into five clusters with centroids: 3.2 mm, 7.7 mm, 16.4 mm, 24.1 mm, and 32.8 mm. Map LoC_y (Table 1) showed only a main effect for overlap ($p < 0.001$, $\eta^2 = 0.998$, large effect size). There were multiple comparison differences between all overlaps ($p < 0.001$), and data were grouped into six clusters with centroids: 3.5 mm, 8.2 mm, 17.6 mm, 25.9 mm, 34.5 mm, and 35.9 mm.

Map entropy (Table 1) showed a main effect for both overlap ($p < 0.001$, $\eta^2 = 0.998$, large effect size) and window length ($p < 0.001$, $\eta^2 < 0.04$, small effect size), and there was interaction ($p < 0.001$, $\eta^2 < 0.04$, small effect size). There were multiple comparison differences between 50 ms and all window lengths ($p < 0.001$). Data were grouped into five clusters with centroids: 1.8 d.u., 2.4 d.u., 2.9 d.u., 3.0 d.u., and 4.3 d.u.

Map moment-1 (Table 1) showed a main effect for the window length ($p < 0.001$, $\eta^2 < 0.04$, small effect size). There were differences between 50 ms and 1,000 ms ($p = 0.036$), 50 ms and 150 ms ($p = 0.004$), 50 ms and 250 ms ($p = 0.001$),

50 ms and 500 ms ($p = 0.001$), and 50 ms and 1000 ms ($p < 0.004$). Data were grouped into five clusters with centroids: 0.06 d.u., 0.09 d.u., 0.13 d.u., 0.18 d.u., and 0.24 d.u. Map moment-2 (Table 1) showed a main effect for the window length ($p < 0.001$, $\eta^2 < 0.04$, small effect size). There were differences between 50 ms and all window lengths ($p < 0.001$). Data were grouped into one cluster. Map moment-3 (Table 1) showed a main effect for the window length ($p < 0.001$, $\eta^2 < 0.04$, small effect size). There were differences between 50 ms and all window lengths ($p < 0.001$), 100 ms and 150 ms ($p = 0.005$), and 100 ms and the rest of the window lengths ($p < 0.001$). Data were grouped into one cluster. Map moment-4 (Table 1) showed a main effect for the window length ($p < 0.001$, $\eta^2 < 0.04$, small effect size). There were differences between 50 ms and the rest of the window lengths ($p < 0.001$), 100 ms and 250 ms ($p = 0.006$), 100 ms and 500 ms ($p < 0.001$), 100 ms and 1,000 ms ($p < 0.001$), and 150 ms and 1000 ms ($p = 0.017$). Data were grouped into one cluster.

Discussion

The most important finding in our study was that the sEMG segmentation parameters (overlap and window length) of activation maps introduce bias, resulting in distorted regional muscle activation compromising the map inferences. For example, we can conclude about regional sEMG activation with or without clear regional sEMG activation when there were not, e.g., the statistical error types (Akobeng, 2016). The topological dimensional reduction and feature extraction of the sEMG maps confirmed it. Outer segmentation parameters tested here have caused the highest distortion in the activation maps; independently, no-overlap and small window length trends reduce the activation map region, while large overlap and window length trends increase the activation map region. Thus, sEMG map generation can modify the spatial myoelectrical activity and should be carefully considered by their physiological and clinical repercussions, i.e., wrong rehabilitation or performance planning. Furthermore, many clinical and sport science studies did not fully consider it in the past, and there is high variability in the choice of segmentation parameters (Botter and Vieira, 2015; Guzmán-Venegas et al., 2015; Jordanic et al., 2016; Falla et al., 2017; Jordanić et al., 2017; Zhu et al., 2017; Martinez-Valdes et al., 2018; Vinti et al., 2018; Watanabe et al., 2018; Hegyi et al., 2019) and truncation use (Stadler et al., 2007; Guzmán-Venegas et al., 2015; Falla et al., 2017; Jordanić et al., 2017).

The high-dimensional sEMG maps embedded into a low-dimensional dataset were studied through their entropy and volume. These variables permitted an understanding of three regions of activation. Overlap showed an increased volume

and decreased entropy at outer parameters (two regions) and increased entropy with low volume at central parameters (one region). The window length showed decreased entropy at outer parameters (two regions) and higher entropy at central parameters (one region), while the volume trended to be constant. The entropy of sEMG polyhedrons quantified the geometrical heterogeneity of the embedding data (Franch et al., 2019), which represents the chance to order the fuzzy nodes projected from the RMS of MUAPs spatially distributed in our study. Thus, the decreased entropy shows a most regular geometry (homogeneity) due to decreased local connectivity (McInnes et al., 2020; Sánchez-Rico and Alvarado, 2019), which occurred with a large volume, suggesting more distance between nodes (less similar RMS of MUAPs). Consequently, there was less chance to order the fuzzy nodes projected from the RMS of MUAPs. This last distorted muscle activation suggests that two scenarios occurred in the outer parameters, an attenuated map for small overlap and window length, where there was a more significant proportion of low RMS of MUAPs (blue pixels; please visualize the sEMG maps of Figure 1), and a blurred map for large overlap and window length, where there was a more significant proportion of high RMS of MUAPs (yellow pixels; please visualize the sEMG maps of Figure 1).

On the other hand, an increased entropy shows a most irregular geometry (heterogeneity) due to increased local connectivity (McInnes et al., 2020; McInnes, 2018; Sánchez-Rico and Alvarado, 2019), which occurred with a small volume suggesting a lower distance between nodes (more similar RMS of MUAPs). Central parameters with higher entropy and lower volume were found near 50% overlap, while for window length, higher entropy and lower volume were found between 100 ms and 500 ms. A case of the total loss of connectivity was found for 1,000 ms, and 90% of overlap in coherence with findings of gene studies using UMAP (please, see Figure 2) (Dorrity et al., 2020).

Regarding the extracted features from sEMG activation maps, the LoC_x , LoC_y , and entropy confirmed a main distorted effect of the overlap on maps. The clustering analysis permitted decomposing data in coherence with the multiple comparison results. For y-coordinates, six clusters were found, suggesting that overlap 0% had two centroids, meaning that there were two sub-groups of 50 ms. For x-coordinates and entropy, five clusters were found in coherence with overlapping. Regarding the window length, only the x-coordinate and entropy showed differences (small effect size). In consequence, the 50 ms without overlap generated the most dissimilar sEMG map. These findings agree with discontinuities that can be introduced by small window lengths and the artifacts caused without window sliding (Yip et al., 2017). This last issue is caused by truncation ringing (Gibbs artifact), where small windowing abruptly magnifies intensity

changes like a high-pass filter (Stadler et al., 2007). Thus, overlapping and small windowing can be an essential source to create a synthetic bias on the sEMG activity distorting the MUAP visualization techniques (Stadler et al., 2007; Vigotsky et al., 2017).

Finally, the image moments changed the sEMG activation maps but with a small effect size. This change suggests a lower sensitivity of image moments to detect biased sEMG maps compared to UMAP, LoC, and entropy of map features. The main limitation to the current study was the sEMG available grid used, which is related to the level of the spatial resolution of the sEMG intensity maps. The space aliasing was set according to our available electrode (inter-electrode distance of 10 mm). The standard acquisition of sEMG map indicates a relative acceptable use of 10 mm and sampling frequency in space higher than 200 samples/m (Merletti and Muceli, 2019; Merletti and Cerone, 2020). Also, the maximal spatial sampling may be appreciated using 90% of the spatial power density distribution on the x-axis, y-axis, or both (Afsharipour et al., 2019). However, electrodes lower or equal to 8 mm would obtain better spatial resolution. Although there are many options for selecting the shape of the window function, we used a rectangular one as a fixed and controlled experimental factor. Here, the effect of the window type on myoelectric manifestations is outside the scope of our study, and these limitations have been addressed in a previous publication (Tan and Jiang, 1984). The pinnate architecture of medial gastrocnemius limits our results only for this kind of muscle.

Conclusion

Here, we demonstrate that embedded sEMG maps and features of image extraction change the spatial muscle activation by segmentation parameters. The instantaneous sEMG maps were primarily affected by outer parameters of the overlap, followed by the outer parameters of the window length. Consequently, choosing the window length and overlap parameters can introduce bias in sEMG activation maps, resulting in distorted regional muscle activation.

Data availability statement

Original datasets are available in a publicly accessible repository: (1) https://www.researchgate.net/publication/365904692_Biased_instantaneous_regional_muscle_activation_maps_embedded_fuzzy_topology_and_image_features_analysis_datapart1 and (2) https://www.researchgate.net/publication/365904985_Biased_instantaneous_regional_muscle_activation_maps_embedded_fuzzy_topology_and_image_features_analysis_datapart2.

Ethics statement

The studies involving human participants were reviewed and approved by Universidad de los Andes. The patients/participants provided written informed consent to participate in this study.

Author contributions

CD, AW, AN, CC-M, RS, and FC: conceptualization, methodology, software, validation, formal analysis, data curation, writing—review and draft, writing—review and editing, visualization, and supervision. OV, PP, and FP: conceptualization, methodology, software, validation, formal analysis, data curation, writing—review and draft, writing—review and editing, visualization, and supervision.

Funding

This study was supported by the “Fondo interdisciplina del departamento de ciencias de la salud de la Pontificia Universidad Católica de Chile,” and “Grant support for publication of the Carrera de kinesiología del departamento de Ciencias de la Salud de la Pontificia Universidad Católica de Chile.” FC was supported by a CNPq research fellowship. CD was supported by the De Luca Foundation and Delsys Inc. through Delsys’ donation initiative

References

- Afsharipour, B., Soedirdjo, S., and Merletti, R. (2019). Two-dimensional surface EMG: The effects of electrode size, interelectrode distance and image truncation. *Biomed. Signal Process. Control* 49, 298–307. doi:10.1016/j.bspc.2018.12.001
- Akobeng, A. K. (2016). Understanding type I and type II errors, statistical power and sample size. *Acta Paediatr.* 105, 605–609. doi:10.1111/apa.13384
- Ali, M., Jones, M. W., Xie, X., and Williams, M. (2019). TimeCluster: Dimension reduction applied to temporal data for visual analytics. *Vis. Comput.* 35, 1013–1026. doi:10.1007/s00371-019-01673-y
- Beniczky, S., and Schomer, D. L. (2020). Electroencephalography: Basic biophysical and technological aspects important for clinical applications. *Epileptic Disord.* 22, 697–715. doi:10.1684/epd.2020.1217
- Botter, A., and Vieira, T. M. (2015). Filtered virtual reference: A new method for the reduction of power line interference with minimal distortion of monopolar surface EMG. *IEEE Trans. Biomed. Eng.* 62, 2638–2647. doi:10.1109/TBME.2015.2438335
- Brown, M., and Godman, M. (2011). *Simple pattern recognition via image moments*. New Mexico Institute of Mining and Technology, Socorro, New Mexico.
- Campanini, I., Disselhorst-Klug, C., Rymer, W. Z., and Merletti, R. (2020). Surface EMG in clinical assessment and neurorehabilitation: Barriers limiting its use. *Front. Neurol.* 11, 934. doi:10.3389/fneur.2020.00934
- De la Fuente, C., Martínez-Valdes, E., Priego-Quesada, J. I., Weinstein, A., Valencia, O., Kunzler, M. R., et al. (2021). Understanding the effect of window length and overlap for assessing sEMG in dynamic fatiguing contractions: A non-linear dimensionality reduction and clustering. *J. Biomech.* 125, 110598. doi:10.1016/j.jbiomech.2021.110598
- Dorrity, M. W., Saunders, L. M., Queitsch, C., Fields, S., and Trapnell, C. (2020). Dimensionality reduction by UMAP to visualize physical and genetic interactions. *Nat. Commun.* 11, 1537. doi:10.1038/s41467-020-15351-4
- Falla, D., Cescon, C., Lindstroem, R., and Barbero, M. (2017). Muscle pain induces a shift of the spatial distribution of upper trapezius muscle activity during a repetitive task: A mechanism for perpetuation of pain with repetitive activity? *Clin. J. Pain* 33, 1006–1013. doi:10.1097/AJP.0000000000000513
- Farina, D., Leclerc, F., Arendt-Nielsen, L., Butelli, O., and Madeleine, P. (2008). The change in spatial distribution of upper trapezius muscle activity is correlated to contraction duration. *J. Electromyogr. Kinesiol.* 18, 16–25. doi:10.1016/j.jelekin.2006.08.005
- Ferguson, C. J. (2009). An effect size primer: A guide for clinicians and researchers. *Prof. Psychol. Res. Pract.* 40, 532–538. doi:10.1037/a0015808
- Franch, G., Jurman, G., Coviello, L., Pendesini, M., and Furlanello, C. (2019). MASS-UMAP: Fast and accurate analog ensemble search in weather radar archives. *Remote Sens.* 11, 2922. doi:10.3390/rs11242922
- Ghaderi, P., and Marateb, H. R. (2017). Muscle activity map reconstruction from high density surface EMG signals with missing channels using image inpainting and surface reconstruction methods. *IEEE Trans. Biomed. Eng.* 64, 1513–1523. doi:10.1109/TBME.2016.2603463
- Guzmán-Venegas, R. A., Biotti Picand, J. L., and de la Rosa, F. J. B. (2015). Functional compartmentalization of the human superficial masseter muscle. *PLoS ONE* 10, e0116923. doi:10.1371/journal.pone.0116923
- Hegyi, A., Csala, D., Péter, A., Finni, T., and Cronin, N. J. (2019). High-density electromyography activity in various hamstring exercises. *Scand. J. Med. Sci. Sports* 29, 34–43. doi:10.1111/sms.13303
- Jordanić, M., Rojas-Martínez, M., Mañanas, M. A., Alonso, J. F., and Marateb, H. R. (2017). A novel spatial feature for the identification of motor tasks using high-density electromyography. *Sensors (Basel)* 17, 1597. doi:10.3390/s17071597
- Jordanic, M., Rojas-Martínez, M., Mañanas, M. A., and Alonso, J. F. (2016). Spatial distribution of HD-EMG improves identification of task and force in patients with incomplete spinal cord injury. *J. Neuroeng. Rehabil.* 13, 41. doi:10.1186/s12984-016-0151-8
- Martínez-Valdes, E., Negro, F., Falla, D., De Nunzio, A. M., and Farina, D. (2018). Surface electromyographic amplitude does not identify differences in neural drive to

2020. OV was supported by “Fondo de Ayuda a la Investigación” (Universidad de los Andes, Santiago, Chile) with project number INV-IN201701.

Acknowledgments

FC acknowledges the support from the Conselho Nacional de Desenvolvimento Científico e Tecnológico (CNPq, Brazil). AW was supported by grant BASAL FB0008.

Conflict of interest

The authors declare that the research was conducted in the absence of any commercial or financial relationships that could be construed as a potential conflict of interest.

Publisher’s note

All claims expressed in this article are solely those of the authors and do not necessarily represent those of their affiliated organizations, or those of the publisher, the editors, and the reviewers. Any product that may be evaluated in this article, or claim that may be made by its manufacturer, is not guaranteed or endorsed by the publisher.

synergistic muscles. *J. Appl. Physiol.* 124, 1071–1079. doi:10.1152/japplphysiol.01115.2017

McInnes, L., Healy, J., and Melville, J. (2020). Umap: Uniform Manifold approximation and projection for dimension reduction. [Online] <http://arxiv.org/abs/1802.03426> Jul 4, 2020).

McInnes, L. (2018). Scientific computing with python. UMAP: Uniform Manifold approximation and projection for dimensional reduction. [Online] <https://www.youtube.com/watch?v=nq6iPZVUxZU> Dec 20, 2020).

Meehan, C., Meehan, S., and Moore, W. (2020). Uniform Manifold approximation and projection (UMAP). [Online]. MATLAB Central File Exchange <https://www.mathworks.com/matlabcentral/fileexchange/71902> Aug 11, 2020).

Merletti, R., and Cerone, G. L. (2020). Tutorial. Surface EMG detection, conditioning and pre-processing: Best practices. *J. Electromyogr. Kinesiol.* 54, 102440. doi:10.1016/j.jelekin.2020.102440

Merletti, R., and Muceli, S. (2019). Tutorial. Surface EMG detection in space and time: Best practices. *J. Electromyogr. Kinesiol.* 49, 102363. doi:10.1016/j.jelekin.2019.102363

Oskolkov, N. (2019). How exactly UMAP works. [Online]. Medium <https://towardsdatascience.com/how-exactly-umap-works-13e3040e1668> Dec 14, 2020).

Pincheira, P. A., Martinez-Valdes, E., De la Fuente, C., Palma, F., Valencia, O., Redenz, G., et al. (2020). Quantifying topographical changes in muscle activation: A statistical parametric mapping approach. *Proceedings* 49, 71. doi:10.3390/proceedings2020049071

Pincheira, P. A., Martinez-Valdes, E., Guzman-Venegas, R., Falla, D., Garrido, M. I., Cresswell, A. G., et al. (2021). Regional changes in muscle activity do not underlie the repeated bout effect in the human gastrocnemius muscle. *Scand. J. Med. Sci. Sports* 31, 799–812. doi:10.1111/sms.13912

Sánchez-Rico, M., and Alvarado, J. M. (2019). A machine learning approach for studying the comorbidities of complex diagnoses. *Behav. Sci. (Basel)* 9, 122. doi:10.3390/bs9120122

Stadler, A., Schima, W., Ba-Ssalamah, A., Kettenbach, J., and Eisenhuber, E. (2007). Artifacts in body MR imaging: Their appearance and how to eliminate them. *Eur. Radiol.* 17, 1242–1255. doi:10.1007/s00330-006-0470-4

Tan, L., and Jiang, J. “Chapter 4 - discrete fourier transform and signal spectrum,” (1984). in *Digital signal processing*. Editors L. Tan and J. Jiang. 3rd Edition (Cambridge, MA, USA: Academic Press), 91–142.

Theisen, D., Rada, I., Brau, A., Gette, P., and Seil, R. (2016). Muscle activity onset prior to landing in patients after anterior cruciate ligament injury: A systematic Review and meta-analysis. *PLoS One* 11, e0155277. doi:10.1371/journal.pone.0155277

Vieira, T. M. M., Loram, I. D., Muceli, S., Merletti, R., and Farina, D. (2011). Postural activation of the human medial gastrocnemius muscle: Are the muscle units spatially localised? *J. Physiol.* 589, 431–443. doi:10.1113/jphysiol.2010.201806

Vigotsky, A. D., Halperin, I., Lehman, G. J., Trajano, G. S., and Vieira, T. M. (2017). Interpreting signal amplitudes in surface electromyography studies in sport and rehabilitation sciences. *Front. Physiol.* 8, 985. doi:10.3389/fphys.2017.00985

Vinti, M., Gracies, J.-M., Gazzoni, M., and Vieira, T. (2018). Localised sampling of myoelectric activity may provide biased estimates of cocontraction for gastrocnemius though not for soleus and tibialis anterior muscles. *J. Electromyogr. Kinesiol.* 38, 34–43. doi:10.1016/j.jelekin.2017.11.003

Watanabe, K., Kouzaki, M., Ogawa, M., Akima, H., and Moritani, T. (2018). Relationships between muscle strength and multi-channel surface EMG parameters in eighty-eight elderly. *Eur. Rev. Aging Phys. Act.* 15, 3. doi:10.1186/s11556-018-0192-z

Xu, Y., Liu, H., Hao, D., Taggart, M., and Zheng, D. (2022). Uterus modeling from cell to organ level: Towards better understanding of physiological basis of uterine activity. *IEEE Rev. Biomed. Eng.* 15, 341–353. doi:10.1109/RBME.2020.3023535

Yip, E., Yun, J., Wachowicz, K., Gabos, Z., Rathee, S., and Fallone, B. G. (2017). Sliding window prior data assisted compressed sensing for MRI tracking of lung tumors. *Med. Phys.* 44, 84–98. doi:10.1002/mp.12027

Zhu, M., Yu, B., Yang, W., Jiang, Y., Lu, L., Huang, Z., et al. (2017). Evaluation of normal swallowing functions by using dynamic high-density surface electromyography maps. *Biomed. Eng. OnLine* 16, 133. doi:10.1186/s12938-017-0424-x



OPEN ACCESS

EDITED BY

Suvash C. Saha,
University of Technology Sydney, Australia

REVIEWED BY

Tyler Brown,
Boise State University, United States
Weijie Fu,
Shanghai University of Sport, China

*CORRESPONDENCE

Chaoyi Chen,
✉ chenchaoyi@nbu.edu.cn
Yaodong Gu,
✉ guyaodong@nbu.edu.cn

SPECIALTY SECTION

This article was submitted to
Biomechanics,
a section of the journal
Frontiers in Bioengineering and
Biotechnology

RECEIVED 06 August 2022

ACCEPTED 20 January 2023

PUBLISHED 30 January 2023

CITATION

Tong J, Lu Z, Cen X, Chen C, Ugbole UC
and Gu Y (2023), The effects of ankle
dorsiflexor fatigue on lower limb
biomechanics during badminton forward
forehand and backhand lunge.
Front. Bioeng. Biotechnol. 11:1013100.
doi: 10.3389/fbioe.2023.1013100

COPYRIGHT

© 2023 Tong, Lu, Cen, Chen, Ugbole and
Gu. This is an open-access article
distributed under the terms of the [Creative
Commons Attribution License \(CC BY\)](#).
The use, distribution or reproduction in
other forums is permitted, provided the
original author(s) and the copyright
owner(s) are credited and that the original
publication in this journal is cited, in
accordance with accepted academic
practice. No use, distribution or
reproduction is permitted which does not
comply with these terms.

The effects of ankle dorsiflexor fatigue on lower limb biomechanics during badminton forward forehand and backhand lunge

Jianhua Tong¹, Zhenghui Lu¹, Xuanzhen Cen^{1,2}, Chaoyi Chen^{1*},
Ukadike Chris Ugbole³ and Yaodong Gu^{1,2,4*}

¹Faculty of Sports Science, Ningbo University, Ningbo, China, ²Doctoral School on Safety and Security Sciences, Obuda University, Budapest, Hungary, ³School of Health and Life Science, University of the West of Scotland, Scotland, United Kingdom, ⁴Research Academy of Medicine Combining Sports, Hwa Mei Hospital, University of Chinese Academy of Sciences, Ningbo, China

Background: Local muscle fatigue may have an adverse effect on the biomechanics of the lunge movement and athletic performance. This study analyzed the biomechanical indicators of the forward lunge in badminton players before and after fatigue of the ankle dorsiflexors.

Methods: Using the isometric muscular strength testing system, 15 badminton players underwent an ankle dorsiflexor fatigue test. Before and after the fatigue experiment, five lunges were done in both the forehand forward (FH) and backhand forward (BH) directions, five in each direction. A Vicon motion capture system and an AMTI force measuring station were used to record lower limb kinematic and ground reaction force (GRF). Pre-fatigue and post-fatigue variability were determined using paired-samples t-tests, Wilcoxon signed rank test, and Statistical Non-parametric Mapping (SNPM).

Result: The results showed that after fatigue, the peak angle of ankle dorsiflexion was significantly reduced ($p = 0.034$), the range of motion (ROM) of the ankle sagittal plane ($p = 0.000$) and peak angle of ankle plantarflexion ($p = 0.001$) was significantly increased after forehand landing. After fatigue, ankle inversion was significantly increased after forehand and backhand landings (FH: $p = 0.033$; BH: $p = 0.015$). After fatigue, peak knee flexion angles increased significantly (FH: Max: $p = 0.000$, Min: $p = 0.000$; BH: Max: $p = 0.017$, Min: $p = 0.037$) during forehand and backhand landings and ROM in knee flexion and extension increased ($p = 0.009$) during forehand landings. Knee inversion range of motion was significantly increased after fatigue ($p = 0.024$) during forehand landings. Peak hip flexion angle ($p = 0.000$) and range of motion ($p = 0.000$) were significantly reduced in forehand landings after fatigue. The mean loading rate ($p = 0.005$) and the maximum loading rate ($p = 0.001$) increased significantly during backhand landings after fatigue. Post-fatigue, the center of pressure (COP) frontal offset increased significantly (FH: $p = 0.000$; BH: $p = 0.000$) in the forehand and backhand landings.

Conclusion: These results indicate that when the ankle dorsiflexors are fatigued, the performance of the forehand is significantly negatively affected, and the impact force of the backhand is greater.

KEYWORDS

badminton, muscle fatigue, lunge, biomechanics, lower limb

1 Introduction

Badminton is one of the most popular sports in the world, and it is a non-contact racket sport. Participants in badminton need to perform running, jumping, stopping abruptly, and lunging (Shariff et al., 2009; Kuntze et al., 2010; Phomsoupha and Laffaye, 2015), with the lunge accounting for 15% or more of the total number of movements in a single game (Lam et al., 2020). Due to the rapid and violent impact, the lower limbs are subjected to a greater load than walk or run during the lunge heel landing phase of badminton, which may increase the risk of damage to the lower limbs (Cronin et al., 2003; Robinson and O'Donoghue, 2008; Lam W. K. et al., 2017; Dempster et al., 2021). The rate of injury per badminton player is 0.85 per year, and the proportion of lower limb injuries is approximately 58% (Boesen et al., 2011). The ankle and knee joints account for the majority of lower limb injuries among badminton players, whereas a well-executed lunge increases the deceleration of ground reaction forces (GRF) and the stability of the lower extremity landing position, thus reducing the possibility of ankle and knee injuries (Krøner et al., 1990; Valdecabres et al., 2020a).

During the lunge landing, the athlete's lower limb joints are subjected to heavy loads and adapt to rapid changes in body posture, which exerts greater demands on their muscle strength, ability to absorb stress in the lower limbs, and lower limb joint stability than general body sports (e.g., running, walking) (Huang et al., 2014; Al-Nuaim and Safi, 2022; Xiang et al., 2022; Xu et al., 2022). In addition, fatigue has negative effects on athletic performance as well as the coordination and precision of motor postural control (Kellis and Liassou, 2009), which has a significant impact on the participation experience of athletes and is a major cause of injury.

Systemic fatigue has been shown to increase ankle inversion angle and knee stiffness during typical badminton lunge landings (Valdecabres et al., 2018; Herbaut and Delannoy, 2020), thereby increasing the risk of ankle sprains and knee loading in badminton players. It has been revealed that the angle of the ankle and knee joints during landing is also a significant determinant of joint stability (Bates et al., 1978). However, current fatigue protocols rarely link muscle fatigue to biomechanical changes in badminton (Sarshin et al., 2011; Valdecabres et al., 2020b; Herbaut and Delannoy, 2020). Local muscle fatigue may have effects exercise performance and loading, causing the stress distribution on the musculoskeletal structure to change (RADIN, 1986; Christina et al., 2001; Kellis and Liassou, 2009; Tiwari et al., 2021; Yahya et al., 2022). As a major player in ankle motion, the dorsiflexors use concentric contraction to increase dorsiflexion before landing in a lunge to provide adequate landing cushion range (Kim et al., 2017). With a greater range of motion (ROM) in the ankle dorsiflexion, the body can take less impact when landing and be more cushioned. During the landing phase of the lunge, the dorsiflexors alternate with the plantar flexors; although the plantar flexors are dominant, the dorsiflexors also have an irreplaceable role. It has been shown that when the knee is flexed beyond 90°, the plantar flexors' eccentric contraction increases during lunge landing, but the dorsiflexors also increase their activity and contribute to ankle stability (Lees and Hurley, 1994; Kim et al., 2017; Lee and Loh, 2019). Furthermore, the effect of dorsiflexor fatigue on ankle motion during landing is currently unknown. In previous

research on local muscle fatigue, it was found that dorsiflexor fatigue increased the magnitude of postural sway and impaired dynamic postural stability, thereby increasing the risk of ankle injury (Lundin et al., 1993).

Previous studies have been conducted on the impact of ankle dorsiflexor fatigue on the kinematics, kinetics, and stability of the lower extremities during running (Lundin et al., 1993; Flynn et al., 2004; Kellis and Liassou, 2009; Mattes et al., 2015). The effects of dorsiflexor fatigue are currently unclear on badminton lunge motions. In badminton singles, players frequently lunge forward to hit the shuttlecock, accounting for approximately 37% of all movements (Hu et al., 2015; Phomsoupha and Laffaye, 2015). On the forward lunge, previous studies have found that the lower limb joint loads and plantar pressures vary based on the lunge's direction (Hong et al., 2014; Hu et al., 2015). Forward forehand (FH) and backhand lunges (BH) are two of the most critical forward lunge techniques (Hong et al., 2014; Hu et al., 2015; Valdecabres et al., 2018). In addition, due to the asymmetrical nature of badminton, players hold their racket with their dominant hand and maintain balance by adopting an asymmetrical posture. Different lateral limbs move in different movement patterns, so the effect of fatigued ankle dorsiflexors on the FH and BH may vary (Lin et al., 2015).

This study aimed to determine the effect of fatigued ankle dorsiflexors on the lower limb biomechanics of badminton players during FH and BH. This study hypothesized that fatigue of the dorsiflexor muscle groups would result in a decrease in ankle dorsiflexion angle, an increase in peak vertical ground reaction force (VGRF) and impact loading rates, and a decrease in dynamic postural stability in badminton players performing FH and BH.

2 Methods

2.1 Participants

The sample size was determined using data from previous studies. At least 15 participants were selected using G*Power3.1 with an alpha value of 0.05 and a power value of 0.80 and effect size of 0.80 (Hu et al., 2015; Nielsen et al., 2020; Lin et al., 2021). This study recruited 15 right-handed male professional badminton players with dominant right legs (Age: 23.30 ± 2.00 years; Body mass: 74.93 ± 3.98 kg; Height: 1.76 ± 0.02 m; Years of Experience: 5.90 ± 1.23 years) (Mei et al., 2017; Herbaut and Delannoy, 2020; Nielsen et al., 2020). Participants were selected on the basis of consistent badminton practice (at least 2 h per week) and at least 2 years of competition experience. Prior to the test, participants provided written consent and were informed of the testing procedures and requirements. Participants had no upper or lower extremity injuries in the previous 6 months. Subjects did not engage in high-intensity training or competition for 2 days before the experiment. The testers gave each participant the same type and brand of badminton shoes in order to eliminate the confounding effect of footwear (Fu, 2011; Mei et al., 2017). The local ethics committee approved the experiment (RAGH202108253005.7).

2.2 Experimental protocol and procedures

Before the experiment began, the participants' basic information (height and weight) was gathered. And the subject's leg length (distance between the right anterior superior iliac spine and the outer ankle of the ankle joint) was measured to assist in the measurement of movement distance for each individual. Fatigue-inducing process: data collection prior to fatigue, the fatigue process, and data collection after fatigue. Before fatigue, static stance trials were conducted to determine the joint center and axis of rotation. Kinematic and kinetic data were gathered during the lunge [Figure 1](#) shows the experimental design. According to previous studies, the forehand lunge is defined by moving in the direction of the racket hand, causing the chest to face the net, hitting the ball with the racket, and returning to the starting position as quickly as possible; each lunge should be completed within 3 s, with the lunge moving 1.5 times the length of the leg, whereas the backhand lunge has the back facing the net ([Mei et al., 2017](#); [Lam et al., 2018](#); [Nielsen et al., 2020](#)). Each participant completed a total of 10 successful lunges in both directions, five in each direction, with 30–60 s between each movement, with the FH and BH completed randomly.

After becoming familiar with the dorsiflexion fatigue task (dorsiflexion of the ankle at maximum ROM until fatigue), the participant laid supine on an isometric ergometer with fully extended knees. After sufficient movement of the ankle joint to warm up (to avoid muscle strain), participants performed three maximum isometric contractions in ankle dorsiflexion (120°/s) to determine the maximum peak moment that the participants can exert. After determining the maximum peak moment of the subject, a 4-min rest period was administered ([Salavati et al., 2007](#); [Boyas et al., 2011](#); [Gautrey et al., 2013](#)). The subjects were then instructed to repeat the dorsiflexion motion as rapidly as possible until they became fatigued. Fatigue of the dorsiflexor group is judged by three consecutive repetitions below 50 percent of the peak moment value ([Yaggie and McGregor, 2002](#); [Gribble and Hertel, 2004](#); [Salavati et al., 2007](#); [Boyas et al., 2011](#)). During the fatigue process, participants were encouraged with positive cues to exert their maximum peak moment with each movement ([McNair et al., 1996](#)). After fatigued, kinematic and kinetic data on the lunge were collected.

2.3 Collection and processing

According to a previous study, 36 reflective markers (6DOF) were placed in the lower extremities and pelvis ([Schafer et al., 2018](#); [Xu et al., 2020](#); [Jiang et al., 2021](#)). The reflective markers are located at the big toe, the first and fifth metatarsal heads, the heel, the medial and lateral sides of the ankle, the middle of the tibia, the middle of the femur, the internal and external of the femoral condyles, the anterior superior iliac spine, and the posterior superior iliac spine. An eight-camera Vicon motion system (Oxford Metrics Ltd., Oxford, United Kingdom) was used to collect the kinematic data of the right lower limb of the subject during a lunge with a sampling frequency of 200 Hz. The C3D files generated by the Vicon Nexus software were imported into Visual 3D (c-motion Inc., Germantown, MD, United States) for further kinematic data processing. Embedded in the floor and synchronized with the Vicon system, an AMTI force plate

(AMTI, Watertown, MA, United States) was used to collect kinetic data with a sampling frequency of 1,000 Hz. Kinematic and kinetic data were gathered during the lunge contact period, which was defined as the time between the impact of the dominant leg's heel on the force plate and the withdrawal of the toe from the force plate ([Lam et al., 2018](#)). The kinematics and kinetics data were filtered with fourth-order zero-phase low pass Butterworth filters at 10 Hz and 20 Hz ([Lam W.-K. et al., 2017](#); [Jiang et al., 2021](#)). An isometric muscle test device was applied to test the fatigue of the ankle dorsiflexor group (CON-TREX-MJ, PHYSIOMED, GER).

2.4 Statistical analyses

All analyses were conducted with SPSS 26.0 (SPSS Inc., Chicago, IL, United States) and MATLAB R2019a (The MathWorks, Natick, MA, United States). Max and Min for kinematic data are both the maximum and minimum values of the angles of the three joints in the sagittal and frontal planes during the lunge landing (by numerical comparison), and ROM is the difference between the maximum and minimum values (Max-Min). GRF data includes peak vertical ground reaction force, peak horizontal ground reaction force, maximum loading rate, and average loading rate ([Kuntze et al., 2010](#); [Lam W. K. et al., 2017](#); [Lam et al., 2018](#)). Briefly, the peak vertical ground reaction force and the peak horizontal ground reaction force were defined as the maximum value of the vertical and horizontal GRF, respectively ([Lam et al., 2018](#)). The maximum loading rate is the maximum slope of the VGRF curve between consecutive data points, ranging from 20% to 90% prior to the initial peak impact ([Lam W.-K. et al., 2017](#); [Lam et al., 2018](#)), the mean loading rate is the average slope of the VGRF curve between consecutive data points, ranging from 0% to 100% prior to the impact of the initial peak ([Lam et al., 2018](#)). The displacement of the COP sagittal plane is the total offset of the COP on the Y-axis of the force table coordinate system, and the displacement of the frontal plane is the total offset of the COP on the X-axis of the force table coordinate system. Prior to statistical analysis, the Shapiro-Wilk test was used to examine the normality of discrete variables and sagittal and frontal waveform data of the ankle, knee, and hip joints. Pre-fatigue and post-fatigue data were compared using a paired-samples *t*-test; non-normally distribution data were examined using the Wilcoxon signed rank test, with a significance level of $p < 0.05$ and Bonferroni correction. The sagittal and frontal waveform data of the three joints not to be normally distributed ($p < 0.05$), hence Statistical Non-parametric Mapping (SNPM) was utilized to examine the waveform data of the ankle, knee, and hip joints.

3 Results

3.1 Lower limb joint angle and range of motion

[Table 1](#) shows the differences in joint angles and ROM in the sagittal and frontal planes between badminton players who did the FH and BH before and after their dorsiflexors got fatigued. [Figures 2, 3](#) demonstrate the angle changes and ROM of the lower limb joints in the sagittal and frontal planes of badminton players who performed the FH and BH before and after their dorsiflexors became fatigued.

TABLE 1 Comparison of pre-fatigue and post-fatigue means standard deviations for joint angles and ROM values during the strike phase of the FH and BH (unit: degrees).

Variables		FH				BH			
		Pre (°)	Post (°)	t/z	DF	Pre (°)	Post (°)	t/z	DF
Hip flexion (+)	Max	79.59 ± 7.25	73.15 ± 5.78	5.774	-6.44 ± 9.92	79.16 ± 6.73	77.84 ± 9.12	1.175	-1.33 ± 11.76
	Min	36.93 ± 3.20	36.89 ± 3.76	0.051	-0.04 ± 4.88	39.27 ± 2.61	39.69 ± 2.65	-0.920	0.42 ± 3.34
	ROM	42.66 ± 7.64	36.26 ± 6.18	5.210	-6.39 ± 9.41	40.18 ± 7.05	38.05 ± 8.23	1.967	-2.13 ± 11.68
Hip adduction (+)	Max	15.78 ± 8.39	13.88 ± 7.51	1.282	-1.9 ± 12.21	10.70 ± 7.73	9.55 ± 7.07	1.396	-1.15 ± 7.70
	Min	-0.81 ± 11.01	-0.90 ± 9.49	0.044	-0.09 ± 12.78	-6.30 ± 9.93	-6.52 ± 8.33	0.155	-0.22 ± 14.23
	ROM	16.60 ± 6.09	14.77 ± 4.52	1.551	-1.83 ± 8.32	16.77 ± 4.19	16.82 ± 4.06	-0.063	0.05 ± 5.87
Knee flexion (+)	Max	55.73 ± 11.61	64.61 ± 6.90	-5.600	8.88 ± 13.55	65.03 ± 12.64	69.87 ± 5.35	-2.482	4.84 ± 15.32
	Min	34.93 ± 4.81	44.61 ± 5.07	-10.042	9.68 ± 6.44	40.84 ± 8.70	44.97 ± 1.16	-2.143	4.13 ± 8.43
	ROM	21.13 ± 6.79	24.70 ± 8.60	-2.716	3.58 ± 9.89	24.19 ± 8.84	24.89 ± 8.65	-0.474	0.7 ± 11.41
Knee adduction (+)	Max	10.09 ± 5.68	10.82 ± 5.42	-0.600	0.72 ± 6.52	11.06 ± 6.02	12.05 ± 5.73	-1.062	0.99 ± 6.79
	Min	2.70 ± 3.92	0.21 ± 4.93	-1.839 ^a	-2.49 ± 7.28	0.83 ± 5.66	1.00 ± 5.83	-0.710 ^a	0.17 ± 6.81
	ROM	7.96 ± 4.69	10.25 ± 5.18	-2.336	2.28 ± 8.00	11.22 ± 4.51	10.69 ± 3.88	0.579	-0.54 ± 5.88
Ankle Dorsi-flexion (+)	Max	15.06 ± 8.73	11.52 ± 9.56	2.176	-3.53 ± 12.35	15.70 ± 9.04	12.75 ± 9.93	-1.250 ^a	-2.95 ± 11.63
	Min	-18.41 ± 16.89	-30.08 ± 15.26	-3.403 ^a	-15.02 ± 21.79	-28.90 ± 15.45	-32.35 ± 13.78	-0.989 ^a	-3.45 ± 24.06
	ROM	33.47 ± 10.82	41.59 ± 9.51	-3.820	8.11 ± 13.51	44.60 ± 8.67	45.10 ± 7.25	-0.334	8.12 ± 15.29
Ankle Inversion (+)	Max	15.51 ± 8.32	15.61 ± 10.54	-1.028 ^a	0.1 ± 13.12	18.96 ± 8.26	15.44 ± 10.50	3.840	-3.52 ± 9.93
	Min	1.47 ± 10.54	-0.70 ± 13.51	-1.300 ^a	-2.17 ± 14.77	4.64 ± 10.21	-0.75 ± 13.62	4.542	-5.39 ± 11.02
	ROM	14.18 ± 4.24	16.05 ± 4.42	-2.191	1.86 ± 5.73	14.36 ± 3.45	15.66 ± 4.04	-2.517	1.3 ± 4.83

Note: FH, forehand lunge; BH, backhand lunge; Pre, pre-fatigue, Post, post-fatigue. Significant *p*-values (<0.05) are shown in bold. DF: The difference between post-fatigue and pre-fatigue.

^aWilcoxon signed rank test results for non-normally distributed variables.

Before and after fatigue of the dorsiflexor group, significant differences in ankle joint angles occurred between 0% and 10% ($p = 0.021$) and 93%–100% ($p = 0.012$) throughout the movement cycle when badminton players performed FH, and between 0% and 7% ($p = 0.013$) and 90%–100% ($p = 0.006$) during the BH (Figure 2).

In the sagittal plane, peak ankle plantarflexion angle was significantly increased ($t = 2.176$, $p = 0.034$) and peak ankle dorsiflexion angle ($t = -3.403$, $p = 0.001$) were significantly reduced when athletes performed FH after fatigue of the dorsiflexor, hence ankle plantarflexion-dorsiflexion ROM was significantly increased ($t = -3.820$, $p = 0.001$) (Table 1). The peak knee flexion angle (Max: $t = -5.600$, $p < 0.001$; Min: $t = -10.042$, $p < 0.001$) and knee sagittal ROM ($t = -2.716$, $p = 0.009$) were significantly greater than pre-fatigue during the FH. Peak hip flexion angle ($t = 5.774$, $p < 0.001$) and hip sagittal ROM ($t = 5.210$, $p < 0.001$) were significantly reduced than pre-fatigue during the FH (Table 1). After fatigue, the peak knee flexion angle was significantly greater during BH than before fatigue (Max: $t = -2.482$, $p = 0.017$; Min: $t = -2.143$, $p = 0.037$) (Table 1).

In the frontal plane, after fatigue than that before fatigue of the dorsiflexors, the peak ankle inversion angle was significantly smaller than before fatigue when athletes performed BH (Max: $t = 3.840$, $p < 0.001$; Min: $t = 4.542$, $p < 0.001$), but the ankle frontal plane ROM was significantly greater than before fatigue ($t = -2.517$, $p = 0.015$) (Table 1).

3.2 Ground reaction force

Table 2 and Figure 4 illustrate the characteristics of GRF when an athlete performs FH and BH before and after dorsiflexor fatigue. Before fatigue of the dorsiflexor group, the peak horizontal reaction force of athletes performing FH was significantly lower than after fatigue ($t = 3.721$, $p = 0.001$) (Table 2). The maximum loading rate ($t = -2.91$, $p = 0.005$) and the mean loading rate ($t = -3.531$, $p = 0.001$) were significantly higher when the BH was performed by the athletes after dorsiflexor fatigue than before fatigue (Table 2).

3.3 Center of pressure

Table 3 and Figure 5 illustrate the pre-fatigue and post-fatigue COP displacement quantities in the sagittal and frontal planes during FH and BH. The frontal plane displacements during the FH and BH were significantly greater than before fatigue (FH: $t = 4.394$, $p < 0.001$; BH: $t = 6.001$, $p < 0.001$) (Table 3).

4 Discussion

This study aimed to investigate the effect of ankle dorsiflexor group fatigue on the biomechanics of FH and BH in badminton

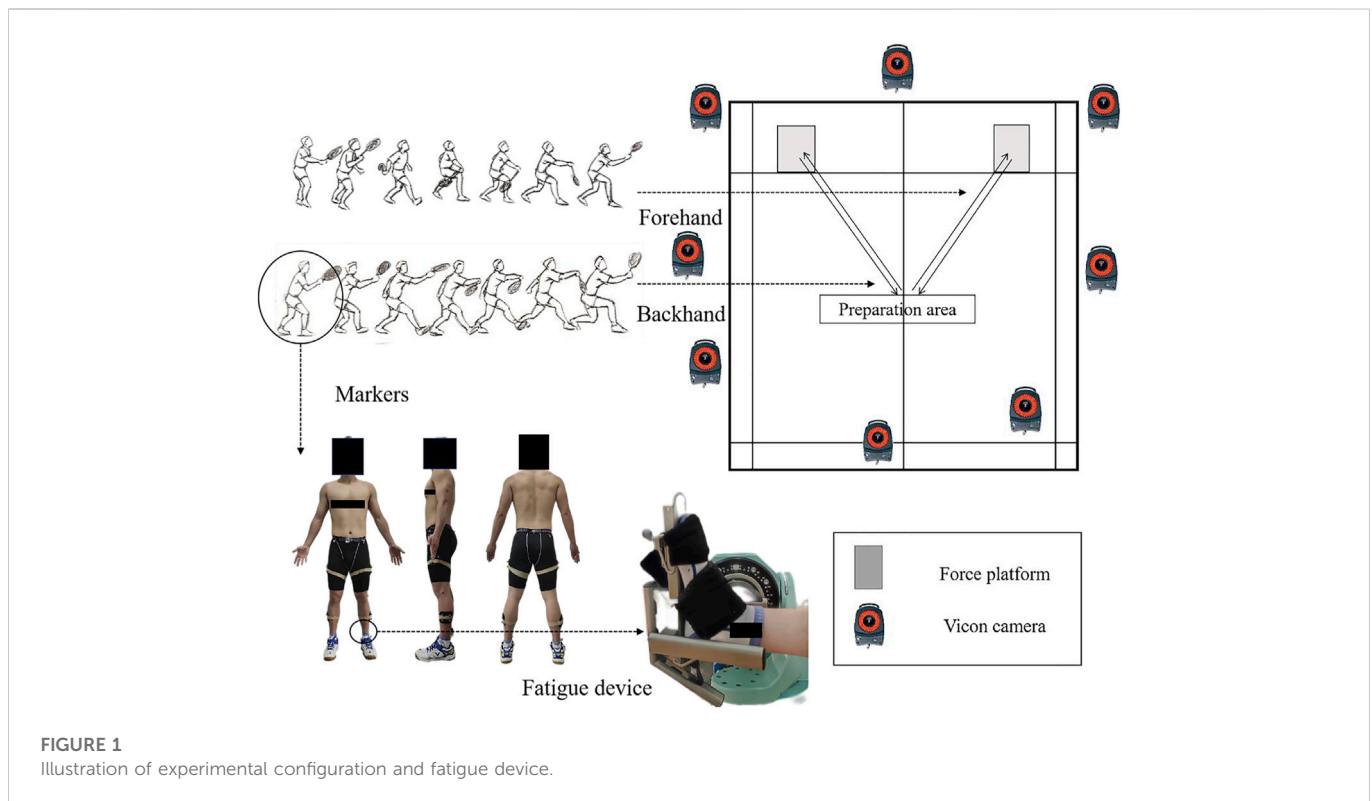


FIGURE 1
Illustration of experimental configuration and fatigue device.

players. Consistent with the hypothesis, after dorsiflexor fatigue, badminton players had decreased ankle dorsiflexion angle and decreased dynamic postural stability during FH and BH; impact loading rate increased significantly during BH. The VGRF and impact loading rate were not affected significantly before and after fatigue of the dorsiflexors during FH, did not support the hypothesis.

In badminton, it is critical to perform a great lunge and return to the starting position for the following stroke, which can affect the outcome of the entire game (Lam et al., 2020). Previous research has shown that fatigue negatively affects the quality of movement performance, whereas a substandard lunge landing increases the risk of lower extremity injury (Bulat et al., 2019; Buckthorpe, 2021). Thus, kinematic and kinetic data were gathered during the lunge landing for this study. According to previous research, a significant increase of 10° in ankle plantarflexion increases the tendency for calf muscle fatigue and overuse injuries in the foot (Lee and Loh, 2019), it may also induce Achilles tendon and anterior calcaneal ligament fatigue and damage (Fahlström et al., 1998; Fahlstrom et al., 2002; Fong et al., 2009; Mei et al., 2017; Lee and Loh, 2019). The previous study's significant increase in plantarflexion may have been attributable to differences in skill level, with better badminton players employing a more efficient landing method (less plantarflexion). Consistent with previous studies, the current participants exhibited a significant increase in peak ankle plantarflexion angle of 11.5° after fatigue, which may be due to a significant decrease in peak ankle dorsiflexion angle of 3.5° and a significant increase in ankle sagittal ROM of 8° during FH. Participants exhibited less dorsiflexion, possibly due to dorsiflexor fatigue resulting in insufficient dorsiflexor muscle strength and relatively high plantarflexion strength. Under normal circumstances, moderate ankle valgus and foot pronation can help the lower extremity

absorb vertical and rotational forces, which makes jumping and landing, running, and other activities less likely to cause injury (Dubin et al., 2011). Some studies have demonstrated a positive correlation between increased ROM in ankle valgus and a decreased risk of lower extremity injury (Hoch et al., 2015; Padua et al., 2019). In our study, the current participants showed a significant decrease in peak ankle valgus angle by 5° and an increased tendency to valgus after fatigue, which may be caused by an increase in peak plantarflexion angle by 3.4° and peak knee flexion angle by 4.8° during BH. Because when the ankle plantarflexion increases, the moment arm of the GRF increases and the ankle joint's stability decreases; concurrently, due to the directional nature of the motion and the increased knee flexion, the trunk tends to move toward the left front, resulting in an increase in ankle valgus (Wright et al., 2000; Herbaut and Delannoy, 2020). An increase in ankle valgus ROM may provide sufficient cushioning to the lateral ankle collateral ligament. Therefore, this may be the body's protective mechanism against harm. In addition, previous research revealed that amateur badminton players had a significantly greater ROM of 2.2 degrees of ankle inversion compared to professional badminton players (Fu et al., 2017). This was attributed to the lack of stability of the muscles surrounding the ankle joint in amateur players (Fong et al., 2009; Dubin et al., 2011). Such a change is apparently similar to our study, where participants showed a significant increase in ankle inversion ROM of 2.1° at FH and 1.3° at BH after dorsiflexor fatigue. This could be caused by the increased tendency of ankle valgus after fatigue. Hence, dorsiflexor fatigue may also affect the work of the unstable muscles around the ankle joint, which causes increased ROM in the frontal plane of the athlete.

Different degrees of knee flexion may result in varying movement performance and joint impact forces. It has been shown that elite

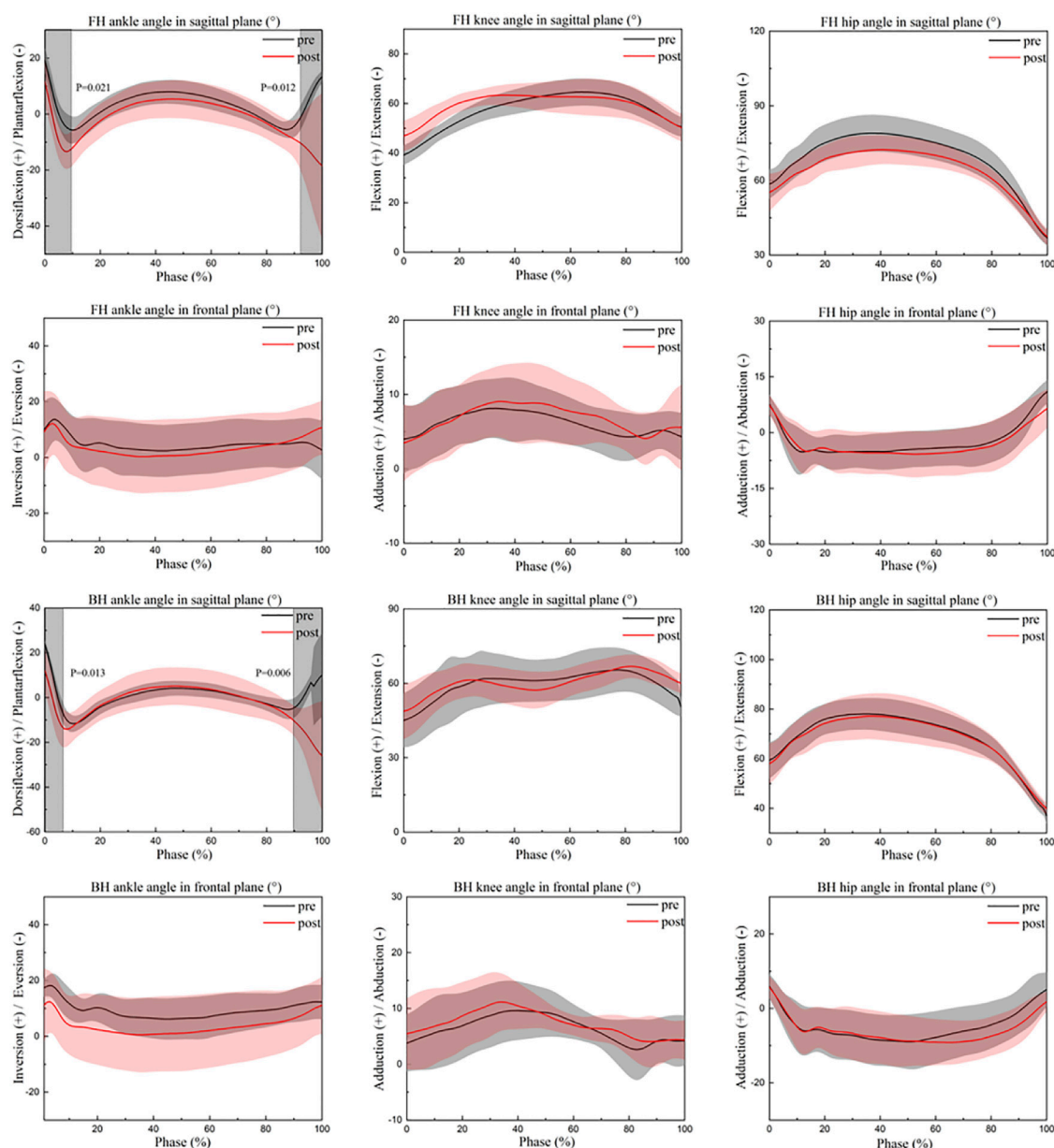


FIGURE 2

Changes in the lower limb angles in the sagittal-frontal plane during the strike phase. FH, forehand lunge; BH, backhand lunge; pre, pre-fatigue, post, post-fatigue.

badminton players show less knee flexion (9° less maximum flexion angle and 12° less minimum flexion angle) during the forehand lunge than recreational badminton players, enabling them to recover from their starting position and prepare for the next stroke more quickly (Mei et al., 2017). Interestingly, one study noted that during the lunge, athletes with knee injuries would reduce knee injuries and cushion the impact of landing on the joint by increasing knee flexion (2.8° compared to ROM in non-injured athletes) while boosting dynamic stability by lowering the center of mass (Huang et al., 2014). Again, in relation to our study, after dorsiflexor fatigue, the current subjects showed more flexed knee posture across the entire lunge in both FH and BH; a significant increase in knee flexion maximum of 8.9° and a minimum of 9.7° at FH; a significant

increase in knee flexion maximum of 4.8° and a significant increase in minimum of 4.1° at BH. Such an increase is similar to previous studies. This may be because badminton players reduce the risk of injury by increasing knee flexion and decreasing athletic performance after dorsiflexor fatigue, which may be a neuromuscular protective mechanism of their own. Because it has been shown that at the moment of landing, each degree of knee flexion decreases the ground reaction force by 68 N, and greater knee flexion also increases the impact attenuation rate (Gerritsen et al., 1995; Lafortune et al., 1996; Duquette and Andrews, 2010). In the sagittal plane of the knee, greater flexion may be associated with a decreased risk of injury and a worsen in athletic performance, whereas the opposite may be true in the frontal plane. Studies have shown that the

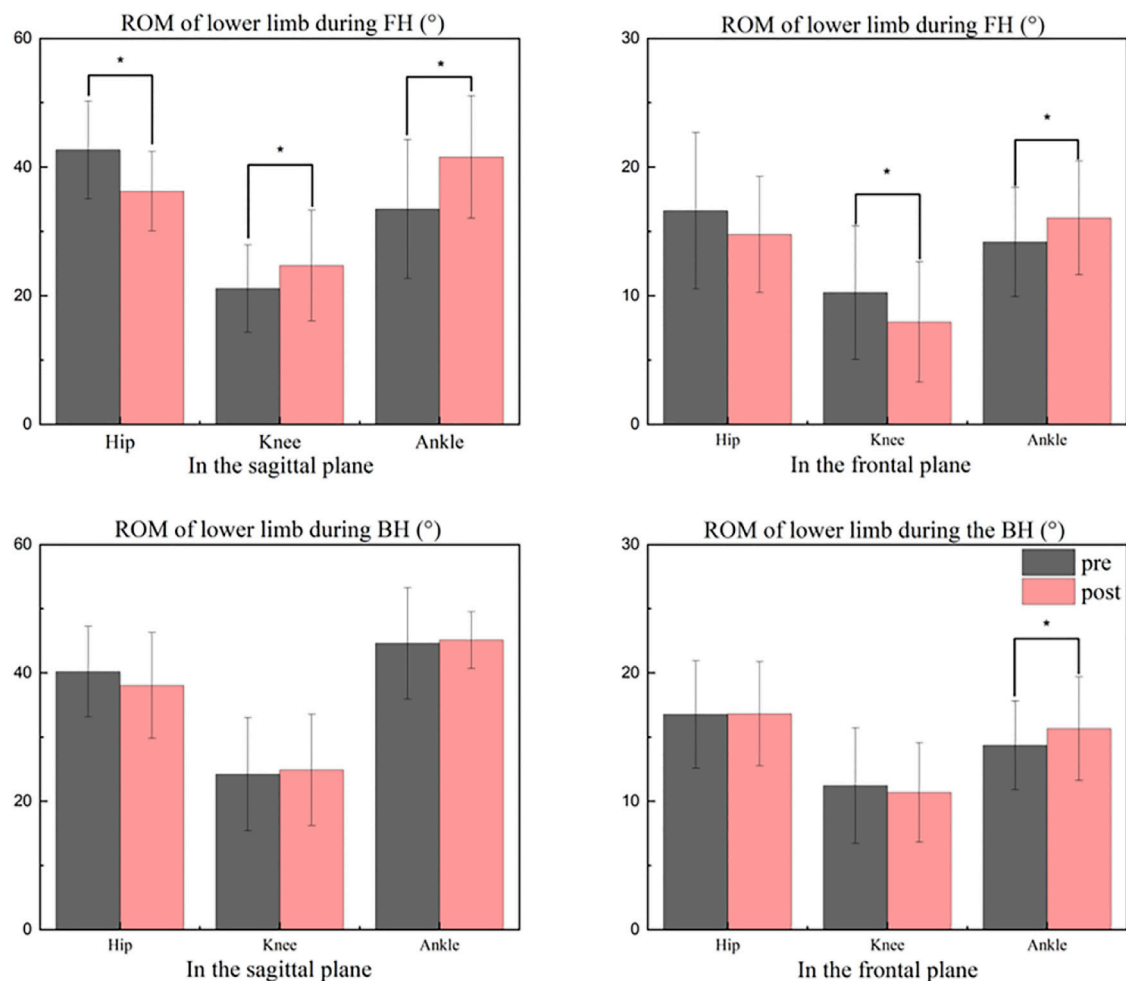


FIGURE 3

Comparisons between pre and after ROM levels during the strike period. FH, forehand lunge; BH, backhand lunge; pre, pre-fatigue, post, post-fatigue. *Significant differences at the hip, knee, and ankle ($p < 0.05$).

TABLE 2 Comparison of pre-fatigue and post-fatigue means standard deviations for the ground reaction forces (GRFs) characteristics of the FH and BH.

Variables	FH				BH			
	Pre	Post	t	DF	Pre	Post	t	DF
Peak vertical GRF (BW)	1.55 ± 0.19	1.52 ± 0.22	0.717	−0.03 ± 0.31	1.50 ± 0.17	1.51 ± 0.22	−0.161	0.01 ± 0.30
Peak horizontal force (BW)	−0.38 ± 0.06	−0.35 ± 0.06	3.721	0.03 ± 0.10	−0.43 ± 0.09	−0.41 ± 0.09	−1.682	0.02 ± 0.11
Maximum loading rate (BW/S)	109.14 ± 31.70	103.58 ± 43.49	0.780	−5.56 ± 67.72	103.10 ± 29.16	114.01 ± 31.55	−2.911	10.90 ± 43.80
Mean loading rate (BW/S)	85.71 ± 27.50	80.79 ± 34.78	0.467	−4.92 ± 37.47	78.74 ± 22.11	92.24 ± 27.23	−1.682	13.5 ± 35.04

Note: FH, forehand lunge; BH, backhand lunge; Pre, pre-fatigue, Post, post-fatigue. Significant p -values (<0.05) are shown in bold. DF: The difference between post-fatigue and pre-fatigue.

knee frontal ROM of elite badminton players is 4° greater than that of recreational badminton player. Moreover, studies have also shown that the frontal ROM of the knee joint of athletes with knee joint injuries is significantly larger than that of athletes without knee joint injuries by 3.4°. In addition, research has demonstrated that tiredness has no effect on the frontal ROM of the knee joint in badminton players. The reason for this phenomenon could be the difference in skill level or gender between the participants (Huang et al., 2014; Mei

et al., 2017; Valdecabres et al., 2018). In general similarity to previous studies, the current subjects showed a significantly 2.3° increase in knee frontal ROM after fatigue, which may be the result of a cascade effect caused by a significant 4° increase in ankle frontal ROM during FH. According to previous studies, dorsiflexion of the ankle is negatively linked with knee frontal plane displacement (Sigward et al., 2008). When the range of dorsiflexion is decreased, the frontal plane compensatory motion of the ankle joint increases,

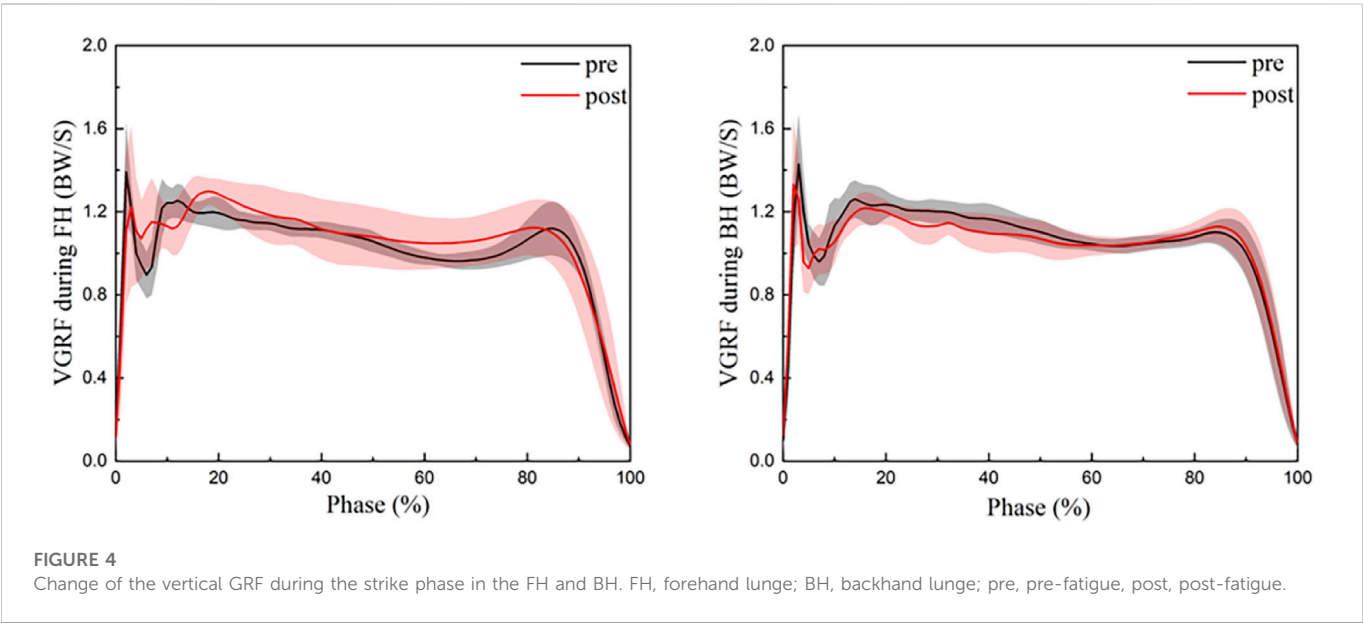
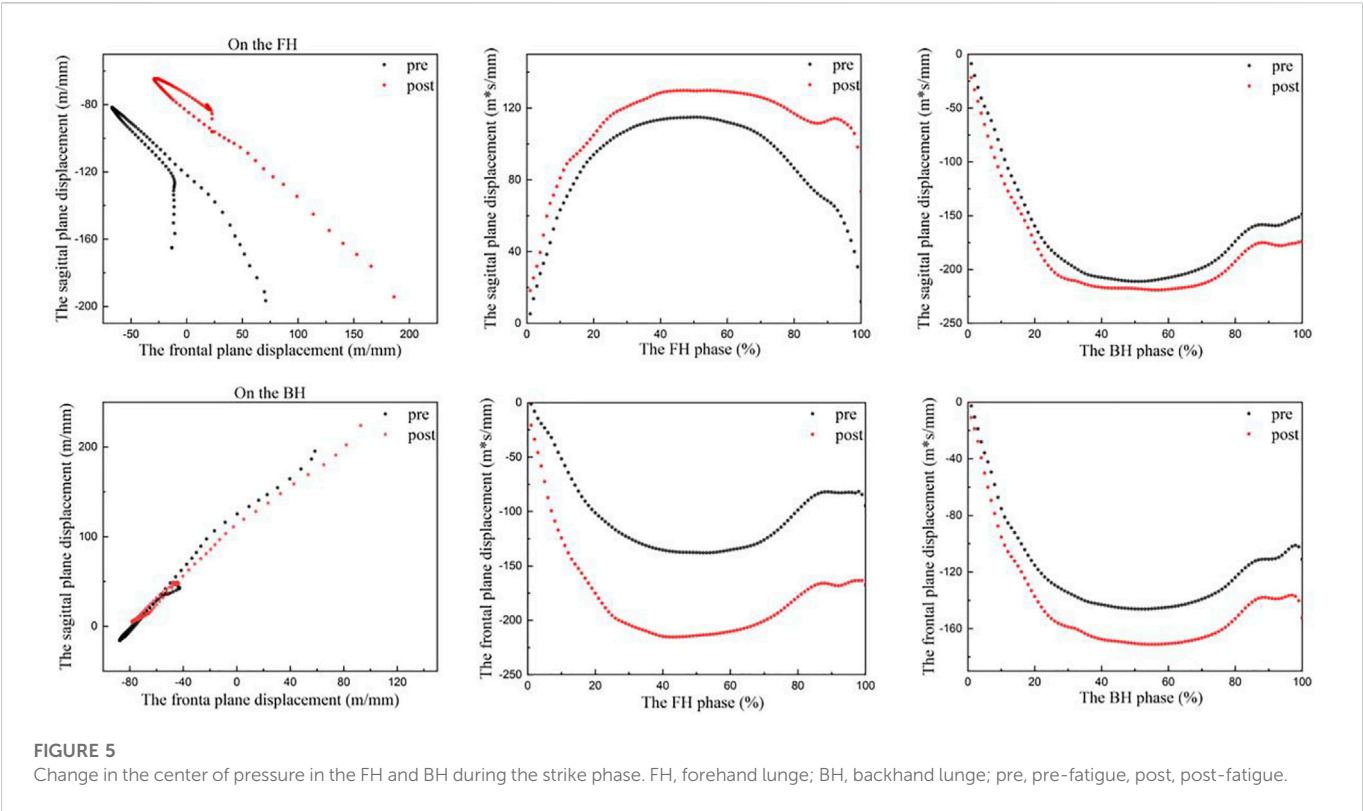


TABLE 3 Comparison of pre-fatigue and post-fatigue means standard deviations for center of pressure displacement characteristics in the FH and BH.

Variables	FH				BH			
	Pre	Post	t	DF	Pre	Post	t	DF
The Sagittal plane displacement (m*s/mm)	9.98 ± 3.19	10.85 ± 4.20	-1.381	0.88 ± 5.47	17.16 ± 2.34	17.64 ± 2.21	0.211	0.48 ± 2.87
The Front plane displacement (m*s/mm)	16.21 ± 2.55	18.54 ± 2.70	4.394	2.33 ± 3.69	12.02 ± 2.36	14.40 ± 2.34	6.001	2.39 ± 3.33

Note: FH, forehand; BH, backhand; Pre, pre-fatigue, Post, post-fatigue. Significant *p*-values (<0.05) are shown in bold. DF: The difference between post-fatigue and pre-fatigue.



which contributes to the movement of the tibia in the knee joint, resulting in an increase in the frontal plane motion of the knee joint (Gross, 1995; Baker and Juhn, 2000; Joseph et al., 2008). This will improve athletic performance and increase the dynamic stability of the knee joint, but it will also increase the loading on the knee joint (Huang et al., 2014).

In the lunge movement, the knee joint's movement is closely linked to the hip joint's movement. Previous research has shown that badminton players with knee injuries have less forward trunk movement (reduced trunk angle, that is the angle of the hip joint to the vertical axis) in order to reduce knee stress during the FH because of greater knee flexion (Huang et al., 2014). This phenomenon of reduced hip flexion (elite badminton players have a significantly greater peak hip flexion angle of 14° than recreational players) is also associated with good athletic performance, which can assist the player in returning quickly to the starting position (Handbook, 2014; Mei et al., 2017). Participants in our study had a significant reduction in hip ROM of 6.4° after fatigue, which might be related to a significant reduction in hip flexion angle at peak during FH of 6.4° . In combination with previous studies, the significant decrease in peak hip flexion angle can be explained by an increase in knee flexion and a shift of body weight forward because of fatigue (Lin et al., 2015; Leporace et al., 2020). During the lunge, the body employs compensatory strategies to alleviate the stress on the lower extremity joints by increasing knee flexion and decreasing hip flexion. Previous research has shown that the peak joint contact force and the ground reaction force develop proportionally to the distal-to-proximal extent of flexion of the lower limb joints, with the ankle joint, knee joint, and hip joint proportions being 2.63–2.75, 4.59–4.63, and 3.82–3.82, respectively (Zhang et al., 2000; Chen et al., 2020). As the major cause of energy dissipation, the knee extensors and hip extensors use eccentric contractions to relieve pressure on the lower limbs and preserve the dynamic balance of the movements as much as possible (Zhang et al., 2000).

In an excellent lunge, badminton players are subjected to ground reaction forces that are approximately 2–3 times their body weight, which greatly increases the stress on the lower limb joints (Lam et al., 2018). The magnitude of the impact loading rate is positively correlated with the risk of stress fracture (Milner et al., 2006; Hansen et al., 2008; Puddle and Maulder, 2013). In a previous study, the vertical ground reaction force and loading rate were not significantly different before and after fatigue (Valldcabres et al., 2018). In contrast, the current participants had a significant increase in maximum loading rate of 11 BW/S and an average loading rate of 13.5 BW/S during FH after fatigue in our study. This may be a result of the differences generated by various fatigue schemes. Previous research on fatigue schemes focused on overall fatigue, but ours focused on local fatigue. The significant increase in loading rate may be the result of a decreased ankle dorsiflexion range, which reduces the body's ability to absorb high impact forces during fatigue and increases the risk of stress fractures in the lower limbs (Lee et al., 2018; Radcliffe et al., 2021). Common knee injuries in badminton, such as anterior cruciate ligament (ACL) injuries, can be the result of repeated high impact stresses (Shariff et al., 2009; Lam et al., 2018). Horizontal reaction force is closely related to it, and in a lunge to resist a greater horizontal reaction force, eccentric contraction of the knee extensors increases and knee flexion

increases, resulting in ACL overuse (Chappell et al., 2005; Lam et al., 2018). After fatigue, the current participants showed a significant decrease in peak horizontal reaction force of 0.03 BW, which corresponded to an increase in knee flexion. However, this is not conducive to kicking off the ground and returning to the starting position late in the lunge (Fukashiro et al., 1995; Kuntze et al., 2010).

The existence of better postural control is also seen as an indirect predictor of better athletic performance and a lower injury propensity (Edis et al., 2016; Pau et al., 2019). Additionally, the flexibility of the ankle joint and the muscle strength of the ankle and knee joints influence dynamic postural stability (Williams et al., 2016). After fatigue, the current participants showed a significant increase in frontal plane displacement of $2.3 \text{ m}^*\text{s}/\text{mm}$ during FH and $2.4 \text{ m}^*\text{s}/\text{mm}$ during BH. This may be caused by fatigue of the dorsiflexors leading to increased ROM of the frontal plane of the ankle and a tendency to ankle valgus, which results in a significant increase in body displacement in the left-right direction and less body control of posture than before fatigue (Padua et al., 2019). Thus, dorsiflexor fatigue may also negatively influence dynamic postural stability.

The study presented in this paper also has some limitations. At first, the participants were professional badminton players. In future studies, it should be considered whether experimental results (e.g., different athletic performance, ground reaction forces, etc.) occur before and after fatigue in amateur players that differ from those of professional players. Second, this study only looked at men, and gender differences should be taken into account in future studies. Third, mental and metabolic fatigue can also have an effect on muscle fatigue. What does this effect look like? How big is the effect? It is unknown as well. In addition, there are constraints in the recovery of local muscle fatigue (speed of recovery, etc.) that I hope future researchers will take into consideration.

5 Conclusion

The results of the study showed that when badminton players performed forehand lunges, more significant changes in lower limb joint angles and ROM occurred before and after fatigue of the dorsiflexor group. Fatigue may have a profound effect on the FH performance of badminton players, this may be a compensating mechanism employed by the body to reduce the risk of damage. After dorsiflexor fatigue, badminton players performed the backhand lunge with a subtle change in joint angle and range of motion, while the impact loading rate increased significantly. When developing a training program, it should be considered to enhance the training of the dorsiflexors of the ankle joint. Badminton players in a state of dorsiflexor fatigue can minimize the use of the backhand lunge in order to reduce the occurrence of injury. But forehand lunge sports performance is more negatively affected by fatigue. The advantages and disadvantages of performing these two movements after fatigue are pointed out for the athletes.

Data availability statement

The raw data supporting the conclusion of this article will be made available by the authors, without undue reservation.

Ethics statement

The studies involving human participants were reviewed and approved by Ningbo University ethics committee. The patients/participants provided their written informed consent to participate in this study.

Author contributions

JT, ZL, and CC developed the original idea and wrote the manuscript. XC, UU, and YG provided critical input and contributed to the final version. All authors were involved in the final direction of the paper and contributed to the final version of the manuscript. All authors have read and agree to the published version of the manuscript.

Funding

This study was sponsored by the Major Program of the National Natural Science Foundation of China (19ZDA352), Zhejiang Provincial Key Research and Development Program of China (2021C03130), Zhejiang Provincial Natural Science Foundation of

China for Distinguished Young Scholars (LR22A020002), Philosophy and Social Sciences Project of Zhejiang Province, China (22QNYC10ZD and 22NDQN223YB), Educational science planning project of Zhejiang Province (2021SCG083), Ningbo Natural Science Foundation (20221JCGY010532 and 20221JCGY010607), Public Welfare Science and Technology Project of Ningbo, China (2021S134) and K. C. Wong Magna Fund in Ningbo University.

Conflict of interest

The authors declare that the research was conducted in the absence of any commercial or financial relationships that could be construed as a potential conflict of interest.

Publisher's note

All claims expressed in this article are solely those of the authors and do not necessarily represent those of their affiliated organizations, or those of the publisher, the editors and the reviewers. Any product that may be evaluated in this article, or claim that may be made by its manufacturer, is not guaranteed or endorsed by the publisher.

References

- Al-Nuaim, A., and Safi, A. (2022). The impact of environment on physical activity levels and obesity among Saudi arabia youth: Comparison of urban; rural farm and rural desert geographical locations. *Phys. Activity Health* 6 (1), 86–95. doi:10.5334/paah.188
- Baker, M. M., and Juhn, M. S. (2000). Patellofemoral pain syndrome in the female athlete. *Clin. sports Med.* 19 (2), 315–329. doi:10.1016/s0278-5919(05)70206-4
- Bates, B., Osternig, L., Mason, B., and James, S. (1978). Lower extremity function during the support phase of running. *Biomech. VI-b* 31, 39.
- Boesen, A. P., Boesen, M. I., Koenig, M. J., Bliddal, H., Torp-Pedersen, S., and Langberg, H. (2011). Evidence of accumulated stress in Achilles and anterior knee tendons in elite badminton players. *Knee Surg. Sports Traumatol. Arthrosc.* 19 (1), 30–37. doi:10.1007/s00167-010-1208-z
- Boyas, S., Remaud, A., Bisson, E. J., Cadieux, S., Morel, B., and Bilodeau, M. (2011). Impairment in postural control is greater when ankle plantarflexors and dorsiflexors are fatigued simultaneously than when fatigued separately. *Gait posture* 34 (2), 254–259. doi:10.1016/j.gaitpost.2011.05.009
- Buckthorpe, M. (2021). Recommendations for movement re-training after ACL reconstruction. *Sports Med.* 51 (8), 1601–1618. doi:10.1007/s40279-021-01454-5
- Bulat, M., Can, N. K., Arslan, Y. Z., and Herzog, W. (2019). Musculoskeletal simulation tools for understanding mechanisms of lower-limb sports injuries. *Curr. Sports Med. Rep.* 18 (6), 210–216. doi:10.1249/jsr.0000000000000601
- Chappell, J. D., Herman, D. C., Knight, B. S., Kirkendall, D. T., Garrett, W. E., and Yu, B. (2005). Effect of fatigue on knee kinetics and kinematics in stop-jump tasks. *Am. J. sports Med.* 33 (7), 1022–1029. doi:10.1177/0363546504273047
- Chen, T. L., Wang, Y., Wong, D. W., Lam, W. K., and Zhang, M. (2020). Joint contact force and movement deceleration among badminton forward lunges: A musculoskeletal modelling study. *Sports Biomech.* 21, 1249–1261. doi:10.1080/14763141.2020.1749720
- Christina, K. A., White, S. C., and Gilchrist, L. A. (2001). Effect of localized muscle fatigue on vertical ground reaction forces and ankle joint motion during running. *Hum. Mov. Sci.* 20 (3), 257–276. doi:10.1016/s0167-9457(01)00048-3
- Cronin, J., McNair, P., and Marshall, R. (2003). Lunge performance and its determinants. *J. sports Sci.* 21 (1), 49–57. doi:10.1080/0264041031000070958
- Dempster, J., Dutheil, F., and Ugbole, U. C. (2021). The prevalence of lower extremity injuries in running and associated risk factors: A systematic review. *Phys. Activity Health* 5 (1), 133–145. doi:10.5334/paah.109
- Dubin, J. C., Comeau, D., McClelland, R. I., Dubin, R. A., and Ferrel, E. (2011). Lateral and syndesmotank ankle sprain injuries: A narrative literature review. *J. Chiropr. Med.* 10 (3), 204–219. doi:10.1016/j.jcm.2011.02.001
- Duquette, A. M., and Andrews, D. M. (2010). Tibialis anterior muscle fatigue leads to changes in tibial axial acceleration after impact when ankle dorsiflexion angles are visually controlled. *Hum. Mov. Sci.* 29 (4), 567–577. doi:10.1016/j.humov.2010.03.004
- Edis, Ç., Vural, F., and Vurgun, H. (2016). The importance of postural control in relation to technical abilities in small-sided soccer games. *J. Hum. Kinet.* 53 (1), 51–61. doi:10.1515/hukin-2016-0010
- Fahlström, M., Björnstig, U., and Lorentzon, R. (1998). Acute achilles tendon rupture in badminton players. *Am. J. Sports Med.* 26 (3), 467–470. doi:10.1177/03635465980260032201
- Fahlstrom, M., Lorentzon, R., and Alfredson, H. (2002). Painful conditions in the achilles tendon region: A common problem in middle-aged competitive badminton players. *Knee Surg. Sports Traumatol. Arthrosc.* 10 (1), 57–60. doi:10.1007/s00167-001-0255-x
- Flynn, J. M., Holmes, J. D., and Andrews, D. M. (2004). The effect of localized leg muscle fatigue on tibial impact acceleration. *Clin. Biomech.* 19 (7), 726–732. doi:10.1016/j.clinbiomech.2004.04.015
- Fong, D. T., Chan, Y.-Y., Mok, K.-M., Yung, P. S., and Chan, K.-M. (2009). Understanding acute ankle ligamentous sprain injury in sports. *BMC Sports Sci. Med. Rehabilitation* 1 (1), 14. doi:10.1186/1758-2555-1-14
- Fu, L., Ren, F., and Baker, J. S. (2017). Comparison of joint loading in badminton lunging between professional and amateur badminton players. *Appl. Bionics Biomech.* 2017, 1–8. doi:10.1155/2017/5397656
- Fu, W. J. (2011). The role of footwear on plantar pressure performance during badminton movements. *Appl. Mech. Mater.* 55–57, 1675–1678. doi:10.4028/www.scientific.net/AMM.55-57.1675
- Fukashiro, S., Komi, P. V., Järvinen, M., and Miyashita, M. (1995). In vivo achilles tendon loading during jumping in humans. *Eur. J. Appl. physiology Occup. physiology* 71 (5), 453–458. doi:10.1007/bf00635880
- Gautrey, C. N., Watson, T., and Mitchell, A. (2013). The effect of isokinetic testing speed on the reliability of muscle fatigue indicators during a hip abductor-adductor fatigue protocol. *Int. J. Sports Med.* 34 (7), 646–653. doi:10.1055/s-0032-1321801
- Gerritsen, K. G. M., Vandenbogert, A. J., and Nigg, B. M. (1995). Direct dynamics simulation of the impact phase in heel-toe running. *J. Biomechanics* 28 (6), 661–668. doi:10.1016/0021-9290(94)00127-p
- Gribble, P. A., and Hertel, J. (2004). Effect of hip and ankle muscle fatigue on unipedal postural control. *J. Electromyogr. Kinesiol* 14 (6), 641–646. doi:10.1016/j.jelekin.2004.05.001
- Gross, M. T. (1995). Lower quarter screening for skeletal malalignment—Suggestions for orthotics and footwear. *J. Orthop. Sports Phys. Ther.* 21 (6), 389–405. doi:10.2519/jospt.1995.21.6.389
- Handbook, B.-V. B.-B. (2014). *Training, tactics, competition*. Maidenhead: Meyer and Meyer Sport (UK) Ltd.
- Hansen, U., Zioupos, P., Simpson, R., Currey, J. D., and Hynd, D. (2008). The effect of strain rate on the mechanical properties of human cortical bone. *J. Biomechanical Engineering-Transactions Asme* 130 (1), 011011. doi:10.1115/1.2838032

- Herbaut, A., and Delannoy, J. (2020). Fatigue increases ankle sprain risk in badminton players: A biomechanical study. *J. Sports Sci.* 38 (13), 1560–1565. doi:10.1080/02640414.2020.1748337
- Hoch, M. C., Farwell, K. E., Gaven, S. L., and Weinhandl, J. T. (2015). Weight-bearing dorsiflexion range of motion and landing biomechanics in individuals with chronic ankle instability. *J. Athl. Train.* 50 (8), 833–839. doi:10.4085/1062-6050-50.5.07
- Hong, Y., Wang, S. J., Lam, W. K., and Cheung, J. T.-M. (2014). Kinetics of badminton lunges in four directions. *J. Appl. biomechanics* 30 (1), 113–118. doi:10.1123/jab.2012-0151
- Hu, X., Li, J. X., Hong, Y., and Wang, L. (2015). Characteristics of plantar loads in maximum forward lunge tasks in badminton. *PLoS One* 10 (9), e0137558. doi:10.1371/journal.pone.0137558
- Huang, M. T., Lee, H. H., Lin, C. F., Tsai, Y. J., and Liao, J. C. (2014). How does knee pain affect trunk and knee motion during badminton forehand lunges? *J. Sports Sci.* 32 (7), 690–700. doi:10.1080/02640414.2013.848998
- Jiang, X., Yang, X., Zhou, H., Baker, J. S., and Gu, Y. (2021). Prolonged running using bionic footwear influences lower limb biomechanics. *Healthc. MDPI* 9, 236. doi:10.3390/healthcare9020236
- Joseph, M., Tiberio, D., Baird, J. L., Trojjan, T. H., Anderson, J. M., Kraemer, W. J., et al. (2008). Knee valgus during drop jumps in national collegiate athletic association division I female athletes: The effect of a medial post. *Am. J. sports Med.* 36 (2), 285–289. doi:10.1177/0363546507308362
- Kellis, E., and Liassou, C. (2009). The effect of selective muscle fatigue on sagittal lower limb kinematics and muscle activity during level running. *J. Orthop. Sports Phys. Ther.* 39 (3), 210–220. doi:10.2519/jospt.2009.2859
- Kim, Y.-w., Kim, T.-h., Yang, M.-n., Yon, Y.-s., and Lee, J.-h. (2017). Comparison of activities of tibialis anterior, peroneus longus, and tibialis posterior muscles according to lunge squats and Bulgarian split squats in a healthy population. *J. Musculoskelet. Sci. Technol.* 1 (1), 26–30. doi:10.29273/jkema.2017.1.1.26
- Krøner, K., Schmidt, S., Nielsen, A., Yde, J., Jakobsen, B., Møller-Madsen, B., et al. (1990). Badminton injuries. *Br. J. Sports Med.* 24 (3), 169–172. doi:10.1136/bjism.24.3.169
- Kuntze, G., Mansfield, N., and Sellers, W. (2010). A biomechanical analysis of common lunge tasks in badminton. *J. Sports Sci.* 28 (2), 183–191. doi:10.1080/02640410903428533
- Lafortune, M. A., Hennig, E. M., and Lake, M. J. (1996). Dominant role of interface over knee angle for cushioning impact loading and regulating initial leg stiffness. *J. biomechanics* 29 (12), 1523–1529. doi:10.1016/s0021-9290(96)80003-0
- Lam, W.-K., Ryue, J., Lee, K.-K., Park, S.-K., Cheung, J. T.-M., and Ryu, J. (2017a). Does shoe heel design influence ground reaction forces and knee moments during maximum lunges in elite and intermediate badminton players? *PLoS One* 12 (3), e0174604. doi:10.1371/journal.pone.0174604
- Lam, W. K., Ding, R., and Qu, Y. (2017b). Ground reaction forces and knee kinetics during single and repeated badminton lunges. *J. Sports Sci.* 35 (6), 587–592. doi:10.1080/02640414.2016.1180420
- Lam, W. K., Lee, K. K., Park, S. K., Ryue, J., Yoon, S. H., and Ryu, J. (2018). Understanding the impact loading characteristics of a badminton lunge among badminton players. *PLoS One* 13 (10), e0205800. doi:10.1371/journal.pone.0205800
- Lam, W. K., Wong, D. W., and Lee, W. C. (2020). Biomechanics of lower limb in badminton lunge: A systematic scoping review. *PeerJ* 8, e10300. doi:10.7717/peerj.10300
- Lee, J. J., and Loh, W. P. (2019). A state-of-the-art review on badminton lunge attributes. *Comput. Biol. Med.* 108, 213–222. doi:10.1016/j.combiomed.2019.04.003
- Lee, J., Song, Y., and Shin, C. S. (2018). Effect of the sagittal ankle angle at initial contact on energy dissipation in the lower extremity joints during a single-leg landing. *Gait Posture* 62, 99–104. doi:10.1016/j.gaitpost.2018.03.019
- Lees, A., and Hurley, C. (1994). Forces in a badminton lunge movement. *Sci. racket sports* 1994, 249–256.
- Leporace, G., Tannure, M., Zeitoune, G., Metsavaht, L., Marocolo, M., and Souto Maior, A. (2020). Association between knee-to-hip flexion ratio during single-leg vertical landings, and strength and range of motion in professional soccer players. *Sports Biomech.* 19 (3), 411–420. doi:10.1080/14763141.2018.1494207
- Lin, C. F., Hua, S. H., Huang, M. T., Lee, H. H., and Liao, J. C. (2015). Biomechanical analysis of knee and trunk in badminton players with and without knee pain during backhand diagonal lunges. *J. Sports Sci.* 33 (14), 1429–1439. doi:10.1080/02640414.2014.990492
- Lin, K.-C., Wei, C.-W., Lai, C.-L., Cheng, I., and Chen, N.-S. (2021). Development of a badminton teaching system with wearable technology for improving students' badminton doubles skills. *Educ. Technol. Res. Dev.* 69 (2), 945–969. doi:10.1007/s11423-020-09935-6
- Lundin, T. M., Feuerbach, J. W., and Grabiner, M. D. (1993). Effect of plantar flexor and dorsiflexor fatigue on unilateral postural control. *J. Appl. Biomechanics* 9 (3), 191–201. doi:10.1123/jab.9.3.191
- Mattes, K., Eldin, A. H. W., Schaffert, N., and Manzer, S. (2015). Local concentric muscle fatigue of the ankle dorsiflexors and plantar flexors: A reproducibility study. *Isokinet. Exerc. Sci.* 23, 87–92. doi:10.3233/IES-150568
- McNair, P. J., Depledge, J., Brett Kelly, M., and Stanley, S. N. (1996). Verbal encouragement: Effects on maximum effort voluntary muscle: Action. *Br. J. sports Med.* 30 (3), 243–245. doi:10.1136/bjism.30.3.243
- Mei, Q., Gu, Y., Fu, F., and Fernandez, J. (2017). A biomechanical investigation of right-forward lunging step among badminton players. *J. Sports Sci.* 35 (5), 457–462. doi:10.1080/02640414.2016.1172723
- Milner, C. E., Ferber, R., Pollard, C. D., Hamill, J., and Davis, I. S. (2006). Biomechanical factors associated with tibial stress fracture in female runners. *Med. Sci. Sports Exerc.* 38 (2), 323–328. doi:10.1249/01.mss.0000183477.75808.92
- Nielsen, M. H., Lund, J. N., Lam, W. K., and Kersting, U. G. (2020). Differences in impact characteristics, joint kinetics and measurement reliability between forehand and backhand forward badminton lunges. *Sports Biomech.* 19 (4), 547–560. doi:10.1080/14763141.2018.1501086
- Padua, E., D'Amico, A. G., Alashram, A., Campoli, F., Romagnoli, C., Lombardo, M., et al. (2019). Effectiveness of warm-up routine on the ankle injuries prevention in young female basketball players: A randomized controlled trial. *Med. Kaunas.* 55 (10), 690. doi:10.3390/medicina55100690
- Pau, M., Porta, M., Arippa, F., Piloni, G., Sorrentino, M., Carta, M., et al. (2019). Dynamic postural stability, is associated with competitive level, in youth league soccer players. *Phys. Ther. Sport* 35, 36–41. doi:10.1016/j.ptsp.2018.11.002
- Phomsoupha, M., and Laffaye, G. (2015). The science of badminton: Game characteristics, anthropometry, physiology, visual fitness and biomechanics. *Sports Med.* 45 (4), 473–495. doi:10.1007/s40279-014-0287-2
- Puddle, D. L., and Maulder, P. S. (2013). Ground reaction forces and loading rates associated with parkour and traditional drop landing techniques. *J. sports Sci. Med.* 12 (1), 122–129.
- Radcliffe, C. R., Colman, C. E., and Spratford, W. A. (2021). The effect of fatigue on peak Achilles tendon force in Irish dancing-specific landing tasks. *Sports Biomech.* 2021, 1–14. doi:10.1080/14763141.2021.1951826
- Radin, E. L. (1986). Role of muscles in protecting athletes from injury. *Acta Medica Scand.* 220 (S711), 143–147. doi:10.1111/j.0954-6820.1986.tb08943.x
- Robinson, G., and O'Donoghue, P. (2008). A movement classification for the investigation of agility demands and injury risk in sport. *Int. J. Perform. Analysis Sport* 8 (1), 127–144. doi:10.1080/24748668.2008.11864828
- Salavati, M., Moghadam, M., Ebrahimi, I., and Arab, A. M. (2007). Changes in postural stability with fatigue of lower extremity frontal and sagittal plane movers. *Gait Posture* 26 (2), 214–218. doi:10.1016/j.gaitpost.2006.09.001
- Sarshin, A., Mohammadi, S., Shahrabad, H. B. P., and Sedighi, M. (2011). The effects of functional fatigue on dynamic postural control of badminton players. *Biol. Exerc.* 7 (2). doi:10.4127/jbe.2011.0047
- Schafer, Z. A., Perry, J. L., and Vanicek, N. (2018). A personalised exercise programme for individuals with lower limb amputation reduces falls and improves gait biomechanics: A block randomised controlled trial. *Gait Posture* 63, 282–289. doi:10.1016/j.gaitpost.2018.04.030
- Shariff, A. H., George, J., and Ramlan, A. A. (2009). Musculoskeletal injuries among Malaysian badminton players. *Singap. Med. J.* 50 (11), 1095–1097.
- Sigward, S. M., Ota, S., and Powers, C. M. (2008). Predictors of frontal plane knee excursion during a drop land in young female soccer players. *J. Orthop. sports Phys. Ther.* 38 (11), 661–667. doi:10.2519/jospt.2008.2695
- Tiwari, A., Singh, O., and Bhatia, D. (2021). A review on motor neuron disabilities and treatments. *Int. J. Biomed. Eng. Technol.* 37 (2), 154–175. doi:10.1504/ijbet.2021.119502
- Valdecabres, R., Casal, C. A., Chiminazzo, J. G. C., and De Benito, A. M. (2020a). Players' on-court movements and contextual variables in badminton world championship. *Front. Psychol.* 11, 1567. doi:10.3389/fpsyg.2020.01567
- Valdecabres, R., de Benito, A. M., Littler, G., and Richards, J. (2018). An exploration of the effect of proprioceptive knee bracing on biomechanics during a badminton lunge to the net, and the implications to injury mechanisms. *PeerJ* 6, e6033. doi:10.7717/peerj.6033
- Valdecabres, R., Richards, J., and De Benito, A. M. (2020b). The effect of match fatigue in elite badminton players using plantar pressure measurements and the implications to injury mechanisms. *Sports Biomech.* 21, 940–957. doi:10.1080/14763141.2020.1712469
- Williams, V. J., Nagai, T., Sell, T. C., Abt, J. P., Rowe, R. S., McGrail, M. A., et al. (2016). Prediction of dynamic postural stability during single-leg jump landings by ankle and knee flexibility and strength. *J. Sport Rehabil.* 25 (3), 266–272. doi:10.101123/jsr.2015-0001
- Wright, I., Neptune, R., van den Bogert, A. J., and Nigg, B. (2000). The influence of foot positioning on ankle sprains. *J. biomechanics* 33 (5), 513–519. doi:10.1016/s0021-9290(99)00218-3
- Xiang, L., Mei, Q., Wang, A., Shim, V., Fernandez, J., and Gu, Y. (2022). Evaluating function in the hallux valgus foot following a 12-week minimalist footwear intervention: A pilot computational analysis. *J. Biomechanics* 132, 110941. doi:10.1016/j.jbiomech.2022.110941
- Xu, D., Jiang, X., Cen, X., Baker, J. S., and Gu, Y. (2020). Single-leg landings following a volleyball spike may increase the risk of anterior cruciate ligament injury more than landing on both-legs. *Appl. Sci.* 11 (1), 130. doi:10.3390/app11010130
- Xu, D., Quan, W., Zhou, H., Sun, D., Baker, J. S., and Gu, Y. (2022). Explaining the differences of gait patterns between high and low-mileage runners with machine learning. *Sci. Rep.* 12 (1), 2981–3012. doi:10.1038/s41598-022-07054-1
- Yaggie, J. A., and McGregor, S. J. (2002). Effects of isokinetic ankle fatigue on the maintenance of balance and postural limits. *Arch. Phys. Med. Rehabil.* 83 (2), 224–228. doi:10.1053/apmr.2002.28032
- Yahya, U., Senanayake, S. A., and Naim, A. G. (2022). Characterising leg-dominance in healthy netballers using 3D kinematics-electromyography features' integration and machine learning techniques. *Int. J. Biomed. Eng. Technol.* 39 (1), 65–92. doi:10.1504/ijbet.2022.10047887
- Zhang, S.-N., Bates, B. T., and Dufek, J. S. (2000). Contributions of lower extremity joints to energy dissipation during landings. *Med. Sci. sports Exerc.* 32 (4), 812–819. doi:10.1097/00005768-200004000-00014



OPEN ACCESS

EDITED BY

Zhen (Jeff) Luo, University of Technology
Sydney, Australia

REVIEWED BY

Rahim Mutlu,
University of Wollongong in Dubai, United
Arab Emirates
Lorenzo Masia,
Heidelberg University, Germany

*CORRESPONDENCE

Hyung-Soon Park,
✉ hyungspark@kaist.ac.kr

SPECIALTY SECTION

This article was submitted to
Bionics and Biomimetics,
a section of the journal
Frontiers in Bioengineering and
Biotechnology

RECEIVED 14 March 2022

ACCEPTED 20 January 2023

PUBLISHED 02 February 2023

CITATION

Park CB and Park H-S (2023), Portable 3D-
printed hand orthosis with spatial stiffness
distribution personalized for assisting
grasping in daily living.
Front. Bioeng. Biotechnol. 11:895745.
doi: 10.3389/fbioe.2023.895745

COPYRIGHT

© 2023 Park and Park. This is an open-
access article distributed under the terms
of the [Creative Commons Attribution
License \(CC BY\)](#). The use, distribution or
reproduction in other forums is permitted,
provided the original author(s) and the
copyright owner(s) are credited and that
the original publication in this journal is
cited, in accordance with accepted
academic practice. No use, distribution or
reproduction is permitted which does not
comply with these terms.

Portable 3D-printed hand orthosis with spatial stiffness distribution personalized for assisting grasping in daily living

Chan Beom Park and Hyung-Soon Park*

Department of Mechanical Engineering, Korea Advanced Institute of Science and Technology (KAIST),
Daejeon, South Korea

Stroke survivors having limited finger coordination require an active hand orthosis to assist them with grasping tasks for daily activities. The orthosis should be portable for constant use; however, portability imposes constraints on the number, size, and weight of the actuators, which increase the difficulty of the design process. Therefore, a tradeoff exists between portability and the assistive force. In this study, a personalized spatial stiffness distribution design is presented for a portable and strengthful hand orthosis. The spatial stiffness distribution of the orthosis was optimized based on measurements of individual hand parameters to satisfy the functional requirements of achieving sufficient grip aperture in the pre-grasping phase and minimal assistive force in the grasping phase. Ten stroke survivors were recruited to evaluate the system. Sufficient grip aperture and high grip strength-to-weight ratio were achieved by the orthosis via a single motor. Moreover, the orthosis significantly restored the range of motion and improved the performance of daily activities. The proposed spatial stiffness distribution can suggest a design solution to make strengthful hand orthoses with reduced weight.

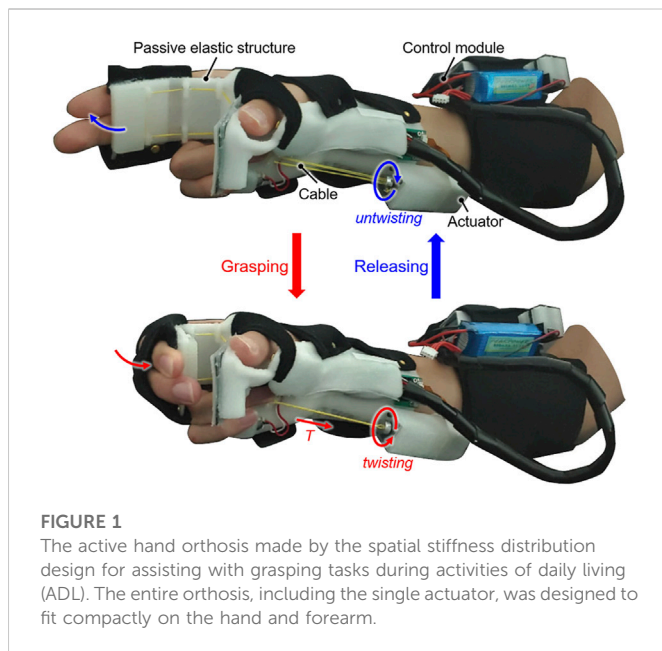
KEYWORDS

hand orthosis, personalized, portable, spatial stiffness distribution, strengthful, stroke

1 Introduction

Stroke is a cerebrovascular event that occurs in 13 million people worldwide every year (Lindsay et al., 2019). Often, it leads to neurological deficits such as spasticity, muscle weakness, and muscle co-contraction in the upper extremities, which negatively affects activities of daily living (ADL) (Chae et al., 2002; Kuo and Hu, 2018). Early in the post-stroke stage, intensive and task-specific training is implemented with the help of therapists and rehabilitation devices to restore impaired motor functions (Bayona et al., 2005; Waddell et al., 2014). However, ~65% of stroke survivors in the chronic stage cannot use their affected hands to perform ADL owing to challenges in hand function recovery (Dobkin, 2005; Wang et al., 2019). Portable hand orthoses, which can assist with finger movements according to user intentions, are necessary to aid stroke survivors with grasping tasks for ADL (Peters et al., 2017).

For stroke survivors, the limited finger coordination because of spasticity and muscle weakness is the primary obstacle for performing grasping tasks with the affected hand (Kamper et al., 2006; Kuo and Hu, 2018). In particular, flexor spasticity and extensor muscle weakness limit the range of motion (ROM) of finger joints (Hoffmann et al., 2016; Kuo and Hu, 2018). Thus, the orthosis should support both finger flexion and extension. Including actuators, a portable orthosis should weigh <500 g because of its constant use and for easy donning/doffing (Nycz et al., 2016; Ates et al., 2017; Lambelet et al., 2020). Moreover, it should be able to



counteract spasticity in the pre-grasping phase to ensure a sufficient grip aperture, and it should generate a grip strength above 15 N (Yurkewich et al., 2019).

Many types of hand orthoses have been developed. Most existing hand orthoses include multiple actuators to assist dexterous finger movements for rehabilitation purposes. The hand orthoses comprise exoskeletons (Ryu et al., 2008; Chiri et al., 2009; Ho et al., 2011; Ates et al., 2015), tendon-driven gloves (Wege and Zimmermann, 2007; Ueki et al., 2012; Aiple and Schiele, 2013; Borboni et al., 2016; Xiloyannis et al., 2016; Kim and Park, 2018; Burns and Vinjamuri, 2020; Alicea et al., 2021), and inflatable robotic gloves (Cappello et al., 2018; Nuckols et al., 2020). The exoskeletal orthoses can assist fingers with accurately controlled joint movements; however, they inherently suffer from poor portability due to their heavy weight. The soft orthoses considerably reduce applied weight on the hand using gloves made from lightweight silicone or fabric; however, they are less convenient to be used in daily living due to multiple actuators with long tendon sheaths and tubes required to transfer assistive force from the actuators to the gloves.

Several portable hand orthoses have been developed by reducing the number of actuators in the soft orthoses for assistive purposes in daily living (In et al., 2015; Polygerinos et al., 2015; Thielbar et al., 2016; Popov et al., 2017; Yap et al., 2018; Yurkewich et al., 2019; 2020). Some portable orthoses (Popov et al., 2017; Yurkewich et al., 2019; 2020) even do not require any long tendon sheaths and tubes for convenient use. Although multiple portable hand orthoses have been developed for stroke survivors, they have not been quantitatively evaluated for their effectiveness at assisting with grasping tasks for ADL due to an issue regarding grip strength. It is because the assistive force of portable hand orthoses is limited by the allowable number, size, and weight of actuators, which inhibits finger extension and grip strength (Yurkewich et al., 2019; 2020). Many researchers have developed portable orthoses of which actuation modules are remotely mounted on the body such as on the waist (Polygerinos et al., 2015; Thielbar et al., 2016; Yap et al., 2018) to reduce the external

weight on the hand; however, heavy actuators are still associated with poor usability.

An elastic structure can be used for portable orthoses (Arata et al., 2013; Nycz et al., 2016) to ensure passive finger extension, thus reducing the required number of actuators for grasping assistance. The stiffness of the structure significantly affects grasping performance for each individual; the low stiffness would result in limited grip aperture in the pre-grasping phase by spastic finger joints while the high stiffness would lead to limited grip strength in the grasping phase by requiring unnecessarily high assistive force for flexion. Thus, it is desirable to personalize the spatial stiffness distribution of the structure based on individual degrees of spasticity (Park et al., 2016) to achieve sufficient grip aperture and grip strength with actuators constrained by number, size, and weight. However, there are limited design guidelines to determine the spatial stiffness distribution of hand orthoses for each individual.

This study presents a personalized spatial stiffness distribution design for a portable and strengthful hand orthosis to assist with grasping tasks (Figure 1). The spatial stiffness distribution is designed as per individuals to achieve a sufficient grip aperture against spasticity in the pre-grasping phase and a minimal assistive force in the grasping phase. Because the degree of spasticity is unique to each stroke survivor, the spatial stiffness distribution is optimized based on measurements of individual hand parameters. The orthosis having the personalized spatial stiffness distribution is made using a 3D printer, and it was evaluated by recruiting chronic stroke survivors with impaired hand functionality. By using only a single small (10 Ø) motor, the orthosis can assist with grasping tasks by generating a sufficient grip aperture and high grip strength. The rest of this study is organized as follows. Section 2 presents an overview of the orthosis design and describes the procedure for optimizing the stiffness of the orthosis. Section 2 also presents the experimental evaluation. Section 3 presents the experimental results. Section 4 discusses the significance and implications of the results in this study and concludes the paper.

2 Materials and methods

2.1 Overall design

The specifications of the orthosis made by the spatial stiffness distribution design are determined as follows based on the results of previous studies and interviews with clinicians.

- 1) Portability: The orthosis including the actuators should weigh <500 g (Nycz et al., 2016; Ates et al., 2017; Lambelet et al., 2020) because it will be in constant use throughout the day. Thus, the number of actuators should be minimized.
- 2) Grasping assistance: The orthosis should assist with the bidirectional movement of the fingers to aid with grasping tasks. The target grip aperture and minimal required grip strength are set to 80 mm (>70 mm (Feix et al., 2014)) and 15 N (Yurkewich et al., 2019), respectively.
- 3) Comfort and safety: The orthosis should not induce pain, hyperextension, and skin damage during use. The application of a compressive force to finger joints must be avoided when it is assisting with finger movement.

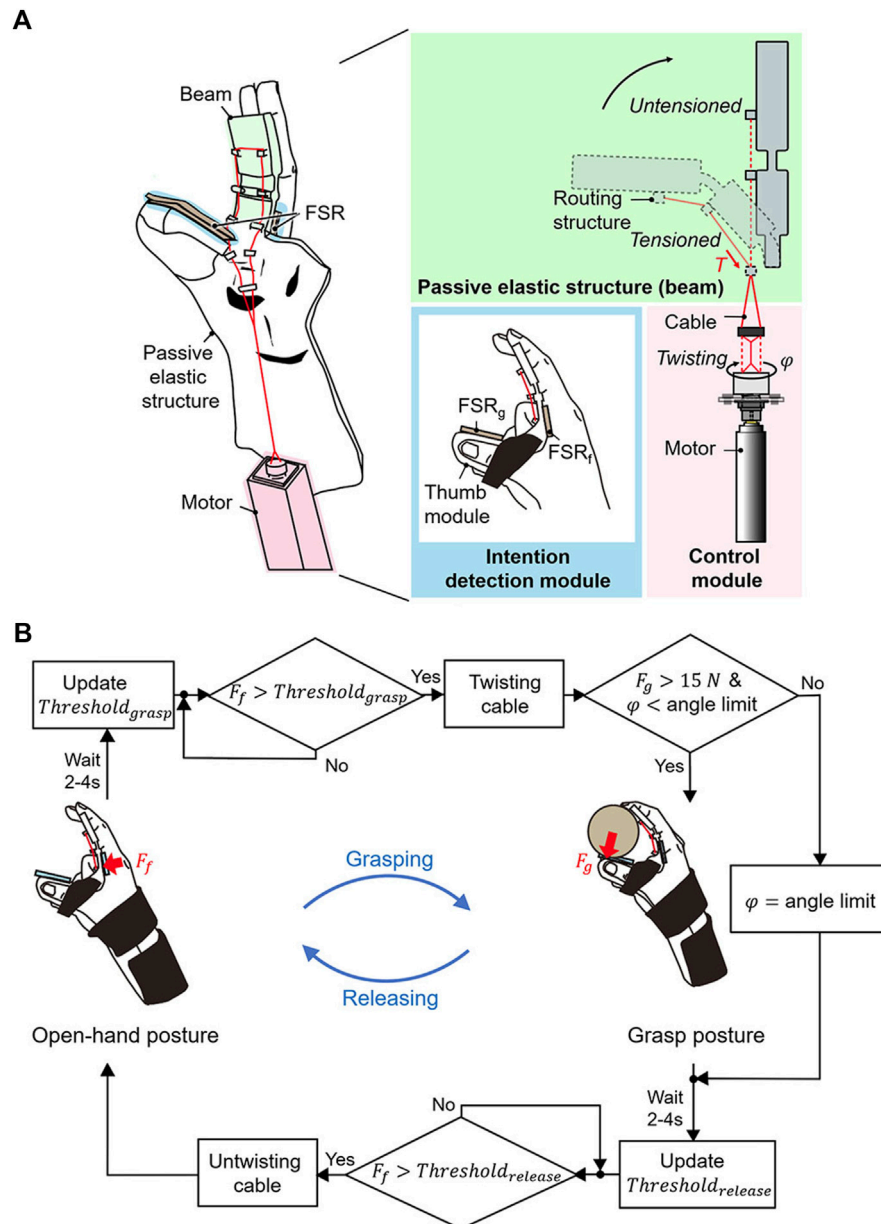


FIGURE 2

Design overview of the active hand orthosis. **(A)** The orthosis consists of a passive elastic structure for passive extension, a control module for active flexion, and an intention detection module. The rotation angle (φ) of the motor is adjusted to twist the cable, which generates the assistive force (T). The assistive force is applied to routing structures of the beam. Two force-sensing resistors (FSR_g, FSR_l) are used as the intention detection module. **(B)** Working principle of the orthosis based on user intention. The grasping and releasing tasks are initiated when the user applies a flexion force (F_f) over the pre-set $Threshold_{grasp}$ and $Threshold_{release}$. A grasping task is achieved by rotating the motor from the initial angle, which was set when the cable was completely untwisted, to the holding angle when a grip strength (F_g) reaches a 15 N. The releasing task is done by rotating the motor from the holding angle to the initial angle.

The number of grasp types that the orthosis can assist with is limited because the underactuation of the orthosis is inevitable for portability. Because tripod grasp achieved by three fingers (i.e., the thumb, index finger, and middle finger) was similar with the grasping posture achieved by one of the postural synergies required for a tool use (Santello et al., 1988), it was considered that common objects can be grasped by the tripod grasp. Thus, the tripod grasp is selected for emulation using a single motor.

The orthosis comprises a passive elastic structure (including a beam) fabricated from thermoplastic polyurethane (TPU; Hyvision System, Inc. Seongnam, South Korea), an intention detection module, and a control module (Figure 2A). The orthosis has a total weight of 454 g, and it compactly fits on the affected hand and forearm. The passive elastic structure is made using a 3D printer (Cubicon Single, Hyvision System, Inc. Seongnam, South Korea) and reduces the number of actuators required by realizing the passive extension of

fingers. The passive elastic structure allows independent donning/doffing of the orthosis and avoids joint compression during extension of spastic finger joints. The beam of the passive elastic structure where the fingers make contact is designed to optimize the stiffness for ensuring a sufficient grip aperture in the pre-grasping phase and minimizing the required antagonistic assistive force (T) for grasping. The passive elastic structure excluding the beam is designed as per the hand geometry of each user for comfort. Because of finger contracture in the affected hand, a 3D scanner (Sense2, 3D Systems Inc. Rock Hill, SC, United States) is used to scan the unaffected hand when the user grasps an 80-mm-diameter cylinder. The affected hand geometry is generated by mirroring the 3D scanning results assuming symmetry of the hands (Kulaksiz and Gözil, 2002). The thumb module is designed based on the affected hand geometry using the software Geomagic Freeform (3D Systems, Inc. Rock Hill, SC, United States) so that the palmar aspect of the thumb is rigidly fixed at the abducted posture as the user grasps an 80-mm-diameter cylinder.

The control module comprises a small motor (10 Ø, 46.8 mm length, 64:1, 315172, MAXON Inc. Sachseln, Switzerland), cable (Power Pro, Shimano Inc. Caringbah, Australia), motor driver (446023, MAXON Inc. Sachseln, Switzerland), Arduino Micro, and battery (800 mAh-11.1V, PEAKPOWER Engineering Inc. Lakewood, United States). The cable contraction for active flexion of the beam is driven by a twisted string actuation (TSA) mechanism (Palli et al., 2013). The contraction length of the cable is adjusted by controlling the rotation angle (φ) of the motor. A contraction force (assistive force) is applied at routing structures of the beam. The battery continuously lasts for 170 min, and 2,260 cycles of active flexion were continuously achieved during that period. It was also confirmed that the orthosis could withstand ~40,000 cycles of active flexion without break. The intention detection module comprises two force-sensing resistors (FSRs) (FSR01CE, OHMITE Manufacturing Co., Warrenville, IL, United States) that are respectively positioned on the beam and thumb module. In particular, the FSR on the beam (FSR_b) can sense the flexion force of the affected hand, and the FSR on the thumb module (FSR_t) can measure how much grip strength is applied to a grasped object.

Because stroke survivors cannot voluntarily extend their fingers because of extensor muscle weakness, the grasping and releasing intentions are detected solely using the FSR_t that can measure the flexion force. The grasping and releasing intentions are detected when the FSR_t detects a force that exceeds the pre-set values $Threshold_{grasp}$ and $Threshold_{release}$, respectively (Figure 2B). To calculate $Threshold_{grasp}$ and $Threshold_{release}$, the voluntary force of the user is first calculated during voluntary grasping in a setup procedure. The user applies the maximal flexion force for a grasping task while wearing the orthosis. The FSR_t measures the peak value for five attempts, and the values are then recorded. The baseline force, which corresponds to the force at rest, is measured before the voluntary grasping. The minimum difference between the peak and baseline forces is defined as the voluntary force. $Threshold_{grasp}$ and $Threshold_{release}$ were defined as the sum of the calculated voluntary force and baseline force. These values are updated at the end of every grasping and releasing task because the baseline force varies with spastic contractions over time. At the end of a grasping and releasing task, a waiting period of 2–4 s is implemented until the spastic response settles down, and the force measured after the waiting period is set as the baseline force for the next tasks. The waiting period is determined as per the time required for the force to settle

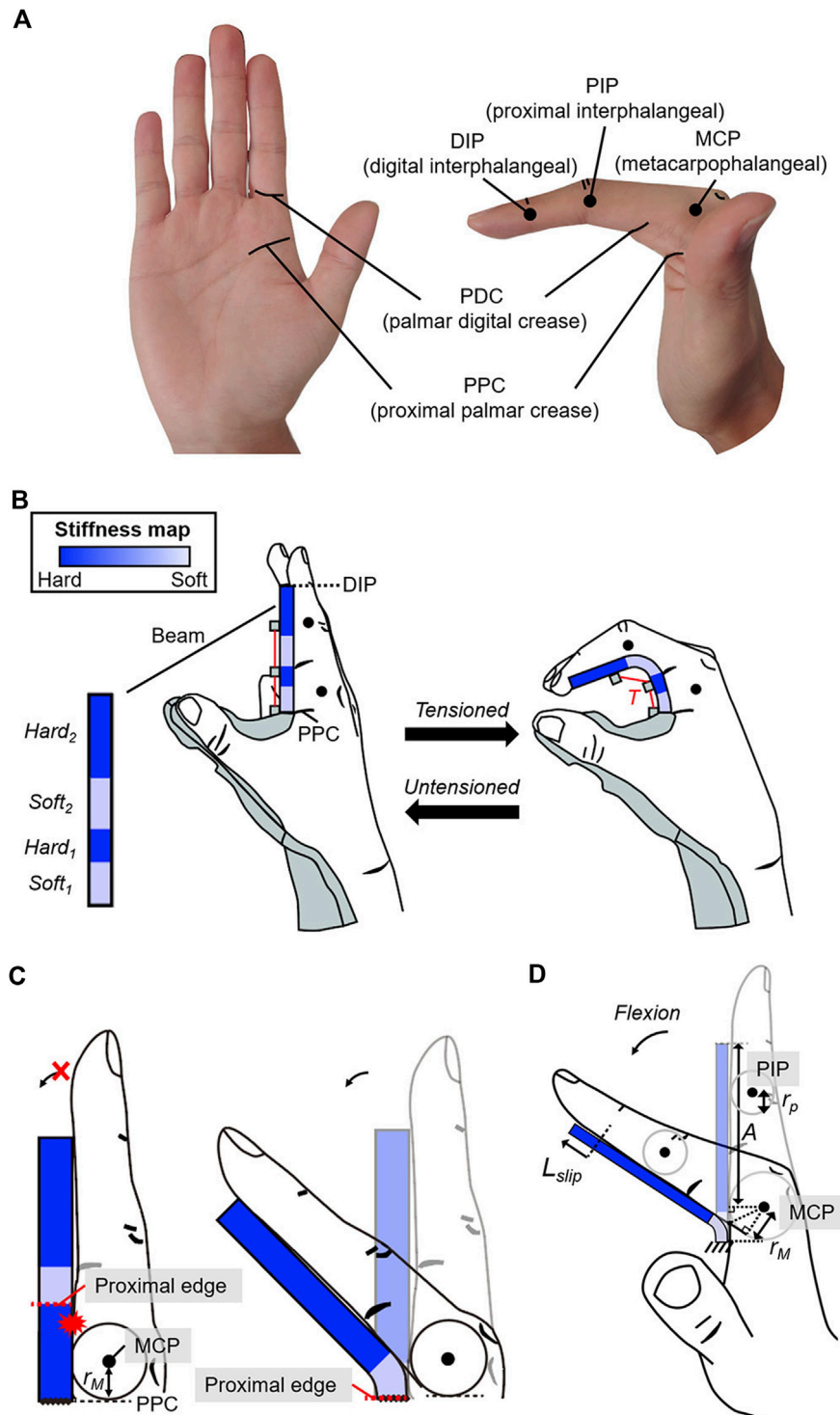
down to 110% of the baseline force that is measured before the voluntary grasping during the setup procedure.

The grasping and releasing tasks are initiated when the user applies a flexion force (F_f) that exceeds the pre-set values ($Threshold_{grasp}$, $Threshold_{release}$). In the initial state, the fingers are passively extended (open-hand posture) at the initial angle of the motor, which is set when the cable is completely untwisted. Active flexion of the beam is initiated once the user applies a force that exceeds $Threshold_{grasp}$. The active flexion is driven by rotating the motor to twist the cable under a nominal step input current. The motor rotates until the angle limit, which is set to when the end of the beam makes contact with the thumb module. Once the rotation angle reaches the angle limit, a proportional–integral–derivative (PID) controller maintains the angle limit for safety. When the grip strength (F_g) reaches 15 N (Yurkewich et al., 2019) before the motor rotates to the angle limit, the PID controller holds the rotation angle to maintain the holding angle that grasps objects at a 15-N grip strength. The minimally required grip strength of 15 N for grasping (Yurkewich et al., 2019) is used to increase the life cycle of the cable, which can break because of abrasion during twisting. To release an object, the user should flex the fingers to apply a force over $Threshold_{release}$. Passive extension is achieved by reversely rotating the motor under a nominal input current, which untwists the cable. Once the rotation angle reaches the initial angle, the PID controller holds the initial angle. For false activation (i.e., unintended grasping and releasing) caused by physical perturbation, the user must reapply a force to return their hand to the desired posture.

2.2 Beam design

The beam geometry was designed to satisfy two conditions: it should passively extend the fingers in the pre-grasping phase, and it must be bendable to allow finger flexion under the action of the assistive force in the grasping phase. To achieve these conditions, the geometric constraints of the beam were determined based on the kinematics of the finger movement. The kinematics varies depending on the anthropometric dimensions of an individual hand. The positions of hand landmarks were used as a reference to measure the anthropometric dimensions and determine the geometric constraints on the beam design. The finger joints and following skin creases were selected as hand landmarks (Figure 3A): the palmar digital crease (PDC) and proximal palmar crease (PPC). Note that the PPC is where the proximal phalanx is folded toward the palm to achieve 90° metacarpophalangeal (MCP) flexion. To satisfy the first condition, the beam was designed to cover the proximal and middle phalanges of index and middle fingers (Figure 3B). This design allows the MCP and proximal interphalangeal (PIP) joints to be passively extended while sensory feedback is obtained via the fingertips.

To meet the second condition, the stiffness of the beam was designed as follows. Active flexion requires that the beam deflection along the MCP and PIP joints be significantly larger than in other regions; thus, stiffness close to the MCP and PIP joints should be less than that in other regions. The beam comprises two soft regions ($Soft_1$ and $Soft_2$) and two hard regions ($Hard_1$ and $Hard_2$) (Figure 3B). Because the beam is at the palmar aspect of the fingers, the proximal edge of soft regions was constrained to be more proximal than the corresponding joint by at least the radius

**FIGURE 3**

Geometric constraints of the beam to enable passive extension and active flexion of the fingers. (A) Hand landmarks used to design the beam. (B) The beam covers the palmar aspect from the PPC to the DIP to enable passive extension of the MCP and PIP joints. The stiffness near the MCP and PIP joints is set lower than that in other regions to allow active flexion of the joints under the assistive force (T). (C) The proximal edge of the soft region is set more proximal than the joint by a length greater than the radius of the joint to allow joint flexion. (D) Slip distance (L_{slip}) considered for locating $Soft_2$. A is the length between the MCP and DIP joints. r_M and r_P are respectively the radius of the MCP and PIP joints.

of the joint to allow finger flexion (Figure 3C). The proximal edge of $Soft_1$ was assigned to the PPC, which is more proximal than the MCP joint by the radius of the MCP joint (r_M) for all users. The position of

$Soft_2$ was determined by considering the slip occurrence between the beam and fingers during MCP flexion. The beam slips with respect to the fingers (Figure 3D) during MCP flexion. Thus, the proximal edge

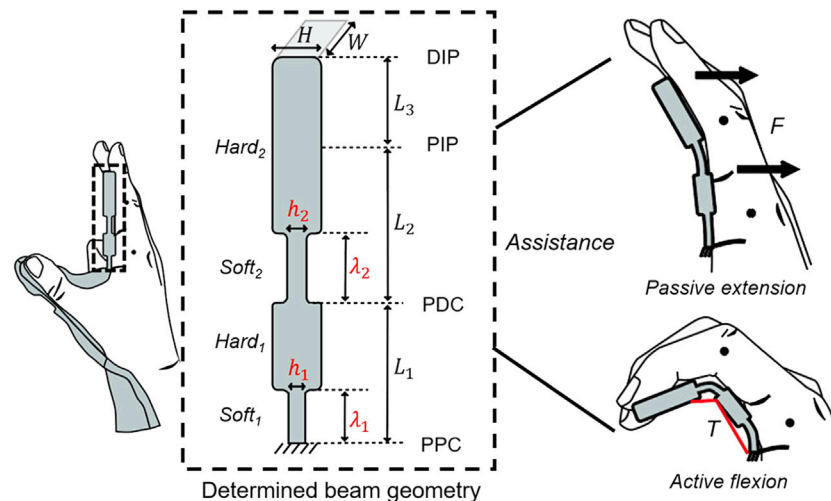


FIGURE 4

Determined beam geometry consisting of two soft regions ($Soft_1$ and $Soft_2$) and hard regions ($Hard_1$ and $Hard_2$) under the geometric constraints. The stiffness of the soft regions is determined by the design variables ($h_1, h_2, \lambda_1, \lambda_2$) calculated via stiffness optimization. The other variables are set when the anthropometric dimensions of individual hands are measured.

of $Soft_2$ was set to be more proximal than the PIP joint by a length that is greater than the sum (L_{const2}) of the slip distance (L_{slip}) and radius of the PIP joint (r_p). Because 35° of MCP flexion has been reported to occur during tripod grasping (Park et al., 2014), L_{const2} that occurs during MCP flexion was used as a geometric constraint for $Soft_2$, and it can be calculated as follows:

$$\begin{aligned}
 L_{const2} &= L_{slip} + r_p \\
 &\approx \left(A + r_M \tan\left(\frac{35^\circ}{2}\right) \right) \\
 &\quad - \left(A - r_M \tan\left(\frac{35^\circ}{2}\right) \right) + r_p \\
 &= 2r_M \tan\left(\frac{35^\circ}{2}\right) + r_p
 \end{aligned} \quad (1)$$

A (Figure 3D) is the length between the distal interphalangeal (DIP) and MCP joints at full extension. r_M and r_p are the radii of the MCP and PIP joints, respectively. The proximal edge of $Soft_2$ was set to the PDC considered to be more proximal than the PIP joint by length greater than the L_{const2} (An et al., 1983; Buryanov and Kotiuk, 2010). Thus, the determined beam geometry comprises two soft regions ($Soft_1$ and $Soft_2$) and two hard regions ($Hard_1$ and $Hard_2$) at predefined locations to allow bidirectional finger movement.

The stiffness can be adjusted by changing the thickness along the beam (Figure 4). The stiffness of $Soft_1$ and $Soft_2$ is determined by design variables ($\lambda_1, \lambda_2, h_1, h_2$), where λ_1, λ_2 and h_1, h_2 are the longitudinal length and thickness of the soft regions, respectively, and are determined via stiffness optimization to achieve sufficient grip aperture in the pre-grasping phase and minimal assistive force in the grasping phase. The other variables (L_1, L_2, L_3, W , and H) are determined as per the measured anthropometric dimensions of an individual hand. In particular, L_1, L_2 , and L_3 are the lengths between the PPC and PDC, PDC and PIP, and PIP and DIP, respectively. W is the width of the index and middle fingers. H is the thickness of the hard regions. To ensure high

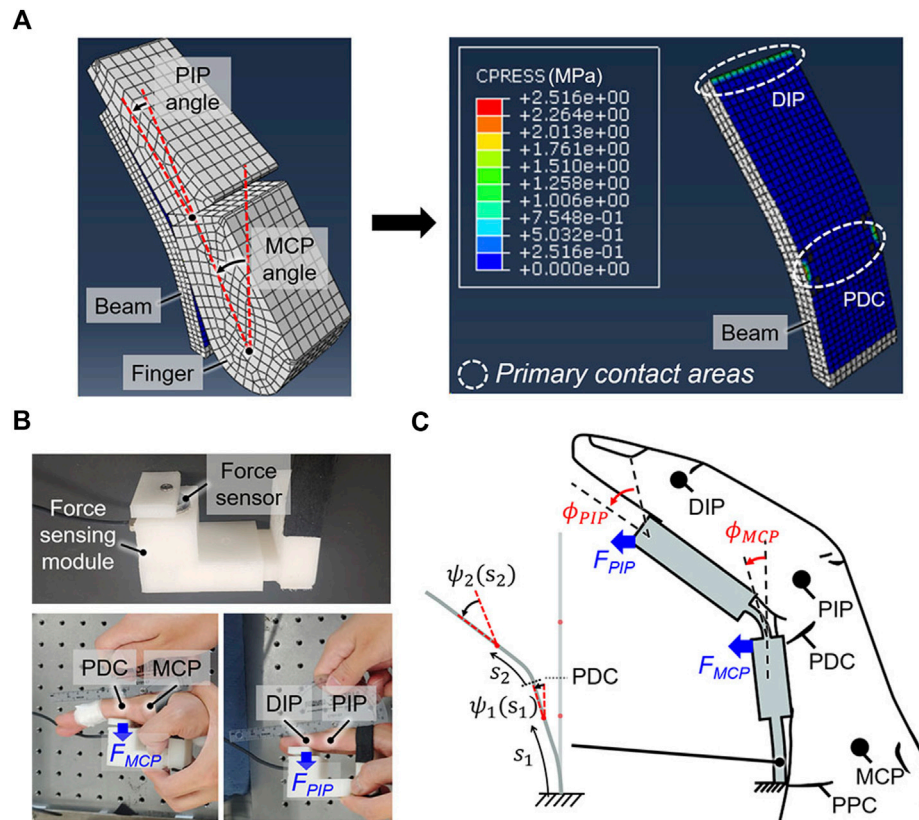
stiffness in the hard regions and the applicability of the Euler–Bernoulli theory, H is set so that the aspect ratio of the entire beam slightly exceeds 10. As geometric constraints, the distal edge of $Soft_1$ should be more proximal than PDC ($\lambda_1 < L_1$), and the distal edge of $Soft_2$ should be more proximal than PIP joint ($\lambda_2 < L_2$). The routing structures are positioned along the PPC, PDC, and PIP joint to deflect each of $Soft_1$ and $Soft_2$ under the assistive force.

2.3 Stiffness optimization

There exists a tradeoff between an achievable grip aperture and grip strength because an increase in the spatial stiffness leads to an increase in the grip aperture and required assistive force for grasping. The stiffness optimization enables the orthosis to achieve a target grip aperture in the pre-grasping phase while minimizing the required assistive force in the grasping phase. It would enable the orthosis to grasp common objects with increased grip strength by a given small-sized motor. Because stroke survivors have different joint characteristics (Kim et al., 2019) such as degree of spasticity, the stiffness should be optimized as per the measurements of individual hand parameters. Otherwise, the spatial stiffness distribution that is equally designed for all stroke survivors may result in a limited grip aperture for users with a severe degree of spasticity and or require an unnecessarily large amount of assistive force for users with flaccid hands. The stiffness optimization process has two steps: obtaining stiffness solutions that can achieve the target grip aperture and identifying the optimal solution that requires a minimal assistive force.

2.3.1 Stiffness solutions for passive extension

Before determining the stiffness of $Soft_1$ and $Soft_2$, the relevant individual hand parameters should be measured. The anthropometric dimensions of the hand are the primary parameters. In this study, the dimensions were measured using a goniometer (Model 12-1012, Baseline®, Fabrication Enterprises, Inc. NY, United States), and

**FIGURE 5**

Obtaining the stiffness solutions of the beam to achieve passive extension. (A) The contact pressure is concentrated at the primary contact areas, which are located near the PDC and DIP when the finger is flexed against the beam to achieve a target grip aperture of 80 mm. (B) The joint resistive forces (F_{MCP} , F_{PIP}) at the primary contact areas, which are respectively applied to extend the MCP and PIP joints, were measured using a force sensor. (C) Calculating the stiffness solutions for which the beam deflection angles (ψ_1 , ψ_2) at the primary contact areas equal the individually measured joint angles (ϕ_{MCP} , ϕ_{PIP}) for yielding an 80-mm grip aperture. The stiffness solutions were obtained based on the coordinates (s_1 , s_2) of each beam segment, which were divided by the position of the PDC.

they are used to determine L_1 , L_2 , L_3 , W , and H of the beam. Because finger contracture made it difficult to measure the affected hand, the dimensions were measured for the unaffected hand assuming the symmetry of both hands (Kulaksiz and Gözil, 2002). The joint angles that yield the target grip aperture of 80-mm (ϕ_{MCP} and ϕ_{PIP}) are the secondary parameters. The target joint angles that should be maintained are used to determine the stiffness of $Soft_1$ and $Soft_2$. Because the joint angles differ among individuals because of the dissimilar hand size, the joint angles should be measured for each user and then be used to set constraints in determining the stiffness of $Soft_1$ and $Soft_2$. The joint angles were measured using the goniometer as a user grasps an 80-mm-diameter cylinder with their unaffected hand. The force applied to the beam by the fingers (i.e., joint resistive force) deflects $Soft_1$ and $Soft_2$ and decreases the grip aperture. This joint resistive force should be known to determine the necessary stiffness for $Soft_1$ and $Soft_2$ to achieve passive extension. Thus, the joint resistive force is the tertiary parameter. Because the joint resistive force differs depending on the degree of spasticity, it should be measured for each user.

Before measuring the force, the location where the force is applied was obtained by static analysis under the condition that the finger and beam contact each other. In this study, finite element analysis (FEA) was used using ABAQUS (6.14, Dassault Systèmes Simulia Corp. Providence, RI, United States) for static analysis. An

individual hand-beam model was developed (Figure 5A) that uses the measured dimensions of the index finger and position of the center of the joint rotation. The kinematics of the middle finger was assumed the same as that of the index finger for simplicity. The beam comprises two soft regions and two hard regions as per geometric constraints. Three longitudinal lengths (i.e., min, mid, and max) were used for each soft region of the beam. Because there is no thickness information for the beam, a constant thickness that satisfies the aspect ratio criterion was used for the entire beam. The hard regions were modeled to be rigid by applying kinematic constraints. A dynamic flexural modulus of 46.49 MPa was applied to the beam; this value was measured for TPU by operating a three-point bending test system (DTS Company, Menlo Park, CA, United States) at a strain rate of 0.1/s. The TPU was modeled as an elastic material because the TPU showed a linear stress-strain curve at low strain regions occurred during the active flexion. The modeled finger was flexed based on the individually measured joint angles, and it was found that the contact pressure is concentrated near the PDC and DIP joint (i.e., primary contact areas). Thus, the joint resistive forces were assumed to concentrate at positions of the PDC and DIP joint.

The joint resistive forces (F_{MCP} and F_{PIP}) for the user were measured based on the positions of primary contact areas (Figure 5B). In this study, a force-sensing module containing a

force sensor (KTOYO 247SA, KTOYO, Ltd. Uijeongbu, South Korea) was used for measurements. The user sits in a chair that is adjusted such that the base of the sternum is approximately parallel to the tabletop. The user then rests their affected arm on the table and extends the elbow as much as possible. The wrist is externally maintained in a neutral posture by the experimenter, and a force sensor at the position of the PDC (i.e., primary contact area) of the index finger to maintain fully extended MCP joint is used to measure F_{MCP} . The PIP joints are taped to prevent fingertips from touching the force-sensing module. A force sensor at the position of the DIP joint (i.e., primary contact area) of the index finger to maintain fully extended PIP joint is used to measure F_{PIP} . For this measurement, the experimenter externally holds the MCP joints in full extension. During the measurement, the force was nearly constant when the spastic response occurred right after the extension settled down. To eliminate the contribution of the spastic response immediately after movement, the force was measured for 1 min, and the average force over the last 10 s is considered as F_{MCP} or F_{PIP} .

The measured hand parameters are used to obtain the stiffness of $Soft_1$ and $Soft_2$ such that the beam can maintain the required joint angles against the joint resistive forces. The beam can be divided into two segments as per the position of the PDC. Thereafter, h_1 and h_2 were calculated with respect to λ_1 and λ_2 as follows, respectively (Beléndez et al., 2005):

$$\begin{aligned} \frac{d^2\psi_1}{ds_1^2} &= \frac{12}{EWh(s_1)^3} (-(F_{MCP} + F_{PIP}) \cos(\psi_1)) \\ \text{B.C}_1: \psi_1(0) &= 0 \\ \psi_1(L_1) &= \phi_{MCP} \text{ and } M_1(L_1) = M_2(0) \\ \frac{d^2\psi_2}{ds_2^2} &= \frac{12}{EWh(s_2)^3} - (F_{PIP} \cos(\psi_1 + \phi_{MCP})) \\ \text{B.C}_2: \psi_2(0) &= 0 \\ \psi_2(L_2 + L_3) &= \phi_{PIP} \text{ and } M_2(L_2 + L_3) = 0 \end{aligned} \quad (2)$$

where $\psi_1(s_1)$ and $\psi_2(s_2)$ are the beam deflection angles at s_1 and s_2 , which are the arc lengths between the fixed end and a point on the corresponding segment (Figure 5C). $h(s_1)$ and $h(s_2)$ are the thickness at s_1 and s_2 . M_1 , M_2 , and E are the corresponding bending moments and Young's modulus. The beam stiffness should be set to ensure a grip aperture of 80 mm. The difference between the beam deflection angles and joint angles at the primary contact areas is $< 2.95^\circ$ on average (Figure 5A). Thus, the boundary conditions (B.C₁ and B.C₂) were set to make the beam deflection angles at the primary contact areas equal to the individually measured joint angles (ϕ_{MCP} and ϕ_{PIP}). $Hard_1$ and $Hard_2$ were assumed to be sufficiently stiff to ensure that any changes in $\psi_1(s_1)$ and $\psi_2(s_2)$ are negligible. In this study, MATLAB (2018a, MathWorks Inc. Natick, MA, United States) was used to calculate h_1 and h_2 based on λ_1 and λ_2 , which are pre-set to change in increments of 1 mm within the geometric constraints. Then, stiffness solutions that satisfy Eq. 2 can be obtained.

The Young's modulus of TPU was measured under the condition of a quasi-static strain rate (0.0021/s) using a high-precision micromechanical test system (DTS Co., Menlo Park, CA, United States). This measured Young's modulus (22.35 MPa) was used as E in Eq. 2 and associated with the target deflection required to maintain a grip aperture of 80 mm. In particular, the beam deflection was designed such that it would approach the target deflection over time because of creep. The creep-induced beam deflection was

considered to ensure that the grip aperture asymptotically converged to 80 mm during the wearing period.

The spasticity of the flexor muscles can change over time and made it difficult to guarantee that the beam, which has fixed spatial stiffness distribution, would maintain the target grip aperture. A grip aperture less than the target of 80 mm would present a challenge in positioning common objects within the hand for grasping in the pre-grasping phase. Thus, a safety factor was applied to the degree of spatial stiffness; the spatial stiffness distribution was designed to achieve the target grip aperture against maximal joint resistive forces. The joint resistive forces are greatest when the fingers are fully extended. Thus, the maximal joint resistive forces statically measured at the fully extended posture (F_{MCP} and F_{PIP}) were used in Eq. 2 to find the stiffness solutions.

2.3.2 Optimizing the stiffness for active flexion

To identify the optimal solution that requires a minimal assistive force for active flexion among the stiffness solutions, the amount of beam deflection required to emulate the tripod grasp (i.e., target grasp type) should be determined first. The ROMs of finger joints during a tripod grasp were used to determine the required beam deflection. The ROMs were measured during tripod grasping tasks using the unaffected hand (Figure 6A). In this study, the average results from three trials were recorded. Reflective markers were placed atop the fingertip, metacarpal, MCP, PIP, and DIP joints of the index finger to enable motion analysis with a motion capture system (OptiTrack V120: Trio, NaturalPoint, Inc. Corvallis, OR, United States). Principal component analysis was then applied to the 3D trajectory data of the reflective markers to identify the planes of flexion/extension movements. The 3D trajectory data was projected on the plane of flexion/extension, and the joint angles were calculated based on the projected trajectory data for relieving the influence of the abduction/adduction movement (Randazzo et al., 2017). Because the determined beam geometry allows finger flexion under beam deflection, the target beam deflection angles at hard regions were assumed the measured ROMs for assisting fingers with tripod grasping.

In this study, FEA was used to simulate the active flexion of stiffness solutions to obtain the relationship between beam deflection angles (ψ_{MCP} , ψ_{PIP}) and assistive forces (T_1 , T_2) (Figure 6B). The beam as per the stiffness solutions was used for the simulations. Each beam was divided in two segments (Seg 1 and Seg 2) as per the position of the PDC, where the routing structure was located. The relationships were obtained for each beam segment because the assistive force in Seg 2 does not generate a moment in Seg 1. For the simulation, the assistive force was applied at the positions of the routing structures, and the beam segments were meshed with C3D20 elements and subjected to the dynamic flexural modulus (46.49 MPa). Plastic deformation resulting from active flexion was not considered because the plastic strain was expected to be small owing to the thinness of the beam.

The measured ROMs and relationships were used to determine the optimal solution that achieves the tripod grasp with the minimal assistive force. The ROM measurement results for the MCP and PIP joints were set as the targeted beam deflection angles of each segment for calculating T_1 and T_2 . In particular, T_1 and T_2 that yield ψ_{MCP} and ψ_{PIP} corresponding to the ROMs were calculated for each stiffness solution based on the relationships shown in Figure 6B. The calculated T_1 and T_2 were then used to identify the optimal solution that required the minimal assistive force among the stiffness solutions (represented as λ_1 and λ_2 in Figure 6C).

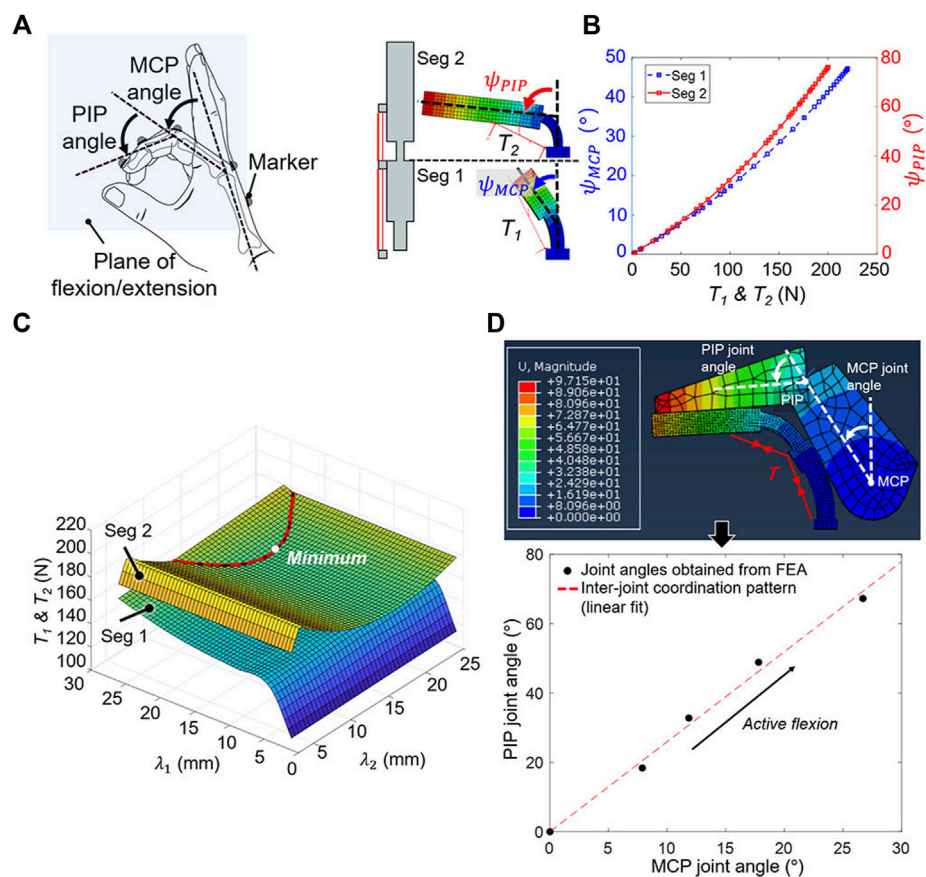


FIGURE 6 Finding the optimal solution among stiffness solutions that minimizes the assistive force for active flexion. **(A)** The MCP and PIP joint ROMs of the unaffected hand during tripod grasping were measured by capturing the 3D trajectories of the reflective markers. **(B)** The relationship between the assistive force (T_1, T_2) and beam deflection angle (ψ_{MCP}, ψ_{PIP}) was obtained via FEA of each beam segment (Seg 1, Seg 2) of the stiffness solutions, where the segment was divided by the position of the PDC. **(C)** The assistive force that yields the same beam deflection angles as the ROM measurements was calculated for the stiffness solutions. The optimal stiffness solution required minimal assistive force. λ_1, λ_2 represent the longitudinal lengths of the soft regions of the stiffness solutions. **(D)** An individual hand-beam model was deflected under the assistive force (T), and finger joint angles when the finger makes contact with the beam were obtained.

TABLE 1 Stroke participant demographics and beam profiles.

Participant number	Months post-stroke	MAS	Aff/Dom hand	Gender	Age (yrs)	F_{MCP} (N)	F_{PIP} (N)	h_1/λ_1 (mm/mm)	h_2/λ_2 (mm/mm)	W (mm)
P1	95	2	R/R	F	52	1.55	0.88	3.45/16.0	2.73/12.3	40
P2	568	0	L/R	F	67	0.33	0.16	1.54/21.0	1.11/12.5	42
P3	237	0	L/R	F	69	0.28	0.47	2.23/15.4	1.64/8.9	40
P4	288	1+	R/R	M	61	0.84	1.33	2.66/7.2	3.25/14.1	43
P5	86	1	R/R	M	59	0.17	0.84	2.60/17.0	1.74/10.3	42
P6	131	2	L/R	M	63	0.54	1.79	2.97/10.6	2.66/17.8	40
P7	146	1+	L/R	F	61	0.73	0.73	2.82/18.0	1.50/4.0	38
P8	109	1	R/R	F	66	0.18	0.39	2.10/19.0	1.16/5.3	35
P9	104	1+	L/R	F	77	0.99	0.93	3.11/21.0	1.64/6.3	40
P10	69	3	L/R	M	70	4.62	6.95	5.95/19.9	4.71/16.8	43

Ten chronic stroke participants with different hand anthropometric dimensions and degrees of spasticity were recruited.
* F_{MCP} , F_{PIP} , denote joint resistive forces and $h_1, h_2, \lambda_1, \lambda_2, W$ denote dimensions of the beam (thickness, longitudinal length, and width).

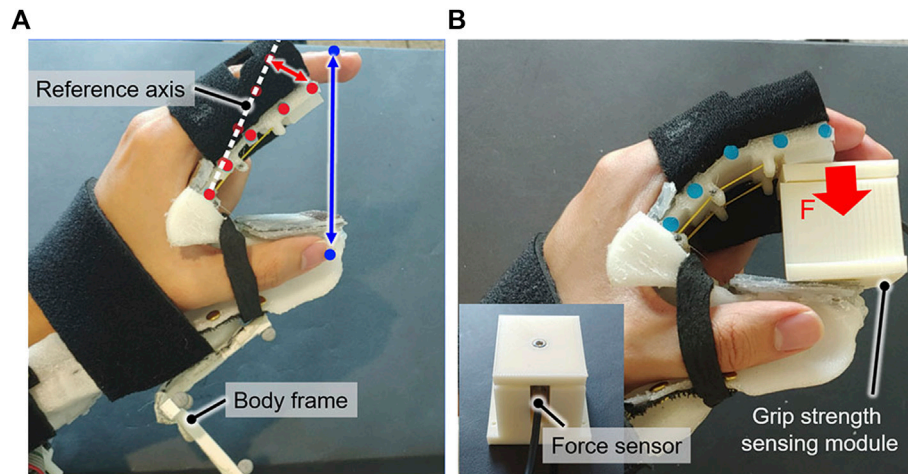


FIGURE 7

Experimental setup for evaluating the orthosis. (A) The beam deflection at the tip (red arrow) and grip aperture (blue arrow) were measured by tracking reflective markers, which were attached to the upward-facing side of the beam (red dot) and fingertips (blue dot). The beam deflection was measured with respect to the reference axis, which was determined based on the markers prior to the orthosis being worn. (B) The grip strength of the orthosis was measured using a grip strength-sensing module under an applied assistive force.

The finger joint angles during active flexion were obtained using an individual hand-beam model. For the model, the optimal solution was used for the beam, and measured dimensions were used for the hand (Figure 6D). The beam was deflected under the assistive force (T), and finger joint angles when the finger makes contact with the beam were calculated. It was confirmed that the PIP joint angle increased linearly with respect to the MCP joint angle, and this inter-joint coordination pattern of the joint angles was obtained to check whether finger joint angles of users increase in accordance with the obtained inter-joint coordination pattern during assistance.

2.4 Experimental evaluation

2.4.1 Participant recruitment

Ten stroke survivors having varying degrees of spasticity were recruited (Table 1) to evaluate the performance of the proposed orthosis at assisting with grasping tasks. The recruited participants were in the chronic stage with limited voluntary ROM. They could follow instructions and had no severe risk of skin breakdown for safety. The participants who scored a MAS grade of four were excluded because passive movement is physically difficult. Moreover, the participants with botulinum toxin type A injection were excluded because the injection can affect the degree of spasticity. The orthosis was personalized as per individuals and 3D-printed. Because the required assistive force for grasping increases as the stiffness of the orthosis increases, the motor that can actively flex the orthosis having the highest stiffness was selected and used for all orthoses to ease the design. The research was approved by the Institutional Review Board of KAIST (KH2020-59, 04/07/2020), and written consent was obtained from each participant after the experiment was explained.

2.4.2 Evaluation criteria

The following criteria were used to evaluate the performance of the proposed orthosis design.

- 1) Beam deflection and grip aperture: The beam deflection was measured to confirm whether it was equal to the target deflection. The target deflection was obtained using FEA by applying the maximal joint resistive force to the beam having the measured Young's modulus. The increase in the deflection of the distal end of the beam was used (Figure 7A) to determine whether the beam is deflected closed to the target deflection to yield the target grip aperture. It was measured immediately after being donned by tracking five reflective markers that were positioned along the upward-facing side of the beam. Because it has been reported that no significant plastic deformation occurs after four cycles of active flexion (Qi and Boyce, 2005), the beam deflection was measured again after four repetitions of active flexion. The grip aperture was measured based on markers attached to the index fingertip and thumb tip to verify whether it achieved the target grip aperture of 80 mm.
- 2) ROM measurement: The ROMs for the MCP and PIP joints of the index finger were measured before and after the orthosis was applied to the affected hand. Reflective markers were placed atop the metacarpal, MCP, PIP, and DIP joints and the fingertip of the index finger for tracking, and joint angles were obtained based on the 3D trajectory data of the markers. The voluntary ROM (i.e., $ROM_{voluntary}$), for which participants flexed their fingers to achieve a closed-hand posture from the maximal extended posture, was calculated from a single trial. The assisted ROM (i.e., $ROM_{assisted}$) was calculated from a single trial when the beam was deflected until contact was made with the thumb module. The increase in ROM (i.e., ΔROM_{total}) was calculated as follows:

$$\begin{aligned}\Delta ROM_{total} &= \Delta ROM_{MCP} + \Delta ROM_{PIP} \\ &= ROM_{assisted} - ROM_{voluntary} \\ \Delta \theta &= \theta_{voluntary} - \theta_{assisted}\end{aligned}\quad (3)$$

where ΔROM_{MCP} and ΔROM_{PIP} are the increases in the ROMs of the MCP and PIP joints, respectively. The increase in joint extension (i.e., $\Delta \theta$) was obtained, where $\theta_{voluntary}$ and $\theta_{assisted}$ are the maximal unassisted and assisted extension angles, respectively.

- 3) Grasp performance: The maximum grip strength with the orthosis, in addition to the ability of the orthosis to grasp various objects, were evaluated. The objects applied for this test were selected based on the previous study (Kang et al., 2016), and they were as follows: a glass cup, baseball, stapler, golf ball, banana, and rectangular battery. The maximum grip strength was measured at the angle limit of the motor when the participant grasped a rectangular 40-mm-height (i.e., 50% of the target grip aperture) grip strength-sensing module without any voluntary force. For this measurement, the motor was rotated until the angle limit regardless of the grip strength measured by the FSR sensor. The force sensor (KTOYO 247SA, KTOYO, Ltd. Uijeongbu, South Korea) was embedded in the grip strength-sensing module (Figure 7B).
- 4) Functional assessment and questionnaire: Each participant was instructed to perform nine ADL tasks from the Chedoke Arm and Hand Activity Inventory (CAHAI)-9 (Barreca et al., 2004) to evaluate the assistive performance of the orthosis with grasping tasks. All nine tasks were bimanual activities: 1) opening a jar of coffee, 2) dialing an emergency number, 3) drawing a line with a ruler, 4) pouring a glass of water, 5) wringing out a washcloth, 6) fastening five buttons, 7) drying the back with a towel, 8) putting toothpaste on a toothbrush, and 9) cutting medium-resistance putty. The performance of each ADL task was evaluated on a scale of 1–7 by the experimenter according to the CAHAI-9 criteria (Jane Rowland et al., 2011). Both hands were positioned on the table, and the participants were instructed to refrain from placing their elbows on the table. Because the participants lacked fine control of the affected arm, it was supported by a gravity compensator and experimenter. The participants first performed all nine tasks without the orthosis. After a 5 min break, they repeated tasks with the orthosis under the same environmental conditions. The performance improvement was quantitatively evaluated by comparing the scores with and without the orthosis. After conducting the functional assessment, the participants were asked to answer a questionnaire comprising 1) the weight of the orthosis is manageable, 2) the assistance of the orthosis is satisfactory, and 3) the orthosis is comfortable while using. The questions were determined based on the orthotics and prosthetics user's survey (OPUS) (Heinemann et al., 2003). The satisfaction of the participants was ranked from one to five, in which the value increases with higher satisfaction.

3 Results

3.1 Beam deflection and grip aperture

The beam deflection was less than the target deflection, thereby yielding a grip aperture larger than the target grip aperture of 80 mm. The distal end of the beam deflected by 12.17 ± 10.00 mm immediately after donning, generating the grip aperture of 94.26 ± 10.73 mm. This measured deflection was less than the target deflection of 40.08 ± 7.37 mm primarily owing to viscosity of the TPU. Because of creep occurred after donning and plastic deformation by active flexion, the beam deflection increased by 9.38 ± 5.48 mm after

four repetitions of active flexion, which corresponded to an average decrease of 6.74 mm for the grip aperture. Nonetheless, the measured beam deflection of 21.54 ± 9.36 mm still did not equal to the target deflection of 40.08 ± 7.37 mm, yielding a grip aperture of 87.52 ± 6.40 mm. The error for the beam deflection would be because of the safety factor considered in designing the stiffness of the beam. The beam stiffness was set to yield the target grip aperture against the maximal joint resistive force; however, fingers would apply force less than the maximal joint resistive force on the beam. This would primarily make the measured deflection be less than the target deflection, which led to increase in the grip aperture.

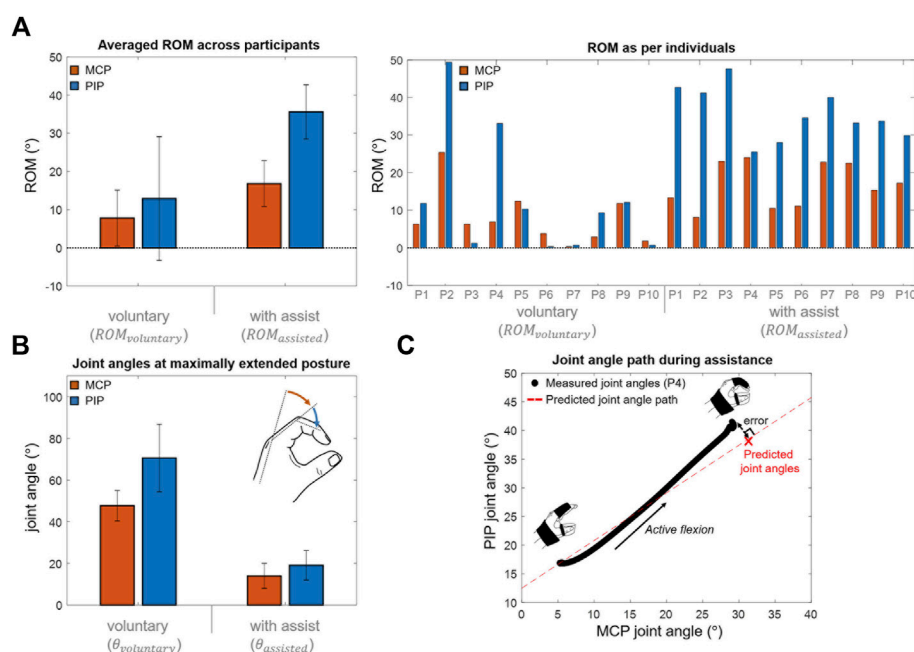
3.2 ROM measurement

The orthosis effectively assisted the finger joints for all participants (Figures 8A, B). All participants demonstrated a limited voluntary ROM of 20.7° on an average because of spastic finger joints. They were only able to flex their fingers from a neutral posture to a closed-hand posture. Although the orthosis-enabled finger flexion was limited by the thumb module, the orthosis increased the joint ROM by $31.7^\circ \pm 26.6^\circ$. Note that the finger flexion was not restricted by the thumb when the voluntary ROM was measured. The ROMs of the MCP and PIP joints were increased by $9.0^\circ \pm 12.1^\circ$ and $22.8^\circ \pm 18.2^\circ$, respectively. Moreover, the orthosis provided passive assistance to yield a maximal assisted extension angle of $33.2^\circ \pm 12.0^\circ$; the fingers were significantly more extended compared to the maximal voluntary extension (maximal unassisted extension angle of $118.2^\circ \pm 25.8^\circ$).

The finger joint angles increase in accordance with the inter-joint coordination pattern obtained by the individual hand-beam model. The “Measured joint angles” in Figure 8C was obtained based on the measurement results during active flexion. The “Predicted joint angle path” in Figure 8C was obtained by increasing joint angles from the maximal assisted extension posture according to the inter-joint coordination pattern. It was confirmed that the joint angles increase in accordance with the inter-joint coordination pattern. The error between the joint angles at maximal flexed posture and predicted joint angles were $4.9^\circ \pm 2.9^\circ$ which were respectively $4.3^\circ \pm 2.6^\circ$ in the MCP joint and $2.2^\circ \pm 1.4^\circ$ in the PIP joint. The joint resistive force was not considered in the hand-beam model to obtain the inter-joint coordination pattern, and it would result in the error which was only 9.3% of assisted joint ROM on average. The inter-joint coordination of the MCP and PIP joints during assistance can be controlled by spatial stiffness distribution design.

3.3 Grasp performance

All participants could grasp each object with the orthosis. Furthermore, they were able to establish contact between their fingertips and large-size objects (i.e., the glass cup and baseball). However, the large slip between the fingers and beam prevented the fingertips from contacting the small-size objects (i.e., banana, stapler, golf ball, and battery). The maximum grip strength was

**FIGURE 8**

Experimental results. **(A)** Averaged ROM across participants during voluntary and assisted flexions (mean difference of MCP and PIP joint ROMs = 9.0°, 22.8°; paired t-test, $p = 0.0427$, 0.0033) and the ROM of individuals. **(B)** Averaged joint angles across participants at maximally extended posture without and with assistance (mean difference of MCP and PIP joint angles = 33.6°, 51.4°; paired t-test, $p = 2.1e-5$, 3.1e-5). **(C)** The measured joint angle path during active flexion. The finger joint angles increased in accordance with the inter-joint coordination pattern obtained from the individual hand-beam model. The "Measured joint angles" was obtained from 3D trajectories of markers attached on the finger. The "Predicted joint angle path" was obtained by increasing joint angles from the maximal assisted extension posture according to the calculated inter-joint coordination pattern.

TABLE 2 Characteristics of active hand orthoses.

Device	Actuators	Number of actuators	Number of assisted fingers	Weight (orthosis/total)	Maximum grip strength	Maximum grip strength/Total weight
Hand of Hope (Ho et al., 2011)	motors, cable-driven	5	5	700 g/n/a	12 N (pinch)	n/a
Yap et al., 2018	pneumatic, fabric-reinforced	5	5	180 g/1260 g	36.2 N (power)	0.029 N/g
Nycz et al., 2016	motors, cable-driven	4	4	113 g/867 g	8.7 N (pinch)	0.01 N/g
Graspy-Glove (Popov et al., 2017)	motors, cable-driven	4	4	250g/340 g	16 N (pinch)	0.047 N/g
Ryu et al., 2008	hydraulics, cable-driven	3	3	2,620 g/2,740 g	12 N (pinch)	0.004 N/g
SNU Exo-Glove (In et al., 2015)	motors, cable-driven	3	3	194 g/n/a	20 N (pinch)	n/a
HERO grip glove (Yurkewich et al., 2020)	motor, cable-driven	2	5	n/a/284 g	11.0 N (pinch)	0.039 N/g
HERO glove (Yurkewich et al., 2019)	motor, cable-driven	1	5	n/a/192 g	0 N (pinch)	0 N/g
Proposed orthosis (this paper)	motor, cable-driven	1	3	259g/454 g	26.27 N (pinch)	0.058 N/g

TABLE 3 Task-based functional assessment results.

Participant number	Task 1	Task 2	Task 3	Task 4	Task 5	Task 6	Task 7	Task 8	Task 9	Total score	Performance improvement
P1	2/4	1/1	2/4	1/4	2/4	1/1	2/4	2/3	2/1	15/26	11
P2	1/4	1/1	1/4	1/4	2/4	1/1	1/4	2/3	1/1	11/26	15
P3	1/4	1/1	1/4	1/4	1/4	1/1	1/4	2/3	1/1	10/26	16
P4	2/4	1/1	1/4	2/4	2/4	1/1	1/4	2/3	1/1	13/26	13
P5	1/4	1/1	2/4	1/4	2/4	1/1	2/4	2/3	1/1	13/26	13
P6	1/4	1/1	2/4	1/4	2/4	1/1	1/4	2/3	1/1	12/26	14
P7	1/4	1/1	1/4	1/4	1/4	1/1	1/4	1/3	1/1	9/26	17
P8	1/4	1/1	1/4	1/4	1/4	1/1	1/4	2/3	1/1	10/26	16
P9	1/4	1/1	2/4	1/4	2/4	1/1	1/4	2/3	1/1	12/26	14
P10	1/4	1/1	2/4	1/4	2/4	1/2	1/4	2/3	1/1	12/27	15
Mean (SD)											14.40 (1.78) $p = 1.01\text{e-}09$

ADL, performance (without orthosis/with orthosis) was quantitatively scored based on the criteria for the CAHAI-9, clinical test. Task 1-9 are respectively opening a jar of coffee, dialing an emergency number, drawing a line with a ruler, pouring a glass of water, wringing out a washcloth, fastening five buttons, drying the back with a towel, putting toothpaste on a toothbrush, and cutting medium-resistance putty. The p -value was calculated using a paired t-test.

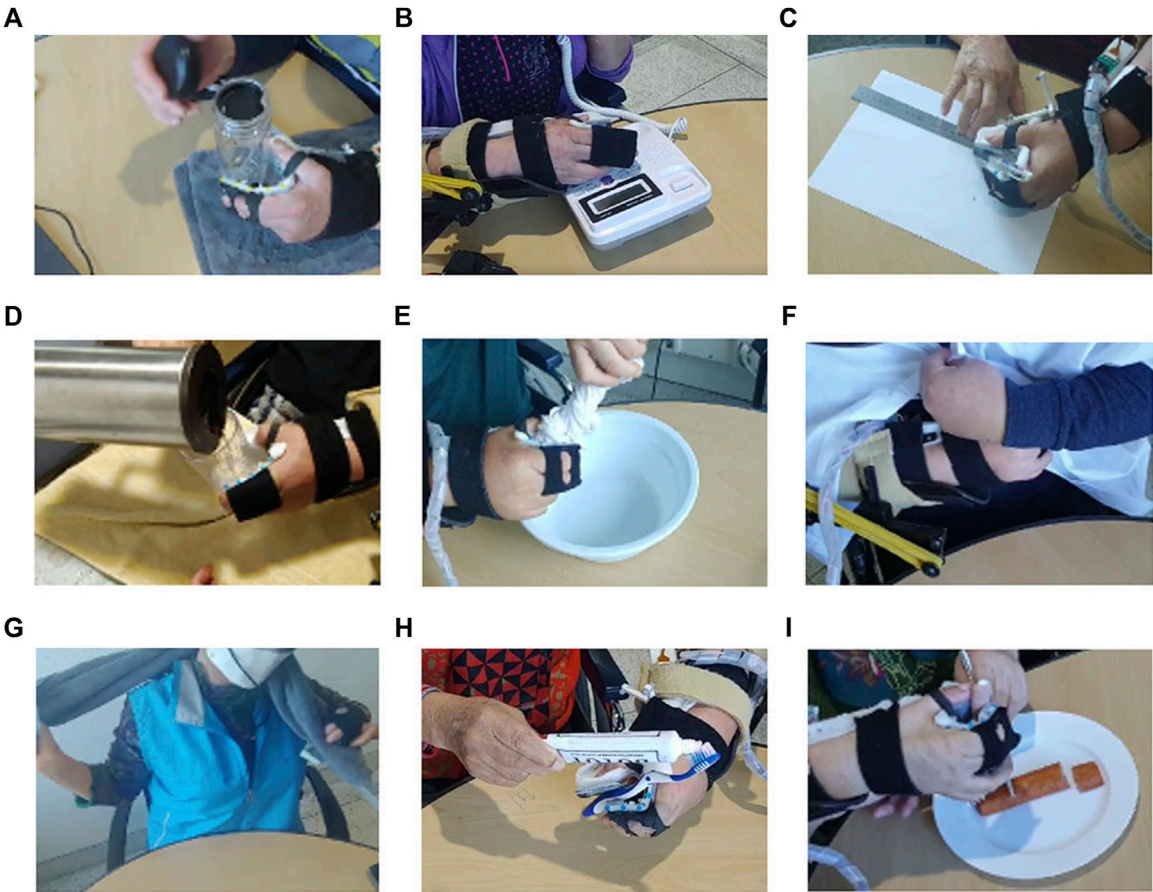


FIGURE 9
Tasks 1–9 from the Chedoke Arm Hand Activity Inventory (CAHAI)-9. **(A)** Task 1: Opening a jar of coffee. **(B)** Task 2: Dialing an emergency number. **(C)** Task 3: Drawing a line with a ruler. **(D)** Task 4: Pouring a glass of water. **(E)** Task 5: Wringing out a washcloth. **(F)** Task 6: fastening five buttons, **(G)** Task 7: Drying the back with a towel. **(H)** Task 8: Putting toothpaste on a toothbrush. **(I)** Task 9: Cutting medium-resistance putty.

measured as 26.27 ± 3.90 N, and the orthosis showed a high grip strength-to-weight ratio (Table 2).

3.4 Functional assessment and questionnaire

The results of the CAHAI-9 tasks (Table 3) demonstrated that all participants had difficulty without the orthosis owing to contracture and low grip strength. The score of one or two was assigned for all tasks because participants do not voluntarily show any manipulation of the affected hand. With orthosis, all participants were able to complete the tasks except for tasks 2, 6, and 9 with only arm support and cueing (Figure 9). The orthosis increased the grip aperture and grip strength of participants to improve their performance of most tasks (score increase: 14.40 ± 1.78). To precisely locate targeted objects along the beam for grasping, the unaffected hand was used for positioning because the orthosis cannot assist with in-hand and upper-limb manipulations. Nonetheless, with only the passive assistance of the arm, the orthosis enabled the participants to independently accomplish bimanual tasks by stably holding targeted objects with the affected hand. Specifically, for task 1, they could open a lid of the jar using the unaffected hand because the affected hand could hold a jar. For task 3, they could draw a line by grasping a pen with the affected hand while the unaffected hand is fixing the ruler. For task 4, participants held a glass cup using the affected hand while pouring water with the unaffected hand. For task 5, one side of a washcloth was held by the affected hand, and the unaffected hand wrung out a wash cloth. For task 7, one side of a towel was held by the affected hand, and the unaffected hand dried the back with a towel. Thus, stroke survivors were assigned score of four for these tasks because they can accomplish 100% of tasks with arm support. For task 8, although it was possible to hold a toothpaste using the affected hand to make the unaffected hand unscrew a lid, squeezing the toothpaste using only the affected hand was impossible with the control algorithm used for the orthosis. Thus, a score of three was assigned for task eight by considering that 50% of the task is accomplished. The orthosis could not provide adequate assistance in tasks 6 and 9 because the tripod grasp type was insufficient to manipulate the object. Task two was not completed because the participants were unable to prevent their ring and little fingers from pushing non-targeted buttons.

The participants answered that the device is sufficiently lightweight (score: 4.3 ± 0.7) and comfortable (score: 4.2 ± 0.5). Moreover, they were satisfied with the assistance of the orthosis (score: 4.3 ± 0.48).

4 Discussion

In this study, a personalized spatial stiffness distribution is presented for a portable and strengthful hand orthosis. The stiffness was optimized for each participant based on measurement of individual hand parameter to satisfy predetermined requirements for the orthosis: maintaining a minimum grip aperture of 80 mm and minimizing the assistive force needed to achieve flexion. The stiffness optimization of the passive elastic structure assists individuals with finger flexor spasticity to achieve the target grip aperture to grasp common objects while minimizing the antagonistic assistive force to

generate sufficient grip strength. The experimental results demonstrated that the orthosis achieves a high grip strength-to-weight ratio and weighs only 454 g, including all of the motor, electronics, and battery located at the hand and forearm. It was demonstrated that the strengthful all-in-one orthosis achieved by the spatial stiffness distribution design can assist participants with the bidirectional movement of the affected hand to grasp various objects and thus can aid with bimanual tasks for ADL.

The passive elastic structure enabled spastic finger joints to be extended even for a participant who has MAS grade of three. Previous orthoses (Lee et al., 2014; Nycz et al., 2016; Popov et al., 2017; Kim and Park, 2018; Yurkewich et al., 2020) assist with extension using cables as exotendons. However, for stroke survivors with a severe degree of spasticity, the tension applied by exotendons to assist with extension may apply a relatively large compressive force on the finger joints, which is a safety concern (Felson, 2013; Kim et al., 2019). The proposed orthosis includes a passive elastic structure that is positioned on the palmar aspect of the affected hand to eliminate the requirement for exotendons and increase the moment arms of the extending forces applied at finger joints. Participants replied that they did not feel any pain and discomfort during assisted finger joint extension. The passive elastic structure would enable the orthosis to assist finger extension against spastic finger joints with reduced joint compression.

The spatial stiffness distribution design of the orthosis significantly affects ROMs of finger joints during assistance. In this study, by adjusting the stiffness along the beam considering the slip between the fingers and beam, the limited increase in ROM during assistance is avoided. In particular, the hard region of beam can limit the ROM of the PIP joint when the slip during finger flexion is not considered in the spatial stiffness distribution design. The soft regions were respectively positioned close to the finger joints considering the slip, and their stiffness were adjusted to emulate the tripod grasp. The proposed design prevents the beam from blocking finger flexion and enables users to conduct tripod grasp. The proposed orthosis was demonstrated to increase the ROM of finger joints by an average of 31.7° , which is similar to that of a previous orthosis (i.e., 46.3°) (Yurkewich et al., 2019).

The results highlight the importance of a user-specific orthosis design. To maximize user compliance and increase grip strength through reduced actuator size and weight, orthosis was personalized for each participant based on the measurements of hand parameters. This was achieved by first considering the individual hand geometry. With the exception of the beam component, the passive elastic structure was designed based on the affected hand geometry generated by 3D scanning. All participants reported that the orthosis was comfortable. The second individualized characteristic that was considered was the joint resistive force, particularly for MCP and PIP joints. The spatial stiffness distribution was personalized based on measurement results of joint resistive force to ensure sufficient grip aperture and high enough grip strength, and it was shown that the orthosis can achieve grasping assistance with a high grip strength-to-weight ratio. The required motor size and weight for grasping assistance would be reduced by considering individual joint characteristics in the spatial stiffness distribution design.

The TSA mechanism was selected to improve the portability of the orthosis using its high contraction force-to-torque ratio and

mechanical simplicity. Owing to its characteristics, the actuating module adopting the TSA mechanism becomes compact in comparison with the other actuating modules such as soft fluidic actuators (Zhang et al., 2019). However, the TSA mechanism has the disadvantage of contraction length. It can maximally generate contraction length as 30% of its untwisted length, and this should be considered in hardware design. In this study, the motor was mounted at the forearm to provide the untwisted length required for generating contraction length to flex the orthosis.

The proposed orthosis does have limitations. First, the cable of the TSA mechanism can break during use. The cable breaks after being twisted several times (Palli et al., 2013), which may decrease the usability. Devising an easily replaceable cable module may solve this limitation. Second, the orthosis was unable to assist with two tasks from CAHAI-9 (i.e., cutting medium-resistance putty and fastening five buttons). This is because the single tripod grasp was insufficient to perform these tasks. In particular, the limited degrees of freedom of the orthosis ultimately hindered manipulation of the objects, which prevented it from assisting the participants with tasks requiring dexterous manipulation. For the putty-cutting task, the applied torque caused the fork to rotate when the participant attempted to pierce the putty. For button fastening, dexterous manipulation was required to pull holes in the cloth toward the buttons.

In this study, a personalized spatial stiffness distribution design is presented for a portable and strengthful hand orthosis to assist with grasping tasks. The objective was to design spatial stiffness distribution that can assist bidirectional finger movement with a sufficient grip aperture in the pre-grasping phase and high enough grip strength in the grasping phase. The orthosis includes a passive elastic structure with an individually optimized stiffness and a cable contracted by TSA mechanism using a single motor. In the experiment, the orthosis can assist with grasping tasks for ADL by providing a sufficient grip aperture and grip strength. The orthosis increased the grip aperture and grip strength of all participants, enabling successful grasping even by those with severe degrees of spasticity.

Data availability statement

The raw data supporting the conclusions of this article will be made available by the authors, without undue reservation.

References

- Aiple, M., and Schiele, A. (2013). Pushing the limits of the CyberGrasp™ for haptic rendering. *Proc. IEEE ICRA* 2013, 3541–3546. doi:10.1109/ICRA.2013.6631073
- Alicea, R., Xiloyannis, M., Chiaradia, D., Barsotti, M., Frisoli, A., and Masia, L. (2021). A soft, synergy-based robotic glove for grasping assistance. *Wearable Technol.* 2, e4. doi:10.1017/wtc.2021.3
- An, K.-N., Ueba, Y., Chao, E., Cooney, W., and Linscheid, R. (1983). Tendon excursion and moment arm of index finger muscles. *J. biomechanics* 16, 419–425. doi:10.1016/0021-9290(83)90074-X
- Arata, J., Ohmoto, K., Gassert, R., Lamercy, O., Fujimoto, H., and Wada, I. (2013). A new hand exoskeleton device for rehabilitation using a three-layered sliding spring mechanism. *Proc. IEEE ICRA* 2013, 3902–3907. doi:10.1109/ICRA.2013.6631126
- Ates, S., Haarman, C. J., and Stienen, A. H. (2017). SCRIPT passive orthosis: Design of interactive hand and wrist exoskeleton for rehabilitation at home after stroke. *Auton. Robots* 41, 711–723. doi:10.1007/s10514-016-9589-6
- Ates, S., Mora-Moreno, I., Wessels, M., and Stienen, A. H. (2015). Combined active wrist and hand orthosis for home use: Lessons learned. *Proc. ICORR* 2015, 398–403. doi:10.1109/ICORR.2015.7281232
- Barreca, S., Gowland, C. K., Stratford, P., Huijbregts, M., Griffiths, J., Torresin, W., et al. (2004). Development of the Chedoke arm and hand activity inventory: Theoretical constructs, item generation, and selection. *Top. Stroke Rehabil.* 11, 31–42. doi:10.1310/JU8P-UVK6-68VW-CF3W
- Bayona, N. A., Bitensky, J., Salter, K., and Teasell, R. (2005). The role of task-specific training in rehabilitation therapies. *Top. Stroke Rehabil.* 12, 58–65. doi:10.1310/BQM5-6YGB-MVJ5-WVCR

Ethics statement

The studies involving human participants were reviewed and approved by Institutional Review Board, Korea Advanced Institute of Science and Technology. The patients/participants provided their written informed consent to participate in this study. Written informed consent was obtained from the individual(s) for the publication of any potentially identifiable images or data included in this article.

Author contributions

All authors listed have made a substantial, direct, and intellectual contribution to the work and approved it for publication.

Funding

This work was supported by the National Research Foundation of Korea (NRF) grant funded by the Korea government (MSIT) (No. NRF-2020R1A2C2012641).

Conflict of interest

The authors declare that the research was conducted in the absence of any commercial or financial relationships that could be construed as a potential conflict of interest.

Publisher's note

All claims expressed in this article are solely those of the authors and do not necessarily represent those of their affiliated organizations, or those of the publisher, the editors and the reviewers. Any product that may be evaluated in this article, or claim that may be made by its manufacturer, is not guaranteed or endorsed by the publisher.

Supplementary material

The Supplementary Material for this article can be found online at: <https://www.frontiersin.org/articles/10.3389/fbioe.2023.895745/full#supplementary-material>

- Beléndez, T., Pérez-Polo, M., Neipp, C., and Beléndez, A. (2005). Numerical and experimental analysis of large deflections of cantilever beams under a combined load. *Phys. Scr.* 2005, 61. doi:10.1238/Physica.Topical.118a00061
- Borboni, A., Mor, M., and Faglia, R. (2016). Glove—Hand robotic rehabilitation: Design, mechanical model, and experiments. *J. Dyn. Syst. Meas. Control* 138, 111003–111015. doi:10.1115/1.4033831
- Burns, M. K., and Vinjamuri, R. (2020). “Design of a soft glove-based robotic hand exoskeleton with embedded synergies,” in *Advances in motor neuroprostheses* (Springer), 71–87. doi:10.1007/978-3-030-38740-2_5
- Buryanov, A., and Kotiuk, V. (2010). Proportions of hand segments. *Int. J. Morphol.* 28, 755–758. doi:10.4067/S0717-95022010000300015
- Cappello, L., Meyer, J. T., Galloway, K. C., Peisner, J. D., Granberry, R., Wagner, D. A., et al. (2018). Assisting hand function after spinal cord injury with a fabric-based soft robotic glove. *J. neuroengineering rehabilitation* 15, 59–10. doi:10.1186/s12984-018-0391-x
- Chae, J., Yang, G., Park, B. K., and Labatia, I. (2002). Muscle weakness and cocontraction in upper limb hemiparesis: Relationship to motor impairment and physical disability. *Neurorehabil. Neural Repair* 16, 241–248. doi:10.1177/154596830201600303
- Chiri, A., Giovacchini, F., Vitiello, N., Cattin, E., Roccella, S., Vecchi, F., et al. (2009). Handexos: Towards an exoskeleton device for the rehabilitation of the hand. *Proc. IEEE IROS* 2009, 1106–1111. doi:10.1109/IROS.2009.5354376
- Dobkin, B. H. (2005). Rehabilitation after stroke. *N. Engl. J. Med.* 352, 1677–1684. doi:10.1056/NEJMc043511
- Feix, T., Bullock, I. M., and Dollar, A. M. (2014). Analysis of human grasping behavior: Object characteristics and grasp type. *IEEE Trans. Haptics* 7, 311–323. doi:10.1109/TOH.2014.2326871
- Felson, D. T. (2013). Osteoarthritis as a disease of mechanics. *Osteoarthr. Cartil.* 21, 10–15. doi:10.1016/j.joca.2012.09.012
- Heinemann, A. W., Bode, R., and O'reilly, C. (2003). Development and measurement properties of the orthotics and prosthetics users' survey (OPUS): A comprehensive set of clinical outcome instruments. *Prosthet. Orthot. Int.* 27, 191–206. doi:10.1080/03093640308726682
- Ho, N., Tong, K., Hu, X., Fung, K., Wei, X., Rong, W., et al. (2011). An EMG-driven exoskeleton hand robotic training device on chronic stroke subjects: Task training system for stroke rehabilitation. *Proc. IEEE ICORR* 2011, 5975340. doi:10.1109/ICORR.2011.5975340
- Hoffmann, G., Conrad, M. O., Qiu, D., and Kamper, D. G. (2016). Contributions of voluntary activation deficits to hand weakness after stroke. *Top. Stroke Rehabil.* 23, 384–392. doi:10.1179/1945511915y.0000000023
- In, H., Kang, B. B., Sin, M., and Cho, K.-J. (2015). Exo-glove: A wearable robot for the hand with a soft tendon routing system. *EEE Robotics & Automation Magazine* 22, 97–105. doi:10.1109/MRA.2014.2362863
- Jane Rowland, T., Turpin, M., Gustafsson, L., David Henderson, R., and James Read, S. (2011). Chedoke arm and hand activity inventory-9 (CAHAI-9): Perceived clinical utility within 14 days of stroke. *Top. stroke rehabilitation* 18, 382–393. doi:10.1310/tsr1804-382
- Kamper, D. G., Fischer, H. C., Cruz, E. G., and Rymer, W. Z. (2006). Weakness is the primary contributor to finger impairment in chronic stroke. *Arch. Phys. Med. Rehabil.* 87, 1262–1269. doi:10.1016/j.apmr.2006.05.013
- Kang, B. B., Lee, H. H., Jeong, U., Chung, J., and Cho, K.-J. (2016). Development of a polymer-based tendon-driven wearable robotic hand. *Proc. IEEE ICRA* 2006, 3750–3755. doi:10.1109/ICRA.2016.7487562
- Kim, D. H., Lee, S. W., and Park, H. S. (2019). Development of a biomimetic extensor mechanism for restoring normal kinematics of finger movements post-stroke. *IEEE Trans. Neural Syst. Rehabil. Eng.* 27, 2107–2117. doi:10.1109/TNSRE.2019.2938616
- Kim, D. H., and Park, H.-S. (2018). Cable actuated dexterous (CADEX) glove for effective rehabilitation of the hand for patients with neurological diseases. *Proc. IEEE IROS* 2018, 2305–2310. doi:10.1109/IROS.2018.8594336
- Kulaksiz, G., and Gözil, R. (2002). The effect of hand preference on hand anthropometric measurements in healthy individuals. *Ann. Anat.* 35, 257–265. doi:10.1016/S0940-9602(02)80119-4
- Kuo, C.-L., and Hu, G.-C. (2018). Post-stroke spasticity: A review of epidemiology, pathophysiology, and treatments. *Int. J. Gerontol.* 12, 280–284. doi:10.1016/j.jig.2018.05.005
- Lamblet, C., Temiraliyul, D., Siegenthaler, M., Wirth, M., Woolley, D. G., Lambercy, O., et al. (2020). Characterization and wearability evaluation of a fully portable wrist exoskeleton for unsupervised training after stroke. *J. Neuroeng. Rehabil.* 17, 1–16. doi:10.1186/s12984-020-00749-4
- Lee, S. W., Landers, K. A., and Park, H.-S. (2014). Development of a biomimetic hand extensor device (BiomHED) for restoration of functional hand movement post-stroke. *IEEE Trans. Neural Syst. Rehabil. Eng.* 22, 886–898. doi:10.1109/TNSRE.2014.2298362
- Lindsay, M. P., Norrving, B., Sacco, R. L., Brainin, M., Hacke, W., Martins, S., et al. (2019). World stroke organization (WSO): Global stroke fact sheet 2019. *Int. J. Stroke* 14, 806–817. doi:10.1177/1747493019881353
- Nuckols, K., Hohimer, C. J., Glover, C., De Lucena, D. S., Moyo, W., Wagner, D., et al. (2020). “Effects of a soft robotic glove using a high repetition protocol in chronic stroke: A pilot study,” in 2020 8th IEEE RAS/EMBS International Conference for Biomedical Robotics and Biomechanics (BioRob): IEEE, 428–433. doi:10.1109/BioRob49111.2020.9224291
- Nycz, C. J., Bützer, T., Lambercy, O., Arata, J., Fischer, G. S., and Gassert, R. (2016). Design and characterization of a lightweight and fully portable remote actuation system for use with a hand exoskeleton. *IEEE Robot. Autom. Lett.* 1, 976–983. doi:10.1109/LRA.2016.2528296
- Palli, G., Natale, C., May, C., Melchiorri, C., and Wurtz, T. (2013). Modeling and control of the twisted string actuation system. *IEEE ASME Trans. Mechatron.* 18, 664–673. doi:10.1109/TMECH.2011.2181855
- Park, J., Seo, N. J., Son, J., Kim, W., and Cheong, J. (2014). Postural variation of hand precision grips by object size. *J. Mech. Sci. Technol.* 28, 1641–1651. doi:10.1007/s12206-014-0309-x
- Park, S., Bishop, L., Post, T., Xiao, Y., Stein, J., and Ciocarlie, M. (2016). On the feasibility of wearable exotendon networks for whole-hand movement patterns in stroke patients. *Proc. IEEE ICRA* 2016, 3729–3735. doi:10.1109/ICRA.2016.7487560
- Peters, H. T., Page, S. J., and Persch, A. (2017). Giving them a hand: Wearing a myoelectric elbow-wrist-hand orthosis reduces upper extremity impairment in chronic stroke. *Arch. Phys. Med. Rehabil.* 98, 1821–1827. doi:10.1016/j.apmr.2016.12.016
- Polygerinos, P., Wang, Z., Galloway, K. C., Wood, R. J., and Walsh, C. J. (2015). Soft robotic glove for combined assistance and at-home rehabilitation. *Robotics Aut. Syst.* 73, 135–143. doi:10.1016/j.robot.2014.08.014
- Popov, D., Gaponov, I., and Ryu, J.-H. (2017). Portable exoskeleton glove with soft structure for hand assistance in activities of daily living. *IEEE ASME Trans. Mechatron.* 22, 865–875. doi:10.1109/TMECH.2016.2641932
- Qi, H. J., and Boyce, M. C. (2005). Stress-strain behavior of thermoplastic polyurethanes. *Mech. Mater.* 37, 817–839. doi:10.1016/j.mechmat.2004.08.001
- Randazzo, L., Iturrate, I., Perdakis, S., and Millán, J. d. R. (2017). mano: A wearable hand exoskeleton for activities of daily living and neurorehabilitation. *IEEE Robot. Autom. Lett.* 3, 500–507. doi:10.1109/LRA.2017.2771329
- Ryu, D., Moon, K.-W., Nam, H., Lee, Y., Chun, C., Kang, S., et al. (2008). Micro hydraulic system using slim artificial muscles for a wearable haptic glove. *Proc. IEEE IROS* 2008, 3028–3033. doi:10.1109/IROS.2008.4651159
- Santello, M., Flanders, M., and Soechting, J. F. (1998). Postural hand synergies for tool use. *J. Neurosci.* 18, 10105–10115. doi:10.1007/s002210000420
- Thielbar, K. O., Triandafilou, K. M., Fischer, H. C., O'Toole, J. M., Corrigan, M. L., Ochoa, J. M., et al. (2016). Benefits of using a voice and EMG-driven actuated glove to support occupational therapy for stroke survivors. *IEEE Trans. Neural Syst. Rehabil. Eng.* 25, 297–305. doi:10.1109/TNSRE.2016.2569070
- Ueki, S., Kawasaki, H., Ito, S., Nishimoto, Y., Abe, M., Aoki, T., et al. (2012). Development of a hand-assist robot with multi-degrees-of-freedom for rehabilitation therapy. *IEEE ASME Trans. Mechatron.* 17, 136–146. doi:10.1109/TMECH.2010.2090353
- Waddell, K. J., Birkenmeier, R. L., Moore, J. L., Hornby, T. G., and Lang, C. E. (2014). Feasibility of high-repetition, task-specific training for individuals with upper-extremity paresis. *Am. J. Occup. Ther.* 68, 444–453. doi:10.5014/ajot.2014.011619
- Wang, H., Arceo, R., Chen, S., Ding, L., Jia, J., and Yao, J. (2019). Effectiveness of interventions to improve hand motor function in individuals with moderate to severe stroke: A systematic review protocol. *BMJ Open* 9, e032413. doi:10.1136/bmjopen-2019-032413
- Wege, A., and Zimmermann, A. (2007). Electromyography sensor based control for a hand exoskeleton. *Proc. ROBIO* 2007, 1470–1475. doi:10.1109/ROBIO.2007.4522381
- Xiloyannis, M., Cappello, L., Khanh, D. B., Yen, S.-C., and Masia, L. (2016). “Modelling and design of a synergy-based actuator for a tendon-driven soft robotic glove,” in 2016 6th IEEE International Conference on Biomedical Robotics and Biomechanics (BioRob): IEEE, 1213–1219. doi:10.1109/BIOROB.2016.7523796
- Yap, H. K., Lim, J. H., Nasrallah, F., and Yeow, C.-H. (2018). Corrigendum: Design and preliminary feasibility study of a soft robotic glove for hand function assistance in stroke survivors. *Front. Neurosci.* 12, 323. doi:10.3389/fnins.2018.00323
- Yurkewich, A., Hebert, D., Wang, R. H., and Mihailidis, A. (2019). Hand extension robot orthosis (HERO) glove: Development and testing with stroke survivors with severe hand impairment. *IEEE Trans. Neural Syst. Rehabil. Eng.* 27, 916–926. doi:10.1109/TNSRE.2019.2910011
- Yurkewich, A., Kozak, I. J., Hebert, D., Wang, R. H., and Mihailidis, A. (2020). Hand extension robot orthosis (HERO) grip glove: Enabling independence amongst persons with severe hand impairments after stroke. *J. Neuroeng. Rehabil.* 17, 33–37. doi:10.1186/s12984-020-00659-5
- Zhang, J., Sheng, J., O'Neill, C. T., Walsh, C. J., Wood, R. J., Ryu, J.-H., et al. (2019). Robotic artificial muscles: Current progress and future perspectives. *IEEE Trans. robotics* 35, 761–781. doi:10.1109/TRO.2019.2894371



OPEN ACCESS

EDITED BY

Zhen Luo,
University of Technology Sydney,
Australia

REVIEWED BY

Eduardo Palermo,
Sapienza University of Rome, Italy
Antonio J. del-Ama,
Rey Juan Carlos University, Spain

*CORRESPONDENCE

Carlos A. Cifuentes,
✉ carlos.cifuentes@uwe.ac.uk

SPECIALTY SECTION

This article was submitted to
Biomechanics,
a section of the journal
Frontiers in Bioengineering and
Biotechnology

RECEIVED 17 August 2022

ACCEPTED 14 March 2023

PUBLISHED 10 April 2023


CITATION

Sánchez-Manchola M,
Arciniegas-Mayag L, Múnera M,
Bourgain M, Provot T and Cifuentes CA
(2023), Effects of stance control via
hidden Markov model-based gait phase
detection on healthy users of an active
hip-knee exoskeleton.
Front. Bioeng. Biotechnol. 11:1021525.
doi: 10.3389/fbioe.2023.1021525

COPYRIGHT

© 2023 Sánchez-Manchola, Arciniegas-
Mayag, Múnera, Bourgain, Provot and
Cifuentes. This is an open-access article
distributed under the terms of the
[Creative Commons Attribution License](#)
(CC BY). The use, distribution or
reproduction in other forums is
permitted, provided the original author(s)
and the copyright owner(s) are credited
and that the original publication in this
journal is cited, in accordance with
accepted academic practice. No use,
distribution or reproduction is permitted
which does not comply with these terms.

Effects of stance control via hidden Markov model-based gait phase detection on healthy users of an active hip-knee exoskeleton

Miguel Sánchez-Manchola¹, Luis Arciniegas-Mayag²,
Marcela Múnera^{1,3}, Maxime Bourgain ^{4,5}, Thomas Provot^{4,5} and
Carlos A. Cifuentes^{3,6*}

¹Department of Biomedical Engineering, Colombian School of Engineering Julio Garavito, Bogotá, Colombia, ²LabTel, Electrical Engineering Department at Federal University of Espírito Santo, Vitória, Brazil, ³Bristol Robotics Laboratory, University of the West of England, Bristol, United Kingdom, ⁴EPF Graduate School of Engineering, Cachan, France, ⁵Arts et Métiers Institute of Technology, Institut de Biomécanique Humaine Georges Charpak, Paris, France, ⁶School of Engineering, Science and Technology, Universidad Del Rosario, Bogotá, Colombia

Introduction: In the past years, robotic lower-limb exoskeletons have become a powerful tool to help clinicians improve the rehabilitation process of patients who have suffered from neurological disorders, such as stroke, by applying intensive and repetitive training. However, active subject participation is considered to be an important feature to promote neuroplasticity during gait training. To this end, the present study presents the performance assessment of the AGoRA exoskeleton, a stance-controlled wearable device designed to assist overground walking by unilaterally actuating the knee and hip joints.

Methods: The exoskeleton's control approach relies on an admittance controller, that varies the system impedance according to the gait phase detected through an adaptive method based on a hidden Markov model. This strategy seeks to comply with the assistance-as-needed rationale, i.e., an assistive device should only intervene when the patient is in need by applying Human-Robot interaction (HRI). As a proof of concept of such a control strategy, a pilot study comparing three experimental conditions (i.e., unassisted, transparent mode, and stance control mode) was carried out to evaluate the exoskeleton's short-term effects on the overground gait pattern of healthy subjects. Gait spatiotemporal parameters and lower-limb kinematics were captured using a 3D-motion analysis system Vicon during the walking trials.

Results and Discussion: By having found only significant differences between the actuated conditions and the unassisted condition in terms of gait velocity ($p = 0.048$) and knee flexion ($p \leq 0.001$), the performance of the AGoRA exoskeleton seems to be comparable to those identified in previous studies found in the literature. This outcome also suggests that future efforts should focus on the improvement of the fastening system in pursuit of kinematic compatibility and enhanced compliance.

KEYWORDS

adaptive gait phase detection, assisted-as-needed, hidden markov model, lower-limb exoskeleton, robot-assisted gait training, stance control, stroke

1 Introduction

Mobility is considered one of the most important human faculties which can be defined as the ability of an individual to move freely through multiple environments and perform activities of daily living with ease (Winter 2009). Following a neurological dysfunction, such as stroke, mobility may be affected and only a short-time period might remain to take advantage of the inherent adaptability and plasticity of the central nervous system for recovery (Wolpert et al., 2011). Reestablishing effective mobility for individuals with lower-limb impairments is often a complex challenge and frequently involves the interdisciplinary efforts of many medical, surgical, and rehabilitative specialists (Pasquina et al., 2017). Within this context, robot-based training has risen in the past years as a potential clinical aid for both patients and health professionals. Preliminary results on its influence on stroke survivors undergoing the sub-acute phase, i.e., within the first 3 months, suggest that combining rehabilitation devices with a conventional rehabilitation program appears to be more effective than overground gait training alone in the recovery of independent walking (Schwartz and Meiner, 2015; Mehrholz et al., 2017).

Most-commercially, available lower-limb assistive devices move the patient's limbs along a predefined, fixed trajectory frequently drawn from healthy subjects (Knaepen et al., 2014). However, it has already been proven that a monotonous repetition of the same gait pattern results in decreased neuromuscular activity, increased energy consumption, and learned disuse (Taub et al., 2006; Knaepen et al., 2014). In order to induce motor learning based on the principle of neuroplasticity, studies have shown that therapy is only effective if task-oriented activities are performed whereby patient effort is promoted (Lagoda et al., 2012). Therefore, to interact with humans, wearable robots are expected to be flexible, adaptable, and, most importantly, safe. One of the benchmarks to achieve this is compliance. Compliance plays an important role in human adaptations to environmental changes and securing stable gait (Geyer et al., 2006). However, compliance has not yet found its way into commercial wearable robots, which usually use direct-drive actuation due to its high bandwidth and controllability (Bacek et al., 2018).

In pursuit of compliance, researchers have developed a new class of controllers to provide "assistance-as-needed" (AAN). For instance, strategies based on impedance modulation (Tsuji and Tanaka, 2005; Marchal-Crespo and Reinkensmeyer, 2009) help the subject only when away from a reference pattern (kinematic in most cases) by exerting proportional restoring forces. On the other hand, strategies based on proportional myoelectric control (Ferris et al., 2006) render control outputs that are directly proportional to the magnitude of surface electromyography (EMG) signals. However, this method relies on clean and reliable EMG acquisition from nominal, functional muscles which may be affected when working with patient groups (Dzeladini et al., 2016). Thus, the benchmark for the control of active lower-limb orthoses remains to be the impedance modulation. As a matter of fact, adaptive-impedance control strategies have proven to provide a gait training session as effective as that provided by physical therapists (Dzahir and Yamamoto, 2014).

Within this context, and based on the fact that humans change their joint impedance throughout gait by regulating their posture

and muscle contraction levels for the sake of stability, some robotic devices use a particular strategy commonly known as stance control (SC). SC applies impedance modulation to provide stability and prevent the lower limb joints from collapsing during the stance phase, whereas it releases them to allow free movement during the swing phase (Ir and Azuan AO, 2015). Studies, which have used this strategy, have reported that it can increase walking speed, reduce energy expenditure and gait asymmetry (for both paretic and non-paretic limbs), thus decreasing muscle stress in patients with muscular weakness (Zissimopoulos et al., 2007; Zacharias and Kannenberg, 2012; Rafiaei et al., 2016).

In particular, Dzeladini et al. implemented an SC strategy based on neuromuscular control (NMC) to command an actuated ankle orthosis using few sensory inputs. Preliminary results involving two healthy subjects show a reduction in net metabolic cost and muscle activity, whereas walking dynamics remained relatively unchanged (Dzeladini et al., 2016). Conversely, similar to the current study, Villa-Parra et al. proposed a novel method to modulate the impedance on an active non-backdriveable knee orthosis by using variable gains which vary as a function of the user's anthropometric measurements and gait phases extracted through footswitch signals. Both moment-based and velocity-based gain patterns appeared to be suitable to assist the knee joint under the SC strategy (Villa-Parra et al., 2017). Similarly, Ortlieb et al. featured a variable impedance controller that modulates its stiffness constant based on a 3-gait-phase model to actuate hip and knee joint along the sagittal plane during overground walking. Gait phases are detected through hip flexion velocity. Low compliance on a healthy user shows greater effects on the walking speed and step length (Ortlieb et al., 2019). Finally, the SC approach has also exhibited a positive influence on patients with paraplegia while used in hybrid neuroprostheses (HNP), i.e., the combination of functional neuromuscular stimulation (FNS) with a lower-limb orthosis. HNPs incorporating controllable knee mechanisms operating under the SC premise reduce the amount of stimulation required as compared to FNS systems only (To et al., 2011). Also, a pilot study involving one disabled subject shows that stance phase knee flexion is closer to the nominal condition (i.e., healthy walking) and knee hyperextension after initial contact decreases during walking with HNP compared to FNS-only gait (Bulea et al., 2013).

Other studies which vary the impedance in lower-limb joints focus on the rehabilitation or assistance of only one joint, particularly in the sagittal plane. For instance, by taking advantage of the fact that the swing phase requires free knee rotation, some quasi-passive devices have been developed and can be found in the literature (Shamaei et al., 2013a; Shamaei et al., 2014; Shamaei et al., 2014). Other studies feature devices that vary the knee stiffness by employing a spring system to generate loading profiles based on two gait phases detected by an instrumented insole. The implementation of compliant actuators (Cestari et al., 2015), described as a not-bulky device, and a two-phase gait detection method (namely, stance and swing phases) render three desirable stiffness states (i.e., Minimum, Medium, and High Stiffness). Further, a control strategy proposed for the HUALEX exoskeleton (Tran et al., 2016), featured a fuzzy-based impedance control strategy that changes the impedance

applied by the exoskeleton to the user also for only two gait phases.

Even though the afore-mentioned studies highlight the promising results that the application of varying stiffness in active lower-limb devices have shown in the past years, most of the proposed control strategies consider only the main gait phases (i.e., stance and swing phases). Since the human hip and knee joint stiffness shows significant variations during the stance phase (Shamaei et al., 2013b), the control strategy output could be improved by using an online gait subphase detection with increased granularity. In addition, most studies apply robot-assisted gait training while assisting a single human joint, or rely on pressure sensors instrumented in customized insoles or multiple sensory inputs to divide the user's gait cycle. Nonetheless, footswitch signals have demonstrated poor performance compared to, e.g., inertial sensors, on account of their short durability and the need for professional personnel to locate them precisely (Gouwanda and Gopalai, 2015). Also, although using multiple sensor interfaces seems to be reasonable for prosthetic devices (such as the one found in (Dzeladini et al., 2016)) since they are mounted to the prosthesis itself, in the case of orthoses, a minimal number of sensors should be pursued for the sake of clinical usability and the patient's comfort (Gams et al., 2013). For these reasons, this work utilizes a more reliable, more versatile gait phase detection module (Sánchez Manchola et al., 2019) and a control strategy based on Stance Control (SC) to compensate for the rigid nature of the AGoRA exoskeleton. By combining these three main features: i) an adaptable inertial-based method to accurately segment the gait cycle, and ii) an impedance modulation performed according to the gait phase detected to adjust iii) a non-backdrivable hip-knee exoskeleton, the present study intends to find the short-term effects in terms of gait parameters and user perception of their interplay. Healthy subjects are involved in seeking a preliminary assessment of the proposed prototype as a means of debugging possible hard and software issues prior to trials with pathological individuals.

The document follows its track as shown hereby: Section 2 describes the hardware used in the active exoskeleton (together with an overview of its gait phase detection module and SC approach), followed by the experimental protocol, data processing, and statistical analysis of results. Subsequently, Section 3 presents the results in terms of gait spatio-temporal parameters and lower-limb kinematics, whereas Section 4 discusses the implications of such outcomes. Finally, Section 5 summarizes the findings and includes some recommendations to take into account in further iterations of the wearable device used.

2 Materials and methods

The proposed orthosis controller comprises two main components. The first (Section 2.2) is a Hidden Markov Model (HMM) that uses angular velocity components from a single Inertial Measurement Unit (IMU) placed on the user's foot instep to accurately segment their gait cycle into four events of interest. The second component (Section 2.3.3) relies on an admittance controller, which works as a function of the detected gait phase, to generate a stance behavior on the active orthotic device whose hardware architecture is described as follows.

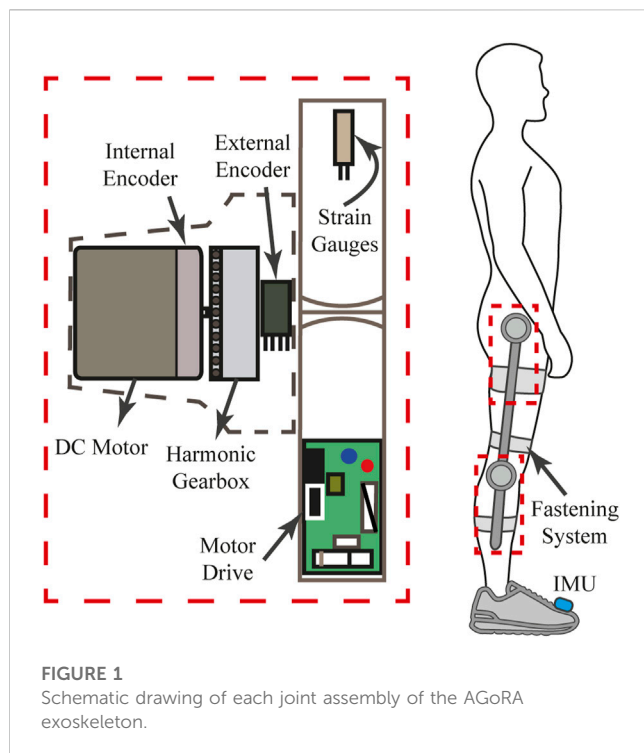
2.1 Active hip-knee exoskeleton

The AGoRA exoskeleton is an active assistive device intended as a rehabilitation tool for stroke patients. It is mainly addressed for overground gait training in a clinical environment as a bilateral wearable device. The exoskeleton comprises two actuated Degrees of Freedom (DoF) to the hip and the knee flexion-extension (i.e., movement along the sagittal plane) as shown in Figure 1. An additional passive DoF in the hip joint allows the abduction/adduction movements for lateral balance support (Rietdyk et al., 1999). Also, most of its mechanical structure is made of duralumin: a light, high-resistant, and low corrosive material whose attributes are considered to be important in the design of wearable robots (Pons et al., 2008). These design criteria allow the device to have a total estimated weight of 15 kg with the actuation mechanisms mounted on both hip and knee joints. For further information on the mechanical structure of the AGoRA exoskeleton, you may refer (Sánchez-Manchola et al., 2018), where the entire infrastructure of the device is detailed.

Regarding the actuation mechanism used, a brushless flat DC motor (EC-60 flat 408057, Maxon Motor AG, Switzerland) is coupled with a harmonic drive gear (CSD-20-160-2AGR, Harmonic Drive LLC, United States) (see Figure 1) to actuate the hip and the knee joints of the AGoRA exoskeleton. This actuation system was chosen because this construction provides more torque at lower speeds (gear ratio of 160:1) while preserving lightweight and reduced volume (Zoss and Kazerooni, 2006). The proposed assembly provides a continuous net torque of 35 Nm and peak torques of 180 Nm, which meets the design requirements for most patients (Bayón et al., 2017). As control strategies meant to assist the human gait cycle do not require continuous torque but high torque profiles at specific times, the peak torque of the selected actuators appears to be sufficient for the application presented in this work (Colombo et al., 2000).

To command these actuation mechanisms, we opted for a distributed architecture with motor drives commanding each joint module independently for the sake of modularity. The exoskeleton joints were equipped with an EPOS4 driver (Maxon Motors AG, Switzerland) which has been developed by the manufacturer specifically for the brushless DC motors previously described (see Figure 1). The motor drives are in charge of the sensor data acquisition and provide three built-in low-level control loops: current, position, and velocity regulation. The data bus used to connect all functional modules consists of a network structure with a deterministic real-time communication based on Controller Area Network (CAN) technology running at 1 Mbps. (Bortole, 2014; Bayón et al., 2017). In order to power the overall architecture, a lithium-ion battery pack of 36 V_{DC} and 4.4 Ah is used while being kept inside a small backpack worn by the user.

Further, in pursuit of kinematic compatibility, i.e., the correct alignment of the exoskeleton hinges with the biological axes of rotation (Hughes et al., 2009), the length of each exoskeleton segment can be adjusted to different anthropometric measures without losing functionality. Via a mechanism of two telescopic bars, the thigh and shank segments can be adjusted to encompass a setting spectrum covering a target population whose height



generally ranges from 1.70 to 1.83 m and whose maximum bodyweight may reach up to 90 kg. Additionally, adjustable rounded 3D-printed leg braces carriers with Velcro straps are used as a means of fastening (as may be seen in Figure 1).

In regards to sensors, the AGoRA exoskeleton is designed in such a way that there are no sensors physically attached to the subject's skin. The exoskeleton is equipped with two types of sensors: kinematic and kinetic. Kinematic sensors are used for measuring hip and knee angular position, and foot angular velocity. Besides the internal relative incremental encoder of each DC motor (used for the implementation of position and impedance controllers), the exoskeleton has an absolute magnetic encoder placed concentrically to each joint assembly (see Figure 1). Conversely, kinetic sensors measure the interaction forces between the user's limbs and the mechanical structure of the exoskeleton. In particular, strain gauges (632-180, RS Pro, United Kingdom) mounted on each exoskeleton link are used as force sensors (see Figure 1) while being bonded to its metal rods. These force sensors are connected in a half Wheatstone bridge configuration to enhance their measurement accuracy and to correct changes resulting from temperature variations. A commercial 24-bit Analog-Digital Converter for weighing scales (HX711, Avia Semiconductors, Czech Republic) is used to balance the bridge and to amplify the output 50 times. Its output signal covers torque measurements ranging from -40 to 40 Nm, thus complying with the maximum continuous torque of the actuators.

In addition to the above-mentioned sensors, an IMU (BNO055, BOSCH, Germany) placed on the dorsal side of the foot, which integrates a triaxial 14-bit accelerometer and an accurate close-loop triaxial 16-bit gyroscope, is used to accurately classify the gait cycle (see Figure 1). The IMU sensor is calibrated using a software library provided by the manufacturer which captures data while the following process is

performed: the device is kept still on a flat surface for about 5 s (gyroscope calibration) and then it is rotated by 45-degree increments across one axis (accelerometer calibration). Despite conventional sensors (e.g., pressure sensors on customized insoles or motion capture systems) are widely used for experimental purposes, they are also well-known to be either too fragile for activities of daily living and difficult to set up, or limited to indoor applications (Smith et al., 2002; Attal et al., 2018). Thus, we decided to use inertial sensors over other sensors on the basis of their cost-effectiveness (Caldas et al., 2017) and the fact that inertial quantities present typical waveform features throughout a gait cycle (Taborri et al., 2016).

2.2 Gait phase detection

This detection module, presented in previous work (Sánchez Manchola et al., 2019), relies on the most widespread model for wearable robots, i.e., a four-event model, to segment the gait cycle into: i) the initial foot contact with the ground or Heel Strike (HS); ii) the loading response phase or Flat Foot (FF); iii) the heel lifting or Heel-Off (HO); and iv) the initial Swing Phase (SP) (Taborri et al., 2016). For the correct positioning of the inertial sensor, we opted for fastening it to the dorsal side of the foot because of the better performance that scalar classifiers have shown with the sensor placed in this location, even compared to other vectorial classifiers that involve further inertial signals captured from different lower-limb locations (Taborri et al., 2014). Thus, the foot instep poses a location that requires a minimum number of sensors and guarantees classification accuracy.

A Hidden Markov Model (HMM) is chosen to be the detection method for this particular application since the use of wearable sensors such as IMU sensors along with an algorithm based on HMM has shown high accuracy in the recognition of activities of daily living (Panahandeh et al., 2013; Bennett et al., 2016). HMM has even demonstrated to be more accurate in the context of motor activity recognition compared to different supervised and unsupervised methods such as k-means, Gaussian Mixture Model, Linear Discriminant Analysis, Dynamic Time Warping, and threshold-based algorithms (Mannini and Sabatini, 2010; Attal et al., 2015; Sánchez Manchola et al., 2019; Martin, 2020).

An HMM is a doubly stochastic process with N underlying discrete states that are not observable, i.e., its state sequence is hidden to the observer who only has access to the emissions of each state (Rabiner, 1989). The second embedded stochastic process describes the emissions from Y observations, i.e., either the sensor readout or feature vectors extracted from them, in terms of discrete probabilities or probability density functions (Rabiner, 1989). HMM is a statistical model widely used to estimate a sequence of hidden states in a time series (Taborri et al., 2015), which for the case of gait phase detection corresponds to the gait events ($N = 4$, for this case).

HMM can be expressed as a function of a set λ of statistical measures:

$$\lambda = (A, B, \pi) \quad (1)$$

which includes the probability distribution matrix of state transition A , the probability distribution matrix of observation symbols B , and the initial state distribution vector π .

The development of a continuous HMM entails two main procedures: a training stage and a test stage. The first phase refers to the adjustment of model parameters λ to optimally adapt them to an observed training dataset (Rabiner, 1989). The Baum-Welch algorithm, the most common solution to this issue, is implemented in the present work to optimize the transition and emission probabilities starting from an initial parameter set (Sánchez Manchola et al., 2019). Subsequently, the test stage allows the feature classification based on the trained model achieved in the training phase, i.e., the search for the optimal state sequence is undertaken. The Viterbi algorithm represents a widely used optimality criterion to tackle this testing procedure (Rabiner, 1989). However, and despite its computational efficiency, this algorithm is not suitable for real-time implementation since the indicators it uses are computed based on a whole observation dataset (Sánchez Manchola et al., 2019). Thus, its real-time implementation becomes fundamental for it to be used in a lower-limb rehabilitation robot.

On this basis, a new online decoding approach known as the Forward-Only Viterbi (FOV) has been implemented to overcome this limitation. The FOV algorithm is applied to each signal in order to find the l -th state of likely sequence at a certain time t_n (l_{t_n}) and the probability associated at each i -th state $\delta_{t_n}(i)$ (Taborri et al., 2014). Particularly, this decoding approach can be deployed by implementing the pseudo-code presented in Algorithm 1. A study performed by Mannini and Sabatini, however, found that this Viterbi decoding alternative is plagued by erroneous events that consist of missed and additionally detected gait strides Mannini and Sabatini (2012). Contrary to the mentioned study, in which a heuristic strategy discarded detected gait strides if their time duration was less than 250 ms, we do not take into account gait phases that last less than 150 ms (i.e., the shortest period for HS in healthy subjects during comfortable walking (Lemke et al., 2000)).

Require:

- 1: procedure INITIALIZATION
- 2: $\delta_{t_0}(i) \leftarrow \pi_i b_i(Y(t_0))$, $1 \leq i \leq N$;
- 3: $l_{t_0} \leftarrow \operatorname{argmax}_{1 \leq i \leq N} \delta_{t_0}(i)$;
- 4: end procedure

Ensure: l_{t_n}

- 5: for each new frame b do
- 6: $\delta_{t_n}(i) \leftarrow \max(\delta_{t_{n-1}}(i) A_{ij}) \times B_i(Y(t_n))$;
- 7: $l_{t_n} \leftarrow \operatorname{argmax}_{1 \leq i \leq N} \delta_{t_n}(i)$;
- 8: end for

Algorithm 1. FOV algorithm

The HMM algorithm applied in this study (Sánchez Manchola et al., 2019) was assessed using a custom insole as a reference system. The custom insole comprised four force-sensitive resistors placed in the hallux, the first and fifth metatarsophalangeal, and the heel. These pressure centers are selected because they show unique pattern characteristics in the estimation of ground reaction forces (Lim et al., 2017). After

using standardized parameters training (SPT), the system showed an accuracy of 81.4% in healthy users and 78.06% in patients who had suffered some pathology that affected their gait pattern. A complete description of this gait phase detection module and its validation is available in (Sánchez Manchola et al., 2019).

2.3 Control architecture

Human-Robot Interaction (HRI) involves different control architectures to assist a user's lower limbs. In recent decades, multiple lower limb exoskeletons have been designed with a multi-layer control architecture (Minchala et al., 2017; Al-Shuka et al., 2019; Kumar et al., 2019; Lee et al., 2020). This control architecture is usually composed of a low-level controller comparable to standard controllers such as PID, PI, and PD. This controller changes based on the desired activity that the user intends to execute (Tijjani et al., 2022). The mid-level controller is used for two tasks: in the first one, a standard controller applies the control strategy; and in the second one, mathematical equations are considered to estimate the HRI and convert it into supported values used by the low-level controller (Vantilt et al., 2019). Finally, a high-level controller may involve machine-learning methods to calculate the control gain variations in accordance with the user's desired activity (Minchala et al., 2017; Vantilt et al., 2019). For the case of the AGoRA exoskeleton, its control architecture comprises a multilevel control structure which encompasses the gait pattern estimation, the torque/force or angular values estimation, and the standard controllers to apply estimated parameters on the exoskeleton actuation system (Figure 2). This section shows the AGoRA exoskeleton's multilevel control architecture for the SC application.

2.3.1 Low-level controller

This module comprises a PI speed controller and a PI current controller. The velocity control has been used as part of the admittance controller to express the user's motion intention in terms of angular velocity values. The outcome of the admittance controller is thus used as an input for the speed controller which commands the exoskeleton's actuation mechanism.

The velocity controller internally uses a PI current controller which comes as an out-of-the-box tool on the Maxon's EPOS4 driver. Figure 3 shows a simplified model of this current controller. Its corresponding gains were estimated by using the EPOS Studio software (Maxon Motors, v.3.2) which provides an auto-tuning option, where a chirp signal is applied to the actuation mechanism. For this tuning process, the exoskeleton was coupled to a rigid structure (test bench) to allow free hip and knee movements, as shown in Figure 4. As a result, the following PI were obtained: $p = 955671 \mu V/A$, $I = 485188 \mu V/As$ for the hip joint, and $p = 937294 \mu V/A$, $I = 430053 \mu V/As$ for the knee joint.

A velocity controller is also a built-in tool of the EPOS4 driver and its schematic is shown in Figure 5. The characterization of the corresponding PI gains was performed in a similar way as for the current controller and the resulting values are $p = 385000 \mu As/rad$,

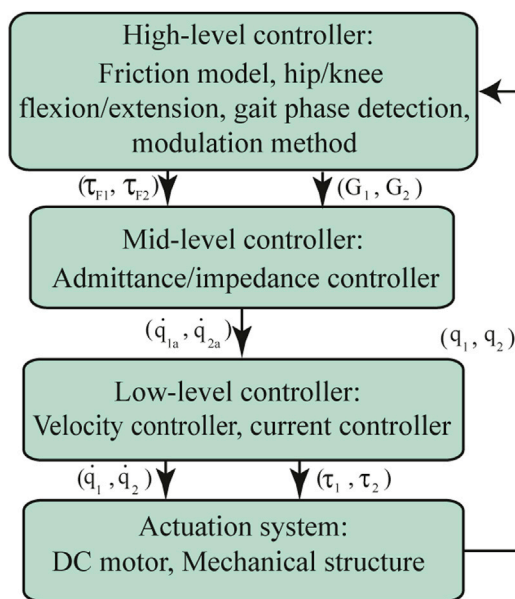


FIGURE 2

The control architecture of the AGoRA exoskeleton is comprised of 3 control levels: a high-level controller, comprised by a friction model with a resulting compensation torque τ_F and a modulation method that calculates the admittance controller gains according to each gait phase detected (G); a mid-level controller which uses an admittance/impedance controller, where \dot{q}_n is the resulting angular velocity profile; and a low-level controller that involves a speed controller and a current controller, where \dot{q} is the resulting angular velocity and τ corresponds to the low-level controller output. Subindexes 1 and 2 correspond to the hip and knee joints, respectively.

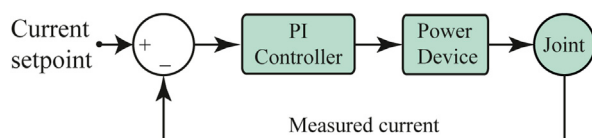


FIGURE 3

Schematic of the PI current controller implemented in the AGoRA exoskeleton as a low-level controller.

$I = 4515922 \mu A/rad$ for the hip joint, and $p = 427769 \mu A/rad$, $I = 4442130 \mu A/rad$ for the knee joint.

2.3.2 Mid-level controller

Even though the actuation mechanism used for the AGoRA exoskeleton can exert torque profiles which are sufficient to assist human lower limbs (as depicted in Section 2.1), the motor-gearbox assembly employed in each exoskeleton joint does not allow the unpowered hardware to comply with the user's command. Since such behavior could eventually cause injuries to the patient by restricting their natural gait pattern, the implementation of compliant control strategies appears to be necessary to mitigate these adverse effects.

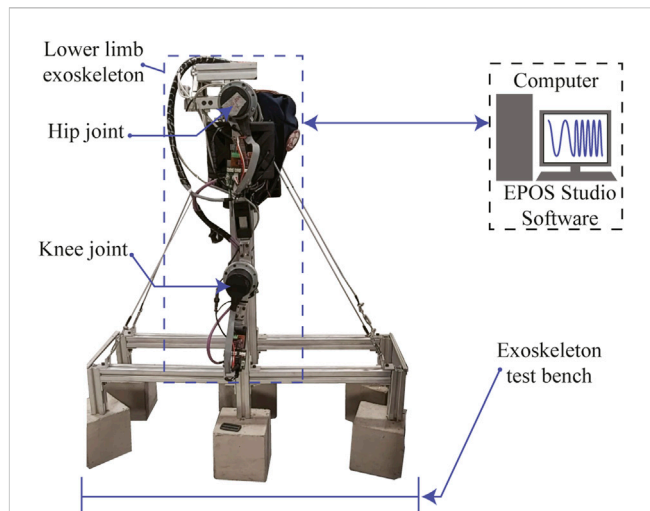


FIGURE 4

Experimental setup for the gain tuning of the AGoRA exoskeleton's low-level controller.

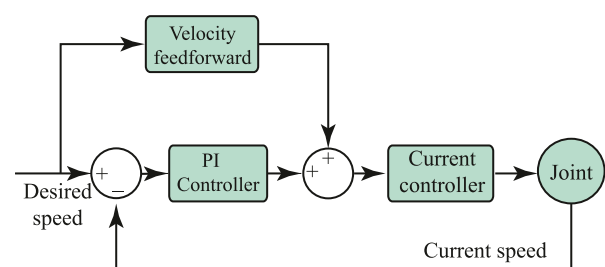
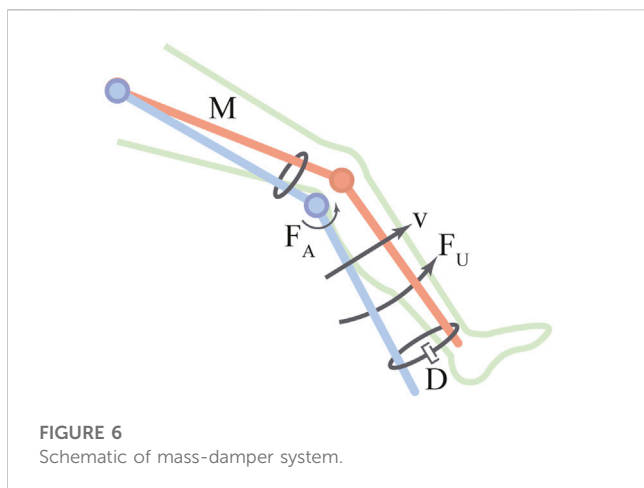


FIGURE 5

Schematic of the PI speed controller implemented in the AGoRA exoskeleton as a low-level controller.

The admittance controllers have proven to be stable in high stiffness conditions (del Ama Espinosa, 2013). An admittance controller is a variation of the impedance controller (designed by Hogan in 1984 (Hogan, 1984)) whose performance highly depends on the actuator position and the actuator velocity. If the mechanical impedance of the exoskeleton could be zero (infinite admittance), its user would not feel any resistance while wearing it. However, this zero-impedance behavior is only ideal, given the actuator's intrinsic inertia and friction, and the controller time delay (Hoogen et al., 2002). Low impedance, nonetheless, can be achieved if the control system takes into account the user's motion intention. This low impedance behavior is widely known as backdrivability (Krebs et al., 2000), and good backdrivability provides numerous benefits in robot-assisted gait training, e.g., the ability to act as a monitoring tool for health professionals (Ichinose et al., 2003). In particular, an admittance controller is implemented in the AGoRA exoskeleton by modeling both the hip and the knee joints as a mass-damper system. In this sense, the motion of each exoskeleton joint will depend on its angular velocity and a damping constant, resulting in a system that simulates stiffness as shown in Eq. (2). Here, D is the damping



constant, v is the angular velocity differential, and F_d is the force generated by the virtual damping.

$$Dv = F_d \quad (2)$$

The dynamic behavior of the HRI present in the AGoRA exoskeleton can be modeled as shown in Figure 6. In this model, the exoskeleton is assumed to have a given mass M and a damping constant D . Thus, the equation that describes the system velocity (v) is given by Eq. (3).

$$M\dot{v} + Dv = F_i \quad (3)$$

The interaction force F_i is measured by the strain gauges used as force sensors. In the frequency domain, Eq. (3) can be expressed as in Eq. (4).

$$v(s) = F_i / (Ms + D) \quad (4)$$

The output velocity value is passed through the low-level velocity controller (embedded within the motor drive) as an input. Using Eq. (4), the rendered admittance (Y) can be modeled as in Eq. (5).

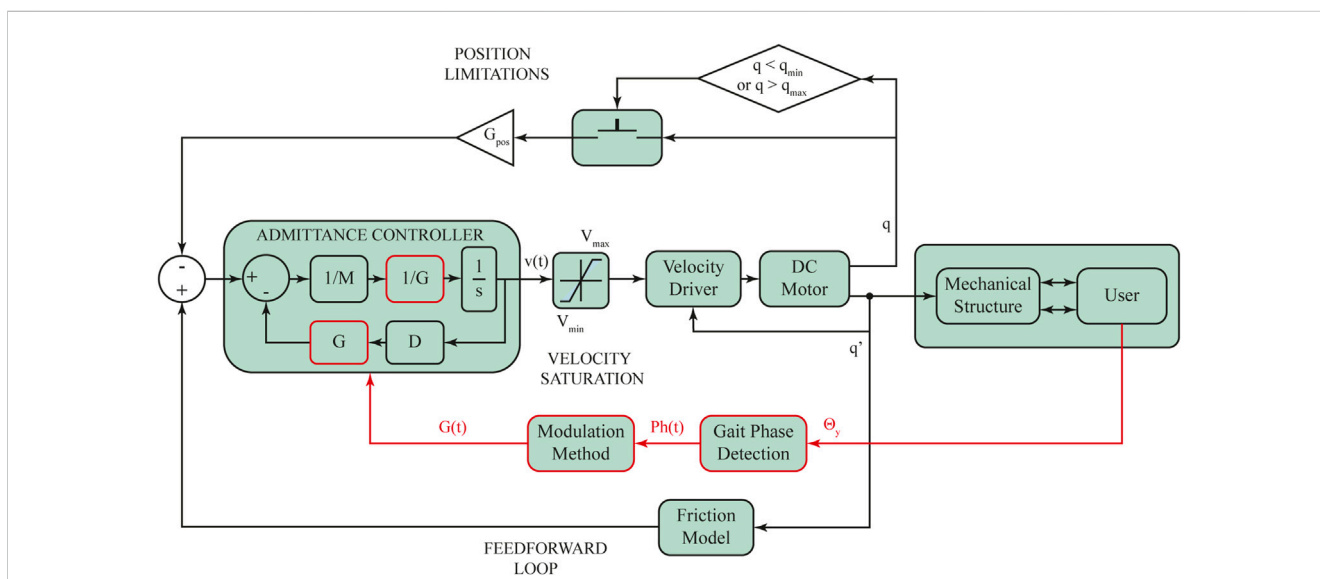
$$Y(s) = (Ms + D)^{-1} \quad (5)$$

The rationale behind the admittance control is thus to make the actuation mechanism show low impedance (high admittance) when moved by the patient's extremities (see Admittance Controller in Figure 7). The admittance controller receives the calculated forces mentioned in Eq. (4) as input and renders velocity values accordingly as output. The impedance parameters M and D are set to 0.25 kg and 2.5 N/(m/s), respectively. These values were obtained empirically during tests undertaken on a test bench and adjusted for each exoskeleton joint during preliminary walking trials.

2.3.3 High-level controller

A feedforward control loop is included within the control scheme to anticipate and compensate the dynamics of the exoskeleton structure. By modeling the exoskeleton as a 2-DoF robot, a friction model may be proposed (see Feedforward Loop in Figure 7). The friction model (Wu et al., 2016) depicts the torque value the actuation mechanism needs to exert to compensate for the influence of friction. Eq. (6) defines the proposed friction model, where F_c is the Coulomb friction, \dot{q} is the joint's angular velocity, and T_m and F_s are the starting torque and the static friction torque, respectively, which are defined using the gearbox datasheet.

$$T_f = \begin{cases} F_c \operatorname{sgn}(\dot{q}) & \dot{q} \neq 0 \\ T_m, |T_m| < |F_s| & \dot{q} \approx 0 \\ F_s, |T_m| \geq |F_s| & \dot{q} \approx 0 \end{cases} \quad (6)$$



Further, to avoid exceeding joint limits and subsequently causing damage or instability to the user, limitations in terms of position (q_{min} , q_{max}) and velocity (V_{min} , V_{max}) are also taken into consideration (as depicted as *Position Limitations* and *Velocity Saturation* respectively, in Figure 7).

In order to deploy an SC strategy with the admittance controller already described, an impedance modulation is achieved by directly multiplying a variable gain G by the controller constants M and D (as shown in red in Figure 7) (Villa-Parra et al., 2017). G is directly proportional to the system impedance and is updated according to the different gait sub-phases to adapt both joint impedances during gait. When varying the controller gain G in terms of four gait partitions (as shown in Figure 8A), typical lower limb moment during gait (as shown in Figures 8B, D, for knee and hip joints, respectively) should be displayed. In this context, G is defined and smoothly varied for each detected gait phase i following a pattern based on typical moment variations throughout gait (as reported in a public dataset of overground walking kinematics and kinetics in healthy subjects (Fukuchi et al., 2018)). Figures 8C, E show an example of such G variations within a single gait cycle for the knee and hip joints, respectively. And so, for the case of the knee joint, the highest gain value is given during HS when the knee experiences its first flexion, and then it gradually decreases with a slight increase during HO (as found by (Villa-Parra et al., 2017)). Following the same premise applied to the knee joint, the impedance modulation for the hip joint keeps the controller gain at high values throughout the stance phase, while there is a significant gain decrease during SP, in pursuit of stability during loading response. For both patterns, the proposed impedance modulation seeks to promote a shock-damping behavior during gait phases associated with weight acceptance (i.e., HS and FF where knee and hip apply a large moment value).

Regardless of the exoskeleton joint, G_i , $1 \leq i \leq 4$ require suitable time spans Δt_i , $1 \leq i \leq 4$, in which the controller gain linearly decreases/increases until it reaches the desired value for HS, FF, HO, and SP, respectively. Such linear change allows the admittance controller to exert smooth velocity profiles according to each subject's gait pattern. Considering that the weight and gait velocity are the anthropometric measures that most affect the knee mechanical behavior (Shamaei and Dollar, 2011), these parameters are considered here to define the corresponding G and Δt values (Villa-Parra et al., 2017).

More specifically, time spans Δt_i are established using Eq. (7) which defines these time periods as a function of known physical properties: the corresponding gait phase (i), the sampling frequency (f_s), and the user's height (H) and velocity (v_u) (Villa-Parra et al., 2017).

$$\Delta t_i = \frac{0.0413 \cdot i \cdot H \cdot f_s}{v_u} \quad (7)$$

Moreover, knee moment-based pattern (shown in Figure 8C) is configured to reach the following gain values: $G_1 = 0.7 \cdot W$, $G_2 = 0.2 \cdot W$, $G_3 = 0.3 \cdot W$ and $G_4 = 0.1 \cdot W$, whereas hip moment-based pattern (shown in Figure 8E) is set to follow these gain values: $G_1 = 0.6 \cdot W$, $G_2 = 0.8 \cdot W$, $G_3 = 0.4 \cdot W$ and $G_4 = 0.1 \cdot W$, with W being the user's weight in kg.

Algorithm 2 shows the pseudo-code implemented in the Robot Operative System (ROS) for the online gain pattern generation (see

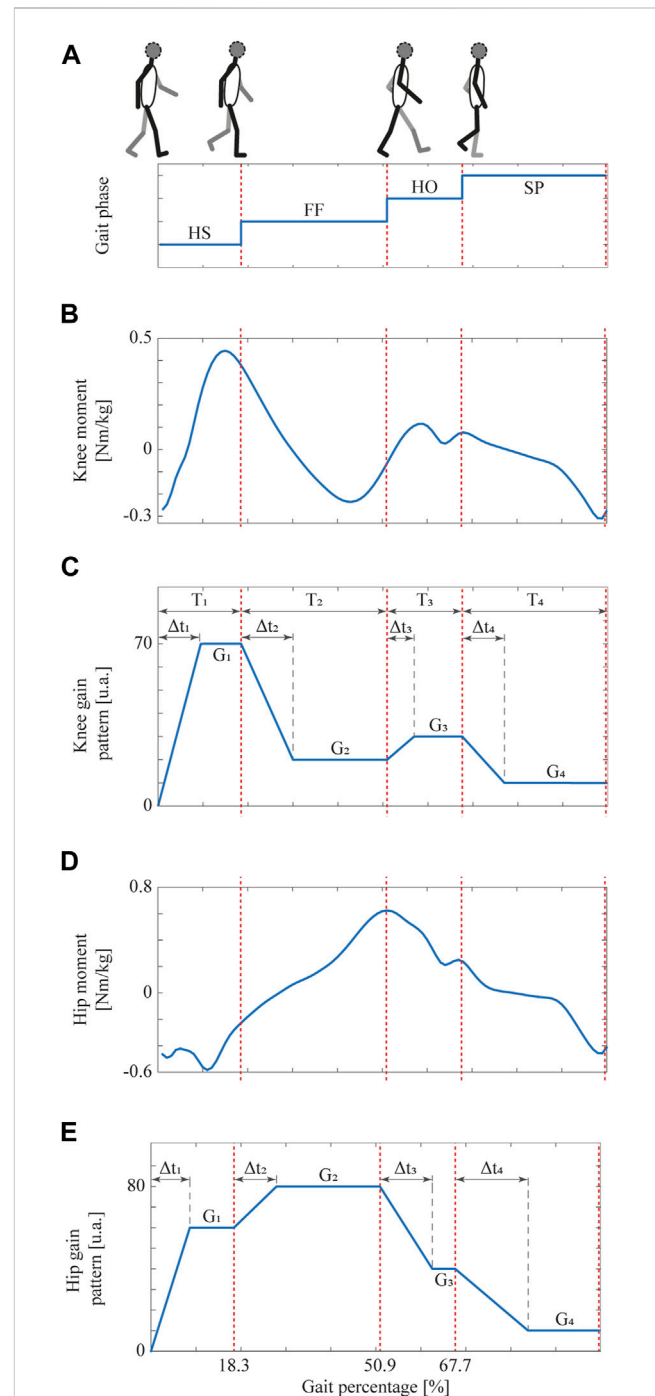


FIGURE 8

The gait phase detected schematic during the walking activity, taking into account the time spans (Δt_i) for each gait phase.; (A) Gait phases detected by means of the inertial-based partitioning method. (B) Knee and (D) Hip moment throughout the gait cycle in healthy subjects at a comfortable speed (Fukuchi et al., 2018). Also, gain patterns based on the (C) knee and (E) hip moment which ensures smooth transitions between gait phases. Adapted from (Villa-Parra et al., 2017).

Modulation Method in Figure 7), where Ph_d is the default phase from which the pattern begins to be generated, Ph_c is the current gait phase detected through the inertial-based algorithm, and ΔG is the gain increment added every sample.

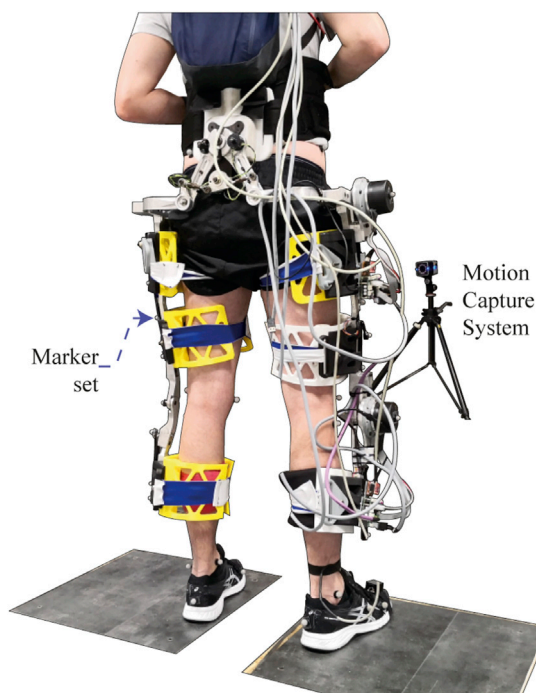


FIGURE 9
Experimental setup for trials with healthy subjects wearing the AGoRA exoskeleton.

Require:

```

1: procedure INITIALIZATION
2:  $G_i; \Delta t_i \leftarrow (0.0413 \cdot i \cdot H \cdot f_s) / v_u$ ;
3:  $Ph \leftarrow Ph_d; G \leftarrow G_{Ph_d}$ ;
4:  $step \leftarrow 1; \Delta G \leftarrow 0$ ;
5: end procedure

```

Ensure: G

```

6: for each new phase  $Ph$  do
7: if  $Ph_c \neq Ph$  then
8:  $\Delta G \leftarrow (G_{Ph_c} - G) / \Delta t_{Ph_c}$ ;
9:  $step \leftarrow 1$ ;
10:  $Ph \leftarrow Ph_c$ ;
11: else
12:  $G \leftarrow G + \Delta G$ ;
13:  $step \leftarrow step + 1$ ;
14: if  $step > \Delta t_{Ph}$  then
15:  $\Delta G \leftarrow 0$ ;
16: end if
17: end if
18: end for

```

Algorithm 2. Online Gait Pattern Modulation

2.4 Experimental protocol

The experimental protocol comprises two phases to evaluate the SC response during the walking activity. First, a preliminary test was carried out on a treadmill to assess the SC response in terms of angular hip position, angular knee position, detected gait phase, and the calculated

SC gains for the knee and the hip joints. Second, an overground walking test was implemented to assess the gait spatiotemporal parameters in healthy subjects using the SC in the AGoRA exoskeleton. The details about each test are featured below.

2.4.1 SC test in treadmill

The stance controller was tested through a pilot study that involved a healthy user (i.e., they did not suffer from any gait-associated pathology) who used the AGoRA exoskeleton while walking over a conventional treadmill. A six-minutes walking test (6MWT) was performed on the treadmill at $\frac{3\text{Km}}{\text{h}}$ (such a speed was determined during a preliminary 10-m walking test applied to the user). During this preliminary trial, the angular position, angular velocity, detected gait phase, and computed controller gains were obtained for both hip and knee joints. Data acquisition was executed through sensor recording features available within ROS.

2.4.2 SC test during overground walking

A pilot study was conducted involving six neurologically intact subjects (6 males, 25.5 ± 6.1 y.o., height of 1.8 ± 0.03 m, and weight of 71.5 ± 10.9 kg) to assess the SC influence on spatiotemporal parameters and lower-limbs kinematics in healthy subjects during exoskeleton-assisted overground gait. A unilateral version of the exoskeleton was used for this study, i.e., the right hip and knee joints were actuated while the left leg was only attached to the mechanical frame (no actuation mechanisms were assembled), as may be seen in Figure 9.

At the beginning of the test, the subject's anthropometric features were measured to adjust the exoskeleton segments accordingly and to set up the initial parameters of the admittance controller on the basis of the user's weight and height. The user then performed a 10-m overground walking test while wearing the IMU on the tip of their dominant foot and the acquisition module on their back for the training stage of the gait phase detection module. Subsequently, the AGoRA exoskeleton was mounted on the volunteer by attaching the Velcro straps to their limbs and donning the backpack containing the battery and the main board. An emergency button was then handed to the subject, as he was instructed to press it in any situation that might compromise their safety or comfort to completely shut down the device. Once the exoskeleton was already worn and powered, the user was encouraged to walk for a short period (not longer than 10 min) so he would accommodate the device. Ten level-ground 10-m walking trials were subsequently performed for each of the three experimental conditions: i) a Transparent Mode (TM) that used the admittance control described in Section 2.3.2 to compensate for the rigid nature of the unpowered device, ii) the actual SC mode, and iii) the unassisted mode (baseline level of this study) assessed after the exoskeleton was removed from the volunteer. The two initial conditions were randomized for each subject in such a way that they were not aware of which operation mode they were experiencing. All subjects were encouraged to walk at their self-selected comfortable speed, while different kinematic and kinetic data were captured. A 3D-motion analysis system Vicon, equipped with 12 high-speed infrared cameras (Vicon Motion Systems Ltd., Vicon-Oxford, United Kingdom), was used to monitor human and exoskeleton joint angular displacements at a sampling rate of 200 Hz. The marker set consisted of 27 reflective markers (configuration adapted from (Bourgain et al., 2018) and focused on lower limbs and pelvis), thus allowing a lower-limb analysis in an indoor analysis laboratory (see Figure 9). The subject was instructed to tap the floor

once firmly at the beginning of each trial so that a distinctive peak was recognizable by both measurement systems as a means of data synchronization.

The experimental protocol, including all the proposed procedures involving healthy subjects, were approved by the local Ethics Committee at the Colombian School of Engineering. All participants recruited for this study signed a written informed consent in which they stated to be aware of the possible risks they were facing while undergoing these trials and agreed to participate in spite of them. The volunteers of this study were selected based on their health status and physical conditions by taking into account the inclusion criteria listed below.

- Male able-bodied adults aged between 18 and 65 y.o.
- No history of a neurological, neuromuscular or physical disability that may hinder their normal gait pattern.
- Height within the range of 170–185 cm.
- Weight not greater than 90 kg.
- Some specific anthropometric measurements:
 - Femur length: 42–48 cm.
 - Distance between trochanters: 32–37 cm.
 - Tibia length: 28–31 cm.

These criteria were established based on the functional range within which the exoskeleton can be adjusted (see Section 2.1).

2.5 Data processing

Marker trajectories were first smoothed with an average sliding window (five values) with two passes in reverse direction to minimize the shifting effect. Any gaps in the raw motion data were filled using a C2-spline interpolation (gaps shorter than 15 frames) within the Vicon's software Nexus (Hybois et al., 2019). Marker trajectories and kinetic data were then imported into OpenSim v.3.3. software and processed through a multibody kinematic optimization technique. To this end, a lower-limb model was implemented based on Raabe's model (Raabe and Chaudhari, 2016) to generate a generic model with seven segments and 12 generalized

coordinates. The generic model was then scaled to each participant on the basis of a static acquisition captured before all walking trials. All trials were finally processed using the final model and the inverse kinematics tool available on the OpenSim software in order to obtain gait spatiotemporal parameters and hip-knee kinematics (Zacharias and Kannenberg, 2012; Knaepen et al., 2014).

2.6 Statistical and user's satisfaction analysis

Regarding statistical analysis, gait spatiotemporal parameters (e.g., step length, cadence, etc.) and hip and knee flexion/extension values from the six involved subjects were loaded into the SPSS software v.23.0 (IBM-SPSS Inc., Armonk, NY, United States), and either one-way repeated-measures ANOVA tests were conducted to compare among experimental conditions with a statistical significance level of $p < 0.05$ or Friedman tests (non-parametric version of ANOVA test) depending on whether the data exhibited a normal distribution or not (Shapiro-Wilk test). Bonferroni's tests were carried out as a *post hoc* test in case significant differences were found.

Finally, a questionnaire (adapted Quebec User Evaluation of Satisfaction with Assistive Technology, QUEST 2.0) was used to evaluate the subject's perception towards the assistive device (Demers et al., 2002). Only the questions related to assistive technology (e.g., weight, safety, durability, simplicity of use, and comfort) were used in this study since the AGoRA exoskeleton is still undergoing validation stages. The score for each question ranges from 1 to 5 (1: not satisfied at all; 2: not very satisfied; 3: more or less satisfied; 4: quite satisfied; and 5: very satisfied), and a final score is obtained as the median \pm the interquartile range of the valid responses.

3 Results

3.1 SC response during treadmill walking

Figure 10 shows the system response under treadmill walking conditions in terms of angular position, angular

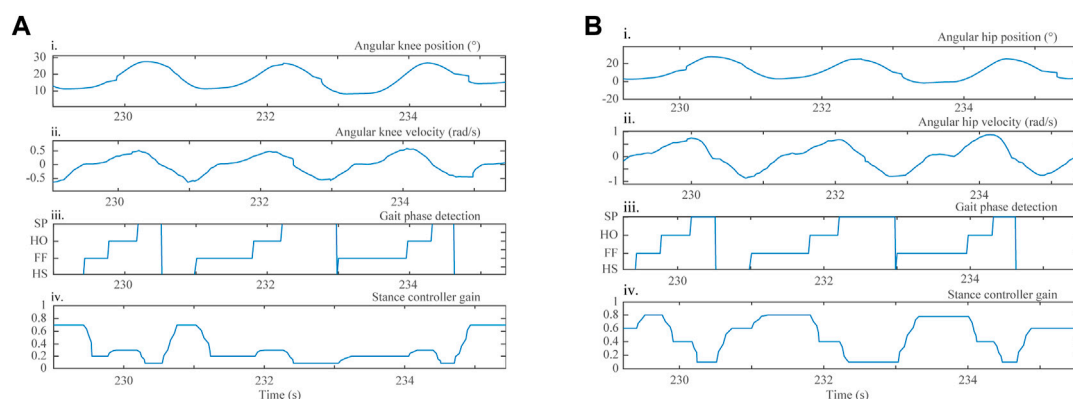


FIGURE 10

Three gait cycles of a healthy subject during a 6-min treadmill walking test, in terms of the following parameters: (i) angular joint position; (ii) angular joint velocity acquired with the AGoRA exoskeleton incremental encoders; (iii) gait phase detection outcome, determined using the gait phase detection module; and (iv) modulation method response, for the (A) knee and (B) hip joints.

TABLE 1 Spatiotemporal gait parameters calculated by the 3D-motion analysis system Vicon for all experimental conditions assessed: Unassisted, Transparent Mode (TM), and Stance Control (SC) (mean \pm std). Asterisks indicate significant differences from the unassisted condition (Bonferroni, $p < 0.05$).

Parameter	Unassisted	TM	SC
Gait velocity [m/s]	1.12 \pm 0.34	0.78 \pm 0.35	0.66 \pm 0.23*
Cadence [steps/min]	83.38 \pm 21.71	61.95 \pm 21.21	58.77 \pm 18.33
Stride length [cm]	161.68 \pm 9.47	146.88 \pm 20.91	135.88 \pm 27.77
Step duration (right leg) [s]	0.90 \pm 0.46	1.16 \pm 0.60	1.15 \pm 0.65
Step duration (left leg) [s]	0.70 \pm 0.096	1.06 \pm 0.51	1.14 \pm 0.4
Stride duration [s]	1.59 \pm 0.51	2.21 \pm 1.02	2.28 \pm 0.94
Stance phase (right leg) [%]	53.8 \pm 9.52	50.32 \pm 11.9	48.28 \pm 13.07
Stance phase (left leg) [%]	45.91 \pm 9.6	49.32 \pm 12.01	51.31 \pm 13.09

velocity, the gait phase detected through the inertial-based method, and the resulting controller gain across few gait cycles for both hip and knee exoskeleton joints. Such outcome exhibits angular position (Figure 10Ai; Figure 10Bi) and angular velocity values (Figure 10Aii; Figure 10Bii) which are typical for healthy subjects (Knaepen et al., 2014) and the way the modulation method (described Section 2.3.3 and shown in Figure 10Aiii; Figure 10Biii) successfully renders reasonable gain values for the admittance controller (described in Section 2.3.3 and shown in Figure 10Aiv; Figure 10Biv).

3.2 Gait parameters during overground walking

Spatiotemporal gait parameters among the three experimental conditions, i.e., unassisted, TM, and SC, are presented in Table 1. For the six involved participants, these results only demonstrate a significant difference from the unassisted condition for the case of gait velocity while walking in SC ($p = 0.048$). Conversely, the other spatiotemporal parameters show no significant difference from the unconstrained baseline (i.e., unassisted condition) which lies close to typical gait parameters found previously for healthy subjects (Knaepen et al., 2014).

3.3 Human joint kinematics during overground walking

Likewise, the peak joint angles during unassisted walking and exoskeleton-assisted gait are presented in Table 2. Significant differences from the unconstrained condition were found for the peak knee flexion on the right leg (i.e., the actuated side) during both operation modes: TM ($p = 0.001$) and SC ($p = 0.000$). Also, the left side, i.e., the inactive side, shows a significant reduction in peak knee flexion during TM ($p = 0.01$). On the other hand, hip kinematics remains untouched while being assisted by the AGoRA exoskeleton since no noteworthy differences were found while the peak hip flexion/extension values lie close to typical values found for healthy subjects during unconstrained overground walking (Ward et al., 2017; Fukuchi et al., 2018).

Additionally, the user survey regarding their satisfaction towards the AGoRA exoskeleton controlled by the proposed approaches produced the following outcomes: weight: 4 ± 1 , dimensions: 3 ± 1 , adjustment (meaning the user's perception towards the system used to attach the exoskeleton to their limbs, i.e., the fastening system and telescopic bars): 3 ± 1 , safety: 5 ± 0.25 , stability (meaning how close the subject felt as though they were about to fall): 4 ± 0.25 , durability: 3 ± 1.25 , ease of use (i.e., how intuitive it is to use): 4 ± 1 , and comfort: 3 ± 0.25 , within a range between 0 and 5.

Based on the experiences gained during the experimental trials, further use with the designed platform would require a therapist or assistant well aware and capable of adjusting and mounting the exoskeleton on the user. The total time needed for the donning process was found to be around 25–30 min when the orthosis is being used for the first time since more time is required to measure the subject's anthropometric measurements and properly adjust the length of thigh and shank segments.

4 Discussion

This work presents the performance assessment of the AGoRA exoskeleton during two experimental phases. The first phase evaluates the SC response with a healthy user performing a 6MWT over a treadmill in terms of angular position, angular velocity, detected gait phase, and controller gain. The second

TABLE 2 Lower-limb kinematics calculated by the 3D-motion analysis system Vicon for all experimental conditions assessed: Unassisted, Transparent Mode (TM), and Stance Control (SC) (mean \pm std). Asterisks indicate significant differences from unassisted condition (Bonferroni, $p < 0.05$).

Parameter	Unassisted	TM	SC
Peak knee flexion (right leg) [°]	−66.80 \pm 5.59	−47.33 \pm 7.10*	−46.48 \pm 5.44*
Peak knee flexion (left leg) [°]	−64.02 \pm 5.65	−52.37 \pm 9.46*	−53.84 \pm 11.47
Peak hip flexion (right leg) [°]	26.00 \pm 4.62	25.62 \pm 7.35	21.97 \pm 9.45
Peak hip flexion (left leg) [°]	24.74 \pm 4.67	25.04 \pm 4.94	26.30 \pm 7.71
Peak hip extension (right leg) [°]	−17.22 \pm 4.41	−11.58 \pm 6.08	−13.86 \pm 7.28
Peak hip extension (left leg) [°]	−17.38 \pm 4.02	−17.00 \pm 3.58	−18.83 \pm 5.22

phase features the short-term effects on the walking pattern of six healthy subjects during overground walking. This lower-limb active orthosis operates using a TM that suppresses the dynamics of a non-backdrivable structure to some extent, and an SC that is meant to provide support to both knee and hip joints during the stance phase whereas it allows free movement during the swing phase. This SC approach varies hip and knee impedances on the basis of two anthropometric measurements: height and weight. Such consideration has been widely taken into account in previous designs of SC orthoses (Rafiei et al., 2016; Villa-Parra et al., 2017). However, by using an adaptive method based on a machine-learning model and a minimal number of inertial sensors for gait phase estimation purposes, we expect to further research the effects of this control strategy on healthy subjects.

First, the treadmill-walking experimental phase served as a pilot study to evaluate the overall performance of the device and to fix minor hard- and software bugs before conducting experimental trials with it operating in a more autonomous manner (i.e., overground walking). The angular velocity profiles exhibited for both assisted joints are the result of stiffness values generated through the SC gain (varied as a function of the detected gait phase, as explained in Section 2.3.3) and show a pattern already observed in healthy subjects in previous studies (Knaepen et al., 2014). For instance, the knee modulation response (shown in Figure 10Aiv) exhibits low stiffness values during knee extension and progressively increased stiffness values during knee flexion, as reported in (Shamaei et al., 2013b). Likewise, the modulation method response for the hip joint (shown in Figure 10Biv) is in agreement with previous work as high stiffness values are applied during the HS gait phase (Huang and Wang, 2016; Akl et al., 2020).

And so, during the overground-walking experimental phase, regarding spatiotemporal gait parameters, only the gait velocity appeared to be significantly affected by the exoskeleton while operating in SC. Even though a slight reduction in gait velocity during robot-assisted training is not ideal, previous studies have demonstrated that this parameter can reduce up to 0.57 m/s while wearing an orthosis commanded by an SC approach (Rafiei et al., 2016). Also, the gait velocity obtained applying SC is close to further results registered in (Knaepen et al., 2014; Villa-Parra et al., 2017; Ortlieb et al., 2019). Thus, such a variation seems not to be critical, also because further gait parameters did not demonstrate any significant influence by the exoskeleton while they remained close to those which are considered typical among able-bodied individuals. For instance, a study with similar experimental conditions to those imposed in this study found cadence to be around 79.7 ± 3.66 steps/min, whereas the step duration was equal to 0.76 ± 0.04 and 0.75 ± 0.03 s for right and left legs respectively, during normal overground walking (Knaepen et al., 2014). Furthermore, a study of gait analysis using an active knee orthosis reports the swing phase to be between 36% and 51% of the gait cycle (Arazpour et al., 2016), thus complying with the stance phase percentages found in this work for exoskeleton-aided walking (as may be seen in Table 1). Finally, although the stride length decreases between unassisted and assisted conditions, it remains in range with the parameters estimated for the AUTONOMYO exoskeleton (Ortlieb et al., 2019), for instance.

Regarding lower-limb kinematics, at least one significant difference per side was found for the case of the peak knee flexion, with a mean peak value of approximately 46.48° during the SC condition. Normally,

the human knee joint needs 67° of flexion during the swing phase in healthy subjects during normal walking. However, the maximum knee flexion is highly dependent on the user's gait speed. Knee peak values close to 67° have been registered when users walk at approximately 1.25 m/s, whereas values between 40° and 50° are associated to gait velocities near 0.5 m/s (Asseldonk et al., 2008). Even more, using an SC orthosis has proven to reduce this value to 40° in healthy subjects (Arazpour et al., 2014). Such outcomes along with other studies, where the knee stiffness is controlled through robot-aided assistance and similar knee kinematics are displayed (Shamaei et al., 2013a; Cestari et al., 2015; Ortlieb et al., 2019), suggest that the influence of the AGoRA exoskeleton on the user's knee is in accordance with what is found in the literature. In the same way, the peak hip flexion and extension registered during the SC assessment are similar to those presented in (Asseldonk et al., 2008), HUALEX exoskeleton (Tran et al., 2016), and the unilateral orthosis reported in (Hussain et al., 2013).

For this particular setting, such a reduction in terms of knee angular displacement seems to be attributable to some hardware issue (in particular, to the fastening system), since the left side, which has no actuation mechanism assembled and thus perceives no electromechanical activation, also shows a significant reduction in peak knee flexion during TM. An improper attachment to the user's limbs mainly produces joint misalignments which are a well-known problem when dealing with physically coupled systems, e.g., humans wearing exoskeletons (Gordon et al., 2018). If perfectly-aligned joints are assumed, exoskeleton forces can be modeled as equal. Nevertheless, the presence of joint misalignment results in the imperfect transmission of torque from the exoskeleton to the user's body (Schiele and van der Helm, 2006), thus introducing undesirable forces parallel to the human limb which can cause discomfort or unintended changes in the behavior of the control system. In spite of this, hip kinematics present no considerable change from the baseline condition, which may imply a better attachment to the pelvic region, and thus, better compliance of the exoskeleton's control system on the hip joint. Overall, it cannot be ruled out that the differences among experimental conditions could have been much lower if the users had been fitted with an optimal orthosis system.

Concerning user satisfaction, results show that the lowest score (3) was related to the items regarding "dimensions", "durability", "comfort", and "adjustment". It is worth noting that the insight concerning dimensions might be related to the inherent protrusion of the actuation mechanisms which are placed laterally, and whose bulkiness is even more notorious in a unilateral device such as the version proposed for this study. Likewise, the comfort factor in wearable devices has been commonly associated with features such as sensors, straps, and weight (Huo et al., 2016). Besides, offering unilateral hip and knee assistance for healthy subjects may be an additional factor that promotes the discomfort experienced by the participants, since some of them expressed feeling some pain in the upper back after wearing the exoskeleton. Physiological theories have been developed to address these limitations (Li et al., 2015), but this issue remains a major problem for powered autonomous orthoses. Finally, the remark on the adjustment system seems to be in accordance with the analysis drawn from the kinematic outcomes and thus encourages some hardware modifications to obtain a more robust system, e.g., new materials able to properly adjust the exoskeleton and to suppress relative movement between human and machine.

Finally, it is important to note that this study is limited by the reduced number of subjects recruited for the study, which

compromises to some extent the power of the applied statistical tests. However, since the participants were rather homogeneous in terms of age and anthropometric measures due to the reduced operating spectrum that the exoskeleton provides, the outcomes should allow the debugging of several hard and software issues (discovered during experimental trials) for further iterations of the device and future trials with mobility-impaired patients. Besides, although the results found in terms of spatiotemporal gait parameters and lower-limb kinematics are similar to those presented in the literature, the use of a single sensor unit attached to the user might be useful for clinical settings where wearability is critical and donning times are expected to be reduced.

5 Conclusion

The performance evaluation of the AGoRA exoskeleton in the short term in healthy subjects has been featured in the present study. Six neurologically-intact subjects were recruited to perform several overground trials under three experimental conditions: unassisted walking, and exoskeleton-assisted walking while operating in TM and SC. Spatiotemporal gait parameters and lower-limb kinematics were processed from measurements captured by a motion capture system based on passive optical markers. Additionally, in order to assess the exoskeleton's performance both objectively and subjectively, a user survey was conducted to collect data regarding their satisfaction with the implemented technology.

Most spatiotemporal parameters did not exhibit any significant change from the unassisted condition for both operation modes, and only knee kinematics was compromised while the user was wearing the exoskeleton. However, given the fact that the sample size of the present study does not guarantee statistical power, the results here presented should be taken with caution and should not be considered as definitive proof of the efficiency of the approach implemented. Furthermore, an improper attachment to the subject's limbs, as a consequence of a deficient fastening system, did not ensure kinematic compatibility and could have influenced the effect of the torque profiles coming out of the control system.

Thus, the research conducted in this study together with the results obtained should only serve as a preliminary evaluation to validate the alterations in the gait pattern generated by the non-backdrivable exoskeleton applying a control strategy based on stance control. The gait alterations for an entire significant population are not discussed in this study. On the other hand, this work is not intended to prove its effectiveness within a gait rehabilitation program. Although the gait pattern of healthy subjects seems to remain unaffected by the actuation of the exoskeleton, further studies should involve actual stroke survivors so that a real comparison with respect to traditional therapy is feasible. To this end, a larger sample size is recommended. It has been estimated that at least 384 participants should be involved in the future to achieve a confidence level of 95% and an error margin of $\pm 5\%$. Also, further modifications of the device should be carried out in the hardware and software architectures to facilitate its donning and command by healthcare professionals within a clinical setting, such as the

improvement of the fastening system to make it easier to adjust and more robust to misalignments, and the development of a graphical user interface.

Data availability statement

The original contributions presented in the study are included in the article/Supplementary Material, further inquiries can be directed to the corresponding author.

Ethics statement

The studies involving human participants were reviewed and approved by the Ethics Committee at the Colombian School of Engineering. The patients/participants provided their written informed consent to participate in this study.

Author contributions

MS-M, LA-M, MB, TP, MM, and CC contributed to the conception and design of the study. MS-M organized the database and performed the statistical analysis. MS-M and LA-M wrote the first draft of the manuscript. All authors contributed to manuscript revision, read, and approved the submitted version.

Funding

This work was supported by the Colombian Ministry of Science, Technology and Innovation Minciencias (grant ID No. 801–2017), CYTED research network REASISTE (grant 216RT0505), and funding from the Colombian School of Engineering Julio Garavito and the mobility chair of the EPF foundation: Sport and Rehabilitation Tech & Design Education.

Conflict of interest

The authors declare that the research was conducted in the absence of any commercial or financial relationships that could be construed as a potential conflict of interest.

Publisher's note

All claims expressed in this article are solely those of the authors and do not necessarily represent those of their affiliated organizations, or those of the publisher, the editors and the reviewers. Any product that may be evaluated in this article, or claim that may be made by its manufacturer, is not guaranteed or endorsed by the publisher.

References

- Akl, A. R., Baca, A., Richards, J., and Conceição, F. (2020). Leg and lower limb dynamic joint stiffness during different walking speeds in healthy adults. *Gait Posture* 82, 294–300. doi:10.1016/j.gaitpost.2020.09.023
- Al-Shuka, H. F., Rahman, M. H., Leonhardt, S., Ciobanu, I., and Berteau, M. (2019). Biomechanics, actuation, and multi-level control strategies of power-augmentation lower extremity exoskeletons: An overview. *Int. J. Dyn. Control* 7, 1462–1488. doi:10.1007/s40435-019-00517-w
- Arazpour, M., Ahmadi, F., Bani, M. A., Hutchins, S. W., Bahramizadeh, M., Ghomshe, F. T., et al. (2014). Gait evaluation of new powered knee-ankle-foot orthosis in able-bodied persons: A pilot study. *Prosthetics Orthot. Int* 38, 39–45. doi:10.1177/0309364613486917
- Arazpour, M., Moradi, A., Samadian, M., Bahramizadeh, M., Joghataei, M., Bani, M. A., et al. (2016). The influence of a powered knee-ankle-foot orthosis on walking in poliomyelitis subjects: A pilot study. *Prosthetics Orthot. Int* 40, 377–383. doi:10.1177/0309364615592703
- Asseldonk, E. H. V., Veneman, J. F., Ekkelenkamp, R., Buurke, J. H., Helm, F. C. V. D., and Kooij, H. V. D. (2008). The effects on kinematics and muscle activity of walking in a robotic gait trainer during zero-force control. *IEEE Trans. Neural Syst. Rehabilitation Eng.* 16, 360–370. doi:10.1109/TNSRE.2008.925074
- Attal, F., Amirat, Y., Chibani, A., and Mohammed, S. (2018). Automatic recognition of gait phases using a multiple regression hidden markov model. *IEEE/ASME Trans. Mechatronics* 1, 1. doi:10.1109/TMECH.2018.2836934
- Attal, F., Mohammed, S., Dedabrishvili, M., Chamroukhi, F., Oukhellou, L., and Amirat, Y. (2015). Physical human activity recognition using wearable sensors. *Sensors Switz.* 15, 31314–31338. doi:10.3390/s151229858
- Bacek, T., Moltedo, M., Rodriguez-Guerrero, C., Geeroms, J., Vanderborcht, B., and Lefeber, D. (2018). Design and evaluation of a torque-controllable knee joint actuator with adjustable series compliance and parallel elasticity. *Mech. Mach. Theory* 130, 71–85. doi:10.1016/j.MECHMACHTHEORY.2018.08.014
- Bayón, C., Ramírez, O., Serrano, J., Castillo, M. D., Pérez-Somarriba, A., Belda-Lois, J., et al. (2017). Development and evaluation of a novel robotic platform for gait rehabilitation in patients with cerebral palsy: CPWalker. *Robotics Aut. Syst.* 91, 101–114. doi:10.1016/j.ROBOT.2016.12.015
- Bennett, T. R., Wu, J., Kehtarnavaz, N., and Jafari, R. (2016). Inertial measurement unit-based wearable computers for assisted living applications: A signal processing perspective. *IEEE Signal Process. Mag.* 33, 28–35. doi:10.1109/MSP.2015.2499314
- Bortole, M. (2014). “Robotic exoskeleton with an assist-as-needed control strategy for gait rehabilitation after stroke.” Ph.D. thesis (Getafe: Univ. Carlos III de Madrid).
- Bourgain, M., Hybois, S., Thoreux, P., Rouillon, O., Rouch, P., and Sauret, C. (2018). Effect of shoulder model complexity in upper-body kinematics analysis of the golf swing. *J. Biomechanics* 75, 154–158. doi:10.1016/j.jbiomech.2018.04.025
- Bulea, T. C., Kobetic, R., Audu, M. L., and Triolo, R. J. (2013). Stance controlled knee flexion improves stimulation driven walking after spinal cord injury. *J. NeuroEng. Rehab.* 10, 68. doi:10.1186/1743-0003-10-68
- Caldas, R., Mundt, M., Potthast, W., Buarque de Lima Neto, F., and Markert, B. (2017). A systematic review of gait analysis methods based on inertial sensors and adaptive algorithms. *Gait Posture* 57, 204–210. doi:10.1016/j.gaitpost.2017.06.019
- Cestari, M., Sanz-Merodio, D., Arevalo, J. C., and García, E. (2015). An adjustable compliant joint for lower-limb exoskeletons. *IEEE/ASME Trans. Mechatronics* 20, 889–898. doi:10.1109/TMECH.2014.2324036
- Colombo, G., Joerg, M., Schreier, R., and Dietz, V. (2000). Treadmill training of paraplegic patients using a robotic orthosis. *J. rehab. res. dev.* 37, 693–700.
- del Ama Espinosa, A. J. (2013). “Hybrid walking therapy with fatigue management for spinal cord injured individuals.” Ph.D. thesis (Getafe: Univ. Carlos III de Madrid).
- Demers, L., Monette, M., Lapierre, Y., Arnold, D. L., and Wolfson, C. (2002). Reliability, validity, and applicability of the Quebec User Evaluation of Satisfaction with assistive Technology (QUEST 2.0) for adults with multiple sclerosis. *Disabil. Rehab* 24, 21–30. doi:10.1080/09638280110066352
- Dzahir, M., and Yamamoto, S.-i. (2014). Recent trends in lower-limb robotic rehabilitation orthosis: Control scheme and strategy for pneumatic muscle actuated gait trainers. *Robotics* 3, 120–148. doi:10.3390/robotics3020120
- Dzeladini, F., Wu, A. R., Renjewski, D., Arami, A., Burdet, E., van Asseldonk, E., et al. (2016). “Effects of a neuromuscular controller on a powered ankle exoskeleton during human walking.” in 2016 6th IEEE Int. Conf. on Biomedical Robotics and Biomechatronics (BioRob), Singapore, 26–29 June 2016 (IEEE), 617–622. doi:10.1109/BIOROB.2016.7523694
- Ferris, D. P., Gordon, K. E., Sawicki, G. S., and Peethambaran, A. (2006). An improved powered ankle-foot orthosis using proportional myoelectric control. *Gait Posture* 23, 425–428. doi:10.1016/j.gaitpost.2005.05.004
- Fukuchi, C. A., Fukuchi, R. K., and Duarte, M. (2018). A public dataset of overground and treadmill walking kinematics and kinetics in healthy individuals. *PeerJ* 6, e4640. doi:10.7717/peerj.4640
- Gams, A., Petric, T., Debevec, T., and Babic, J. (2013). Effects of robotic knee exoskeleton on human energy expenditure. *IEEE Trans. Biomed. Eng.* 60, 1636–1644. doi:10.1109/TBME.2013.2240682
- Geyer, H., Seyfarth, A., and Blickhan, R. (2006). Compliant leg behaviour explains basic dynamics of walking and running. *Proc. Biol. Sci.* 273, 2861–2867. doi:10.1098/rspb.2006.3637
- Gordon, D. F. N., Henderson, G., and Vijayakumar, S. (2018). Effectively quantifying the performance of lower-limb exoskeletons over a range of walking conditions. *Front. Robotics AI* 5, 61. doi:10.3389/frobt.2018.00061
- Gouwanda, D., and Gopalai, A. A. (2015). A robust real-time gait event detection using wireless gyroscope and its application on normal and altered gaits. *Med. Eng. Phys.* 37, 219–225. doi:10.1016/j.medengphy.2014.12.004
- Hogan, N. (1984). “Impedance control: An approach to manipulation,” in 1984 Am. Control Conf, San Diego, CA, USA, 06–08 June 1984, 304–313. doi:10.23919/ACC.1984.4788393
- Hoogen, J., Rienen, R., and Schmidt, G. (2002). Control aspects of a robotic haptic interface for kinesthetic knee joint simulation. *Control Eng. Pract.* 10, 1301–1308. doi:10.1016/S0967-0661(02)00085-0
- Huang, Y., and Wang, Q. (2016). Torque-stiffness-controlled dynamic walking: Analysis of the behaviors of bipeds with both adaptable joint torque and joint stiffness. *IEEE Robotics Automation Mag.* 23, 71–82. doi:10.1109/MRA.2015.2510753
- Hughes, A., Freeman, C., Burrage, J., Chappell, P., Lewin, P., and Rogers, E. (2009). Feasibility of iterative learning control mediated by functional electrical stimulation for reaching after stroke. *Neurorehab. Neural Repair* 23, 559–568. doi:10.1177/1545968308328718
- Huo, W., Mohammed, S., Moreno, J. C., and Amirat, Y. (2016). Lower limb wearable robots for assistance and rehabilitation: A state of the art. *IEEE Syst. J.* 10, 1068–1081. doi:10.1109/JSYST.2014.2351491
- Hussain, S., Xie, S. Q., and Jamwal, P. K. (2013). Adaptive impedance control of a robotic orthosis for gait rehabilitation. *IEEE Trans. Cybern.* 43, 1025–1034. doi:10.1109/TSMCB.2012.2222374
- Hybois, S., Puchaud, P., Bourgain, M., Lombart, A., Bascou, J., Lavaste, F., et al. (2019). Comparison of shoulder kinematic chain models and their influence on kinematics and kinetics in the study of manual wheelchair propulsion. *Med. Eng. Phys.* 69, 153–160. doi:10.1016/j.medengphy.2019.06.002
- Ichinose, W. E., Reinkensmeyer, D. J., Aoyagi, D., Lin, J. T., Ngai, K., Edgerton, V. R., et al. (2003). A robotic device for measuring and controlling pelvic motion during locomotor rehabilitation. *Annu. Int. Conf. IEEE Eng. Med. Biol. - Proc.* 2, 1690–1693. doi:10.1109/iembs.2003.1279715
- Ir, M., and Azuan Ao, N. (2015). Stance-control-orthoses with electromechanical actuation mechanism: Usefulness, design analysis and directions to overcome challenges. *J. Neurol. Neurosci.* 6, 4. doi:10.21767/2171-6625.100049
- Knaepen, K., Beyl, P., Duerinck, S., Hagman, F., Lefeber, D., and Meeusen, R. (2014). Human-robot interaction: Kinematics and muscle activity inside a powered compliant knee exoskeleton. *IEEE Trans. Neural Syst. Rehab. Eng.* 22, 1128–1137. doi:10.1109/TNSRE.2014.2324153
- Krebs, H. I., Volpe, B. T., Aisen, M. L., and Hogan, N. (2000). Increasing productivity and quality of care: Robot-aided neuro-rehabilitation. *J. Rehab. Res. Dev.* 37, 639–652.
- Kumar, S., Wöhrle, H., Trampler, M., Simnófske, M., Peters, H., Mallwitz, M., et al. (2019). Modular design and decentralized control of the recupera exoskeleton for stroke rehabilitation. *Appl. Sci. Switz.* 9, 626. doi:10.3390/app9040626
- Lagoda, C., Moreno, J. C., and Pons, J. L. (2012). Human-robot interfaces in exoskeletons for gait training after stroke: State of the art and challenges. *Appl. Bionics Biomechanics* 9, 193–203. doi:10.1155/2012/901483
- Lee, H., Ferguson, P. W., and Rosen, J. (2020). “Chapter 11. Lower limb exoskeleton systems—overview,” in *Wearable robotics: Systems and applications*. Editors J. Rosen and P. W. Ferguson (Cambridge: Academic Press). doi:10.1016/B978-0-12-814659-0.00011-4
- Lemke, M. R., Wendorff, T., Mieth, B., Buhl, K., and Linnemann, M. (2000). Spatiotemporal gait patterns during over ground locomotion in major depression compared with healthy controls. *J. psychiatric res.* 34, 277–283. doi:10.1016/S0022-3956(00)00017-0
- Li, N., Yan, L., Qian, H., Wu, H., Wu, J., and Men, S. (2015). Review on lower extremity exoskeleton robot. *Tech. rep.*
- Lim, D. H., Kim, W. S., Kim, H. J., and Han, C. S. (2017). Development of real-time gait phase detection system for a lower extremity exoskeleton robot. *Int. J. Precis. Eng. Manuf.* 18, 681–687. doi:10.1007/s12541-017-0081-9
- Mannini, A., and Sabatini, A. M. (2012). Gait phase detection and discrimination between walking jogging activities using hidden Markov models applied to foot motion data from a gyroscope. *Gait Posture* 36, 657–661. doi:10.1016/j.gaitpost.2012.06.017

- Mannini, A., and Sabatini, A. M. (2010). Machine learning methods for classifying human physical activity from on-body accelerometers. *Sensors* 10, 1154–1175. doi:10.3390/s100201154
- Marchal-Crespo, L., and Reinkensmeyer, D. J. (2009). Review of control strategies for robotic movement training after neurologic injury. *J. NeuroEng. Rehab.* 6, 20. doi:10.1186/1743-0003-6-20
- Martin, C. (2020). Comparison of machine learning models: Gesture recognition using a multimodal wrist orthosis for tetraplegics. *J. Purdue Undergrad. Res.* 10, 14. doi:10.7771/2158-4052.1435
- Mehrholz, J., Thomas, S., Werner, C., Kugler, J., Pohl, M., and Elsner, B. (2017). Electromechanical-assisted training for walking after stroke. *Cochrane Database Syst. Rev.* 5, CD006185. doi:10.1002/14651858.CD006185.pub4
- Minchala, L. I., Astudillo-Salinas, F., Palacio-Baus, K., and Vazquez-Rodas, A. (2017). “Mechatronic design of a lower limb exoskeleton,” in *Design, control and applications of mechatronic systems in engineering*. Editor S. Yildirim (London, United Kingdom: intechopen). doi:10.5772/67460
- Ortlieb, A., Lichard, P., Dzeladini, F., Baud, R., Bleuler, H., Ijspeert, A., et al. (2019). “Investigation on variable impedance control for modulating assistance in walking strategies with the autonomy exoskeleton,” in *Biosystems and biorobotics* (Springer Int. Publishing), 75–79. doi:10.1007/978-3-030-01887-0_15
- Panahandeh, G., Mohammadi, N., Leijon, A., and Handel, P. (2013). Continuous hidden markov model for pedestrian activity classification and gait analysis. *IEEE Trans. Instrum. Meas.* 62, 1073–1083. doi:10.1109/TIM.2012.2236792
- Pasquina, P. F., Emba, C. G., and Corcoran, M. (2017). *Lower limb disability: Present military and civilian needs*. New York.
- Pons, J. L., Ceres, R., and Caldern, L. (2008). “Introduction to wearable robotics,” in *Wearable robots* (Chichester, UK: John Wiley & Sons), 1–16. doi:10.1002/9780470987667.ch1
- Raabe, M. E., and Chaudhari, A. M. (2016). An investigation of jogging biomechanics using the full-body lumbar spine model: Model development and validation. *J. Biomechanics* 49, 1238–1243. doi:10.1016/j.jbiomech.2016.02.046
- Rabiner, L. (1989). A tutorial on hidden Markov models and selected applications in speech recognition. *Proc. IEEE* 77, 257–286. doi:10.1109/5.18626
- Rafaei, M., Bahramizadeh, M., Arzpour, M., Samadian, M., Hutchins, S. W., Farahmand, F., et al. (2016). The gait and energy efficiency of stance control knee-ankle-foot orthoses: A literature review. *Prosthetics Orthot. int* 40, 202–214. doi:10.1177/0309364615588346
- Rietdyk, S., Patla, A. E., Winter, D. A., Ishac, M. G., and Little, C. E. (1999). Balance recovery from medio-lateral perturbations of the upper body during standing. *J. Biomechanics* 32, 1149–1158. doi:10.1016/S0021-9290(99)00116-5
- Sánchez Manchola, M. D., Pinto Bernal, M. J., Munera, M., and Cifuentes, C. A. (2019). Gait phase detection for lower-limb exoskeletons using foot motion data from a single inertial measurement unit in hemiparetic individuals. *Sensors* 19, 2988. doi:10.3390/s19132988
- Sánchez-Manchola, M., Gómez-Vargas, D., Casas-Bocanegra, D., Múnera, M., and Cifuentes, C. A. (2018). “Development of a robotic lower-limb exoskeleton for gait rehabilitation: Agora exoskeleton,” in 2018 IEEE ANDESCON, Santiago de Cali, Colombia, 22–24 August 2018, 1–6. doi:10.1109/ANDESCON.2018.8564692
- Schiele, A., and van der Helm, F. C. T. (2006). Kinematic design to improve ergonomics in human machine interaction. *IEEE Trans. Neural Syst. Rehab. Eng.* 14, 456–469. doi:10.1109/TNSRE.2006.881565
- Schwartz, I., and Meiner, Z. (2015). Robotic-assisted gait training in neurological patients: Who may benefit? *Ann. Biomed. Eng.* 43, 1260–1269. doi:10.1007/s10439-015-1283-x
- Shamaei, K., Cenciarini, M., Adams, A. A., Gregorczyk, K. N., Schiffman, J. M., and Dollar, A. M. (2014). Design and evaluation of a quasi-passive knee exoskeleton for investigation of motor adaptation in lower extremity joints. *IEEE Trans. Biomed. Eng.* 61, 1809–1821. doi:10.1109/TBME.2014.2307698
- Shamaei, K., and Dollar, A. M. (2011). On the mechanics of the knee during the stance phase of the gait. *IEEE Int. Conf. Rehab. Robotics*. 2011, 5975478. doi:10.1109/ICORR.2011.5975478
- Shamaei, K., Napolitano, P. C., and Dollar, A. M. (2013a). A quasi-passive compliant stance control knee-ankle-foot orthosis. *IEEE Int. Conf. Rehabil. Robot.* 2013, 6650471. doi:10.1109/ICORR.2013.6650471
- Shamaei, K., Sawicki, G. S., and Dollar, A. M. (2013b). Estimation of quasi-stiffness of the human knee in the stance phase of walking. *PLoS ONE* 8, e59993. doi:10.1371/journal.pone.0059993
- Smith, B., Coiro, D., Finson, R., Betz, R., and McCarthy, J. (2002). Evaluation of force-sensing resistors for gait event detection to trigger electrical stimulation to improve walking in the child with cerebral palsy. *IEEE Trans. Neural Syst. Rehab. Eng.* 10, 22–29. doi:10.1109/TNSRE.2002.1021583
- Taborri, J., Palermo, E., Rossi, S., and Cappa, P. (2016). Gait partitioning methods: A systematic review. *Sensors* 16, 66. doi:10.3390/s16010066
- Taborri, J., Rossi, S., Palermo, E., Patané, F., and Cappa, P. (2014). A novel HMM distributed classifier for the detection of gait phases by means of a wearable inertial sensor network. *Sensors* 14, 16212–16234. doi:10.3390/s140916212
- Taborri, J., Scalona, E., Rossi, S., Palermo, E., Patané, F., and Cappa, P. (2015). “Real-time gait detection based on Hidden Markov Model: Is it possible to avoid training procedure?,” in 2015 IEEE Int. Symp. on Med. Measurements and Applications (MeMeA), Turin, Italy, 07–09 May 2015, 141–145. doi:10.1109/MeMeA.2015.7145188
- Taub, E., Uswatte, G., Mark, V. W., and Morris, D. M. (2006). The learned nonuse phenomenon: Implications for rehabilitation. *Eura Medicophys* 42, 241–256.
- Tijjani, I., Kumar, S., and Boukhebbi, M. (2022). A survey on design and control of lower extremity exoskeletons for bipedal walking. *Appl. Sci.* 12, 2395. doi:10.3390/app12052395
- To, C. S., Kobetic, R., Bulea, T. C., Audu, M. L., Schnellenberger, J. R., Pinault, G., et al. (2011). Stance control knee mechanism for lower-limb support in hybrid neuroprostheses. *J. Rehab. Res. Dev.* 48, 839. doi:10.1682/JRRD.2010.07.0135
- Tran, H. T., Cheng, H., Rui, H., Lin, X. C., Duong, M. K., and Chen, Q. M. (2016). Evaluation of a fuzzy-based impedance control strategy on a powered lower exoskeleton. *Int. J. Soc. Robotics* 8, 103–123. doi:10.1007/s12369-015-0324-9
- Tsuji, T., and Tanaka, Y. (2005). Tracking control properties of human-robotic systems based on impedance control. *IEEE Trans. Syst. Man, Cybern. - Part A Syst. Humans* 35, 523–535. doi:10.1109/TSMCA.2005.850603
- Vantilt, J., Tanghe, K., Afschrift, M., Bruijnes, A. K., Junius, K., Geeroms, J., et al. (2019). Model-based control for exoskeletons with series elastic actuators evaluated on sit-to-stand movements. *J. NeuroEngineering Rehabilitation* 16, 65. doi:10.1186/s12984-019-0526-8
- Villa-Parra, A., Delisle-Rodriguez, D., Souza Lima, J., Frizera-Neto, A., and Bastos, T. (2017). Knee impedance modulation to control an active orthosis using insole sensors. *Sensors* 17, 2751. doi:10.3390/s17122751
- Ward, S., Wiedemann, L., Stinear, C., Stinear, J., and McDaid, A. (2017). “The influence of the Re-Link Trainer on gait symmetry in healthy adults,” in IEEE Int. Conf. on Rehab. Robotics, London, UK, 17–20 July 2017 (IEEE), 276–282. doi:10.1109/ICORR.2017.8009259
- Winter, D. A. (2009). *Biomechanics and motor control of human movement*. 4 edn. Hoboken: Wiley.
- Wolpert, D. M., Diedrichsen, J., and Flanagan, J. R. (2011). Principles of sensorimotor learning. *Nat. Rev. Neurosci.* 12, 739–751. doi:10.1038/nrn3112
- Wu, J., Gao, J., Song, R., Li, R., Li, Y., and Jiang, L. (2016). The design and control of a 3DOF lower limb rehabilitation robot. *Mechatronics* 33, 13–22. doi:10.1016/J.MECHATRONICS.2015.11.010
- Zacharias, B., and Kannenberg, A. (2012). Clinical benefits of stance control orthosis systems: An analysis of the sci. Literature. *JPO J. Prosthetics Orthot.* 24, 2–7. doi:10.1097/JPO.0b013e3182435db3
- Zissimopoulos, A., Fatone, S., and Gard, S. A. (2007). Biomechanical and energetic effects of a stance-control orthotic knee joint. *J. rehab. res. dev.* 44, 503–513. doi:10.1682/jrrd.2006.09.0124
- Zoss, A., and Kazerooni, H. (2006). Design of an electrically actuated lower extremity exoskeleton. *Adv. Robot.* 20, 967–988. doi:10.1163/156855306778394030



OPEN ACCESS

EDITED BY

Suvash C. Saha,
University of Technology Sydney,
Australia

REVIEWED BY

Viviana Toro-Ibacache,
University of Chile, Chile
Gianluca Tartaglia,
University of Milan, Italy

*CORRESPONDENCE

Przemysław Stróżyk,
✉ przemyslaw.strozyk@pwr.edu.pl

RECEIVED 13 July 2022

ACCEPTED 25 April 2023

PUBLISHED 11 May 2023

CITATION

Stróżyk P and Bałchanowski J (2023),
Application of numerical simulation
studies to determine dynamic loads
acting on the human masticatory system
during unilateral chewing of
selected foods.
Front. Bioeng. Biotechnol. 11:993274.
doi: 10.3389/fbioe.2023.993274

COPYRIGHT

© 2023 Stróżyk and Bałchanowski. This is
an open-access article distributed under
the terms of the [Creative Commons
Attribution License \(CC BY\)](https://creativecommons.org/licenses/by/4.0/). The use,
distribution or reproduction in other
forums is permitted, provided the original
author(s) and the copyright owner(s) are
credited and that the original publication
in this journal is cited, in accordance with
accepted academic practice. No use,
distribution or reproduction is permitted
which does not comply with these terms.

Application of numerical simulation studies to determine dynamic loads acting on the human masticatory system during unilateral chewing of selected foods

Przemysław Stróżyk^{1*} and Jacek Bałchanowski²

¹Faculty of Mechanical Engineering, Department of Mechanics, Materials and Biomedical Engineering, Wrocław University of Science and Technology, Wrocław, Poland, ²Faculty of Mechanical Engineering, Department of Fundamentals of Machine Design and Mechatronic Systems, Wrocław University of Science and Technology, Wrocław, Poland

Introduction: This paper presents its kinematic-dynamic computational model (3D) used for numerical simulations of the unilateral chewing of selected foods. The model consists of two temporomandibular joints, a mandible, and mandibular elevator muscles (the masseter, medial pterygoid, and temporalis muscles). The model load is the food characteristic (i), in the form of the function $F_i = f(\Delta h_i)$ —force (F_i) vs change in specimen height (Δh_i). Functions were developed based on experimental tests in which five food products were tested (60 specimens per product).

Methods: The numerical calculations aimed to determine: dynamic muscle patterns, maximum muscle force, total muscle contraction, muscle contraction corresponding to maximum force, muscle stiffness and intrinsic strength. The values of the parameters above were determined according to the mechanical properties of the food and according to the working and non-working sides.

Results and Discussion: Based on the numerical simulations carried out, it can be concluded that: (1) muscle force patterns and maximum muscle forces depend on the food and, in addition, the values of maximum muscle forces on the non-working side are 14% lower than on the working side, irrespective of the muscle and the food; (2) the value of total muscle contraction on the working side is 17% lower than on the non-working side; (3) total muscle contraction depends on the initial height of the food; (4) muscle stiffness and intrinsic strength depend on the texture of the food, the muscle and the side analysed, i.e., the working and non-working sides.

KEYWORDS

dynamic patterns of a muscles, dynamic characteristics of foods, numerical simulation, kinematic-dynamic model of unilateral chewing, experimental tests of food

1 Introduction

Food consumption is one of the most important activities (Lund, 1991), necessary to sustain life processes at the same time as a complex kinematic-dynamic process (Daumas et al., 2005; Hedjazi et al., 2013; Peck et al., 2000; Piancino et al., 2008; Slager et al., 1997; Stróżyk and Bałchanowski, 2018), which is controlled by the central nervous system (Dellow and Lund, 1971; Lund, 1991). Mastication is also a multi-parametric issue encompassing many complex and synchronised processes for preparing a bolus for swallowing. The most important processes may include: 1) the dynamic processing of the food (Stokes et al., 2013) dependent on its position on the dental arch (Manns and Díaz, 1988), 2) the continuous change in the geometric dimensions and mechanical properties of the food (Lenfant et al., 2009; Lillford, 2000; Lucas et al., 2004; Mioche et al., 2002; Stokes et al., 2013) and 3) the performance of complex movements by the mandible during chewing (Hylander, 2006; Koolstra, 2002; Piancino et al., 2012; Posselt, 1952; Quintero et al., 2013; Slavicek, 2010; Weinberg, 1963).

There are many papers in the literature where the authors (Çakir et al., 2011; Hutchings et al., 2012; Kohyama et al., 2007; Kohyama et al., 2008; Santana-Mora et al., 2014; Wang et al., 2010) focus on various parameters related to the act of chewing, e.g., 1) change in food texture, 2) chewing effort, 3) muscle activity, 4) some cycles needed to prepare a bolus of food, 5) degree of wetting of food with saliva, 6) age, 7) pathogenic changes, but most importantly 8) loads that occur during chewing of food. On the other hand, based on the data reported by (Agrawal et al., 1998; Hiimeae et al., 1996; Koolstra, 2002; Mathevon et al., 1995; Shimada et al., 2012), it appears that the mechanical properties of food are important for the function of the masticatory system during symmetric incisal biting and chewing. Furthermore, the work results (Mioche et al., 1999; Stróżyk and Bałchanowski, 2018) indicate that food imposes individual patterns of muscular force that must adapt to different functional requirements (Fitts et al., 1991). Their values are controlled by the central nervous system (Dellow and Lund, 1971; Lund, 1991), based on remembered external stimuli (patterns) perceived by different receptors (Quintero et al., 2013) so that it is adapted to the food consumed (Hiimeae et al., 1996; Knudson, 2007; Murray, 2004).

One of the main ways to determine muscle forces is through electromyography (EMG)-based method and mathematical equations (Ferrario and Sforza, 1996; Itoh et al., 1997; Mioche et al., 1999; Murray et al., 1999; Pruim et al., 1980; Weijs and Hillen, 1985). The method is mainly applied to the masseter muscle and the temporalis muscle. In the case of the medial and lateral pterygoid muscles, measurements are more difficult because they cannot be externally accessed (Koole et al., 1990; Murray et al., 1999; Widmalm et al., 1987; Wood et al., 1986). Consequently, determining muscle forces requires intra-oral access, which makes measurements during chewing difficult due to the possibility of interference with the natural act of chewing.

Since using EMG during chewing makes it impossible to determine the forces in all the mandibular elevator muscles, it is a good option to use a numerical computational model of the masticatory system. The model developed for numerical calculations provides reproducibility but requires the preparation of basic data, e.g., the geometry of the mandible, the muscle attachment sites, the muscle model and the mode of support. As chewing is a dynamic issue, a model should be developed based on solid mechanics, i.e., a kinematic-dynamic model (Stróżyk and Bałchanowski, 2016; Stróżyk and

Bałchanowski, 2018; Stróżyk and Bałchanowski, 2020). The load of the model should be the characteristics of the food in the form of the function $F_i = f(\Delta h_i)$ —force (F_i) vs. change in specimen height (Δh_i), determined during experimental tests, while the movement of the mandible is set in the path of mastication determined for the tested food.

Preliminary analysis of the function of the masticatory system in terms of: 1) the position of the food (bite force) on the dental arch, 2) the number of cycles and 3) the muscle activity on the left and right sides of the mandible indicate that, in mechanical terms, unilateral chewing will be an interesting case of physiological load on the masticatory system.

In the literature, it is possible to find publications in which the authors model unilateral chewing, but these are static models in which the position of the mandible corresponds to the closure of the mouth (Koriath et al., 1992; Pinheiro and Alves, 2015; Pachnicz and Stróżyk, 2021; Reina et al., 2007). Interesting information on unilateral chewing can be found in (Harrison et al., 2014). However, the authors focus on dynamic changes in the mechanical properties of the food rather than on changes in the values of the muscular forces acting on the masticatory system. Analysing other publications on chewing (Choi et al., 2005; Jahadkbar et al., 2016; Lee et al., 2017; Luo et al., 2017; Marková and Gallo, 2016; Reina et al., 2007), we find that none of them present changes in muscle force values (muscle functioning patterns) to dynamic changes occurring in the food during mastication.

The primary aim of this study was to determine computational model of unilateral chewing, loaded with the dynamic patterns of food (i) determined in experimental tests. The model prepared in this way made it possible to determine, firstly, selected dynamic parameters of the mandibular elevator muscles, i.e., total muscle contraction (q_i) and dynamic muscle forces (F_i) as functions, $q_i = q_i(t)$ and $F_i = F_i(t)$, respectively. The parameters obtained allowed the determination of muscle dynamic patterns in the function $F_i = f(q_i)$. From the results obtained, parameters such as muscle stiffness (K_i) and intrinsic strength (k_i) were also determined as a function of food.

As mastication is a complex mechanical process (Stokes et al., 2013), the study was limited to first cycle.

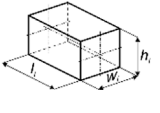





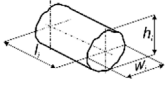
The results demonstrate the feasibility of using a hybrid model (based on experimental tests of food and numerical simulation of unilateral chewing) to show how the dynamic parameters of the mastication system change as a function of the mechanical properties of the food and its geometric dimensions.

The proposed computational model, the adopted boundary conditions and the calculation method can be one possibility for determining muscular forces. On the other hand, the results obtained can be used to model complex issues concerning the biomechanics of the masticatory system requiring knowledge of loads.

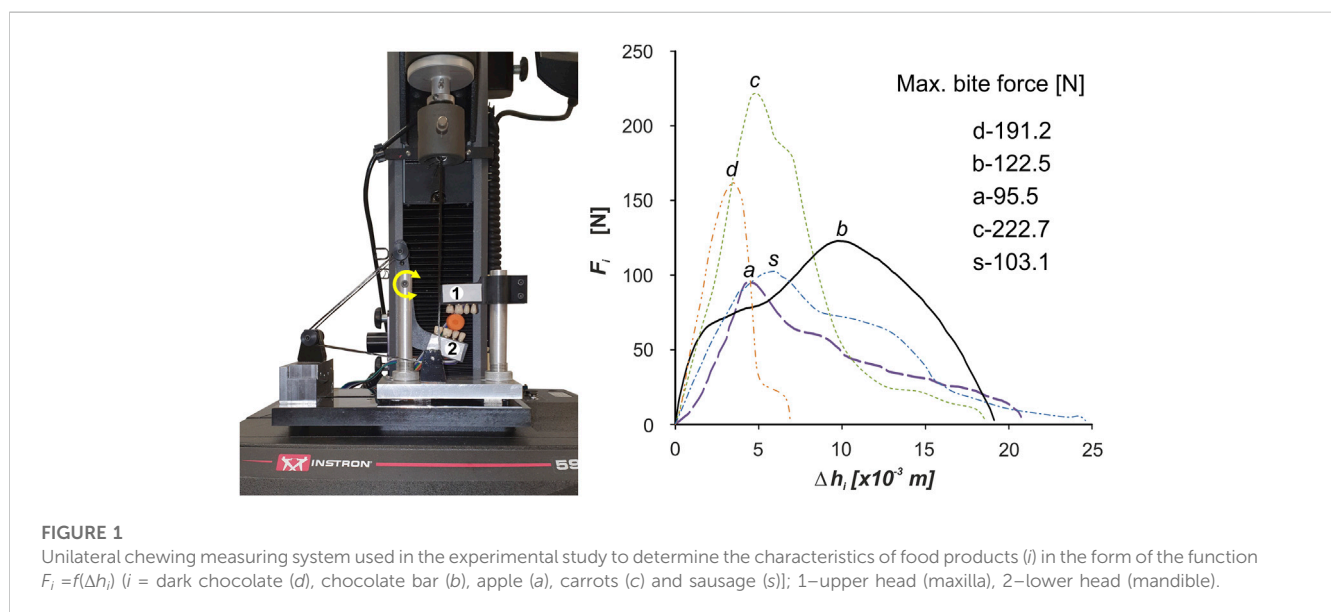
2 Materials and methods

The use of numerical simulation to determine force patterns for the mandibular elevator muscles (the masseter muscle-M, the medial pterygoid muscle-MP and the temporalis muscle-T) during unilateral chewing required, first of all, the construction of a numerical model of the human masticatory system consisting of the mandible, TMJ and muscles. In addition, this necessitated: 1) determining how to support the model and 2) defining and

TABLE 1 Food product (*i*), its mean height (h_i), width (w_i) and length (l_i) and mean chewing time (t_i).

Parameters	Dark chocolate (<i>d</i>)	Chocolate bar (<i>b</i>)	Apple (<i>a</i>)	Carrots (<i>c</i>)		Sausage (<i>s</i>)	
							
							
$h_i / ^1 [\times 10^{-3} \text{ m}]$	9.1 ± 0.8	20.1 ± 0.4	23.5 ± 1.2	}	19.6 ± 1.5	}	27.2 ± 1.8
$w_i / ^1 [\times 10^{-3} \text{ m}]$	17.1 ± 1.2	17.4 ± 1.4	18.6 ± 0.8				
$l_i / ^1 [\times 10^{-3} \text{ m}]$	26.2 ± 0.8	30.3 ± 0.7	26.5 ± 0.6		16.8 ± 1.1		17.4 ± 1.3
$t_i / ^1 [\text{ s}]$	0.51 ± 0.03	1.12 ± 0.07	1.31 ± 0.09	1.08 ± 0.08		1.51 ± 0.09	

¹ the values are means \pm SD, ($i = d, b, a, c, s$).



determining the parameters (input data) responsible for the load and initial position (for time $t = 0 \text{ s}$) of the model.

2.1 Determination of model load and food characteristics

During the numerical simulations, forces in the muscles were determined for loads corresponding to different foods; therefore the basic parameter responsible for the mandibular force is the food characteristic (*i*), in the form of the function $F_i = f(\Delta h_i)$ —force (F_i) vs. change in high of food specimen (Δh_i), determined in experimental studies. In the numerical model, the above function is decomposed into two functions in which force

and change in high of food specimen are time-dependent, i.e., $F_i(t)$ and $\Delta h_i(t)$.

The general algorithm for determining food characteristics was similar to that presented in (Stróżyk and Bałchanowski 2018). Five foods were prepared for the study ($i = c, a, d, b, s$): 1) vegetables—carrot (*c*); 2) fruits—apple (*a*); 3) sweets—dark chocolate (*d*) and a chocolate bar (*b*) and 4) meat and cold cuts—sausage (*s*), different in terms of structure, mechanical properties and method of production (natural and artificial). The products were purchased from a single selected grocery shop and stored at 7°C until the specimens were prepared. The specimens were then normalised at 21°C for approximately 60 min until the tests began.

The aim of the experimental study was not to determine typical mechanical parameters but only the function $F_i = f(\Delta h_i)$. The

specimens in terms of dimensions [height (h_i), width (w_i), and length (l_i)] were similar to a typical bite of food, while the shape depended on the product (Table 1). To determine the characteristics, 60 specimens were prepared for each food.

In the experimental tests, we used our own test stand design (Figure 1) [developed on the basis of a patent application—(Stróżyk, 2021)], consisting of two measuring heads, i.e., upper (maxilla) and lower (mandible), imitating fragments of the dental arches.

The lower head is mounted on a cantilever and thus can perform a rotational. In addition, acrylic dental prostheses, used in dental prosthetics, were attached to the heads to make the act of chewing similar to natural chewing. During testing, the test stand was mounted on an Instron 5944 test machine.

Based on the information provided in (Fitts et al., 1991; Dick and Wakeling, 2017; Koolstra, 2002), muscle force is dependent on the speed of mandibular movement, while speed is dependent on the mechanical parameters of the food, i.e., high force and low speed (hard food) or low force and high speed (soft food). Furthermore, based on the analysis of (Anderson et al., 2002; Foegeding and Drake, 2007; Foster et al., 2006; Meullenet et al., 2002; Williams et al., 2005) it appeared that the range of reported mandibular movement speeds (in this case, chewing speed) for different foods is extensive. Therefore, it was decided that all foods would be masticated at a constant velocity of $v_t = 0.02$ m/s (Stróżyk and Bałchanowski, 2016; Stróżyk and Bałchanowski, 2018; Stróżyk and Bałchanowski, 2020). Maintaining a constant v_t required performing a kinematic analysis of the simulator and, based on this, developing a control program for the Instron 5944 machine (Bluehill ver. 3). In addition, the chewing time (t_i) was determined for each food product based on the nominal food height (h_i) and the set velocity v_t (Table 1).

Figure 1 shows the characteristics of selected products (i), in the form of the function $F_i = f(\Delta h_i)$, developed on the basis of measurement results and elementary statistical calculations.

2.2 Numerical model of the human masticatory system

In order to carry out a kinetostatic analysis of the chewing process of selected foods, a computational model of the human masticatory system was developed, consisting of two elements: a fixed skull (Synbone 8500) and a movable mandible (Synbone 8596). The temporomandibular joints (TMJ) were modelled as shaped joints, with constraints in the form of contact forces between the articular surface of the condyle of the mandible and the articular tuber of the temporal bone (Stróżyk and Bałchanowski, 2018). The forces in the muscles were modelled using non-linear force vectors applied at the anatomical points of muscle attachment.

The numerical model had 4 degrees of freedom, which means that 4 active muscle force unknowns can be determined from the equilibrium equations. Hence, the model assumed the unknowns were the two temporalis muscle forces (FT_{Wi} , FT_{Ni}). In contrast, the forces in the masseter muscle (FM_{Wi} , FM_{Ni}) and the medial pterygoid muscles (FMP_{Wi} , FMP_{Ni}) were replaced by the resultant forces (FV_{Wi} , FV_{Ni}) (Prium et al., 1980), on the left and right sides (Figure 2).

The muscles were modelled using linear kinematic excursions to simulate the elongation and contraction of the muscles that allow the

mandible to move in relation to the maxilla during mastication. In the numerical model of the skull–mandible, four linear kinematic excursions were used for the temporalis muscle and the resultant. The active forces FT_{Wi} , FT_{Ni} , in the enforcing qT_{Wi} , qT_{Ni} represent the temporalis muscle, while the active forces FV_{Wi} , FV_{Ni} in the enforcing qV_{Wi} and qV_{Ni} represent the results of the masseter and medial pterygoid muscles (Figure 2).

The external force on the model [modelling the occlusal force (Stróżyk et al., 2018; Stróżyk and Bałchanowski, 2016; Stróżyk and Bałchanowski, 2018)] was the force F_i , as a function of $F_i = f(\Delta h_i)$, applied at point IW on the occlusal surface of the first molar (46) (Figure 2).

2.3 Boundary conditions for the numerical model

Based on an analysis based on solid mechanics and analytical geometry, it appears that the parameters that will have a significant effect on the alignment of the mandible with respect to the maxilla will be: 1) product height (h_i) and 2) unilateral contraction of the lateral pterygoid muscle. The height of h_i is responsible for establishing the distance between the upper and lower incisors, whereas contraction of the muscle on the non-working side (N) is responsible for lateral movement of the mandible, resulting in the appearance of a path of mastication and asymmetrical displacement of the processes in the TMJ during unilateral chewing. Since there is a lack of data in the available literature on the preload (muscle force) and corresponding stiffness of the lateral pterygoid muscle, it was decided to use the effect of its action as a parameter defining mandibular preposition and movement.

The appropriate association of the height of the h_i and the mastication path (effect) and the appropriate alignment of the mandibular processes at the TMJ enable the initial position of the model to be determined during unilateral chewing.

Based on the analysis of data reported in (Bhatka et al., 2004; Buschang et al., 2007; Nishigawa et al., 1997; Piancino et al., 2012; Slavicek, 2010), a hypothetical path of mastication was prepared for each product, in the frontal plane (Figure 3A), in shape close to an ellipse (Hedjazi et al., 2013), in such a way that its geometric parameters (height and width) were synchronised with the food height (h_i), i.e., the initial distance between a pair of corresponding first molars.

The path of mastication prepared in this way are the parameter by which it is possible to reproduce the trajectory of the incisal point during a single or one cycle of unilateral chewing.

The results of preliminary calculations showed that the introduction of the mastication path significantly affects the values of the length of the condylar trajectories (Δd_i). In addition, analysis of the results showed that the condyles move according to the mandibular kinematics reported in (Weinberg, 1963), i.e., the working condylar rotates and little lateral Bennett's movement. In contrast, the non-working condylar movement is sloped downward, forward, and medially.

For the non-working side, the length of the trajectory of the condylar is: chocolate $\Delta d_d = 0.0031$ m, chocolate bar $\Delta d_b = 0.0068$ m, apple $\Delta d_a = 0.0079$ m, carrot $\Delta d_c = 0.0065$ m, and sausage $\Delta d_s = 0.0102$ m, and is on average as much as seven times greater than on the working side. Therefore, in the numerical simulation, it was assumed that there would be a fixed centre of rotation of the mandible in the condylar on the working side,

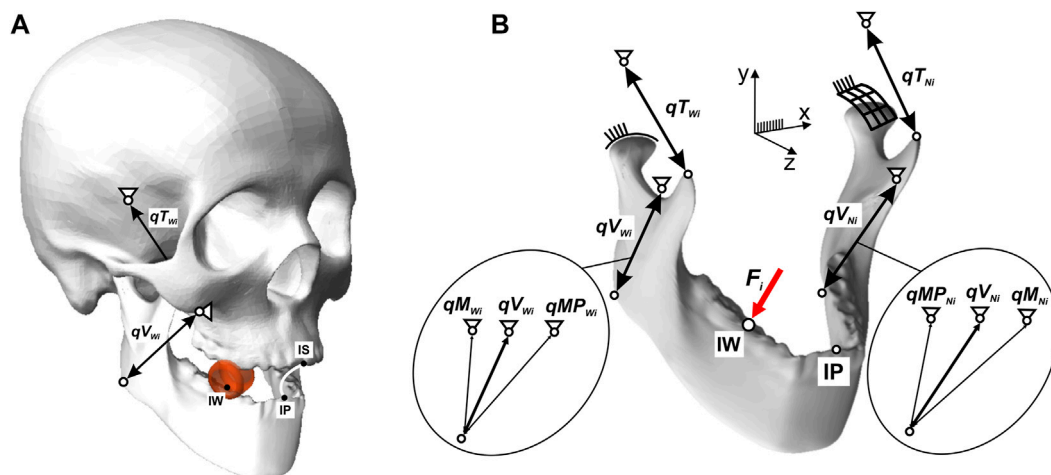


FIGURE 2
Computational model of the human masticatory system: (A) general view, (B) force forcing diagram of the mandible.

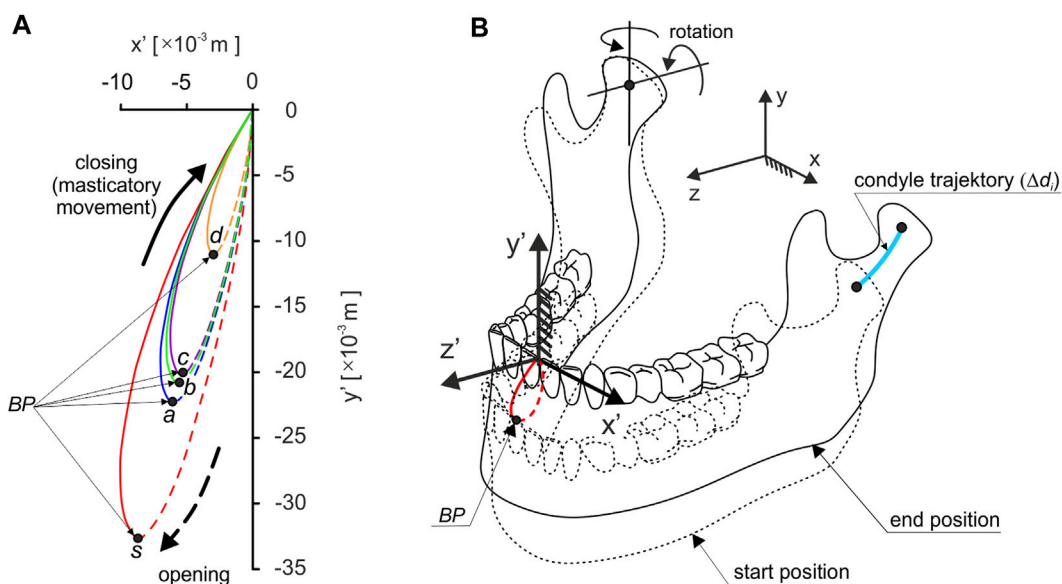


FIGURE 3
Trajectory of: (A) the incisal point in the frontal plane (path of chewing), depending on the foods and (B) the mandibular condyle on the non-working side during unilateral chewing; Black point (BP) indicates the point at which chewing begins.

through which the instantaneous axes of rotation would pass. On the non-working side, on the other hand, the condylar will have the possibility of rotation and translation (Figure 3B).

The mandibular model is fixed in the TMJ and the origin attachment sites of the masseter, medial pterygoid, and temporalis muscles. Based on the developed chewing paths, there are kinematic contact pairs with 5 degrees of freedom (3 rotations and 2 displacements) in the TMJ on the working and non-working sides. The displacement values depend on the type of food and the chewing side (Table 1).

The proposed way of supporting the model, especially in the TMJ, made it possible to simulate the complex movement of the lower

incisors during chewing (Figures 2, 3). A detailed description of the model is given in (Stróżyk and Bałchanowski, 2018).

2.4 Numerical simulations of unilateral chewing

Simulation studies consisted in moving the incisal point from the lower position (point IP Figure 2A) to the endpoint IS (the origin of the coordinate system Figure 2).

During the simulation of food chewing, the molar to which the force F_i has applied moves with a constant velocity $v_t = 0.02$ m/s. The

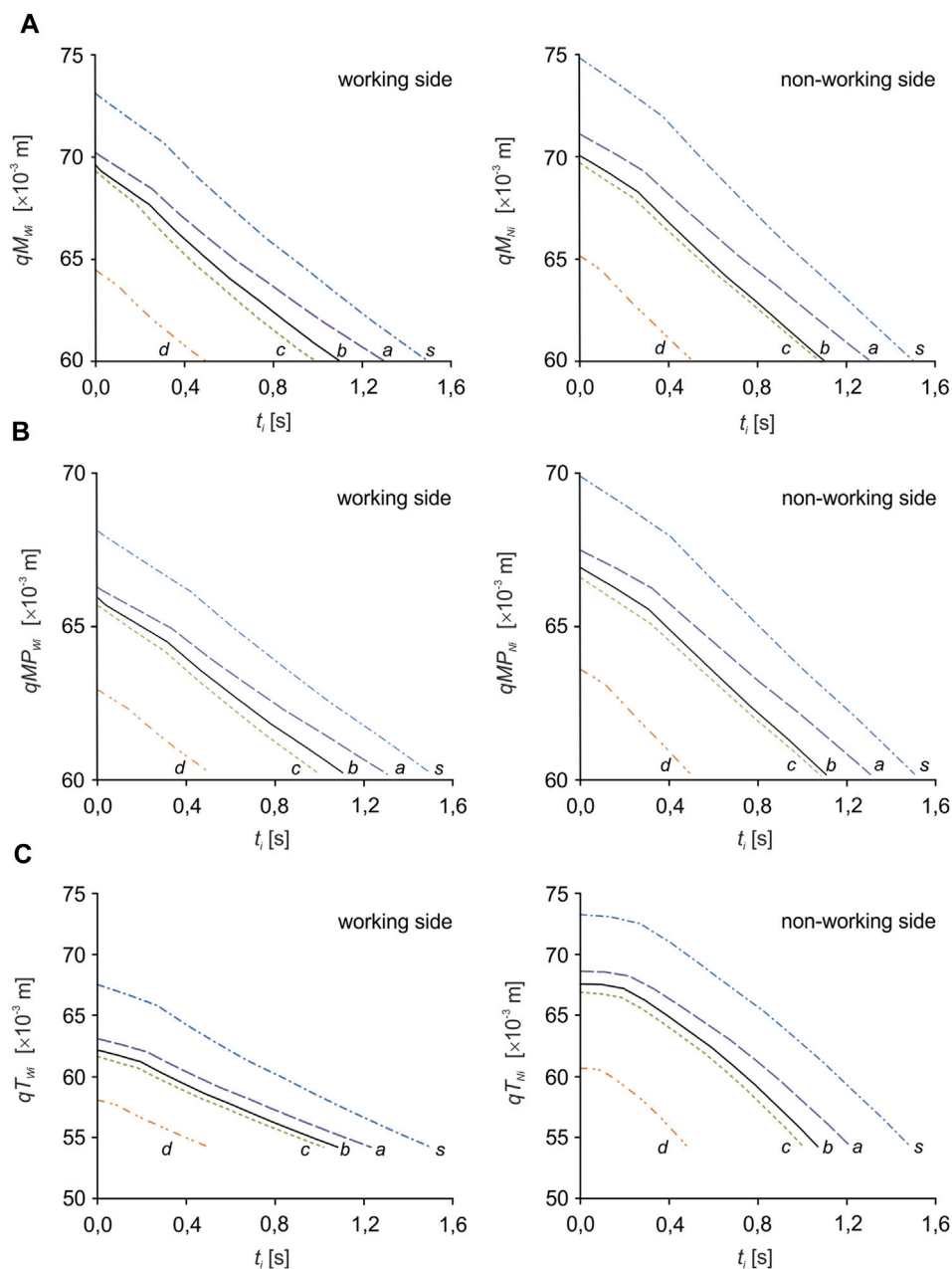


FIGURE 4

Kinematic characteristics of the change in muscle length: (A) the masseter muscle (qM_{Wi} , qM_{Ni}), (B) the medial pterygoid muscle (qMP_{Wi} , qMP_{Ni}) and (C) the temporalis muscle (qT_{Wi} , qT_{Ni}) depending on the food product (i).

developed numerical model is universal and can model variable (nonlinear) chewing velocity. In the simulation studies chewing was modelled at a constant speed because the food patterns were determined experimentally on a testing machine for such speed.

Numerical simulations were carried out in three stages. In the first, the inverse task of the kinematics of motion of the mandibular-cranial system was solved. This consisted in applying a forced mandibular movement along the longitudinal mastication path and determining the mandibular movement at the TMJ on the W and N sides. During this simulation, the changes in muscle length

(contractions) necessary to force the mandibular closure movement were also determined (Figure 4).

In the second stage, proper calculations were performed modelling a simple dynamics task simulating mandibular closure resulting from muscle contractions. Forcing qT_{Wi} , qT_{Ni} , qV_{Wi} and qV_{Ni} were used as changes in muscle length (contractions) determined in the simple task. As a result of calculations, the unknown muscle forces were determined: FM_{Wi} , FM_{Ni} , FMP_{Wi} , FMP_{Ni} and FT_{Wi} , FT_{Ni} . Simulations were performed separately for each food.

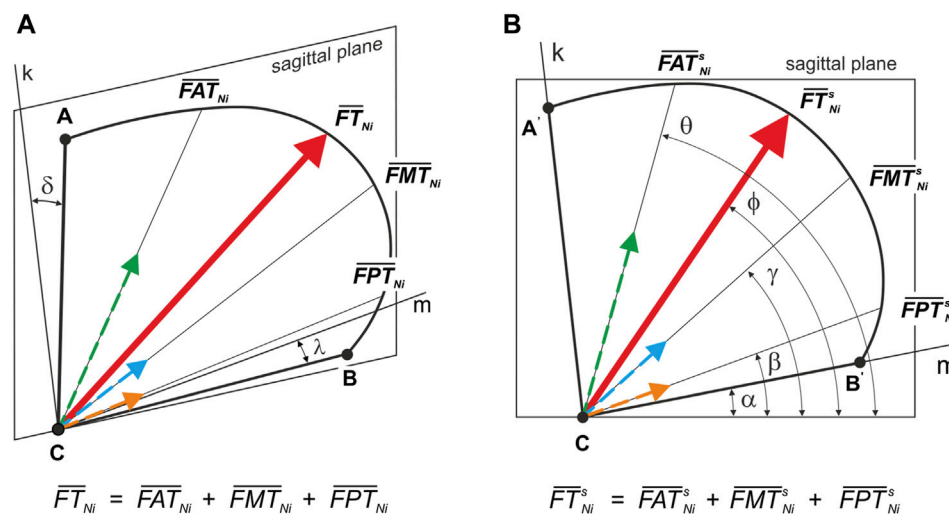


FIGURE 5

Position of the principal vector of the temporalis muscle and its components—working and non-working side: (A) relative to the sagittal plane (\overline{FT}_{Ni} ; \overline{FAT}_{Ni} ; \overline{FMT}_{Ni} ; \overline{FPT}_{Ni}) and (B) on the sagittal plane (\overline{FT}_{Ni}^s ; \overline{FAT}_{Ni}^s ; \overline{FMT}_{Ni}^s ; \overline{FPT}_{Ni}^s). ($\delta = 20^\circ$ i $\lambda = 20^\circ$); Line k and m lie in the sagittal plane.

TABLE 2 Maximum muscle force, contraction corresponding to maximum force and total contraction, respectively for: the masseter muscle [(FM_{HWi} , FM_{HNI}), (ΔqM_{HWi} , ΔqM_{HNI}), (ΔqM_{CWi} , ΔqM_{CNI})], the medial pterygoid [(FMP_{HWi} , FMP_{HNI}), (ΔqMP_{HWi} , ΔqMP_{HNI}), (ΔqMP_{CWi} , ΔqMP_{CNI})] and the temporalis muscle [(FT_{HWi} , FT_{HNI}), (ΔqT_{HWi} , ΔqT_{HNI}), (ΔqT_{CWi} , ΔqT_{CNI})], depending on a product (i).

Side	Parametry		Dark chocolate (d)	Chocolate bar (b)	Apple (a)	Carrots (c)	Sausage (s)
Masseter							
Working	FM_{HWi}	[N]	233.2	149.4	112.2	274.3	126.9
	ΔqM_{HWi}	[$\times 10^{-3}$ m]	2.1	4.4	2.4	2.4	2.9
	ΔqM_{CWi}	[$\times 10^{-3}$ m]	4.2	9.3	10.5	8.9	12.5
Non-working	FM_{HNI}	[N]	200.3	127.8	96.2	235.5	108.8
	ΔqM_{HNI}	[$\times 10^{-3}$ m]	2.5	5.3	2.9	2.8	3.5
	ΔqM_{CNI}	[$\times 10^{-3}$ m]	5.0	11.2	12.7	10.6	14.9
Medial pterygoid							
Working	FP_{HWi}	[N]	209.3	134.5	100.6	244.7	113.5
	ΔqP_{HWi}	[$\times 10^{-3}$ m]	1.4	2.8	1.5	1.5	1.9
	ΔqP_{CWi}	[$\times 10^{-3}$ m]	2.7	5.9	6.7	5.6	8.0
Non-working	FP_{HNI}	[N]	179.2	115.4	86.2	209.8	97.3
	ΔqP_{HNI}	[$\times 10^{-3}$ m]	1.7	3.5	1.9	1.9	2.3
	ΔqP_{CNI}	[$\times 10^{-3}$ m]	3.3	7.3	8.3	6.9	9.8
Temporalis							
Working	FT_{HWi}	[N]	46.1	29.3	22.7	53.4	24.4
	ΔqT_{HWi}	[$\times 10^{-3}$ m]	3.4	7.3	3.9	3.0	4.8
	ΔqT_{CWi}	[$\times 10^{-3}$ m]	6.7	15.4	16.9	14.5	20.6
Non-working	FT_{HNI}	[N]	39.4	25.0	19.4	45.9	20.9
	ΔqT_{HNI}	[$\times 10^{-3}$ m]	4.2	8.9	4.7	4.7	5.8
	ΔqT_{CNI}	[$\times 10^{-3}$ m]	8.2	18.8	20.4	17.5	24.9

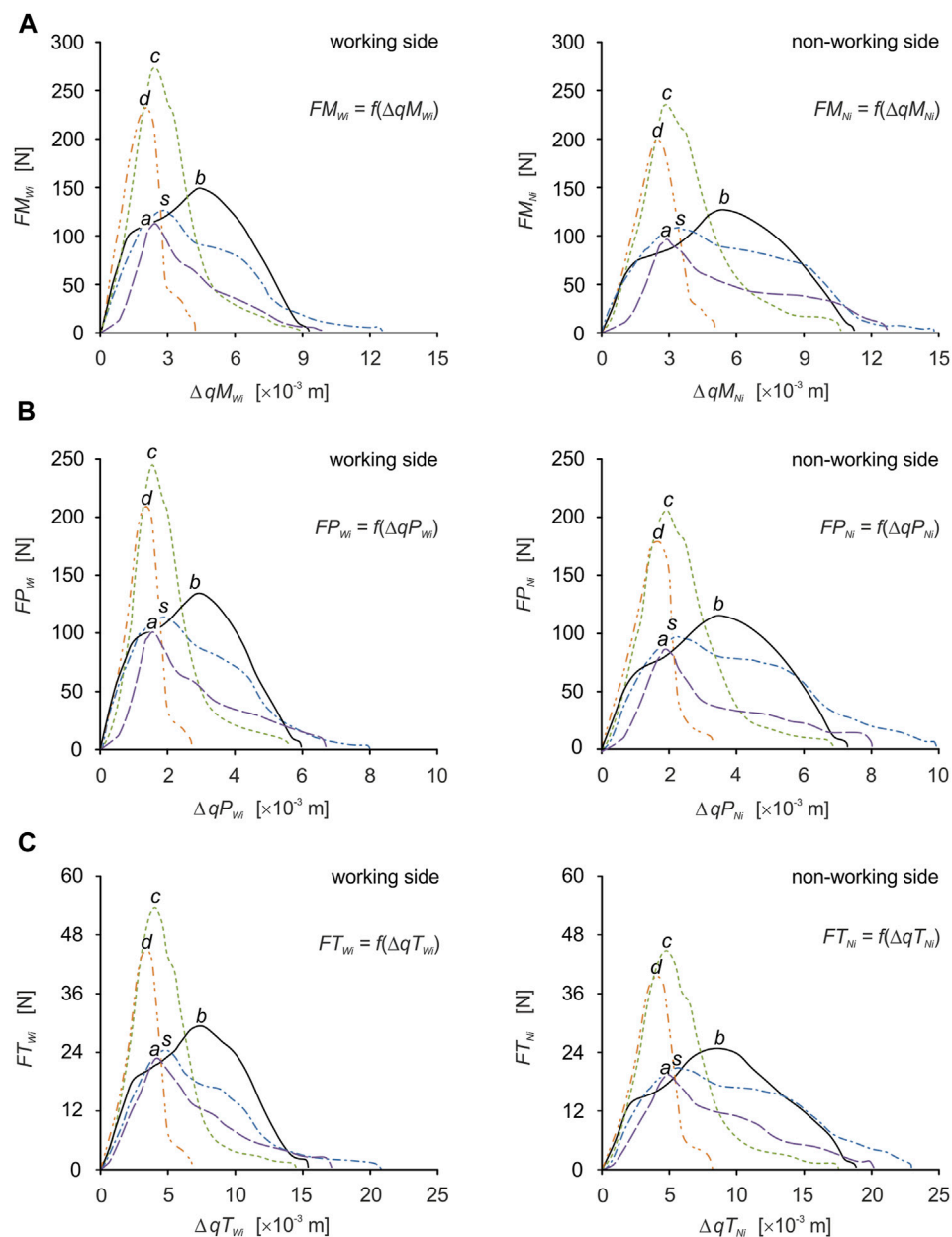


FIGURE 6

Muscle force patterns as a function of muscle force vs. muscle contraction for: (A) the masseter muscle [$FM_{wi} = f(\Delta qM_{wi})$, $FM_{Ni} = f(\Delta qM_{Ni})$], (B) the medial pterygoid muscle [$FP_{wi} = f(\Delta qP_{wi})$, $FP_{Ni} = f(\Delta qP_{Ni})$] and (C) the temporalis muscle [$FT_{wi} = f(\Delta qT_{wi})$, $FT_{Ni} = f(\Delta qT_{Ni})$], during unilateral food chewing (i).

In the third step, based on elementary trigonometric calculations, the principal vector of the temporalis muscle was decomposed (FT_{Ni}) into three components, respectively for: the anterior temporalis (FAT_{Ni}), the middle temporalis (FMT_{Ni}) and the posterior temporalis (FPT_{Ni}). The distribution was performed based on the assumption that muscle force is proportional to physiological cross-sectional area (PCSA) (Koolstra et al., 1988); Figure 5A shows the schematic position of the temporalis muscle (outline—ABC) in relation to the sagittal plane. On the other hand, Figure 5B shows the position of the temporalis muscle (outline—A'B'C) in the sagittal plane and gives the angles determining the position of the B'C edge

($\alpha = 11^\circ$) and the line of action of FT_{Ni} ($\phi = 58^\circ$) and its components, i.e., FAT_{Ni} ($\theta = 76^\circ$), FMT_{Ni} ($\gamma = 42^\circ$) and FPT_{Ni} ($\beta = 22^\circ$), in relation to the sagittal axes.

3 Results

Based on the determined food characteristics (Figure 1), the developed model of the masticatory system (Figure 2), the chewing path (Figure 3), the determined changes in muscle length (Figure 4) and numerical calculations, muscle force patterns were determined,

TABLE 3 Maximum muscle force, contraction corresponding to maximum force and total contraction respectively for: the anterior temporalis [(FAT_{HWi} , FAT_{HNi}), (ΔqAT_{HWi} , ΔqAT_{HNi}), (ΔqAT_{CWi} , ΔqAT_{CNi})], the middle temporalis [(FMT_{HWi} , FMT_{HNi}), (ΔqMT_{HWi} , ΔqMT_{HNi}), (ΔqMT_{CWi} , ΔqMT_{CNi})] and the posterior temporalis [(FPT_{HWi} , FPT_{HNi}), (ΔqPT_{HWi} , ΔqPT_{HNi}), (ΔqPT_{CWi} , ΔqPT_{CNi})] depending on a product (*i*).

Side	Parametry		Dark chocolate (d)	Chocolate bar (b)	Apple (a)	Carrots (c)	Sausage (s)
Anterior temporal							
Working	FAT_{HWi}	[N]	22.1	14.1	10.9	25.7	11.7
	ΔqAT_{HWi}	[$\times 10^{-3}$ m]	2.7	5.8	3.2	3.3	3.8
	ΔqAT_{CWi}	[$\times 10^{-3}$ m]	5.4	12.3	13.9	12.3	16.3
Non-working	FAT_{HNi}	[N]	18.9	12.0	9.3	22.0	10.0
	ΔqAT_{HNi}	[$\times 10^{-3}$ m]	3.4	7.2	3.9	3.8	4.6
	ΔqAT_{CNi}	[$\times 10^{-3}$ m]	6.6	15.1	16.9	14.5	19.7
Middle temporal							
Working	FMT_{HWi}	[N]	13.4	8.5	6.6	15.5	7.1
	ΔqMT_{HWi}	[$\times 10^{-3}$ m]	2.5	5.2	2.9	3.0	3.4
	ΔqMT_{CWi}	[$\times 10^{-3}$ m]	4.7	11.0	12.2	11.0	14.4
Non-working	FMT_{HNi}	[N]	11.4	7.2	5.6	13.3	6.1
	ΔqMT_{HNi}	[$\times 10^{-3}$ m]	2.9	6.3	3.3	3.3	4.0
	ΔqMT_{CNi}	[$\times 10^{-3}$ m]	5.7	13.5	14.7	12.7	17.5
Posterior temporal							
Working	FPT_{HWi}	[N]	10.6	6.7	5.2	12.3	5.6
	ΔqPT_{HWi}	[$\times 10^{-3}$ m]	2.1	4.4	2.4	2.5	3.0
	ΔqPT_{CWi}	[$\times 10^{-3}$ m]	4.1	9.2	10.4	9.3	12.9
Non-working	FPT_{HNi}	[N]	9.1	5.7	4.5	10.6	4.8
	ΔqPT_{HNi}	[$\times 10^{-3}$ m]	2.5	5.4	2.9	2.9	3.5
	ΔqPT_{CNi}	[$\times 10^{-3}$ m]	4.9	11.4	12.6	10.8	15.0

for the masseter muscle, the medial pterygoid muscle and the temporalis muscle and its components (the anterior temporalis, the middle temporalis, the posterior temporalis) (Figure 6). In addition, Tables 2, 3 give the values for maximum bite force and the corresponding values for muscle contraction and total muscle contraction. In contrast, Tables 4, 5 show muscle stiffness and intrinsic strength values.

In the general case, the total contraction of the muscle (Δq_C), the contraction corresponding to the maximum force (Δq_H) and the muscle contraction (Δq_E) were determined from Eqs 1–3. During the calculations, the equations were modified in such a way that the above parameters could be determined on selected muscles depending on the food, separately for the working and non-working sides.

$$\Delta q_C = |q(t) - q(0)| \quad (1)$$

$$\Delta q_H = |q(t_H) - q(0)| \quad (2)$$

$$\Delta q_E = |q(t_E) - q(0)| \quad (3)$$

where:

$q(0)$ —initial muscle length for time $t = 0s$ —open mouth,

$q(t)$ —muscle end length for time t —closed mouth,

$q(t_H)$ —muscle length for time t_H , corresponding to the position of the mandible in which the muscle force reaches its maximum value (F_H),

$q(t_E)$ —muscle length determined for time t_E from the interval $0 \div t$,

3.1 Muscle force patterns

Preliminary analysis indicates significant differences between patterns, force values and contractions. The variation in muscle behaviour is not surprising, as the diversity of characteristics (Figure 1) generates individual conditions for the masticatory system (Mioche et al., 1999), adapted to functional requirements, depending on the input data (Fitts et al., 1991).

For efficient interpretation of the results, muscle patterns were prepared separately for each muscle (Figure 7) and for the components of the temporalis muscle (Figure 5), and separately for the working and non-working sides. Thanks to this, there are 5 muscle patterns on each graph, depending on the food, while the

TABLE 4 Values of stiffness (K_{Wi} , K_{Ni}) for selected muscles in relation to food.

Side	Muscle	Chocolate (d)	Chocolate bar (b)	Apple (a)	Carrots (c)	Sausage (s)
$K_{Wi} [\times 10^3 \text{ N/m}]$						
Working	Masseter	108,9	34,0	46,3	114,8	43,5
	Medial pterygoid	152,1	48,2	65,1	162,7	60,8
	Temporalis	13,6	4,0	5,8	13,7	5,1
	Anterior temporalis	10,3	3,2	4,5	10,7	4,0
	Middle temporalis	6,2	1,9	2,7	6,5	2,4
	Posterior temporalis	4,9	1,5	2,2	5,1	1,9
$K_{Ni} [\times 10^3 \text{ N/m}]$						
Non-Working	Masseter	78,6	24,1	32,8	82,7	31,3
	Medial pterygoid	106,5	33,4	45,0	113,2	42,6
	Temporalis	9,4	2,8	4,1	9,8	3,6
	Anterior temporalis	7,4	2,3	3,2	7,7	2,9
	Middle temporalis	4,5	1,4	1,9	4,7	1,7
	Posterior temporalis	3,6	1,1	1,5	3,7	1,4

TABLE 5 Intrinsic strength values (k_{Wi} , k_{Ni}) for selected muscles in relation to food.

Side	Muscle	$PCSA_j / ^1 [\times 10^{-4} \text{ m}^2]$	Chocolate (d)	Chocolate bar (b)	Apple (a)	Carrots (c)	Sausage (s)
$k_{Wi} [\times 10^4 \text{ N/m}^2]$							
Working	Masseter	6.80	34.3	22.0	16.5	40.3	18.7
	Medial pterygoid	4.37	47.9	30.8	23.0	56.0	26.0
	Temporalis	8.23	5.6	3.6	2.8	6.5	3.0
$k_{Ni} [\times 10^4 \text{ N/m}^2]$							
Non-Working	Masseter	6.80	29.5	18.8	14.1	34.6	16.0
	Medial pterygoid	4.37	41.0	26.4	19.7	47.9	22.3
	Temporalis	8.23	4.8	3.0	2.4	5.6	2.5

¹ Langenbach and Hannam, 1999.

data are given in Tables 2, 3 enable the determination of additional mechanical parameters characterising the muscle functioning.

3.2 Stiffness of the muscle

In the general case, the stiffness (K) is determined from the elementary Eq. 4, in which the force (F) and displacement (x) are directly proportional to each other.

$$K = F / x \text{ [N/m]} \quad (4)$$

Eq. 4 is linear, so its use is limited to problems with a linear relationship between F and x . This means that the stiffness

determined for a range of load ($0 \div F$) or displacement ($0 \div x$) has a constant value.

The above equation can be used for issues of a non-linear nature, but then the stiffness is only determined for a specific value of F or x . Therefore, the value of stiffness has the characteristics of a comparative parameter based on which it is possible to assess the influence of various factors on the functioning of the muscular system, e.g., 1) different ways of biting, 2) the geometry of the masticatory system resulting from individual characteristics and pathological conditions, 3) foods, 4) the state of dentition and 5) changes resulting from surgical procedures (Pachnicz and Stróżyk, 2021).

Based on the considerations above, this paper is limited only to the determination of muscle stiffness (Eq. 4) for the maximum

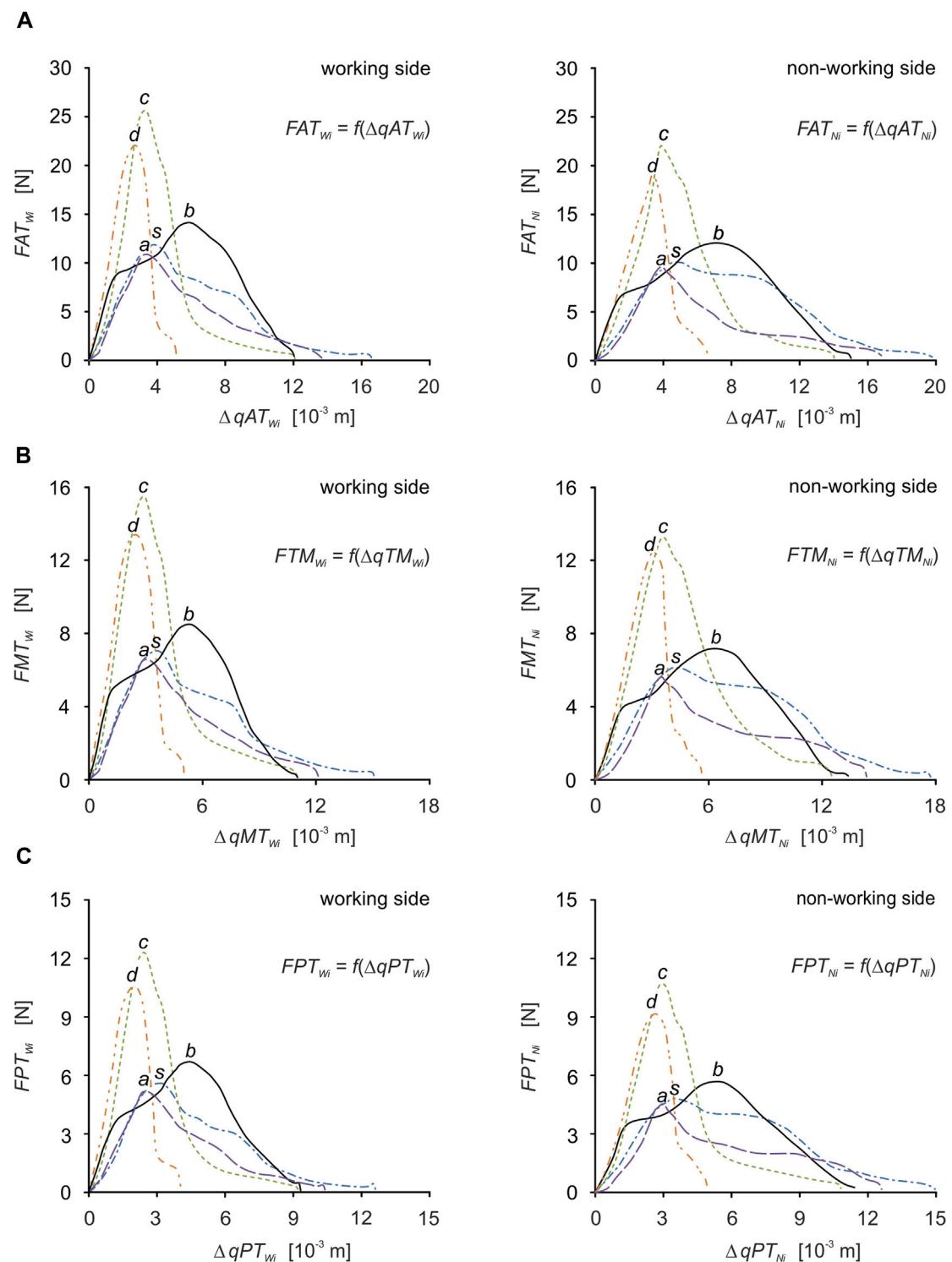


FIGURE 7 Muscle force patterns as a function of muscle force vs. muscle contraction for: (A) the anterior temporalis [$FAT_{wi} = f(\Delta qAT_{wi})$, $FAT_{Ni} = f(\Delta qAT_{Ni})$], (B) the middle temporalis [$FTM_{wi} = f(\Delta qTM_{wi})$, $FTM_{Ni} = f(\Delta qTM_{Ni})$] and (C) the posterior temporalis [$FPT_{wi} = f(\Delta qPT_{wi})$, $FPT_{Ni} = f(\Delta qPT_{Ni})$] during unilateral food chewing (i).

muscle forces (Table 2, 3) for the working (K_{wi}) and non-working (K_{Ni}) sides, respectively.

Of course, Eq. 4 was adjusted so that stiffness could be determined for selected muscles, i.e., $F \rightarrow F_H$ and $x \rightarrow \Delta qH$.

3.3 Intrinsic strength

Based on publications (Koolstra et al., 1988; Koriath and Hannam, 1990; May et al., 2001; Pruim et al., 1980) it can be

TABLE 6 The value of proportionality coefficients R_{FW} and R_{FN} for selected muscles, depending on cases I and II.

Side	Muscle	Case I	Case II
R_{FW}			
Working	Masseter	1.215	
	Medial pterygoid	1.089	
	Temporalis	0.239	–
	Anterior temporalis	–	0.115
	Middle temporalis	–	0.069
	Posterior temporalis	–	0.055
R_{FN}			
Non-Working	Masseter	1.042	
	Medial pterygoid	0.934	
	Temporalis	0.204	–
	Anterior temporalis	–	0.098
	Middle temporalis	–	0.059
	Posterior temporalis	–	0.047

stated that intrinsic strength (k), is used to determine maximum muscle force (F_H) based on Eq. 5 and the relationship between muscle force (F) and EMG measurements according to Eq. 6.

$$F_H = k \times PCSA \quad (5)$$

$$F = k \times PCSA \times EMG_F \quad (6)$$

where: (EMG_F)—scale factor

To calculate intrinsic strength, Eq. 5 was used, which was adjusted for the selected muscles depending on the selected foods, for the working (k_{Wi}) and non-working (k_{Ni}) sides, respectively—Table 5. To determine intrinsic strength, the data given in Table 1–3 were used and it was assumed that the $PCSA$ values on the working and non-working sides are the same.

The values of the temporalis muscle components are not included in Table 5 because their values are identical to those of the principal vector.

4 Discussion

In the work presented here, we used our model of unilateral chewing (Figure 2) developed based on: 1) the anatomical structure of the masticatory system (Synbone skull 8500 and mandible 8596), 2) food patterns Figures 1, 3 chewing paths Figure 3A.

Based on the assumptions made, dynamic patterns were determined for the mandibular elevator muscles in the form of muscle forces and corresponding contractions. Furthermore, the results obtained allowed the calculation of stiffness of the muscle and intrinsic strength. All values of the above parameters were determined in relation to the food and the working and non-working sides for a single chewing cycle.

4.1 Limitations of the model

The model proposed and the assumptions made are a compromise between a correctly anatomical structure of the masticatory system and the physiological mechanism of mastication (act of chewing) and the possibility of reproducing the conditions (parameters) necessary to reproduce physiologically correct unilateral chewing.

Despite the use of simplifications (e.g., same chewing velocity, the muscle is represented by a single principal vector, no friction coefficients, no consideration of the muscle damping coefficient, use of a single geometrical model of the mandible, mechanically correct but basic in terms of the anatomical structure temporomandibular joint), the model meets the basic requirements to carry out calculations in accordance with the principles of solid mechanics and function of the masticatory system.

Since the model does not take into account all the parameters responsible for the correct course of the chewing process, it must be assumed that the results of the calculations show how the mandibular elevator muscles may function during the first unilateral chewing cycle.

4.2 Dynamic patterns of muscle forces

Similar to the authors' previous work (Stróżyk and Bałchanowski 2016; Stróżyk and Bałchanowski, 2018; Stróżyk and Bałchanowski, 2020) and other publications (Agrawal et al., 1998; Hiimae et al., 1996; Koolstra, 2002; Mathevon et al., 1995; Shimada et al., 2012) and the present study, it has been shown that mechanical [$F_i = f(\Delta h_i)$] and geometric [height (h_i)] food

TABLE 7 Values of muscle forces corresponding to unilateral chewing.

Muscle		Pinheiro and Alves (2015)		Reina et al. (2007)		Korioth et al. (1992)	
		Right	Left	Right	Left	Right	Left
Superficial masseter	}	234.1	195.1	106.6	38.1	137.1	114.2
Deep masseter				45.7	16.3	58.7	49.0
Medial pterygoid		191.0	136.4	169	82.2	146.2	104.4
Lateral pterygoid		26.1	56.5	33.5	23.9	20.1	43.5
Anterior temporalis	}	263.6	221.4	102.7	80.6	115.3	91.6
Middle temporalis				57.4	50.7	63.1	64.1
Posterior temporalis				40.8	40.8	44.6	29.5

parameters have a significant influence on the function of the masticatory system, especially the muscular system.

Based on the elementary comparative analysis of the food characteristics (Figure 1) with the muscle force patterns (Figures 6, 7), it can be shown that there is a high similarity between them related to the course of the graphs. Such a relationship occurs in the so-called simple mechanisms (Stróżyk and Bałchanowski, 2016; Stróżyk and Bałchanowski, 2018; Stróżyk and Bałchanowski, 2020) characterised by the fact that the response of the system is in the form of displacements and enforcing forces (muscle forces) is correlated with the force (resistance force posed by food). The correlation between the above-mentioned parameters is manifested, among other things, by their values increasing at the same rate and reaching maximum values at the same time. Of course, the above statement is fulfilled for the kinematically correct movement of the masticatory system.

Furthermore, it can also be seen that the patterns of the same muscle on the working and non-working sides have similar characteristics but different values (Tables 2, 3). This is due to the asymmetrical alignment of the mandible concerning the sagittal plane, which is a consequence of including the chewing path.

In addition, significant differences can be observed, irrespective of the muscle, between the values of maximal muscle forces and maximal contractions, depending on the food. However, the comparison of the values of the contractions corresponding to the maximum forces shows that the differences are not as explicit as for the muscle forces (Tables 2, 3).

4.2.1 Maximum muscle force

The results indicate that not only muscle force patterns but also maximum muscle forces are dependent on food (mechanical parameters). Moreover, analysing their values (Tables 2, 3) it was observed that on the working side, they are higher than on the non-working side. This result proves the correctness of the obtained results and compliance with the elementary static principle, from which it follows that the resultant of external forces (occlusion force)

is located closer to the components (muscular forces) with higher values.

A detailed analysis taking into account the values of the maximum muscle forces shows that the forces on the non-working side are on average 14% lower than those on the working side, irrespective of the muscle (the masseter, medial pterygoid and temporalis muscles), the division of the temporalis muscle (Figure 5) and the food (Table 1). The difference is not large, but it balances the non-working and the working side, allowing a stable mandible elevation during unilateral chewing for the given boundary conditions.

The knowledge of the maximum muscle forces (F_{HWi} and F_{HNi}) and the maximum occlusion forces (F_{bmax}) made it possible to show that there is a correlation between them, which can be presented in the form of their ratio (Table 6), corresponding for the working (R_{FW}) and non-working (R_{FN}) sides. Based on the data (Figure 1; Tables 2, 3) R_{FW} and R_{FN} can be determined considering: (1) the principal vectors of the masseter, medial pterygoid and temporalis muscles (case I) and/or (2) the principal vectors of the masseter muscle and the medial pterygoid muscle with simultaneous consideration of the division of the temporalis muscle into three parts (case II)—(Figure 5). The results given in Table 6 indicate that the values of R_{FW} and R_{FN} are constant for the muscles and components of the primary vector of the temporalis muscle, of food, but different for the working and non-working sides.

The relationship between maximum muscle force and maximum occlusion force can also be represented by a linear relationship (Eqs 7, 8) in which the proportionality coefficient is R_{FW} and R_{FN} .

$$F_{HWi} = R_{FW} \times F_{i,max} \quad (7)$$

$$F_{HNi} = R_{FN} \times F_{i,max} \quad (8)$$

In the literature, it is possible to find publications in which authors model bilateral and unilateral chewing, among others (Choi et al., 2005; Pinheiro and Alves, 2015; Jahadakbar et al., 2016; Lee et al., 2017; Luo et al., 2017; Marková and Gallo, 2016; Orassi et al., 2021; Pachnicz and Stróżyk, 2021; Reina et al., 2007); however, these are models corresponding to static occlusion and the muscle force

TABLE 8 Values of proportionality coefficients R_{qW} and R_{qN} for selected muscles, depending on cases I and II.

Side	Muscle	Case I	Case II
R_{qW}			
Working	Masseter	0.46	
	Medial pterygoid	0.29	
	Temporalis	0.74	–
	Anterior temporalis	–	0.60
	Middle temporalis	–	0.53
	Posterior temporalis	–	0.46
R_{qN}			
Non-Working	Masseter	0.55	
	Medial pterygoid	0.36	
	Temporalis	0.90	–
	Anterior temporalis	–	0.73
	Middle temporalis	–	0.64
	Posterior temporalis	–	0.55

values used are based, primarily, on the data reported in (Korioth et al., 1992; Korioth and Hannam, 1994) and in (Ferrario et al., 2004).

Despite the use of static models in the above-mentioned publications, it was decided to relate the obtained maximum values of muscle forces to those works in which the authors take into account the unilateral loading of the mandible—Table 7. Taking into account the data provided by (Pinheiro and Alves, 2015), it follows that the values of forces in the muscles differ significantly from those reported in Tables 2, 3. According to the authors of the above-mentioned publication, the main role in generating occlusal force is played by the temporalis muscle, which muscular force is greater than that of the masseter muscle and the medial pterygoid muscle, both on the working and non-working sides. On the basis of the results obtained in Tables 2, 3, it follows that during unilateral chewing the muscle forces generated by the masseter muscle and the medial pterygoid muscle are significantly greater than the values determined for the temporalis muscle. A similar regularity regarding the values of muscle forces can be found in the work of (Korioth et al., 1992).

Based on the muscle force values reported by (Reina et al., 2007), it appears that the medial pterygoid muscle is the dominant muscle. The analysis performed indicates that on the working side, the medial pterygoid muscle has the highest values, while the superficial the masseter muscle and the temporalis muscle have similar values. On the non-working side, the medial pterygoid muscle and the

posterior temporalis muscle have similar values, while the masseter muscle has a value ~2 times lower than them. In contrast, the results are shown in Tables 2, 3 indicate that regardless of the product and side, the masseter muscle has the highest value, and the temporalis muscle has the lowest value. The muscle force values of the medial pterygoid muscle are only 10% less than those of the masseter muscle.

Furthermore, in the works (Korioth et al., 1992; Reina et al., 2007), the temporalis muscle is decomposed into 3 components (Table 7), between which there is the same relationship as shown in Table 3, i.e., the anterior temporalis muscle has the highest value of muscle force, the middle temporalis muscle intermediate and the posterior temporalis muscle the lowest, regardless of the side.

4.2.2 Muscle contraction

On the basis of the data given in Tables 2, 3, it can be shown that for the working side, the total contraction of the mandibular elevator muscles is 17% lower on average than on the non-working side.

Analysis of the results also showed that total contraction was dependent on the initial food height (Table 1), i.e., the distance between a pair of corresponding molars.

Detailed analysis showed that the height of the food influences: 1) the size of the chewing path (mainly height, but also width (Figure 3) and 2) muscle contractions (Tables 2, 3). The relationship between food height and chewing path height in the sagittal plane can be described by Tales' theorem. On the other hand, the relationship between the height of the food (h_i) and the total muscle contraction (Δq_{Ci}) can be determined: 1) by solving tasks in which the movable part (mandible) is suspended on a tendon (muscle) and is simultaneously supported at a point corresponding to the TMJ or 2) using a parameter that is the ratio (ratio) of their values ($\Delta q_{Ci}/h_i$). The ratio was determined separately for the working side (R_{qW}) and the non-working side (R_{qN}). The results of the calculations (Table 8) showed that the values of R_{qW} and R_{qN} are: 1) constant for each muscle and 2) dependent on the considered side, i.e., working or non-working side. Considering the temporalis muscle (Figure 5), the values of R_{qW} and R_{qN} (Table 8) can be presented for 2 cases: 1) without considering the division of the temporalis muscle (case I) and 2) with considering the division of the temporalis muscle into three parts (case II) (Figure 5).

The relationship between (Δq_{Ci}) and (h_i) can be represented by the linear relationship (Eqs 9, 10) in which the proportionality coefficient is R_{qW} and R_{qN} .

$$\Delta q_{CW_i} = R_{qW} \times h_i \quad (9)$$

$$\Delta q_{CN_i} = R_{qN} \times h_i \quad (10)$$

Based on the results presented, it can be assumed that the muscle contraction during unilateral chewing, with the dimensions of the masticatory system fixed, depends on the height of the food bite. Since the height (h_i) changes during biting, therefore, the contraction can be written in the form of a function $\Delta q_E = f(\Delta h_i)$ - the muscle contraction (Δq_E) vs. the height of food specimen (Δh_i). Moreover, the above parameters are time-dependent, i.e., $\Delta q_E(t)$ and $\Delta h_i(t)$. The above conclusion can also be applied to symmetric incisal biting of foodstuffs.

There was no clear relationship between maximum force and corresponding contraction (Tables 2, 3).

4.3 Stiffness of the muscle

As with the other parameters, the stiffness of the muscle (K) is also strongly dependent on: 1) the mechanical properties of the food (texture), 2) the muscle analysed and 3) the side analysed, i.e., working and/or non-working.

Preliminary analysis of the results indicates that similar values of stiffness of the muscle (Table 4) can be obtained for products different in texture, characteristics (Figure 1) and method of manufacture. The results given in Table 4 indicate that with respect to K the selected products can be divided into two groups, i.e., 1) chocolate and carrot and 2) bar, apple and sausage. It can also be observed that the K in the first group is, on average 2.7 times higher than that of the second group, irrespective of the type of muscle and the working and non-working side. Furthermore, analysing the K values in relation to the side, it can be seen that the stiffness of the muscles is lower under the non-working side (K_{Ni}), compared to the working side (K_{Wi}), by an average of 29%.

Analysis of the results given in Tables 2–4 indicates that the greater the stiffness of the muscle, the greater the maximum muscle force.

It should be added that the determined patterns of muscle forces (Figures 6, 7) enable the determination of the non-linear stiffness (K_i) according to the general Eq. 11. However, first, with the help of an appropriate tool (mathematical program), an appropriate mathematical equation should be fitted to the data (patterns), i.e., $F_{Ei} = f(\Delta q_{Ei})$ or $F_{Ei} = F_{Ei}(\Delta q_{Ei})$ (muscle force vs. muscle contraction).

$$K_i = dF_{Ei} / d(\Delta q_i) \quad (11)$$

where: dF_{Ei} —muscle force gains in relation to food and side of the mandible, $d(\Delta q_i)$ —increases in muscle contraction according to food and side of the mandible

The resulting K_{Wi} and K_{Ni} values can be used in numerical calculations where the muscle is modelled as a spring only (Antic et al., 2015; Pachnicz and Stróżyk, 2021). If the calculations involve static loading, it is sufficient to provide a single value corresponding to a given bite force or muscle force, depending on the target. In dynamic calculations, the non-linear function of the muscle must be taken into account (Figure 6), so the stiffness must be entered as a function according to the requirements of the programme. On the other hand, an accurate representation of the performance characteristics of the muscle requires the use of complex models, e.g., 1) Maxwell model, 2) Voigt model, 3) Kelvin model, and 4) Hill model, in which additional parameters regarding elements such as spring elements, damping elements, contractile element and parallel elastic element (elements describing the passive elastic properties of the muscle fibres) must be taken into account (Romero and Alonso, 2016). It is also possible to use the model proposed

by Röhrle and Pullan (2007), in which the muscle is a viscoelastic material.

4.4 Intrinsic strength

Analysis of the data given in Table 5 has shown that the values of intrinsic strength (k): 1) depend on the food, above all on its mechanical properties, 2) depend on the side analysed, i.e., working and/or non-working, 3) regardless of the side and food considered, are the highest for the temporalis muscle and the lowest for the medial pterygoid muscle. However, for the masseter muscle they are smaller than the medial pterygoid muscle by an average of 28%, and 4) they are identical both for the main vector of the temporalis muscle and its components (this results from an assumption related to the decomposition of the main vector into its components (Figure 5).

In the available literature (in recent years), there are few publications concerning the determination of the k -parameter, especially in relation to physiological forces. An interesting publication on the k -parameter, despite the passage of more than 40 years, is the paper by Pruim et al., 1980. In the above-mentioned paper, the authors provide k values determined during experimental studies (*in vivo*) but during bilateral static occlusion at different levels of occlusion force. Moreover, the authors assume the same k value for all muscles, which makes it difficult to compare the results. However, taking the values obtained for chocolate as a reference (lowest height and maximum occlusion force reached in the mandibular position close to the close-up of the teeth) and considering the temporalis muscle (lowest k), it was decided to compare the results given by Pruim et al., 1980 with the values presented in Table 5. Analysis of the value of the k parameter showed that during unilateral chewing, the temporalis muscle has significantly lower average values (more than 20 times lower than bilateral chewing). Considering the masseter muscle and the medial pterygoid muscle, it turns out that the mean values are also smaller, respectively: 4-fold and 3-fold.

Taking into account some of the oldest data concerning the parameter k given in the works by Fick et al. (1904) 1×10^6 N/m², Morris (1948) 0.9×10^6 N/m², Ikai and Fukunaga (1968) 0.7×10^6 N/m² it follows that a value close to the data given in Table 5 is 0.4×10^6 N/m² determined by Hettinger. (2017). A similar value in the 1980s was given by Weijs and Hillen (1985) i.e., $k = 0.37 \times 10^6$ N/m², which is widely used by many authors (Hattori et al., 2003; Koolstra et al., 1988; Koolstra and Eijden, 1992; Koriath and Hannam, 1990; Langenbach and Hannam, 1999; Peck et al., 2000; Zheng et al., 2019). Analysis of the aforementioned papers indicates that the authors use only one value of $k = 0.37 \times 10^6$ N/m² or 0.4×10^6 N/m², although the paper (Slager et al., 1997) used $k = 0.35 \times 10^6$ N/m². Furthermore, the authors used one value of k for all muscles. However, according to the data given in Table 5, it follows that the values of k are different and depend on the food product. This indicates that the mechanical parameters of the product also have a significant influence on the values of the k parameter. The same observations but concerning chewing, can be found in (Stróżyk and Bałchanowski, 2018).

It should also be added that the equations (Eqs 5, 6) from which the value of k was determined are linear and restricted to a point only, i.e., F_H .

It is interesting to note that k is very strongly dependent on PCSA, i.e., for the same muscle force but different values of PCSA, different values of k can be obtained, and each will bear the hallmarks (or give the impression) of a correct value.

It is also worth noting that there is an analogy between intrinsic strength (k) and the classical definition of strain (σ), i.e., the same formula and the same physical unit in the SI system. Considering the general function $\sigma = f(\epsilon)$ (tension vs. strain), which is used for the mathematical notation of the characteristics obtained in the classical compression test, it is possible, on its basis, to propose an elementary function for the parameter k , i.e., $k = f(\epsilon)$, where: $\epsilon = \Delta q_E / q(0)$. On the basis of the above function, it can be shown that k is not a constant value during muscle contraction and changes with the change in load similarly to σ . The equation $k = f(\epsilon)$, does not change the physical meaning of intrinsic strength but extends its applications to the full range of changes in muscle force values, not only the maximum values.

5 Conclusion

The present work shows that the use of a hybrid model based on numerical simulation and experimental studies can provide an advanced (promising) tool for modelling complex processes such as the act of chewing. This paper also shows that muscle forces and mechanical parameters of food can be represented as functions, $F_i = f(q_i)$ and $F_i = f(\Delta h_i)$, respectively. In addition, the advantage of the presented model is that it allows rapid modification of geometric parameters and loading functions tailored to individual patient characteristics. The results of such calculations will allow for better fabrication and fitting of implants or prosthetic components to the patient.

The determined muscle or food force patterns can also be used in numerical simulations based on deformable body mechanics. Such simulations will make it possible to determine stress, strain and displacement at selected points in the mandible, maxilla, teeth and temporomandibular joint.

The conclusions of the present study confirm and complement theories about the mechanisms of the masticatory system during chewing. On the other hand, the computational technique used, using inverse kinematics and dynamics analysis and the application of food patterns, made it possible to

understand the influence of mechanical food parameters on muscle force patterns.

Data availability statement

The raw data supporting the conclusion of this article will be made available by the authors, without undue reservation.

Author contributions

PS and JB designed the study. PS conducted the experimental studies and determined the food characteristics. JB developed the computational models and collected the data. Both authors interpreted the data and wrote and revised the manuscript. In addition, they agree to be responsible for all aspects of the manuscript. All authors contributed to the article and approved the submitted version.

Funding

This paper was supported by Grants-in-Aid from the Wrocław University of Science and Technology, Faculty of Mechanical Engineering, Poland; (K58 and K61—No. 821 1104 160).

Conflict of interest

The authors declare that the research was conducted in the absence of any commercial or financial relationships that could be construed as a potential conflict of interest.

Publisher's note

All claims expressed in this article are solely those of the authors and do not necessarily represent those of their affiliated organizations, or those of the publisher, the editors and the reviewers. Any product that may be evaluated in this article, or claim that may be made by its manufacturer, is not guaranteed or endorsed by the publisher.

References

- Agrawal, K. R., Lucas, P. W., Bruce, I. C., and Prinz, J. F. (1998). Food properties that influence neuromuscular activity during human mastication. *J. Dent. Res.* 77, 1931–1938. doi:10.1177/00220345980770111101
- Anderson, K., Throckmorton, G. S., Buschang, P., and Hayasaki, H. (2002). The effects of bolus hardness on masticatory kinematics. *J. Oral Rehabil.* 29, 689–696. doi:10.1046/j.1365-2842.2002.00862.x
- Antic, S., Vukicevic, A. M., Milasinovic, M., Saveljic, I., Jovicic, G., Filipovic, N., et al. (2015). Impact of the lower third molar presence and position on the fragility of mandibular angle and condyle: A three-dimensional finite element study. *J. Craniomaxillofac Surg.* 43, 870–878. doi:10.1016/j.jcms.2015.03.025
- Bhatka, R., Throckmorton, G. S., Wintergerst, A. M., Hutchins, B., and Buschang, P. H. (2004). Bolus size and unilateral chewing cycle kinematics. *Arch. Oral Biol.* 49, 559–566. doi:10.1016/j.archoralbio.2004.01.014
- Buschang, P. H., Throckmorton, G. S., Austin, D., and Wintergerst, A. M. (2007). Chewing cycle kinematics of subjects with deepbite malocclusion. *Am. J. Orthod. Dentofac. Orthop.* 131, 627–634. doi:10.1016/j.ajodo.2005.06.037
- Çakir, E., Koç, H., Vinyard, C. H. J., Essick, G., Daubert, C. H. R., Drake, M., et al. (2011). Evaluation of texture changes due to compositional differences using oral processing. *J. Texture Stud.* 43, 257–267. doi:10.1111/j.1745-4603.2011.00335.x
- Choi, A. H., Ben-Nissan, B., and Conway, R. C. (2005). Three-dimensional modelling and finite element analysis of the human mandible during clenching. *Aust. Dent. J.* 50, 42–48. doi:10.1111/j.1834-7819.2005.tb00084.x
- Daumas, B., Xu, W. L., and Bronlund, J. (2005). Jaw mechanism modeling and simulation. *Mech. Mach. Theory.* 40, 821–833. doi:10.1016/j.mechmachtheory.2004.12.011
- Dellow, P. G., and Lund, J. P. (1971). Evidence for central timing of rhythmical mastication. *J. Physiol.* 215, 1–13. doi:10.1113/jphysiol.1971.sp009454

- Dick, T. J. M., and Wakeling, J. M. (2017). Shifting gears: Dynamic muscle shape changes and force-velocity behavior in the medial gastrocnemius. *J. Appl. Physiol.* 123, 1433–1442. doi:10.1152/japplphysiol.01050.2016
- Ferrario, V. F., and Sforza, C. (1996). Coordinated electromyographic activity of the human masseter and temporalis anterior muscles during mastication. *Eur. J. Oral. Sci.* 104, 511–517. doi:10.1111/j.1600-0722.1996.tb00134.x
- Ferrario, V., Sforza, C., Serrao, G., Dellavia, C., and Tartaglia, G. (2004). Single tooth bite forces in healthy young adults. *J. Oral Rehabil.* 31, 18–22. doi:10.1046/j.0305-182x.2003.01179.x
- Fick, H. (1904). *Handbuch der Anatomie und Mechanik der Gelenke* G. Fischer Classic reprint–forgotten books. <https://www.forgottenbooks.com/en> (Accessed February 14, 2018).
- Fitts, R. H., McDonald, K. S., and Schluter, J. M. (1991). The determinants of skeletal muscle force and power: Their adaptability with changes in activity pattern. *J. Biomech.* 24, 111–122. doi:10.1016/0021-9290(91)90382-W
- Foegeding, E. A., and Drake, M. A. (2007). Invited review: Sensory and mechanical properties of cheese texture. *J. Dairy Sci.* 90, 1611–1624. doi:10.3168/jds.2006-703
- Foster, K. D., Woda, A., and Peyron, M. A. (2006). Effect of texture of plastic and elastic model foods on the parameters of mastication. *J. Neurophysiol.* 95, 3469–3479. doi:10.1152/jn.01003.2005
- Harrison, S. M., Paul, W., Cleary, P. W., Eyres, G., Sinnotta, M. D., and Lundinc, L. (2014). Challenges in computational modelling of food breakdown and flavour release. *Food Funct.* 5, 2792–2805. doi:10.1039/c4fo00786g
- Hattori, Y., Satoh, C., Seki, S., Watanabe, Y., Ogino, Y., and Watanabe, M. (2003). Occlusal and TMJ loads in subjects with experimentally shortened dental arches. *J. Dent. Res.* 82, 532–536. doi:10.1177/154405910308200709
- Hedjazi, L., Guessasma, S., Yven, C., Della Valle, G., and Salles, C. (2013). Preliminary analysis of mastication dynamics and fragmentation during chewing of brittle cereal foods. *Food Res. Int.* 54, 1455–1462. doi:10.1016/j.foodres.2013.09.041
- Hettinger, T. (2017). Physiology strength. *This edition is published by Muriwai Books – www.pp-publishing.com. Text originally published in 1961 under the same title.* (Editor by M. H. Thurlwell) Charles C Thomas, Springfield, Illinois.
- Hiemae, K., Heath, M. R., Heath, G., Kazazoglu, E., Murray, J., Sapper, D., et al. (1996). Natural bites, food consistency and feeding behaviour in man. *Arch. Oral Biol.* 41, 175–189. doi:10.1016/0003-9969(95)00112-3
- Hutchings, S. C., Foster, K. D., Bronlund, J. E., Lentle, R. G., Jones, J. R., and Morgenstern, M. P. (2012). Particle breakdown dynamics of heterogeneous foods during mastication: Peanuts embedded inside different food matrices. *J. Food Eng.* 109, 736–744. doi:10.1016/j.jfoodeng.2011.11.011
- Hylander, V. L. (2006). “Functional anatomy and biomechanics of the masticatory apparatus,” in *Temporomandibular disorders: An evidenced approach to diagnosis and treatment*. Editors D. M. Laskin, C. S. Greene, and W. L. Hylander (Hanover Park, IL: Quintessence Publishing Co, Inc.).
- Ikai, M., and Fukunaga, T. (1968). Calculation of muscle strength per unit cross-sectional area of human muscle by means of ultrasonic measurement. *Int. Z. Angew. Physiol.* 26, 26–32. doi:10.1007/BF00696087
- Itoh, K., Hayashi, T., and Miyakawa, M. (1997). Controllability of temporomandibular joint loading by coordinative activities of masticatory muscles: A two-dimensional static analysis. *Front. Med. Biol. Eng.* 8, 123–138. doi:10.1109/IEMBS.1996.651895
- Jahadkabar, A., Moghaddam, N. S., Amirhesam Amerinatanz, A., Dean, D., Karaca, H. E., and Elahinia, M. (2016). Finite element simulation and additive manufacturing of stiffness-matched niti fixation hardware for mandibular reconstruction surgery. *Bioengineering* 3, 36. doi:10.3390/bioengineering3040036
- Knudson, D. (2007). *Fundamentals of biomechanics*. New York: Springer Science+Business Media.
- Kohyama, K., Nakayama, Y., Yamaguchi, I., Yamaguchi, M., Hayakawa, F., and Sasaki, T. (2007). Mastication efforts on block and finely cut foods studied by electromyography. *Food Qual. prefer.* 18, 313–320. doi:10.1016/j.foodqual.2006.02.006
- Kohyama, K., Sasaki, T., and Hayakawa, F. (2008). Characterization of food physical properties by the mastication parameters measured by electromyography of the jawclosing muscles and mandibular kinematics in young adults. *Biosci. Biotechnol. Biochem.* 72, 1690–1695. doi:10.1271/bbb.70769
- Koole, P., Beenhakker, F., de Jongh, H. J., and Boering, G. (1990). A standardized technique for the placement of electrodes in the two heads of the lateral pterygoid muscle. *J. Craniomandib. Pract.* 8, 154–162. doi:10.1080/08869634.1990.11678309
- Koolstra, J. H. (2002). Dynamics of the human masticatory system. *Crit. Rev. Oral Biol. Med.* 13, 366–376. doi:10.1177/154411130201300406
- Koolstra, J. H., and van Eijden, T. M. G. J. (1992). Application and validation of a three-dimensional mathematical model of the human masticatory system *in vivo*. *J. Biomech.* 25, 175–187. doi:10.1016/0021-9290(92)90274-5
- Koolstra, J. H., van Eijden, T. M. G. J., Weijis, W. A., and Naeije, M. (1988). A three-dimensional mathematical model of the human masticatory system predicting maximum possible bite forces. *J. Biomech.* 21, 563–576. doi:10.1016/0021-9290(88)90219-9
- Korioth, T. W. P., and Hannam, A. G. (1994). Deformation of the human mandible during simulated tooth clenching. *J. Dent. Res.* 73, 56–66. doi:10.1177/00220345940730010801
- Korioth, T. W. P., and Hannam, A. G. (1990). Effect of bilateral asymmetric tooth clenching on load distribution at the mandibular condyles. *J. Prosthet. Dent.* 64, 62–73. doi:10.1016/0022-3913(90)90154-5
- Korioth, T. W. P., Romilly, D. P., and Hannam, A. G. (1992). Three-dimensional finite element stress analysis of the dentate human mandible. *Am. J. Phys. Anthropol.* 88, 69–96. doi:10.1002/ajpa.1330880107
- Langenbach, G. E. J., and Hannam, A. G. (1999). The role of passive muscle tensions in a three-dimensional dynamic model of the human jaw. *Arch. Oral Biol.* 44, 557–573. doi:10.1016/s0003-9969(99)00034-5
- Lee, J. H., Han, H. S., Kim, Y. Ch., Lee, J. Y., and Lee, B. K. (2017). Stability of biodegradable metal (Mg–Ca–Zn alloy) screws compared with absorbable polymer and titanium screws for sagittal split ramus osteotomy of the mandible using the finite element analysis model. *J. Craniomaxillofac Surg.* 45, 1639–1646. doi:10.1016/j.jcms.2017.06.015
- Lenfant, F., Loret, C., Pineau, N., Hartmann, C., and Martin, N. (2009). Perception of oral food breakdown. The concept of sensory trajectory. *Appetite* 52, 659–667. doi:10.1016/j.appet.2009.03.003
- Lillford, P. J. (2000). The materials science of eating and food breakdown. *MRS Bull.* 25, 38–43. doi:10.1557/mrs2000.252,
- Lucas, P. W., Prinz, J. F., Agrawal, K. R., and Bruce, I. C. (2004). Food texture and its effect on ingestion, mastication and swallowing. *J. Text. Stud.* 35, 159–170. doi:10.1111/j.1745-4603.2004.tb00831.x
- Lund, P. J. (1991). Mastication and its control by the brain stem. *Crit. Rev. Oral Biol. Med.* 2, 33–64. doi:10.1177/10454411910020010401
- Luo, D., Rong, Q., and Chen, Q. (2017). Finite-element design and optimization of a three-dimensional tetrahedral porous titanium scaffold for the reconstruction of mandibular defects. *Med. Eng. Phys.* 47, 176–183. doi:10.1016/j.medengphy.2017.06.015
- Manns, A., and Díaz, G. (1988). *Sistema Estomatognático*. Santiago de Chile: Sociedad Gráfica Almagro Ltda.
- Marková, M., and Gallo, L. M. (2016). The influence of the human TMJ eminence inclination on predicted masticatory muscle forces. *Hum. Mov. Sci.* 49, 132–140. doi:10.1016/j.humov.2016.06.012
- Mathevon, E., Mioche, L., Brown, W. E., and Culioli, J. (1995). Texture analysis of beef cooked at various temperatures by mechanical measurements, sensory assessments and electromyography. *J. Text. Stud.* 26, 175–192. doi:10.1111/j.1745-4603.1995.tb00792.x
- May, B., Saha, S., and Saltzman, M. (2001). A three-dimensional mathematical model of temporomandibular joint loading. *Clin. Biomech.* 16, 489–495. doi:10.1016/s0268-0033(01)00037-7
- Meullenet, J. F., Finney, M. L., and Gaud, M. (2002). Measurement of biting velocities, and predetermined and individual crosshead speed instrumental imitative tests for predicting cheese hardness. *J. Texture Stud.* 33, 45–58. doi:10.1111/j.1745-4603.2002.tb01334.x
- Mioche, L., Bourdiol, P., Martin, J. F., and Noël, Y. (1999). Variations in human masseter and temporalis muscle activity related to food texture during free and side imposed mastication. *Arch. Oral Biol.* 44, 1005–1012. doi:10.1016/s0003-9969(99)00103-x
- Mioche, L., Bourdiol, P., Monier, S., and Martin, J. F. (2002). The relationship between chewing activity and food bolus properties obtained from different meat textures. *Food Qual. prefer.* 13, 583–588. doi:10.1016/S0950-3293(02)00056-3
- Morris, C. B. (1948). The measurement of the strength of muscle relative to the cross-section. *Res. Q. Am. Assoc. Hlth Phys. Educ.* 19, 295–303. doi:10.1080/10671188.1948.10621004
- Murray, G. (2004). “Jaw movement and its control,” in *Occlusion and clinical practice an evidence based approach*. Editors I. Klineberg and J. Rob (London: Elsevier Health Sciences), 13–22.
- Murray, G. M., Orfanos, T., Chan, J. Y., Wanigaratne, K., and Klineberg, I. J. (1999). Electromyographic activity of the human lateral pterygoid muscle during contralateral and protrusive jaw, movements. *Arch. Oral Biol.* 44, 269–285. doi:10.1016/s0003-9969(98)00117-4
- Nishigawa, K., Nakano, M., and Bando, E. (1997). Study of jaw movement and masticatory muscle activity during unilateral chewing with and without balancing side molar contacts. *J. Oral Rehabil.* 24, 691–696. doi:10.1046/j.1365-2842.1997.00553.x
- Orassi, V., Duda, G. N., Heiland, M., Fischer, H., Rendenbach, C., and Checa, S. (2021). Biomechanical assessment of the validity of sheep as a preclinical model for testing mandibular fracture fixation devices. *Front. Bioeng. Biotechnol.* 9, 672176. doi:10.3389/fbioe.2021.672176
- Pachnicz, D., and Stróżyk, P. (2021). A biomechanical analysis of muscle force changes after bilateral sagittal split osteotomy. *Front. Physiol.* 12, 679644. doi:10.3389/fphys.2021.679644

- Peck, C. C., Langenbach, G. E. J., and Hannam, A. G. (2000). Dynamic simulation of muscle and articular properties during human wide jaw opening. *Arch. Oral Biol.* 45, 963–982. doi:10.1016/s0003-9969(00)00071-6
- Piancino, M. G., Bracco, P., Valletlonga, T., Merlo, A., and Farina, D. (2008). Effect of bolus hardness on the chewing pattern and activation of masticatory muscles in subjects with normal dental occlusion. *J. Electromyogr. Kinesiol.* 18, 931–937. doi:10.1016/j.jelekin.2007.05.006
- Piancino, M. G., Isola, G., Merlo, A., Dalessandri, D., Debernardi, C., and Bracco, P. (2012). Chewing pattern and muscular activation in open bite patients. *J. Electromyogr. Kinesiol.* 22, 273–279. doi:10.1016/j.jelekin.2011.12.003
- Pinheiro, M., and Alves, J. L. (2015). The feasibility of a custom-made endoprosthesis in mandibular reconstruction: Implant design and finite element analysis. *J. Craniomaxillofac Surg.* 43, 2116–2128. doi:10.1016/j.jcms.2015.10.004
- Posselt, U. (1952). “Studies in the mobility of the human mandible,” in *Acta odontologica scandinavica* (Copenhagen: Supplementum).
- Pruim, G. J., de Jongh, H. J., and ten Bosch, J. J. (1980). Forces acting on the mandible during bilateral static bite at different bite force levels. *J. Biomech.* 13, 755–763. doi:10.1016/0021-9290(80)90237-7
- Quintero, A., Ichesso, E., Myers, C., Schutt, R., and Gerstner, G. E. (2013). Brain activity and human unilateral chewing. an fMRI study. *J. Dent. Res.* 92, 136–142. doi:10.1177/0022034512466265
- Reina, J. M., Garcia-Aznar, J. M., Dominguez, J., and Doblaré, M. (2007). Numerical estimation of bone density and elastic constants distribution in a human mandible. *J. Biomech.* 40, 828–836. doi:10.1016/j.jbiomech.2006.03.007
- Romero, F., and Alonso, F. J. (2016). A comparison among different Hill-type contraction dynamics formulations for muscle force estimation. *Mech. Sci.* 7, 19–29. doi:10.5194/ms-7-19-2016
- Röhrle, O., and Pullana, A. J. (2007). Three-dimensional finite element modelling of muscle forces during mastication. *J. Biomech.* 40, 3363–3372. doi:10.1016/j.jbiomech.2007.05.011
- Santana-Mora, U., Martínez-Ínsua, A., Santana-Penín, U., del Palomar, A. P., Banzo, J. C., and Mora, M. J. (2014). Muscular activity during isometric incisal biting. *J. Biomech.* 47, 3891–3897. doi:10.1016/j.jbiomech.2014.09.007
- Shimada, A., Yamabe, Y., Torisu, T., Baad-Hansen, L., Murata, H., and Svensson, P. (2012). Measurement of dynamic bite force during mastication. *J. Oral Rehabil.* 39, 349–356. doi:10.1111/j.1365-2842.2011.02278.x
- Slager, G. E. C., Otten, E., van Eijden, T. M. G. J., and van Willigen, J. D. (1997). Mathematical model of the human jaw system simulating static biting and movements after unloading. *J. Neurophysiol.* 78, 3222–3233. doi:10.1152/jn.1997.78.6.3222
- Slavicek, G. (2010). Human mastication. *Int. J. Stomatol. Occlusion Med.* 3, 29–41. doi:10.1007/s12548-010-0044-6
- Stokes, J. R., Boehm, M. W., and Baier, S. K. (2013). Oral processing, texture and mouthfeel: From rheology to tribology and beyond. *Curr. Opin. Colloid Interface Sci.* 18, 349–359. doi:10.1016/j.cocis.2013.04.010
- Stróżyk, P., and Bałchanowski, J. (2020). Effect of foods on selected dynamic parameters of mandibular elevator muscles during symmetric incisal biting. *J. Biomech.* 2020, 109800. doi:10.1016/j.jbiomech.2020.109800
- Stróżyk, P., and Bałchanowski, J. (2016). Effect of foodstuff on muscle forces during biting off. *Acta Bioeng. Biomech.* 18, 81–91. doi:10.5277/ABB-00305-2015-03
- Stróżyk, P., and Bałchanowski, J. (2018). Modelling of the forces acting on the human stomatognathic system during dynamic symmetric incisal biting of foodstuffs. *J. Biomech.* 79, 58–66. doi:10.1016/j.jbiomech.2018.07.046
- Stróżyk, P., Bałchanowski, J., and Szrek, J. (2018). “Modelling of the dynamic loads of the human stomatognathic system during biting off,” in 24th International Conference–Engineering Mechanics. Institute of Theoretical and Applied Mechanics of the Czech Academy of Sciences, Svatka, Czech Republic, May 14 – 17.
- Stróżyk, P. (2021). *The patent application (WIP ST 10/C PL436928 patent Office of the Republic of Poland).*
- Wang, M. Q., He, J. J., Zhang, J. H., Wang, K., Svensson, P., and Widmal, S. E. (2010). SEMG activity of jaw closing muscles during biting with different unilateral occlusal supports. *J. Oral Rehabil.* 37, 719–725. doi:10.1111/j.1365-2842.2010.02104.x
- Weijs, W. A., and Hillen, B. (1985). Cross-sectional areas and estimated intrinsic strength of the human jaw muscles. *Acta Morphol. Neerl Scand.* 23, 267–274.
- Weinberg, L. A. (1963). An evaluation of basic articulators and their concepts. *J. Prosthet. Dent.* 13, 622–644. doi:10.1016/0022-3913(63)90133-1
- Widmalm, S. E., Lillie, J. H., and Ash, M. M. (1987). Anatomical and electromyographic studies of the lateral pterygoid muscle. *J. Oral Rehabil.* 14, 429–446. doi:10.1111/j.1365-2842.1987.tb00738.x
- Williams, S. H., Wright, B. W., Truong, V. D., Daubert, C. R., and Vinyard, C. J. (2005). Mechanical properties of foods used in experimental studies of primate masticatory function. *Am. J. Primatol.* 67, 329–346. doi:10.1002/ajp.20189
- Wood, W. W., Takada, K., and Hannam, A. G. (1986). The electromyographic activity of the inferior part of the human lateral pterygoid muscle during clenching and chewing. *Arch. Oral Biol.* 31, 245–253. doi:10.1016/0003-9969(86)90056-7
- Zheng, K., Liao, Z., Yoda, N., Fang, J., Chen, J., Zhang, Z., et al. (2019). Investigation on masticatory muscular functionality following oral reconstruction—An inverse identification approach. *J. Biomech.* 90, 1–8. doi:10.1016/j.jbiomech.2019.04.007



OPEN ACCESS

EDITED BY

Suvash C. Saha,
University of Technology Sydney,
Australia

REVIEWED BY

Yongtao Lu,
Dalian University of Technology (DUT),
China
Laura Maria Vergani,
Polytechnic University of Milan, Italy

*CORRESPONDENCE

Carlos A. Cifuentes,
✉ carlos.cifuentes@uwe.ac.uk,
✉ carlosan.cifuentes@urosario.edu.co

RECEIVED 04 July 2022

ACCEPTED 25 September 2023

PUBLISHED 11 October 2023

CITATION

Ramos O, de Arco L, Cifuentes CA,
Moazen M, Wurdemann H and Múnera M
(2023), Mechanical assessment of novel
compliant mechanisms for
underactuated prosthetic hands.
Front. Bioeng. Biotechnol. 11:985901.
doi: 10.3389/fbioe.2023.985901

COPYRIGHT

© 2023 Ramos, de Arco, Cifuentes,
Moazen, Wurdemann and Múnera. This is
an open-access article distributed under
the terms of the [Creative Commons
Attribution License \(CC BY\)](#). The use,
distribution or reproduction in other
forums is permitted, provided the original
author(s) and the copyright owner(s) are
credited and that the original publication
in this journal is cited, in accordance with
accepted academic practice. No use,
distribution or reproduction is permitted
which does not comply with these terms.

Mechanical assessment of novel compliant mechanisms for underactuated prosthetic hands

Orion Ramos¹, Laura de Arco², Carlos A. Cifuentes^{1,3*},
Mehran Moazen⁴, Helge Wurdemann⁴ and Marcela Múnera^{3,5}

¹School of Engineering, Science and Technology, Universidad Del Rosario, Bogota, Colombia,

²Telecommunications Laboratory (LABTEL), Electrical Engineering, Federal University of Espirito Santo (UFES), Vitória, Brazil, ³Bristol Robotics Laboratory, University of the West of England, Bristol, United Kingdom, ⁴Department of Mechanical Engineering, University College London, London, United Kingdom, ⁵Biomedical Engineering Department, Colombian School of Engineering Julio Garavito, Bogota, Colombia

This paper proposes novel compliant mechanisms for constructing hand prostheses based on soft robotics. Two models of prosthetic hands are developed in this work. Three mechanical evaluations are performed to determine the suitability of the two designs for carrying out activities of daily living (ADLs). The first test measures the grip force that the prosthesis can generate on objects. The second determines the energy required and dissipated from the prosthesis to operate. The third test identifies the maximum traction force that the prosthesis can support. The tests showed that the PrHand1 prosthesis has a maximum grip force of 23.38 ± 1.5 N, the required energy is 0.76 ± 0.13 J, and the dissipated energy is 0.21 ± 0.17 J. It supports a traction force of 173.31 ± 5.7 N. The PrHand2 prosthesis has a maximum grip force of 36.13 ± 2.3 N, the required energy is 1.28 ± 0.13 J, the dissipated energy is 0.96 ± 0.12 J, and it supports a traction force of 78.48 ± 0 N. In conclusion, the PrHand1 prosthesis has a better performance in terms of energy and tensile force supported. The difference between the energy and traction force results is related to two design features of the PrHand2: fully silicone-coated fingers and a unifying mechanism that requires more force on the tendons to close the prosthesis. The grip force of the PrHand2 prosthesis was more robust than the PrHand1 due to its silicone coating, which allowed for an improved grip.

KEYWORDS

compliant mechanism, hand prosthetics, soft-actuators, mechanical assessment, grasping

1 Introduction

As the number of amputees and people with upper extremity disabilities continues to grow, robotic hands are increasingly viewed as a solution to improve their quality of life (Jelačić et al., 2020). According to current estimates, it is expected there will be 3.6 million amputees in the United States alone by 2050 (Jelačić et al., 2020). In developing countries, the number of amputees without access to an assistive device was estimated at 30 million (del Carmen Malbrán, 2011). According to Colombia's 2020 social protection report SISPRO, there were more than half a million people with mobility disabilities in their upper limbs (34.93% of the Colombian population) (SISPRO 2020).

Upper limb amputations generate numerous issues, including reduced self-esteem and physical problems that can prevent a person from performing activities of daily living (ADL) (Ziegler-Graham et al., 2008; Daniels et al., 2020). Therefore, the development of devices such as robotic hands aims to help people with disabilities (Robinson et al., 2014). However, a significant portion of the world's vulnerable population cannot access these types of devices, further deepening health inequality (Borg and Östergren, 2015).

Prosthetic devices replace the missing part of the human hand, and the main objective of prosthetic devices is to achieve the best possible functionality to help people with disabilities, regardless of aesthetics. In addition, prosthetic manufacturers seek to reduce costs and improve manufacturing methods to make the devices more widely accessible (Tian et al., 2017a). In the field of robotics, the construction of assistive hand devices seeks to combine the functionality of the prosthesis with the application of new technologies to achieve similar functioning as the human hand (Huaroto et al., 2020). Robotic hands have evolved from devices with limited functionality to systems capable of understanding and replicating human hand movements (Salvietti, 2018). The improvement of functionalities is related to increasing degrees of freedom (DoF) and different manufacturing technologies (Cordella et al., 2016). Previously, robotic hands were manufactured with rigid elements and industrial materials that generated heavy devices (Shintake et al., 2018). Actuation methods were based on motors and gears, which were required for each DoF of the device (Zappatore et al., 2017). A number of new techniques have emerged to reduce the weight and facilitate the manufacturing process of the devices. These processes include 3D printing technologies, new actuation techniques (Ten Kate et al., 2017), the use of motors to pull joint-actuating tendons (Jing et al., 2019), and design techniques that reduce the number of actuators needed for DoF (i.e., underactuated devices) (Massa et al., 2002; Niola et al., 2014). Finally, the inclusion of new soft materials in the manufacturing process has also reduced the fabrication time, cost, and weight of the devices (Polygerinos et al., 2017).

Robotic hands built using 3D printing can be divided into two classes: those that use pins as joints in rigid parts (Wahit et al., 2020) and those that use compliant mechanisms and flexible materials (Mutlu et al., 2015). Tendon drive techniques can be used in both types of joints, allowing for the reduction of actuators in this type of device. Soft robotics—devices using soft actuators and materials—is another option. For example, the design of fingers with silicone actuators for a robotic hand (Fras and Althoefer, 2018), improvements in grip functionality with specialized actuators for the palm (Li et al., 2019), or others where the type of actuator and its control is evaluated (Deimel and Brock, 2016; Tian et al., 2017b).

The use of techniques based on soft robotics aims to solve significant challenges faced by conventional robotic hands. For example, soft robotics allows for weight reduction, faster production, and improve safety human-device interaction (Laschi et al., 2016). However, the new technology cannot yet fully replace a conventional prosthesis due to the maximum force it is capable of exerting and the complexity of control involved in these actuators (Laschi et al., 2016). Soft materials have infinite DoF, which causes the joints to bend in undesired directions during force execution. However, soft joints with compliant mechanisms and tendon

routing can establish fully controlled actuation. Links with guided soft joints can move and exert forces on predefined axes. However, they can flex and adapt to the environment when perturbations are greater than a certain threshold. This property makes manipulators with compliant mechanisms more adaptable and durable (Liu et al., 2018).

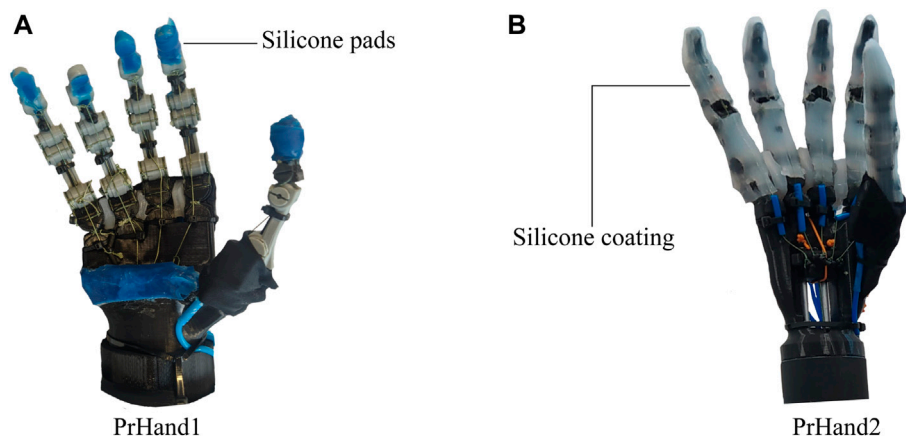
Current state-of-the-art prosthetic technologies rarely implement degrees of abduction of the middle fingers, especially in devices with rigid components (Owen et al., 2018), with existing devices using gear and motor methods for this DoF (Vulliez et al., 2018). Robotic hands using compliant mechanisms have also implemented the degree of abduction in the main fingers. In this technology, robotic hands have been developed with passive degrees of abduction, i.e., they are not controllable. Passive DoFs only give a plus in drop tolerance, and increased adaptation in grasping objects (Liu et al., 2019; Mottard et al. 2017). In the case of soft-actuated robotic hands, two types of abduction are observed: passive abduction and abduction joint designed to be actuated. In the former, the soft material itself generates abduction by having infinite DoF. Therefore, the degree of abduction exists but without being designed to be actuated (Godfrey et al., 2018). The other type of abduction is when the joint is designed to be actuated. In most cases, this occurs pneumatically using silicone actuators. A design of this joint can generate different motions that increase the dexterity and functionality of the robotic hand (Tian et al., 2017a; Xu et al., 2018).

The addition of abduction degrees of freedom and the use of new manufacturing ultimately aim to improve users' quality of life by improving the performance of robotic hands. However, these devices face complex challenges. Devices made of rigid materials must become more compatible with humans, and devices based on soft robotics must be able generate higher forces and better control.

Mechanical tests allow for the evaluation of the mechanical capacities of the prosthesis and its resistance to the different loads encountered as part of ADL. One of the most commonly used tests to determine maximum mechanical capacity is grip force, which measures the force that the prosthesis can generate on a grasped objects (Cuellar et al., 2020). A grip force of 10 N is considered sufficient to carry almost all objects related to ADL (Smit and Plettenburg, 2010a), and most of the current developments manage to exceed this value (Cuellar et al., 2020 Moreo, 2016).

In any electromechanical device, the aim is to reduce the amount of energy required and dissipated from the system. Therefore, if two devices performing the same task are compared, the one requiring less energy is considered more efficient. Similarly, the less energy the system dissipates, the more efficient the mechanisms are. This is because they transfer the input energy better and do not dissipate it in the form of heat or other energy. For example, in tendon-actuated prostheses, the dissipation of energy by transmission should be minimal. This reduces the input effort required by the actuator and produces a higher grasping force. This mechanical test determines the system's efficiency by finding the energy needed to close the hand and how much of the energy is lost in the operation of the prosthesis (Smit et al. 2015). The energy ranges (both required and dissipated) in current hands are around 1,058–2,292J (Smit and Plettenburg, 2010a).

The traction test is intended to determine the maximum force that the prosthesis can be subjected to. The traction force appears

**FIGURE 1**

The hand prostheses constructed for this study are based on compliant mechanisms and soft actuators. **(A)** The PrHand1 prosthesis has silicone coatings only at specific points. **(B)** PrHand2 prosthesis has fingers completely coated with silicone.

when a vertical force opposite to the force exerted by the hand is generated, e.g., when carrying a market bag or lifting a heavy object. The traction test typically takes the mechanisms to their limit by generating permanent mechanical damage, such as shaft breakage or deformation of prosthesis parts. Based on the Yale-CMU-Berkeley (YCB) standardized object set (Calli et al., 2015), the heaviest object used as part of ADL measurements weighs 3.1 kg, so a minimum traction force of 30 N is required to hold an object of this weight without damage.

These tests allow the mechanical comparison of different prosthesis designs. Therefore, this study aims to determine whether new construction techniques based on soft robotics and compliant mechanisms can build a prosthesis capable of meeting the mechanical requirements of grip force, energy, and traction force for ADL requirements. To investigate this research question, two prostheses with design differences will be constructed and evaluated mechanically.

2 Methodology and materials

In this study, two prostheses were constructed using compliant mechanism techniques and soft actuators (see Figure 1). Both designs are constructed with guided soft joints (Culha et al., 2017). Each finger link is made of rigid material (PLA) and 2.85 Filaflex tendons (Recreus, España) with elastic properties to perform their actuation. Finger abduction is achieved by the force generated by pneumatic silicone actuators. The two designs use a Dynamixel MX-106 motor (Robotis, USA) to actuate the flexion of the five fingers and an air pump (MITSUMI, Japan) to pressurize the abduction actuators. The system for the two designs uses a 12 V, 5A supply for operation. The hand control was performed in ROS on a Raspberry Pi 3.

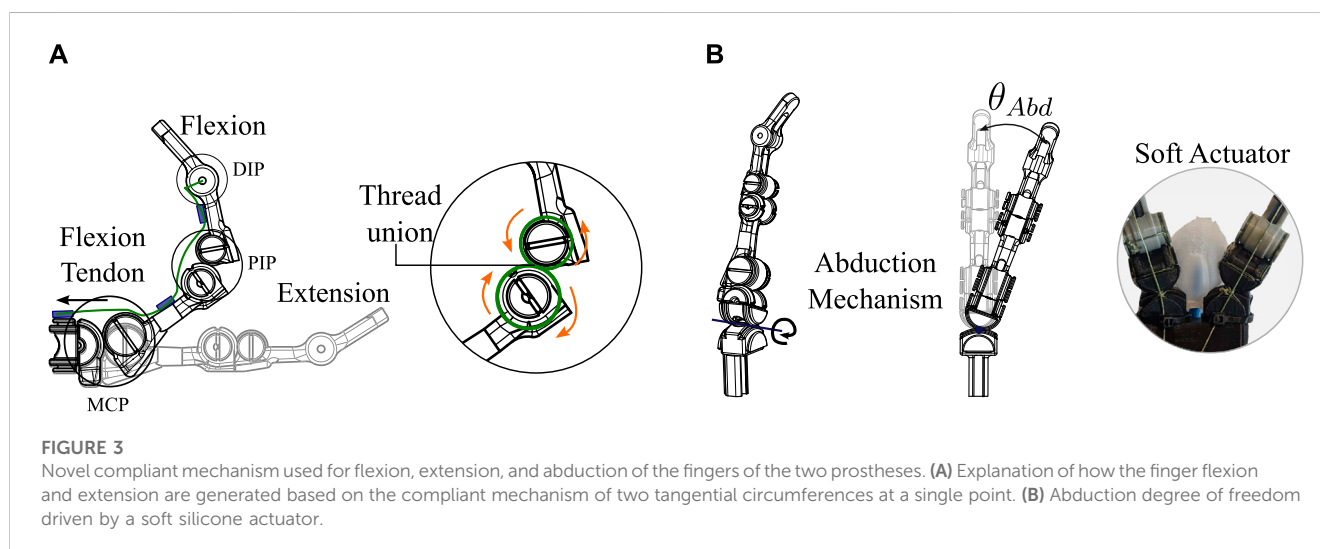
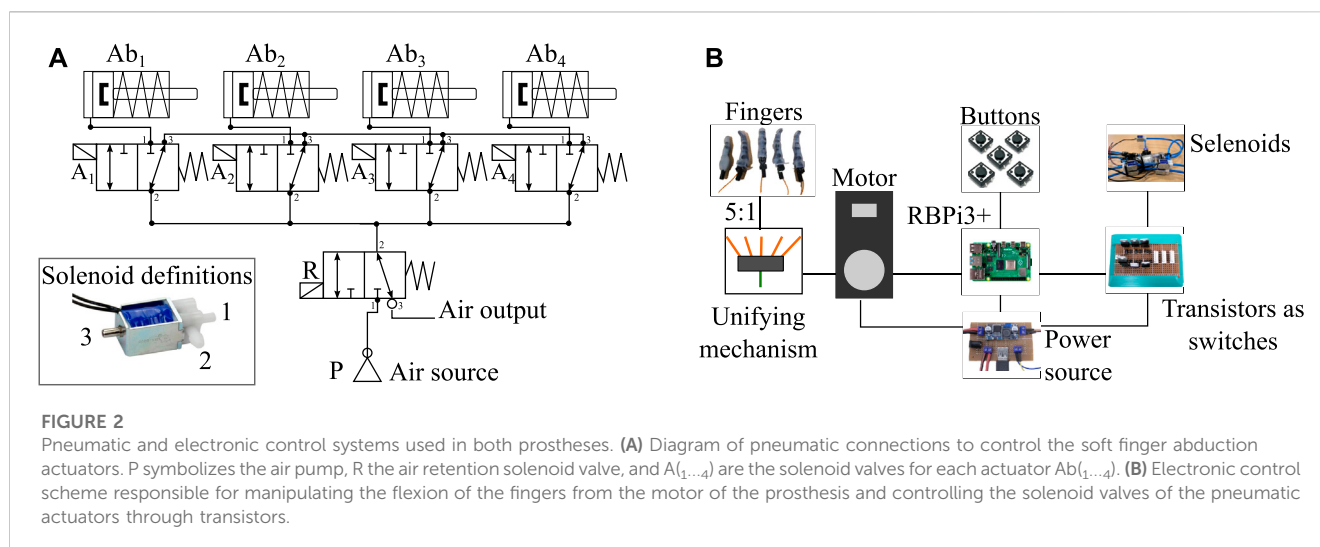
Both devices use the same pneumatic and electronic control system since the same components are used for their actuation. To achieve the abduction movements in the prostheses, silicone actuators controlled by open three-way mini-solenoid valves with two positions for each actuator are used (Generic 3/2, China). Each

solenoid valve is actuated through the Raspberry Pi independently according to the type of grip to be performed. The general pneumatic connection of the solenoid valves $A_{(1...4)}$, air pump (P) and actuators $Ab_{(1...4)}$ is shown in Figure 2A. To reduce energy consumption, the activation of the air pump is also controlled using the Raspberry Pi. The pump is only turned on when pressure is required by the actuators.

As with the pneumatic control system, the two prostheses share the same electromechanical control scheme. The entire system is powered by a 12-volt supply passing through a regulator that provides 5 volts to power the various electronic components. Since only one motor is used in the design of these devices for the flexion of the fingers, the five tendons (one per finger) must be unified into a single tendon tensioned by the motor. This system is called a unifying mechanism, and this mechanism is different in each version of the prosthesis. Both the flexion of the fingers and the activation of the pneumatic actuators are controlled by physical push buttons. The electromechanical scheme shared by the two devices can be seen in Figure 2B.

2.1 Novel finger compliant mechanism joint

The main characteristic of the prosthesis design under investigation is the flexion and extension mechanism of the fingers. The mechanism is based on compliant mechanisms constructed from a single material (Hill and Canfield, 2016). However, two circumferences are used, joined by a tension element such as a rigid thread (Sufix 832, USA) that allows rigid materials for its construction, such as PLA. The finger flexion is achieved using the tension force generated to the joint through a tendon, as shown in Figure 3A. Unlike a traditional revolute joint, this joint does not rotate about a fixed axis; instead, the joint rotates and translates tangentially about a circumference. This novel joint is more similar to joints in the human body (Xu and Todorov, 2016). These properties facilitate construction and assembly by making the joint's exact alignment with an axis unnecessary. The faces of the two circumferences only touch at one point in their movement; there is



no friction and, therefore, no wear. Finally, another advantage of this joint is due to the union of the two circumferences being made with thread. Although it is rigid, the joint allows small deformations in situations of shocks or great forces, preventing any part from breaking. Two of these novel joints were used to flex and extend the metacarpophalangeal (MCP) and interphalangeal (PIP) joint of the finger. The distal interphalangeal (DIP) joint in these designs was not constructed to be a degree of freedom. The location of the joints are seen in Figure 3.

This same novel mechanism is used for the degree of freedom of abduction in the fingers of the two prostheses. Unlike the flexion and extension degrees already presented, the degree of abduction is driven by a force generated by the silicone actuators, as shown in Figure 3B. In this case, the tangent circumferences are at 90 degrees to the axis of the flexion and extension joints. The final angle of abduction (θ_{Abd}) of each finger depends on how much pressure is applied to the pneumatic actuators. In this application, the angle θ_{Abd} does not require any sensor or control to be generated; only the timing of the solenoid valve is defined to allow air to enter the actuator.

By not behaving as a typical revolute joint, different behavior in flexion and extension of the fingers is exhibited. To kinematically explain how flexion is generated with this joint, the forward and inverse kinematics equations are calculated. PIP degree of freedom is used for the explanation as presented in Figure 4A. The reference point of the system and the endpoint (x,y) for the kinematic calculation of the joint can be seen in Figure. The variables required for the joint kinematic solution include principal angles θ , α and the links' distances, (a , L and r).

The equations that determine the final coordinate (x, y) of the link to the principal angle θ in the novel joint can be seen in Eq. 1. Unlike the solution of a traditional revolute joint (Eq. 2), these equations are composed of the two terms that depend on the angle θ and α . Where

$$\alpha = \frac{R_2}{R_1 + R_2} \theta,$$

$$a = R_1 + R_2$$

and R_1 , R_2 are the radius of the circumferences.

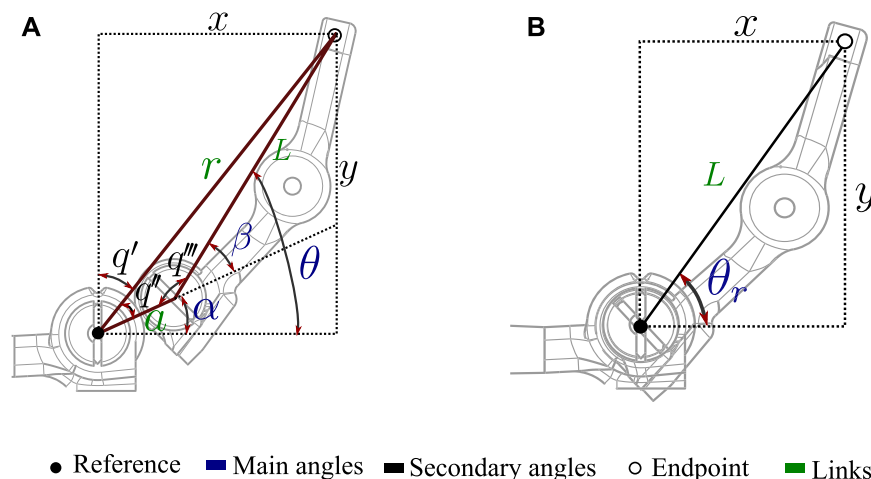


FIGURE 4

Variables involved in the kinematic solution of articulations. (A) Variables of the novel joint based on the compliant mechanism used in the prostheses constructed in this study. (B) Related variables in a traditional revolute joint.

$$\begin{bmatrix} x \\ y \end{bmatrix} = \begin{bmatrix} a \cos(\alpha) \\ a \sin(\alpha) \end{bmatrix} + \begin{bmatrix} L \cos(\theta) \\ L \sin(\theta) \end{bmatrix} \quad (1)$$

The variables involved in a typical revolute joint can be seen in Figure 4B. The forward kinematics of this joint is presented in Eq. 2. The equations show how only one term is dependent on θ_r and defines the final coordinate (x, y).

$$\begin{bmatrix} x \\ y \end{bmatrix} = \begin{bmatrix} L \cos(\theta_r) \\ L \sin(\theta_r) \end{bmatrix} \quad (2)$$

To complete the kinematic solution of the proposed joint for prosthetic fingers, Eq. 3 shows the inverse kinematics solution. Where α depends on the (x, y) coordinates as seen in Eq. 4 and β only depends on known joint parameters (Eq. 5). Moreover, Eq. 6 shows the solution of the inverse kinematics of the revolute joint.

$$\theta = \beta + \alpha \quad (3)$$

$$\alpha = 90 - \arctan\left(\frac{x}{y}\right) - \arccos\left(\frac{r^2 + a^2 - L^2}{2ar}\right) \quad (4)$$

$$\beta = 180 - \arccos\left(\frac{a^2 + L^2 - r^2}{2aL}\right) \quad (5)$$

$$\theta_r = \arctan\left(\frac{y}{x}\right) \quad (6)$$

These equations can be used to compare the behavior of the novel joint based on a compliant mechanism and a traditional revolute joint. Moreover, this approach to kinematics allows the entire motion of the fingers to be calculated in series by using only the two flexion degrees of freedom (MCP and PIP).

The kinematic equations are important for understanding the movement and behavior of the joint, which can be beneficial for optimizing the design and performance of the prosthesis in the future. Furthermore, it is important to establish a baseline for the kinematics of this new mechanism in order to have a reference point for future studies and comparisons. Overall, while the kinematic equations may not be necessary for evaluating the immediate

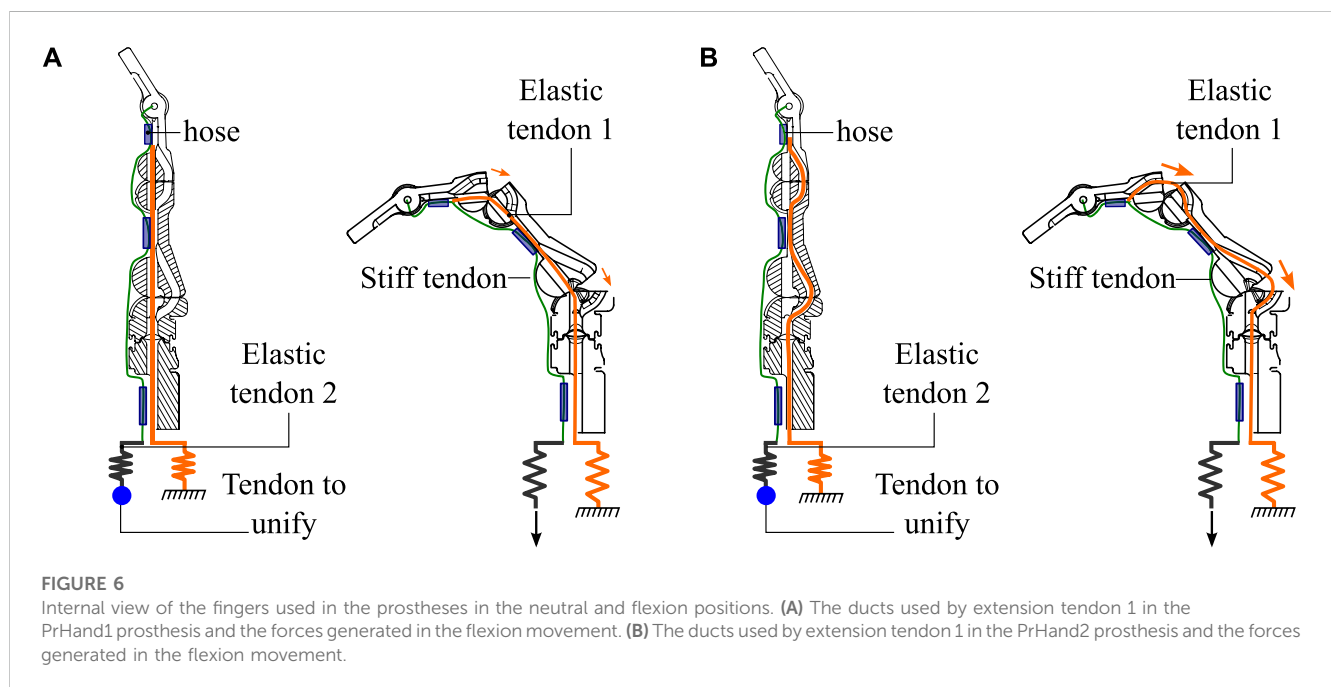
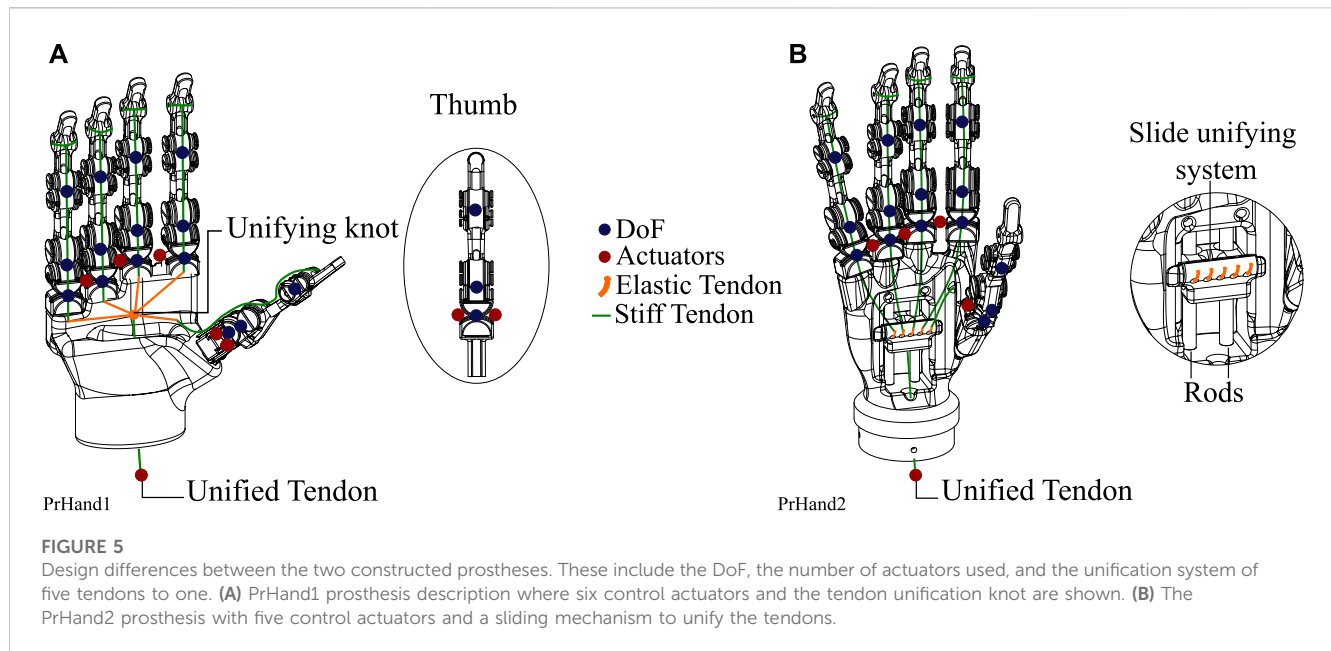
performance of the prosthesis, they provide valuable information for understanding and improving the technology in the long term.

The similarities between the designs include the novel compliant mechanism for the degrees of freedom of the fingers, the actuators used, the pneumatic scheme, and the electromechanical control scheme. The key differences between PrHand1 and PrHand2 are: the number of soft actuators used for abduction, the location of the actuators, the actuation of the thumb, the coating of the fingers to increase grip friction, the location of the extension tendon, and the unification system. A detailed description of each prosthesis is presented below.

2.1.1 PrHand1

The PrHand1 design uses an Ecoflex 00–50 silicone coating in localized parts of the fingers and palm of the prosthesis, which do not generate any restriction in the flexion movement (see Figure 1A). In this version, five soft actuators are used to control the abduction degrees of freedom. The thumb's initial position in the PrHand1 prosthesis is 45 degrees to the palm, as is the thumb of the human hand (Huang and Huang, 2019). This initial position requires two soft actuators to control the abduction and adduction of the thumb. Each prosthetic finger of the PrHand1 design has three degrees of freedom: two degrees of freedom of these (PIP and MCP) are for flexion of the prosthetic fingers. The other degree of freedom is for the abduction of the central fingers. This distribution of the joints in the main fingers does not mimic the DIP degree of freedom in the human hand. In this design, this joint is fixed with an angle of 30° degrees. In total, this prosthesis design has 15 degrees of freedom distributed in the fingers only (see Figure 5A).

An elastic tendon pulled by a single motor moves the PIP and MCP joints of the four main fingers simultaneously. Likewise, the tension in the tendon moves the IP and MCP joints of this finger, together with the thumb, to generate flexion. The unifying system of the five tendons connects to a single tendon which is driven by the motor pulley is a knot that collects the tendons, as seen in Figure 5A.



To achieve low-level independence in each finger, elastic tendon sections were used, allowing for independent deformation of each finger. When flexion is generated, the fingers take the shape of the object they are holding. The longer the elastic tendon section, the more compliant the grip, and the less force it can exert. The size of the elastic tendon can be modified by simply making the union knot at a different point, thus lengthening or shortening the distance between the elastic tendons.

The fingers of the PrHand1 prosthesis have an internal elastic tendon that generates a counter force to flexion to avoid the need for an actuator responsible for finger extension. This tendon is called the extension tendon. This design is located on the center or neutral line

of the flexion motion, as seen in [Figure 6A](#). Thus, the extension tendon does not generate high opposing forces to the flexion motion.

2.1.2 PrHand2

The PrHand2 design uses Ecoflex 00–50 silicone coating around the fingers except for the joints. This is because the silicone generates high flexion restriction (see [Figure 1B](#)). In this version, four soft actuators are used only to control the abduction degrees of freedom, and, unlike the PrHand1 prosthesis, the initial position of the thumb is located at 90 degrees to the palm. This was done to remove a soft actuator and reduce the complexity of grip types. Like the PrHand1 design, each prosthetic finger of the design has three

TABLE 1 Summary of mechanical properties of the proposed designs.

Property	PrHand1	PrHand2
Palm length [cm]	10	8.1
Hand length [cm]	19	19.5
Palm width [cm]	8.5	6.8
Palm depth [cm]	4	2.8
DoF	15	15
Actuators	6	5

degrees of freedom: two degrees of freedom (PIP and MCP) are responsible for the flexion of the prosthetic fingers, and the other degree of freedom is to generate abduction in the main fingers. This distribution of the joints in the main fingers does not take into account the DIP degree of freedom of the human hand. In total, this design has 15 degrees, as seen in [Figure 5B](#).

The unifying mechanism in the PrHand2 prosthesis is more complex than the unifying knot of the PrHand1 design. For this prosthesis, a sliding mechanism was used to collect the elastic tendons of the fingers and attach them to a moving part that slides using two parallel rods. The movement of the mobile piece is generated by the rigid tendon connected to the motor ([Figure 5B](#)). As in PrHand1, elastic tendons were used to generate compliant grips in the PrHand2 prosthesis. In this case, the unifying mechanism of this prosthesis holds five elastic tendons, one for each finger. The unifying mechanism then transforms the five elastic tendons into a single rigid tendon pulled by the motor. In this mechanism, the elastic elements are the same size for each finger. However, modifying their size to allow for more or less deformation is not possible after the mechanism is assembled. This system allows the assembly and attachment of each tendon to be independent, which makes the assembly of the device more practical than the PrHand1 prosthesis.

Internally, the fingers of the PrHand2 prosthesis differs from PrHand1 because the extension tendon does not pass through the center or neutral line of the joint. Instead, the extension tendon is displaced to the limit of the motion circumferences, which generates a force that returns the joint to its original position ([Figure 6B](#)). This displacement increases the force required by the motor to achieve finger flexion. The overall dimensions of the two prostheses and the number of actuators used in each design can be seen in [Table 1](#).

In this section we delve deeper into the methodology used to evaluate the PrHand1 and PrHand2 prostheses from a mechanical perspective. In particular, the configurations and sensors used to measure the various variables in subsections 2.2, 2.3 and 2.4 are examined. In addition, subsection 2.5 provides a detailed explanation of the statistical analysis methodology used to classify and compare the results of each test.

2.2 Grasping force

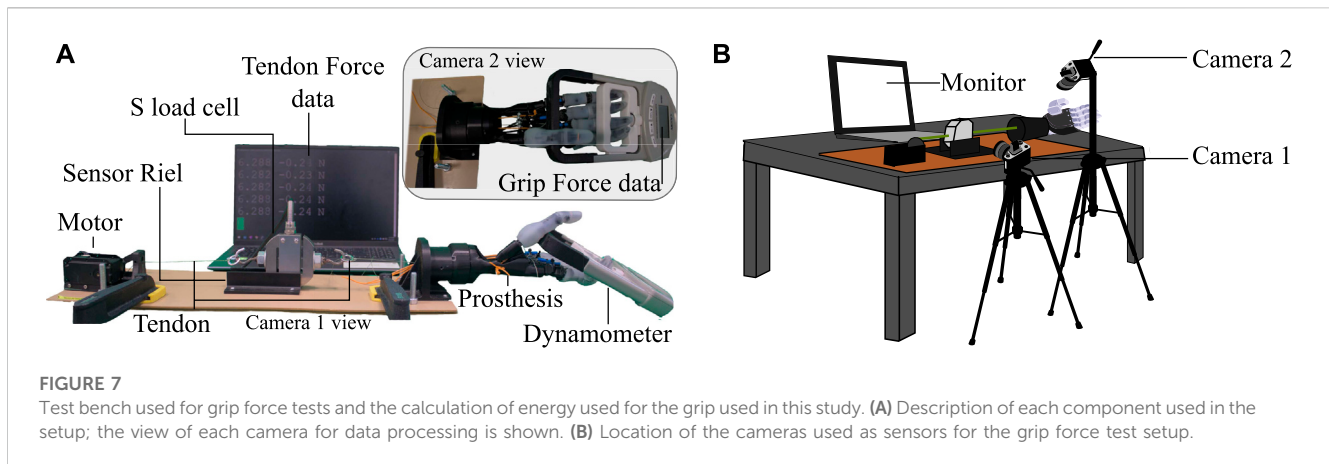
This test aims to find the maximum grip force achieved by hand prostheses driven by tendons and motors. Determining the maximum grip force in the constructed prostheses was based on

applying the maximum force of the motor and measuring the generated grip force in the fingers of the prosthesis with a hand dynamometer (EH101 CAMRY, USA) ([Cuellar et al., 2020](#); [Cuellar et al., 2019](#)). The variables of this experiment are the maximum force generated in the grip and the maximum force generated in the flexion tendon. A standard hand dynamometer (EH101 CAMRY, USA) was used to measure the grip force in kg, and an S-type load cell (50 kg Lexus, China) was used to measure the tension in the flexion tendon of each prosthesis. The acquisition of the load cell data requires an HX711 amplifier (Avia semiconductor, China) which is collected by an Arduino UNO (Arduino, USA). The drive motor must be decoupled from the prosthesis to locate the S-type load cell between the unifying mechanism and the motor, as seen in [Figure 7A](#). The dynamometer is a commercial device that does not allow real-time data collection with a data acquisition device; instead cameras were used as sensors to record the results of the dynamometer during the test. A second camera was used to record the load cell results displayed on a monitor to relate tendon force to grip force overtime. The location of the cameras is seen in [Figure 7B](#).

The experiment starts by placing the dynamometer on the prosthesis in the grip position, as shown in [Figure 7A](#) camera 2 view. In the resting or initial position, the zero in the load cell is established. To determine the maximum grip force generated by the prosthesis, the present study measured grip force using a power grip, as this type of grip is known to produce the highest force in prosthetic hands due to its use of all five fingers in its grip ([Halim et al., 2019](#); [Fransson and WINKEL, 1991](#)). The placement of the dynamometer was carefully determined based on the movement of the prosthetic fingers to ensure optimal force measurement.

Using ROS and the Dynamixel motor position control, the motor position is increased to close the prosthetic fingers that apply force on the dynamometer. The motor position is increased to the maximum range allowed by the motor in normal mode (180°). This last position is maintained for five seconds before a return to the initial position releases the force on the dynamometer. The motor position is controlled by a potentiometer that sends the position value directly to the setpoint of the Dynamixel motor controller. The whole procedure is recorded with audio by two cameras at 60 FPS. The test was performed six times for each prosthesis.

Since the dynamometer data were not accessible for processing with a data acquisition board, the generated force data had to be collected manually from the videos recorded by camera 2. Using the video editing software DaVinci Resolve 17 (Blackmagic Design, USA), the videos from the two cameras were synchronized, using the clip alignment function based on the audio waveform that the software provides. This process was performed for the six experiments of each prosthesis, unifying the results of each prosthesis into a single video. The results were determined by finding the maximum value reached in the dynamometer (camera 2) and averaging the five values of the tendon force observed in the monitor (camera 1). Two vectors of 6 data were obtained for each prosthesis: maximum grip force (GmF) and force applied to achieve maximum grip (TmF). This test indicates which prosthesis generates more grip force and if this value allows a prosthesis to meet ADL requirements.



2.3 Required and dissipated energy

This test experimentally finds the energy required to open and close each prosthesis evaluated in this study. To calculate the energy, the variables involved are the distance traveled by the tendon and the force generated in the flexion tendon of each prosthesis. The required values were measured with the S-type load cell (50 kg Lexus, China) and a camera that simultaneously recorded the monitor and the displacement of the tendon in the experiment. The same electronic setup used in Section 2.2 was employed to collect the load cell data, and the test bench in Figure 7 was likewise used. Camera 1 recorded the movement of the S-type sensor during the test, allowing the displacement required for the energy calculation to be determined.

Each of the tests in this experiment starts from an initial position of an open prosthetic hand. The hand is then closed completely using the maximum range of the Dynamixel motor (180°). When the hand is fully closed, this position is held for five seconds before the prosthesis is returned to its fully open position, and the motor is returned to its initial state (Cuellar et al., 2020; Smit et al., 2015; Cuellar et al., 2019). The experiment was recorded with camera 1 at 60 FPS. This experiment was performed six times for each prosthesis (PrHand1 and PrHand2).

It is possible to calculate the required energy (R_E) and the dissipated energy (D_E) when opening and closing the prosthesis by force generated's integral in the flexion tendon for the displacement of the prosthesis when it is closed, as shown in the Eq. 7. The energy dissipated is calculated by subtracting the energy obtained in the backward movement of the prosthesis (from closed to open) from the energy required, as shown in the Eq. 8.

$$R_E = \int_0^l F(x)dx, \quad (7)$$

where $F(x)$ is the force exerted on the tendons until the hand closes completely and l is the distance traveled by the tendons to the same point.

$$D_E = R_E - \int_0^{l_1} F_1(x)dx, \quad (8)$$

where l_1 is the displacement of the tendon until the hand opens completely and $F_1(x)$ is the force exerted on the tendons to the same point.

The tendon force is displayed in real-time through the setup monitor. The tendon displacement was recorded utilizing the open-source video processing software Kinovea beta 0.9.4 (KINOVEA, France). With this tool, it is possible to take a fixed reference point and measure the tendon displacement based on the displacement of the S-type load cell. Obtaining a sample of tendon displacement and a sample of the force on the tendon (average of the five values seen on the monitor) was performed every n meters of increase in tendon displacement. The calculation of n is independent in each video and is calculated with Eq. 9.

$$n = \frac{TDT}{\#samples}, \quad (9)$$

where TDT is the total distance traveled by the S-Type load cell, and $\#samples$ is the number of samples to take from video.

The n meter increment ensures that the same amount of data is available for each test performed in the experiment. The data obtained allow a curve of tendon force vs. tendon displacement to be plotted. From each of the six tests performed for this experiment, a vector of two variables and n samples [tendon force, tendon displacement] was obtained. Energy R_E and D_E were calculated using the integral function of Matlab software to determine which prosthesis requires and dissipates less energy.

2.4 Traction force

This experiment determines the maximum weight the prosthesis can support in its flexion state (closed hand). The maximum weight supported by the prosthesis in this test is easily converted to the traction force (TrF) using the value of gravity. The cylindrical grip is used to achieve the maximum force. This type of grip distributes the load over the 4 main fingers, making it possible to generalize the maximum force on the prosthesis.

The primary variables involved in this experiment are the weight supported by the prosthesis (kg) and the traction force (N). The secondary variables are the length of time the weight is lifted and the distance the prosthesis has to lift the supported weight. For both prostheses, the same power supply (12V, 5A) and the same motor (Dynamixel MX-106) were used to achieve hand closure. In this

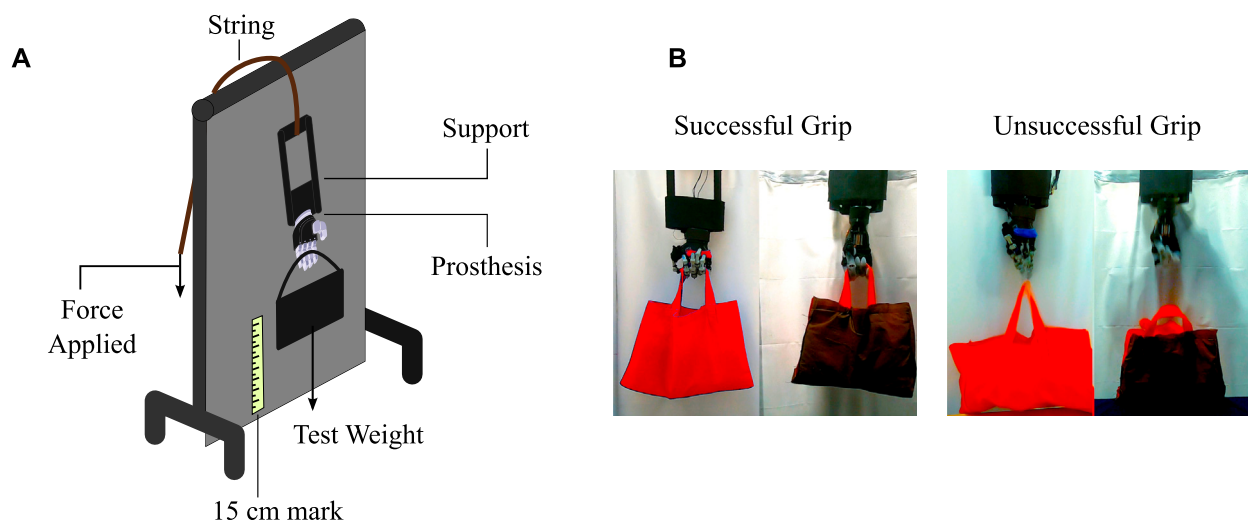


FIGURE 8

The bench needed to perform the experiment to calculate the traction force. (A) The components of the traction test. (B) Definition of successful and unsuccessful grips used in the traction test.

experiment, sensors were not used to obtain the test data. The test bench used to find the traction force of each prosthesis is seen in Figure 8A. The setup shows the vertical location of the prosthesis, the container where the weight is placed, and how to lift the prosthesis using a string attached to a prosthesis's base.

The test consists of placing an initial weight of 1 kg in the container held by the prosthesis, followed by the application of force on the prosthesis's string to lift the weight of the container. The prosthesis must move 15 cm from the reference, then hold this position for 10 s before returning to the reference position (Choi et al., 2017; Mio et al., 2019). The whole procedure is performed at low speeds to avoid accelerations and abrupt forces. If the prosthesis does not suffer any mechanical damage or does not drop the weight of the container, the weight is increased in 1 kg increments and the procedure is repeated. Examples of successful and unsuccessful grips from the test are illustrated in Figure 8B. When the prosthesis fails to perform the entire test, the weight at which it fails is recorded and reduced 2 kg before performing the test again. For each test, three unsuccessful grips are obtained to allow three values for the analysis. A failure analysis is carried out after each unsuccessful grasp.

The failure report is made by quantifying the damage of each prosthesis according to four categories: permanent mechanical damage, permanent aesthetic damage, temporary mechanical damage, and temporary aesthetic damage. In the category of permanent mechanical damage, the number of broken, fractured, or bent elements are counted. The damage must make it impossible for the prosthesis to function, and the element must be replaced by a new one to repair the damage. Permanent aesthetic damage is when some of the external parts of the device break and must be changed for it to function. In this category, such damage relates to fabrics and silicone coatings. In the category of temporary mechanical damage, elements should be quantified that make it impossible for the device to function due to dislocations, sliding between tendons, or any other damage. However, the elements do not need to be exchanged for replacements; only the failed element is assembled, joined, or corrected. Finally, damage to

elements such as silicone coatings and external fabrics which can be solved with adhesive are considered temporary aesthetic damage. The total number of failures will demonstrate which prosthesis suffered the most damage during the traction force test.

2.5 Data analysis

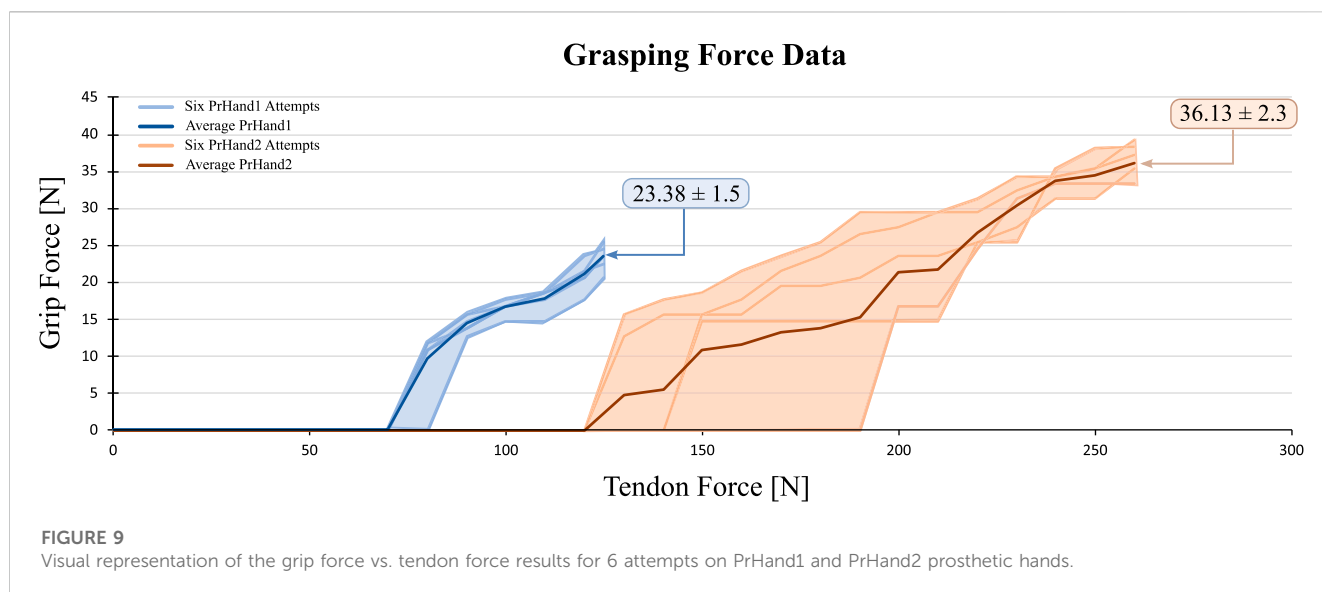
The statistical analysis of the three tests was carried out in two ways: (i) descriptive statistics to organize and visualize the data graphically from the mean and deviation, and (ii) inferential statistics to find the relevant differences between the two prostheses in each test. This analysis compares the mean results of the two prostheses and defines if there are significant differences between them. The inferential tests were the Mann-Whitney test and t-test according to the normality and the variance of the data. The Shapiro-Wilk test verified the normality, and the variance between the data was analyzed according to the f-test. The statistical analysis was implemented in RStudio (Version 1.3.1093, USA).

3 Results

This section describes the results after data processing is performed for each test. For each result set, a descriptive statistics procedure was used to visualize the results, and an inferential statistics procedure was performed to find significant differences between the PrHand1 and PrHand2 prostheses. See [Supplementary Material](#) for a video summary.

3.1 Grasping force

Regarding the grip force test, Figure 9 shows the grip force versus tendon force. these data were taken from the videos of camera



1 and 2. The Figure 9 shows the 6 experiments and the average of the results. It is evident that the PrHand1 prosthesis reaches the maximum GmF value much earlier than the PrHand2 prosthesis. In general, it can be seen that PrHand2 achieves a higher grip force value than PrHand1, but requires more tendon force to achieve it. The maximum values for both prostheses are: 23.38 ± 1.5 N for PrHand1 compared to PrHand2's 36.130 ± 2.3 N of GmF. PrHand1 achieves 127.16 ± 2.8 N and PrHand1 achieves 251.81 ± 15 N of TmF.

The GmF coefficient of variation (CV) of this test is calculated. For PrHand1, a CV of 7.22% is obtained, and for PrHand2, 6.95%. This means that the variation between the results according to the mean in grip force is moderate. Therefore, it is essential to perform a statistical test to ensure significant differences between the mean values to confirm if one of the prostheses generates more grip force than the other. The data's normality, the variance between them, and the number of results for each prosthesis were reviewed to select the inferential statistical test. For the GmF variable, the data follow a normal distribution and homogeneous variance, so a t-test is performed. This test confirmed significant differences in the results of the GmF, with a p -value = $1e^{-6}$, signifying that PrHand2 generates more grasping force than PrHand1.

An inferential statistical test was likewise performed to identify a significant difference in the results of TmF in the two prostheses. The initial results for PrHand1 indicate there is a minor variation between the data (CV = 2.44%), whilst great variation (CV = 6.66%) is shown in PrHand2.

For the TmF of this test, the six results for each prosthesis follow a normal distribution. However, the variance is not homogeneous among the data, so a t-test with Welch's correction was used. The p -value for the TmF in the tendon is = $5e^{-6}$. The result indicates a significant difference between PrHand1 and PrHand2 in terms of TmF, indicating PrHand1 generates less force on the tendon than PrHand2 under the same conditions. For the statistical tests, a reliability value of 0.05 was assumed so that significant differences were present in the two variables. The summary of the grip force test results is presented in Table 2.

TABLE 2 Summary of mechanical test results.

	PrHand1	PrHand2	p -value
TmF [N]	127.16 ± 2.80	251.81 ± 15.00	$5e^{-6}$
GmF [N]	23.38 ± 1.50	36.13 ± 2.30	$1e^{-6}$
R_E [J]	0.76 ± 0.13	1.28 ± 0.13	$4e^{-5}$
D_E [J]	0.21 ± 0.17	0.96 ± 0.12	$2e^{-6}$
TrF [N]	173.31 ± 5.70	78.48 ± 0.00	0.001

3.2 Required and dissipated energy

The results of the energy test were consolidated into two variables. The required energy R_E, as seen in Eq. 7, and the dissipated energy D_E (see Eq. 8). Regarding R_E, PrHand1 obtained a value of 0.76 ± 0.12 J and PrHand2 a value of 1.28 ± 0.13 J. The results of the D_E variable were 0.21 ± 0.17 J and 0.96 ± 0.12 J for PrHand1 and PrHand2, respectively. The results of one of the experiments in our study of energy required and dissipated are shown in Figure 10. The visual representation provided by the figure makes it easy to understand the importance of each variable in the equations used for the calculation.

In both results, there is a considerable difference between the averages of PrHand1 and PrHand2. However, the value of the CV in the results is high. The CV of R_E of PrHand1 is 15%, and for PrHand2 is 10%. The CV of PrHand1 in the D_E was 72%, and for PrHand2 was 13%.

To confirm if the difference between the averages of the results generates significant differences, the Student's t-test was performed on unrelated samples. The data of the two prostheses follow a normal distribution, and the variance is homogeneous. These inferential tests were as follows: p -value of $4e^{-5}$ for the R_E and a p -value of $2e^{-6}$ for the D_E. Assuming test reliability of 5%, it can be stated that there are significant differences between PrHand1 and PrHand2 for the R_E and D_E in opening and closing the hand. The results show that the PrHand1 device requires and dissipates less

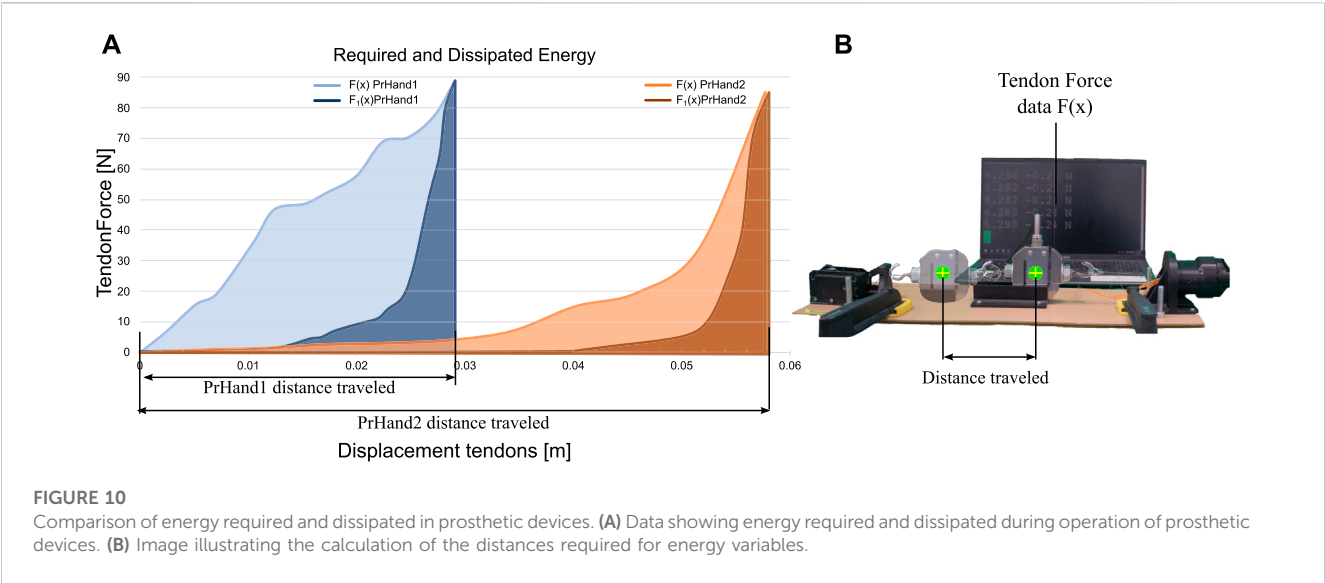


TABLE 3 Mechanical failure report.

	PrHand1	PrHand2
Permanent mechanical damage	0	0
Permanent esthetic damage	4	0
Temporary mechanical damage	1	0
Temporary esthetic damage	0	4
Total	5	4

The result was put in bold to emphasize.

energy, making it more efficient than the PrHand2 device for the same task.

3.3 Traction force

In this experiment, two results were obtained: a numerical result and a condition report of the prostheses after the test. The numerical result is the average maximum traction force (TrF), and the report on the condition of the prosthesis specifies the number of damaged mechanical or aesthetic elements. The numerical results for the TrF variable showed that PrHand1 measured 173.31 ± 5.7 N compared to PrHand2's 74.48 ± 0 N.

Table 3 quantifies the permanent and temporary failures that the prostheses suffered during the test. According to the results, PrHand2 completed the traction test and underwent fewer failures than PrHand1.

Expanding on the values in Table 3, neither prosthesis experienced permanent mechanical damage. In the category of permanent aesthetic damage, the coverings of the four main fingers of PrHand1 wholly detached and therefore received a value of 4. The PrHand1 also suffered a dislocation of the middle finger (Figure 11A), which generated an unsuccessful grip in the test and prevented the prosthesis from functioning. This mechanical dislocation was temporary damage since the repositioning of the finger did not affect the subsequent

functioning. Regarding temporary aesthetic damage, the finger coverings of PrHand2 broken and one of the joint pads detached from the finger, as seen in Figure 11B. This damage could be fixed with adhesive. PrHand1 did not experience any temporary aesthetic damage.

Unsuccessful grasps of PrHand2 always occurred at the same weight (8 Kg), and as the variation of weights in the test was performed every 1 kg, there are no intermediate values in the measurement, generating this zero standard deviation. for that reason, it is not possible to perform traditional inferential statistical tests to compare the means. However, to confirm the difference between the TrF results variable, the one-sample t-test was performed. The result of this statistical test confirms a significant difference in the TrF with a p -value = 0.001.

4 Discussion

This section presents an interpretation of the results, a discussion of how the results may be helpful in the development of prostheses, a comparison with similar studies, and limitations of the study.

4.1 Gripping force

The grip force test results show that PrHand2 have 54.5% stronger grip to PrHand1 since it generates greater GmF, and there is a statistically significant difference. Achieving high values in this variable is positive for a prosthesis because it allows for the manipulation more ADL objects. Mechanically, the GmF variable results can be associated with the complete silicone coating of PrHand2. This coating facilitates the hand dynamometer's grip and reduces the loss of force due to the sliding of the sensor. The unification system is another reason PrHand2 generates more GmF: the elastic tendons of the unification system are shorter and allow less elongation, increasing energy transmission. This allows a better transfer of force from the motor to the finger flexion in the prosthesis.

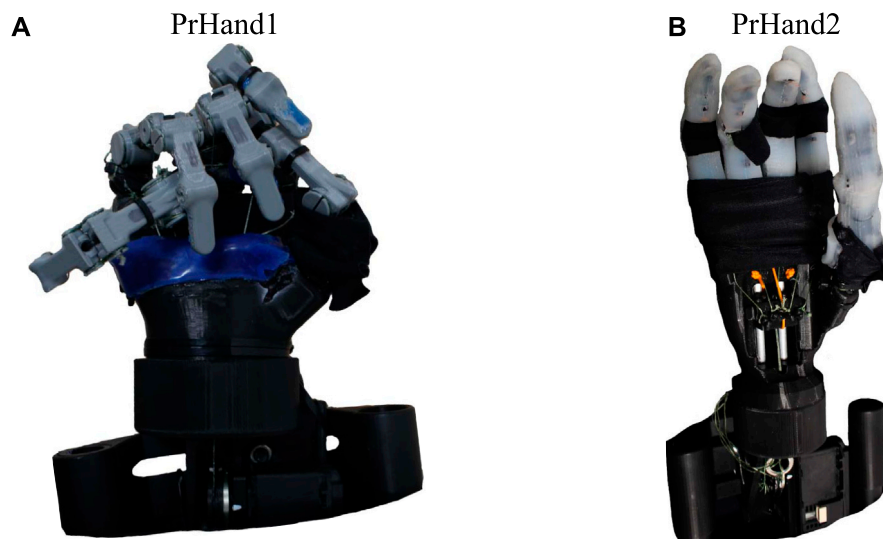


FIGURE 11

Prosthesis condition after performing the maximum supported traction test. **(A)** PrHand1 prosthesis with a dislocated finger (separated from the base). **(B)** PrHand2 prosthesis with aesthetic failures in the finger coverings.

The results of TmF show that 98% more force was applied in the tendon of PrHand 2 than in PrHand1. This result demonstrates that the forces opposing flexion motion in the fingers are generated by the silicone coatings and the internal path of the elastic tendon in the fingers are higher in PrHand2.

It is possible to use the GmF value to estimate if the prosthesis is functional for ADL requirements. It is estimated that values in the range of 10 N of grip strength allow for robust use of a hand prosthesis (Smit and Plettenburg, 2010b). Based on this, PrHand1 and PrHand2 can be used without grip force limitations for ADL since PrHand1 is 133.8% above the 10 N reference and PrHand2 is 261% above it.

Although the reduction in an actuator's price, size, and weight is not a priority in the research prostheses (Tian et al., 2017b), the unification system of PrHand2 is more efficient according to the results of this test. This difference allows a smaller, more accessible motor to be used in developing countries.

It is necessary to compare the performances of PrHand1 and PrHand2 as well as results from the literature. However, the previous research does not use the same actuators or conditions as the experiment performed in this study, so the fairest way to compare the results is to select a force on the tendon as input and compare the grip force only. Grip force values generated at 100 N of applied force on the tendon were found in different studies so that the value is the point of comparison (Cuellar et al., 2020; Moreo, 2016; Cuellar et al., 2019; Smit et al., 2015; Smit, 2020). As the tendon force results of this study are not 100 N, a review of the videos that collected the data from the experiment was necessary. The review found that PrHand1 exerts 16.5 N on the grip at 100 N input, while PrHand2 did not generate a force on the dynamometer at 100 N input. PrHand1 generates similar values to the prostheses in the current literature. For example, the rigid prosthesis constructed by Cuellar et al. (Cuellar et al., 2020) generated 16.84 N of grip force, which is not significantly different from the value generated by PrHand1. Two prostheses from the literature

generate 15 N in the grip (Smit et al., 2015; Smit, 2020), and there is a statistically significant difference between this value and the 16.5 N of PrHand1. This difference indicates that PrHand1 generates more force than the rigid prostheses constructed by Smit et al. (Smit et al., 2015; Smit, 2020), as well as generating 175.23% more force than the 2019 prosthesis 2019 (Cuellar et al., 2019), which generates 6 N of grip force. The prosthesis built by Moreo et al. (Moreo, 2016) achieved values of almost 20 N in the grip force test with 100 N of tendon input. All statistical tests performed to compare data from the literature studies were performed with the one-sample t-test. These results show that PrHand1 generates competitive values using new technologies. The summary of the literature comparison is presented in Table 4.

Prosthetic hand development aims to reduce the force required on tendons to increase efficiency. One way to achieve this is by optimizing the tension in the extension tendon. This can lead to a reduction in the force required in the flexion tendons, and ultimately, to achieving the lowest possible tension in the extension tendon while allowing the fingers to return to their initial position. In this particular study, the optimization process was not implemented due to the lack of instrumentation to measure pre-tension in each tendon. However, the study provides valuable insights into the potential benefits of optimizing tension in the extension tendon. It is worth noting that optimizing the tension in the extension tendon would not only reduce the total force required in the tendons, but would also increase the force of the grip. This is because the prosthesis would be able to use its resources more efficiently, resulting in a stronger grip for the user. Therefore, integrating a sensor to measure pre-tension accurately would be necessary to adjust the tension in the extension tendon, making the prosthetic hand more functional and effective for users. Specifically, the optimization process would focus on finding the pre-tension in the extension tendon that generates the highest grip force for each finger and allows the finger to return to its initial position. This

TABLE 4 Mechanical compilation of literature prosthesis results.

	GmF [N]	R_E [J]	D_E [J]	TrF [N]
Cuellar et al. (2020)	16.84	0.38	0.32	-
Smit et al. (2015)	15.00	0.88	0.64	-
Smit (2020)	15.00	-	-	-
Moreo (2016)	20	-	-	-
Cuellar et al. (2019)	6	0.10	0.05	-
Choi et al. (2017)	-	-	-	226.22
Mio et al. (2019)	-	-	-	112.40
PrHand1	16.5	0.76	0.21	173.31
PrHand2	0	1.28	0.96	74.48

could be done by iteratively adjusting the pre-tension until the desired results are achieved. Alternatively, a differential model of the tendon and force or a finite state simulation could be used to find the optimum pre-tension (Buccino et al. 2022).

4.2 Required and dissipated energy

The energy test results calculate which device requires the least amount of energy to operate and which dissipates the least energy, indicating the most energy-efficient device. The percentage of energy dissipated is derived from losses due to friction, heat, or deformations in the device elements. The PrHand1 prosthesis requires 39.4% less energy than the PrHand2 prosthesis, indicating significant mechanical differences in the devices. As the test was performed with the same power system (both mechanical and electrical), the variation in the results are caused by the design differences presented in Section 2, particularly the partial silicone coating of the fingers and the frictionless unification system of the PrHand1 prosthesis. These differences contribute to reducing the force of the hand closure by reducing the required energy of the system. In contrast, these same systems in the PrHand2 prosthesis make the hand closure movement more difficult. The complete covering of the fingers, the extension tendon that generates a force in opposition to the movement, and the rail-based unification system increase the required energy in this prosthesis.

PrHand1 dissipates only 27.6% of the energy it requires, while PrHand2 dissipates 75% of the required energy, which is inefficient. The energy dissipated is evidence of how easily the hand returns to its initial position, which directly links to the unification mechanism, the finger coating, and the extension tendons in each prosthesis. Although the extension tendons and silicone coating of PrHand2 help in the finger return, the friction generated in the rods of the sliding unification mechanism is high; as a result, the energy dissipation is due to the unification mechanism and the friction generated from it. An improvement for future iterations of the device should reduce the friction in the unification mechanism and reduce the opposing force of the extension tendon in the fingers.

The results of this test are relevant for commercial prostheses needing to reduce power consumption and energy waste whilst

employing smaller batteries and increasing the time between recharges. Although both devices can be used in assistive applications, PrHand2 would have fewer operating hours than PrHand1 with the same battery.

PrHand2 requires 45.5% more energy than the most energy-intensive prosthesis of those reviewed in the literature (Smit et al., 2015), whereas PrHand1 is in alignment with other research. For example, there are no significant differences between the values of required energy (0.88 J) presented by Smit et al. Smit et al. (2015) and PrHand1. However, PrHand1 requires 104% and 676% more energy than the prostheses of Cuellar et al. Cuellar et al. (2020) and Cuellar and Smit et al. Cuellar et al. (2019), respectively.

Regarding dissipated energy, PrHand2 has higher values compared to the prostheses reviewed in the literature. It dissipates 50% more energy than (Smit et al. 2015). In contrast, PrHand1 only has significant differences with the prosthesis by Smit et al. (Smit et al. 2015), and the energy dissipated by PrHand1 is 67% less. There are no significant differences in the energy dissipated compared to the other prostheses reviewed (Table 4).

PrHand1 requires and dissipates energy values similar to the values of the prostheses currently considered state of the art. Compared to the literature, the novel compliant mechanism used in both prostheses requires more energy to actuate than traditional systems. The energy reduction depends mainly on the friction in the unification mechanism and the opposing force generated by the silicone coating and the extension tendons in each finger. Improvements for future iterations of the prosthesis will reduce the friction in the unification mechanism and reduce the opposing force of the extension tendon in the fingers.

4.3 Traction force

The final experiment identified that the PrHand1 prosthesis achieves 132.7% more traction force than the PrHand2 prosthesis. The difference is due to the energy dissipation. The cause of PrHand2's unsuccessful grips in the traction test was due to the motor overheating and not to mechanical failures as expected. In the PrHand1 prosthesis, the unsuccessful grips were generated by dislocation of the middle finger and an overstretched tendon, indicating the prosthesis does not distribute the loads proportionally to each finger. This does not happen in the mechanism of the PrHand2 prosthesis since it allows the tensioning of each tendon and enables the adjustment of each finger if necessary. However, as the energy required to close this prosthesis is high, little power remains to lift the weight in the test, leading to the motor overheating at the same weight in each trial.

Based on the failure report in Table 3, PrHand1 finished the test with more aesthetic damage than PrHand2, but the mechanisms of PrHand2 were not pushed to the extreme due to the excessive power consumption of the motor. Of the categories evaluated in the report, the only permanent failure suffered by PrHand1 was the detachment of the silicone patch on the fingertips. As this is an easy fix, it is not considered serious damage. The finger dislocation that was the primary cause of PrHand1's unsuccessful grip is an easily correctable failure that did not damage the device.

This test is typically destructive to rigid prostheses since high weight-bearing values cause permanent damage to axes or

elements such as gears and pinions. However, using new design techniques such as novel compliant joints and elastic elements allows testing without severe damage, which demonstrates the advantages of these technologies for applications in commercial systems.

For example, the PrHand1 frictionless unifying mechanism is desirable in future iterations because this mechanism reduces the required energy needed to control the system. From the PrHand2 design, the finger coating allows a better grip and thus a higher grasping force, which is an essential element for future versions.

5 Conclusion and future work

Two versions of underactuated hand prostheses were constructed and mechanically evaluated to develop new technologies based on soft robotics and compliant joints. This paper presents the mechanical evaluation of the grip force, required energy/dissipated energy, and traction force. Although both versions of the PrHand prosthesis generate sufficient force for the user to perform typical ADLs, PrHand2 can generate a higher grip force with the same actuation system. The energy test shows that PrHand1 has a more efficient system because it requires less energy to close the hand, and the energy dissipation is less than 30%. In contrast, PrHand2 requires more energy and dissipates more than 70%. The energy consumption of the PrHand2 prosthesis is associated with the full silicone coating on the fingers and the sliding mechanism in the unification system. Therefore, it is necessary to redesign the unification system to improve this system. Finally, the traction force supported by PrHand1 is greater than that supported by PrHand2. This is due to PrHand2's motor overheating and is also associated with the motor's prosthesis consumption.

This study illustrates that both prosthesis designs built with soft robotics techniques and compliant mechanisms meet the mechanical requirements necessary to carry out ADL requirements. In addition, it suggests that these technologies are robust and efficient for this type of prosthesis application as neither design suffered a permanent failure. Based on this research, a third version is proposed to improve the performance by combining the best characteristics of each design. Our forthcoming study involving prostheses will focus on evaluating their functionality and various types of grips. To accomplish this, we will replicate the AHAP protocol (Llop-Harillo et al., 2019) and utilize 28 objects commonly used in daily living activities to assess the prostheses' performance. Additionally, we plan to design an object capable of measuring grip force at various points along the finger to obtain more precise and real-time data for analysis. Based on the results obtained from these evaluations, we will subsequently

assess a version with enhanced mechanical and functional performance with amputee patients.

Data availability statement

The original contributions presented in the study are included in the article/Supplementary Material, further inquiries can be directed to the corresponding author.

Author contributions

OR, LA, MAM, HW, MM, and CC contributed to the conception and design of the study. OR and LA organized the database and performed the statistical analysis. OR and LA wrote the first draft of the manuscript. All authors contributed to the article and approved the submitted version.

Funding

This work was supported by the Royal Academy of Engineering–Industry–Academia Partnership Programme Colombia/UK (IAPP18-19\264), PrExHand Project. This work has been partially funded by the Engineering and Physical Sciences Research Council (Grant Number: EP/V01062X\1).

Conflict of interest

The authors declare that the research was conducted in the absence of any commercial or financial relationships that could be construed as a potential conflict of interest.

Publisher's note

All claims expressed in this article are solely those of the authors and do not necessarily represent those of their affiliated organizations, or those of the publisher, the editors and the reviewers. Any product that may be evaluated in this article, or claim that may be made by its manufacturer, is not guaranteed or endorsed by the publisher.

Supplementary material

The Supplementary Material for this article can be found online at: <https://www.frontiersin.org/articles/10.3389/fbioe.2023.985901/full#supplementary-material>

References

- Borg, J., and Östergren, P.-O. (2015). Users' perspectives on the provision of assistive technologies in Bangladesh: awareness, providers, costs and barriers. *Disabil. Rehabilitation assistive Technol.* 10, 301–308. doi:10.3109/17483107.2014.974221
- Buccino, F., Bunt, A., Lazell, A., and Vergani, L. M. (2022). Mechanical design optimization of prosthetic hand's fingers: novel solutions towards weight reduction. *Materials* 15, 2456. doi:10.3390/ma15072456

- Calli, B., Walsman, A., Singh, A., Srinivasa, S., Abbeel, P., and Dollar, A. M. (2015). Benchmarking in manipulation research: using the yale-cmu-berkeley object and model set. *IEEE Robotics Automation Mag.* 22, 36–52. doi:10.1109/mra.2015.2448951
- Choi, K. Y., Akhtar, A., and Bretl, T. (2017). A compliant four-bar linkage mechanism that makes the fingers of a prosthetic hand more impact resistant. *Proc. - IEEE Int. Conf. Robotics Automation* 6694, 6694–6699. doi:10.1109/ICRA.2017.7989791
- Cordella, F., Ciano, A. L., Sacchetti, R., Davalli, A., Cutti, A. G., Guglielmelli, E., et al. (2016). Literature review on needs of upper limb prosthesis users. *Front. Neurosci.* 10, 209. doi:10.3389/fnins.2016.00209
- Cuellar, J. S., Plettenburg, D. H., Azadpoor, A., Breedveld, P., and Smit, G. (2020). Design of a 3D-printed hand prosthesis featuring articulated bio-inspired fingers. *Proc. Institution Mech. Eng. Part H* 235, 336–345. doi:10.1177/0954411920980889
- Cuellar, J. S., Smit, G., Breedveld, P., Zadpoor, A. A., and Plettenburg, D. (2019). Functional evaluation of a non-assembly 3d-printed hand prosthesis. *Proc. Inst. Mech. Eng. H* 233, 1122–1131. doi:10.1177/0954411919874523
- Culha, U., Hughes, J., Rosendo, A., Giardina, F., and Iida, F. (2017). Design principles for soft-rigid hybrid manipulators. in *Soft robotics: trends, applications and challenges* (Springer), 87–94.
- Daniels, C. A., Olsen, C. H., Scher, A. I., McKay, P. L., and Niebuhr, D. W. (2020). Severe upper limb injuries in us military personnel: incidence, risk factor and outcomes. *Mil. Med.* 185, e146–e153. doi:10.1093/milmed/usz139
- Deimel, R., and Brock, O. (2016). A novel type of compliant and underactuated robotic hand for dexterous grasping. *Int. J. Robotics Res.* 35, 161–185. doi:10.1177/0278364915592961
- del Carmen Malbrán, M. (2011). World report on disability. *J. Policy Pract. Intellect. Disabil.* 4, 290. doi:10.1111/j.1741-1130.2011.00320.x
- Fransson, C., and Winkel, J. (1991). Hand strength: the influence of grip span and grip type. *Ergonomics* 34, 881–892. doi:10.1080/00140139108964832
- Fras, J., and Althoefer, K. (2018). “Soft biomimetic prosthetic hand: design, manufacturing and preliminary examination,” in 2018 IEEE/RSJ International Conference on Intelligent Robots and Systems (IROS) (IEEE), 1–6.
- Godfrey, S. B., Zhao, K. D., Theuer, A., Catalano, M. G., Bianchi, M., Breighner, R., et al. (2018). The soft-hand pro: functional evaluation of a novel, flexible, and robust myoelectric prosthesis. *PLoS one* 13, e0205653. doi:10.1371/journal.pone.0205653
- Halim, I., Umar, R. Z. R., Mohamed, M. S. S., Ahmad, N., Padmanathan, V., and Saptari, A. (2019). The influence of hand tool design on hand grip strength: a review. *Int. J. Integr. Eng.* 11, 53–69. doi:10.30880/ijie.2019.11.06.007
- Hill, S., and Canfield, S. (2016). “An assessment of fused deposition modeling for the manufacturing of flexural pivots in an anthropomorphic robotic hand design,” in International Design Engineering Technical Conferences and Computers and Information in Engineering Conference (American Society of Mechanical Engineers), 50169, V05BT07A066.
- Huang, M.-B., and Huang, H.-P. (2019). Innovative human-like dual robotic hand mechatronic design and its chess-playing experiment. *IEEE Access* 7, 7872–7888. doi:10.1109/access.2019.2891007
- Huaroto, J. J., Suárez, E., and Vela, E. A. (2020). Wearable mechatronic devices for upper-limb amputees. in *Control theory in biomedical engineering* (Elsevier), 205–234.
- Jelačić, Z., Dedić, R., and Dindo, H. (2020). Chapter 1 - the challenges of prosthetic design and control. in *Active above-knee prosthesis*. Editors Z. Jelačić, R. Dedić, and H. Dindo (Academic Press), 1–17. doi:10.1016/B978-0-12-818683-1.00001-9
- Jing, X., Yong, X., Li, G., Jiang, J., and Yokoi, H. (2019). “Design of a prosthetic hand for multiple hand motions,” in 2019 IEEE International Conference on Robotics and Biomimetics (ROBIO) (IEEE), 2814–2819.
- Laschi, C., Mazzolai, B., and Cianchetti, M. (2016). Soft robotics: technologies and systems pushing the boundaries of robot abilities. *Sci. robotics* 1, eaah3690. doi:10.1126/scirobotics.aah3690
- Li, Y., Wei, Y., Yang, Y., and Chen, Y. (2019). A novel versatile robotic palm inspired by human hand. *Eng. Res. Express* 1, 015008. doi:10.1088/2631-8695/ab2f69
- Liu, C.-H., Chen, T.-L., Chiu, C.-H., Hsu, M.-C., Chen, Y., Pai, T.-Y., et al. (2018). Optimal design of a soft robotic gripper for grasping unknown objects. *Soft Robot.* 5, 452–465. doi:10.1089/soro.2017.0121
- Liu, H., Xu, K., Siciliano, B., and Ficiucello, F. (2019). “The mero hand: a mechanically robust anthropomorphic prosthetic hand using novel compliant rolling contact joint,” in 2019 IEEE/ASME International Conference on Advanced Intelligent Mechatronics (AIM) (IEEE), 126–132.
- Llop-Harillo, I., Pérez-González, A., Starke, J., and Asfour, T. (2019). The anthropomorphic hand assessment protocol (ahap). *Robotics Aut. Syst.* 121, 103259. doi:10.1016/j.robot.2019.103259
- Massa, B., Roccella, S., Carrozza, M. C., and Dario, P. (2002). “Design and development of an underactuated prosthetic hand,” in Proceedings 2002 IEEE international conference on robotics and automation (Cat. No. 02CH37292) (IEEE), 4, 3374–3379.
- Mio, R., Sanchez, M., Valverde, Q., Lara, J., and Rumiche, F. (2019). Mechanical testing methods for body-powered upper-limb prostheses: a case study. *Adv. Sci. Technol. Eng. Syst.* 4, 61–68. doi:10.25046/aj040508
- Moreo, M. (2016). *Parametric design of a 3d printable hand prosthesis for children in developing countries*. TU Delft Research Repository.
- Mottard, A., Laliberté, T., and Gosselin, C. (2017). Underactuated tendon-driven robotic/prosthetic hands: design issues. *Robotics sci. Syst.* 12.
- Mutlu, R., Alici, G., het Panhuis, M., and Spinks, G. (2015). Effect of flexure hinge type on a 3d printed fully compliant prosthetic finger. In 2015 IEEE International Conference on Advanced Intelligent Mechatronics (AIM) (IEEE), 790–795.
- Niola, V., Rossi, C., Savino, S., and Troncone, S. (2014). “An underactuated mechanical hand: a first prototype,” in 2014 23rd International Conference on Robotics in Alpe-Adria-Danube Region (RAAD) (IEEE), 1–6.
- Owen, M., Au, C., and Fowke, A. (2018). Development of a dexterous prosthetic hand. *J. Comput. Inf. Sci. Eng.* 18. doi:10.1115/1.4038291
- Polygerinos, P., Correll, N., Morin, S. A., Mosadegh, B., Onal, C. D., Petersen, K., et al. (2017). Soft robotics: review of fluid-driven intrinsically soft devices; manufacturing, sensing, control, and applications in human-robot interaction. *Adv. Eng. Mater.* 19, 1700016. doi:10.1002/adem.201700016
- Robinson, H., MacDonald, B., and Broadbent, E. (2014). The role of healthcare robots for older people at home: a review. *Int. J. Soc. Robotics* 6, 575–591. doi:10.1007/s12369-014-0242-2
- Salviati, G. (2018). Replicating human hand synergies onto robotic hands: a review on software and hardware strategies. *Front. neurobotics* 12, 27. doi:10.3389/fnbot.2018.00027
- Shintake, J., Caccuciolo, V., Floreano, D., and Shea, H. (2018). Soft robotic grippers. *Adv. Mater.* 30, 1707035. doi:10.1002/adma.201707035
- SISPRO (2020). *ASIS disability indicators*.
- Smit, G. (2020). Mechanical evaluation of the “Hüfner hand” prosthesis. *Prosthetics Orthot. Int.* 45, 54–61. doi:10.1177/0309364620952900
- Smit, G., and Plettenburg, D. (2010a). Efficiency of voluntary closing hand and hook prostheses. *Prosthetics Orthot. Int.* 34, 411–427. doi:10.3109/03093646.2010.486390
- Smit, G., and Plettenburg, D. H. (2010b). Efficiency of voluntary closing hand and hook prostheses. *Prosthetics Orthot. Int.* 34, 411–427. doi:10.3109/03093646.2010.486390
- Smit, G., Plettenburg, D. H., and Helm, F. C. T. V. D. (2015). The lightweight delft cylinder hand: first multi-articulating hand that meets the basic user requirements. *IEEE Transac Neural Syst. Rehabil. Eng.* 23, 431–440. doi:10.1109/TNSRE.2014.2342158
- Ten Kate, J., Smit, G., and Breedveld, P. (2017). 3d-printed upper limb prostheses: a review. *Disabil. Rehabilitation assistive Technol.* 12, 300–314. doi:10.1080/17483107.2016.1253117
- Tian, L., Magnenat Thalmann, N., Thalmann, D., and Zheng, J. (2017a). The making of a 3d-printed, cable-driven, single-model, lightweight humanoid robotic hand. *Front. Robotics AI* 4, 65. doi:10.3389/frobt.2017.00065
- Tian, M., Xiao, Y., Wang, X., Chen, J., and Zhao, W. (2017b). Design and experimental research of pneumatic soft humanoid robot hand. in *Robot intelligence technology and applications 4* (Springer), 469–478.
- Vulliez, P., Gazeau, J.-P., Laguillaumie, P., Mnyusiwalla, H., and Seguin, P. (2018). Focus on the mechatronics design of a new dexterous robotic hand for inside hand manipulation. *Robotica* 36, 1206–1224. doi:10.1017/s0263574718000346
- Wahit, M. A. A., Ahmad, S. A., Marhaban, M. H., Wada, C., and Izhar, L. I. (2020). 3d printed robot hand structure using four-bar linkage mechanism for prosthetic application. *Sensors (Basel, Switz.)* 20, 4174. doi:10.3390/s20154174
- Xu, Z., Bai, Y., Ni, R., Yang, N., Sun, Y., and Qi, P. (2018). “Anthropomorphic soft pneumatic fingers towards full dexterity of human hand,” in 2018 IEEE-RAS 18th International Conference on Humanoid Robots (Humanoids) (IEEE), 381–386.
- Xu, Z., and Todorov, E. (2016). “Design of a highly biomimetic anthropomorphic robotic hand towards artificial limb regeneration,” in 2016 IEEE International Conference on Robotics and Automation (ICRA) (IEEE), 3485–3492.
- Zappatore, G. A., Reina, G., and Messina, A. (2017). Analysis of a highly underactuated robotic hand. *Int. J. Mech. Control* 18, 17–24.
- Ziegler-Graham, K., MacKenzie, E. J., Ephraim, P. L., Trivison, T. G., and Brookmeyer, R. (2008). Estimating the prevalence of limb loss in the United States: 2005 to 2050. *Archives Phys. Med. rehabilitation* 89, 422–429. doi:10.1016/j.apmr.2007.11.005

Frontiers in Bioengineering and Biotechnology

Accelerates the development of therapies,
devices, and technologies to improve our lives

A multidisciplinary journal that accelerates the
development of biological therapies, devices,
processes and technologies to improve our lives
by bridging the gap between discoveries and their
application.

Discover the latest Research Topics

[See more →](#)

Frontiers

Avenue du Tribunal-Fédéral 34
1005 Lausanne, Switzerland
frontiersin.org

Contact us

+41 (0)21 510 17 00
frontiersin.org/about/contact



Frontiers in
Bioengineering
and Biotechnology

